Edited by
Agata Godula-Jopek

Hydrogen Production

by Electrolysis

Related Titles

Stolten, D., Emonts, B. (eds.)

Hydrogen Science and Engineering
Materials, Processes, Systems and Technology

2015
Print ISBN: 978-3-527-33238-0

Oldham, K.K., Myland, J.J., Bond, A.A.

Electrochemical Science and Technology – Fundamentals and Applications

2012
Print ISBN: 978-0-470-71085-2

Zhang, J., Zhang, L., Liu, H., Sun, A., Liu, R. (eds.)

Electrochemical Technologies for Energy Storage and Conversion

2012
Print ISBN: 978-3-527-32869-7

Stolten, D., Emonts, B. (eds.)

Fuel Cell Science and Engineering
Materials, Processes, Systems and Technology

2012
Print ISBN: 978-3-527-33012-6

Godula-Jopek, A., Jehle, W., Wellnitz, J

Hydrogen Storage Technologies
New Materials, Transport and Infrastructure

2012
Print ISBN: 978-3-527-32683-9

Gileadi, E.

Physical Electrochemistry
Fundamentals, Techniques and Applications

2011
Print ISBN: 978-3-527-31970-1

Daniel, C., Besenhard, J.O. (eds.)

Handbook of Battery Materials
2nd Edition

2011
Print ISBN: 978-3-527-32695-2

Aifantis, K.E., Hackney, S.A., Kumar, R.V. (eds.)

High Energy Density Lithium Batteries
Materials, Engineering, Applications

2010
Print ISBN: 978-3-527-32407-1

Stolten, D. (ed.)

Hydrogen and Fuel Cells
Fundamentals, Technologies and Applications

2010
Print ISBN: 978-3-527-32711-9

Edited by Agata Godula-Jopek

Hydrogen Production

by Electrolysis

With a Foreword by Detlef Stolten

WILEY-VCH
Verlag GmbH & Co. KGaA

Editor

Dr.-Habil. Ing. Agata Godula-Jopek FRSC
Airbus Group Innovations
Willy Messerschmitt Str. 1
81663 Munich
Germany

and

Polish Academy of Sciences
Institute of Chemical Engineering
ul. Baltycka 5
44100 Gliwice
Poland

Cover:

The picture shows a modern PEM water electrolyzer with ancillary equipment in a container (by permission from CETH2).

All books published by Wiley-VCH are carefully produced. Nevertheless, authors, editors, and publisher do not warrant the information contained in these books, including this book, to be free of errors. Readers are advised to keep in mind that statements, data, illustrations, procedural details or other items may inadvertently be inaccurate.

Library of Congress Card No.: applied for

British Library Cataloguing-in-Publication Data
A catalogue record for this book is available from the British Library.

Bibliographic information published by the Deutsche Nationalbibliothek
The Deutsche Nationalbibliothek lists this publication in the Deutsche Nationalbibliografie; detailed bibliographic data are available on the Internet at <http://dnb.d-nb.de>.

© 2015 Wiley-VCH Verlag GmbH & Co. KGaA, Boschstr. 12, 69469 Weinheim, Germany

All rights reserved (including those of translation into other languages). No part of this book may be reproduced in any form – by photoprinting, microfilm, or any other means – nor transmitted or translated into a machine language without written permission from the publishers. Registered names, trademarks, etc. used in this book, even when not specifically marked as such, are not to be considered unprotected by law.

Print ISBN: 978-3-527-33342-4
ePDF ISBN: 978-3-527-67653-8
ePub ISBN: 978-3-527-67652-1
Mobi ISBN: 978-3-527-67651-4
oBook ISBN: 978-3-527-67650-7

Typesetting Laserwords Private Limited, Chennai, India
Printing and Binding Markono Print Media Pte Ltd., Singapore

Printed on acid-free paper

Contents

Foreword *XIII*
Preface *XV*
List of Contributors *XIX*

1 Introduction *1*
Agata Godula-Jopek
1.1 Overview on Different Hydrogen Production Means from a Technical Point of View *10*
1.1.1 Reforming *13*
1.1.2 Electrolysis *14*
1.1.3 Gasification *16*
1.1.4 Biomass and Biomass-Derived Fuels Conversion *16*
1.1.5 Water Splitting *18*
1.2 Summary Including Hydrogen Production Cost Overview *21*
References *28*

2 Fundamentals of Water Electrolysis *33*
Pierre Millet
2.1 Thermodynamics of the Water Splitting Reaction *33*
2.1.1 Thermodynamic Functions of State *33*
2.1.2 Selection Criteria for Operating Temperature *35*
2.1.3 Electrochemical Water Splitting *36*
2.1.4 pH Dependence of Water Dissociation Voltage *37*
2.1.5 Temperature Dependence of Water Dissociation Voltage *39*
2.1.6 Pressure Dependence of Water Dissociation Voltage *41*
2.1.6.1 General Pressure Dependence *42*
2.1.6.2 Detailed Pressure Dependence *44*
2.2 Efficiency of Electrochemical Water Splitting *46*
2.2.1 Water Splitting Cells: General Characteristics *46*
2.2.2 Main Sources of Energy Dissipation in Electrochemical Cells *48*
2.2.3 Energy Efficiency of Water Electrolysis Cells *50*
2.2.4 Faradaic Efficiency of Water Electrolysis Cells *51*
2.3 Kinetics of the Water Splitting Reaction *52*

2.3.1 Half-Cell Reaction Mechanism in Acidic Media *52*
2.3.1.1 HER *52*
2.3.1.2 OER *53*
2.3.1.3 Kinetics *54*
2.3.2 Half-Cell Reaction Mechanism in Alkaline Media *56*
2.3.3 Role of Operating Temperature on the Kinetics *56*
2.3.4 Role of Operating Pressure on the Kinetics *58*
2.4 Conclusions *59*
Nomenclature *59*
Greek symbols *60*
Subscripts or superscripts *60*
Acronyms *60*
References *61*

3 PEM Water Electrolysis *63*
Pierre Millet
3.1 Introduction, Historical Background *63*
3.2 Concept of Solid Polymer Electrolyte Cell *65*
3.3 Description of Unit PEM Cells *67*
3.3.1 General Description *67*
3.3.2 Membrane Electrode Assemblies *68*
3.3.2.1 Electrocatalysts *68*
3.3.2.2 Coating Processes *69*
3.3.2.3 Electrocatalytic Layers *71*
3.3.3 Current–Gas Distributors *72*
3.3.4 Spacers *74*
3.3.5 Bipolar Plates *74*
3.4 Electrochemical Performances of Unit PEM Cells *76*
3.4.1 Polarization Curves *76*
3.4.2 Characterization of Individual Electrodes *78*
3.4.3 Charge Densities and Electrode Roughness *79*
3.4.3.1 Half-Cell Characterization *80*
3.4.3.2 Full-Cell Characterization *82*
3.4.4 EIS Characterization *84*
3.4.5 Pressurized Water Electrolysis and Cross-Permeation Phenomena *87*
3.4.5.1 Origins of Cross-Permeation Phenomena *87*
3.4.5.2 Hydrogen and Oxygen Solubility in SPEs *88*
3.4.5.3 Nafion Permeability to Hydrogen and Oxygen *89*
3.4.5.4 A Simple Model to Account for Gas Cross-Permeation *90*
3.4.6 Durability Issues: Degradation Mechanisms and Mitigation Strategies *92*
3.5 Cell Stacking *94*
3.5.1 Different Stack Configurations *94*
3.5.2 Design of PEM Water Electrolysis Stack *94*

3.5.3 Stack Performances *96*
3.5.4 Diagnosis Tools and Maintenance *97*
3.6 Balance of Plant *100*
3.6.1 General Description *100*
3.6.2 Cost Analysis *100*
3.7 Main Suppliers, Commercial Developments and Applications *102*
3.7.1 Commercial Status *102*
3.7.2 Markets and Applications *104*
3.8 Limitations, Challenges and Perspectives *105*
3.8.1 Replacement of Platinum with Non-Noble Electrocatalysts *107*
3.8.2 Replacement of Iridium with Non-Noble Electrocatalysts *108*
3.8.3 New Polymeric Proton Conductors for Operation at More Elevated Temperatures *109*
3.8.4 Operation at Elevated Current Densities *110*
3.8.5 Operation at Elevated Pressures *110*
3.9 Conclusions *111*
Nomenclature *113*
Greek symbols *113*
Subscripts or superscripts *114*
Acronyms *114*
References *114*

4 Alkaline Water Electrolysis *117*
Nicolas Guillet and Pierre Millet
4.1 Introduction and Historical Background *117*
4.2 Description of Unit Electrolysis Cells *121*
4.2.1 General Description *121*
4.2.2 Electrolyte *123*
4.2.3 Electrodes and Catalysts *124*
4.2.4 Diaphragm/Separator *128*
4.2.4.1 Zero-Gap Assembly *131*
4.2.4.2 Anionic Membranes *132*
4.3 Electrochemical Performances of Alkaline Water Electrolysers *137*
4.3.1 Polarization Curves *137*
4.3.2 Comparison of Electrolyser Performances *138*
4.3.3 Operation at Elevated Temperatures *139*
4.3.3.1 Thermodynamics *140*
4.3.3.2 Kinetics *142*
4.3.3.3 Electrolyte Conductivity *142*
4.3.4 Operation at Elevated Pressures *142*
4.3.4.1 Hydrogen Compression *143*
4.3.4.2 Pressurized Electrolysers *144*
4.3.4.3 Advantages and Disadvantages *144*
4.3.4.4 Best Solution? *146*
4.4 Main Suppliers, Commercial Developments and Applications *147*

4.4.1 Markets for Electrolysers *147*
4.4.1.1 Small-Scale Electrolyser Market (Less than 1 $Nm^3H_2\,h^{-1}$) *147*
4.4.1.2 Medium-Scale Electrolysers Market (1 – 10 $Nm^3H_2\,h^{-1}$) *147*
4.4.1.3 Large Scale Electrolysers (10 to More than 100 $Nm^3H_2 \cdot h^{-1}$) *148*
4.4.2 Commercially Available Electrolyser Designs *150*
4.4.2.1 Oerlikon-Type Electrolyser *150*
4.4.2.2 Norsk Hydro-Type Electrolyser *154*
4.4.2.3 Zdansky/Lonza-Type Electrolyser *155*
4.4.3 Advanced Designs *156*
4.4.3.1 Metal Foam as Electrodes *156*
4.4.3.2 Gas Diffusion Electrodes *159*
4.4.3.3 Very High-Pressure Electrolysers *160*
4.5 Conclusions *161*
Nomenclature *162*
Greek Symbols *162*
Subscripts or Superscripts *162*
Acronyms *163*
References *163*

5 Unitized Regenerative Systems *167*
Pierre Millet
5.1 Introduction *167*
5.2 Underlying Concepts *168*
5.2.1 Thermodynamics *168*
5.2.2 Half-Cell Reactions *171*
5.2.3 Process Reversibility *172*
5.3 Low-Temperature PEM URFCs *174*
5.3.1 Principles *174*
5.3.2 Cell Structure and URFC Stack *175*
5.3.3 Performances *176*
5.3.3.1 Water Electrolysis Mode *176*
5.3.3.2 Fuel Cell Mode *177*
5.3.3.3 URFC Mode *178*
5.3.4 Limitations and Perspectives *180*
5.4 High-Temperature URFCs *182*
5.4.1 Principles *182*
5.4.2 Cell Structure *182*
5.4.3 Performances *184*
5.4.3.1 Water Electrolysis Mode *184*
5.4.3.2 Fuel Cell Mode *184*
5.4.3.3 URFC Mode *185*
5.4.4 Limitations and Perspectives *186*
5.5 General Conclusion and Perspectives *187*
Nomenclature *187*
Greek Symbols *188*

Subscripts or Superscripts *188*
Acronyms *188*
References *189*

6 High-Temperature Steam Electrolysis *191*
Jérôme Laurencin and Julie Mougin
6.1 Introduction *191*
6.2 Overview of the Technology *191*
6.3 Fundamentals of Solid-State Electrochemistry in SOEC *197*
6.3.1 Cell Polarization Curve *198*
6.3.1.1 Expression of the Cell Voltage $U(i)$ *198*
6.3.1.2 Ohmic Losses and Contact Resistances *199*
6.3.1.3 Anode and Cathode Polarization: Role of the Electrochemical Process on the Cell Polarization Curve *200*
6.3.1.4 Global Decomposition of the Cell Polarization Curve *206*
6.3.2 Fundamental for Electrochemistry, Mass and Charge Transfer in SOEC Electrodes *209*
6.3.2.1 Electronic and Ionic Charge Transport into the Electrode *209*
6.3.2.2 Gas Transport in the Electrode *215*
6.3.2.3 Expression of the Source Terms: Kinetic of the Electrochemical Process *219*
6.3.2.4 Specific Operating Mechanisms of Single-Phase SOEC Anode *223*
6.3.2.5 Role of Microstructure in the Electrode Behaviour *228*
6.3.3 Role of Temperature in SOEC Operation *236*
6.3.3.1 Cell Thermal Regimes *236*
6.3.3.2 Impact of Cell Temperature on Polarization Curve *239*
6.3.4 Summary and Concluding Remarks *243*
6.4 Performances and Durability *244*
6.4.1 Performances *244*
6.4.2 Durability *249*
6.4.3 Stack Electrochemical and Thermal Management *252*
6.5 Limitations and Challenges *253*
6.5.1 Degradation Issues *254*
6.5.2 System Integration and Economical Considerations *257*
6.6 Specific Operation Modes *259*
6.6.1 Pressurized Operation *259*
6.6.2 Reversible Operation *260*
6.6.3 Co-Electrolysis *261*
List of Terms *262*
Roman symbols *262*
Greek Symbols *263*
Abbreviations *264*
References *264*

7 Hydrogen Storage Options Including Constraints and Challenges *273*
Agata Godula-Jopek
7.1 Introduction *273*
7.2 Liquid Hydrogen *276*
7.2.1 Liquid Hydrogen Storage Systems *279*
7.3 Compressed Hydrogen *281*
7.3.1 Compressed Hydrogen Storage Systems *282*
7.4 Cryo-Compressed Hydrogen *284*
7.4.1 Cryo-Compressed Hydrogen Storage Systems *284*
7.5 Solid-State Hydrogen Storage Including Materials and System-Related Problems *286*
7.5.1 Physical Storage – Overview *290*
7.5.2 Chemical Storage – Overview *297*
7.5.2.1 Solid-State Hydrogen Storage System Coupled with Electrolyser *301*
7.6 Summary *304*
References *306*

8 Hydrogen: A Storage Means for Renewable Energies *311*
Cyril Bourasseau and Benjamin Guinot
8.1 Introduction *311*
8.2 Hydrogen: A Storage Means for Renewable Energies (RE) *312*
8.2.1 Renewable Energy Sources: Characteristics and Impacts on Electrical Networks *312*
8.2.1.1 Intermittency and Limited Forecast of Renewable Production and Electrical Load *312*
8.2.1.2 Impacts of Non-Dispatchable Power Sources on Electrical Networks *314*
8.2.1.3 Solutions for Higher Penetration of Renewable Energies *316*
8.2.2 Energy Storage on Electrical Networks *318*
8.2.2.1 Technologies Characteristics *318*
8.2.2.2 Past, Present and Future Technology Choices *319*
8.2.2.3 Possible Roles of Energy Storage on the Grid *320*
8.2.3 Hydrogen for Energy Storage *323*
8.2.3.1 Power to Hydrogen: Use of Electrolysis to Store Electrical Energy *323*
8.2.3.2 Attractiveness of Hydrogen: Not Only an Energy Carrier *324*
8.2.3.3 Use of Hydrogen to Produce Electricity *326*
8.3 Electrolysis Powered by Intermittent Energy: Technical Challenges, Impact on Performances and Reliability *327*
8.3.1 Effect of Intermittency on System Design and Operation *327*
8.3.1.1 Impact on Power Electronics and Process Control *329*
8.3.1.2 Requirements to Allow Dynamic Operation *332*
8.3.1.3 Impact on Downstream Elements *334*

8.3.2 System Performances and Reliability under Dynamic Operation *334*
8.3.2.1 Impact on Hydrogen Production Characteristics *335*
8.3.2.2 Impact on System Efficiency *337*
8.3.2.3 Impact of Intermittency on Reliability and Durability *341*
8.3.2.4 Specificities of High-Temperature Steam Electrolysis *343*
8.3.3 Improvements on Design and Operation to Manage Intermittency *345*
8.3.3.1 Improvements on System Design *345*
8.3.3.2 Improvements on Operating Strategies *347*
8.3.3.3 Which Technology Best Suited to Intermittent Sources? *349*
8.4 Integration Schemes and Examples *351*
8.4.1 Autonomous Applications *351*
8.4.1.1 Production of Renewable Hydrogen *352*
8.4.1.2 Stand-Alone Power System with Hydrogen as Storage of Electrical Energy *353*
8.4.2 Grid-Connected Applications *356*
8.4.2.1 Production of Renewable Hydrogen with Grid Assistance *356*
8.4.2.2 Electrolysis for Renewable Energy Storage *357*
8.4.2.3 Renewable Source, Grid and Electrolysis Integrated Energy System *358*
8.4.3 High-Temperature Steam Electrolysis Integration with Renewable Source *361*
8.5 Techno-Economic Assessment *362*
8.5.1 Hydrogen from Electrolysis: Future Markets *362*
8.5.1.1 Hydrogen for Off-Grid Applications *363*
8.5.1.2 Hydrogen for Mobility *363*
8.5.1.3 Power to Hydrogen – A Way to Provide Services to the Network *364*
8.6 The Role of Simulation for Economic Assessment *365*
8.6.1 Objectives of the Simulation *365*
8.6.2 Simulation's Main Input Data – Impact on the Robustness of the Results *367*
8.6.2.1 Components, Architectures and Component Models *368*
8.6.2.2 Control Strategies *371*
8.6.2.3 Simulation Temporal Characteristics *372*
8.6.2.4 Simulation Results *373*
8.6.3 Optimization and Sensitivity Analysis *375*
8.6.3.1 Principles *375*
8.6.3.2 Objectives *375*
8.6.3.3 Main Difficulty and Solutions Related to Simulation *376*
8.6.4 Example of Existing Software Products for Techno-Economic Assessments of Hydrogen-Based Systems *376*
8.7 Conclusion *378*
References *379*

9 **Outlook and Summary** *383*
Agata Godula-Jopek and Pierre Millet
9.1 Comparison of Water Electrolysis Technologies *387*
9.2 Technology Development Status and Main Manufacturers *387*
9.2.1 Alkaline Water Electrolysis *387*
9.2.2 PEM Water Electrolysis *389*
9.2.3 Solid Oxide Water Electrolysis *390*
9.3 Material and System Roadmap Specifications *390*
9.3.1 Alkaline Water Electrolysis *392*
9.3.2 PEM Water Electrolysis *392*
9.3.3 Solid Oxide Water Electrolysis *393*
References *393*

Index *395*

Foreword

The most impressive property of hydrogen is not just a single technical one, but the capability to provide reason for implementation even under shifting paradigms. In other words, hydrogen is very versatile and clean. In the 1970s hydrogen was investigated under the pressure of the oil price shocks and it was thought to be very much in line with photovoltaics and clean energy. In the following years a decreasing oil price marginalized these efforts until hydrogen was eyed as an extremely clean fuel by the car industry together with fuel cells, delivering zero-emissions tailpipe. Today, renewable energy, primarily wind power, but also photovoltaics, has reached a level of economics that strategies using hydrogen for storage and as a fuel in transportation are starting to make not just technical and ecological, but also economical sense. Particularly important in this context is the mass production of hydrogen from wind power and photovoltaics via water electrolysis.

Long-standing research and development efforts of the car industry have recently turned into the first automated production of fuel cell vehicles, and other manufacturers have announced to follow within the next 1–3 years. Fuel cell cars benefit from a cruising range similar to those of existing gasoline cars with the option of quick and easy refilling with hydrogen. As there is a broad consensus of the car industry that hydrogen is the best fuel for fuel cell vehicles it is crucial and timely to make the most important way to produce hydrogen from renewable sources – water electrolysis – well known to scientists and the technical community.

In this context, this book makes a great contribution to disseminate the state-of-the-art science and technology of water electrolysis and the challenges thereof.

July 2014 *Detlef Stolten*
Jülich, Germany

Preface

"Low-cost hydrogen will foster a new era of energy sustainability, based on hydrogen."

Over the last decades, severe economic and environmental constraints have appeared on global hydrocarbon-based energy economy. Growing demands for increasing energy leads to reduced capacity in fossil fuels and as such will threaten global energy supply and put more strain on the environment. Therefore it is of vital importance to look for a replacement for hydrocarbon fuels. One promising alternative is hydrogen, which itself presents several advantages. It adds flexibility to energy production and end use chain by making a bridge between fossil, nuclear and renewable energy sources and electrical energy. When produced by electrolysis from renewable energies, it can be considered as a low carbon footprint energy carrier. Furthermore, hydrogen as a product is also used in several industrial applications, which grant electrolysis multiple opportunities of valorization. Hydrogen also appears as an excellent chemical for the transformation of carbon dioxide into synthetic carbonaceous fuels. A most significant part of hydrogen economy is hydrogen production in a sustainable, efficient and environmental-friendly way.

Due to the international energy situation, water electrolysis remains a fast-evolving field. Its high potential for transforming zero-carbon electricity sources into the supply of zero-carbon hydrogen and oxygen for miscellaneous end uses has attracted renewed attention over the last decade and many research and development (R&D) programmes have been launched in many countries to develop new integrated technologies for the management of renewable energy sources.

The transition towards this global 'hydrogen economy' is not expected to take place within a few years, but publicly supported R&D efforts and deployment of a hydrogen infrastructure will certainly contribute to making this vision a reality. In the recent years, the European Union (EU) has adopted ambitious energy and climate change objectives for 2020 and beyond. Long-term commitments to the decarbonization path of the energy and transport system have been made. Security of energy supply is also high on the political agenda. These strategic objectives have been reflected in the proposal of the European Commission for Horizon

2020, the research and innovation pillar of Europe 2020. Fuel cell and hydrogen (FCH) technologies have the potential to contribute in achieving these goals, and they are part of the SET Plan, the technology pillar of the EU's energy and climate policy. These technologies have made significant progress in the last 10 years in terms of efficiency, durability and cost reduction. Competitiveness with incumbent technologies is contemplated for 2015–2020, and targets in terms of performance have been established for that purpose and are considered reachable with a sufficient effort on R&D. Commercialization within some niche applications has already started, which is reflected in a fast-growing market, expected to be US$ 43 billion and US$ 139 billion annually over the next 10–20 years, from a forecasted US$ 785 million in 2012. Several hundreds of thousands of jobs may be created as a consequence of this growth.

The question is how Europe can capture a maximum share of this nascent sector, and what has to be done in the next few years. In this general context, water electrolysis and more specifically polymer electrolyte membrane (PEM) water electrolysis is expected to play an increasing role.

New markets are appearing for hydrogen of electrolytic grade because water splitting appears to be the best option to convert transient electricity load profiles into easy-to-store-and-distribute chemical fuels. New materials have been developed for operation over an extended range of temperature. Existing technologies have been optimized and new technologies have been developed.

Hydrogen production from electrolysis presents rather interesting features. It is indeed a suitable technology for renewable energy sources as it can adapt its power consumption to available input power. It also offers the advantage of being a fully scalable technology, allowing systems in the range of a few kilowatts to several tenths of megawatts. Unlike most storage technologies (batteries, flywheels, etc.), electrolysis allows the separation of the charging power and the stored energy, which can be of a great interest when designing a system with contrasted power and energy needs.

The book provides an overview of water electrolysis technologies based on alkaline electrolysis and PEM water electrolysis for the production of hydrogen and oxygen of electrolytic grade. A brief introduction to the historical background and a general description of the technologies are presented, including electrochemical performances, techniques used for stacking individual electrolysis cells into electrolysers of larger capacity and the performance and characteristics of these stacks. Details about process flowsheet, ancillary equipment and balance of plant are provided as well for both technologies. Last but not the least, current technological developments and applications are presented including discussions on existing limitations, challenges and future perspectives. Furthermore, a deep insight into high-temperature steam electrolysis (HTSE) technology is presented with details on fundamentals of solid-state electrochemistry in HTSE, performances and durabilities, limitations and challenges as well as specific operation modes. Moreover, different hydrogen storage options have been presented and compared taking into consideration existing limitations and targets set by the US Department of Energy (DOE).

It seems important to bring to the reader's attention the challenges related to the coupling of renewable sources with electrolyser systems. A comprehensive review of the associated requirements and their impact on system design, power electronics and process control is presented, including analysis of the impact of intermittency on electrolysis system performances and reliability in terms of produced hydrogen characteristics, efficiency and system lifetime. On the basis of selected key criteria, a qualitative comparison is provided on the suitability of PEM, alkaline and HTSE for integration with renewable energy sources.

The ambition of the authors was to edit a reference textbook in that field and discuss existing limitations and future perspectives. As such, the book offers a comprehensive review of the state of the art, covering different aspects of water electrolysis and high-temperature electrolysis (materials, technologies) and provides a comparison of the existing technologies in terms of performance and cost.

Last but not the least, I wish to acknowledge the excellent cooperation of all the authors, submitting manuscripts and corrections on time. Many thanks are also due to Dr Waltraud Wuest, Dr Heike Noethe and other colleagues from Wiley-VCH Weinheim, Germany, for help with obtaining permissions for reprinting figures and for an excellent job in editing the manuscript of the book.

October 2014 *Agata Godula-Jopek*
Munich, Germany

List of Contributors

Cyril Bourasseau
CEA Grenoble
DRT/LITEN/DTBH/SCSH/LPH
17, rue des Martyrs
38054 Grenoble Cedex 9
France

Agata Godula-Jopek
Airbus Group Innovations—TX6
Willy Messerschmitt Str. 1
81663 Munich
Germany

and

Polish Academy of Sciences
Institute of Chemical
Engineering
ul. Baltycka 5
44100 Gliwice
Poland

Nicolas Guillet
University of Grenoble Alpes
F-38000 Grenoble

and

CEA, LITEN
F-733575 Le Bourget-du-Lac
France

Benjamin Guinot
CEA Grenoble
DRT/LITEN/DTBH/SCSH/LPH
17, rue des Martyrs
38054 Grenoble Cedex 9
France

Jérôme Laurencin
CEA Grenoble
DRT/LITEN/DTBH/SCSH/LPH
17, rue des Martyrs
38054 Grenoble Cedex 9
France

Pierre Millet
Université Paris-Sud 11
Chemistry Department, ICMMO
Bâtiment 410
15 rue Georges Clémenceau
91405 Orsay Cedex
France

Julie Mougin
CEA Grenoble
DRT/LITEN/DTBH/SCSH/LPH
17, rue des Martyrs
38054 Grenoble Cedex 9
France

1
Introduction

Agata Godula-Jopek

> *We find ourselves on the cusp of a new epoch in history, where every possibility is still an option. Hydrogen, the very stuff of the stars and our own sun, is now being seized by human ingenuity and harnessed for human ends. Charting the right course at the very beginning of the journey is essential if we are to make the great promise of a hydrogen age a viable reality for our children and a worthy legacy for the generations that will come after us.*
> Jeremy Rifkin [1].

Hydrogen is being considered as an important future energy carrier, which means it can store and deliver energy in a usable form. At standard temperature and pressure (0 °C and 1013 hPa), hydrogen exists in a gaseous form. It is odourless, colourless, tasteless, non-toxic and lighter than air. The stoichiometric fraction of hydrogen in air is 29.53 vol%. Abundant on earth as an element, hydrogen is present everywhere, being the simplest element in the universe representing 75 wt% or 90 vol% of all matter. As an energy carrier, hydrogen is not an energy source itself; it can only be produced from other sources of energy, such as fossil fuels, renewable sources or nuclear power by different energy conversion processes. Exothermic combustion reaction with oxygen forms water (heat of combustion 1.4×10^8 J kg^{-1}) and no greenhouse gases containing carbon are emitted to the atmosphere.

Selected physical properties of hydrogen based on Van Nostrand are presented in Table 1.1 [2].

The energy content of hydrogen is 33.3 kWh kg^{-1}, corresponding to 120 MJ kg^{-1} (lower heating value, LHV), and 39.4 kWh kg^{-1}, corresponding to 142 MJ kg^{-1} (upper heating value, UHV). The difference between the UHV and the LHV is the molar enthalpy of vaporization of water, which is 44.01 kJ mol^{-1}. UHV is obtained when as a result of hydrogen combustion water steam is produced, whereas LHV is obtained when the product water is condensed back to liquid.

Because of its high energy-to-weight ratio, hydrogen has commonly been used in a number of applications for the last 100 years and a lot of experience has been gained since its production and use, with it becoming the fuel of choice. Hydrogen application for transportation has a long history. One of the first demonstrated

Hydrogen Production: by Electrolysis, First Edition. Edited by Agata Godula-Jopek.
© 2015 Wiley-VCH Verlag GmbH & Co. KGaA. Published 2015 by Wiley-VCH Verlag GmbH & Co. KGaA.

Table 1.1 Selected physical properties of hydrogen.

Parameter	Value	Unit
Molecular weight	2.016	Mol
Melting point	13.96	K
Boiling point (at 1 atm)	14.0	K
Density solid at 4.2 K	0.089	$g\,cm^{-3}$
Density liquid at 20.4 K	0.071	$g\,cm^{-3}$
Gas density (at 0 °C and 1 atm)	0.0899	$g\,l^{-1}$
Gas thermal conductivity (at 25 °C)	0.00044	$cal{\cdot}cm\,s^{-1}\,cm^{-2}\,°C^{-1}$
Gas viscosity (at 25 °C and 1 atm)	0.0089	cP
Gross heat of combustion (at 25 °C and 1 atm)	265.0339	$kJ\,g^{-1}\,mol^{-1}$
Net heat of combustion (at 25 °C and 1 atm)	241.9292	$kJ\,g^{-1}\,mol^{-1}$
Autoignition temperature	858	K
Flammability limit in oxygen	4–94	%
Flammability limit in air	4–74	%

Source: By permission of Wiley VCH.

applications took place in the eighteenth century in Paris. The first manned flight (Jacques Charles and Nicolas Robert) had been demonstrated in a balloon called "hydrogen gas aerostat" for about 45 min, covering a distance of about 21 km.

A car with an internal combustion engine (ICE) that used a mixture of hydrogen and oxygen for fuel was invented by Francoise Isaac de Rivaz from Switzerland in January 1807 and it was the first internal combustion-powered automobile. The main application of hydrogen in the twentieth century was noted for nuclear submarines, airships and launching systems from the 1960s, and the first experimental investigations of liquid hydrogen for propulsion was started in the United States in 1945. Later it became a fuel of choice for rockets and launchers. The development of fuel cells was a major milestone in successful hydrogen application in the transportation sector. At present hydrogen-powered cars based on the polymer electrolyte membrane fuel cell (PEMFC) are being demonstrated worldwide. Fuel cell usage allows significant advantages such as energy-efficient drive train, silent mode of operation and high efficiency in well-to-wheel assessment.

When compared with other fuels such as methanol, petrol, diesel or kerosene, it is obvious that hydrogen yields much higher energy per unit weight than any other fuel. Hydrogen has a high energy-to-weight ratio (about three times more than gasoline, diesel or kerosene) and can be hazardous to handle. The flammability range is highest for hydrogen, but as long as it stays in an area that is properly ventilated there is no risk of reaching this limit. In addition, hydrogen has a relatively high ignition temperature of 858 K, as opposed to an ignition temperature of 501 K for gasoline. Hydrogen ignites very easily and burns with a wide range of mixtures with oxygen or air as compared to any other fuel.

When compared with most hydrocarbons, hydrogen has a much wider flammability range, from 4 (lower flammability limit, LFL) to 75 vol% (upper flammability limit, UFL) in air (4–95 vol% in oxygen) and detonability limits of 11–59 vol% in

air [3, 4]. Flammability limits of hydrogen increase with temperature. The lower limit drops from 4 vol% at Normal Temperature and Pressure (NTP (20 ° C, 1 atm)) to 3% at 100 °C; detonability limits expand with the scale of a mixture [5]. Hydrogen has very low minimum ignition energy (MIE) of 0.017 MJ in air and 0.0012 MJ in oxygen at 25 °C and 1 bar [6]. For comparison, MIE values for most combustibles are in the range of 0.1 – 0.3 MJ and values for oxygen are at least an order of magnitude lower [6] (Table 1.2).

Because of its low density, hydrogen does not collect near the ground but dissipates in air, as opposed to gasoline and diesel fuel. Hydrogen and methanol have been evaluated by Adamson and Pearsons [7] with regard to safety, economics and emissions. Comparative risks analysis in case of accident in enclosed and ventilated areas showed that both hydrogen and methanol are safer than petrol, but in certain situations hydrogen may be of higher risk than methanol. The fraction of heat radiated from the flames is certainly an important factor in case of fire. As can be seen in the Table 1.2, hydrogen and methanol, due to lower values of heat in radiative form, are less likely to catch fire than petrol. Hake *et al.* [8] compared different fuels and fuel storage systems of exemplary passenger cars with regard to the safety features of gasoline, diesel, methanol, methane and hydrogen. Hydrogen could be risky depending on the infrastructure, which is not the case with diesel or gasoline. Although hydrogen's physical properties are well established, actual risks and hazards can only be determined with real systems and long-operating experience. The present lack of operating experience with hydrogen systems has been recognized as a significant barrier to their application. Several international efforts have been initiated to develop regulations, codes and standards (RCS). For example, the European Union has used the EIHP2 (European Integrated Hydrogen Project phase 2) project methodology to outline inputs for regulatory and standardization activities on

Table 1.2 Selected properties of hydrogen compared with other fuels.

Fuel	Gravimetric energy density		Volumetric energy density		Flammability limits	Explosive limits	Fraction of heat in radiative form
	MJ kg^{-1}	kWh kg^{-1}	MJ l^{-1}	kWh l^{-1}	vol%	vol%	
Hydrogen compared 200 bar	120	33.3	2.1	0.58	—	—	—
Hydrogen liquid	120	33.3	8.4	2.33	4 – 75	18.3 – 59.0	17 – 25
Methanol	19.7	5.36	15.7	4.36	6 – 36.5	6 – 36	17
Petrol	42	11.36	31.5	8.75	1 – 7.6	1.1 – 3.3	30 – 42
Diesel	45.3	12.58	35.5	9.86	—	0.6 – 7.5	—
Kerosene	43.5	12.08	31.0	8.6	—	0.7 – 5	—

Source: By permission of Wiley VCH.

a European and global level, thus allowing safe development, introduction and daily operation of hydrogen-fuelled vehicles on public roads and their associated hydrogen refuelling stations [9]. A generic risk-based maintenance and inspection protocol for hydrogen refuelling stations has also been developed. A study has been undertaken to define the potential for the introduction of environmentally friendly hydrogen technologies in stand-alone power systems (H-SAPS). Barriers and potential benefits of promoting new technological applications on a wide scale and the market potential for SAPS have been widely analysed in select cases of existing small- and medium-sized systems with power rating from 8 to 100 kW (Gaidouromantra, Kythnos Island, Greece/PV-diesel-battery/~8 kW; Fair Isle, UK/wind-diesel/~100 kW; Rauhelleren, Norway/diesel/~30 kW; Rambla del Aqua, Spain/PV-battery/~11 kW) [10]. On the basis of the analysis, several interesting observations have been made. In order to introduce hydrogen energy technologies in autonomous power systems, a renewable energy source should be incorporated and in addition it should always be overdimensioned to cover power demand and use an excess electricity to produce hydrogen. It was shown that the replacement of conventional power sources with hydrogen is probably more economically viable in power systems having year-round load demand than those having seasonal power demand (power systems with seasonal power demand require seasonal energy storage; thus water electrolyser and hydrogen storage should be overdimensioned). The cost of fossil fuels in remote locations is higher (due to the increasing costs of fuel transportation); therefore the replacement of conventional power equipment by hydrogen energy equipment is expected to be beneficial from the financial point of view. Furthermore, such systems can successfully be used in short to medium market niche applications and have certain environmental advantages, especially in remote communities [10]. It is expected that hydrogen may play a considerable role in the future global energy systems. As stated by MacCurdy [11], "The degree of civilization of any epoch, people, or group of peoples, is measured by ability to utilize energy for human advancement or needs." Growing interest of hydrogen in transportation sector has been recognized and hydrogen-powered fuel cell vehicles (FCVs) are demonstrated successfuly in Asia, the United States and Europe. Hydrogen-fuelled cars are reported to be about 1.5–2.5 times more efficient than gasoline-advanced cars on a TtW basis (tank to wheels) and produce no emissions, thus offering good performance; a distance of 500 or more kilometres can be refuelled within a few minutes [12]. A very famous example is the BMW seven series with a compressed hydrogen tank and with more than 35 years of experience in hydrogen usage (Figure 1.1).

As transitioning to hydrogen fuels and fuel cells still remains a challenge, there may be a need for an intermediate phase, where both hydrogen and conventional fuels are used together in the same vehicle. As stated, "The solution to meet this transitional requirement is the manufacturing of bi-fuel vehicles running on both hydrogen and gasoline using current internal combustion engine technologies … This bi-fuel approach will stimulate the creation of a hydrogen-refuelling network thus allowing for a full transition to a hydrogen powered vehicle economy" [13]. It

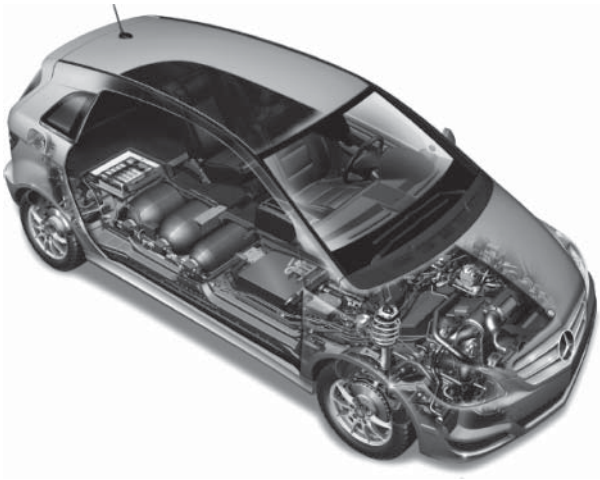

Figure 1.1 B class fuel cell car from Daimler with compressed hydrogen tank. (By permission of Wiley VCH.)

is estimated that cars with a bi-fuel system will increase their autonomy range by using hydrogen and will be able to cover a distance of approximately 200–300 km on hydrogen and up to 500 km on gasoline. A comparison between several vehicles on the market and the bi-fuel prototype by Alset Technology LLC is given in Table 1.3.

The deployment of completely new infrastructure for transportation is one of the key challenges on the technical, economic and financial fronts. The rechargeable vehicles market (battery electric vehicles, BEVs and plug in electric vehicles, PHEVs), which started a few years ago, will require new infrastructure,

Table 1.3 Comparison between several vehicles on the market and bi-fuel prototype vehicle by Alset.

Model	Engine	Capacity (l)	Power		Torque (Nm)	Specific power	
			HP	kW		HP l^{-1}	kW l^{-1}
BMW Hydrogen 7	V12 bivalent	6.0	260	191.23	390	43.3	31.87
Ford Focus C-Max	4cyl-inline monovalent	2.2	112	82.32	?	49.8	37.42
Quantum Prius H2-Hybrid	4cyl-inline hybrid	1.5	71	52.18	111	47.4	34.78
Ford Shuttle E-450	V10 monovalent	6.8	272	199.0	1110	40.0	29.39
Alset H2 Bi-Fuel 1.0	4cyl-inline bivalent	2.0	150	110.25	390	75.2	55.125

Source: Adapted from [13].

with contribution from both the private and public sectors and from different locations. France is one of the leading countries in the market for electric vehicles, aspiring towards 10% market share by 2020 [14]. For the development of the future hydrogen economy, an efficient and safe way of storing hydrogen in different applications, mobile, stationary and portable, is mandatory. Several means of hydrogen storage include compressed hydrogen gas (CGH_2), liquid cryogenic hydrogen (LH_2) and solid state hydrogen storage (SSH_2). Onboard hydrogen storage is one of the key fundamental barriers for commercialization of hydrogen-fuelled light vehicles. Hydrogen storage activities are currently focused on low-pressure material-based technologies allowing *per saldo* driving range above 500 km per vehicle. This means that a mass of more than 5 kg of hydrogen has to be carried, which requires meeting rigorous structural demands with regard to hydrogen tanks, costs, safety and performance requirements in order to be competitive with comparable vehicles available on the market. The current US Department of Energy (DoE) targets for onboard hydrogen storage systems for light-duty vehicles require that in 2017 hydrogen gravimetric and volumetric capacities reach a level of 5.5 wt% and 0.04 kg l^{-1}, respectively, corresponding to usable specific energy of 1.8 kWh kg^{-1} from hydrogen [15]. Selected DoE Technical Targets for Onboard Hydrogen Storage Systems for Light-Duty Vehicles (complete system including tanks, materials, valves, regulators and pipes) are presented in Table 1.4.

The vision on how hydrogen could be introduced in the energy system played a major role in the HyWays (the European Hydrogen Energy Roadmap) project [16]. It was highlighted that if hydrogen is introduced into the energy system, the costs to reduce one unit of CO_2 will decrease by 4% by 2030 and 15% by 2050. About 85% of the reduction of emissions is related to road transport, with the projection that CO_2 emissions from road transport will reduce by 50% by 2050 (Figure 1.2).

Introducing hydrogen technologies into the transport sector (cars, light-duty vehicles, heavy trucks) will also have a significant impact on non-CO_2 emissions into the atmosphere. The projections for the emission levels of CO, NO_x, volatile organic components (VOCs) and particulate matter (PM – solid or liquid particles found in the air) are that the levels will be reduced by more than 70% for NO_x and other pollutants [17]. The main markets for hydrogen end-use applications are passenger transport, light-duty vehicles and city buses. About half of the transport sector is expected to make a fuel shift towards hydrogen. Heavy-duty transport (trucks) and long distance vehicles are expected to switch to alternative fuels. The involvement of hydrogen in the residential and tertiary sector is expected to be limited to remote areas and specific niche applications, where a hydrogen infrastructure is already present [16]. The main challenges in introducing hydrogen into the energy system still remain the same: cost reduction for end-use application with the main focus on road transport; also, policy support continues to be an issue – the key finding of HyWays was that hydrogen is not high enough on the policymakers' agendas and more demonstration projects are needed in order to increase the awareness about hydrogen perspectives.

Table 1.4 Selected DoE technical targets for onboard hydrogen storage systems for light-duty vehicles [15].

Storage parameter	Units	2010	2017	Ultimate
System gravimetric capacity	$kWh\,kg^{-1}$	1.5	1.8	2.5
Usable specific energy from H_2	$kg\,H_2/kg$ system	0.045	0.055	0.075
System volumetric capacity	$kWh\,l^{-1}$	0.9	1.3	2.3
Usable energy density from H_2	$kg\,H_2/l$ system	0.028	0.040	0.070
Storage system costs	\$/kWh net	4	TBD	TBD
Fuel cost	\$/gge[a] at pump	3–7	2–4	2–4
System fill time (5 kg)	min	4.2	3.3	2.5
	$kg\,H_2/min$	1.2	1.5	2.0
Minimum full flow rate	$G\,s^{-1}\,kW^{-1}$	0.02	0.02	0.02
Operating ambient temperature	°C	−30/50 (sun)	−40/60 (sun)	−40/60 (sun)
Minimum/maximum delivery temperature	°C	−40/85	−40/85	−40/85
Operational cycle life (1/4 tank to full)	Cycles	1000	1500	1500
Fuel purity	$\%\,H_2$	99.97% dry basis SAE J2719 and ISO/PDTS 14687-2		

a) gge, gasoline gallon equivalent = 1.3×10^8 J.

A summary of the deployment phases, targets (targets for 2020 together with the European Hydrogen and Fuel Cell Platform have been elaborated on) and required main actions until 2050 are shown in Figure 1.3 [17]. Snapshot 2020 refers to the point where production volumes are significantly increased (breaking level at least 100 000 units per year) and snapshot 2030 refers to the maximum growth point where hydrogen and fuel cells are fully competitive with other technologies on the market.

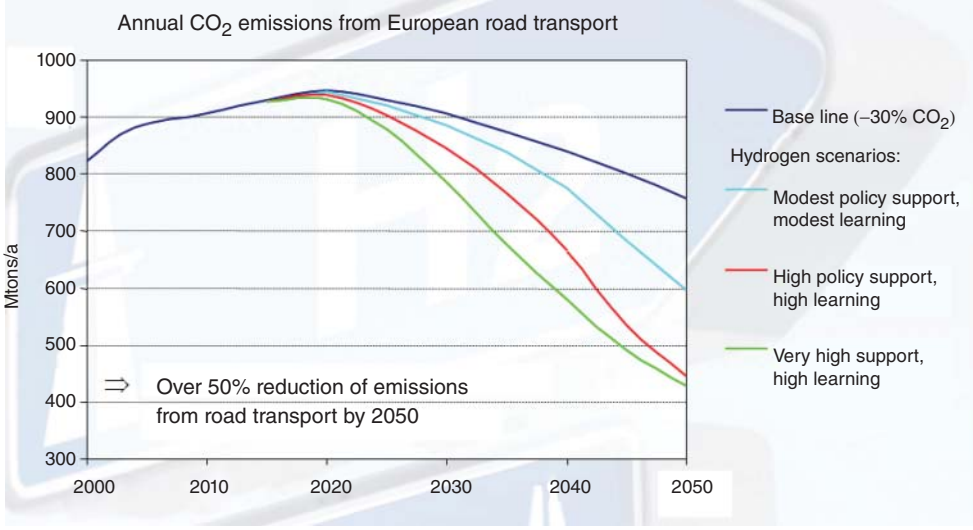

Figure 1.2 Annual CO_2 emission levels from European road transport; current status and predictions until 2050 based on several hydrogen scenarios on policy support (modest, high and very high). (HyWays and ECN [17].)

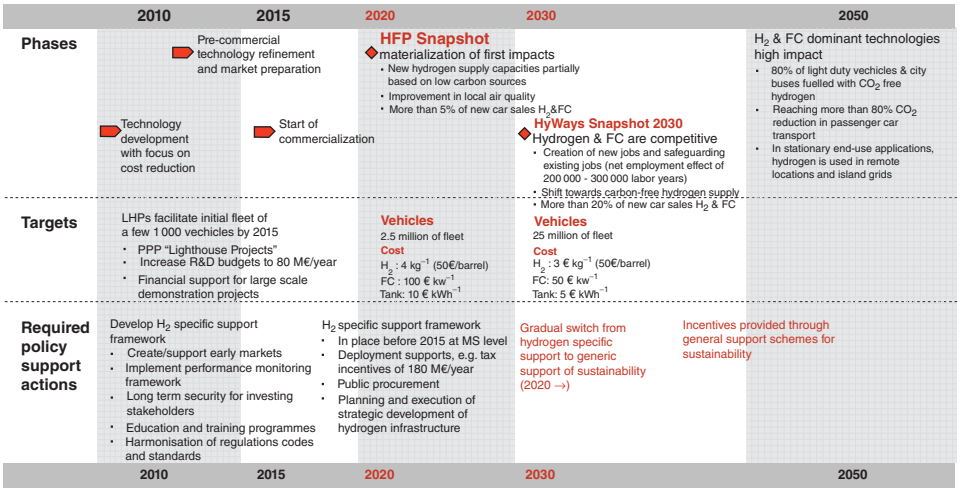

Figure 1.3 A summary of the deployment phases, targets and main actions until 2050. (HyWays and ECN [17].)

On the basis of the HyWays project findings, several key R&D areas for mobile and stationary hydrogen and fuel cells have been formulated. They include significant cost reduction for the H_2 drive train (improvement of PEM fuel cells and its periphery components, onboard storage, hydrogen ICE integration and system optimization), cost reduction for the hydrogen production chains, system integration for hydrogen systems and intensified development of RCS for

hydrogen. Last but not the least, it is of importance to comply with long-term sustainability requirements (production of hydrogen from renewable power sources, fossil fuels with carbon capture and storage – CCS, nuclear power and with closed fuel cycle) [17]. The main challenges that have been listed by the US DoE [18] can be summarized as follows: hydrogen is currently more expensive than gasoline and hydrogen storage systems for automotives cannot meet driving range expectations (above 300 miles) presently without occupying additional space. Given the technology status, the risk of hydrogen delivery infrastructure is still high. Within the scope of the German HyTrust project a current state of public acceptance in hydrogen technology in the mobility sector has been analysed. On the basis of results from interviews, focus groups, conferences and representative surveys, it can be stated that the German population has a very positive attitude towards hydrogen-powered cars, viewing them as a possibility of being mobile without harming the environment. People have no safety concerns regarding hydrogen or hydrogen cars, but they expect that the hydrogen that is used for Fuel Cell Electric Vehicles (FCEV) is produced from electricity based on renewable sources. What is interesting is that there are no safety concerns towards hydrogen and hydrogen-powered vehicles in the population because there is a basic trust in the German technology system [19]. Detailed analysis on prospects for hydrogen in different energy scenarios has been performed [8], and the relevant cases were based on (i) the study commission of the German Parliament "Nachhaltige Energieversorgung unter den Bedingungen der Globalisierung und der Liberalisierung" (Final Report of the Study Commission of the German Parliament in 2002), (ii) scenario study of the European Energy and Transport Trends to 2030 in 2003 and (iii) and the "World Energy Outlook 2002" of the International Energy Agency (IEA) in 2002. The three bodies estimated prospects for hydrogen in future energy systems differently. In Germany it is assumed that hydrogen will be introduced into the final energy carrier market after 2020, reaching about 2% of the total consumption of all fuels by 2050. Hydrogen usage will focus on the transportation market for fuel cells in passenger cars and buses. Around 25% of the hydrogen is to be used for electricity production. To sum up, the role of hydrogen is assumed to be very small for the next five decades. According to the European Commission (EC), the demand for new energy carriers such as hydrogen will grow, but will be insignificant till 2030 as a result of no significant market share for new vehicle technologies such as FCEV. This is also due to the lack of sufficient infrastructure for the supply and distribution of hydrogen. On the other hand, the world energy outlook of the IEA sees prospects for hydrogen use in power generation. It is assumed that global energy use will increase steadily through 2030. Global primary energy demand is projected to increase by 1.7% per year from 2000 to 2030, reaching an annual level of 650 EJ. In that scenario, hydrogen from reformed natural gas converted in fuel cells for electricity generation is expected to emerge as a new source of power generation, especially after 2020. All three scenarios are discussed below (Figures 1.4–1.6).

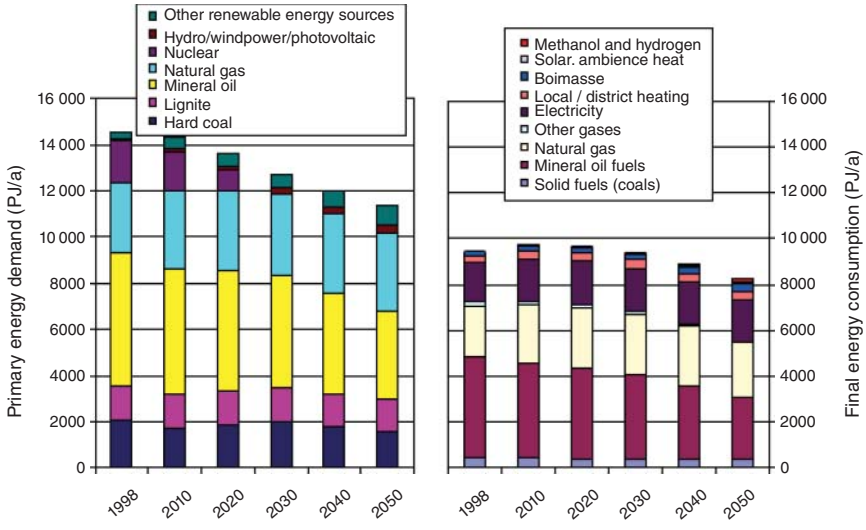

Figure 1.4 Primary energy demand and final energy consumption and hydrogen in Germany [8].

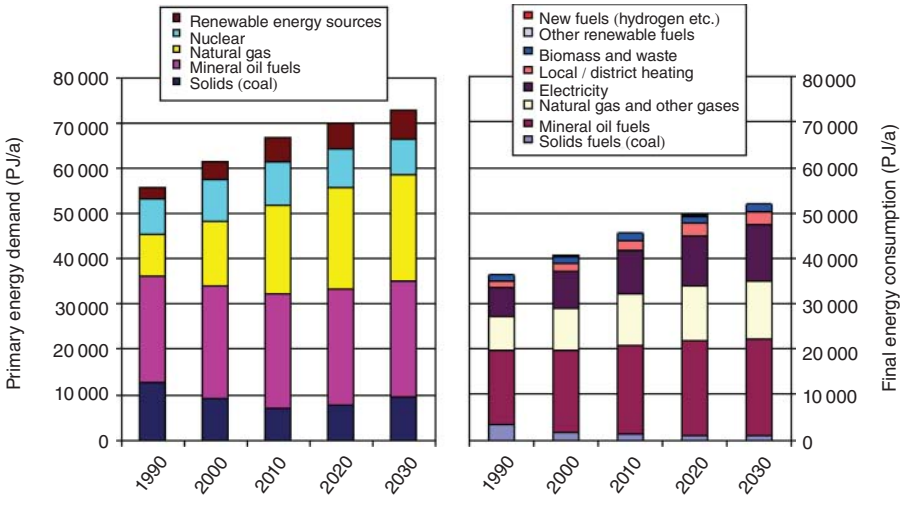

Figure 1.5 EU-15 baseline scenario of primary energy demand and final energy consumption [8].

1.1
Overview on Different Hydrogen Production Means from a Technical Point of View

Hydrogen production is the main step towards transitioning to a hydrogen economy, wherein hydrogen will replace fossil fuels. Hydrogen can be produced by processing a multitude of primary energy resources such as fossil fuels (coal, crude

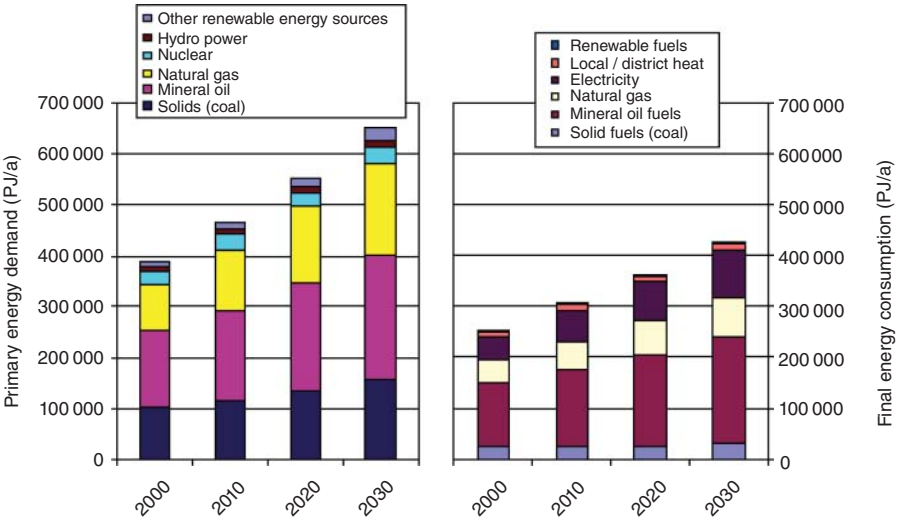

Figure 1.6 World of primary energy demand and final energy consumption by fuel [8].

oil, natural gas, etc.), nuclear fuels (e.g. deuterium, thorium, uranium), geothermal (heat that is stored in underground streams or in hot rocks beneath the earth) as well as solar, wind and tidal energy. These energy sources can also be classified into two groups: renewable (which are non-exhaustible and provide continuous energy supply such as solar or wind energy) and non-renewable, where resources are exhaustible and limited such as fossil fuels. The aim of this section is to give a short overview on the current ways of producing hydrogen such as reforming processes, electrolysis or gasification as well as methods that are in the R&D stage. The major hydrogen production technologies are those producing hydrogen from fossil fuels, from biomass or from water. As can be seen in Figure 1.7, hydrogen can be produced from fossil fuels by steam reforming of natural gas, thermal cracking of natural gas, partial oxidation (POX) of heavy fractions or coal gasification; from biomass by burning, fermenting, pyrolysis, gasification followed by liquefaction or biological production; from water by electrolysis, photolysis, thermochemical processes, thermolysis and combinations of biological, thermal and electrolytic processes. More details on different hydrogen production routes can be found, for example, in [20–26].

Hydrogen can be used in ICE as well as converted to electricity to power electric motors by means of fuel cells, mainly PEMFC. In transportation hydrogen is used in passenger cars, buses and light-duty vehicles. A general illustration of the supply → demand chain as well as the classification of end-users of hydrogen is presented in Figure 1.8.

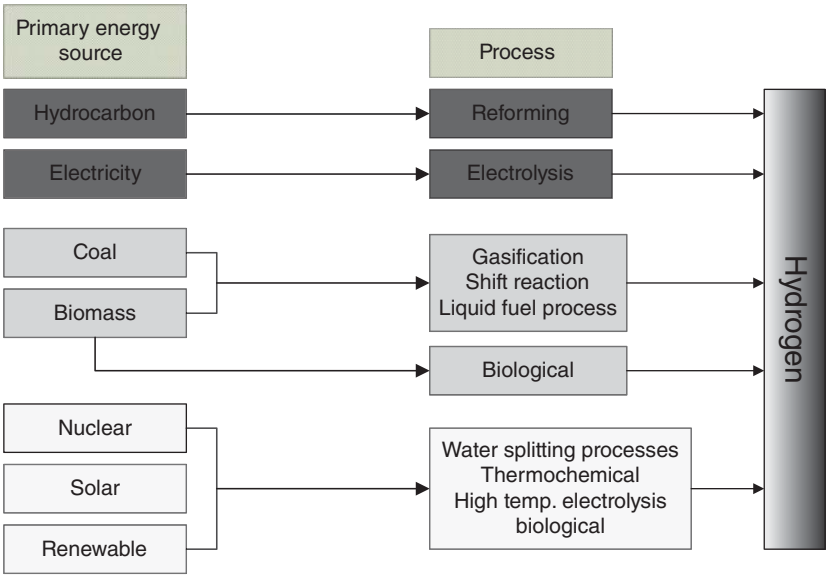

Figure 1.7 General pathways of hydrogen production. (By permission of Wiley VCH.)

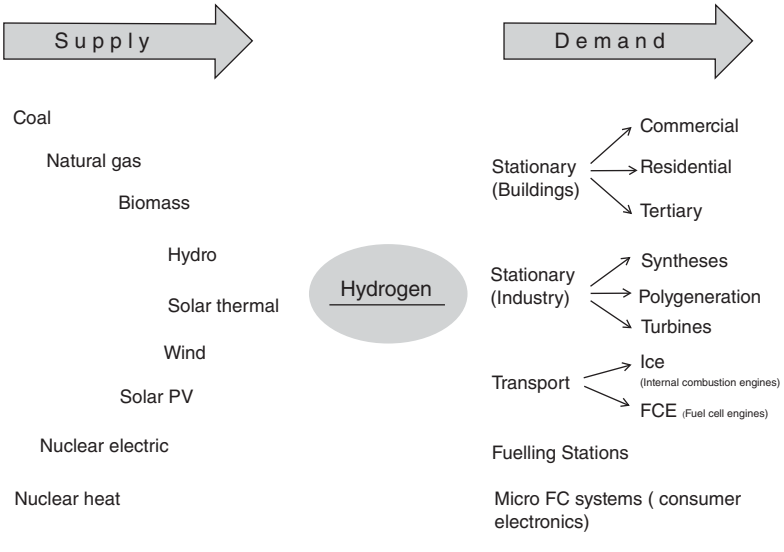

Figure 1.8 Hydrogen by means of different sources and its potential application in stationary, transportation and portable sectors [20]. (By permission of Wiley VCH.)

1.1.1 Reforming

Reforming processes, especially steam reforming, in combination with fossil fuels are the dominant processes for hydrogen production today. Typical feedstock is natural gas, but liquid hydrocarbons such as gasoline can also be used. Three reforming methods that are briefly presented here are catalytic steam reforming (CSR), POX and autothermal reforming (ATR). The chemistry of fuel processing methods, state of the art of catalyst technology for fuel processing applications, fuel processing reactors and balance of plant components has been described in detail by Kolb [27]. Steam reforming of natural gas is currently the cheapest, technically and commercially well-established way to produce hydrogen and is mainly used in the petrochemical and chemical industries. The cost of hydrogen production from steam reforming strongly depends on the costs and availability of natural gas feedstock.

Steam reforming is highly endothermic – high reaction temperatures, typically above 600 K, and pressure of about 2–3 MPa [28] are needed for gas phase conversion in the presence of Fe- or Ni-based catalysts supported on Al_2O_3 and $MgAl_2O_4$.

The efficiency of steam reforming is around 65–70% [20]. Steam reforming of light hydrocarbons is also a well-established industrial process. One of the benefits of using methanol is that the reforming reaction can be carried out at a lower temperature – endothermic steam reforming can be carried out at around 300 °C over a Co–Zn catalyst [29], whereas about 800 °C is required for hydrocarbons. Theoretically, steam reforming of methanol can produce 75% hydrogen concentration at 100% CO_2 selectivity; in practice, it is more than 70% with various catalysts [30]. Higher temperatures (850–1500 °C) are required for the steam reforming of ethanol because of its C–C bond [31]. POX reforming is an exothermic reaction that uses a substoichiometric amount of oxygen, generally from air, to convert the fuel to a H_2-containing stream. The substoichiometric amount of O_2 used results in significant production of carbon monoxide (CO). The process is much faster than steam reforming and can occur with or without the presence of catalysts. The non-catalytic Texaco process operates at temperatures in the range of 1200–1500 °C and pressure above 3 MPa. Catalytic POX uses lower temperatures of around 1000 °C, but for production of pure hydrogen it is less efficient and more costly than steam reforming. Catalysts include supported nickel (NiO–MgO), nickel-modified hexa-aluminates, platinum group metals Pt, Rh, Pd/alumina on ceria-containing supports or on titania [20]. In case of POX, only fuel and feed air is required for the reaction; there are no evaporation processes with the typical by-product methane. The disadvantage of the POX process is catalyst deactivation due to coke deposition and CO. ATR or oxidative steam reforming combines the endothermic steam reforming process with the exothermic POX reaction; therefore it is called autothermal. In such combination, the energy generated by the POX reaction provides the energy for the steam reforming reaction. These systems can be very productive and fast

starting and have been demonstrated with methanol, gasoline and natural gas. ATR has several advantages such as improved heat integration, faster start-up and lower operating temperatures. As in the case of the POX product stream, the autothermal reformate stream contains CO and the H_2 is further diluted by the nitrogen added from air. Among various onboard processing methods for liquid fuels oxidative methanol reforming (OMR) is regarded as the most promising for supplying hydrogen to PEMFCs in a vehicle. The OMR reaction is a combination of POX with steam reforming at a ratio where the overall reaction is thermally neutral or modestly exothermic. It has been confirmed that the high activity of the process of methanol conversion and the high selectivity of hydrogen production are enhanced by the presence of a Pd–ZnO catalyst [32].

Respective reforming reactions in a general way are as follows [27]:

Steam reforming:

$$C_nH_m + nH_2O \rightarrow nH_2 + \left(\frac{(n+m)}{2}\right)CO; \quad \Delta H^0_{298} > 0$$

$$CO + H_2O \rightarrow CO_2 + H_2; \quad \Delta H^0_{298} = -40.4\ \text{kJ mol}^{-1}$$

(water gas shift reaction, WGSR)

WGSR increases the hydrogen concentration of reformate. It occurs in two stages, as high temperature shift (HTS) at around 350 °C and as low temperature shift (LTS) at around 200 °C. Ideally, WGS reactions should reduce the CO level down to less than 5000 ppm.

POX:

$$C_xH_yO_z + \frac{(x-z)}{2}(O_2 + 3.76\ N_2) \rightarrow xCO + \frac{y}{2}H_2 + 3.76\frac{(x-z)}{2}N_2$$

ATR:

$$C_xH_yO_z + n(O_2 + 3.76N_2) + (x - 2n - z)H_2O \rightarrow xCO + \left(x - 2n - z + \frac{y}{2}\right)H_2 + 3.76N_2$$

1.1.2 Electrolysis

This section presents main state-of-the-art alkaline and PEM water electrolysers and a review of manufacturers worldwide. Detailed information on the relevant technologies including operational principles, characteristics, applications and limitations and challenges will be presented in the respective parts of the book. Chapter 2 provides dedicated information on water electrolysis technologies: both alkaline and PEM based. Chapter 3 provides detailed information on high-temperature steam electrolysis. Despite more than 100 years of experience in alkaline electrolysis systems and thousands of installed plants all over the world, only a few systems or industries that provide the state of the art on

this technology remain. Several examples are given in Table 1.7. According to Carmo *et al.* [33] and Mergel *et al.* [23], this could be because of the cost of electrical energy. Electrolytic hydrogen costs are not being able to compete with the production costs for hydrogen by conventional steam reforming of fossil fuels. Challenges of alkaline electrolyser technology concern system lifetimes and maintenance costs. There is currently increased interest with regard to PEM electrolysis technology and over the past 20 years new companies have appeared on the market and new projects have been established in the field. The efficiency of PEM technology could reach a level from 55% to 70%. Key worldwide players in PEM electrolysers area are provided in Tables 1.5 and 1.6 [33]. PEM water electrolysis is still rather expensive due to platinum-based family catalysts and proton exchange membrane. Nevertheless, PEM electrolysis is well suited to be coupled with wind and solar energy.

Table 1.5 Realized alkaline water electrolyser manufacturers [33].

Manufacturer	Rated power (kW)	H_2 production rate ($Nm^3\ h^{-1}$)	Specific energy consumption ($kWh\ Nm^{-3}$)	Maximum pressure (bar)	Location
Brown Bovery (KIMA)	165 000	33 000	—	—	Aswan – Egypt
De Nora	150 000	30 000	4.6	atm	Nangal – India
Norsk Hydro	140 000	28 000	4.1	atm	Ryukan – Norway
Norsk Hydro	135 000	27 000	4.1	atm	Ghomfjord – Norway
Que Que	105 000	21 000	—	—	Zimbabwe
Electrolyser Inc.	76 000 – 10 5000	15 200 – 21 000	4.9	atm	Trail – Canada
Lurgi	22 500	4500	4.3	3	Cuzco – Peru
IHT	511.5 – 3534	110 – 760	4.65 to 4.3	32	Switzerland
NEL Hydrogen Technologies – Statoil	43 – 2 150 $10 – 500	4.3	atm	Norway	—
ELT (Barisic)	13.8 – 1 518	3 – 330	4.6 to 4.3	atm	Germany
Linde	N.a.	5 – 250	N.a.	25	Germany
AccaGen	6.7 – 487	1 – 100	6.7 to 4.87	10 (optional 30 and 200)	Switzerland
Idroenergy	3 – 377	0.4 – 80	7.5 to 4.71	1.8 – 8	Italy
Hydrogenics	54 – 312	10 – 60	5.4 to 5.2	10 (optional 25)	Canada
Teledyne Energy Systems	N.a.	2.8 – 56	N.a.	10	USA
H2Logic	3.6 – 213	0.66 – 42.62	5.45 to 5	4 (optional 12)	Denmark
Claind	N.a.	0.5 – 30	N.a.	15	Italy
Erredue	3.6 – 108	0.6 – 21.3	6 to 5.1	2.5 – 4	Italy
PIEL, division of ILT Technology	2.8 – 80	0.4 – 16	7 to 5	1.8 – 18	Italy
Sagim	5 – 25	1 – 5	5	10	France
Avalence	2 – 25	0.4 – 4.6	5.43 to 5	448	USA

Source: By permission of EFCF Luzern 2013, *www.efcf.com*.

Table 1.6 Main PEM water electrolyser manufacturers [33].

Manufacturer	Rated power (kW)	H_2 production rate ($Nm^3\ h^{-1}$)	Specific energy consumption ($kWh\ Nm^{-3}$)	Maximum pressure (bar)	Location
Proton Onsite	1.8–174	0.265–30 (concept: 90)	7.3 to 5.8	13.8–15 (optional 30)	USA
ITM Power	3–40	0.6–7	4.9–5.5	15	UK
Giner	20	3.7	5.4	85	USA
H-TEC Systems	1.5–20	0.3–3.6	5–5.5	30	Germany
Hydrogenics	7.2	1	7.2	7.9	Canada
Siemens	N.a.	20	N.a.	50	Germany
Treadwell Corp.	N.a.	1.2–10.2	N.a.	75.7	USA

Source: By permission of the EFCF Luzern 2013, *www.efcf.com*.

1.1.3
Gasification

Systems based on gasification can utilize coal, petroleum coke, biomass and municipal and hazardous wastes. In principle the process is similar to POX of heavy oils and involves three main steps: conversion of coal feedstock in the presence of oxidant (typically oxygen or air and steam) to syngas at high temperatures of 1000–1500 °C in a gasification reactor, catalytic shift reaction and purification of the produced hydrogen, typically from residual carbon and ash. Depending on the gasification technology, some water, CO_2 and CH_4 could be present in the syngas including traces of components such as hydrogen cyanide (HCN), hydrogen chloride gas (HCl), hydrogen sulphide (H_2S) and carbonyl sulphide (COS). Generated syngas can either be used directly to produce electricity or be further processed to pure hydrogen to be used for hydrocracking of petroleum or ammonia production (Figure 1.9).

During the pyrolytic process the biomass is heated at 370–550 °C at 0.1–0.5 MPa in the absence of air to convert it into liquid oils, solid charcoal and gaseous compounds. A variety of different types of biomass have been pyrolytically processed for hydrogen generation. They include, for example, pelletized peanut shells [34–36], post-consumer residues such as plastics, trap grease, mixed biomass and synthetic polymers [37] as well as bagasse, switchgrass and a nutshell mixture composed of 40% almond nutshells, 40% almond prunings and 20% walnut shells [38].

1.1.4
Biomass and Biomass-Derived Fuels Conversion

Biomass and biomass-derived fuels are renewable energy sources that can be used to produce hydrogen in a sustainable way. Generally speaking, four main types of

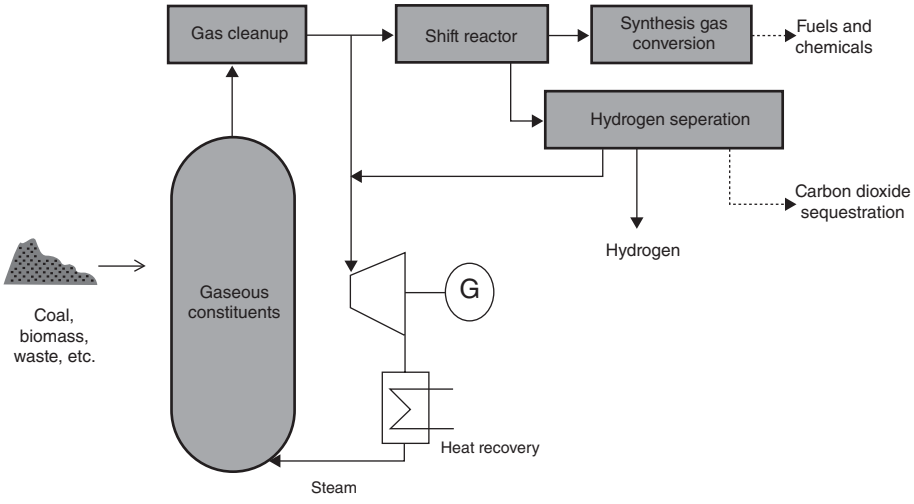

Figure 1.9 Gasification-based energy conversion options. (By permission of Wiley VCH.)

biomass feedstock can be distinguished: (i) energy crops including herbaceous, woody, industrial, agricultural and water, (ii) agricultural residues and waste, (iii) forest waste and residues and (iv) industrial and municipal wastes [39]. The use of a variety of biomass instead of fossil fuels for hydrogen generation may reduce CO_2 emissions to the atmosphere, because the CO_2 released when the biomass is gasified has previously been absorbed from the atmosphere and fixed by photosynthesis in the growing plants. It is estimated that about 12% of today's world energy supply comes from biomass, and the contribution from developing countries is significant higher, about 40–50% [39]. A wide range of technologies exists for transforming biomass into hydrogen, as can be seen in Figure 1.10 [20]. Processes can be divided into thermochemical and biological (fermentation) routes, relevant in both the near term and the mid term. In the long term hydrogen can be produced using photobiological processes, such as photosynthesis in cyanobacteria and algae.

Hydrogen can be produced via purely biological routes through the fermentation of biomass using microorganisms, or directly from cyanobacteria, purple bacteria and microalgae. All biological hydrogen production processes depend on the presence of hydrogen-producing enzymes (nitrogenase, Fe hydrogenase and NiFe hydrogenase). Algae and some microbial fermentations use photosynthesis to produce hydrogen. Other fermentation processes and direct production of hydrogen from cyanobacteria can take place in the absence of light. In Table 1.7, the advantages and disadvantages of different biological routes for hydrogen production are listed.

Research on biomass fermentation for hydrogen is increasing rapidly, especially on thermophilic bacteria and hydrogenases. Photobiological processes appear promising, but are not likely to become commercially available for some years [12].

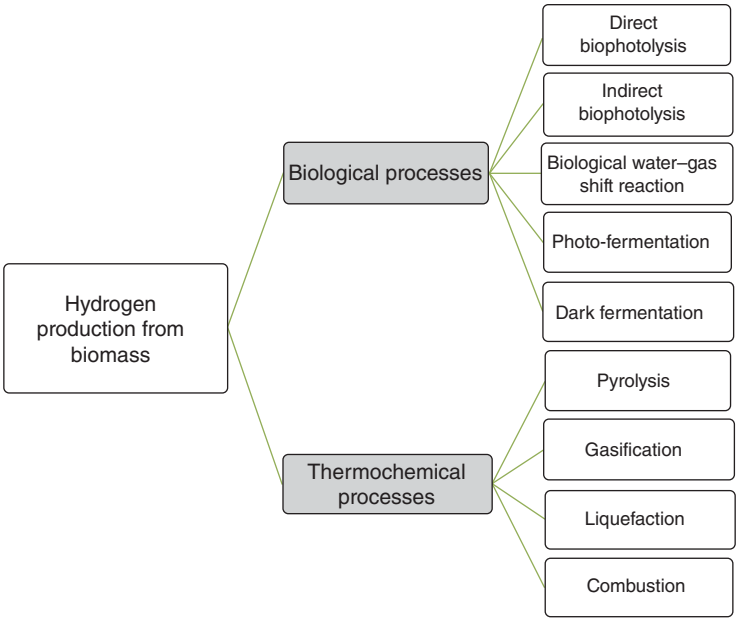

Figure 1.10 Technologies for hydrogen production from biomass [20]. (By permission of Wiley VCH.)

Photobiological hydrogen production is based on photosynthesis in bacteria and green algae. Hydrogen production in photobiological systems is presently limited by low energy conversion efficiencies. Markov *et al.* [40] have reviewed the state of the art of the development of bioreactors, dividing them into two categories based on the nature of hydrogen-evolving reactions. One category consists of photobioreactors based on hydrogen photoproduction and includes three types: (i) photobioreactors incorporating cyanobacteria, (ii) photobioreactors incorporating green algae and (iii) photobioreactors incorporating purple bacteria. To the second category belong bioreactors based on dark anaerobic hydrogen production with three types: (i) "water gas shift reaction" bioreactors incorporating purple bacteria, (ii) anaerobic fermentation bioreactors incorporating chemotrophic bacteria and (iii) bioreactors with immobilized enzymes. Biological processes for hydrogen generation are still at an early stage of development, mainly on a laboratory scale; however, there is intensive research under way to find ways to improve hydrogen yield and hydrogen production rates.

1.1.5
Water Splitting

Hydrogen can also be produced by splitting water and here three processes can be distinguished: electrolysis, photochemical processes and thermochemical cycles. Electrolytical water and steam splitting processes will be discussed in detail in

Table 1.7 Advantages and disadvantages of different biological processes for hydrogen production depending on the type of microorganism [20].

Type of microorganism	Advantages	Disadvantages
Green algae		
Chlamydomonas reinhardtii *Chlamydomonas moevussi* *Scenedesmus obliquus*	Can produce H_2 from water Solar conversion energy increased by 10-fold as compared to trees, crops	Require light for H_2 production O_2 can be dangerous for the system
Cyanobacteria		
Anabaena azollae *Anabaena CA* *Anabaena cylindrica* *AnabaenaCarlabilis* *Nostoc muscorum* *Nostoc sponglaeforme* *Westiellopsis prolifica*	Can produce H_2 from water Nitrogenase enzyme mainly produces H_2 Has the ability to fix N_2 from atmosphere	Uptake hydrogenase enzyme needs to be removed to stop degradation of H_2 Require sun light About 30% of O_2 is present in gas mixture with H_2 CO_2 is present in the gas O_2 has inhibitory effect on nitrogenise
Photosynthetic bacteria		
Rhodobacter sphaeroides *Rhodobacter capsulatus* *Rhodobacter sulidophilus* *Rhodopseumodomonas sphaeroides* *Rhodopseumodomonas paluxtris* *Rhodopseumodomonas capsulate* *Rhodospilillum rubnum* *Holabacterium halobium* *Chlorobium limícola* *Chloroflexu aurantiacus* *Thiocapsa roseopersicina*	Can use different materials such as whey, distillery effluents Can use wide spectrum of light	Require light for H_2 production Fermented broth causes water pollution problem
Fermentative bacteria		
Enterobacter aerogenes *Enterobacter cloacae* *Clostridium butyricum* *Clostridium pasteurianum* *Desulfovibrio vulgaris* *Magashaera elsdenii* *Citrobacter intermedius* *Escherichia coli*	Can produce H_2 all day long without light Can utilize different carbon sources such as starch, cellobiose, sucrose, xylose Different types of raw materials can be used Produces valuable metabolites such as butyric acid, lactic acid as by-products Anaerobic process, therefore no oxygen limitation problems	Fermented broth is required to undergo further treatment before disposal; otherwise it causes water pollution problem CO_2 present in the gas

the respective chapters of the book. In case of thermochemical cycles, water is decomposed directly into hydrogen and oxygen through numerous endothermic and exothermic chemical reactions at temperatures oscillating above 2500 °C in order to obtain significant dissociation rates. Light is used to light up a semiconductor-based photocatalyst immersed in an aqueous electrolyte or water [41, 42]. Hydrogen can be generated using the nuclear energy of thermochemical cycles (e.g. sulphur–iodine or UT-3) and hybrid cycles with the electrolytic and thermochemical steps. This process requires a large amount of heat or electricity to generate hydrogen, which can be supplied by nuclear energy. It is estimated that one of the most promising thermochemical cycles for massive-scale hydrogen production is the sulphur–iodine (S–I) cycle (originally developed by General Atomic) with thermal to hydrogen efficiency of 52% and adiabatic UT-3 cycle (calcium–bromine cycle) developed at the University of Tokyo with efficiency of around 50% [20].

The sulphur–iodine cycle (S–I cycle) is probably the most studied thermochemical cycle. It consists of two successive reactions taking place at 180 and 400 °C, respectively [43]

$$I_2 + SO_2 + 2H_2O \rightarrow 2HI + H_2SO_4 \quad 2HI \rightarrow H_2 + I_2$$

This hydrogen production way is particularly interesting for the concentrated solar power (CSP) technologies.

In the feasibility study for a commercial plant, the UT-3 cycle in Japan showed a hydrogen capacity of 20 000 $Nm^3\ h^{-1}$. Japan Atomic Energy Research Institute (JAEARI) aimed at connecting a nuclear system with a chemical process producing hydrogen. High-temperature steam electrolysers using nuclear energy are able to generate hydrogen without the corrosive conditions associated with thermochemical processes and greenhouse gas emissions associated with hydrocarbon processes [44]. In general, there are more than 300 water splitting processes reported in the literature allowing a temperature reduction from 2500 °C, but they usually work at higher pressures. Some examples are the Ispra Mark process, sulphur acid decomposition and the SynMet process of ZnO reduction and methane reforming in a solar reactor developed at the Paul Scherrer Institute. Thermochemical cycles coupled to a solar energy source work at lower temperatures (around 1200–1800 °C) and have been investigated in various research studies by using a laboratory demonstrator on a pilot scale over years. The German Aerospace Center (DLR) is working since the 1970s on directly using solar energy, including photovoltaics and solar thermal, and on iron-based thermochemical cycle processes [45]. After successful solar thermochemical hydrogen production in pilot tests (HYDROSOL-2) at the DLR, Cologne, the process was introduced in the Spanish Platforma Solar de Almeria (PSA) in Tabernas. A demonstration of the process by operating a solar receiver–reactor has shown repeatable hydrogen production in multiple cycles and is summarized by Neises [46]. The author also discussed investigations on the two-step thermochemical cycle using silicon carbide honeycombs coated with a zinc ferrite redox system. Another concept is

based on the photoelectrochemical cell (PEC cell). In the PEC cell, oxidation and reduction take place on locally separated electrodes. One of the main key challenges, apart from complicated and expensive architecture of the devices, is the requirement for an efficient photocatalyst. It should be cheap, easy to produce and non-toxic. Moreover, it should not contain scarce or expensive chemical elements. The potential of various photocatalysts has been reviewed by Ashokkumar [47], whereas a review and recent developments in photocatalytic water splitting for H_2 production using titanium oxide can be found in [48]. A very interesting material class in this context includes perovskite-type-related oxynitrides, which offer the possibility to absorb visible light and to be adapted to the numerous requirements by defect engineering and substitution. It has been demonstrated that the activity of $LaTiO_2N$, which is used as a photoanode in PEC cells, can be improved by substitution and that modifications in the microstructure and in the particle size influence its performance [49].

1.2 Summary Including Hydrogen Production Cost Overview

The most significant part of the hydrogen economy is hydrogen production in a sustainable, efficient and environmentally friendly way. The key challenge of different hydrogen production methods from various sources is to reduce costs. "Low-cost hydrogen will foster a new era of energy sustainability, based on hydrogen" [50]. Table 1.8 presents US DoE estimated targets and costs of producing hydrogen by selected technological processes [18].

Table 1.9 depicts an overview of hydrogen production costs from different processes taking into account numerous literature sources.

Table 1.10 concentrates exclusively on hydrogen production costs from electrolysis.

From Tables 1.9 and 1.10 it can be observed that the cost windows of steam reforming of light hydrocarbons and electrolysis slightly overlap, making electrolysis competitive with steam reforming in some specific situations. However, these two tables also highlight large disparities in hydrogen production costs. They can be explained on the basis of the different assumptions made by the authors of the mentioned studies. Factors of influence that have been identified are essentially:

- Maturity of the technology (pilot plant, industrial plant)
- Investment, operation, maintenance and replacement costs of the different equipments
- Size of the production plant
- Cost of energy source (coal, electricity, natural gas, etc.)
- Efficiency, capacity factor, and lifetime of the plant
- Purity of produced hydrogen.

Table 1.8 DoE technical targets for hydrogen production from a variety of feedstock.

Distributed production of hydrogen from bioderived renewable liquids					
Parameters	**Units**	**2006**	**2012**	**2017 target**	
Production unit energy efficiency	%	70.0	72.0	65–75	
Capital costs (uninstalled)	$	1.4 M	1.0 M	600 K	
Total hydrogen costs	$/gge	4.40	3.80	<3.00	
Distributed hydrogen production from natural gas					
Parameters	Units	2003	2006	2010	2015
Production unit energy efficiency	% (LHV)	65.0	70.0	72.0	75.0
Production unit capital costs (uninstalled)	$	12.3 M	1.1 M	900 K	580 K
Total hydrogen costs	$/gge H_2	5.00	3.00	2.50	2.00
Distributed water electrolysis hydrogen production					
Parameters	Units	2003	2006	2012	2017 target
Hydrogen costs	$/gge	5.15	4.80	3.70	<3.00
Electrolyser capital cost	$/gge ($/kW)	NA	1.2 (665)	0.70 (400)	0.30 (125)
Electrolyser energy efficiency	% (LHV)	NA	62	69	74
Central wind water electrolysis					
Parameters	Units	2006	2012	2017 target	
Hydrogen costs (plant gate)	$/gge	5.90	3.10	<2.00	
Electrolyser capital cost	$/gge ($/kW)	2.20 (665)	0.80 (350)	0.20 (109)	
Electrolyser energy efficiency	% (LHV)	62	69	74	
Biomass gasification/pyrolysis hydrogen production					
Parameters	Units	2005	2012	2017 target	
Hydrogen costs (plant gate)	$/gge	<2.00	1.60	1.10	
Total capital investment	$M	<194	150	110	
Energy efficiency	%	>35	43	60	
Solar-driven high-temperature thermochemical hydrogen production					
Parameters	Units	2008	2012	2017 target	
Hydrogen costs (HTTC)	$/gge H_2	10.00	6.00	3.00	
Heliostat capital cost	$/m^2	180	140	80	
Process energy efficiency	%	25	30	>35	
Photochemical hydrogen production					
Parameters	Units	2003	2006	2013	2018 target
Usable semiconductor bandgap	eV	2.8	2.8	2.3	2.0
Chemical conversion process efficiency	%	4	4	10	12
Plant solar to hydrogen efficiency	%	NA	NA	8	10
Durability	h	NA	NA	1000	5000

Table 1.8 (*Continued*)

Distributed production of hydrogen from bioderived renewable liquids					
Parameters	**Units**	**2006**	**2012**	**2017 target**	
Photolytic biological hydrogen production from water					
Parameters	Units	2003	2006	2013	2017 target
Utilization efficiency of solar light energy	%	10	15	15	20
Efficiency of incident light energy to H_2 from water	%	0.1	0.1	2	5
Duration of continuous photoproduction	Time units	NA	NA	30 min	4 h
O_2 tolerance (half life in air)	Time units	1 s	1 s	10 min	2 h
Dark fermentation hydrogen production					
Parameters	Units	2003	2006	2013	2018
Yield of H_2 production from glucose	mol H_2/mol glucose	2	2	4	6
Feedstock cost	cents/lb sugar	13.5	13.5	10	8
Duration of continuous production	Time units	17 d	17 d	3 mo	6 mo
Photosynthetic bacterial hydrogen production					
Parameters	Units	2003	2006	2013	2018
Efficiency of incident solar light energy to H_2 from organic liquids	%	1.9	1.9	3.0	4.5
Molar yield of carbon conversion to H_2 (depends on nature of organic substrate	% of maximum	42	42	50	65
Duration of continuous photoproduction	Time units	6 d	6 d	30 d	3 mo

Source: Adapted from [18].

According to [43], 45–50 million tons of hydrogen are produced each year. The majority of this production comes from reforming of light hydrocarbons or oxidation of heavy hydrocarbons as depicted in Figure 1.11.

It has been noticed that hydrogen production from electrolysis represents a very small part of the total production (4%). The amount of hydrogen produced by the other technologies mentioned previously can be considered negligible.

Among all these different production means, some of them are practical from an industrial point of view (although of different maturity levels) and present the advantage to produce clean hydrogen and solve the environmental issues related to the production of hydrogen from reforming of light hydrocarbons or oxidation of heavy hydrocarbons. Water electrolysis, thermochemical transformation of biomass, photosynthetic microorganisms, photoelectrolysis of water and thermochemical cycles could be distinguish here. It is worth pointing out once again that electrolysis can be considered a sustainable way to produce hydrogen only if

Table 1.9 Overview of hydrogen production from different processes.

Process	Production costs (€/kg$_{H2}$)	Comments	Sources
Steam reforming of light hydrocarbons	[1.06; 2.08]		[28, 51, 52]
Partial oxidation of heavy hydrocarbons	[0.72; 1.41]	According to [53] hydrogen production cost from coal may drop down to 0.54 €/kg in the future thanks to R&D efforts (standardization of plant design and execution concept, improvements in reliability, gas cooler designs, etc.)	[28, 51–53]
Thermochemical transformation of biomass	[1.03; 5.39]	These costs are based on evaluations and mainly differ due to assumptions on biomass cost and on the use of either a pilot plant or an industrial plant	[51, 54, 55]
Photosynthetic microorganisms	[0.40; 9.47]	These costs are based on evaluations and disparities mainly depend on assumptions on hydrogen storage capacity, requirement for compression or cost of photobioreactor	[56]
Photoelectrolysis of water	[1.07; 13.5]	These costs are based on evaluations and disparities mainly depend on assumptions on the process used, efficiency, plant lifetime and photoelectrochemical reactor cost	[42]
Thermal dissociation of water	—	The high temperature required for the dissociation reaction to take place requires very resistant materials. Because of these requirements this hydrogen production method is still in the research phase; as such, no solid estimate of costs can be made	—
Thermochemical cycles	[2.66; 9.40]	These costs estimates are based on the cadmium oxide and sulphur–iodine cycles. Disparities can be attributed to assumptions such as cost of electricity, capital cost and capacity factor	[57, 58]

the electricity used comes from renewable sources. Similarly, for thermochemical cycles to be qualified as a clean hydrogen production mean, the heat required must come from a renewable source or must be wasted heat from an industrial process.

Consequently, it is important to realize that local considerations play an important role in the final cost of the produced hydrogen (costs to import the required equipment, local costs of energy, etc.).

Table 1.10 Overview of hydrogen production costs from electrolysis.

Electrolysis technology	Production costs (€/kg H_2)	Comments	Sources
Alkaline and PEM	[1.94; 8.60]	These costs mainly differ due to assumptions on: – The size of the electrolyser (from 100 W to several megawatts) – The origin and cost of electrical energy (direct coupling with wind electricity, PV electricity, grid electricity, etc.) The efficiency of the electrolyser (technology, system design, etc.)	[59–64]
High temperature	[2.00; 3.5]	These costs are based on evaluations with nuclear energy as electricity and heat sources. Variations in costs depend on the nature of the nuclear reactor and assumptions on performances and durability	[65–67]

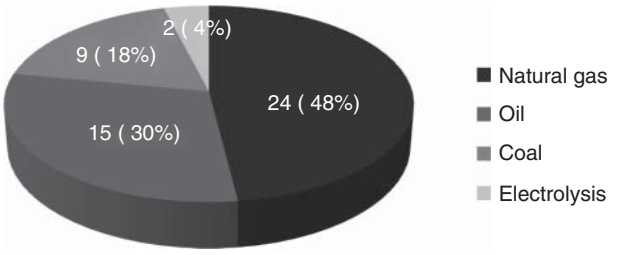

Figure 1.11 Estimated world hydrogen production in million tonnes per year in 2008.

Furthermore, it is worth mentioning that the difficulty in comparing different production means rises from the fact that the obtained product (hydrogen) may have different characteristics in terms of pressure and purity. Some industrial processes may require very pure hydrogen, which, for example, cannot come directly from a steam reforming installation without a purification step. Similarly, some applications may require pressurized hydrogen. For example, in order to reduce the tank size in hydrogen vehicles, hydrogen is stored at high pressure, requiring a compressor to reach 350 or 700 bars. Consequently, comparing different means of hydrogen production would require the definition of a common functional unit that comprises not only a unit of mass of hydrogen (e.g. 1 kg) but also specifications in terms of pressure and purity.

In addition to costs it is essential to also consider a contribution of primary energy conversion processes to greenhouse gases emissions, which at the end

lead to climate change. No doubt CO_2 is the most dominant gas with the maximum influence on climate changes, followed by methane (CH_4), N_2O and fluorine gases (hydrofluorocarbons – HFCs, perfluorocarbons – PFCs and sulphur hexafluoride – SF_6). Global warming potentials (GWPs) of different greenhouse gases as a function of time (20, 100 and 500 years horizon) have been summarized by Stolten *et al.* [68]. When looking at the CO_2 emission status, the majority comes from the energy sector at 37% with a significant share of electricity generation, which accounts for a share of 30%. Eleven percent of emissions comes from the residential sector and about 31% is generated by industry (19%), trade and commerce (4%) and agriculture (8%) [68].

As shown in Figure 1.9 [69], hydrogen production from natural gas and especially from coal (about 550 g CO_2/kWh H_2) generates a significant amount of CO_2. The CO_2 capture and sequestration (CCS) process can significantly reduce the level. Emissions from nuclear or solar energy tend to zero level. Because of the maturity level of the industry, hydrogen production from natural gas has the lowest costs; slightly higher costs can be observed for hydrogen generated from coal, whereas the expenses associated with generating energy from renewable fuels are rather high as the technologies are still not fully developed to enter market levels. Because of the current goal to reduce greenhouse and hazardous emissions only

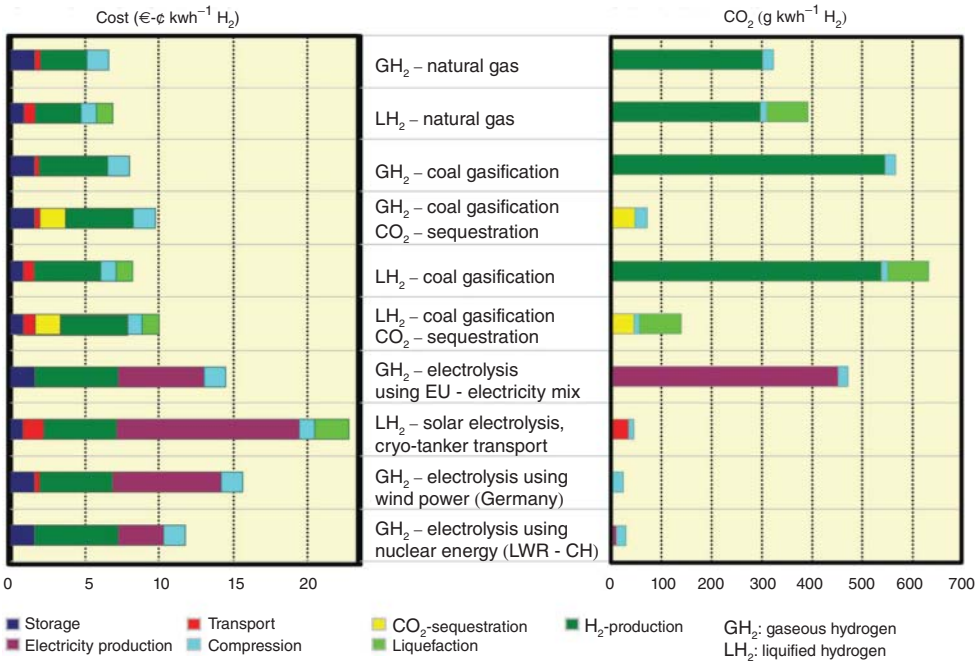

Figure 1.12 Hydrogen costs and CO_2 emissions per kWh H_2 from selected hydrogen production from non-renewable (natural gas, coal) and renewable sources (solar and nuclear) [69].

renewable or carbon-reduced energy carriers can be viewed as a long-term option for the future energy sector (Figure 1.12).

Hydrogen production based on renewable energy sources significantly increases costs when compared with conventional fuels. In Germany, for example, hydrogen produced from biomass is tax free, that from regenerative electricity is tax exempt, whereas hydrogen as fuel is taxed at the mineral oil tax rate for natural gas, which is 13.9 €/MWh, and this rate will continue until 2020 [8]. As can be seen in Figure 1.13, almost two-thirds of Germans encourage the production of hydrogen in an environmentally friendly way. The general opinion is that hydrogen must be green from the beginning in order to contribute to reducing CO_2 emissions in the transport sector. A majority would also prefer hydrogen production in a decentralized way [19].

On the basis of the analysis of hydrogen energy technologies in autonomous power systems [70] it seems that autonomous systems not interconnected to the main grid power systems will be the first market application, where hydrogen can be technically and economically feasible and viable for short-term use. The study has shown that the most suitable way for the production of hydrogen for autonomous power systems is water electrolysis based on renewable energy sources, then reforming of biofuels, followed by the reforming of fossil fuels.

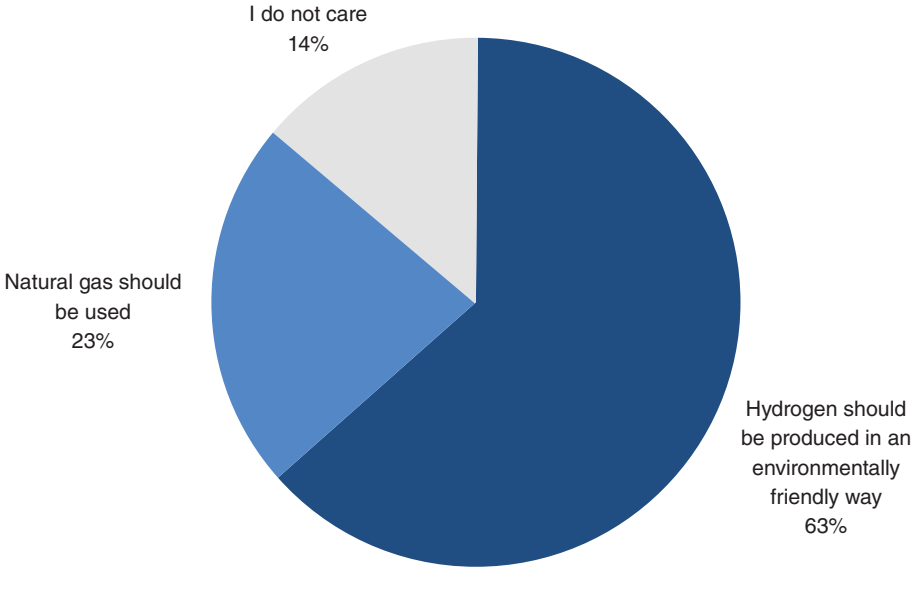

Figure 1.13 Expectations of the Germans with regard to the environmentally friendly production of hydrogen (Survey 01/2013, $n = 1012$) [19]. (By permission of the EFCF Luzern 2013, *www.efcf.com*.)

References

1. Rifkin, J. (2002) *The Hydrogen Economy. The Creation of the Worldwide Energy Web and the Redistribution of Power on Earth*, Penguin Group (USA) Inc., New York, ISBN: 1-58542-193-6.
2. Van Nostrand, R. (2005) *Encyclopaedia of Chemistry*, 5th edn, John Wiley & Sons, Inc., Hoboken, NY, ISBN: 0-471-61525-0.
3. Zabetakis, M.G. (1965) *Flammability Characteristics of Combustible Gases and Vapors*, Bulletin 627, U.S. Department of the Interior, Bureau of Mines.
4. HySafety. Biennial Report on Hydrogen, *http://www.hysafe.org/BRHS* (accessed 4 September 2014).
5. Molkov, V. (2007) Hydrogen safety research: state-of-the-art. Proceedings of the 5th International Seminar on Fire and Explosion Hazards, Edinburgh, Scotland, 2007, pp. 28–43.
6. Kuchta, J.M. (1985) *Investigation of Fire and Explosion Accidents in the Chemical, Mining and Fuel Related Industries*, vol. **680**, Bulletin/U.S Department of the Interior, Bureau of Mines.
7. Adamson, K.-A. and Pearsons, P. (2000) Hydrogen and methanol: a comparison of safety, economics, efficiences and emissions. *J. Power Sources*, **86**, 548–555.
8. Hake, J.-F., Linssen, J., and Walbeck, M. (2006) Prospects for hydrogen in the German energy system. *Energy Policy*, **34**, 1271–1283.
9. L-B Systemtechnik GmbH (2004) European Integrated Hydrogen Project – Phase 2 Joint Final Technical Report 36 Month, Publishable Version, 30 April 2004. ENK6-CT2000-00442, L-B Systemtechnik GmbH.
10. Zoulias, E.I. (2008) Techno-economic analysis of hydrogen technologies integration in existing conventional autonomous power Systems – case studies, in *Hydrogen Based Autonomous Power Systems* (eds N. Lymberopoulos and E.I. Zoulias [Buchverf.]), Springer, London. ISBN: 978-1-84800-246-3.
11. MacCurdy, G.G. (1924) *Human Origins: A Manual of Prehistory*, D. Appleton and Company, New York.
12. Ogden, J. (2013) Introduction to a future hydrogen infrastructure, in *Transition to Renewable Energy Systems* (eds D. Stolten and V. Scherer [Buchverf.]), Wiley-VCH Verlag GmbH & Co. KGaA, Weinheim, ISBN: 978-3-527-33239-7.
13. Galindo, J.I. (2010) Transitioning to the future of hydrogen mobility, in *Sustainable Automotive Technologies 2010: Proceedings of the 2nd International Conference* (eds A. Subic, M. Leary, and J. Wellnitzeds [Buchverf.]), Springer-Verlag.
14. Lucchese, P. (2013) Low FCEV and infrastructure deployment: what could be learned from early stages of electric infrastructures in France for rechargeable vehicles. 4th European PEFC and H2 Forum, Luzerne, Switzerland, July 2–5, 2013.
15. US Department of Energy (2009) Targets for Onboard Hydrogen Storage Systems for Light-Duty Vehicles, September 2009, *http://www1.eere.energy.gov/hydrogenandfuelcells/storage/pdfs/targets_onboard_hydro_storage_explanation.pdf* (accessed 4 September 2014).
16. HyWays *www.hyways.de* (accessed 4 September 2014).
17. European Commission (2008) HYWAYS – The European Hydrogen Roadmap. Contract No. SES6-502596.
18. US Department of Energy (2007) Hydrogen, Fuel Cells and Infrastructure Technologies Program Multi-Year Research, Development and Demonstration Plan Planned Program Activities for 2005–2015, October 2007. DOE/GO-102007-2430.
19. Zimmer, R., Welke, J., and Kaiser, M. (2013) Full steam ahead? Public acceptance of hydrogen technology. 4th European PEFC and H2 Forum, Luzerne, Switzerland, 2–5 July 2013.
20. Godula-Jopek, A., Jehle, W., and Wellnitz, J. (2012) *Hydrogeh Storage Technologies. New Materials, Transport and Infrastructure*, Wiley VCH Verlag & Co. KGaA, Weinheim, ISBN: 978-527-32683-9.

21. Hocevar, S. and Summers, W. (2008) Hydrogen production, in *Hydrogen Technology. Mobile and Portable Applications* (ed. A. Leon [Buchverf.]), Springer-Verlag, Berlin, Heilderberg, ISNB: 978-3-540-79027-3.
22. Sorensen, B. (2005) *Hydrogen and Fuel Cells*, Elsevier Academic Press, ISBN: 0-12-655281-9.
23. Mergel, J., Carmo, M., and Fritz, D. (2013) Status on technologies for hydrogen production by water electrolysis, in *Transition to Renewable Energy Systems* (eds D. Stolten and V. Scherer [Buchverf.]), Wiley VCH & Co. KGaA, Weinheim, ISBN: 978-3-527-33239-7.
24. Agrafiotis, C., von Storch, H., Roeg, M., and Satter, C. (2013) Hydrogen production by solar thermal methane reforming, in *Transition to Renewable Energy Systems* (eds D. Stolten and V. Scherer [Buchverf.]), Wiley VCH & Co. KGaA, Weinheim, ISBN: 978-3-527-33239-7.
25. F. Muller-Langer, A. Grongroft, S. Majer, S. O"Keeffe and M. Klemm. Options for biofuel production – status and perspectives D. Stolten and V. Scherer [Buchverf.]. *Transition to Renewable Energy Systems.* Weinheim Wiley VCH & Co. KGaA, ISBN: 978-3-527-33239-7, 2013.
26. Millet, P. (2012) Water electrolysis for hydrogen generation, in *Electrochemical Technologies for Energy Storage and Conversion*, vol. **2** (eds L. Zhang, X. Sun, H. Liu, J. Zhang, and R.-S. Liu [Buchverf.]), Wiley-VCH Verlag & Co. KGaA, Weinheim, ISBN: 978-3-527-32869-7.
27. Kolb, G. (2008) *Fuel Processing for Fuel Cells*, Viley-VCH Verlag GmbH & Co, Weinheim, ISBN: 978-3-527-31581-9.
28. French Association of Hydrogen and Fuel Cell (2011) Production d'hydrogene a partir des procedes de reformage et d'oxidation partielle, Memento de l'hydrogene Fiche 3.1.1, French Association of Hydrogen and Fuel Cell.
29. Wieland, S., Melin, T., and Lamm, A. (2002) Membrane reactors for hydrogen production. *Chem. Eng. Sci.*, **57**, 1571–1578.
30. Ghenziu, A.F. (2002) Review of fuel processing for hydrogen production in PEM fuel cell systems. *Curr. Opin. Soild State Mater. Sci.*, **6**, 389–399.
31. Onsan, Z.I. (2007) Catalytic processes for clean hydrogen production from hydrocarbons. *Turk J. Chem.*, **31**, 531–550.
32. Liu, S., Takahashi, K., and Ayabe, M. (2003) Hydrogen production by oxidative methanol reforming on Pd/ZnO catalyst: effects of Pd loading. *Catal. Today*, **87**, 247–253.
33. Carmo, M., Fritz, D., Mergel, J., and Stolten, D. (2013) Water electrolysis for hydrogen production. Paving the way to renewables. 4th European PEFC and H2 Forum, Lucerne Switzerland, July 2–5, 2013.
34. Evans, R., Boyd, L., Elam, C., Czernik, S., French, R., Feik, C., Philips, S., Chaornet, E., and Patern, Y. (2003) Hydrogen from Biomass-Catalytic Reforming of Pyrolysis Vapors. FY 3003, Hydrogen, Fuel Cells, and Infrastructure Technologies, Progress Report, National Renevable Energy Laboratory.
35. Yeboah, Y.D., Bota, K.B., and Wang, Z. (2003) Hydrogen from Biomass for Urban Transportation. FY 2003, Hydrogen, Fuel Cells, and Infrastructure Technologies, Progress Report, National Renewablw Energy Laboratory.
36. Abedi, J., Yeboah, Y.D., Realff, M., McGee, D., Howard, J., and Bota, K.B. (2001) An integrated approach to hydrogen production from agricultural residues for use in urban transportation. Proceedings of the 2001 DOE Hydrogen Program Review, NREL/CO-570-30535, National Renewable Energy Laboratory.
37. Czernik, S., French, R., Evans, R., and Chornet, E. (2003) Hydrogen from Post-Consumer Residues. FY 2003, Hydrogen, Fuel Cells, and Infrastructure Technologies, Progress Report, National Renewable Energy Laboratory.
38. Bowen, D.A., Lau, F., Zabransky, R., Remick, R., Slimane, R., and Doong, S. (2003) Techno-Economic Analysis of Hydrogen Production by Gasification of Biomass. FY 2003 Progress Report, Hydrogen, Fuel Cells, and Infrastructure Technologies, National Renewable Energy Laboratory.

39. Ni, M., Leung, D.Y.C., Leung, M.K.H., and Sumathy, K. (2006) An overview of hydrogen production from biomass. *Fuel Process. Technol.*, **87**, 461–472.
40. Markov, S., Eivazova, E., and Stom, D. (2013) Bioreactors for hydrogen production. 4th European PEFC and H2 Forum, Luzerne, Switzerland, July 2–5th, 2013.
41. French Association of Hydrogen and Fuel Cell (2011) Photo-electrolyse de l'eau. Memento de l'Hydrogene Fiche 3.2.3, French Association of Hydrogen and Fuel Cell.
42. (2009) Technoeconomic Analysis of Photoelectrochemical (PEC) Hydrogen Production. Deliverable Task 5.1: Draft Project Final Report, Directed Technologies Inc.
43. French Association of Hydrogen and Fuel Cell (2012) Production d'hydrogene par dissociation de l'eau partir d'un reacteur nucleaire. Memento de l'Hydrogene Fiche 3.2.2, French Association of Hydrogen and Fuel Cell.
44. Marchetti, C., Spitalnik, J., Hori, M., Herring, J.S., O'Brien, J.E., Stoots, C.M., Lessing, P.A., Anderson, R.P., Hartvigsen, J.J., Elangovan, S., Vitart, X., Martinez Val, J.M., Talavera, J., Alonso, A., Miller, A.I., and Wade, D.C. (2004) *Nuclear Production of Hydrogen – Technologies and Perspectives for Global Deployment*, International Nuclear Societies Council, ISBN: 0-89448-570-9.
45. Evers, A.A. (2009) A new approach to a flexible power system. 8th European Fuel Cell Forum, Luzerne, PA, 2009. C0007-Abstract 001.
46. Neises, M. (2011) *Investigations of Mixed Oron Oxides Coated on Ceramic Honeycomb Structures for Thermochemical Hydrogen Production*, VDI Verlag GmbH, Dusseldorf, ISBN: 0178-3-138-392103-4.
47. Ashokkumar, M. (1998) An overview on semiconductor particulate systems for photoproduction of hydrogen. *Int. J. Hydrogen Energy*, **23** (6), 1–14.
48. Meng, N., Leung, M.K.H., Leung, D.Y.C., and Sumathy, K. (2007) A review and recent developments in photocatalytic water-splitting using TiO2 for hydrogen production. *Renew. Sustain. Energy Rev.*, **11**, 401–425.
49. Pokrant, S., Maegli, A., Trottmann, M., Sagarna, L., Otal, E., Hisatomi, T., Steier, L., Grätzel, M., and Weidenkaff, A. (2013) Photocatalytic water splitting with modified LaTiO2N. 4th European PEFC and H2 Forum, Luzerne, Switzerland.
50. Dincer, I. and Naterer, G. (2010) Novel hydrogen production technologies and applications, editorial. *Int. J. Hydrogen Energy*, **35**, 4787.
51. Carbon Counts (2010) CCS Roadmap for Industry: High Purity CO2 Sources, Sectoral Assessment – Final Draft Report, 025 CCS Roadmap for Industry, Carbon Counts Company (UK) Ltd.
52. US DOE (2012) Hydrogen Production Cost Using Low-Cost Natural Gas, US Department of Energy, Record 12024.
53. Brown, B. *http:/hamptonroadshydrogen.com* (accessed 01 April 2014).
54. French Association of Hydrogen and Fuel Cell (2003) Production de bio-hydrogene par transformation thermochimique de la biomasse. Memento de l'Hydrogene Fiche 3.3.1, French Association of Hydrogen and Fuel Cell.
55. US National Renewable Energy Laboratory (2011) Hydrogen Production Cost Estimate Using Biomass Gasification, NREL/MP-560-35593, US National Renewable Energy Laboratory.
56. US National Renewable Energy Laboratory (2004) Updated Cost Analysis of Photobiological Hydrogen Production from Chlamydomonas Reinhardtii Green Algae, NREL/MP-560-35593, US National Renewable Energy Laboratory.
57. (2011) Solar Thermochemical Hydrogen Production Research (STCH), SAND 2011–3622, Sandia National Laboratories.
58. Baerecke, T., Mansilla, C., Avril, S., Bouchon-Meunier, B., Detyniecki, M., and Werkhoff, F. (2011) Fuzzy sets for assessing the profitability of hydrogen production by the sulphur-iodine thermochemical cycle. *Int. J. Hydrogen Energy Environ. Econ.*, **19** (1–2) 119–132.
59. (2008) The Impact of Increased Use of Hydrogen on Petroleum Consumption and Carbon Dioxide Emissions.

SR/IOAF-CNEAF/2008-04, US Energy Information Administration.

60. French Association of Hydrogen and Fuel Cell (2006) Etude Technico-Economique Prospective sur le cout de l'Hydrogene. Memento de l'Hydrogene Fiche 3.3.1, French Association of Hydrogen and Fuel Cell.
61. Current (2009) State-of-the-Art Hydrogen Production Cost Estimate Using water Electrolysis. NREL/BK-6A1-46676, US National Renewable Energy Laboratory.
62. Wind Electrolysis (2011) Hydrogen Cost Optimisation, NREL/TP-5600-50408, US national Renewable Energy Laboratory.
63. ITM Power. Hydrogen Costs Below EU 2015 Targets. *http:/www.itm-power.com/news-item/hfuel-cost-structure* (accessed 01 April 2014).
64. FCH JU (2014) Development of Water Electrolysis in the European Union, Fuel Cells and Hydrogen Joint Undertaking.
65. Hauch, A., Ebbesen, S.D., Jensen, S.H., and Mogensen, M. (2008) Highly efficient high temperature electrolysis. *J. Mater. Chem.*, **18**, 2331–2340.
66. Int. En. Agency (2008) Task 25: High Temperature Hydrogen Production Process, International Energy Agency, IEA/HIA.
67. Rivera-Tinoco, R. and Mansilla, C. (2008) Hydrogen production by high temperature electrolysis coupled with EPR, SFR or HTR: techo-economic study and coupling possibilities. *Int. J. Nucl. Hydrogen Prod. Appl.*, **1**, 249–266.
68. Stolten, D., Edmonds, B., Grube, T., and Weber, M. (2013) Hydrogen as an enabler for renewable energies, in *Transition to Renewable Energy Systems* (eds D. Stolten and V. Scherer [Buchverf.]), Wiley-VCH Verlag GmbH & Co. KGaA, Weinheim, ISBN: 978-3-527-33239-7.
69. Winter, C.-J. (2009) Hydrogen energy – abundant, efficient, clean: a debate over the energy system of change. *Int. J. Hydrogen Energy*, **34**, S1–S52.
70. Zoulias, E.I. and Lymberopoulos, N. (2008) *Hydrogen-Based Autonomous Power Systems, Techno-Economic Analysis of the Integration of Hydrogen in Autonomous Power Systems*, Springer-Verlag, London. ISBN: 978-1-84800-246-3.

2
Fundamentals of Water Electrolysis

Pierre Millet

2.1
Thermodynamics of the Water Splitting Reaction

2.1.1
Thermodynamic Functions of State

Liquid water can be dissociated into its elemental components (molecular hydrogen and oxygen) according to:

$$H_2O(l) \rightarrow H_2(g) + \frac{1}{2} O_2(g) \tag{2.1}$$

In standard conditions of temperature and pressure ($T° = 298$ K, $P° = 1$ bar), water is liquid and H_2 and O_2 are gaseous. Enthalpy, entropy and free (Gibbs) energy standard changes for reaction (2.1) are, respectively [1]:

$$\Delta H_d°(H_2O(l)) = +285.840 \text{ kJ mol}^{-1}$$

$$\Delta S_d°(H_2O(l)) = +163.15 \text{ J mol}^{-1} \text{ K}^{-1}$$

$$\Delta G_d°(H_2O(l)) = \Delta H_d°(H_2O(l)) - T \cdot \Delta S_d°(H_2O(l)) = +237.22 \text{ kJ mol}^{-1}$$

In spite of a favourable entropic contribution due to the formation of 1.5 mole of gaseous species, the enthalpy change is strongly endothermic and, as a result, the Gibbs free energy change is positive and the reaction is non-spontaneous.

Water vapour can also be dissociated into gaseous hydrogen and oxygen according to:

$$H_2O(vap) \rightarrow H_2(g) + \frac{1}{2} O_2(g) \tag{2.2}$$

Enthalpy, entropy and free (Gibbs) energy standard changes for reaction (2.2) are respectively [2]:

$$\Delta H_d°(H_2O(vap)) = +241.80 \text{ kJ mol}^{-1}$$

$$\Delta S_d°(H_2O(vap)) = +44.10 \text{ J mol}^{-1} \text{ K}^{-1}$$

$$\Delta G_d°(H_2O(l)) = \Delta H_d°(H_2O(l)) - T \cdot \Delta S_d°(H_2O(l)) = +228.66 \text{ kJ mol}^{-1}$$

Hydrogen Production: by Electrolysis, First Edition. Edited by Agata Godula-Jopek.
© 2015 Wiley-VCH Verlag GmbH & Co. KGaA. Published 2015 by Wiley-VCH Verlag GmbH & Co. KGaA.

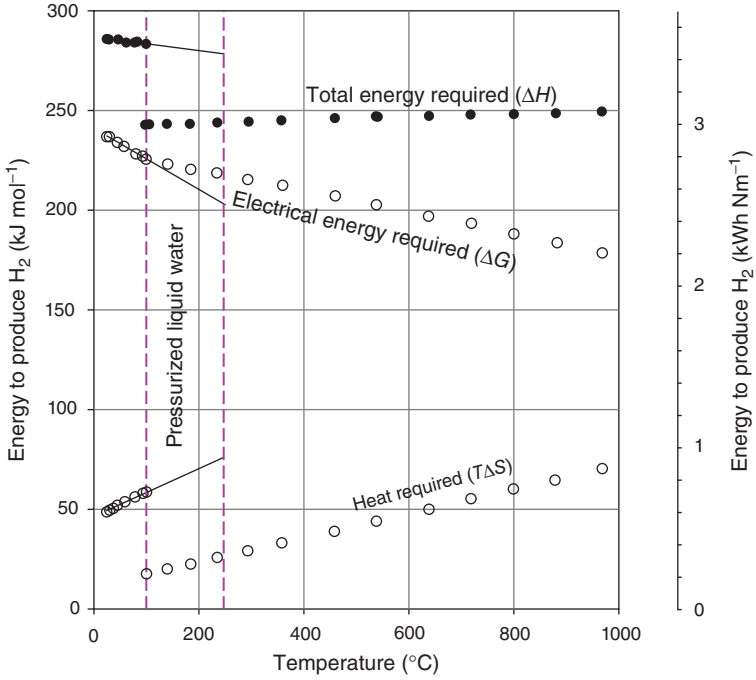

Figure 2.1 $\Delta G(T)$, $\Delta H(T)$ and $T\Delta S(T)$ of the water splitting reaction at $P = 1$ bar. (—) data for pressurized liquid water up to 250 °C.

$\Delta H_d{}^\circ(H_2O(l)) - \Delta H_d{}^\circ(H_2O(vap)) = +44.04$ kJ mol^{-1} is the difference of enthalpy change due to water vapourization (reaction 2.3) in standard conditions:

$$H_2O(l) \rightarrow H_2O(vap) \tag{2.3}$$

$\Delta S_d{}^\circ(H_2O(l)) - \Delta S_d{}^\circ(H_2O(vap)) = +119.05$ J mol^{-1} K^{-1} is the difference of entropy change due to water vapourization.

State function changes with temperature ($\Delta G(T)$, $\Delta H(T)$ and $T \cdot \Delta S(T)$) for reaction (2.1) at 1 bar are plotted in Figure 2.1. The total energy ΔH required to split 1 mole of water is almost constant over the entire temperature range of practical interest. The entropy change ΔS is also approximately constant and positive and the entropic contribution $T \cdot \Delta S$ increases with temperature. The Gibbs free energy change $\Delta G = \Delta H - T \cdot \Delta S$ is positive but decreases when increasing the operating temperature. ΔG becomes negative at high temperatures (>2500 K). Few if any materials can sustain such conditions and, therefore, the direct thermodissociation of water is not considered for practical applications. Discontinuities on $\Delta H(100\,°C, 1b)$ and $T \cdot \Delta S(100\,°C, 1b)$ observed at 100 °C are due to water vapourization. The magnitude of the enthalpy discontinuity is equal to the standard enthalpy of water vapourization ($\approx +45$ kJ mol^{-1}) and equal to the decrease of the entropic contribution. The slope difference of $T \cdot \Delta S(T)$, before and after

100 °C, reflects the entropy change after water vapourization. In Figure 2.1, solid lines between 100 and 250 °C show the situation for the electrolysis of liquid water above 100 °C (electrolysis of pressurized liquid water).

In conclusion, a higher operating temperature facilitates the dissociation of water by decreasing the electrolysis voltage. At room temperature, 15% of the total energy required for electrolysing water comes from heat and 85% from electricity. At 1000 °C, one-third comes from heat and two-third from electricity. This is why high-temperature water electrolysis is interesting when heat is available: electrolysis requires less electricity (which is more expensive than heat).

2.1.2
Selection Criteria for Operating Temperature

According to Figure 2.1, water electrolysis can be performed at different operating temperatures. The question is, What is the best temperature? At any operating temperature T, $\Delta H(T)$ is the total amount of energy that is required to split 1 mole of water, $\Delta G(T)$ is the amount of electrical work needed and $T \cdot \Delta S(T)$ is the heat demand. The following relationship is satisfied:

$$\Delta H(T,1) = \Delta G(T,1) + T \cdot \Delta S(T,1) \tag{2.4}$$

ΔH (the total amount of energy required to split 1 mole of water) is temperature-independent but the higher the operating temperature, the less electricity is required and the more heat can be used. A first criterion that can be used to select the operating temperature is the cost ratio of the kilowatt hours of electricity to the kilowatt hours of electricity, which is usually close to 3–5. Indeed, when heat is used in the industry to produce electricity, the overall efficiency is close to the Carnot efficiency, which is ≈30% in conventional systems. In Europe, the cost of industrial heat is ≈10–15 € MWh^{-1} and the cost of industrial electricity is ≈50–100 € MWh^{-1}. Therefore, operational expenses (opexs) are less for high-temperature electrolysis than for low-temperature electrolysis. As a result, the electricity consumption is higher at low temperature (4–6 kWh Nm^{-3} H_2 for PEM/alkaline technology (polymer electrolyte membrane = PEM)) than at high temperature (3.4 kWh Nm^{-3} H_2 for solid oxide water electrolysis (SOWE)). Another advantage of high-temperature water electrolysis is that it can potentially be used to value industrial heat wastes (200–300 °C is sufficient to vapourize liquid water, the heat of vapourization being a significant energy term in the water splitting reaction). A second criterion (the maturity of the technology) is less favourable to high-temperature technology, which is facing several problems (mostly from material science viewpoints, differential dilatation and interdiffusion phenomena being the source of high and still unacceptable degradation rates) and limitations (e.g. pressurized high-temperature water electrolysis cannot be envisioned in the near future due to severe leak management problems). A more detailed discussion on these issues is provided in the next sections.

2.1.3
Electrochemical Water Splitting

Thermodynamics tells us that the water splitting reaction is a non-spontaneous transformation. However, it can be driven externally by providing energy to the system, for example, electricity. This is a so-called endergonic transformation and the device used for the process is an electrolyser. An electrolyser contains at least one electrolysis cell. An electrolysis has two electrodes (electronic conductor) placed face to face and separated by a thin layer of ionic conductor (the electrolyte). In water electrolysis cells, electrical work is provided to the cell to split water molecules into gaseous hydrogen and oxygen. Half-cell reactions (and associated mechanisms) depend on electrolyte pH. In acidic media, water splitting occurs according to:

$$\text{anode}: \ H_2O(l) \rightarrow \frac{1}{2}O_2(g) + 2H^+ + 2e^- \tag{2.5}$$

$$\text{cathode}: \ 2H^+ + 2e^- \rightarrow H_2(g) \tag{2.6}$$

$$\text{full reaction}: \ H_2O(l) \rightarrow H_2(g) + \frac{1}{2}O_2(g) \tag{2.7}$$

Equation 2.5 is the oxygen evolution reaction (OER) and Equation 2.6 is the hydrogen evolution reaction (HER). In aqueous media, protons formed at the oxygen-evolving anode are solvated to form hydronium ions H_3O^+. Because of the electric field set across the cell, H_3O^+ species migrate through the electrolyte layer down to the cathode where they are reduced into molecular hydrogen while solvating water molecules are released. It terms of mass balance, there is a net consumption of water molecules at the anode and production of gases at each of the two-electrode/electrolyte interfaces. From the energy viewpoint and according to the first principle of thermodynamics, the amount of electricity (nFE) required at equilibrium to split 1 mole of water according to Equation 2.7 is equal to the Gibbs free energy change (ΔG_d) of the water dissociation reaction:

$$\Delta G_d - nFE = 0 \ \text{ where } \ \Delta G_d > 0 \tag{2.8}$$

where $n = 2$ is the number of electrons exchanged during the electrochemical splitting of one water molecule; $F \approx 96\,485 \ \text{C mol}^{-1}$ is the Faraday constant, that is, the electric charge of 1 mole of electrons; and E (in volts) is the free energy electrolysis voltage associated with reaction (2.7). ΔG_d (in J mol^{-1}) is the free energy change associated with reaction (2.7).

For transformations occurring at constant temperature T and pressure P, one can write:

$$\Delta G_d(T,P) = \Delta H_d(T,P) - T\,\Delta S_d(T,P) > 0 \tag{2.9}$$

$\Delta H_d(T,P)$, ΔS_d (T,P) and $\Delta G_d(T,P)$ are, respectively, the enthalpy change (in J mol^{-1}), the entropy change (in J mol^{-1} K^{-1}) and the Gibbs free energy change (in J mol^{-1}) of reaction (2.7) occurring at T and P. As shown with Figure 2.1, ΔG_d (J mol^{-1}) of electricity and $T \cdot \Delta S_d$ (J mol^{-1}) of heat are required to split 1 mole of water.

Two different thermodynamic voltages are usually used to characterize water electrolysis.

The free energy electrolysis voltage E in volts is defined as:

$$E\ (T,P) = \frac{\Delta G_{\mathrm{d}}\ (T,P)}{n\ F} \tag{2.10}$$

The enthalpy or thermo-neutral voltage V in volts is defined as:

$$V\,(T,P) = \frac{\Delta H\,(T,P)}{n\ F} \tag{2.11}$$

Different situations occur depending on the value of $U(T,P)$, the cell voltage applied to the electrolysis cell. For $U(T,P)\ E(T,P)$, electrolysis does not start. For $E(T,P) < U(T,P) < V(T,P)$, there is enough electricity to initiate the process but not enough to maintain isothermicity. Because an electrolysis cell is an open system, the cell tends to take the heat required by the process from the surroundings. If not, the internal temperature should decrease. In fact, current starts to flow for $U(T,P)\ >\ E(T,P)$ and heat is produced internally by different irreversibility sources. Also, there is no practical interest to perform electrolysis in this voltage range because current density is so low that capital expenses (capexs) would be by far too expensive. Finally, for $U(T,P)\ >\ V(T,P)$, the current density increases and increasing amounts of heat are produced.

Reference electrolysis voltages are usually calculated in standard conditions of temperature ($T^{\circ} = 298$ K) and pressure ($P^{\circ} = 1$ bar). Water is liquid, H_2 and O_2 are gaseous and standard free energy, enthalpy and entropy changes for reaction (2.7) are:

$$\Delta G_{\mathrm{d}}{}^{\circ}(\mathrm{H_2O}) = +237.22\ \mathrm{kJ\ mol^{-1}} \Rightarrow E^{\circ} = \frac{\Delta G_{\mathrm{d}}{}^{\circ}(\mathrm{H_2O})}{2F} = 1.2293\ \mathrm{V} \approx 1.23\ \mathrm{V}$$

$$\Delta H_{\mathrm{d}}{}^{\circ}(\mathrm{H_2O}) = +285.840\ \mathrm{kJ\ mol^{-1}} \Rightarrow\ V^{\circ} = \frac{\Delta H_{\mathrm{d}}{}^{\circ}(\mathrm{H_2O})}{2F} = 1.4813\ \mathrm{V} \approx 1.48\ \mathrm{V}$$

$$\Delta S_{\mathrm{d}}{}^{\circ}(\mathrm{H_2O}) = +163.15\ \mathrm{J\ mol^{-1}\ K^{-1}}.$$

It should be noted that the electrolysis of water vapour in standard conditions (this is a fictitious state because liquid water is stable in such conditions) is less than the value for liquid water:

$$\Delta G_{\mathrm{d}}{}^{\circ}(\mathrm{H_2O(vap)}) = +241.80\ \mathrm{kJ\ mol^{-1}} \Rightarrow\ E^{\circ}\ = \frac{\Delta G_{\mathrm{d}}{}^{\circ}(\mathrm{H_2O})}{2F} \approx 1.18\ \mathrm{V}.$$

2.1.4
pH Dependence of Water Dissociation Voltage

In acidic media, half-cell reactions are given by Equations 2.5 and 2.6. On the anodic side, using the Nernst equation, one obtains:

$$E^{+} = E_{\mathrm{H_2O/O_2}}{}^{\circ} + \frac{R_{\mathrm{PG}}\ T}{nF}\ \mathrm{Ln}\,\frac{(a^{2}_{\mathrm{H^+}})\ (f^{1/2}_{\mathrm{O_2}})}{a_{\mathrm{H_2O}}} \tag{2.12}$$

where a_{H^+} is the activity of protons in the electrolyte phase; f_{O_2} is the fugacity of oxygen in the anodic compartment and a_{H_2O} is the activity of water.

A simplified but still accurate expression can be obtained using the following simplifying assumptions:

- The acidic electrolyte is sufficiently diluted to assume that the activity coefficient of protons is close to unity; therefore, their activity is equal to their molar concentration and simply related to pH.
- Pure oxygen is evolved during electrolysis (effect of saturated water vapour is neglected) and fugacity is equal to partial pressure, which is equal to 1 bar.
- Activity of water is close to unity because the electrolyte is diluted (in 1 M proton solutions, there is 98% of water molecules).

On the basis of these three assumptions, Equation 2.12 simplifies into (the reference is the normal hydrogen electrode or NHE):

$$E^+ \approx 1.23 - 0.06\text{pH} \tag{2.13}$$

On the cathodic side:

$$E^- = E_{H_2/H^+}{}^\circ + \frac{R_{PG}\ T}{nF}\ \text{Ln}\frac{a^2_{H^+}}{f_{H_2}} \approx -\ 0.06\text{pH} \tag{2.14}$$

Using the same assumptions as before, at 298 K and when the pressure of hydrogen is 1 bar (ideal gas), Equation 2.14 simplifies into:

$$E^- \approx -0.06\text{pH} \tag{2.15}$$

Therefore, the cell voltage required to split water in acidic media is a constant independent of pH:

$$E_{cell} = E^+ - E^- = 1.23\ \text{V} \tag{2.16}$$

In alkaline media, the following half-cell reactions take place:

$$\text{anode}\ (+):\ 2\ OH^- \rightarrow\ H_2O\ +\ \frac{1}{2}\ O_2(g)\ +\ 2\ e^- \tag{2.17}$$

$$\text{cathode}\ (-):\ 2\ H_2O\ +\ 2\ e^- \rightarrow\ H_2(g)\ +\ 2\ OH^- \tag{2.18}$$

$$\text{full reaction}:\ H_2O(l) \rightarrow\ H_2(g)\ +\ \frac{1}{2}\ O_2(g) \tag{2.19}$$

From the Nernst equation, it follows that:

$$E^+ = E_{H_2O/O_2}{}^\circ + \frac{R_{PG}\ T}{nF}\ \text{Ln}\frac{(a_{H_2O})\ (f^{1/2}_{O_2})}{a^2_{HO^-}} \tag{2.20}$$

At 298 K, when the pressure of oxygen is 1 bar (ideal gas), Equation 2.20 simplifies into:

$$E^+ \approx 1.23 + \text{pKe} - 0.06\text{pH}$$

On the cathodic side:

$$E^- = E_{H_2O/H_2}{}^\circ + \frac{R_{PG}\ T}{nF}\ \text{Ln}\frac{a^2_{H_2O}}{f_{H_2}\ a^2_{HO^-}} \tag{2.21}$$

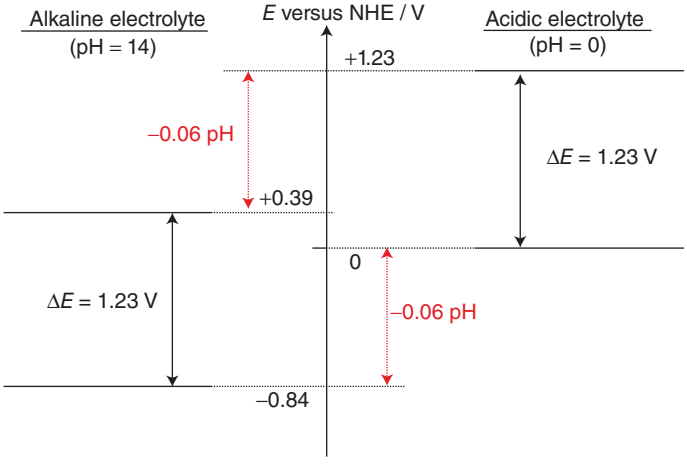

Figure 2.2 Electrode potential versus pH for the water splitting reaction.

At 298 K, when the pressure of hydrogen is 1 bar (ideal gas), Equation 2.21 simplifies into:

$$E^{-} \approx \mathrm{pKe} - 0.06\mathrm{pH} \tag{2.22}$$

Therefore, the voltage required to split water in alkaline media is:

$$E_{\mathrm{cell}} = E^{+} - E^{-} = 1.23\ \ \mathrm{V} \tag{2.23}$$

Therefore, the free energy electrolysis voltage required to split water into hydrogen and oxygen is pH independent. The only difference between alkaline and acidic media is that the potential of each electrode is shifted along the potential axis, as a function of electrolyte pH (Figure 2.2). Consequences are mostly on electrode material stability. In acidic media, most metals are corroded and, hence, platinum group metals (PGMs) are needed. This is usually unsupported platinum or carbon-supported platinum nano-particles for the HER and iridium dioxide for the OER. In alkaline media, nickel and cobalt are passivated and oxides/hydroxides are electrochemically active.

2.1.5
Temperature Dependence of Water Dissociation Voltage

As discussed above, enthalpy, entropy and free energy changes associated with the water splitting reaction are functions of both temperature and pressure (the two main experimental parameters in water electrolysis). As a result, thermodynamic voltages (enthalpy voltage and free energy voltage) are also functions of operating temperature and pressure, as well as energy efficiencies. Accurate determination of cell efficiency requires a quantitative knowledge of temperature and pressure dependencies of thermodynamic voltages. In the following, the discussion will focus on low-temperature processes.

Table 2.1 Coefficients used in Equations 2.26 and 2.27.

Element	*a*	*b*	*c*	*e*
H_2(g)	26.57	3.77	1.17	—
O_2(g)	34.35	1.92	−18.45	4.06

Under atmospheric pressure, liquid water is electrolysed in the 0–100 °C temperature range and water vapour above 100 °C. $\Delta H(T,1)$ and $\Delta G(T,1)$ are defined as:

$$\Delta H(T,1) = \frac{V(T,1)}{2\ F} = H_{H_2}(T,1) + \frac{1}{2}H_{O_2}(T,1) - H_{H_2O}(T,1) \tag{2.24}$$

$$\Delta G(T,1) = \frac{E(T,1)}{2\ F} = G_{H_2}(T,1) + \frac{1}{2}G_{O_2}(T,1) - G_{H_2O}(T,1) \tag{2.25}$$

Enthalpy and entropy formation of H_2(g) and O_2(g) can be obtained from the following polynomial expressions (coefficients are listed in Table 2.1):

$$H_i(T,1) - H_i^\circ = a(T - T_0) + \frac{b}{2}10^{-3}(T^2 - T_0^2) - c\,10^5\left(\frac{1}{T} - \frac{1}{T_0}\right) - \frac{e}{2}10^8\left(\frac{1}{T^2} - \frac{1}{T_0^2}\right) \tag{2.26}$$

$$S_i(T,1) - S_i^\circ = a(Ln\,T - Ln\,T_0) + b\,10^{-3}(T - T_0) - \frac{c}{2}10^5\left(\frac{1}{T^2} - \frac{1}{T_0^2}\right) - \frac{e}{3}10^8\left(\frac{1}{T^3} - \frac{1}{T_0^3}\right) \tag{2.27}$$

Water enthalpy and entropy of formation are obtained from the steam tables [2]. Data are plotted in Figure 2.1. They can be used directly to calculate $E(T,1)$ and $V(T,1)$. Some empirical expressions of $V(T,P)$ and $E(T,P)$ have also been reported in the literature [3]. They apply only to the electrolysis of liquid water (for $T > 100$ °C, at a pressure sufficiently high to avoid water vapourization).

$$V(T) = 2\ F\ \Delta H(T) = 1.485 - 1.49 \times 10^{-4} * (T - T^0) - 9.84 \times 10^{-8} * (T - T^0)^2 \tag{2.28}$$

$$E(T) = 2\ F\ \Delta G(T) = 1.5184 - 1.5421 \times 10^{-3} * T + 9.523 \times 10^{-5} * T * \mathrm{Ln}(T) + 9.84 \times 10^{-8}\ T^2 \tag{2.29}$$

$E(T)$ and $V(T)$ from Equations 2.28 and 2.29 are plotted in Figure 2.3. Trends are of course similar to those of $\Delta G(T)$ and $\Delta H(T)$. The free energy electrolysis voltage $E(T)$ decreases from 1.23 V at 25 °C down to 1.18 V at 100 °C and down to ≈0.9 V at 1000 °C.

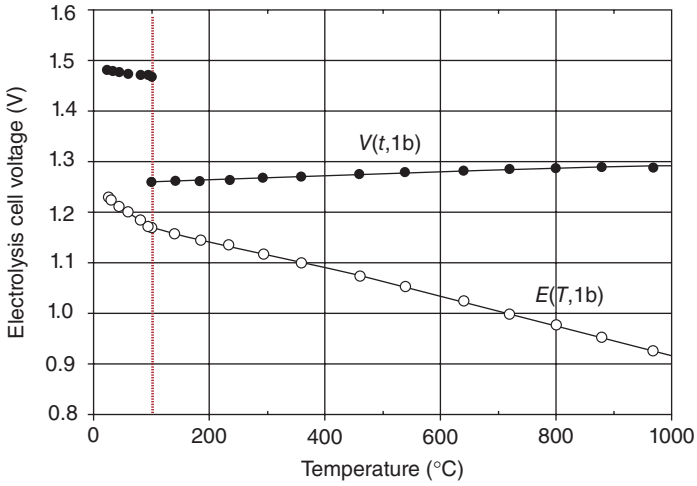

Figure 2.3 Role of operating temperature on the free energy electrolysis voltage $E(T)$ and the enthalpy electrolysis voltage $V(T)$ of water ($P = 1$ bar).

From a practical viewpoint, the maximum temperature accessible to low-temperature technology (≈100–130 °C) comes from material constraints and not from the vapourization of water, which can be easily managed by appropriate pressurization. In PEM technology, for instance, the maximum temperature is 90 °C (as in fuel cell applications) because hydrated polymers (such as perfluorosulphonic Nafion® [4]) lose all mechanical stability above 100 °C. Even if the domain of operating temperature can be extended up to +150 °C using more stable materials (e.g. with short side chains materials originally developed at Dow Chemicals or PBI-based materials), high operating temperatures always negatively impact the stability and durability of membrane-electrode assemblies (MEAs) and catalytic layers.

2.1.6
Pressure Dependence of Water Dissociation Voltage

Hydrogen storage for either mobile or stationary applications is a critical issue. Among different processes, the storage of compressed hydrogen is probably the simplest and most straightforward one. Pressurized vessels that can sustain pressures as high as 700 bars are already available for application in the automotive industry. To fill such tanks with hydrogen of electrolytic grade, there are two options. The first one is to perform water electrolysis at atmospheric pressure and then to compress gaseous hydrogen up to the desired value using an external compressor. The second one is to develop pressurized water electrolysers that can directly deliver pressurized hydrogen at the value of interest (direct electrochemical compression). Different parameters (capex, opex, efficiency) need to be considered to identify the best option. To compare the two processes

more accurately, it is necessary to evaluate the role of operating pressure on the thermodynamics and the kinetics of the water splitting reaction (taking into account the energy required for the injection of liquid water at atmospheric pressure into the pressurized electrolyser). Usually, the best solution is a hybrid one: pressurized electrolysers deliver compressed hydrogen at medium pressure value (15–50 bars) and then the target pressure is reached by mechanical compression. This is because compression energy requirements are more significant at low pressure than at elevated pressure. Although pressurized alkaline water electrolysis is commonly used in the industry (with operating pressure in the 1–50 bar range), the discussion provided in the following is mainly based on PEM water electrolysis for which prototypes operating at very high pressure (several hundred bars) have already been developed and successfully tested.

2.1.6.1 General Pressure Dependence

From basic thermodynamic considerations, the pressure dependence of the free energy electrolysis voltage E is:

$$\left(\frac{\partial E}{\partial P}\right)_{\mathrm{T}} = \frac{1}{nF}\left(\frac{\partial \Delta G}{\partial P}\right)_{\mathrm{T}} = \frac{\Delta \overline{V}}{nF} \tag{2.30}$$

where $\Delta \overline{V}$ is the change of molar volume associated with the compression. Considering the fact the effect of pressure on the volume of condensed phases is small, $\Delta \overline{V}$ can be written by considering only gaseous species. At low pressures, the law of ideal gases prevails (for higher pressure, more accurate state equations are required) and:

$$\Delta \overline{V} = \sum_i \nu_i \frac{R_{\mathrm{PG}}\ T}{p_i} \tag{2.31}$$

where p_i is the partial pressure of species i and ν_i is the stoichiometric factor. Therefore:

$$\left(\frac{\partial E}{\partial P}\right)_{\mathrm{T}} = \sum_i \nu_i \frac{R_{\mathrm{PG}}\ T}{nFp_i} \equiv \sum_i \left(\frac{\partial E}{\partial p_i}\right)_{\mathrm{T}} \tag{2.32}$$

Integration of Equation 2.32 gives:

$$E = E^{\circ} + \sum_i \nu_i \left(\frac{R_{\mathrm{PG}}\ T}{nF}\right) \mathrm{Ln}\left(\frac{p_i}{p^{\circ}}\right) \tag{2.33}$$

Application of Equation 2.33 to water electrolysis yields:

$$E = E^{\circ} + \frac{R_{\mathrm{PG}}\ T}{2F} \mathrm{Ln}\left(\frac{p_{\mathrm{H_2}}}{p^0} \cdot \sqrt{\frac{p_{\mathrm{O_2}}}{p^{\circ}}}\right) \tag{2.34}$$

Let P be the pressure of operation (PEM cells can be operated under a difference of pressure but this case is not considered here). In the case of water electrolysis (almost) pure hydrogen and oxygen are evolved in each compartment. Main impurities are water (saturation at the temperature T of operation), traces of oxygen in hydrogen and of hydrogen in oxygen due to cross-permeation effects and traces

of KOH in the alkaline process. Neglecting the effect of these impurities, then $p_{O_2} = P$ at the anode and $p_{H_2} = P$ at the cathode, and the following relationship is obtained:

$$E = E^{\circ} + \frac{3R_{PG}\ T}{4F}\,\mathrm{Ln}\,(P) \tag{2.35}$$

When the electrolysis pressure changes from P_1 to P_2, then the cell voltage changes by ΔE:

$$\Delta E = \frac{3\ R_{PG}\ T}{4F}\,\mathrm{Ln}\left(\frac{P_2}{P_1}\right) \tag{2.36}$$

In Equation 2.36, setting the reference pressure P_1 at 1 bar, one obtains:

$$E(T,P) = E(T,1) + \frac{3\ R_{PG}\ T}{4\ F}\,\mathrm{Ln}\,(P) \tag{2.37}$$

The free energy voltages (E) calculated from Equation 2.37 for different operating pressures at 298 and 373 K are plotted in Figure 2.4. More accurate calculations can be made using more elaborated state equations, in particular at pressures above 10 bars, when significant differences appear with the law of ideal gas [5]. Figure 2.4 shows that the additional energy cost due to electrochemical compression (approximately 120 mV at 298 K from 1 to 60 bars) remains significantly less than charge transfer overvoltages which appear during operation at high current density (especially the anodic overvoltage of approximately 400–800 mV at 1 A cm^{-2}). This is why electrochemical compression is attracting interest, although the impact on capexs can be quite significant.

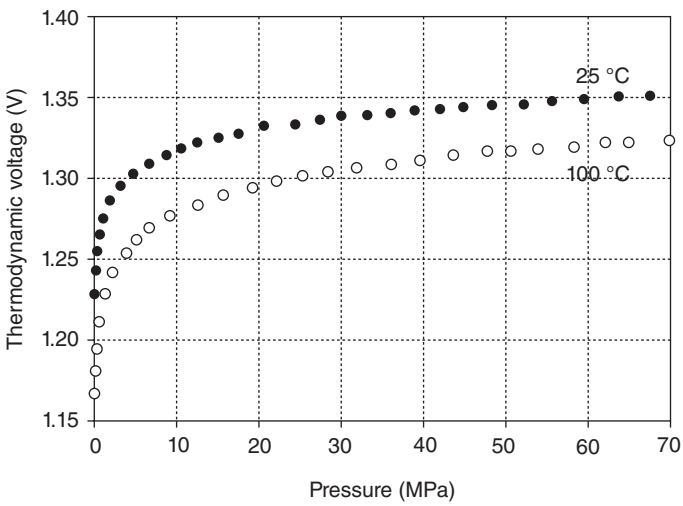

Figure 2.4 Plot of the free energy voltage of water electrolysis as a function of pressure for three different operating temperatures. Data based on the assumption of ideal gases.

2.1.6.2 Detailed Pressure Dependence

Equation 2.37 provides a simple and good approximation for $E(T,P)$ for low pressures (<10 bars). More accurate calculations are required using more elaborated state equations for operating pressure above 10–15 bars. Such expressions can be obtained from the values of $V(298,1)$ and $E(298,1)$ as follows.

$$\Delta H(T,P) = H_{H_2}(T,P) + \frac{1}{2}H_{O_2}(T,P) - H_{H_2O}(T,P) \tag{2.38}$$

$$\Delta S(T,P) = S_{H_2}(T,P) + \frac{1}{2}S_{O_2}(T,P) - S_{H_2O}(T,P) \tag{2.39}$$

$$\Delta G(T,P) = \Delta H(T,P) - T.\Delta S(T,P) = G_{H_2}(T,P) + \frac{1}{2}G_{O_2}(T,P) - G_{H_2O}(T,P) \tag{2.40}$$

$H_i(T,P)$, $S_i(T,P)$ and $G_i(T,P)$ values are obtained in two steps, first by calculating the effect of temperature at constant pressure of 1 bar, then by calculating the pressure effect at target temperature:

$$H_i(T,P) = [H_i(T,P) - H_i(T,1)] - [H_i(T,1) - H_i(298,1)] \tag{2.41}$$

$$S_i(T,P) = [S_i(T,P) - S_i(T,1)] - [S_i(T,1) - S_i(298,1)] \tag{2.42}$$

$$G_i(T,P) = [G_i(T,P) - G_i(T,1)] - [G_i(T,1) - G_i(298,1)] \tag{2.43}$$

Enthalpy and entropy of H_2(g) and O_2(g) formation under 1 bar pressure are obtained from Equations 2.26 and 2.27. Enthalpy and entropy of H_2O(l) formation under 1 bar pressure are obtained from the steam tables [2]. The role of operating pressure is taken into account as follows. Usually, the classical virial expansion (introduced in 1901 by H. Kamerlingh Onnes as a generalization of the ideal gas law) is used to express the pressure of a many-particle system at equilibrium as a power series in the density. Virial coefficients B_i appear as coefficients in the virial expansion of the pressure, thus providing systematic corrections to the ideal gas law. They are characteristic of the interaction potential between the particles and in general depend on the temperature. The second virial coefficient depends only on the pair interaction between the particles, the third depends on two- and non-additive three-body interactions and so on. The pressure change of ΔH and ΔG is given by the following state equations:

$$H(T,P) - H(T,1) = \left(B - T\ \frac{\partial B}{\partial T}\right)\ P + \frac{C - B^2 - 0.5\ \ T\ \left[\frac{\partial C}{\partial T} - 2\ B\ \frac{\partial B}{\partial T}\right]}{R_{PG}\ T}\ P^2 \tag{2.44}$$

$$G(T,P) - G(T,1) = R_{PG}\ T\ \text{Ln}\ P + B\ P + \frac{C - B^2}{2\ R_{PG}\ T}P^2 \tag{2.45}$$

The virial constant B and C can be approximated as function of temperature:

$$B = b_1 + \frac{b_2}{T}\ \ (\text{cm}^3\ \ \text{mol}^{-1}) \tag{2.46}$$

Table 2.2 Coefficients used in Equations 2.46–2.49.

Compound	b_1	b_2	c_1	c_2
$H_2(g)$	20.5	−1857	−351	12 760
$O_2(g)$	42.6	−17 400	−2604	61 457

$$C = c_1 + \frac{c_2}{T^{\frac{1}{2}}} \quad (\mathrm{cm}^6\ \mathrm{mol}^{-2}) \tag{2.47}$$

$$\frac{\mathrm{d}B}{\mathrm{d}T} = -\frac{b_2}{T^2} \quad (\mathrm{cm}^3\ \mathrm{mol}^{-1}\ \mathrm{K}^{-1}) \tag{2.48}$$

$$\frac{\mathrm{d}C}{\mathrm{d}T} = -\frac{c_2}{T^{\frac{3}{2}}} \quad (\mathrm{cm}^6\ \mathrm{mol}^{-2}\ \mathrm{K}^{-2}) \tag{2.49}$$

$H_2(g)$ and $O_2(g)$ coefficients of viral constant for pressures up to 1000 atm are shown in Table 2.2:

Enthalpy and entropy changes of $H_2O(l)$ with pressure are obtained from the steam tables. $E(T,P)$ and $V(T,P)$ obtained from the above set of equations are plotted on Figures 2.5 and 2.6 at different operating temperatures [5].

A comparison of Figures 2.4 and 2.5 shows that the ideal gas assumption is useful to approximate the effect of pressure on the free energy voltage but not sufficient for accurate determination. Although the effect of pressure on the free energy voltage E is significant (+200 mV at 25 °C when the pressure is raised from 1 to

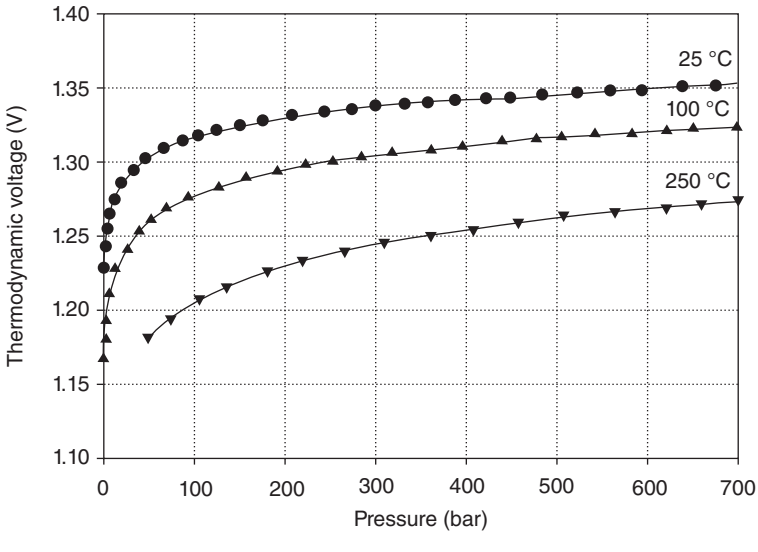

Figure 2.5 Plot of the free energy voltage $E(P)$ of water electrolysis as a function of pressure for three different operating temperatures.

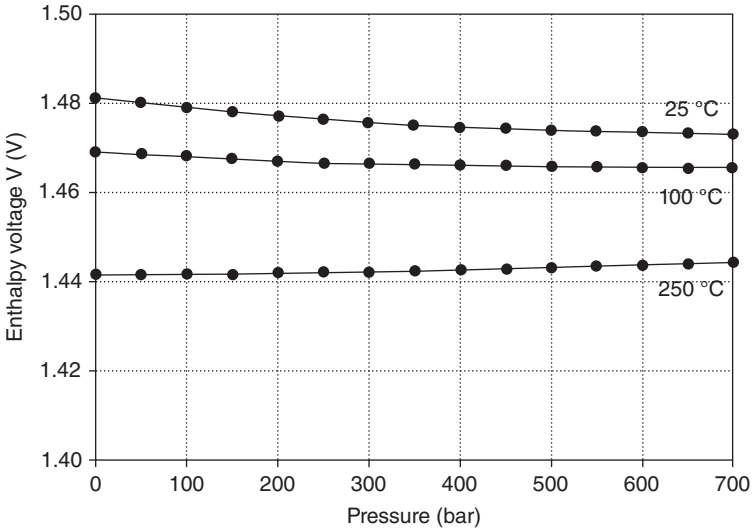

Figure 2.6 Plot of the enthalpy voltage $V(P)$ of water electrolysis as a function of pressure for three different operating temperatures.

700 bar), its effect on the enthalpy voltage V remains limited. The main conclusion from these more accurate data is the confirmation that the energy cost of electrochemical compression is very limited and remains significantly less than charge transfer overvoltages which appear during operation at high current density.

2.2 Efficiency of Electrochemical Water Splitting

2.2.1 Water Splitting Cells: General Characteristics

Electrolysers are devices used to perform endergonic transformations (non-spontaneous chemical reactions that absorb energy in the form of electrical work). Electrolysers contain several (up to hundreds) series-connected elementary electrolysis cells (usually filter-press configuration is preferred to increase compactness and reduce parasite ohmic losses). An electrolysis cell is basically a galvanic chain of planar geometry containing two metallic electrodes placed face to face and clamping a thin electrolytic layer (ions dissolved in liquid polar solvents or ion-conducting polymers or oxygen ion-conducting ceramic). In such electrochemical chains, there are two metal/electrolyte interfaces placed in series. During operation, a continuous current flows across the cell. In the external circuit up to the electrodes, the charge carriers are the electrons, and in the electrolyte, the charge carriers are mobile ions. Electrons can cross interfaces and induce redox transformations of interest (oxygen and hydrogen evolution

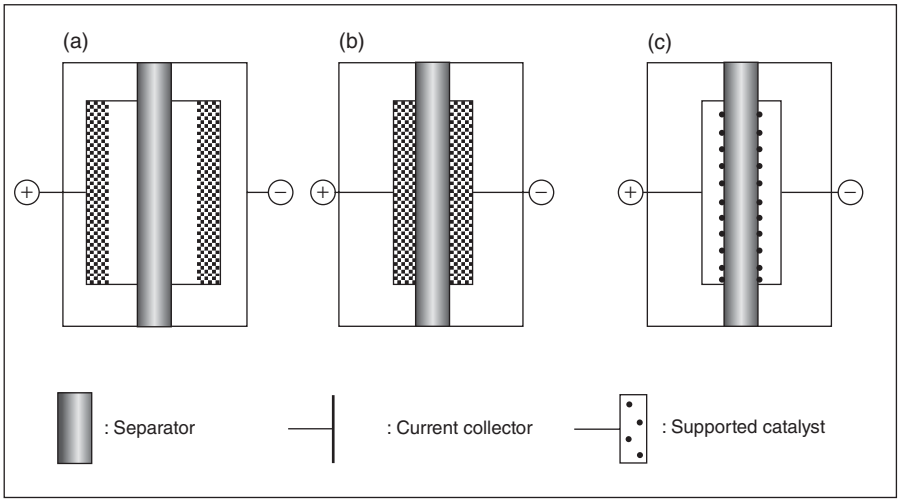

Figure 2.7 Two-dimensional schematic diagrams of (a) a gap cell; (b) a zero-gap cell and (c) a SPE (solid polymer electrolyte) cell.

in the case of water electrolysis). Basically, three different cell concepts are used in industrial devices (Figure 2.7). The first concept (Figure 2.7a) is called a '*gap cell*'. This is the most conventional and simple configuration in which two planar electrodes (usually a cheap electron-conducting substrate surface-covered by a thin layer of a more expensive electrocatalyst) are placed face to face in a liquid electrolyte. A separator (usually a porous diaphragm impregnated with the electrolyte) is introduced in the interpolar gap to prevent the spontaneous recombination of reaction products. In the case of water electrolysis, bubbles of gaseous species form at each interface. The distance between electrodes and diaphragm must be sufficiently large to let gases evolve freely but not too large to reduce ohmic losses. When bubble concentration increases, there is a tendency to form continuous and highly resistive gaseous films over electrode surfaces and therefore the maximum operating current density is usually limited (several hundred mA cm^{-2}) in this kind of cell. The situation can be somewhat improved using the second concept of cell (so-called 'zero-gap cell' shown in Figure 2.7b), which is more appropriate for gas-evolving electrodes. In such cells, porous electrodes are pressed directly onto the separator, to reduce as much as possible the distance between the anode and the cathode (and corresponding ohmic losses). Gaseous products are released through the pores at the backside. Significantly larger current densities can be reached without significant extra voltage losses. The concept is used in advanced and modern alkaline water electrolysers. However, a liquid electrolyte is still needed and this cell design is not appropriate for operation in acidic media. The third concept is called a '*PEM cell*' (Figure 2.7c). PEM stands for proton exchange membrane or polymer electrolyte membrane. The cell separator is a thin ion-conducting polymeric film that is used for the double purpose of conveying electric charges (protons in the case of PEM water electrolysis) from the

anode to the cathode and separating gas products. There is no liquid electrolyte in circulation in this kind of cell. This concept was first proposed for H_2/O_2 fuel cells in the 1950s, at the dawn of the US space programme, to solve the problems associated with the operation of electrochemical cells in a low-gravity environment and those due to the corrosion of metals in acidic media. The idea was used latter for the development of water electrolysers. In a PEM water electrolysis cell, porous catalytic layers are coated on each side of the membrane surface. Electric contacts are obtained by pressing porous current collectors on each side. There is no liquid electrolyte. Only de-ionized water is circulated in the anodic chamber to feed the electrochemical reaction. The same concept of cell is used at high temperature, the separator and electrolyte being a thin oxide-ion-conducting ceramic membrane.

It should be noted that, although more efficient than a liquid electrolyte cell, the PEM cell concept the PEM cell concept adds more geometrical constraints. In a zero-gap cell using a liquid electrolyte (water electrolysis alkaline technology), there is no need to accurately adjust the distance between cell components: the liquid electrolyte fills the entire interpolar region and ensures a homogeneous distribution of current lines. In a PEM cell, the situation is different. The electrolyte is confined inside the membrane. There is a need to adjust the thickness, surface state, dimension and position of all cell components very accurately. There is also a need to pay significant attention to the mechanics of the stack in order to ensure homogenous distributions of compression forces that are critically required for homogeneous distribution of current lines. This difference also contributes to make polymer electrolyte technology more expensive.

2.2.2
Main Sources of Energy Dissipation in Electrochemical Cells

The most significant part (>60%) of electricity supplied to an electrolysis cell is used for the Gibbs free energy change of the endergonic transformation of interest. However, there are several sources of energy degradation (electricity into heat) in a water electrolysis cell. Their magnitude and localization depend on the cell design. Figure 2.8 shows the cross section of a gap cell with liquid electrolyte and the associated distribution of electric potential during operation. Potential drops are located inside bulk electrodes due to internal resistance (1, 1′), across electroactive layers which are not always good electronic conductors (2, 2′), at interfaces where charge transfer processes take place (3, 3′), in solution, across the diffusion layers close to the electrode surface when mass transport phenomena are involved or gaseous species are formed (4, 4′), by transport of ions in the bulk electrolyte (5, 5′) and across the cell separator (6). A similar situation is found in zero-gap and in PEM cells.

Figure 2.9 shows the general shape of the polarization curve measured during water electrolysis at 25 °C, under 1 bar pressure. The free energy electrolysis voltage is 1.23 V. This is usually the most significant voltage contribution. Above this voltage value, current starts to flow across the cell. Additional electric power is

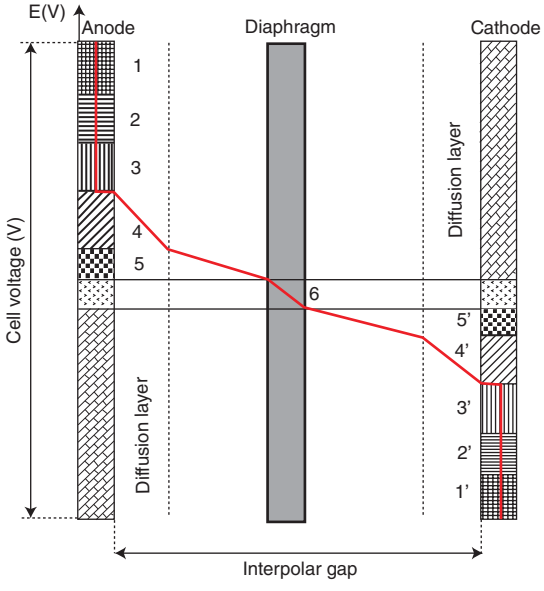

Figure 2.8 Schematic diagram of potential distribution in a gap cell water electrolysis cell.

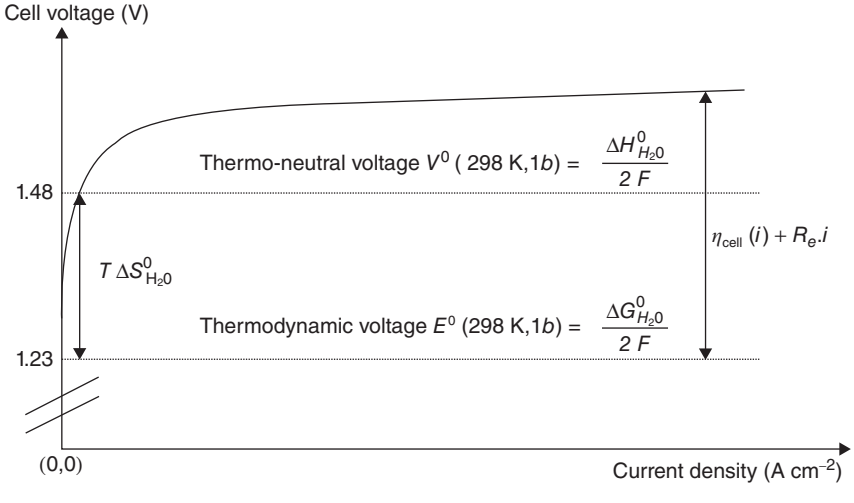

Figure 2.9 Schematic diagram of a water electrolysis polarization curve.

used to overcome some internal resistances and electricity is dissipated as heat to the surroundings. At low current densities, ohmic voltage drops are small whereas charge transfer overvoltages are maximum. The logarithmic shape of the polarization curve is due to these charge transfer phenomena at the anode and the cathode. In the case of water electrolysis, the anodic overvoltage is significantly larger than the cathodic one because the kinetics of the OER is much lower than that of the

HER. Then, as the current density increases, charge transfer resistances decrease and the shape of the polarization curve becomes linear. The shape is dictated by the ohmic resistance of the cell (sum of electronic and ionic resistances) which is therefore a key kinetic parameter. This is especially true in industrial systems of large surface areas where parasite ohmic losses can have a very negative impact on the energy consumption of the cell, especially in PEM cells where there is no liquid electrolyte. Additional parasitic ohmic losses can appear due to inadequate electric contacts between cell components (bipolar plates, current collectors, etc.). This can ultimately lead to unacceptable cell voltages. The quality of an electrolyser must be appreciated by its energy efficiency and its ability to maintain good electrochemical performances on the long term (in the upper range of the $10^4 - 10^5$ h time interval).

It should be noted that when the operating current density is such that Equation 2.50 is satisfied:

$$2F\,(\eta_{\text{cell}} + R_{\text{e}} \cdot i) = T\Delta S_{\text{d}} \tag{2.50}$$

then there is no need to transfer heat from the surroundings to the electrolysis cell. This is the reason why the operating point $V_{\text{d}}(T, P) = \Delta G_{\text{d}}/2F + T\Delta S_{\text{d}}/2F = \Delta H_{\text{d}}/2F$ is called the 'thermo-neutral electrolysis voltage' of the cell.

2.2.3
Energy Efficiency of Water Electrolysis Cells

In water electrolysis cells, the theoretical amount of energy W_{t} required to split 1 mole of water at (T, P) is given from thermodynamic calculations. However, thermodynamics pertains to equilibrium conditions. To reduce capexs, there is a need to operate the cells at high current densities. As the current density increases, an increasing share of the electrical work provided to the cell is degraded into heat. This is a source of inefficiency and increasing opexs. From a practical viewpoint, capex and opex must be balanced and a current density of 1 A cm^{-2} is a good reference value. Electronic conductivity, charge transfer processes at interfaces and ionic transport in the electrolyte are the three main sources of energy degradation.

The efficiency of a water electrolysis cell measures the ratio of the theoretical amount of energy W_{t} to the real amount of energy W_{r} required to split 1 mole of water. Because of heat degradation, $W_{\text{r}} > W_{\text{t}}$. The cell efficiency is defined as:

$$\varepsilon = \frac{W_{\text{t}}}{W_{\text{r}}} \tag{2.51}$$

where $W_{\text{r}} = (U_{\text{cell}} \cdot I \cdot t)$, U_{cell} is the actual cell voltage in volts, I is the current in amperes and t is the duration in seconds. W_{t} can be defined from the free energy voltage E : $W_{\text{t},\Delta G} = (E \cdot I \cdot t)$. W_{t} can also be defined from the thermo-neutral voltage V : $W_{\text{t},\Delta H} = (V \cdot I \cdot t)$.

Therefore, two different definitions can be used to calculate the efficiency of a water electrolysis cell. Because E and V are both functions of operating temperature T and operating pressure P and because U_{cell} is also a function of the

operating current density j, the two different cell efficiencies can also be expressed as a function of T, P and j:

$$\varepsilon_{\Delta G}(T,P,j) = \frac{E(T,P)}{U_{\text{cell}}(T,P,j)} \quad \varepsilon_{\Delta H}(T,P,j) = \frac{V(T,P)}{U_{\text{cell}}(T,P,j)} \tag{2.52}$$

At low current densities, cell efficiencies close to 100% are obtained. Efficiency tends to decrease when current density increases. For example, in conventional PEM water electrolysers, $\varepsilon_{\Delta H} \approx 70\%$ at 1 A cm^{-2}, $T = 90\,^{\circ}\text{C}$ and $P = 1$ bar.

Finally, it should be noted that in low-temperature water electrolysis technology, liquid water is electrolysed and the electrical efficiency should be calculated using the high heating value of the reaction. In high-temperature technology, water vapour is electrolysed and the electrical efficiency should be calculated using the low heating value of the reaction. One interested of high temperature water electrolysis is that waste heat sources can be used for the vapourization of water.

2.2.4
Faradaic Efficiency of Water Electrolysis Cells

The faradaic efficiency ε_{F} is used to measure the efficiency of current flowing across the cell. The faradaic efficiency of each interface can be measured separately. In water electrolysis cells, the relationship between the current and the chemical gas production at each electrode is defined as:

$$(\varepsilon_{\text{F}})^{\text{anodic}} = F\frac{(\mathrm{d}n_{\text{O}_2}/\mathrm{d}t)}{i} \times 100 \tag{2.53a}$$

$$(\varepsilon_{\text{F}})^{\text{cathodic}} = F\frac{(\mathrm{d}n_{\text{H}_2}/\mathrm{d}t)}{i} \times 100 \tag{2.53b}$$

Ideally, ε_{F} should be as close as possible to unity. In water electrolysis cells, gaseous species are formed at both anodic (oxygen) and cathodic (hydrogen) interfaces. It is necessary to collect them separately and to avoid their spontaneous recombination by interdiffusion in the interpolar area. Spontaneous chemical recombination would release the Gibbs free energy change as heat which is a source of inefficiency for the electrical work transferred to the cell. Separators are used to prevent hydrogen/oxygen recombination. In alkaline water electrolysis cell, the separator is an electrolyte-impregnated diaphragm (asbestos was used until it was banned for safety reasons and replaced by various polymeric materials [6, 7]). In PEM water electrolysis cell, the separator is the polymer membrane (a biphasic organic/water material made of water-impregnated perfluorinated perfluorosulphonic polymer). In high-temperature water electrolysis, the separator is an oxide-ion-conducting ceramic.

Ideally, cell separators should be totally gas-proof. In real situations, the solubility of gases (hydrogen and oxygen) in the electrolyte is usually limited but not zero. Mass transport occurs across the separator, especially at high current density and/or high operating pressure. For example, both gases are soluble in aqueous KOH solution and the porous diaphragm is somewhat permeable. The same is true

of the polymer electrolyte in PEM cells whereas pinehole-free ceramics are less prone to interdiffusion of gases. As a consequence, hydrogen can diffuse across the separator from the cathode to the anode and oxygen from the anode to the cathode, the flow being proportional to their respective diffusion coefficients in the media. Hydrogen reaching the anodic compartment can either react chemically with oxygen or be e-oxidized at the anode. Symmetrically, the oxygen reaching the cathodic compartment can react with gaseous or dissolved hydrogen or can be electrochemically reduced at the cathode. From a global viewpoint, this is as if a parasitic current was decreasing the chemical or faradaic efficiency of the cell. Faradaic efficiencies must be measured to optimize cell design and improve cell efficiency.

2.3 Kinetics of the Water Splitting Reaction

In the absence of mass transport limitations, the kinetics of charge transfer processes at any metal/electrolyte interface follows the so-called Butler–Volmer relationship [8]:

$$i = \vec{i} + \overleftarrow{i} = i_0 \left\{ \exp\left[\frac{\beta\ n\ F}{R\ T}\ \eta\right] - \exp\left[-\frac{(1-\beta)\ n\ F}{R\ T}\ \eta\right] \right\} \quad (2.54)$$

where i_0 is the exchange current density (in A cm^{-2}) of the half-cell process considered; β is the symmetry factor [9]; $n = 2$ is the number of electrons exchanged during the electrochemical splitting of one water molecule; $F \approx 96\ 485$ C mol^{-1} is the Faraday constant, that is, the electric charge of 1 mole of electrons; $R = 8.314$ J mol^{-1} K^{-1} is the constant of perfect gas, h is the charge transfer overvoltage (in V) and T is the absolute temperature in Kelvin.

According to Equation 2.54, the main kinetic parameter which determines the efficiency of charge transfer processes is the exchange current density i_0, which is an intensive physical property. The higher the current density, the more reversible is the reaction and the more efficient the charge transfer process. The best electrocatalysts are those having the higher exchange current density for the half-cell reaction of interest. Exchange current densities are expressed per unit surface of geometrical electrode/electrolyte interface. It should be noted that apparent exchange current densities can be increased by developing rough (three dimensions) interfaces.

2.3.1 Half-Cell Reaction Mechanism in Acidic Media

2.3.1.1 HER

The mechanism of HER in acidic media has been extensively studied in the early days of both experimental and theoretical electrochemistry because this is a highly reversible reaction that can be used to set in a very reproducible way the electrode potential. On the basis of the extended work of pioneering electrochemists such

Table 2.3 Two main HER mechanisms on Pt in acidic media.

Mechanism 1	Mechanism 2
$H^+ + 1\,e^- + M \leftrightarrow MH_{ad}{}^{surface}$(step 1)	$H^+ + 1\,e^- + M \leftrightarrow MH_{ad}{}^{surface}$(step 1)
$2\,MH_{ad}{}^{surface} \leftrightarrow H_2(g) + 2\,M$ (step 2)	$H^+ + 1\,e^- + MH_{ad}{}^{surface} \leftrightarrow H_2(g) + M$ (step 2′)

as Frumkin, Conway and Parsons, only two reactions paths involving two steps each are now regarded as likely to occur in acidic media, as described in Table 2.3 where H_{ad} denotes a surface-adsorbed hydrogen ad-atom:

H_{ad} species are formed by proton electronation (Volmer step 1). Molecular hydrogen (gaseous) evolves either by direct chemical recombination of surface hydrogen ad-atoms (Tafel step 2) or by electrochemical recombination (Heyrovsky step 2′). When Pd or Pd-based materials are used as electrocatalysts [10], the HER is in competition with the hydrogen insertion reaction (HIR) that brings two additional reaction steps:

$$MH_{ad}{}^{surface} \leftrightarrow M + H_{ab}{}^{sub\text{-}surface}\text{(step 3)}$$

$$H_{ab}{}^{sub\text{-}surface} \leftrightarrow H_{bulk}\text{(step 4)}$$

where H_{ab} denotes absorbed hydrogen atoms in subsurface regions. Fully hydrided Pd particles are also good HER catalysts. According to Frumkin [11], steps (1) and (3) form one single step whereas according to Bockris *et al.* [12], they are separate steps. On platinum, in acidic media, there is a general agreement that the HER mechanism is that of fast proton discharge followed by rate-determining chemical desorption (mechanism 1). The exchange current density of the HER on Pt in acidic media is 10^{-3} A cm^{-2}. The situation is similar at the cathode of PEM cells [13, 14], even when carbon-supported Pt nano-particles are used in place of bulk Pt particles: the mean diffusion path of surface H adatoms is limited to the nanometre scale due to the geometry of the catalytic powder, and carbon superficial diffusion is unlikely to happen due to strong carbon–hydrogen interactions and low H diffusivity.

2.3.1.2 OER

Many different mechanisms have been reported in the literature to account for the kinetics of the OER in acidic media on metallic oxides [15]. The most often quoted are (Table 2.4):

On Pt electrodes, mechanism 1 usually prevails. Experimental transfer coefficients for the OER and the oxygen reduction reaction (ORR) at high current density are both close to 0.5 (corresponding to a Tafel slope of 118 mV·decade^{-1} at 25 °C and 130 mV·decade^{-1} at 80 °C) [16]. With four electrons exchanged in the overall reaction, this corresponds to a stoichiometric number $\nu = 4$, a value consistent with mechanism 1, the first step being rds. However, Pt is not a good catalyst for the OER (and is thus never used for application in PEM

Table 2.4 Two main OER mechanisms on Pt and IrO_2 (S = reacting site).

Mechanism 1: oxide path (Pt)	Mechanism 2: Krasil'shchikov path (IrO_2)
$4\,Pt + 4\,H_2O \rightarrow 4\,PtOH + 4\,H^+ + 4e^-$ (step 1)	$S + H_2O \rightarrow S-OH + H^+ + 1\,e^-$(step 1)
$4\,PtOH \rightarrow 2\,PtO + 2\,PtH_2O$ (step 2)	$S-OH \rightarrow S-O^- + H^+$(step 2)
$2\,PtO \rightarrow O_2 + 2\,Pt$ (step 3)	$S-O^- \rightarrow S-O + e^-$(step 3)
	$S-O \rightarrow S + \frac{1}{2}\,O_2$(step 4)

water electrolysis cells), the exchange current density (approximately 10^{-9} A cm^{-2} per cm^2 of real interface area) being far too small. Iridium metal or iridium oxides are known as the best OER promoters in acidic media. The exchange current density measured on smooth iridium electrodes is approximately 1000 times higher ($\approx 10^{-6}$ A cm^{-2} per cm^2 of real interface area) [17] than on Pt. According to the literature, this is the Krasil'shchikov path of Table 2.4 [18] which is most frequently found to occur on iridium oxide electrodes [19, 20].

2.3.1.3 Kinetics

Tafel parameters for low-temperature (up to 80 °C) HER and OER in acidic media using PGM catalysts are compiled in Tables 2.5 and 2.6. When current densities are corrected for the roughness of the electrodes, their values are similar to those measured on smooth electrodes.

On the basis of the data of Tables 2.5 and 2.6, the overvoltage–current density relationships for the HER and the OER on smooth PGM surfaces calculated from Equation 2.57 are plotted in Figure 2.10. Curves for the hydrogen oxidation reaction (HOR) and the ORR corresponding to the fuel cell mode are also plotted for comparison. While the shapes of the curves along the potential axis are dictated by the exponential terms of Equation 2.57, the magnitude of the overvoltage is only due to the value of the exchange current density for each reaction.

Table 2.5 Tafel parameters for hydrogen evolution reaction [12, 21, 22].

Electrode (°C)	$d\eta^{cathodic}/d(\log i)$ (mV)	α	Measured i_0 (A cm^{-2}) (geometrical area)	Measured i_0 (A cm^{-2}) (real area)	Roughness factor
Pt					
25	125	0.54	0.17	8×10^{-4}	213
80	105	0.45	0.14	8×10^{-4}	175
Pd					
25	—	0.54	—	1×10^{-3}	—
80		0.45		1×10^{-3}	

Table 2.6 Tafel parameters for oxygen evolution reaction.

Electrode (°C)	$d\eta^{anodic}/d(\log i)$ (mV)	α	Measured i_0 (A cm^{-2}) (geometrical area)	Measured i_0 (A cm^{-2}) (real area)	i_0 (A cm^{-2}) [17]
Pt					
25	110	0.54	1×10^{-7}	6×10^{-10}	1×10^{-9}
80	130	0.45	2×10^{-5}	1×10^{-7}	—
Ir					
25	110	0.54	2×10^{-4}	1×10^{-6}	1×10^{-6}
80	130	0.45	6×10^{-3}	4×10^{-5}	—

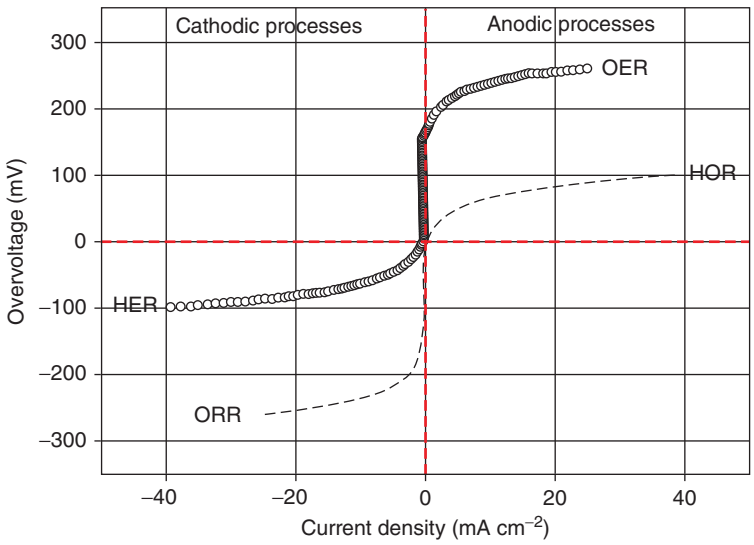

Figure 2.10 Overvoltage–current density relationships on smooth surfaces for: OER = oxygen evolution reaction on Ir°; HER = hydrogen evolution reaction on Pt°; ORR = oxygen reduction reaction on Pt° and HOR = hydrogen oxidation reaction on Pt°.

During water electrolysis, the HER overvoltage remains low whereas the OER overvoltage is larger (Figure 2.11). The relationship between η^+ (the anodic overvoltage) and η^- (the cathodic overvoltage) at any given current density i^* sufficiently large to neglect the reverse term is obtained from Equation 2.54:

$$\frac{\eta^+}{\eta^-} = \frac{\mathrm{Ln}\ (i^*/i_0^+)}{\mathrm{Ln}\ (i^*/i_0^-)} \tag{2.55}$$

whereas $i_0(\mathrm{HER})/i_0(\mathrm{OER}) \approx 1000$, $\eta^+/\eta^- \approx 2.0$ at 1 A cm^{-2} using smooth interfaces.

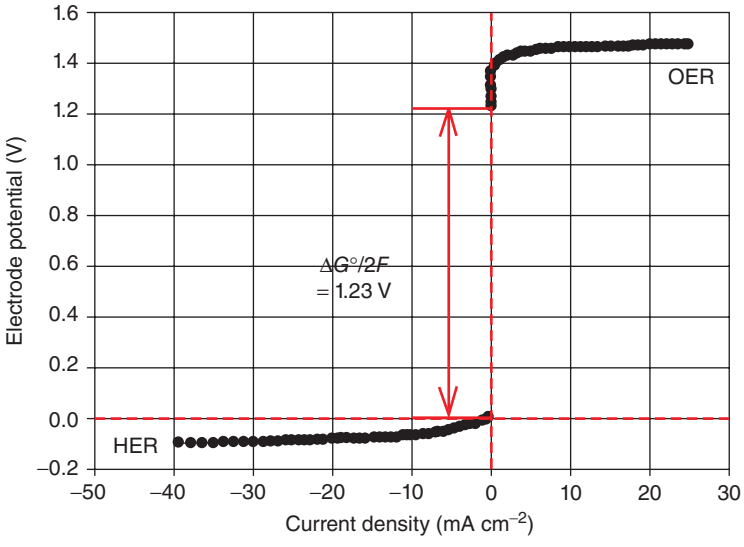

Figure 2.11 Overvoltage–current density relationship calculated at 25 °C from Equation 2.54 for the water splitting reaction in acidic media on smooth Pt and Ir surfaces.

2.3.2
Half-Cell Reaction Mechanism in Alkaline Media

In alkaline water electrolysers, nickel is commonly used as the electrode material. Half-cell reactions are:

$$\text{anode } (+): \ 2\,OH^- \rightarrow H_2O + \frac{1}{2}\,O_2(g) + 2\,e^- \tag{2.17}$$

$$\text{cathode } (-): \ 2\,H_2O + 2\,e^- \rightarrow H_2(g) + 2\,OH^- \tag{2.18}$$

The exchange current density of the HER on smooth Ni foils in alkaline media at 25 °C is $i_0 \approx 7.4 \times 10^{-6}$ A cm^{-2} [23]. Using 3D electrodes (e.g. fresh Ni-coated carbon fibres in 30 wt% KOH at 60 °C [24]), values in the 40–50×10^{-6} A cm^{-2} range have been obtained, corresponding to a roughness factor of approximately 7.

Some reference data for an alkaline water electrolyser are provided in Figure 2.12. The performance of some commercial alkaline water electrolysers are compiled in Table 2.7.

2.3.3
Role of Operating Temperature on the Kinetics

As discussed above, the HER is a fast process but the OER is more sluggish at low temperature. The H^+/H_2 redox system is fully reversible but the H_2O/O_2 redox system is not. The situation appears more clearly by plotting on the same graph the polarization curves of a water electrolyser and a fuel cell at two different temperatures (Figure 2.13). At 90 °C, the kinetic features of the

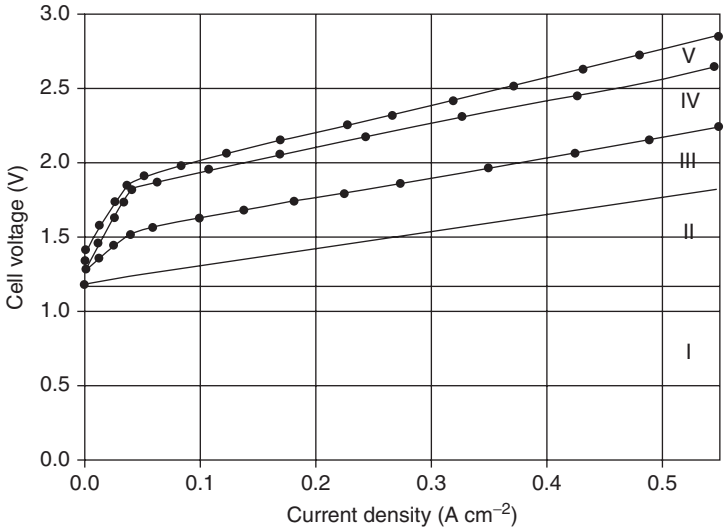

Figure 2.12 Electrochemical performances of a conventional alkaline 'membrane cell' water electrolyser at 90 °C. (I) Thermodynamic voltage (1.18 V); (II) ionic ohmic drop across electrolyte; (III) anodic (O_2) overvoltage; (IV) cathodic (H_2) overvoltage and (V) electronic ohmic drop of electrodes.

Table 2.7 Main characteristics of some commercial alkaline water electrolysers.

Manufacturer (model)	H_2 production (Nm^3 h^{-1})	Production pressure (bar)	Total power (kW)	Energy system (kWh Nm^{-3})	Energy electrolyser (kWh Nm^{-3})	Efficiency (%)
Stuart (IMET 1000)	60	25	290	4.8	4.2	73
Teledyne (EC 750)	42	4-8	235	5.6	—	63
Proton (Hogen 380)	10	14	63	6.3	—	56
Norsk Hydro (5040)	485	30	2330	4.8	4.3	73
Avalence (Hydrofiller 175)	4.6	Up to 700	25	5.4	—	64

water/hydrogen/oxygen system are those of a poorly reversible system. The current requires a significant voltage change (≈500 mV) to see its sign changing and to shift from water electrolysis to fuel cell operation. Despite the fact that the equilibrium voltage is decreasing with temperature (from about 1.23 V at 90 °C corresponding to $\Delta G = 238$ kJ mol^{-1} down to about 0.9 V at 1000 °C corresponding to $\Delta G = 177$ kJ mol^{-1}), the situation gradually changes when the operating temperature is raised, and the system becomes reversible. At 1000 °C (SOWE and solid oxide fuel cell, SOFC, operation), there is a continuous transition between water electrolysis and fuel cell current–voltage polarization curves.

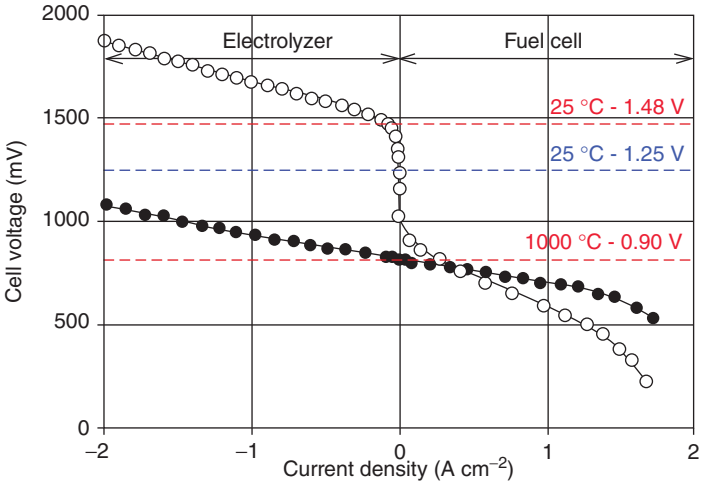

Figure 2.13 Experimental water electrolysis polarization curves measured at (o) 90 °C and (•) 1000 °C.

2.3.4
Role of Operating Pressure on the Kinetics

From the thermodynamic viewpoint, temperature and pressure play an opposite role on the electrolysis voltage. The free energy electrolysis voltage decreases by approximately −0.8 mV °C^{-1} and increases by about +0.3 mV bar^{-1}. From the

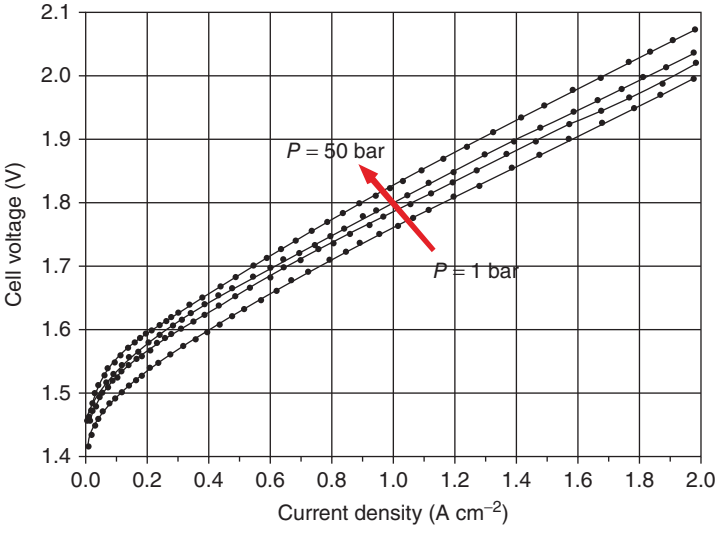

Figure 2.14 Role of operating pressure on the polarization curves of a PEM water electrolysis cell using platinum as the cathodic catalyst and iridium as the anodic catalyst.

kinetic viewpoint, a higher operating pressure usually has limited impact on the kinetics, even at the cathode where the reaction is highly reversible. In some cases (depending on the cell design and the porosity of the current collectors), a higher operating pressure can have positive effects by facilitating transport of gas bubbles. More recent and more accurate measurements show that the effect is limited, at least over the 1–50 bar range (Figure 2.14). It can be concluded that pressurized water electrolysis does not add significant energy costs compared to atmospheric water electrolysis, either in alkaline [25] or in acidic [26, 27] media, thus offering some interesting opportunities for direct storage of compressed gases as long as the capex is not too negatively penalized.

2.4 Conclusions

As discussed in the previous sections, water electrolysis can take place over an extended range of operating temperatures (from room temperature up to 800 °C) and using electrolytes of different pH. Different technologies, each of them having specific advantages and drawbacks, have been developed for operation in these different conditions. At low temperature ($T < 150$ °C), the alkaline technology based on zero-gap cell and liquid electrolyte is the more mature process. The acidic PEM technology based on the concept of a polymer electrolyte cell is more recent and increasingly considered as the water electrolysis technology of the near future. At the same time, as R&D is making progress, different materials (electrolytes and electrocatalysts) have become available. Polymers capable of operation at higher temperature (up to 250–300 °C) are becoming available. Oxide-ion-conducting materials operating down to the less aggressive 650 °C range are appearing and proton-conducting ceramics for operation in the intermediate temperature range are being studied extensively. More details are provided in the next chapters.

Nomenclature

A	membrane area (m^2)
a_i	activity of species i
C_i	concentration of species i in $mol \cdot m^{-3}$
D_i	diffusion coefficient of species i ($m^2 \cdot s^{-1}$)
E	free energy electrolysis voltage (V)
F	Faraday constant (96 485 °C·mol^{-1})
f_i	fugacity of species i
G	Gibbs free energy ($J \cdot mol^{-1}$)
H	enthalpy ($J \cdot mol^{-1}$)
I	current (A)
i	current density (A cm^{-2})
i_0	exchange current density (A cm^{-2})

m	mole number
n	number of electrons exchanged during the electrochemical reaction
P	pressure (Pa)
p_i	partial pressure of component i in a gas mixture (Pa)
R	resistance (Ω)
r	specific resistance ($\Omega \cdot m^2$)
R_{PG}	constant of perfect gas ($0.082\ J.K^{-1} \cdot mol^{-1}$)
S	entropy ($J \cdot mol^{-1} \cdot K^{-1}$)
t	time (s)
T	absolute temperature (K)
U_{cell}	cell voltage (V)
V	thermo-neutral electrolysis voltage (V)
$\overline{V}$	molar volume ($m^3 \cdot mol^{-1}$)
W	electrical work (J)
x, y, z	space coordinates

Greek symbols

δ	membrane thickness (m)
Δ	difference
ε	cell efficiency (%)
η	overvoltage (V)
φ	electrode absolute potential (V)
ρ	electrical resistivity (Ω m)
σ	electrical conductivity ($S\ m^{-1}$)

Subscripts or superscripts

0	standard conditions (298 K, 1 bar)
cell	electrolysis cell
d	dissociation
e	electrolyte
i	species i
r	real
t	theoretical

Acronyms

MEA	membrane-electrode assembly
PEM	polymer electrolyte membrane
PGM	platinum group metals
SPE	solid polymer electrolyte
SOFC	solid oxide fuel cells
SOWE	solid oxide water electrolysis

References

1. Liu, R.S. Sun, X Liu, H. Zhang, L. and Zhang, J. (2011) 'Electrochemical Technologies for Energy Storage and Conversion', *chapter 9, Water electrolysis for hydrogen generation*, (ed. J. Wiley&Sons).
2. Meyer, C.A. (1993) *ASME Steam Tables: Thermodynamic and Transport Properties of Steam*, American Society of Mechanical Engineers, New York.
3. LeRoy, R.L., Bowen, C.T., and Leroy, D.J. (1980) The thermodynamics of aqueous water electrolysis. *J. Electrochem. Soc.*, **127**, 1954.
4. Mauritz, K.A. and Moore, R.B. (2004) State of understanding of nafion. *Chem. Rev.*, **104**, 4535–4585.
5. Onda, K., Kyakuno, T., Hattori, K., and Ito, K. (2004) Prediction of production power for high-pressure hydrogen by high-pressure water electrolysis. *J. Power Sources*, **132**, 64–70.
6. Divisek, J. and Murgen, J. (1983) Diaphragms for alkaline water electrolysis and method for production of the same as well as utilization thereof. US Patent 4,394,244.
7. Vandenborre, H., Leysen, R., Nackaerts, H., Van der Eecken, D., Van Asbroeck, P., Smets, W., and Piepers, J. (1985) Advanced alkaline water electrolysis using inorganic membrane electrolyte (I.M.E.) technology. *Int. J. Hydrogen Energy*, **10** (11), 719–726.
8. Hamann, C.H., Hamnett, A., and Vielstich, W. (1998) *Electrochemistry*, Wiley-VCH Verlag GmbH, Weinheim.
9. Bockris, J.O.'M. and Reddy, A.A.K. (1982) *Comprehensive Treatise of Electrochemistry*, Plenum Press E.
10. Grigoriev, S.A., Mamat, M.S., Dzhus, K.A., Walker, G.S., and Millet, P. (2011) Platinum and palladium nano-particles supported by graphitic nano-fibers as catalyst for PEM water electrolysis. *Int. J. Hydrogen Energy*, **36**, 4143.
11. Frumkin, A.N. (1963) in *Advances in Electrochemistry and Electro- Chemical Engineering*, vol. **3** (ed. P. Delahay), Interscience, New York.
12. Bockris, J.O'M., McBreen, J., and Nanis, L. (1965) The hydrogen evolution kinetics and hydrogen entry into a-iron. *J. Electrochem. Soc.*, **112**, 1025.
13. Millet, P., Durand, R., and Pineri, M. (1989) New solid polymer electrolyte composites for water electrolysis. *J. Appl. Electrochem.*, **19**, 162–166.
14. Marshall, A., Børresen, B., Hagen, G., Tsypkin, M., and Tunold, R. (2009) Hydrogen production by advanced proton exchange membrane (PEM) water electrolyzers-reduced energy consumption by improved electrocatalysis. *Int. J. Hydrogen Energy*, **34**, 4974–4982.
15. Bockris, J.O.'M. (1956) Kinetics theory of adsorption intermediates in electrochemical catalysis. *J. Chem. Phys.*, **24**, 817.
16. Millet, P., Durand, R., and Pinéri, M. (1990) Preparation of new solid polymer electrolyte composites for water electrolysis. *Int. J. Hydrogen Energy*, **15**, 245.
17. Damjanovic, A., Dey, A., and Bockris, J.O.'M. (1966) Electrode kinetics of oxygen evolution and dissolution on Rh, Ir and Pt-Rh alloy electrodes. *J. Electrochem. Soc.*, **113**, 739.
18. Krasil'shchikov, A.I. (1963) *Zh. Fiz. Khim*, **37**, 273.
19. Boodts, J.F.C., Alves, V.A., Da Silva, L.A., and Trasatti, S. (1994) Kinetics and mechanism of oxygen evolution on IrO2 – based electrodes containing Ti and Ce acidic solutions. *Electrochim. Acta*, **39**, 1585.
20. Trasatti, S. (1990) The oxygen evolution reaction, in *Electrochemical Hydrogen Technologies* (ed. H. Wendt), Elsevier, Amsterdam.
21. Millet, P., Alleau, T., and Durand, R. (1993) Characterization of membrane-electrodes assemblies for Solid Polymer Electrolyte water electrolysis. *J. Appl. Electrochem.*, **23**, 322–331.
22. Grigoriev, S., Ilyukhina, L.I., Middleton, P.H., Millet, P., Saetre, T.O., and Fateev, V.N. (2008) A comparative evaluation of palladium and platinum nanoparticles as catalysts in PEM electrochemical cells.

Int. J. Nucl. Hydrogen Prod. Appl., **1-4**, 343–354.

23. Matsuda, A. and Ohmori, T. (1962) *J. Res. Inst. Catal., Hokkaido Univ.*, **10**, 203.
24. Pierozynski, B. (2011) On the hydrogen evolution reaction at nickel-coated carbon fibre in 30 wt. % KOH solution. *Int. J. Electrochem. Sci.*, **6**, 63–77.
25. Schug, C.A. (1998) Operational characteristics of high pressure, high efficiency, water-hydrogen electrolysis. *Int. J. Hydrogen Energy*, **23**, 1113–1120.
26. Engel, R.A., Chapman, G.S., Chamberlin, C.E., and Lehman, P.A. (2004) Development of a high pressure PEM electrolyzer: enabling seasonal storage of renewable energy. Proceeding of the 15th Annual U.S. Hydrogen Conference, Los Angeles, CA, April 26–30, 2004.
27. Marangio, F., Pagani, M., Santarelli, M., and Calì, M. (2011) Concept of a high pressure PEM electrolyser prototype. *Int. J. Hydrogen Energy*, **36**, 7807–7815.

3
PEM Water Electrolysis

Pierre Millet

3.1
Introduction, Historical Background

From a historical perspective, the concept of the solid polymer electrolyte (SPE) cell was introduced in the early 1950s, at the dawn of the US space programme, and was considered at that time as an innovative approach for the development of a new generation of H_2/O_2 fuel cells that could operate efficiently in zero-gravity environments [1]. In these pioneering days of space conquest, operating conditions in space introduced new constraints for electrochemical devices. In particular, the lack of gravity prohibited the use of liquid electrolytes that tend to form liquid bubbles. Homogeneous liquid phases operating in open systems require expensive, complex and energy-consuming technologies (such as centrifugation). Significant progress was accomplished at that time to develop solid matrix impregnated with liquid electrolytes that potentially brought the additional advantage of allowing the use of acidic media, protons being more mobile than hydroxide ions used in alkaline technology. This effort finally led to the synthesis of ionomers, a class of polymers that contain periodical ionized moieties covalently bonded to the main organic backbone. A decisive step was made in the 1960s with the synthesis of sulphonated tetrafluoroethylene-based fluoropolymer–copolymers, developed by the US company DuPont de Nemours, that became famous under the brand name Nafion®. Nafion® products form a class of soft matter materials with fascinating microstructural and physical properties [2] that have raised a lot of scientific interest and have triggered the development of quite versatile technological applications, ranging from fuel cells to water electrolysers. They are characterized by their equivalent weight (EW), that is, the mass of one equivalent of charge. Concerning water electrolysis, these perfluorinated materials are chemically stable and have demonstrated their ability to operate without degradation in quite oxidizing environments, over long periods of time compatible with practical applications. Although their water-swelling and mechanical properties tend to restrict operation to temperatures less than 100 °C, Nafion® products are widely used as the most popular proton-conducting polymer materials in SPE technology. This is mainly due to their elevated proton conductivity (equivalent to

Hydrogen Production: by Electrolysis, First Edition. Edited by Agata Godula-Jopek.
© 2015 Wiley-VCH Verlag GmbH & Co. KGaA. Published 2015 by Wiley-VCH Verlag GmbH & Co. KGaA.

that of 1 M sulphuric acid aqueous solutions) and excellent chemical and mechanical stability. In modern electrochemical literature, SPE cells are referred to as proton exchange membrane or polymer electrolyte membrane (PEM) cells. In a PEM cell, a thin (50–250 μm thick) proton-conducting membrane is used as the 'solid' electrolyte. As a result, very thin electrolysis cells are obtained and elevated current densities of several A cm^{-2} can be achieved. According to the literature, water electrolysis cells can reach an efficiency (based on the higher heating value of hydrogen) of 80% at 1 A cm^{-2}, a value that is common good practice, at least at the lab scale [3, 4]. Because of the highly acidic environment found in these polymers, platinum group metal (PGM) electrocatalysts are required. The acidity would otherwise provoke the dissolution of other metallic catalysts.

PEM water electrolysers (producing up to several tens of H_2 normal cubic metres per hour or Nm^3 H_2 h^{-1}) were first developed for the production of oxygen of electrolytic grade in anaerobic environments such as submarines. Compared to the alkaline process, PEM technology is more expensive. This extra cost is partly due to expensive materials (polymer electrolyte, catalyst, but also other cell components) and partly due to the fact that because the electrolyte is confined in the polymeric membrane, tolerance of cell component dimensions is more demanding and requires sophisticated mechanical tools. But for applications in anaerobic environments, PEM offers several decisive advantages: electrolysers are more compact (PEM water electrolysis cells can be operated in the multi A cm^{-2} range), more efficient at high current density (heat management is simplified), safer (no corrosive liquid electrolyte is required) and offer the possibility to operate more safely under pressure for onboard storage or offboard removal of the hydrogen by-product.

In the 1970s and 1980s, in the follow-up of the first oil crisis that introduced hydrogen as an alternative energy carrier, large-scale hydrogen production by PEM water electrolysis was envisioned from both the technical and financial viewpoints [5]. Cost considerations and lack of industrial maturity were certainly two main disadvantages compared to the alkaline process for large-scale deployment. It is now established that for large production units, operational expenses (opexs) is the key driver and hydrogen from water is and will remain less attractive than hydrogen from methane because of the significant difference in energy requirements. More recently, concerns about large-scale carbon dioxide emissions and associated negative impact on the environment have led to ambitious plans to increase the share of renewable energy sources in our energy mix, and PEM water electrolysis again attracted attention. In the early 2000s when massive public financial support became available in industrialized countries to initiate the development of the hydrogen economy (a new and global energy infrastructure in which hydrogen produced from carbon-free sources can be used as an energy carrier for the promotion of sunlight energy), the technology has been identified as a key process for transforming zero-carbon electricity sources into the supply of zero-carbon hydrogen and oxygen for miscellaneous end uses. In the European Union, the European Commission has provided support through successive framework programmes that finally led to

the creation of a joint public–private partnership on hydrogen technologies (the fuel cell and hydrogen (FCH) joint undertaking) [6]. The effort has recently been renewed in the framework of Horizon 2020, the European R&D programme for the next 5 years. PEM water electrolysis is an efficient, durable and very flexible technology that can sustain successive power on/off cycles (thermal buffering using for example phase transition compounds can be implemented to shave power-off peaks and maintain a high efficiency level with transient power loads) and that is therefore well-suited for water splitting using intermittent power sources but also for the production of hydrogen from off-peak nuclear power electricity. Hydrogen is now considered as the carbon-free energy carrier for mobility and seasonal energy storage applications. Both emerging markets require compressed gas, and pressurized PEM water electrolysis (prototypes operating at several hundred bars have been successfully developed) offers some interesting additional perspectives in view of such applications.

3.2
Concept of Solid Polymer Electrolyte Cell

The general features of a PEM water electrolysis cell are schematically diagrammed in Figure 3.1. In PEM cells, there is no liquid electrolyte as such. Only deionized water circulates. The central component of the cell is a thin (≈0.2 mm thick) membrane of a proton-conduction polymer electrolyte. Such cells are very compact and the efficiency of water splitting is high. The membrane is used for the double purpose of carrying ionic charges (solvated protons) and separating electrolysis products (molecular hydrogen and oxygen), thus preventing their spontaneous exothermic recombination into water. The most popular material used as SPE in these cells is a sulphonated tetrafluoroethylene-based fluoropolymer–copolymer. It was developed in the late 1960s by E.I. DuPont Co., and has become famous under its brand name Nafion® [1]. The organic backbone (Figure 3.2) is fluorinated for the double purpose of fully ionizing the ending sulphonic acid groups (the acidity of hydrated Nafion membrane is similar to 1 M aqueous sulphuric acid solutions) and providing appropriate chemical stability, especially on the anodic side where severe oxidizing conditions are found. On both side of the membrane, two porous catalytic layers are coated. These catalytic layers are connected to an external DC power source that provides electrical work for the reaction. During water electrolysis, the following half-cell reactions take place:

$$\text{anode}: H_2O(l) \rightarrow \frac{1}{2}O_2(g) + 2H^+ + 2e^- \tag{3.1}$$

$$\text{cathode}: 2H^+ + 2e^- \rightarrow H_2(g) \tag{3.2}$$

$$\text{full reaction}: H_2O(l) \rightarrow H_2(g) + \frac{1}{2}O_2(g) \tag{3.3}$$

In these 'SPE cells', DC current is used to split liquid water into gaseous oxygen and protons at the anode (Equation 3.1). In response to the electrical field set across

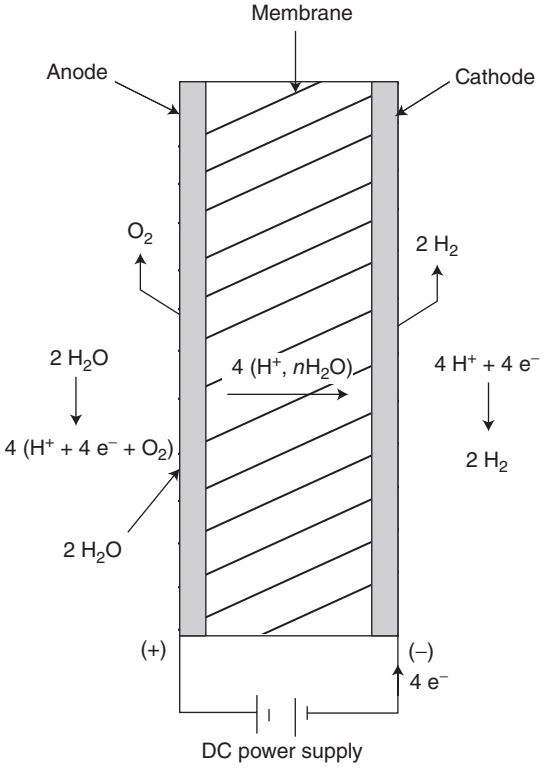

Figure 3.1 Schematic cross section of a PEM water electrolysis cell and half-cell reactions.

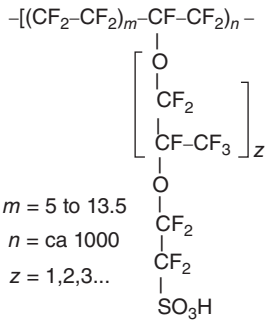

Figure 3.2 Chemical composition of Nafion membranes.

the cell, solvated protons migrate down to the cathode where they are desolvated and reduced into molecular hydrogen (Equation 3.2). The flow of water across the cell is called the electro-osmosis drag (the water to proton mole ratio is a function of EW).

3.3
Description of Unit PEM Cells

3.3.1
General Description

Unit PEM cells (Figure 3.3) contain several components. The electrochemically active central component is the membrane–electrodes assembly (MEA), composed of a SPE membrane (1), coated on each side by two porous layers of electrocatalysts (2) one at the anode (a) for the oxygen evolution reaction (OER) and the other at the cathode (c) for the hydrogen evolution reaction (HER). The MEA is usually clamped between two porous current distributors (3) made of sintered titanium particles. Two hollow bipolar plates (4) are used to convey electric current to the cell and separate two adjacent cells. Channels are used to carry feed water to the anode and to collect liquid–gas mixtures in each cell compartment. Contacts points between current collectors and electrocatalytic layers (5) are critical; the average distance between contact points must be

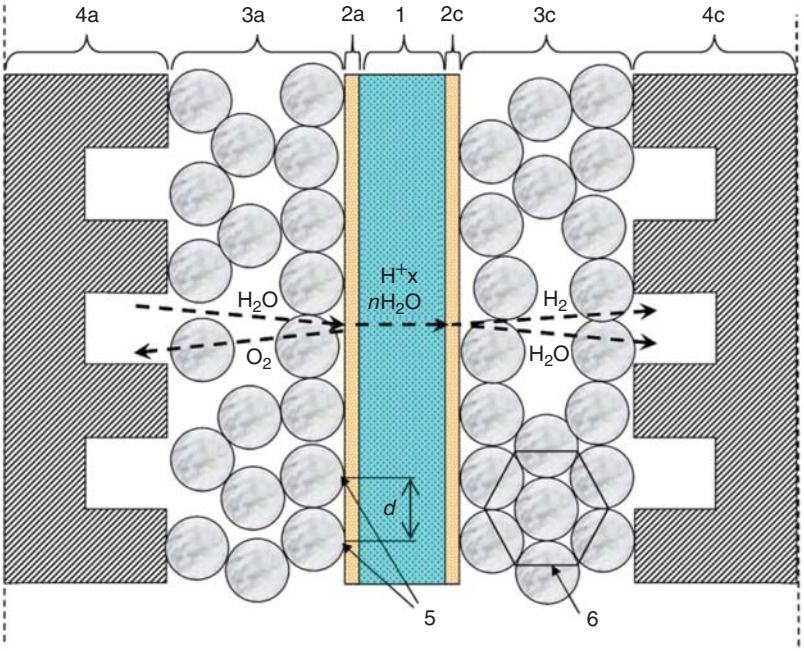

Figure 3.3 Schematic representation (cross-sectional view) of a PEM water electrolysis cell. 1 – PEM; 2 – electrocatalytic layers (a – anodic, c – cathodic); 3 – porous current collectors (a – anodic, c – cathodic); 4 – bipolar plates (a – anodic side, c – cathodic side); 5 – contacts points between current collectors and electrocatalytic layers; *d* – average distance between contact points between a current collector and catalytic layers; 6 – a fragment of a layer with a closely packed hexagonal lattice of particles [7].

sufficiently small (typically several micrometre) to obtain a good distribution of current lines at interfaces. End plates are connected to the external DC power supply. Mechanically soft peripheral gaskets (not represented here) are required to seal the cells. Looking at Figure 3.3, the challenge is to optimize the cell design in such a way that (i) the electronic resistance of non-MEA cell components (bipolar plates and current distributors) is as low as possible so that the externally applied cell voltage is used only to overcome the MEA resistance; (ii) liquid water can be pumped through the anodic compartment with a minimum pressure drop and (iii) liquid water can be homogeneously transferred to the anode through the pores, letting, at the same time, gaseous oxygen flow counterclockwise from the anode to the anodic bipolar plate. In the cathodic compartment, the situation is simpler because flows of both liquid water (electro-osmotic drag) and gaseous hydrogen are linear, from the cathode to the cathodic bipolar plate. All these constraints are satisfied mainly by controlling the pore structure of the current distributors, which has to take into account the maximum current density (gas production rate) and the nominal operating pressure (diameter of gas bubbles vary with pressure).

3.3.2 Membrane Electrode Assemblies

3.3.2.1 Electrocatalysts

In PEM water electrolysis, carbon-supported platinum nanoparticles (Figure 3.4) are used as the electrocatalyst at the cathode for the promotion of HER:

$$H_3O^+ + 1\,e^- \rightarrow H_2O + 1/2H_2 \tag{3.4}$$

Electro-conductive carbon blacks are used as electronic carriers. They are usually prepared by thermal decomposition (acetylene blacks) or partial oxidation

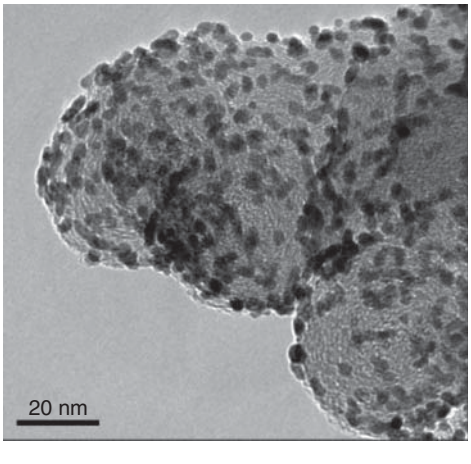

Figure 3.4 SEM image of Pt/C catalyst for HER.

(furnace blacks) of hydrocarbons. Commercial examples of furnace black are Vulcan® or Black Pearls (Cabot Co.) and Ketjen® black (Akzo Nobel Co.). The different methods used for the manufacturing of these carbonaceous substrates lead to carbon blacks of different grades of graphite and amorphous carbon and with specific surface area ranging from 10 to 2000 $m^2\ g^{-1}$. Carbon blacks contain very small particles (10–40 nm thick), which, during the synthesis, tend to form 20–100 nm wide aggregates. The pore network includes the pores of the particles themselves and the pores formed by the aggregation of these particles. As in fuel cell technology, it is desirable to use densely packed small (nanometre range) platinum particles that are obtained by chemical reduction of some platinum precursors such as hexachloro-platinic acid. On the anodic side, there are few if any supporting electronic carriers available. Iridium (metal or oxide) is the most efficient and stable catalyst for the OER in acidic media:

$$H_2O \rightarrow 2H^+ + 2e^- + 1/2O_2 \tag{3.5}$$

Unsupported iridium oxide particles (Figure 3.5), impregnated with polymeric ionomer chains, are usually used to form the anodic catalytic layer.

3.3.2.2 **Coating Processes**

A large variety of coating processes have been reported in the literature for the manufacturing of MEAs. Several options are available to form the electrocatalyst layers: (i) they can be deposited directly onto the SPE or (ii) onto the current distributor, which is then hot-pressed against the membrane. The first approach is now commonly used and several manufacturers are selling MEAs for PEM water electrolysis applications. In the 1980s, several methods describing the chemical reduction of precursor anionic [8] or cationic [9] platinum precursors were reported in the literature. The impregnation–reduction method is a wet (electroless) process. In a first step, an aqueous solution of tetra-ammine platinum salt is first pumped through the plating cell (Figure 3.6) to incorporate the cationic

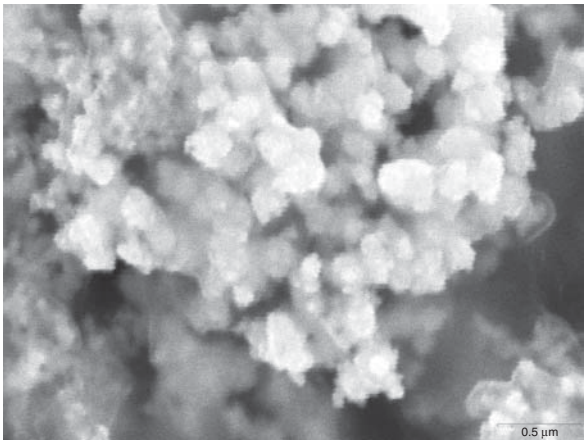

Figure 3.5 SEM image of IrO_2 catalyst for OER.

Figure 3.6 Photograph showing the cell used for electroless deposition of platinum onto the SPE.

platinum precursor into the membrane. The precursor is then reduced using an appropriate chemical reducer such as sodium borohydride [10–12]. As a result, a thin and homogeneous layer of active platinum is deposited over the active section of the SPE. Nowadays, different approaches are used. The wet process leads to the deposition of bulk Pt particles but cost reduction requires the use of carbon-supported nanoparticles. Catalytic inks containing a dispersion of supported catalyst particles dispersed by ultrasonication in a mixture of alcoholic solvent and perfluoro-sulphonated ioner chains are sprayed over the surface of the MEA (Figure 3.7) and then air-dried to remove traces of solvent. The technique is well-adapted for the manufacturing of large surface area MEAs (1200–1500 cm^2 are

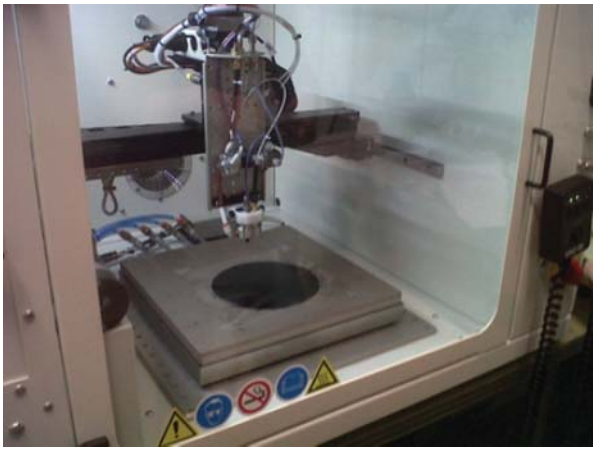

Figure 3.7 Photograph of the ink printer used for spraying a catalytic ink onto the SPE.

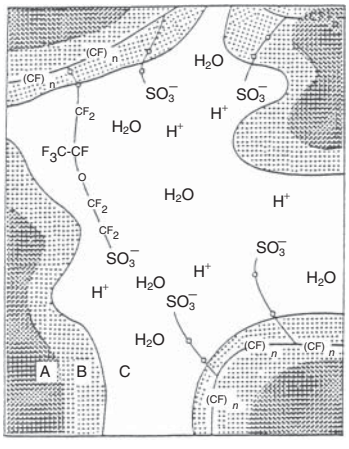

Figure 3.8 Schematic diagram of the microstructure found in Nafion-like SPEs.

becoming available) and the process can be automated. As a result, homogeneous and firmly adherent deposits are formed over the surface of SPEs.

3.3.2.3 Electrocatalytic Layers

The structure of catalytic layers is critical to reduce charge transfer overvoltages during water electrolysis operation and to meet durability specifications imposed by market requirements. The situation is somewhat simpler than in fuel cell technology because gases evolve from a liquid interface and there is no risk of flooding interfaces. However, gas screening phenomena do occur in inappropriately designed PEM cells and it is necessary to pay attention to such problems and design appropriate 3D configurations (triple points where catalytic sites are made of coexisting ion- and electron-conducting phases as well as pores for water and gas transport). Figure 3.8 shows a schematic diagram showing the microstructure of Nafion-like SPEs according to the literature. Ionized ending sulphonic groups tend to cluster into a network of hydrated domains at the nanometre scale. Fraction micrometre thick catalytic layers contain supported or unsupported catalyst particles impregnated with ionomer chains (Figure 3.9). Nanometre large particles trapped inside the SPE subsurface help to anchor the catalytic layer but also to prevent undesirable effects

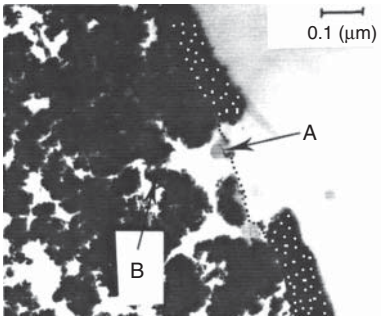

Figure 3.9 TEM image of the microstructure of a Pt/Nafion interface.

associated with gas cross-permeation phenomena and to promote catalytic reoxidation of permeating hydrogen and reduction of permeating oxygen (see Section 3.4.5).

3.3.3
Current–Gas Distributors

Millimetre thick current–gas distributors used in PEM water electrolysis cells are usually made of sintered titanium particles. The porosity of these key cell components needs to be adjusted very carefully because they play a central role (i) in mass transport between bipolar plates and catalytic layers; (ii) in the mechanical compression of the cell and (iii) in the homogeneous distribution of current lines at the interface with the catalytic layer. Concerning mass transport, the situation is rather simple in the cathodic compartment because liquid water (electro-osmotic drag) and gaseous hydrogen flow same way from the catalytic layer to the cathodic bipolar plate. But in the anodic compartment, the situation is more challenging because liquid water flows from the anodic bipolar plate to the anodic catalytic layer while gaseous oxygen flows in the opposite direction, from the catalytic layer to the bipolar plate. Concerning mechanical properties, structures that are too porous should be avoided. More compact ones are more robust and less prone to dimensional changes, and contribute to the homogenous distribution of compression forces over the entire section of the cells. Concerning current flow, there is a need to reduce internal ohmic resistances of the plates by reducing porosity and to pay attention to the structure of the interface with the active catalytic layer, which is critical for the distribution of homogenous current lines. Indeed, because of the small thickness of catalytic layers (usually a fraction of a micrometre), a sufficient number of contact points is required in order to avoid the formation of hot points, especially during operation at elevated current density. From the manufacturing viewpoint, the size and structure of the pore network can be adjusted by using particles of homogeneous size (Figure 3.10) or by mixing particles of two different size populations (Figure 3.11).

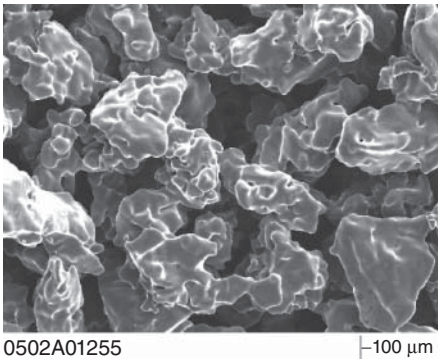

Figure 3.10 SEM image of a porous Ti current collector with homogeneous particle size.

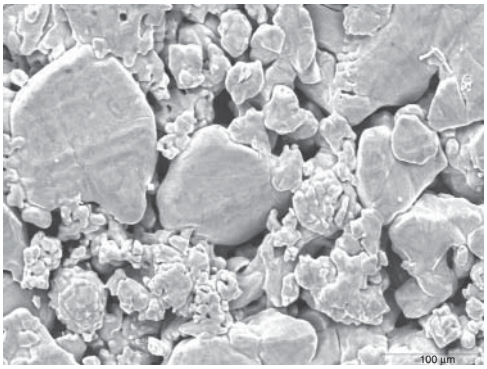

Figure 3.11 SEM image of a porous Ti current collector with heterogeneous particle size.

According to the literature [13], an optimum porosity should lie somewhere in the 30–50% range for operating current densities up to 2A cm^{-2} and atmospheric pressure but more porous structures are required for higher current density values.

The situation prevailing at the anode during operation can be exemplified with Figures 3.12–3.14. Figure 3.12 shows the photograph of a 250 cm^2 titanium disc made of spherical titanium particles (Figure 3.13). Extreme surface titanium particles are pressed against the catalytic layer. Figure 3.14 shows a surface view of an

Figure 3.12 Micrograph of a 250 cm^2 porous Ti current collector.

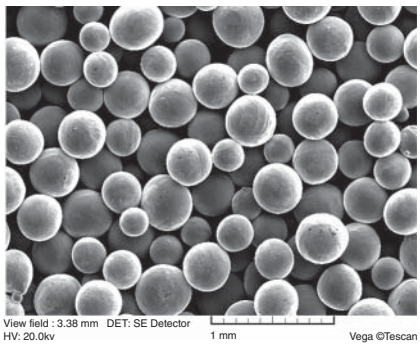

Figure 3.13 SEM image of a porous Ti current collector with spherical particles.

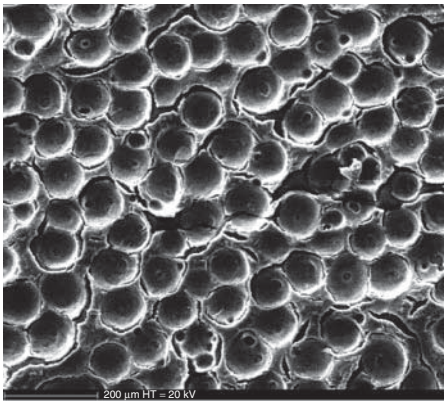

Figure 3.14 SEM image of the surface of an IrO_2 catalytic layer after operation [14].

IrO_2 catalytic layer after operation. The porous current collectors pressed again the MEA form spherical craters around which cracks can be observed. This is the region where evolving oxygen is collected and evacuated backward through the current collector.

3.3.4
Spacers

In a PEM cell, there is a need to manage a void section parallel to the current collectors through which liquid water can be pumped and where gaseous reaction products are collected. Several technology options are available. The first one is similar to what is used in fuel cell technology: a machine-grooved thick bipolar plate is equipped with flow channels. Another option (Figure 3.15) is to use a cell spacer (e.g. a titanium grid) that is sufficiently thick. The mesh structure needs to be optimized, taking into account the nominal current density of operation and the pressure of operation. At the periphery, a polymeric sealant of appropriate mechanical properties is used to ensure water and gas tightness, for water injection and gas collection, and to facilitate the distribution of compression forces in the filter press configuration.

3.3.5
Bipolar Plates

Bulk titanium plates are usually used as bipolar plates between adjacent cells. Although bulk electronic conductivity of titanium is much lower than that of other metals (e.g. stainless steel), titanium is most interestingly prone to surface oxidation and chemically stable in the environment of PEM water electrolysis cells (when contacting highly deionized water with i.e. 10–18 MΩ cm resistivity). Figure 3.16 shows XPS spectra measured on a titanium plate after 1 month passed in oxygen-saturated deionized water at 80 °C. Surface etching (100 s etching

Figure 3.15 Photograph of a grid spacer installed in a srack + details of water injection/gas collection.

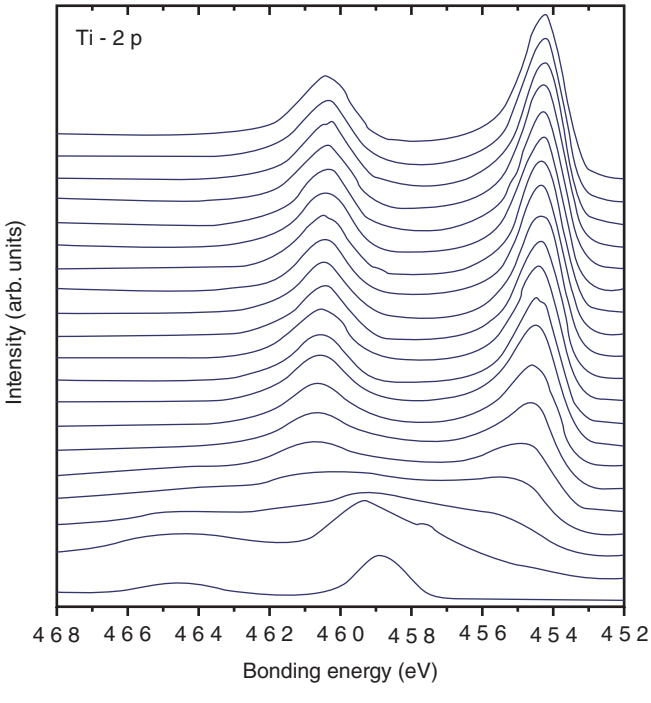

Figure 3.16 XPS profiles as a function of surface etching.

with Ar ions between two consecutive spectra) provides information about the structure and thickness of the passivating surface layer. This is a nanometre thick homogeneous film of TiO_2 that prevents metal dissolution. The next layers contain TiO and Ti_2O_3 but they probably form during the etching process. The

following layers are those of bulk Ti. During electrolysis, the behaviour of this surface oxide layer under polarization is not fully understood but bulk corrosion of the plates is not an issue. Surface coating is sometimes considered as an interesting option to reduce parasite contact ohmic resistances and increase performance durability. Thin noble metal (Au, Pt), Ti carbide or nitride can be used for that purpose. At the cathode, titanium hydrides may form, even at low temperature, but the impact on the durability of both bipolar plates and current distributors is not a matter of concern.

3.4 Electrochemical Performances of Unit PEM Cells

3.4.1 Polarization Curves

As discussed above, carbon-supported platinum nanoparticles are used as an electrocatalyst for the HER, and iridium (metal or oxide) is used for the OER in conventional PEM water electrolysers. Best electrolysis efficiencies ($\varepsilon_{\Delta H} \approx 70\%$ at $1\,A\,cm^{-2}$) can be obtained using noble metal loadings of about $0.5\,mg\,cm^{-2}$ of Pt for the HER and about $2\,mg\,cm^{-2}$ of Ir (or iridium oxide) for the OER [4]. PEM water electrolysis is still considered as an expensive technology due to the use of noble metals but detailed cost analysis reveals that the cost of PGM catalysts is low at the system level, less than a few percentage points of the entire cost. PGM contents can be reduced using for example Pt–Pd alloys or Pd can also be used at the cathode and iridium-based mix oxides at the anode [15].

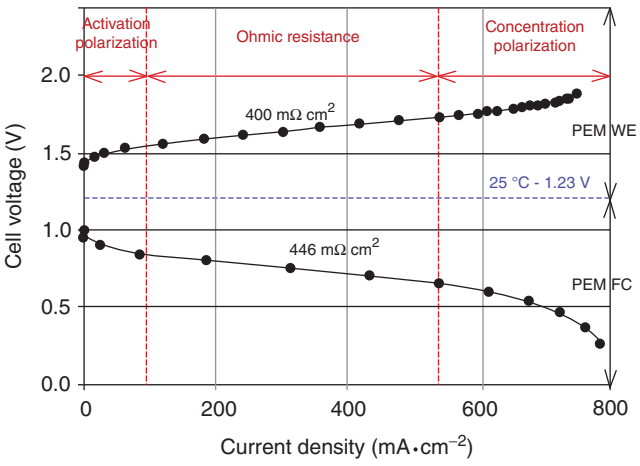

Figure 3.17 Typical PEM fuel cell and water electrolysis cell polarization curves.

Figure 3.17 shows on the same graph typical polarization curves of a PEM H_2/O_2 fuel cell and a PEM water electrolysis cell. In both cases, three distinct domains are observed: (i) at low current density (when the effect of ohmic resistances can be neglected), this is the activation domain where logarithmic relationships due to Butler–Volmer charge transfer kinetics are obtained; (ii) in the intermediate range, the shape is mainly linear; this is a domain of potential where charge transfer resistances are becoming very low and where the cell resistance is becoming predominant and (iii) in the third domain, at high current density, there is a tendency to reach a limiting current density. In fuel cells, this is due to mass transport of gases to the interfaces. In water electrolysis cells, this is usually due to gas screening effects and mass transport limitation across the porous current distributors.

Figure 3.18 shows two reference polarization curves that are characteristic of the performances of modern PEM water electrolysis cells. The grey rectangle area in the middle of the graph delineates a range of performances met by modern electrolysers; 80% enthalpy efficiency at 1 A cm^{-2} is common good practice, at least at the laboratory scale. To further improve the interest for the technology, there is a need to increase current density (more compact systems will contribute to reduced capex's) and to reduce operating cell voltage (leading to higher efficiency and better durability). This can be achieved by developing more efficient electrocatalysts and by using thinner SPEs, in order to reduce the ohmic drop across the membrane (Figure 3.19). There is a limit, however, to such progress, especially in using thinner SPEs, because in conventional membrane materials, gas-cross permeation effects tend to increase more rapidly when the operating pressure is raised and such membranes should be used only for operation at atmospheric pressure.

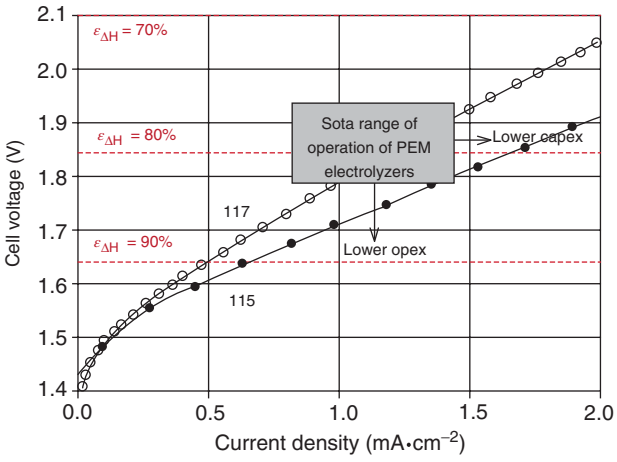

Figure 3.18 Reference polarization curves of PEM water electrolysers.

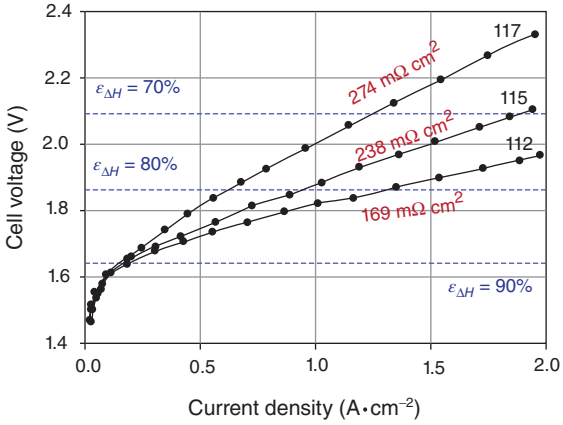

Figure 3.19 Polarization curves measured with Nafion membranes of different thicknesses.

3.4.2
Characterization of Individual Electrodes

In liquid electrolyte cells, electrochemical characteristics of individual electrode/electrolyte interfaces can be investigated separately using reference electrodes. PEM cells are very compact. They use very thin (a fraction of a millimetre thick) and solid MEAs. It is therefore not possible to introduce a conventional (e.g. saturated calomel electrode) reference electrode or even a capillary in order to separately probe anode or cathode responses. However, several techniques described in the literature are using a so-called 'internal reference electrode' to bypass this problem [9, 16]. Figure 3.20 shows the schematic diagram of a PEM cell equipped with such a reference electrode. The cell itself is located at the bottom of the membrane strip and the reference (usually a platinum deposit) is located on top. When hydrogen is supplied to

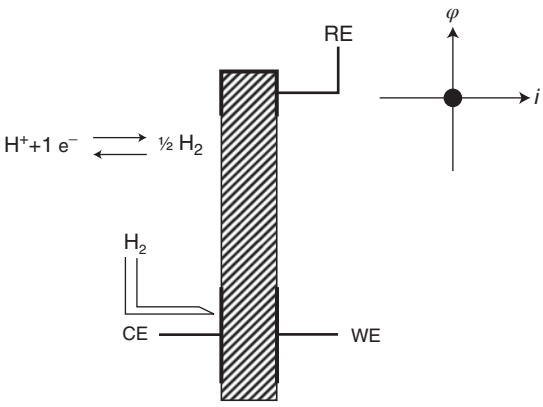

Figure 3.20 Schematic diagram of a reference electrode.

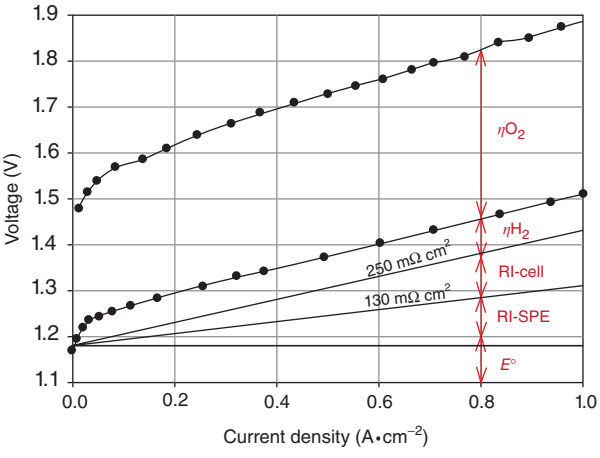

Figure 3.21 Individual voltage terms of the polarization curve of Figure 3.18 in the restricted 0–1 A cm^{-2} range. $T = 90\,°C$, $P = 1$ bar.

the reference, the potential is usually stable and well-defined (corresponding to the normal hydrogen electrode). This configuration is useful to investigate the behaviour of laboratory cells (but not so easily implemented on industrial systems) and separately probe anode and cathode behaviour, both at rest and under current circulation.

Figure 3.21 shows how each term of the cell voltage varies with operating current density at 90 °C. The free energy electrolysis voltage (see section on fundamentals of water electrolysis) at 90 °C is close to 1.18 V.

The ionic resistance of the SPE and the electronic resistance of non-MEA cell components introduce two loss terms that increase linearly with operating current density. A thin membrane and an appropriate cell design are required to keep these resistances as low as possible (a cell resistance of x mΩ·cm^2 will add a voltage drop of x mV at 1 A·cm^{-2}). The HER overvoltage η_{H_2} is usually low because of the high kinetics of the reaction. However, the anodic overvoltage η_{O_2} is usually much higher (IrO_2 is a good OER catalysts; RuO_2 is better but unstable at anodic potentials of interest and Pt is a poor catalyst), being the most significant source of energy loss. Voltage drops vary with operating temperature (Figure 3.22). Optimal operation of PEM water electrolysis cells is found somewhere between 60 and 90 °C but degradation rates tend to increase with operating temperature.

3.4.3
Charge Densities and Electrode Roughness

There are two main parameters that determine the electrocatalytic activity of catalytic layers in PEM water electrolysis cells: the chemical composition of the catalysts (usually Pt for the HER and IrO_2 for the OER) and the surface area of the catalyst/electrolyte interfaces. Surface characteristics are usually determined

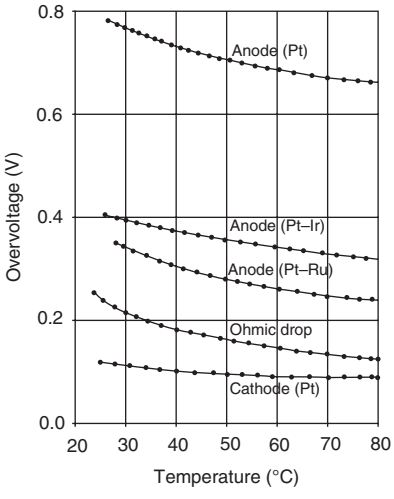

Figure 3.22 Temperature dependence of cell voltage components [4].

by measuring the roughness factor of each electrode. The roughness factor r_f is the dimensionless ratio of the real surface area to the geometrical area. $R_f = 1$ when smooth electrodes are used and can go up to several hundreds for rough interfaces. Cyclic voltammetry provides a convenient way to measure roughness factors because the electric charge that is required to load/unload interface capacitances is proportional to the surface of the interface.

3.4.3.1 Half-Cell Characterization

Figure 3.23 shows the cyclic voltammogram measured at the cathode of a PEM water electrolysis cell using an internal reference electrode. The CV measured on a smooth Pt foil in 1 M sulphuric acid aqueous solution is also plotted for comparison.

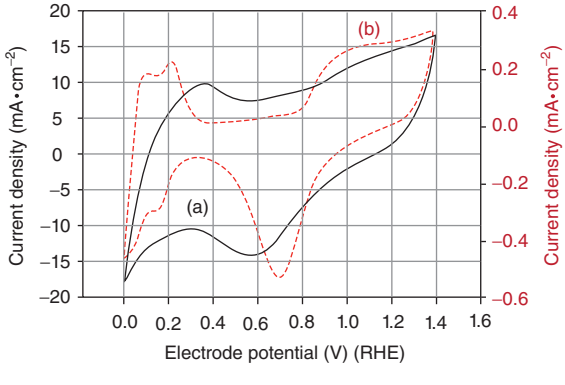

Figure 3.23 (a) Typical CV measured at the C–Pt cathode of a PEM water electrolysis cell and (b) CV on a smooth Pt foil, 1 M H_2SO_4. $v = 50\,mV \cdot s^{-1}$ [17].

The CV measured on the PEM cell is somewhat distorted due to several reasons: (i) traces of dissolved oxygen (due to oxygen cross-permeation from the anode) are difficult to eliminate; at the cathode, they are electrochemically reduced during the cyclic voltammetry experiment and the lower the electrode potential the higher the reduction current, which tends to bend the CV towards negative currents; (ii) the use of a carbon carrier of large surface area at the cathode for HER induces a high capacitive response that tend to smooth out platinum features, in particular in the hydrogen adsorption region of the cycle and (iii) it is difficult to neatly clean the SPE; traces of alcohols used during the plating process tend to adsorb at the surface of the Pt particles and are difficult to remove. Nevertheless, Figure 3.23 shows that the main features of the PEM Pt cathode are sufficiently well-marked to estimate (at least approximately) the roughness factor r_f of the interface, which is the dimensionless ratio of the total Pt electrolyte interface in square centimetre divided by the geometrical surface of the MEA in square centimetre, taking a reference charge of 210 μC cm^{-2} for a smooth Pt surface [17]. On the basis of this assumption, the roughness factor measured in Figure 3.23 is approximately 380. There is of course a direct advantage of using electrodes with high roughness factor and r_f depends mainly on the catalyst particle shape, the thickness of catalytic layer and the coating parameters. In conventional MEAs, the roughness factor of PEM cathodes usually lies in the 100–600 range and it is not an easy task to go beyond such values. A large concentration of nanoparticles are required for this purpose. Nanoparticles can be synthesized separately and then coated over the membrane. They can also be synthesized directly onto the membrane surface, using, for example, the impregnation/reduction method mentioned above. In that case, nanoparticles form directly inside the membrane subsurface. The polymer matrix tends to prevent growth and agglomeration. In such a case (Figure 3.24),

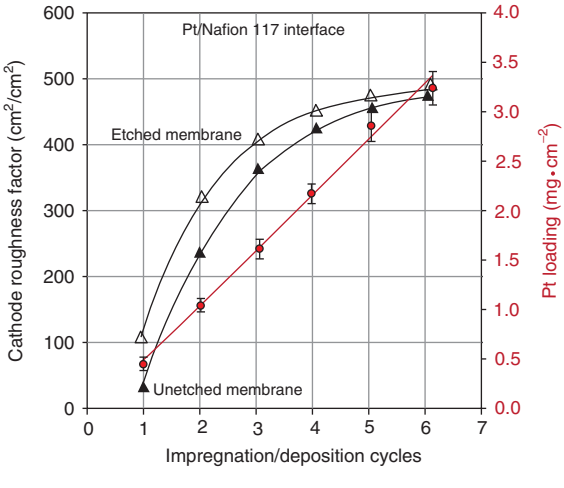

Figure 3.24 Plot of roughness factor as a function of Pt loading at the cathode of a PEMWE cell [4].

a relationship is observed between the roughness factor and noble metal loading but the roughness factor tends to reach a maximum limit at high loading values.

Half-cell measurements can also be used to probe anodes, which is the most critical electrode in a PEM water electrolysis cell (seat of larger charge transfer overvoltage and prone to fast degradation). A typical CV measured on a PEM water electrolysis anode containing unsupported IrO_2 particles is provided in Figure 3.25 for different scan rates. The roughness factor can be estimated integrating the cyclic voltammogram in the 100–1200 mV potential and making comparison with a reference charge of 310 μC cm^{-2} [18]. The roughness factor associated with the CV of Figure 3.25 is approximately 730, which is close to values obtained at cathodes (differences are usually due to high PGM loadings at anodes). An interesting observation is that r_f values tend to decrease markedly when the potential scan rate increases, indicating that some reacting sites are less accessible than others for the charge transfer reactions.

3.4.3.2 Full-Cell Characterization

It is not always possible to use internal reference electrodes to investigate separately the behaviour of PEM water electrolysis anodes and cathodes, in particular in stacks. However, it is still possible to perform cyclic voltammetry experiments (when a three-electrode potentiostat is used, the reference electrode input is short-circuited with the counterelectrode, and a difference of potential is applied between these two short-circuited electrodes and the working electrode). The potential range of the scan must be less than the Gibbs free energy electrolysis voltage (1.23 V in standard conditions), typically ±1 V. A typical example is provided in Figure 3.26. A detailed analysis of the physical meaning of individual peaks is beyond the scope of this chapter but the coulombic charge obtained by the integration of a cyclic voltammogram between potential scan values provides valuable information that is related to the total area of anode/electrolyte and

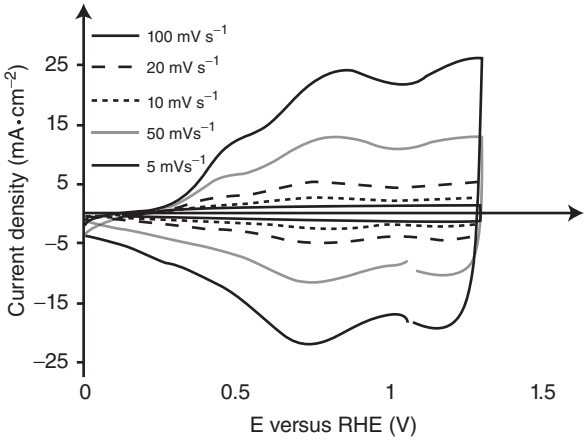

Figure 3.25 Typical CV measured at the IrO_2 anode of a PEM water electrolysis cell (1.8 mg cm^{-2}). $v = 50$ mV s^{-1}.

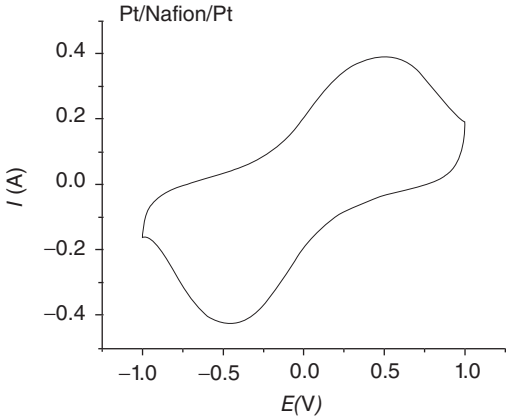

Figure 3.26 CV measured on a Pt/Nafion/Pt MEA using a floating reference point

cathode/electrolyte interfaces, and thus to the cumulative roughness factor of the anode and the cathode. By measuring a reference charge value using, for example, a smooth Pt cathode and a smooth iridium anode in acidic environment, it becomes possible to estimate the roughness of the cell and to follow degradation processes.

The same measurements can be performed at the stack level (Figure 3.27). From a qualitative viewpoint, the superposition of individual cell cyclic voltammograms

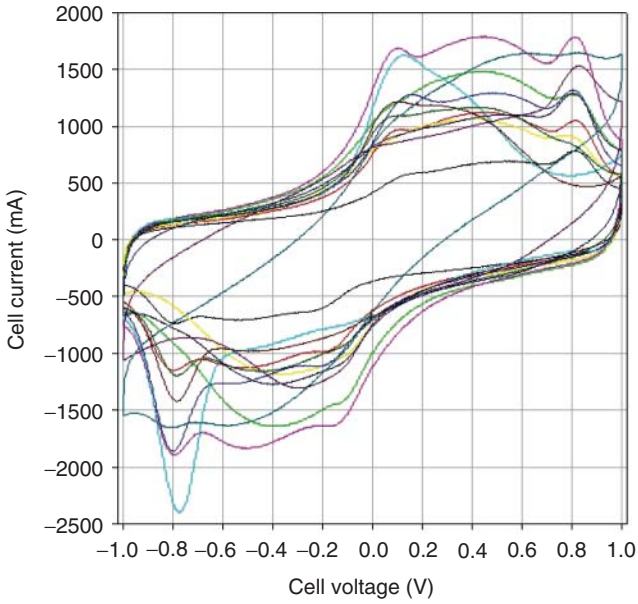

Figure 3.27 CVs measured on the MEAs of a 12 cell stack using a floating reference point.

provides information on the discrepancy of charge density between the different cells. The distribution of electric charge may be due to differences from one MEA to another or from different electrical environments in the stack. What is needed is to optimize internal cell geometry and cell stacking processes in order to reduce as much as possible charge differences among the cells. The method can also be used for maintenance operation, offering the possibility to analyse the behaviour of individual cells along durability tests.

3.4.4 EIS Characterization

Electrochemical impedance spectroscopy (EIS) is another useful tool that can be used to analyse the behaviour of PEM water electrolysis cells. When reference electrodes are available, EIS can be used to measure individual cell interfaces. When no reference is available, EIS can be used to measure the global impedance of the cell for different polarizations, in real water electrolysis conditions. An experimental limitation comes from the maximum current density that can be reached, especially to characterize large MEAs. Modern frequency analysers can be coupled to amperometric boosters that can deliver up to approximately 100 A. Figure 3.28a shows the cross section of a typical

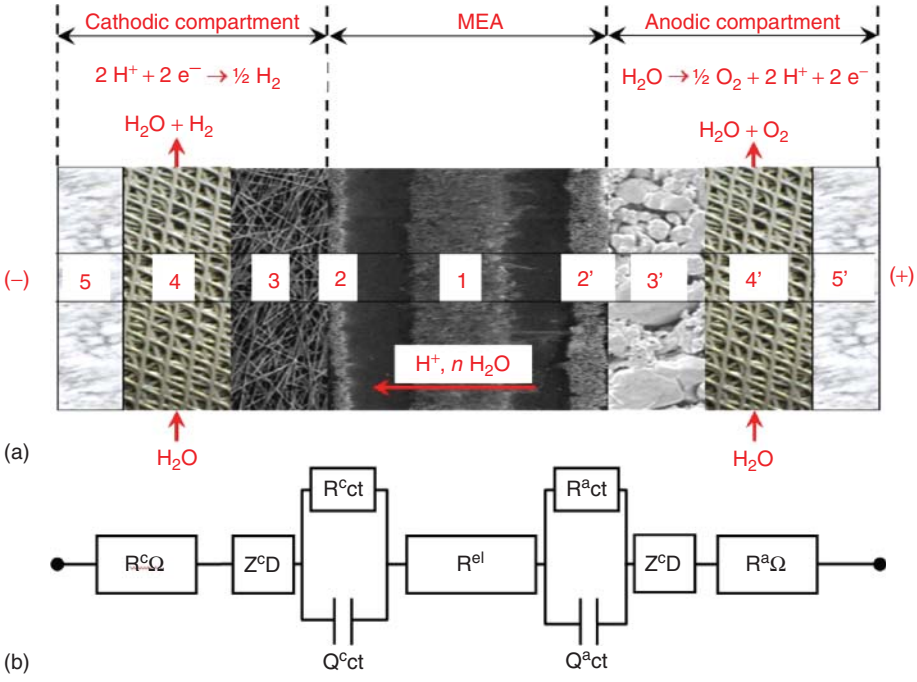

Figure 3.28 (a) Cross section of a PEM water electrolysis cell; and (b) equivalent electric circuit [19].

PEM cell (thicknesses of individual components are not at scale) [19]. The PTFE (poly(tetrafluoroethylene))-reinforced SPE at the centre (1) and its two catalytic layers (2 and 2′) are clamped between a carbonaceous cathodic gas diffusion layer (GDL) and an anodic porous titanium current distributor (3 and 3′). Two grid spacers (4 and 4′) placed close to the end plates (5 and 5′) are used to manage a void for water circulation and gas collection. The equivalent electrical circuit that reflects the different features of the PEM cell are pictured in Figure 3.28b. Different circuit components are:

- R^{c}_{Ω} and R^{a}_{Ω} ($\Omega\,cm^2$): electronic resistance of electron-conducting metallic cell components (bipolar plates, spacers and current collectors) at the cathode and the anode, respectively.
- R^{el} ($\Omega\,cm^2$): ionic resistance of the SPE.
- R^{c}_{ct} ($\Omega\,cm^2$): cathodic polarization (charge transfer) resistance associated with the HER.
- R^{a}_{ct} ($\Omega\,cm^2$): anodic polarization (charge transfer) resistance associated with the OER.
- Q^{c}_{dl} ($F\,cm^{-2}$): cathodic constant phase element, which is used to account for the pseudo-capacitive behaviour of the charged and 3D interface between the porous catalytic layer and the electrolyte.
- Q^{a}_{dl} ($F\,cm^{-2}$): anodic constant phase element for the pseudo-capacitive anode/electrolyte interface.
- Z^{c}_{D} ($\Omega\,cm^2$): cathodic diffusion impedance due to H_2 transport away from the cathode through the porous cathodic current distributor.
- Z^{a}_{D} ($\Omega\,cm^2$): anodic diffusion impedance due to O_2 transport away from the anode and/or to H_2O transport to the anode through the porous anodic current distributor.

Experimental impedance diagrams measured on PEM water electrolysis cells at cell voltages less than the free energy electrolysis voltage (1.23 V in standard conditions and 1.18 V at 80 °C) are pseudo-capacitive in shape. Pseudo-capacitances appear when rough electrochemical interfaces are used. They are modelled using constant phase elements (CPEs). The impedance Z_Q of a CPE noted Q is [20]:

$$Z_Q = \frac{1}{T\ (j\ \omega)^n} \tag{3.6}$$

where T is a frequency-independent constant in $F\,cm^{-2}\,s^{n-1}$ and n is a factor ranging between 0 and 1. $r_f = 1$ is equivalent to n = 1. In such case, T behaves like a puirecapacitance.

When the cell voltage increases, current starts to flow across the cell and the low frequency limit of the impedance spectra bends down towards the real axis (Figure 3.29). The resistance measured at low frequencies on the real axis is equivalent to the slope of the polarization curve at the same current density. In the low current density range where ohmic contributions are small, only one arc that can be described by two depressed semicircles is usually observed. As the current density increases, the arc gradually shrinks towards a single point on the real axis, which is the value of the ohmic cell resistance (Figure 3.30).

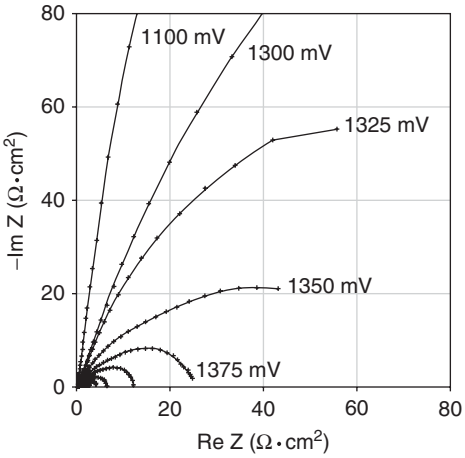

Figure 3.29 EIS impedance spectra (Nyquist coordinates) measured at different cell voltages and 80 °C on a 23 cm^2 PEM water electrolysis cell [17].

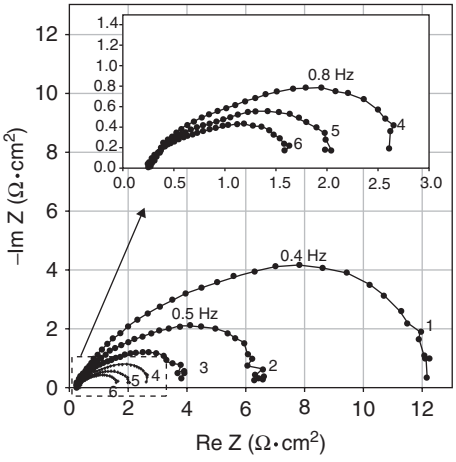

Figure 3.30 Zoom of EIS impedance spectra of Figure 3.29 for E_{cell} (mV) = 1 – 1400; 2 – 1425; 3 – 1450; 4 – 1475; 5 – 1500; 6 – 1525 mV [17].

At higher current densities, when current distributors of appropriate porosity are used, there is no mass transport limitation, and therefore the equivalent circuit of Figure 3.28b can be simplified by neglecting diffusion impedances (Z^c_D and Z^a_D). Half-cell measurements show that the charge transfer resistance associated with the HER at the cathode is usually much lower than the anodic charge transfer resistance associated with the OER (Figure 3.21). This is an indication that the two depressed semi-circles can both be attributed to the OER, which is a two-electron charge transfer process. Experimental impedance diagrams can therefore

be modelled using a simplified circuit that contains only two (resistance//CPE) circuits series connected with the ohmic cell resistance:

$$Z_{\text{cell}} \approx R_{\Omega} + \frac{1}{j\,\omega\,Q_{\text{HF}} + \frac{1}{R_{\text{HF}}}} + \frac{1}{j\,\omega\,Q_{\text{LF}} + \frac{1}{R_{\text{LF}}}} \tag{3.7}$$

where $j = \sqrt{-1}$, ω is the pulsation in rad s^{-1}, R_{Ω}(in Ω cm^2) $= R_{\Omega}^{c} + R^{el} + R_{\Omega}^{a}$ is the ohmic resistance of the cell determined from the high frequency intercept of the impedance spectra with the real axis in Nyquist coordinates, R_{HF} and R_{LF} (in $\Omega\,cm^2$) are the polarization resistances of the high (HF) and low (LF) frequency depressed semicircles, respectively, and Q_{HF} and Q_{LF} (in F cm^{-2} s^{n-1}) are their CPE.

Experimental observations are consistent with the Krasil'shchikov mechanism reported in the literature for the OER on iridium oxide (Table 3.1) and therefore full-cell EIS measurements can be used to measure the features of the anode, which, of the two electrodes found in PEM water electrolysis cells, is the one that is most prone to degradation.

3.4.5
Pressurized Water Electrolysis and Cross-Permeation Phenomena

3.4.5.1 Origins of Cross-Permeation Phenomena

As discussed above, the polymeric membrane used as a cell separator in water electrolysis cells should be totally gas-proof. In a real situation, this is not the case. The solubility of gases (hydrogen and oxygen) in perfluorosulphonated materials such as DuPont Nafion products is usually limited but not zero. This is the reason why the hydrogen content in the oxygen produced at the anode of a PEM cell is not zero and, conversely, the oxygen content in the hydrogen produced at the cathode is also not zero. This situation is due to the microstructure of these biphasic polymeric materials, which is a network of clustered and interconnected hydrophilic areas where proton conductivity takes place. They are surrounded by a continuous perfluorinated polymeric backbone (Figure 3.31, [21]). According to this model, there are ≈40 Å in-diameter clusters of sulphonate-ended perfluoroalkyl ether groups that are organized as inverted micelles and arranged on a lattice. These micelles are connected by pores or channels that are ≈10 Å in size. These $-SO_3^-$-coated channels were invoked to account for intercluster transfer of cations and ion conductivity.

Table 3.1 Two main OER mechanisms on Pt and IrO_2 (S = reacting site).

Mechanism 1: oxide path (Pt)	Mechanism 2: Krasil'shchikov path (IrO_2)
$4Pt + 4H_2O \rightarrow 4PtOH + 4H^+ + 4e-$ (step 1)	$S + H_2O \rightarrow S - OH + H^+ + 1e^-$ (step 1)
$4PtOH \rightarrow 2PtO + 2PtH_2O$ (step 2)	$S - OH \rightarrow S - O^- + H^+$ (step 2)
$2PtO \rightarrow O_2 + 2Pt$ (step 3)	$S - O^- \rightarrow S - O + e^-$ (step 3)
	$S - O \rightarrow S + 1/2O_2$ (step 4)

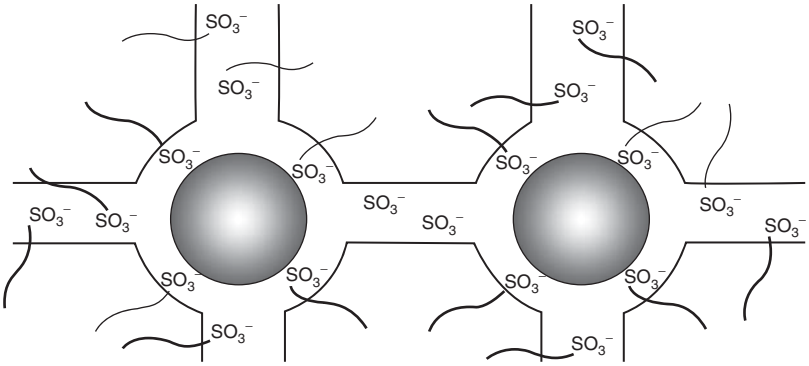

Figure 3.31 Nafion microstructure according to the model developed by Gierke, showing a network of clustered hydrophilic areas inside a main organic phase.

The driving force to the transfer of dissolved gases from one side to the other of the cell is the gradient of chemical potential across the SPE during operation, resulting from the gradient of pressure (concentration). The mass transport mechanism is mostly diffusion-controlled (convection has also been reported but found less significant because the size of ionic clusters in the SPE is very small). Hydrogen reaching the anodic compartment either can react chemically with oxygen or can also be e-oxidized at the anode. Symmetrically, oxygen reaching the cathodic compartment can react with gaseous or dissolved hydrogen or can be electrochemically reduced at the cathode. From a global viewpoint, this is as if a parasitic current was decreasing the chemical or faradaic efficiency of the cell. Faradaic efficiencies must be measured to optimize cell design and improve cell efficiency.

3.4.5.2 Hydrogen and Oxygen Solubility in SPEs

Henry's law constants for H_2 and O_2 are mainly the function of the EW of the polymer, water content, temperature and pressure [22]. Nafion appears to behave water-like below about 50 °C but not above, as also reported for ionic conductivity [23]. Gas solubility values in water can be taken, as a first approximation, for gas solubility in Nafion. For H_2, the following relations can be used in the 0–100 °C temperature range and the 1–10 atm pressure range [24]:

- for $0\,°C < T < 45\,°C$:

$$H_{H_2}^{H_2O} = 7.9 \times 10^6 \ \exp\left(\frac{-545}{T}\right) \times (1 + 0.000071\ P_{H_2}^3) \quad \text{in atm mol}^{-1}\ \text{cm}^3 \tag{3.8}$$

- for $45\,°C < T < 100\,°C$:

$$H_{H_2}^{H_2O} = 8.3 \times 10^5 \exp\left(\frac{-170}{T}\right) \times (1 + 0.000071\ P_{H_2}^3) \quad \text{in atm mol}^{-1}\ \text{cm}^3 \tag{3.9}$$

For O_2, the following relations can be used in the 0–100 °C temperature range, at 1 atm:

- for 0 °C < T < 45 °C:

$$H_{O_2}^{H_2O} = 1.3 \times 10^8 \ \exp\left(\frac{-1540}{T}\right) \quad \text{in} \quad \text{atm mol}^{-1} \ \text{cm}^3 \tag{3.10}$$

- for 45 °C < T < 100 °C:

$$H_{O_2}^{H_2O} = 5.1 \times 10^6 \exp\left(\frac{-500}{T}\right) \quad \text{in} \quad \text{atm mol}^{-1} \ \text{cm}^3 \tag{3.11}$$

3.4.5.3 Nafion Permeability to Hydrogen and Oxygen

The gas permeability P^m relates the flow of gas across the membrane to the difference of pressure set across:

$$P^m = \frac{v}{\Delta P} \ \frac{L}{A} \quad \text{in cm}^2 \ \text{Pa}^{-1} \ \text{s}^{-1} \tag{3.12}$$

In Equation 3.12, v is the rate of gas permeation (e.g. with units of N cm^3 s^{-1}); ΔP is the difference of gas pressure set across the membrane (in Pa); L is the thickness of the membrane (in cm) and A is the section of the membrane in cm^2. The structure of water electrolysis SPE is shown in Figure 3.31.

This is a 3D biphasic medium containing a large organic phase in the bulk of which a network of percolating and hydrophilic ionic clusters is homogeneously embedded. P^m values for hydrogen and oxygen varies markedly with both operating temperature and water content of the polymer electrolyte (Figure 3.32). They bracket those measured on PTFE, which is a characteristic of the SPE organic backbone and liquid water (which is similar to the hydrophilic proton-conducting clusters of the SPE). These measurements clearly show that the transport of hydrogen and oxygen across the SPE membrane is a diffusion-controlled process that

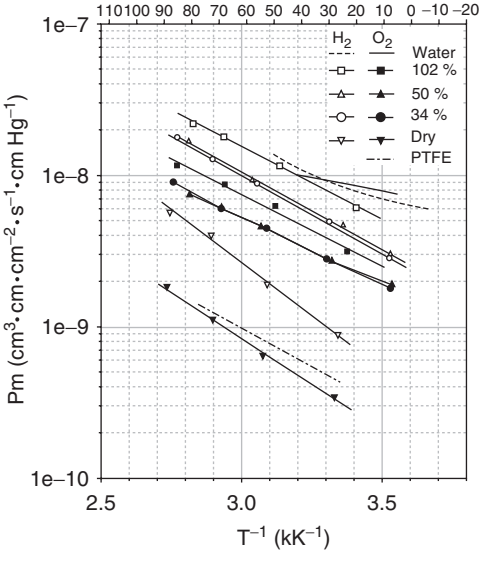

Figure 3.32 Hydrogen (open symbols) and oxygen (closed symbols) permeability of Nafion 117 with temperature and water content [25].

Table 3.2 H_2 and O_2 permeability and diffusion coefficient in fully hydrated Nafion 117 at different temperatures.

T (°C)	10	20	40	60	85
$P^{m}_{O_2}$ ($cm^2\,Pa^{-1}\,s^{-1}$)	2.1×10^{-12}	2.3×10^{-12}	3.7×10^{-12}	5.3×10^{-12}	8.4×10^{-11}
D_{O_2} ($cm^2\,s^{-1}$)	2.1×10^{-7}	2.5×10^{-7}	4.2×10^{-7}	6.5×10^{-7}	1.1×10^{-6}
$P^{m}_{H_2}$ ($cm^2\,Pa^{-1}\,s^{-1}$)	3.8×10^{-12}	4.6×10^{-12}	7.6×10^{-12}	1.2×10^{-11}	2.0×10^{-11}
D_{H_2} ($cm^2\,s^{-1}$)	3.9×10^{-7}	4.9×10^{-7}	8.7×10^{-7}	1.5×10^{-6}	2.6×10^{-6}
D_{H_2}/D_{O_2}	1.9	2.0	2.1	2.3	2.4

involves water-dissolved H_2 and O_2 molecules. Gas transport through the organic matrix can be neglected. PEM water electrolysis cell are fully hydrated and, therefore, H_2 and O_2 permeabilities are at maximum. Permeation flows are related to Fickian diffusion coefficients D_i (expressed in $cm^2 \cdot s^{-1}$) through the following relationship:

$$D_i = P_i^{m}\ R_{PG}\ T\ C_i \tag{3.13}$$

R_{PG} is the constant of perfect gas, T is the temperature in K and C_i is the solubility of species i. Hydrogen and oxygen diffusion coefficients in Nafion 117 at different operating temperatures are compiled in Table 3.2. D_{H_2} is approximately two times larger than D_{O_2} over the 0–100 °C temperature range of operation of PEM water electrolysis cells, and, as a result, the hydrogen content in the oxygen flow is usually larger than the oxygen content in the hydrogen flow.

3.4.5.4 A Simple Model to Account for Gas Cross-Permeation

The main features of gas cross-permeation can be determined from the following simplified permeation model. The model, based on simplifying assumptions, relates the level of contamination (H_2 in O_2 expressed in mol. or vol%) to the water content of the membrane. Model assumptions are: (i) mass transport is diffusion-controlled; (ii) diffusion processes follow Fick's first law of diffusion; (iii) at a given current density, temperature and pressure, the hydrogen concentration C_{H_2} dissolved in the polymer at the cathode is constant and (iv) faradaic efficiency is assumed to be unity. Then, Φ_{H_2}, the flow of hydrogen (in mol $cm^2\,s^{-1}$) across the membrane of thickness L, is given by:

$$\Phi_{H_2 i} = D_{H_2}\ \frac{\Delta C_{H_2}}{L} \tag{3.14}$$

Using Equation 3.12, Equation 3.14 can then be rewritten as:

$$\Phi_{H_2} = \frac{D_{H_2}}{H_{H_2}}\ \frac{(P_1 - P_2)}{L} \quad \text{in mol}\ \ s^{-1}\ \ cm^{-2} \tag{3.15}$$

Let j be the current density (in A cm^{-2}) flowing across the PEM cell. The mole number of oxygen produced at the anode per second and per square centimetre is $n_{O_2} = j/2\ F$ where F is the Faraday constant. The mole number of hydrogen

reaching the anodic compartment by cross-permeation is given by Equation 3.15. In stationary conditions (constant current density, temperature and pressure), the mole percentage of H_2 in O_2 is:

$$\frac{n_{H_2}}{n_{H_2} + n_{O_2}} \times 100 \tag{3.16}$$

The main result of this simplified model is that the H_2 content in O_2 is inversely proportional to current density (at constant temperature and pressure). Experiments show that this is not exactly the case, in particular at low current densities (Figure 3.33).

At low current density where the inverse relationship should be observed, there is a strong discrepancy between the experimental data and the model. It can be attributed to the faradaic efficiency at the anode. Part of the hydrogen reaching the anode by cross-permeation is reoxidized into protons. The fraction of hydrogen that is reoxidized depends on the geometry of the anode/SPE interface. A complete mass balance of the process can be used to determine the faradaic efficiency of each electrode. By taking into account faradaic efficiency, a much better fit can be obtained. However, the model has no general validity because it strongly depends on the particular microstructure of the MEA used in the experiments. These effects are amplified when the pressure is raised. Figure 3.34 shows that the hydrogen content in oxygen and the faradaic efficiency tend to decrease significantly as the operating pressure is raised. Some solutions have been reported in

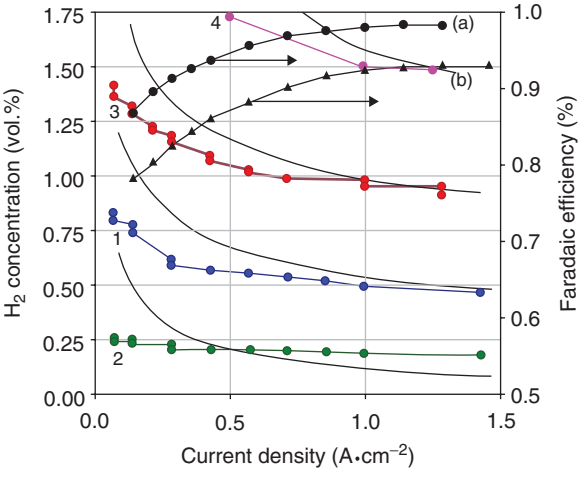

Figure 3.33 (Left) Hydrogen content (vol%) in the anodic oxygen–water vapour mixture, measured at different pressures as a function of operating current density; 50 cm^2 monocell. Pt for the HER, Ir for the OER and Nafion-117 as SPE. $T = 85\,°C$. [26]. (1) 1 bar (current collector is platinized); (2) 1 bar (current collector not platinized); (3) 6 bar (current collector is platinized) and (4) 30 bar (current collector is platinized); Full lines: best fits using Equation 3.13: see text. (Right) Current efficiency at the cathode at (a) 2 bar and (b) 30 bar, as a function of operating current density.

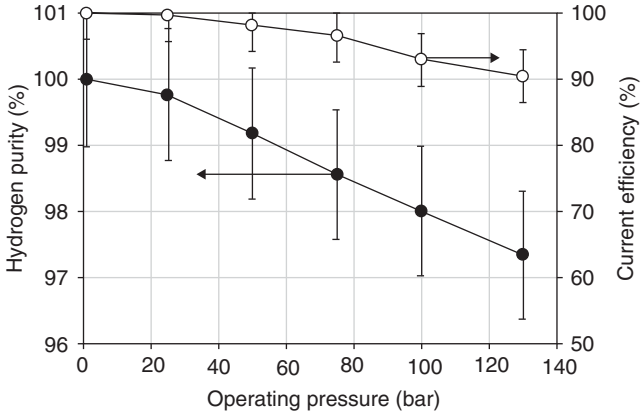

Figure 3.34 Hydrogen purity (●, vol%) in the cathodic compartment and current efficiency (○, %) as a function of operating pressure.

the literature to minimize these negative effects. According to Equation 3.15, the cross-permeating flow of hydrogen can be reduced mainly by decreasing the diffusion coefficient, increasing solubility or increasing membrane thickness but each option comes with additional negative side effects. Thicker SPEs or introduction of PTFE fibres in the SPE (Figure 3.28a) have positive effects on cross-permeation but increase cell resistance at the same time. The same situation prevails when inorganic fillers (such as silica or zirconium oxide) are incorporated into the SPE. Incorporation of zirconium dioxide particles in the SPE can reduce D_{H2} by a factor varying from 0 to about 10, depending on the filler concentration, but the mechanical behaviour of the membrane is also affected. A last option that can be used to reduce the hydrogen content in evolving oxygen and that can help to manage safety issues (but not losses in faradaic efficiency) is to promote internally the catalytic recombination of H_2 with O_2. This can be achieved using so-called internal gas recombiners [26], for example, by adding Pt particles (recombination sites) inside the membrane. Whatever the solution used, the price to pay is always a lesser ionic conductivity of the SPE, an additional ohmic term during electrolysis and a lower cell efficiency.

3.4.6
Durability Issues: Degradation Mechanisms and Mitigation Strategies

Capital expenses of PEM water electrolysis cells are directly related to the durability of PEM cells. Market requires technologies that can maintain electrochemical performances in the upper range of $10^4 - 10^5$ h at nominal operating conditions. According to the literature, the durability of PEM water electrolysis cell is already excellent and durability tests have been performed at a stack level of over 50 000 h of intermittent operation without significant performance losses. Some results are plotted in Figure 3.35.

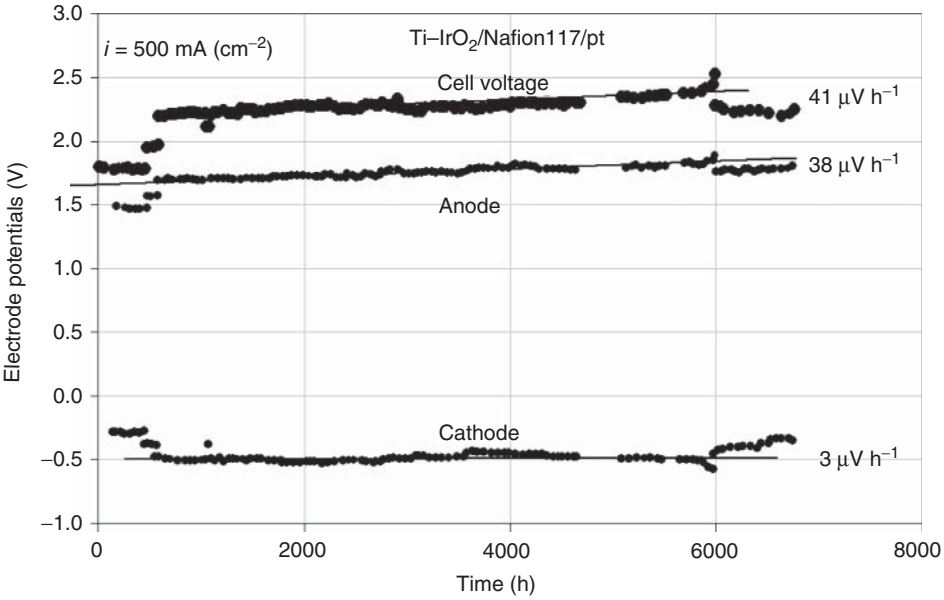

Figure 3.35 Long-term performance of a PEM water electrolysis cell showing individual electrode behaviour.

As in fuel cell technology, degradation rates can be conveniently expressed in $\mu V\,h^{-1}$. Using internal reference electrodes, it is possible to separately record cell voltage and anodic and cathodic electrode potential. In the case reported here (lab-scale experiment using 1.8 MΩ cm deionized water and a strict monitoring of the purity of the feed water), the degradation process is mainly due to a loss of activity at the anode. In fact, there are two main sources of performance degradation: (i) a set of reversible physical processes and (ii) a set of irreversible phenomena that tend to spoil the integrity of MEAs and other cell components. Examples of the first type are gradual loss of electrochemical performances due to the incorporation, into the SPE, of trace amounts of miscellaneous metallic cations. These cationic species are released by the stainless steel tubing of the electrolysis module in contact with highly deionized water. Incorporation into the SPE takes place by ion exchange with the protons of the membrane. In response to the internal electric field, these species tend to migrate to the cathode where they can form underpotential deposits onto platinum particles. As a result, the cathodic overvoltage increases with time and the energy consumption of the stack increases. Usually, this kind of problem can be controlled by a strict monitoring of the quality of the makeup water and by occasional maintenance operations. Examples of the second type of degradation processes are (i) gradual erosion of catalytic layer and loss of active sites; (ii) chemical degradation of the SPE due to the formation of local hot points (this may be caused by uneven repartition of current lines across the cells or to the formation of hydrogen peroxide at rest time). Such degradation mechanisms are very critical because they can ultimately lead to the sudden

perforation and destruction of the MEAs and the electrolysers. Some example are reported in Ref. [7]. The negative impact of degradations phenomena can be avoided by regular maintenance operations.

3.5 Cell Stacking

3.5.1 Different Stack Configurations

Individual PEM cells are of limited production capacity. Individual cells are usually stacked together to adjust the production capacity of the electrolyser to process requirements [27, 28]. Main stack concepts are schematically pictured in Figure 3.36.

The monopolar design (Figure 3.36a) is a design of PEM cells connected in parallel. A better design consists of a series connection of these cells. The most popular and simple design is to apply the stack voltage directly between the two end plates (b). Alternatively (c), a central anode (or cathode) can be used. Figure 3.37 shows the cross-section two MEAs stacked together. Porous current distributors are used in each cell compartment (label 2). Bipolar plates are made of compressed carbon powder with built-in channels (label 3) used for water circulation. On the anodic side the bipolar plate is surface coated by a thin film of tantalum that is used to prevent surface oxidation.

3.5.2 Design of PEM Water Electrolysis Stack

Individual PEM water electrolysis cells are stacked to form electrolysers of larger production capacity (Figure 3.38) [29]. The challenge here is to use a proper design that ensures the homogeneous distribution of liquid water over the entire surface area of anodic catalytic layers and the efficient collection of production liquid – gas

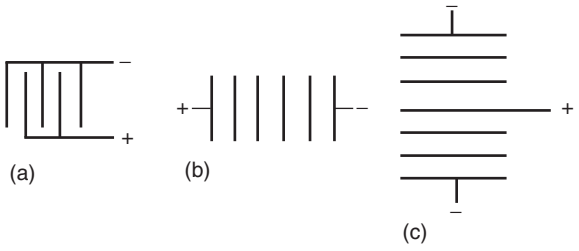

Figure 3.36 Series connection of electrolysis cells: (a) monopolar; (b) bipolar; (c) bipolar with central anode.

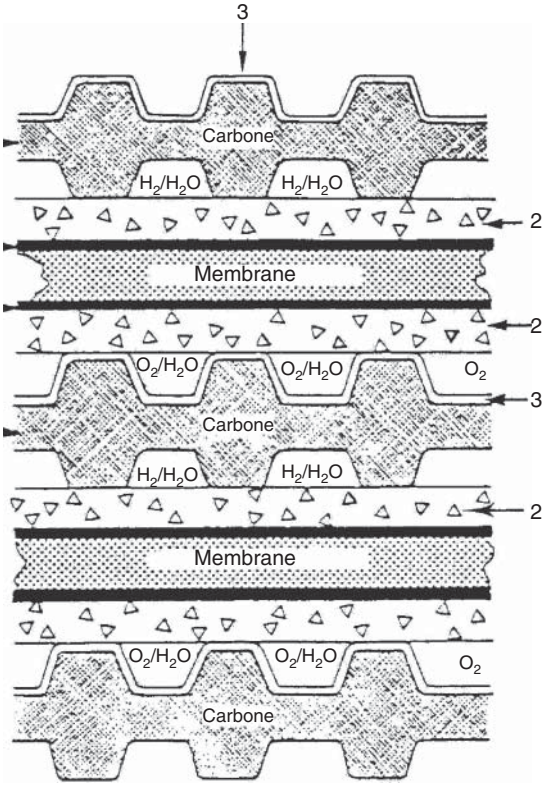

Figure 3.37 Cross section of a PEM water electrolysis stack [5].

Figure 3.38 Photograph of two PEM water electrolysis stacks, 1.6 Nm^3 H_2 h^{-1} each [29].

mixtures in view of separation in a subsequent step. Homogeneous distribution of current lines across the stack is another key challenge that needs to be appropriately managed to avoid unacceptable high degradations rates. This is usually achieved by ensuring the homogeneous distribution of compression mechanical forces across the stack. In PEM water electrolysis stack, polymer-based sealants are used to adjust compression forces and to delineate the volumes of individual cells. They are also used to support the different of pressure between the cells and the atmosphere. Conventional sealants allow operation up to several bars but leaks appear above this level and operation at higher operating pressures requires other approaches. An individual PEM stack can be mounted on individual pressurization chambers or two stacks can be encapsulated in pressurization cylinders. The two PEM water electrolysis stacks of Figure 3.38 (13 MEAs, 250 cm^2 each, delivering a maximum of 1.6 Nm^3 H_2 h^{-1} at 1.2 A cm^{-2}) mounted in a pressurization cylinder are shown in Figure 3.39. Water inlet and liquid–gas mixtures outlet are located on the front flange. For safety reasons, it is better to ensure a flow of pressurized inert gas across the pressurization vessel during electrolysis, in order to remove traces of leaking hydrogen and/or oxygen that would otherwise tend to accumulate inside the vessel. During electrolysis, two high-pressure pumps are used for the circulation of pressurized liquid water in both anodic and cathodic compartments.

3.5.3
Stack Performances

Concerning the design of a PEM water electrolysis stack, the main challenge is to ensure homogeneous distribution of liquid water in anodic cell compartments and homogeneous distribution of current lines across the stack. One of the best merit functions that tells whether the stack is operating appropriately or not is the

Figure 3.39 Photograph of pressurized PEM water electrolysis bistack, 3.2 Nm^3 H_2 h^{-1}, 60 bars [29].

set of individual cell polarization curves. As an example, a set of such data measured on one of the two stacks of Figure 3.28 (equipped with PTFE-reinforced MEAs for operation at elevated pressure) is provided in Figure 3.40. At low current densities (when only charge transfer resistances at the anode and the cathode prevail), some minor differences are already observed. This is the first indication that MEAs do not operate homogeneously but it is difficult to tell if this comes from intrinsic differences (e.g. different roughness factors) or from their individual environment in their respective cells (e.g. heterogeneous contacts with current distributors). In the intermediate current density range, polarization curves exhibit different ohmic slopes, as discussed for Figure 3.18. Because all MEAs are made with the same membrane material, this is a strong indication that individual cell resistances are different. This may be due to surface oxidation of some titanium cell components or more or less resistive MEAs. In the high current density range, unexpected cell voltages rise indicate that a limiting current density of 450–500 mA cm^{-2} can be obtained. This is an indication that gas screening effects are taking place, and probably that current distributors are not firmly pressed against the MEAs (thus explaining the strong ohmic slopes). When the stack is appropriately tightened up, screening effects disappear. Now, new PEM water electrolysers require a period of activation during which thermal equilibrium is reached, clamped MEAs become fully hydrated and gases find their way across current distributors. After that period (Figure 3.41), the system operates more homogeneously.

3.5.4
Diagnosis Tools and Maintenance

Problems of current homogeneity tend to become more critical as the size of MEAs increases. A PEM water electrolysis stack that can deliver up to

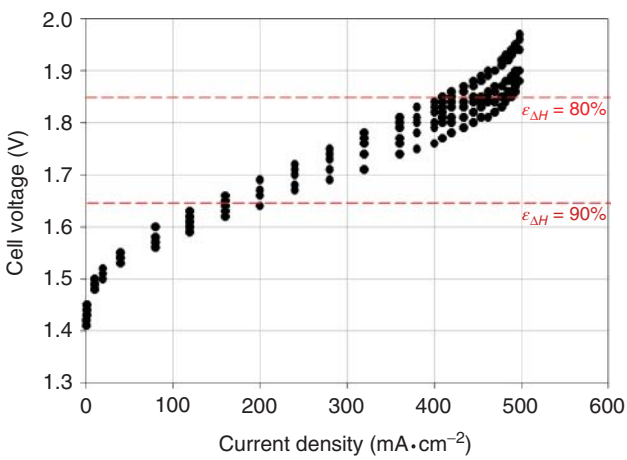

Figure 3.40 Some polarization curves of a 12-cell PEM water electrolysis stack.

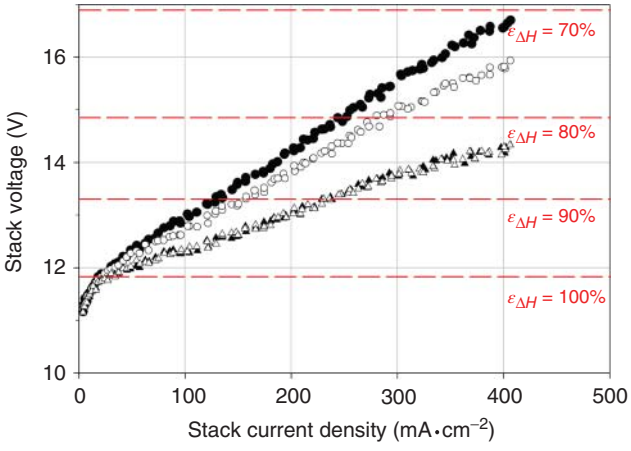

Figure 3.41 Pressurized bistack polarization curves. (● and ○) Before activation; (▲ and Δ) after activation.

10 Nm^3 H_2 h^{-1} (equipped with 600 cm^2 MEAs) is pictured in Figure 3.42 [19]. Again, the challenge is to make individual cells operate under the same conditions (performance discrepancies affect global performances but also durability issues). Figure 3.43 shows a plot of coulombic charge densities (measured by cyclic voltammetry) and internal resistances (the high frequency resistance measured by electrochemical impedance spectroscopy), for each individual cell of the stack.

Measurements were made on a prototype electrolyser that was assembled using simplified procedures in order to evaluate the impact of some assembling tools on stack performances. In this case, measurements show that data are significantly dispersed, indicating quite heterogeneous electrochemical environments for individual MEAs. The dispersion of charge density may come from a dispersion of performances of individual MEAs (e.g. unevenly hydrated) but also from

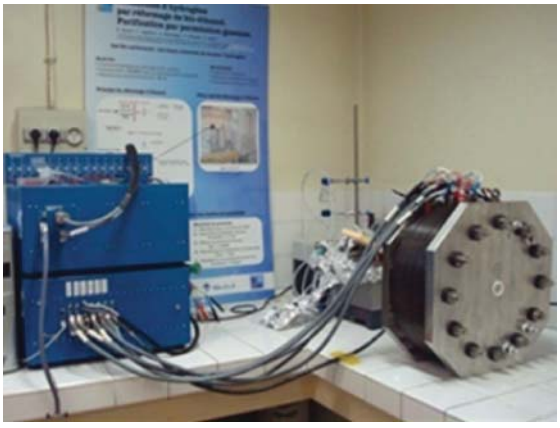

Figure 3.42 Picture of a PEM water electrolysis stack. (Source: CETH2 Co.).

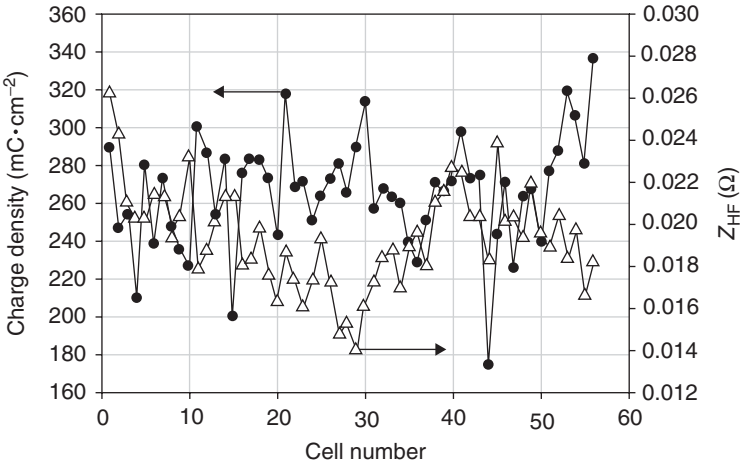

Figure 3.43 Plot of anodic charge density and high-frequency cell impedance of individual cells in the stack of Figure 3.42 [19].

the fact that they all experience a heterogeneous individual electrochemical environment, possibly because of different cell resistances. This is further confirmed by the dispersion of internal resistances measured by EIS. When a better control of the internal mechanics of the stack is achieved, data are less scattered (Figure 3.44). What is desirable for a higher efficiency and a better durability is high value roughness factors and low data dispersion between individual cells.

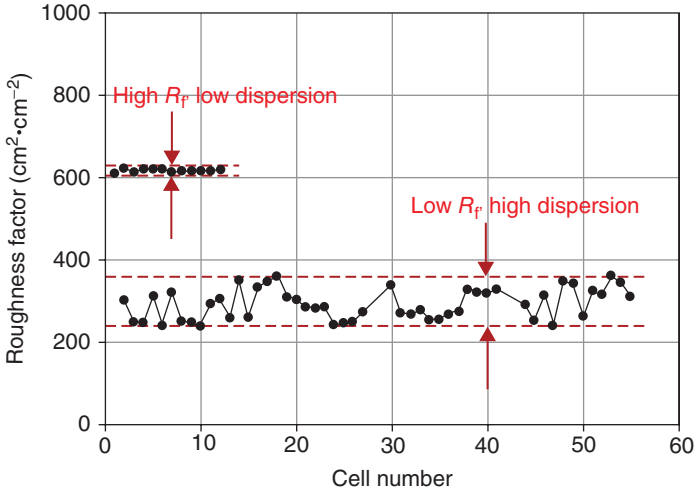

Figure 3.44 Plot of roughness factors as a function of cell number for (top) a 12-cell stack, 250 cm^2 MEAs and (bottom) a 56-cell stack, 600 cm^2 and distribution.

3.6
Balance of Plant

3.6.1
General Description

As discussed in a previous section, there is an interest to perform pressurized water electrolysis. There are several options. The most straightforward one is to pressurize both the anode and the cathode. But PEM technology has also demonstrated its ability to operate under significant pressure differences. An interesting configuration is that of a pressurized cathode and an anode operating at atmospheric pressure. This design was first developed for oxygen generation in anaerobic environments, for example, for breathing purposes aboard submarines. Compressed hydrogen was then easier to dispose of. For application in the hydrogen economy, the advantage of operating PEM electrolysers under pressure differences is mainly with regard to safety issues, the production and release of atmospheric oxygen being significantly less dangerous.

The process flowsheet of a symmetrically pressurized PEM water electrolysis unit is pictured in Figure 3.45.

After purification (a water resistivity in the 0.1-1 Mohm cm range is required…), deionized process water stored in storage tanks under an inert gaseous atmosphere is pumped from atmospheric pressure into the anodic process loop at the pressure of operation using an injection pump (high-pressure water injection requires specific equipment; this is where the energy cost of pressurized water electrolysis is paid and this is a limitation for high-pressure applications). Liquid water is pumped through both anodic and cathodic compartments and the water/gas biphasic mixtures are separated in gravity separators. Process gases are purified (usually using passive autocatalytic recombiners, that is, surfaces coated with platinum nanoparticles that promote the spontaneous recombination of hydrogen and oxygen into water) and pressures are adjusted in view of downstream process applications. After dehydrogenation, the flow of liquid water across the cell from the anode to the cathode (due to the electro-osmotic drag of water appearing in the cathodic compartment (resulting from the desolvation of protons) has to be recycled to the feed water tank or to the anodic loop.

3.6.2
Cost Analysis

A cost target for PEM water electrolysers installed on site is approximately 500 \$ kW^{-1}. Figure 3.46 provides the cost breakdown for a conventional PEM water electrolyser. The cost of stacks amounts to approximately 50% of the entire system cost (deviations depend on system manufacturer). Concerning the stack, bipolar plates and current distributors are main contributors. MEAs account for only one-fourth and the polymer electrolyte is the most expensive cost contributor.

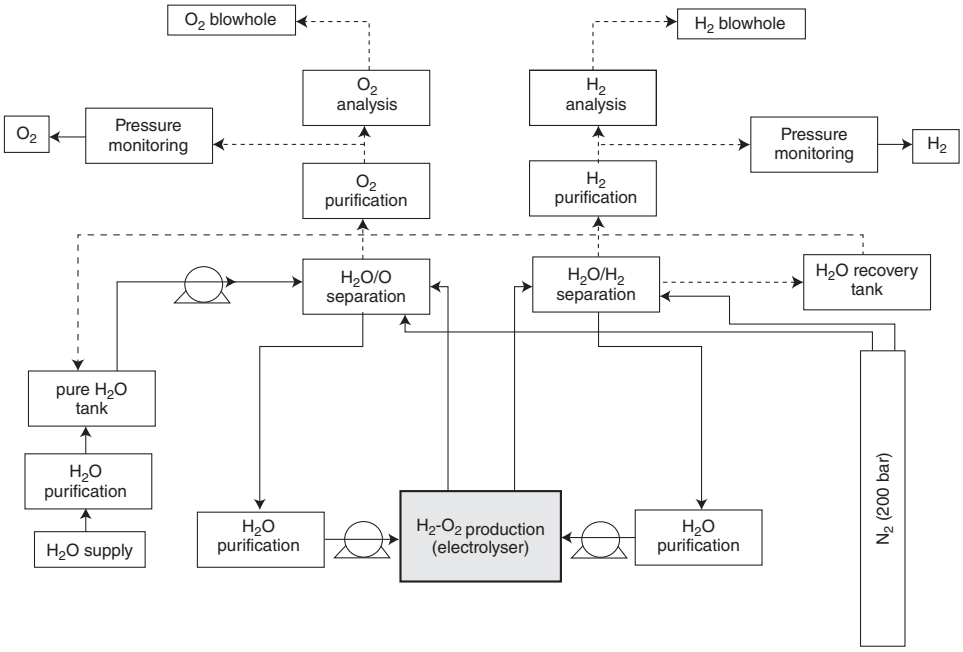

Figure 3.45 Process flowsheet of a PEM water electrolysis unit.

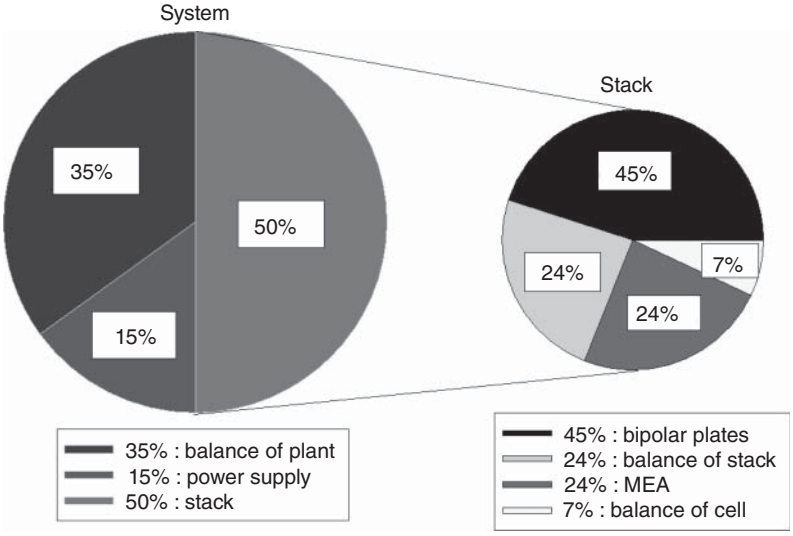

Figure 3.46 PEM water electrolysers: cost breakdown.

Estimated delivery cost for hydrogen using different technology and different hydrogen source feedstock are compiled in Table 3.3. Although it can be expected that in the long term, capex's of steam methane reformers (SMRs) and water electrolysers of similar production capacity will not be significantly different, hydrogen from water is and will remain more expensive than hydrogen from methane because of significant differences in energy requirements (the Gibbs free energy requirement to extract 1 mol of H_2 from methane in standard conditions is +41 kJ while this is +237 kJ from water). Concerning the cost of hydrogen from hydrocarbons such as methane, incorporation of CCS (carbon capture and storage) costs (based on state-of-the-art estimations) is claimed to have no impact on the situation. Of course, the use of renewable energy as a primary energy source also tends to increase the cost of hydrogen.

3.7
Main Suppliers, Commercial Developments and Applications

3.7.1
Commercial Status

A list of some international suppliers and companies active in this field is provided in Table 3.4 but the situation tends to change rapidly due to continuous R&D efforts and emerging markets.

As can be seen from Figure 3.47, modern PEM water electrolysers contain large stacks (>1000 cm^2, up to 100 cell/stack). Autonomous systems are containerized

Table 3.3 Estimated H_2 delivery costs (2010, taxes not included) for different hydrogen production paths (ranges depend on scale).

Production path	Efficiency (% LVH basis)	Cost (€ kg^{-1})
DOE target 2015 for 'green' H_2	—	**1.5–2.5**
Hydrogen from natural gas without CCS (mass production)	*70–75%*	*1–2*
Hydrogen from natural gas with CCS (mass production)	*70–75%*	*1.4*
Hydrogen from natural gas without CCS (steam reforming at fuelling station)	70–75%	2–3
Hydrogen from natural gas (offsite steam reforming + truck delivery)	70–75%	3.5–5
Hydrogen from coal gasification without CCS (mass production)	—	0.5–0.9
Hydrogen from coal gasification with CCS (mass production)	—	0.9–1.1
Hydrogen from biomass (offsite gasification + delivery)	70–75%	1.5–3.5
Hydrogen from wind (onshore and offsite water electrolysis)	30% WE: 75% (1.0 A cm^{-2})	5–7
Hydrogen from solar (offsite water electrolysis)	Solar : 15% WE : 75% at 1.0 A cm^{-2}	6.5–8.5
Hydrogen from nuclear (offsite water electrolysis)	33% WE : 75 (1.0 A cm^{-2})	4.5–6.5
Hydrogen from nuclear (large-scale thermochemical cycles)	50%	4–5.5
Hydrogen from solar (large-scale thermochemical cycles)	50%	4.5–6.5

Table 3.4 Some manufacturers of PEM water electrolysers and system characteristics.

Manufacturer	Country of origin	Capacity range $Nm^3\ h^{-1}$	Pressure (bar g)	Consumed energy $kWh\ Nm^{-3}$ (ΔH efficiency)
Hydrogen Technologies AS	Norway	0–20 0–6	1–16 1–15	No data available
Proton Energy Systems	United States	0–50 0–230	1–15 1–30	— 4.2 (84%)
Hydrogenics	Canada	0–2	1–8	4.9 (72)
Hélion/AREVA	France	0–10	1–50	No data available
CETH2	France	0–5 0–20	1–16 1–16	5.0 (70%) 5.2 (65%)
ITM-Power	United Kingdom	0–5	1–200	6.25–7.14 (57–50%)

Figure 3.47 10 Nm^3 H_2 h^{-1} PEM water electrolysis stack. (Source: Courtesy CETH2 Co.)

Figure 3.48 Modular (four stacks) 24 Nm^3 H_2 h^{-1} PEM water electrolysis stack. (Source: Courtesy CETH2 Co.)

(Figure 3.48) and several stacks are used to adapt capacity to process requirements and to facilitate the management of maintenance operation when necessary.

3.7.2
Markets and Applications

The hydrogen market contains three main segments (Figure 3.49): (i) hydrogen for different chemical applications in the industry; (ii) hydrogen mobility (refuelling stations) and (iii) hydrogen for energy storage (medium-scale systems are required for local needs and grid regulation, and large-scale systems for seasonal storage of renewable energy sources). In terms of cost, hydrogen of electrolytic grade cannot compete with hydrogen from methane. There are several existing market applications in the industry sector that require pure hydrogen free from

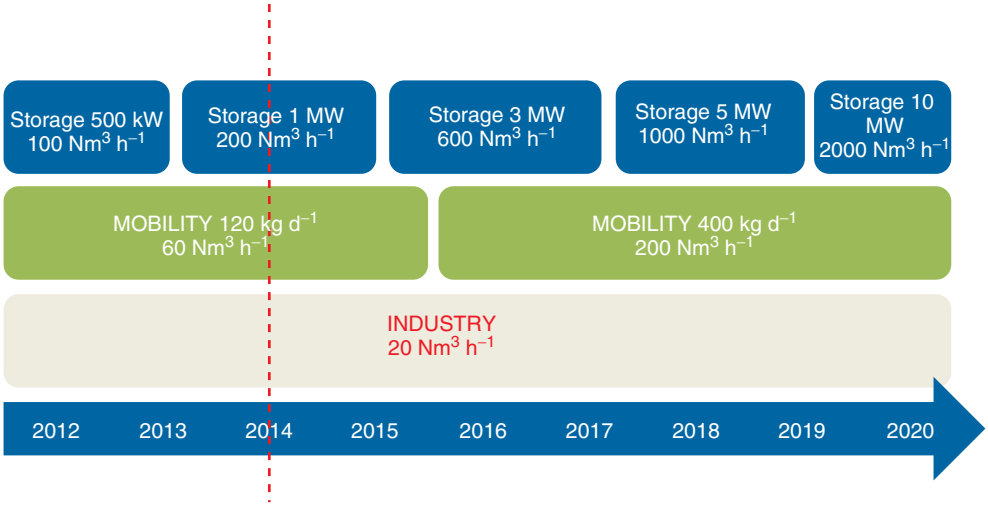

Figure 3.49 Market trends for 2020.

carbon traces although modern pressure swing adsorption (PSA) hydrogen purifiers tend to deliver appropriate purities. The main advantage of water electrolysis is process flexibility and the possibility of onsite modular production. If oxygen can also be used in a nearby process, this is a further advantage. However, if the main power source is coming from a renewable energy source, then storage units are required.

Hydrogen refuelling stations for mobility applications is seen as an emerging market for which water electrolysers can provide an alternative solution to conventional SMRs.

3.8
Limitations, Challenges and Perspectives

In current state of the art, PEM water electrolysis technology is already an efficient process: enthalpic efficiencies up to 80–85% (calculated from the higher heating value of hydrogen) have been demonstrated at the lab scale at 1 A cm^{-2}. The main drawback for market applications comes from the facts that: (i) larger electrolysers (a minimum of 10 kg H_2 h^{-1} is required in the short term to supply hydrogen in refuelling stations) operating at multi A cm^{-2} current densities with extended durability are needed and (ii) market requirements are calling for systems down to the US$ 500/kW range. State-of-the-art performances, short-term targets and ultimate potential of PEM water electrolysers are compiled in Table 3.5 [30]. This is a fast-evolving field and milestones may be reached faster than expected if appropriate R&D efforts financially supported by public funding agencies are made. At the stack level, enhanced performances will require

Table 3.5 State-of-the-art, short-term target and ultimate PEM water electrolysis specifications.

Property	State of the art	Target 2020–2030	Ultimate goal
Operating current density (A cm^{-2})	0–1	0–2	0–5
Operating temperature (°C)	50–80	80–120	100–150
Operating pressure (bar)	1–50	1–350	1–700
Enthalpic efficiency with PGM catalysts	80% at 1 A cm^{-2}	80% at 2 A cm^{-2}	80% at 4 A cm^{-2}
Enthalpic efficiency with non-PGM catalysts	30–40% at 1 A cm^{-2}	60% at 1 A cm^{-2}	60% at 1 A cm^{-2}
SPE voltage drop (mV at 1 A cm^{-2})	150	100	67
SPE ionic conductivity (S cm^{-1} at 80 °C)	0.17	0.20	0.30
SPE gas permeability to H_2 (cm^2 s^{-1} Pa^{-1}) (80 °C, full humidity)	10^{-11}	10^{-9}	10^{-9}
Cathodic PGM (Pt) content (mg cm^{-2})	1.0–0.5	0.5–0.05	<0.05
Anodic PGM (Ir, Ru) contents (mg cm^{-2})	1.0–2.0	0.5–0.1	<0.1
Durability (h)	10^4	10^4–5.10^4	>10^5
Production capacity of electrolysis units	1 kg h^{-1}	>10 kg h^{-1}	>100 kg h^{-1}
	(≈10 Nm^3 h^{-1})	(≈100 Nm^3 h^{-1})	(≈1000 Nm^3 h^{-1})
Energy (kWh kg^{-1} H_2 at 80 °C, 1 A cm^{-2})	56	<50	48
Non-energy cost (€ kg^{-1} H_2)	5	2	1

the development of innovative materials for all cell components. The replacement of platinum family catalysts and expensive SPE remains a challenging issue but all cell components are concerned. Regarding basic research, current development focus on: (i) reduction of iridium loadings at the anode by developing stable catalysts carriers or alloying ruthenium with iridium and an inert oxide (tin, titanium, etc.); (ii) the development of noble metal-free catalysts (PGM are used for benchmarking electrochemical performances) and (iii) research on alternative SPE (R&D is mainly driven by the needs of the fuel cell industry).

Concerning applied research, the focus is on: (i) Reduction of platinum loadings at the cathode using carbon carriers and/or specific printing methods such as screen printing. (ii) Surface treatment of titanium bipolar plates and current collectors to reduce contact resistance (Pt coatings are expensive but nitrides, carbides, etc., can be considered as interesting alternatives). Main challenges for PEM water electrolysis are to identify and synthesize alternative materials with performances similar to those used in state-of-the-art technology.

3.8.1
Replacement of Platinum with Non-Noble Electrocatalysts

In recent years, different compounds have been identified as potential candidates for the replacement of platinum at the cathode of PEM water electrolysers for the HER. In alkaline technology, nickel and cobalt are appropriate elements for the HER and the OER. Bulk metal particles cannot sustain the acidic environment of PEM cells. The idea developed by Millet and colleagues is to use mononuclear molecular compounds that contain cobalt, nickel or iron active centres. Some significant results have been obtained. In particular, boron-capped tris(glyoximato) cobalt (clathrochelate) complexes adsorbed at the surface of carbonaceous electronic carriers of large surface area have been successfully implemented [31, 32]. Some typical results obtained during PEM water electrolysis with such cathodes and IrO_2 anodes are plotted in Figure 3.50 [33].

An activation procedure is required before best cell performances are obtained. The operating temperature and current density are gradually increased, and after a period of several hours, the cell becomes fully activated (the additional charge transfer overvoltage observed at low current densities tend to decrease). The polarization curve of the activated cell is close to the reference curve measured in the same cell with a platinum cathode. Although the cobalt clathrochelate cathode remains less efficient than Pt for the HER, interesting electrochemical performances are, nevertheless, obtained. A cell efficiency $\varepsilon_{\Delta H} \approx 80\%$ is obtained at a current density of 500 mA cm^{-2} and 90 °C. In addition, such cathodes are less prone to surface contamination than platinum and can be operated with less purified feed water. Figure 3.51 shows some results in terms of process durability. During the accelerated ageing test, the cell was powered by step-like

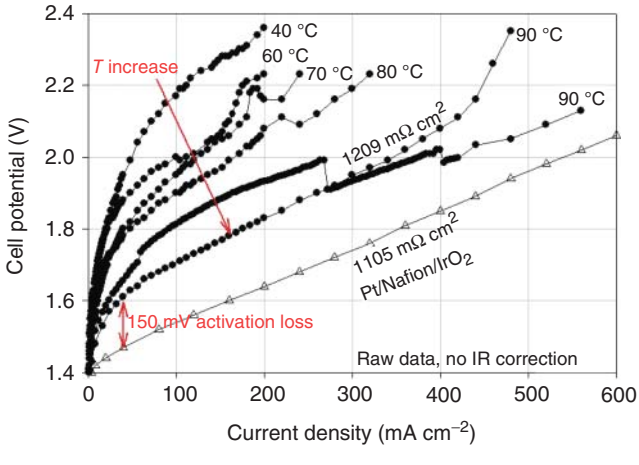

Figure 3.50 Polarization curves measured at different temperatures on 250 cm^2 PEM water electrolysis cells containing an IrO_2 anode and a carbon–boron-capped tris(glyoximato) cobalt complexes cathode. (Δ) Reference curve with Pt at the cathode.

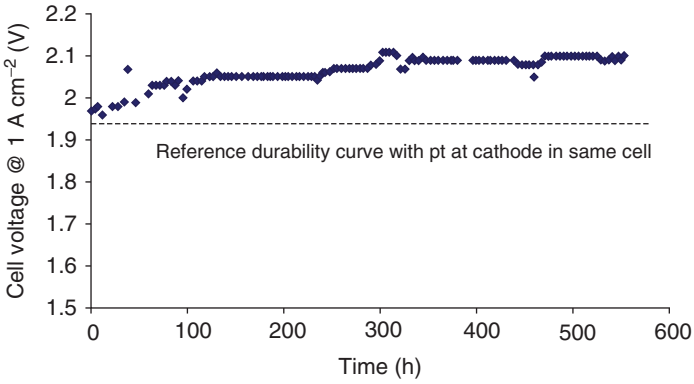

Figure 3.51 Durability test performed at 1 A cm^{-2} and 80 °C on PEM water electrolysis cells containing an IrO_2 anode and a carbon–boron-capped tris(glyoximato) cobalt complexes cathode.

transient current loads ranging from 0 to 2 A cm^{-2}. The cell voltage was recorded at 1 A cm^{-2} every 8 h at the end of ageing cycles. A reference durability curve measured with a conventional Pt/IrO_2 MEA using the same Nafion 117 SPE is also plotted for comparison. In spite of the aggressive conditions of the test, Figure 3.51 shows that the performances remain reasonably stable during the test. This is an illustration that there are some credible alternative for the replacement of platinum in such cells (the situation is of course more challenging for the replacement of iridium dioxide at anodes).

3.8.2
Replacement of Iridium with Non-Noble Electrocatalysts

The replacement of PGM (iridium) at anodes of PEM cells is a much more challenging task. Some research approaches tend to inspire from natural photosynthesis, although operating conditions (potential of operation of the oxygen reaction centre, ORC and turnover) are totally different. In natural oxygen-evolving systems, the OER is located in photosystem II [34]. It was recently discovered that oxidation of water involves a manganese–calcium cluster [35]. Manganese-based di- and trinuclear complexes such as perchlorate salts of mixed valence species $[Mn_2O_2L_2]^{3+}$ (L = dipyridyl (bpy), phenanthrolin (phen) have been tested as OER catalysts in PEM water electrolysis cells [36]. Whereas the chemical stability of such compounds was found sufficient, their efficiency as catalyst for promoting the OER in acidic media was found insufficient and to date, most significant results have been obtained using ruthenium complexes [37].

3.8.3
New Polymeric Proton Conductors for Operation at More Elevated Temperatures

Conventional SPEs (Nafion® products from DuPont Co.) are limited to operating temperatures less than 90 °C. Above this, the water-swelling properties of these materials are such that the water content becomes too high and membranes lose their mechanical properties. This is a concern for all PEM technologies. Research in the field is driven by the development of H_2/O_2 fuel cell for automotive applications. In a PEM fuel cell, approximately 50% of the free energy change of the water-forming reaction is released as heat to the surroundings. Onboard operation at conventional (80–90 °C) temperatures requires a larger heat exchanger compared to those used in internal combustion engines (ICEs)-driven cars. An operating temperature close to 150 °C would be more appropriate. Alternative perfluorosulphonated acid (PFSA) materials to Nafion® (e.g. short-side chain PFSA such as Aquivivion® from Solvay Co.) are stable at such temperatures. They are also interesting for applications in PEM water electrolysis cells (Figure 3.52). An additional problem in fuel cell technology comes from water management issues. Feed gases must be appropriately hydrated and the water produced at the cathode from the reduction of oxygen must be removed to avoid condensation, flooding effects and losses of performance. Such problems are critical and a new trend in research is to develop new polymers involving new proton-conduction mechanisms and operating in quasi-dry conditions. Phosphoric acid-impregnated polybenzimidazole (PBI) materials can be used to extend operating temperature up to 250 °C. It can be expected that the results of all this research will also benefit PEM water electrolysis if chemical stability is increased.

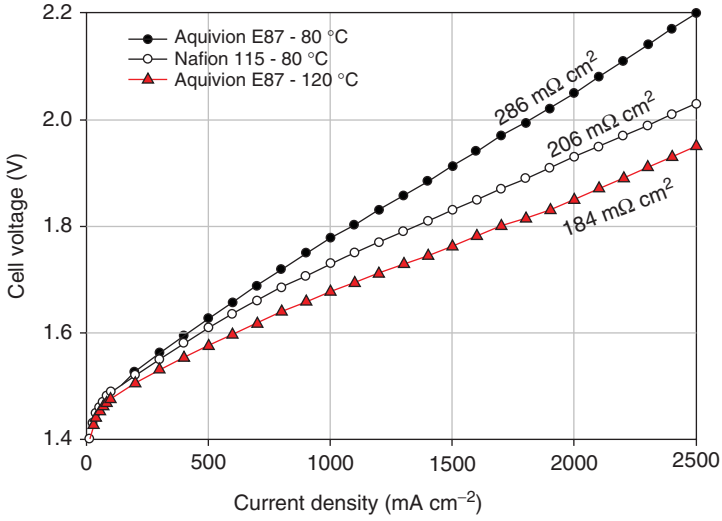

Figure 3.52 PEM water electrolysis polarization curves using Nafion® and Aquivion® SPEs.

3.8.4
Operation at Elevated Current Densities

Conventional alkaline water electrolysers operate up to 200–400 mA cm^{-2} and conventional PEM water electrolysers operate up to 0.8–1.0 A cm^{-2}. PEM systems operating in the 2.0–2.5 A cm^{-2} range have already been developed and successfully tested but, as can be seen from Figure 3.53, PEM water electrolysis cells can sustain much higher operating current density, especially when the cell is pressurized, the volumetric fraction of the gaseous phase being reduced. In the experiment of Figure 3.53, the ohmic resistance of the cell is still high (250 mΩ cm^{-2} whereas less than 100 mΩ cm^{-2} is achievable using appropriate non-MEA cell components). There is an obvious economic advantage at operating PEM cells at such elevated current densities, even if the enthalpy efficiency goes down to less than 60%. There are two main challenges here: (i) development of proper cell design that can sustain such conditions and (ii) above 2.0 V, cell components tend to corrode rapidly and cell durability is significantly impacted.

3.8.5
Operation at Elevated Pressures

PEM water electrolysis is a technology that offers the possibility of delivering directly compressed hydrogen. Some results obtained in the 1–130 bar pressure range with the PEM bistack of Figure 3.39 are compiled in Table 3.6 [29]. Measurements were made under stationary conditions, at a constant current density of 500 mA cm^{-2} and a mean operating temperature of 88 °C.

Cross-permeation phenomena discussed in Section 3.1.4.5 are the main cause of faradic efficiency losses, gas pollution and concern on safety issues. As the operating pressure is raised, the hydrogen purity falls from 99.98% at atmospheric

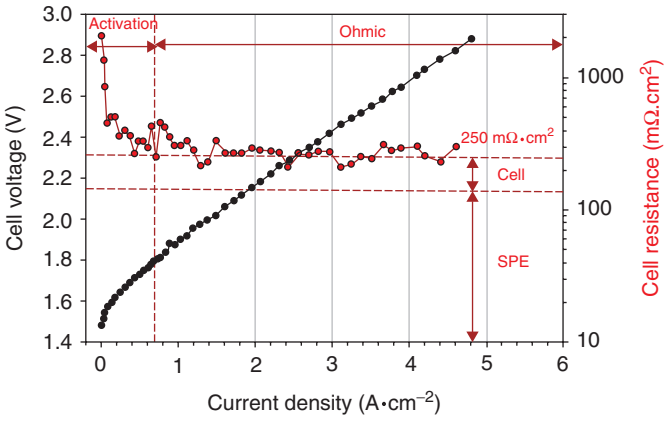

Figure 3.53 (Black filled circle) PEM water electrolysis polarization curve measured under continuous power loads; (red filled circle) internal cell resistance.

Table 3.6 Test results obtained with a high-pressure PEM water electrolysis stack under stationary operating conditions.

Parameter	Unit	Measured value at operating pressure (bar)					
		1	25	50	75	100	130
Electric current	A	123.5	126.5	125.5	124.5	125.0	124.0
Operating temperature	°C	86	87	85	89	84	88
H_2 production rate	$Nm^3\,h^{-1}$	0.68	0.69	0.68	0.65	0.64	0.63
H_2 purity before recombiner	%vol	99.98	99.76	99.18	98.56	98.01	97.34
H_2 purity after recombiner	%vol	99.999	99.999	99.997	99.995	99.993	99.991
Individual cell voltage	V						
1		1.70	1.70	1.71	1.71	1.72	1.73
2		1.68	1.69	1.70	1.71	1.71	1.72
3		1.71	1.71	1.71	1.72	1.71	1.71
4		1.70	1.71	1.71	1.73	1.74	1.74
5		1.71	1.70	1.71	1.71	1.73	1.74
6		1.69	1.69	1.70	1.71	1.73	1.73
7		1.70	1.69	1.69	1.70	1.72	1.73
8		1.68	1.70	1.70	1.73	1.74	1.74
9		1.68	1.69	1.71	1.72	1.73	1.74
10		1.69	1.69	1.71	1.73	1.73	1.74
11		1.70	1.71	1.71	1.72	1.73	1.74
12		1.68	1.69	1.70	1.72	1.73	1.74
13		1.69	1.71	1.71	1.71	1.72	1.74
Stack voltage	V	22.01	22.08	22.17	22.32	22.44	22.54
Power consumption	kW	2.72	2.79	2.78	2.78	2.81	2.79
Specific energy consumption	$kWh\,Nm^{-3}$	4.03	4.08	4.12	4.31	4.38	4.47
Current efficiency	%	99.98	99.68	98.13	96.57	92.91	90.45
Energy efficiency $\varepsilon_{\Delta G}$	%	72.6	72.4	72.1	71.6	71.2	70.9

pressure down to 97.34% (at 130 bars) due to increasing gas crossover. With a lower explosive limit of 4 vol% of hydrogen in air, this is a situation that can potentially lead to hazardous situations. As already pointed out elsewhere [26, 38, 39], the use of internal gas recombiners offers a simple and efficient way to manage explosion hazards and maintain the final purity of hydrogen at levels >99.99%, that is, at values well above the thresholds of explosion mixtures.

3.9 Conclusions

The purpose of this chapter is to review state-of-the-art PEM water electrolysis, to identify some limitations in existing technology and to draw some perspectives in view of future market applications. PEM water electrolysis is a somewhat

young technology that appeared in the 1970s when appropriate polymer electrolyte materials became commercially available. The technology has mostly been used for some niche applications, in particular for oxygen generation in anaerobic environments. Systems that can deliver up to several 10 $Nm^3 H_2 h^{-1}$ have been successfully developed. Main advantages of this technology are: (i) no need for corrosive and leaking electrolytes; (ii) possibility to operate at elevated current densities (the multi A cm^{-2} range is accessible); (iii) possibility to operate safely at elevated pressure (prototypes operating above 100 bars have been successfully tested) and (iv) well-adapted to operation with transient power loads.

Over the last few decades, severe economical and environmental constraints have appeared on our hydrocarbon-based energy economy. The current situation and short-term projections are calling for an increasing share of renewable energy sources in our energy mix. New markets are appearing for hydrogen of electrolytic grade because water splitting appears to be the best option to convert transient electricity load profiles into 'easy to store and distribute' chemical fuels. Hydrogen also appears as an excellent chemical for the transformation of carbon dioxide into synthetic carbonaceous fuels. In the short term, hydrogen refuelling stations are expected to be deployed in industrial countries, offering citizens the possibility to choose ecological transportations means. In the longer term, the possibility of deploying large water electrolysers for seasonal energy storage is also under consideration. The transition towards this global 'hydrogen economy' is not expected to take place within a few years but publicly supported R&D efforts and deployment of a hydrogen infrastructure will certainly contribute to make this vision reality. In the recent years, the European Union has adopted ambitious energy and climate change objectives for 2020 and beyond. Long-term commitments to the decarbonization path of the energy and transport system were made. The security of energy supply is also high on the political agenda. These strategic objectives have been reflected in the proposal of the European Commission for Horizon 2020, the research and innovation pillar of Europe 2020, which puts emphasis on providing support from basic research to market introduction. FCH technologies have the potential to contribute to achieving these goals, and they are part of the SET Plan, the technology pillar of the EU's energy and climate policy. These technologies have made significant progress for the last 10 years in terms of efficiency, durability and cost reduction. Competitiveness with incumbent technologies is contemplated for 2015–2020, and targets in terms of performance have been established for that purpose and are considered reachable with sufficient emphasis on R&D. The commercialization of some niche applications has already started, which is reflected in a fast-growing market that is expected to be US$ 43 billion and US$ 139 billion annually over the next 10–20 years, from a forecasted US$ 785 million in 2012. Several hundreds of thousands jobs may be created as a consequence of this growth. The question is how Europe can capture a maximum share of this nascent sector, and what has to be done in the next few years.

In this general context, water electrolysis and more specifically PEM water electrolysis is expected to play an increasing role. The first systems that can deliver

pressurized hydrogen at the 100 $Nm^3 H_2 h^{-1}$ rate are now available. Some market-driven new applications are boosting R&D and main commercial suppliers active in the field are planning to put on the market systems at the MW scale in the short term. The potential of PEM water electrolysis is still not fully demonstrated. There are signs indicating that future systems will be operating at much higher current densities.

Nomenclature

A	membrane area (m^2)
a_i	activity of species i
C_i	concentration of species i in mol m^{-3}
D_i	diffusion coefficient of species i ($m^2\ s^{-1}$)
E	free energy electrolysis voltage (V)
F	Faraday constant (96 485 C mol^{-1})
f_i	fugacity of species i
G	Gibbs free energy (J mol^{-1})
H	enthalpy (J mol^{-1})
I	current (A)
i	current density (A cm^{-2})
i_0	exchange current density (A cm^{-2})
L	membrane thickness (m)
m	mole number
n	number of electrons exchanged during the electrochemical reaction
P	pressure (Pa)
p_i	partial pressure of component i in a gas mixture (Pa)
R	resistance (Ω)
r	specific resistance (Ω m^2)
R_{PG}	constant of perfect gas (0.082 J K^{-1} mol^{-1})
S	entropy (J mol^{-1} K^{-1})
t	time (s)
T	absolute temperature (K)
U_{cell}	cell voltage (V)
V	thermoneutral electrolysis voltage (V)
$\overline{V}$	molar volume (m^3 mol^{-1})
W	electrical work (J)
x, y, z	space coordinates

Greek symbols

Δ	difference
ε	cell efficiency (%)
η	overvoltage (V)

φ	electrode absolute potential (V)
ρ	electrical resistivity (Ω m)
σ	electrical conductivity (S m^{-1})

Subscripts or superscripts

°	standard conditions (298 K, 1 bar)
cell	electrolysis cell
d	dissociation
e	electrolyte
i	species *i*
r	real
t	theoretical

Acronyms

CCS	carbon capture and storage
EIS	electrochemical impedance spectroscopy
EW	equivalent weight of membrane (equiv. g^{-1})
ICE	internal combustion engine
MW	Mega Watt
PBI	polybenzimidazole
PEM	proton exchange membrane
PFSA	perfluorosulphonated acid
PGM	platinum group metals
PSA	pressure swing adsorption
PSA	pressure swing adsorption
PTFE	polytetrafluoroethylene
SMR	steam methane reforming
SPE	solid polymer electrolyte
XPS	X-Ray photoelectron spectroscopy

References

1. Grubb, W.T. (1959) Batteries with solid ion-exchange electrolytes. *J. Electrochem. Soc.*, **106**, 275–281.
2. Mauritz, K.A. and Moore, R.B. (2004) State of understanding of nafion. *Chem. Rev.*, **104**, 4535–4585.
3. Rasten, E., Hagen, G., and Tunold, R. (2003) Electrocatalysis in water electrolysis with solid polymer electrolyte. *Electrochim. Acta*, **48**, 3945–3952.
4. Millet, P., Durand, R., and Pinéri, M. (1989) New solid polymer electrolyte composites for water electrolysis. *J. Appl. Electrochem.*, **19**, 162–166.
5. (1981) Solid polymer Electrolyte Water Electrolysis Technology Development for Large-Scale Hydrogen Production. US Department of Energ DOE/ET/26 202–1.

6. (2003) Hydrogen Energy and Fuel Cells. Directorate General for Research, Report EUR 20719 EN, European Commission, Brussels.
7. Millet, P., de Guglielmo, F., Grigoriev, S.A., and Porembskiy, V.I. (2012) Cell failure mechanisms in PEM water electrolyzers. *Int. J. Hydrogen Energy*, **37**, 17478–17487.
8. Takenaka, H. and Torikai, E. (1980) Pd structural catalyst for oxygen reduction reaction and its single cell performance. Japanese Patent n° 55,38934, March 18th.
9. Millet, P., Durand, R., and Pinéri, M. (1990) Preparation of new solid polymer electrolyte composites for water electrolysis. *Int. J. Hydrogen Energy*, **15**, 245–253.
10. Millet, P., Durand, R., Dartyge, E., Tourillon, G., and Fontaine, A. (1993) Precipitation of metallic platinum into Nafion ionomer membranes- experimental results. *J. Electrochem. Soc.*, **140**, 1373.
11. Millet, P., Andolfatto, F., and Durand, R. (1995) Preparation of solid polymer electrolyte composites. Investigation of the ion-exchange process. *J. Appl. Electrochem.*, **25**, 227–232.
12. Millet, P., Andolfatto, F., and Durand, R. (1995) Preparation of solid polymer electrolyte composites. Investigation of the precipitation process. *J. Appl. Electrochem.*, **25**, 233–239.
13. Grigoriev, S.A., Millet, P., Volobuev, S.A., and Fateev, V.N. (2009) Optimization of porous current collectors for PEM water electrolysers. *Int. J. Hydrogen Energy*, **34**, 4968–4973.
14. Millet, P., Mbemba, N., Grigoriev, S.A., Fateev, V.N., Aukauloo, A., and Etievant, C. (2011) Electrochemical performances of PEM water electrolysis cells and perspectives, *Int. J. Hydrogen Energy*, **36**, 4134–4142.
15. Marshall, A., Børresen, B., Hagen, G., Tsypkin, M., and Tunold, R. (2009) Hydrogen production by advanced proton exchange membrane (PEM) water electrolyzers-reduced energy consumption by improved electrocatalysis. *Int. J. Hydrogen Energy*, **34**, 4974–4982.
16. Millet, P. (1994) Water electrolysis using EME technology: electric potential distribution inside a Nafion membrane during electrolysis. *Electrochim. Acta*, **39**, 2501.
17. Trasatti, S. and Petri, O.A. (1992) Real surface area measurement in electrochemistry. *J. Electroanal. Chem.*, **327**, 353–376.
18. Savinell, R.F., Iii, R.L.Z., and Adams, J.A. (1990) Electrochemically active surface area voltammetric charge correlations for ruthenium and iridium dioxide electrodes. *J. Electrochem. Soc.*, **137**, 1–6.
19. Rozain, C. and Millet, P. (2014) Electrochemical characterization of polymer electrolyte membrane water electrolysis cells. *Electrochim. Acta*, **131**, 160–167.
20. Brug, G.J., Van Den Eeden, A.L.G., Sluyters-Rehbach, M., and Sluyters, J.H. (1984) The analysis of electrode impedances complicated by the presence of a constant phase element. *J. Electroanal. Chem. Interfacial Electrochem.*, **176**, 275.
21. Gierke, T.D., Munn, G.E., and Wilson, F.C. (1981) The morphology in Nafion perfluorinated membrane products, as determined by wideand small-angle x-ray studies. *J. Polym. Sci., Part B: Polym. Phys.*, **19**, 1687–1704.
22. Grigoriev, S.A., Porembskiy, V.I., Korobtsev, S.V., Fateev, V.N., Auprêtre, F., and Millet, P. (2011) High-pressure PEM water electrolysis and corresponding safety issues. *Int. J. Hydrogen Energy*, **36**, 2721–2728.
23. Ferry, A., Doeff, M.M., and DeJonghe, L.C. (1998) Transport property measurements of polymer electrolytes. *Electrochim. Acta*, **43**, 1387–1393.
24. Mann, R.E., Amphlett, J.C., Peppley, B.A., and Thurgood, C.P. (2006) Henry's law and the solubilities of reactant gases in the modeling of PEM fuel cells. *J. Power. Sources*, **161**, 768–774.
25. Sakai, T., Takenaka, H., Wakabayashi, N., Kawami, Y., and Torikai, E. (1985) Gas permeation properties of Solid Polymer Electrolyte (SPE) membranes. *J. Electrochem. Soc.*, **132**, 1328–1332.
26. Grigoriev, S.A., Millet, P., Korobtsev, S.V., Porembskiy, V.I., Pepic, M., Etiévant, C., Puyenchet, C., and Fateev, V.N. (2009) Hydrogen safety aspects related to

high-pressure polymer electrolyte membrane water electrolysis. *Int. J. Hydrogen Energy*, **34**, 5986–5991.

27. Goodridge, F. and Scott, K. (1995) *Electrochemical Process Engineering: A Guide to the Design of Electrolytic Plant*, Plenum Publishing Corporation.
28. Wendt, H. and Kreysa, G. (1999) *Electrochemical Engineering: Science and Technology in Chemical and Other Industries*, Springer.
29. Millet, P., Grigoriev, S.A., and Porembskiy, V.I. (2013) Development and characterisation of a pressurized PEM Bi-stack electrolyzer, *Int. J. Energy Res.*, **37**, 449–456.
30. Cerri, I., Lefebvre-Joud, F., Holtappels, P., Honegger, K., Stubos, T., and Millet, P. (2012) Scientific Assessment in support of the Materials Roadmap Enabling Low Carbon Energy Technologies, Coordination: Hydrogen and Fuel Cells. JRC Scientific and Technical Reports, Report EUR 25293 EN, European Commission, Brussels.
31. Pantani, O., Anxolabéhère, E., Aukauloo, A., and Millet, P. (2007) Electroactivity of cobalt and nickel glyoximes with regard to the electro-reduction of protons into molecular hydrogen in acidic media. *Electrochem. Commun.*, **9**, 54–58.
32. Pantani, O., Naskar, S., Guillot, R., Millet, P., Anxolabéhère, E., and Aukauloo, A. (2008) Cobalt clathrochelate complexes as hydrogen-producing catalysts. *Angew. Chem. Int. Ed.*, 9948–9950.
33. Millet, P., Rozain, C., Villagra, A., Ragupathy, A., Ranjbari, A. and Guymont, M. (2014) Implementation of cobalt clathrochelates in polymer electrolyte water electrolysers for hydrogen evolution. *Chem. Engineering. Trans*, **41**, in press.
34. Ferreira, K.N., Iverson, T.M., Maghlaoui, K., Barber, J., and Iwata, S. (2004) Architecture of the photosynthetic oxygen-evolving center. *Science*, **303**, 1831–1838.
35. Mishra, A., Wernsdorfer, W., Abboud, K., and Christou, G. (2005) The first high oxidation state manganese-calcium cluster: relevance to the water oxidizing complex of photosynthesis. *Chem. Commun.*, 54–56.
36. Medhoui, T., Anxolabehere, E., Aukauloo, A., and Millet, P. (2006) Biomimetic approaches for the development of non-noble metal electrocatalysts. Application to PEM water electrolysis. Proceeding of the 16th World Hydrogen Energy Conference, Lyon, France, June 13–16, 2006.
37. Mbemba, N., Herrero, C., Ranjbari, A., Aukauloo, A., Grigoriev, S.A., and Millet, P. (2013) Ruthenium-based molecular compounds for oxygen evolution in acidic media. *Int. J. Hydrogen Energy*, **38–20**, 8590–8596.
38. Grigoriev, S.A., Porembskiy, V.I., Korobtsev, S.V., Fateev, V.N., Auprêtre, F., and Millet, P. (2011) High-pressure PEM water electrolysis and corresponding safety issues. *Int. J. Hydrogen Energy*, **36**, 2721–2728.
39. Ströbel, R., Oszcipok, M., and Fasil, M. (2002) The compression of hydrogen in an electrochemical cell based on a PEM fuel cell design. *J. Power Sources*, **105**, 208–215.

4
Alkaline Water Electrolysis

Nicolas Guillet and Pierre Millet

4.1
Introduction and Historical Background

In 1789, Paets van Troostwyk and Deinman published [1] the first observations on experiments conducted with the assistance of Mr. J. Cuthberston on the decomposition of water by electric discharges into 'air inflammable' (flammable air), also named hydrogen, and 'air vital' (life giving air), also known as oxygen gas. During the nineteenth century, with the improvement of electrodynamic generators such as the Gramme machine in 1869, water electrolysis became an economical method for the production of hydrogen. The Russian physicist Prof. D. Latchinof in Saint Petersburg, Dr. A d'Arsonval at the French Collège de France in Paris and Cdt Renard, Director of the French military aerostation institute of Chalais, concurrently developed apparatus for industrial synthesis of hydrogen and oxygen through water electrolysis [2]:

- In the years 1885–1887, d'Arsonval used an electrolyser to generate pure oxygen for its experiment researches on physiology at the Collège de France. An iron perforated cylinder was used as anode and placed into a cloth bag that served as a diaphragm. A 30% solution of KOH was used as electrolyte. A cylindrical vessel (20 cm in diameter and 60 cm high) was used as cathode. The maximum applied current was 60 A, corresponding to 16 mA cm^{-2} of cathode (the nominal current density of operation ranged between 5 and 8 mA cm^{-2} of the cathode). Only oxygen was collected. The apparatus typically produced 100–150 Nm^3 of oxygen per day. The main limitation of this apparatus was the need to frequently replace the diaphragm [3].
- Cdt Renard developed a water electrolyser to supply hydrogen for inflating balloons. Acidic (27 wt%) and alkaline electrolytes (NaOH 15 wt%) were experimented. The electrodes were made of 2 mm iron sheet. The inner electrode, used as anode, was 17.4 cm in diameter and 3.29 m high. It was perforated with 300 holes (10 mm in diameter) and put in an asbestos bag. The outer electrode, serving both as cathode and as electrolyte tank, was 30 cm in diameter, 3.404 m high. Internal resistance was around 7.5 mΩ and the voltage was around 2.7 V

Hydrogen Production: by Electrolysis, First Edition. Edited by Agata Godula-Jopek.
© 2015 Wiley-VCH Verlag GmbH & Co. KGaA. Published 2015 by Wiley-VCH Verlag GmbH & Co. KGaA.

at 365 A (nominal current of operation: 12 mA cm^{-2} of cathode). This apparatus could produce 158 NL h^{-1} of hydrogen.

- Prof. Latchinov developed the first machine that used several bipolar electrodes, separated by sheets of parchment in an iron tank. He used iron electrodes in NaOH 10 wt%. The apparatus was inserted in a 2 m long paraffined wood box, divided into a series of electrochemical cells separated by iron electrode plates. Between these electrode plates were placed diaphragms of parchment. A maximum of 44 electrodes (1.4 m high and 21 cm large) could be placed in the box. The two external plates were connected to the source of the electric current. The current applied was about 100 mA cm^{-2} (300 A) and the average cell voltage was 2.5 V (110 V applied between external cells) [3]. Prof. Latchinov is also considered as the first to develop a pressurized water electrolyser.

In 1900, a patent leading to the production of the first industrial electrolyser based on the filter-press design (Figure 4.1) was proposed by Dr Schmidt [4]. The Schmidt apparatus used asbestos cloth reinforced with rubber on the edges as the diaphragm. Two different types were proposed: a 44-cell type used for 110 V applied voltage and a 26-cell type for 65 V (average voltage per cell: 2.5 V). For each type, five sizes ranging from 15 to 150 A (163–2750 NL h^{-1}) were also proposed.

The Schmidt bipolar electrolyser was manufactured and commercialized in 1902 by the company Maschinenfabril Oerlikon (Switzerland). In the early twentieth century, more than 400 industrial electrolysers were in operation (Figures 4.2) [5]. Such electrolysers were mainly used in industrial applications to produce hydrogen and oxygen for welding or cutting applications (metallurgy, glassware production, jewellery, etc.), thanks to the high temperature of the oxy-hydrogen flame.

In the 1920s and 1930s, increasing amounts of hydrogen were required to produce ammonia as precursors of fertilizer (nitrates) and explosive (ammonium nitrates) following the Haber process: $N_2 + 3H_2 \rightarrow 2\,NH_3$. This need for hydrogen, helped by the low cost of hydroelectricity in mountainous countries, stimulated the development of water electrolysis technology and the industrial market was led by three main companies: Oerlikon (Switzerland), Norsk Hydro (Norway) and Cominco (Canada). The first very large-scale electrolyser was built by Norsk Hydro in 1927 in Vemork, Rjukan (Telemark, Norway). This 125 MW plant could produce 27 900 $Nm^3\,h^{-1}$ of hydrogen. The most important electrolytic ammonia plant was built in 1947 and was operated by Norsk Hydro in Glomfjord (Norway). It required 380 MW hydroelectric power to produce 1300 tons of ammonia and 85 kg of D_2O per day [6].

Since the 1950s, hydrocarbon energy has taken a growing place in industry. Hydrogen can be produced on a large scale through coal gasification and natural gas steam reforming, and at much lower costs than by electrolysis. The economic advantage of water electrolysis gradually diminished and the last Norwegian large-scale plant (Glomfjord) was closed in 1992 (Figure 4.3).

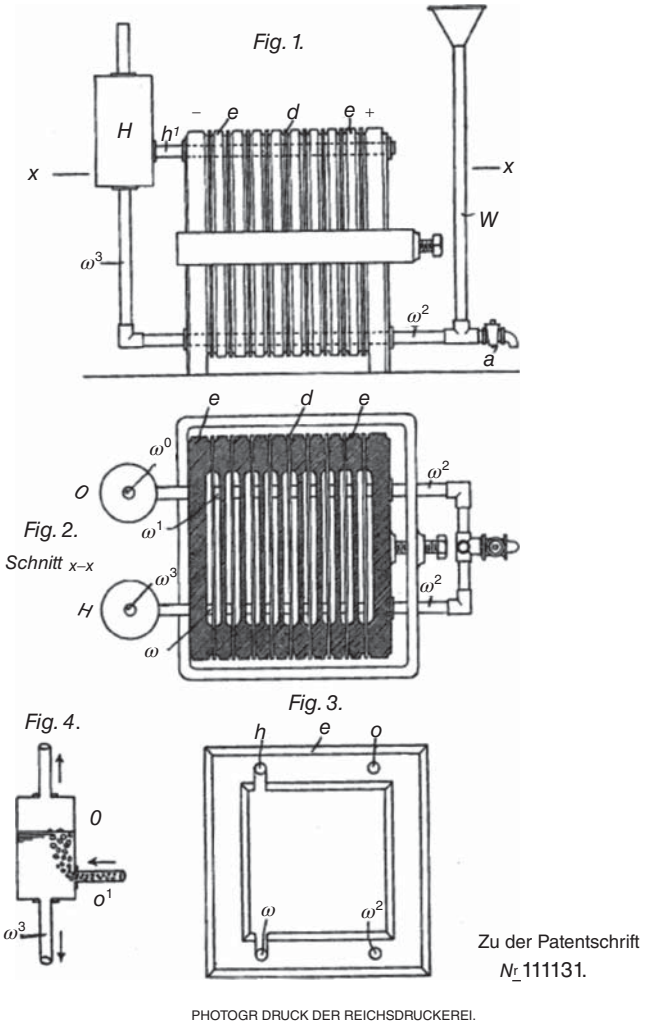

Figure 4.1 Drawing of the Dr. Schmidt water electrolyzer, patent DE 111,131 (1899) [4].

In 2010, industrial hydrogen (≈70 million tons per year) was largely produced from fossil fuels without carbon capture and storage (CCS): 48% from natural gas, 30% from refinery/chemical off-gases, 18% from coal and only 4% by electrolysis. Most of the production is for captive use in the chemical and refinery industries [7]. Electrolytic hydrogen is, however, preferred by the food and pharmaceutical

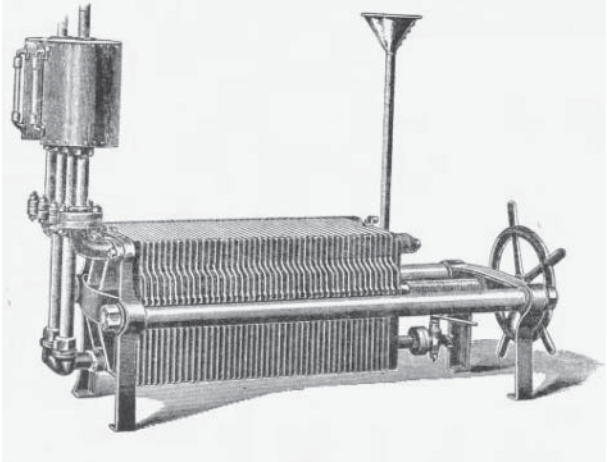

Figure 4.2 View of Dr O. Schmidt electrolyser.

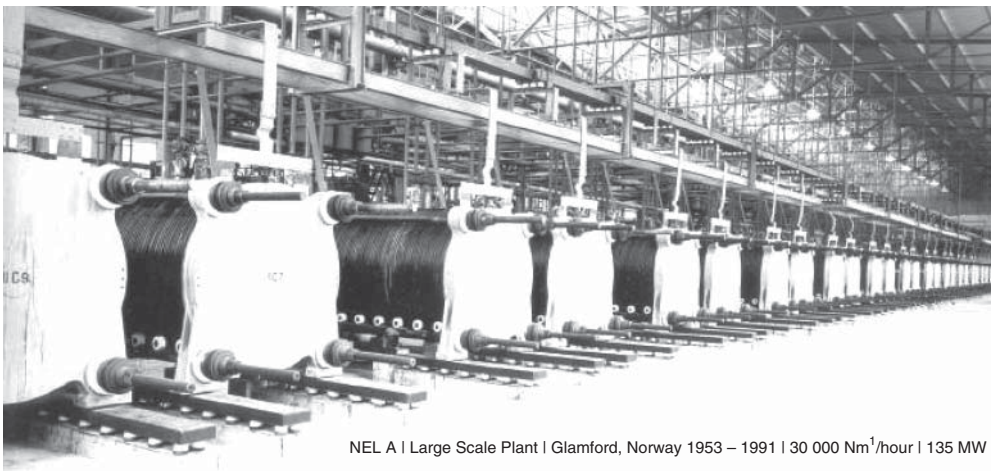

Figure 4.3 Picture of one of the two Glomfjord electrolysis plants. (From *http://www.nel-hydrogen.com/docs/Efficient_Electrolysers_for_Hydrogen_Production.pdf*.)

industries owing to the ease of onsite production and the high purity of the gas (99.999% is quite usual) with no pollutant of hydrogen is water More recently, the development of renewable energy sources (solar and/or wind farms) on a large scale and the need for an efficient way to store energy renewed worldwide interest in water electrolysis. Improving the efficiency of water electrolysis and reducing capital expenses are now two major goals.

4.2 Description of Unit Electrolysis Cells

4.2.1 General Description

The main advantage of alkaline water electrolysis over other water electrolysis technology lies in the fact that alkaline electrolysers can be made of abundant and inexpensive materials: simple iron or nickel steel electrodes are used to produce hydrogen and nickel used for oxygen production. The electrodes are immersed in a highly concentrated alkaline aqueous solution made of concentrated potassium hydroxide (usually close to 6 mol l^{-1}). A porous solid material (diaphragm) that allows transport of hydroxyl ions (OH^-) between the electrodes and exhibits a very low permeability to oxygen and hydrogen (both to gas bubbles and to dissolved gases in the electrolyte) is placed between the anode and the cathode to effectively separate the produced gases and avoid mix-ups that could lead to safety hazards and low faradaic efficiencies. The reaction requires the supply of electrical energy through a potential difference between the two electrodes. In practical operation, the cell voltage lies in the 1.3–2.0 V range. When a sufficient difference of potential is applied between the electrodes, anodic (oxidation of water) and cathodic (reduction of water) reactions take place simultaneously on the anode and cathode, respectively. At the anode, which is polarized at a potential close to 1.8–2.0 V RHE (reversible hydrogen electrode), OH^- ions of the electrolyte are oxidized according to Equation 4.1 into oxygen gas. This is the oxygen evolution reaction or OER. The hydrogen production takes place at the cathode, which is polarized at a negative potential (relative to the RHE). The electrons coming from the external electrical circuit are used to reduce the water in hydrogen gas, bubbling in the electrolyte and OH^- ions (Equation 4.2). This is the hydrogen evolution reaction or HER.

$$\text{anode}: \quad 4\,OH^- \rightarrow O_2 + 2\,H_2O + 4\,e^- \qquad E^\circ = 1.23\ \text{V versus RHE} \tag{4.1}$$

$$\text{cathode}: \quad 4\,H_2O + 4\,e^- \rightarrow 2\,H_2 + 4\,OH^- \quad E^\circ = 0\ \text{V versus RHE} \tag{4.2}$$

Two important points should be noted:

- The two electrochemical reactions occur at the electrode surface: the contact point between the electrolyte (H_2O and OH^-) and the metallic electrode that conducts electrons.
- The amount of gas produced is directly proportional to the current flowing through the electric circuit (Faraday law): whenever four electrons pass through the power supply, an oxygen molecule and two hydrogen molecules are simultaneously produced.

Two different type of water electrolysis cells can be used: (i) the tank cell (unipolar configuration, Figure 4.4) developed by Dr d'Arsonval and Cdt Renard are simple and reliable and (ii) the filter-press cells (bipolar configuration, Figure 4.5)

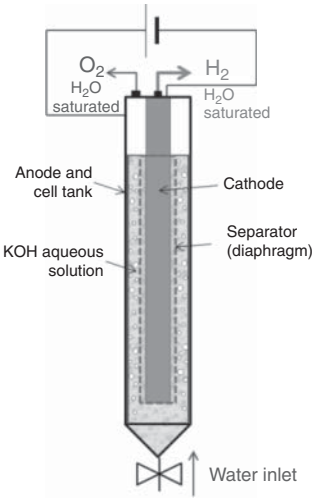

Figure 4.4 Schematic diagram of a unipolar alkaline water electrolysis cell.

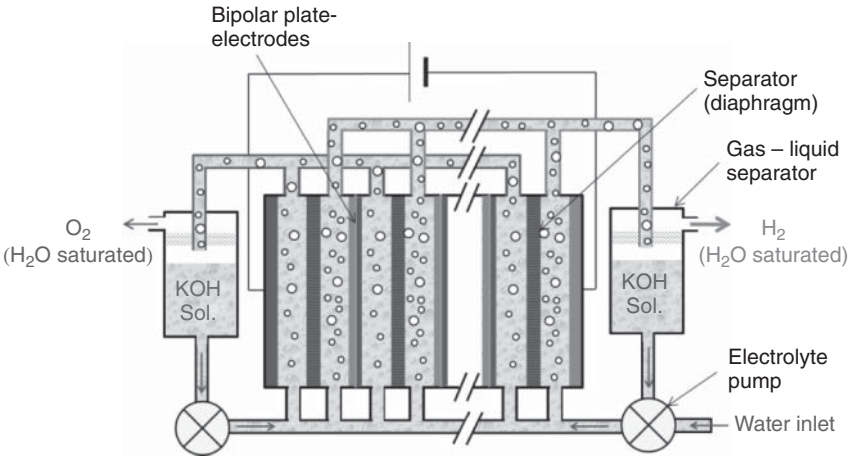

Figure 4.5 Schematic diagram of a bipolar alkaline water electrolysis cell.

developed by Prof. D. Latchinov and Dr O. Schmidt are more compact; they have lower ohmic losses and require less energy for the same production of gases. Disadvantages of bipolar cells are related to their structural complexity, the requirement of electrolyte circulation (pumping) and the use of external gas/electrolyte separators.

Most of the industrial alkaline water electrolysers must be kept operating at a minimum current density (10–20% of rated power). This is due to the fact that the porous material separating the two compartments where oxygen and hydrogen gases are produced, is not perfectly impermeable to the reaction products: gases partly dissolve in the electrolyte. Thus, due to the effect of chemical diffusion (Fick's law), some hydrogen gas passes permanently through the separator

from the cathodic compartment to the anodic compartment and is mixed with the oxygen produced. Similarly, a fraction of oxygen also crosses over the separator for mixing with the produced hydrogen. According to Fick's laws of diffusion, the amount of species diffusing through the separator is proportional to the gradient of the chemical activity (pressure and concentration of dissolved gases). It does not depend on the amount of produced gases. Whatever the operating current density, as long as operating pressure and temperature are kept constant, the amount of products transported by diffusion remains constant. At low current density, only a small amount of gas is produced at each electrode while a constant amount of the products crosses over the separator from one compartment to the other. The oxygen concentration in hydrogen and the hydrogen concentration in oxygen are higher at low current densities. Besides the decrease in the purity of product gases, safety aspects may become critical at low current densities. Indeed, mixtures of hydrogen – oxygen gas can be easily flammable in a large concentration range: the lower explosion limit (LEL) of hydrogen in oxygen is 3.9 mol%, while the upper explosion limit (UEL) is 95.8% [8, 9]. Outside these limits, the gas mixtures are not flammable. It is therefore essential to avoid reaching these limits.

Another limitation of alkaline water electrolysers appears when sudden current changes are applied while the electrodes are immersed in the electrolyte. In case of very rapid rise in current, a large amount of gas is produced very quickly. Then there is a risk that the electrolyte could be expelled from the compartments, in a manner similar to what occurs when opening a bottle of liquid under pressure ('Champagne' effect). The evacuation of a substantial portion of the electrolyte would lead to a significant deficiency of the electrolyser and could potentially damage the system. In other words, alkaline water electrolysers require stationary operating conditions and are not totally well-adapted for operation with transient power sources.

4.2.2
Electrolyte

The volume of the electrolyte stored in the electrochemical cells is determined by the distance (gap) between the electrodes. This distance usually ranges between a millimetre and several centimetres. The ohmic losses in the electrolyte increase with the distance between the electrodes. On the other hand, when the electrolyte volume is too small, the reactant concentrations change rapidly during operation. Aqueous solutions of KOH are often preferred to NaOH because of their highest specific conductivity. The maximum conductivity of KOH aqueous solutions is obtained at about 30 wt% (Figure 4.6). This concentration is commonly used in modern alkaline water electrolysers.

It should be noted that the amount of electrolyte has to be adjusted continuously to counterbalance losses through product gases (typically 1 mg KOH per

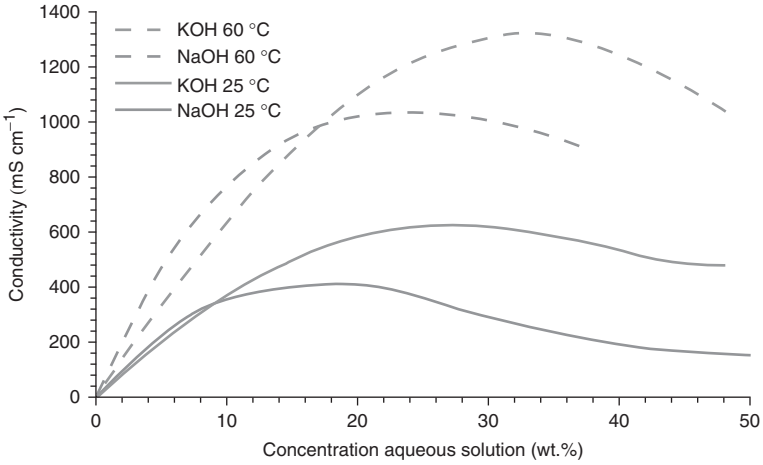

Figure 4.6 Conductivity of aqueous solutions of NaOH and KOH [10, 11].

Nm^3H_2). It also has to be changed at regular time intervals because of the accumulation of impurities coming from water and from electrolyser components (corrosion of metallic parts, degradation of the electrodes and separator) that fouls the electrolyte.

4.2.3
Electrodes and Catalysts

As for any electrochemical application, electrode materials required for alkaline water electrolysis should have good corrosion resistance, high electronic conductivity and high catalytic activity with regard to the two reactions of interest (the hydrogen evolution reaction or HER at the cathode and the oxygen evolution reaction or OER at the anode). Stainless steel and lead oxide were first identified as cheap electrode materials, with low overpotential for the OER, but were found not chemically stable at sufficiently high voltage in highly concentrated alkaline solutions. Nickel is now recognized as one of the best materials for the OER. It offers a rather good resistance to corrosion in alkaline solutions, a good electrochemical activity and a reasonable cost (the average price of nickel over the 2009–2014 period is 13.8 € kg^{-1} [12], compared to 36.6 € g^{-1} for platinum [13]). Plain nickel electrodes have shown a good durability in real operation conditions, even though accelerated corrosion phenomena occur during power-off periods. OER overvoltage on nickel electrodes amounts to several hundreds of millivolts. To increase the electrochemical active surface area (ECSA) of the electrodes, a porous layer of nickel or a nickel–iron alloy is usually coated over steel or nickel plates [14]. In 1925, Raney proposed a patented process for the synthesis of high surface area nickel powders [15]. This process has become famous and the nickel thus obtained is frequently referred to as 'Raney nickel' (Figure 4.7). In this process, nickel and silicon metals are melted together to produce a nickel–silicon

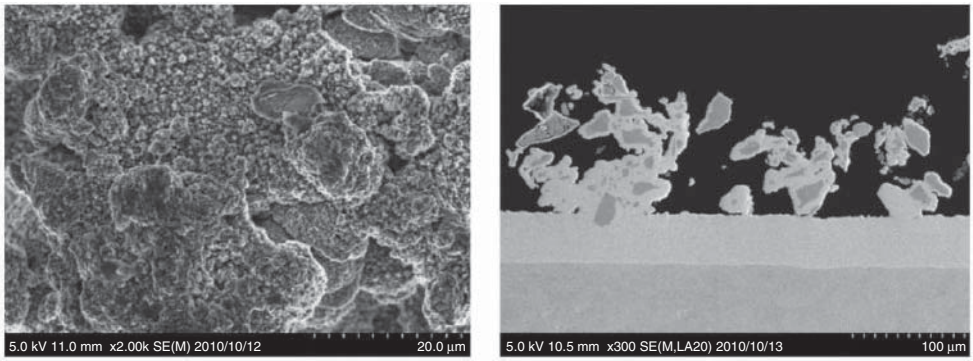

Figure 4.7 SEM images of activated Raney nickel catalyst deposited on a Ni mesh substrate [16].

alloy. The proportion of nickel on silicon can vary from 10% to 80%. After cooling, the alloy is pulverized and treated with sodium hydroxide. Silicon is oxidized to Na_2SiO_3($Si + 2\ NaOH + H_2O \rightarrow Na_2SiO_3 + 2\ H_2$) and eliminated after washing. A high-purity nickel powder with controlled porosity and surface area is then obtained. This process was improved in 1927 by the addition of aluminium [17]. This catalyst was used in alkaline water electrolysers until the end of the 1950s.

It was then shown that the activity of monometallic oxide catalysts for oxygen evolution reaction, such as nickel and cobalt oxides, can be improved by incorporating other metallic ions. Ternary mixed oxides of Fe, Co and Mo were investigated as electrocatalysts [18]. The partial replacement of Co by Fe in the $CoMoO_4$ matrix was shown to increase the specific surface area and the apparent electrocatalytic activity of the oxide. However, it is difficult to predict which formulation will produce the best catalyst. A recently published work presented the results of a parallel screening assay to compare the catalytic activity of diverse mixed metal oxides containing between one and three metals [19]. A fluorescence-based screening method was used to evaluate the electrolytic activity of the mixed oxide catalysts under alkaline conditions. This method uses a chromophore fluorescent oxygen-sensitive paint. The intensity of the fluorescence can be considered as proportional to the amount of oxygen produced. Authors have reported the results of the comparison of catalytic activity of nearly 3500 mixed metal oxide compositions. Some of the mixed oxide catalyst compositions showing the highest fluorescence are summarized in Table 4.1. The activity measured by fluorescence is reported relative to that of NiO.

The highest activities were observed on the oxides containing Ni, Fe and a third element such as Cr, Al, Ga or Ca. These results were verified by electrochemical measurements and the Ni–Fe–Cr, Ni–Fe–Ga and Ni–Fe–Al mixed oxide structures were confirmed as highly effective catalysts.

At the cathode, mild steel is one of the materials mostly used for the HER. Nickel as well as Raney nickel deposition on steel plates is quite usual. The nickel–sulphur alloy is considered as an excellent HER cathode material in

Table 4.1 Average catalyst activity of cobalt- and nickel-based mixed oxides obtained from fluorescence measurements; relative activity, compared to NiO: >1 in white, >3 in light gray and >4 in dark gray [20].

	Cobalt-Based Oxides																		0.4
																			Co
	0.6[a]	0.8	1.0	0.4	0.6	1.0	0.6	0.8	1.6	0.6	0.6	0.6	1.0	0.6	1.0	0.8	0.8	1.2	
	Mg	Al	Ca	Ti	V	Cr	Mn	Fe	Ni	Cu	Zn	Ga	Sr	Mo	Ba	Ce	W	Bi	
		0.2[b]	0	0	0.2	0.8	0.4	2.0	2.0	0.2	0.4	0	0	0	0.8	1.4	0.8	1.0	Mg
			1.2	0	0.4	0.2	0.6	0.6	2.6	0.4	0.4	0.6	1.0	0.8	1.6	1.8	0.8	3.4	Al
Al	1.2[d]			0.2	1.0	1.0	0.4	1.6	3.2	0.6	2.4	1.4	1.4	0.6	0.8	1.8	1.8	2.8	Ca
Ca	2.4	3.4			0	0	0	0	0	0	0	0.6	0	1.2	0	0	1.2	0	Ti
Ti	0	0.8	0			0.6	0	1.6	1.2	0.8	0.6	0.8	1.2	0	0.4	0.4	1.0	0.6	V
V	0.8	1.2	1.0	0.8			0.2	2.0	2.4	1.4	0.6	0.6	1.4	0	2.2	0	2.8	1.2	Cr
Cr	2.4	3.2	3	3.4	2.0			2.0	1.6	0	0.2	0	1.0	0.4	0	0	0.8	0.6	Mn
Mn	0	2.0	0.8	0.6	1.6	1.0			2.4	0.4	1.2	0.8	2.6	2	3	2.6	1.8	0.6	Fe
Fe	3.2	3.8	4.8	0.6	2.0	4.0	2.4			0.2	3.4	2.2	3.4	1.4	3.2	1.6	1.8	1.4	Ni
Co	2.0	2.6	3.2	0	1.2	2.4	1.6	2.4			0.8	**1.4**	**0.4**	**0.4**	**0.8**	**0.2**	**1.4**	**0.8**	Cu
Cu	0.2	1.8	0.4	0	0	1.0	0	0	0.2			0.4	0.8	0.8	2.0	0.4	0	1.8	Zn
Zn	1.4	2.8	3.0	0	1.0	3.4	0.2	1.8	3.4	1.0			1.6	0.8	2.8	1.4	2.4	2.4	Ga
Ga	2.2	2.0	2.8	2.6	1.6	2.4	1.4	3.8	2.2	1.4	1.0			1.0	2	1.2	1.4	1.6	Sr
Sr	1.4	3.0	3.4	0.6	1.4	1.8	0.8	4.4	3.4	0.4	1.2	2.4			1.0	0.4	0	0.6	Mo
Mo	1.0	1.4	2.4	1.6	1.2	1.2	1.6	2.4	1.4	0	2.0	2.2	1.8			1.2	1.4	0.6	Ba
Ba	2.0	2.6	3.6	1.8	1.0	2.6	1.0	4.2	3.2	0.4	1.8	2.4	2.4	1.2			1.2	0	Ce
Ce	1.0	2.2	1.8	0.8	1.6	2.2	1.0	3.2	1.6	0	0	3.0	0.6	0.8	1.2			1.2	W
W	1.4	1.8	1.0	1.2	1.4	1.8	1.4	3.6	1.8	2.8	1.2	2.4	1.6	2.6	1.4	1.6			
Bi	1.8	1.6	3.0	0.4	0	2.6	0.8	1.6	1.4	0.2	1.0	1.0	2.2	1.2	2.0	1.0	0		
	Mg	Al	Ca	Ti	V	Cr	Mn	Fe	Co	Cu	Zn	Ga	Sr	Mo	Ba	Ce	W	Bi	
	1.2[c]	2.4	2.0	1.0	1.0	2.4	1.0	2.4	1.6	1.0	1.4	1.8	1.8	1.6	1.8	1.6	1.0	1.0	
Ni	Nickel-Based Oxides																		
1.0																			

water electrolysis [21]. However, the Ni–S_x film dissolves gradually when the electrolyser is stopped (increase of the cathode potential) and therefore loses its high HER activity, which is an obstacle for large-scale application. The activity of some catalysts consisting of hydrogen storage alloys (metal hydrides), for example, $LaNi_{4.9}Si_{0.1}$ and Ti_2Ni alloys, and Ni–Mo coating, that have a low HER overpotential and high durability under intermittent electrolysis [22] has also been reported in the literature. Addition of hydrogen storage alloys inside the electrodes enhances the overall corrosion resistance against power interruptions. During power-off periods, absorbed hydrogen is electrochemically released at a sufficiently low potential to prevent corrosion. The properties of a composite material that combines a hydrogen storage material and nickel–sulphur alloy have also been reported [23]. The HER activity of this composite was shown to be higher than that of the Ni–S film and stability was also enhanced. During operation, both anodic and cathodic catalysts suffer from a loss of activity and stability. Gas evolution within the pores of these porous electrodes leads to mechanical stress and then crumbling or erosion of catalyst particles. This phenomenon is particularly important during operation in transient power conditions (such as rapid increase of the current density or startup and shutdown procedures). The time variation of anode and cathode potentials following the shutdown of an electrolyser using Raney nickel electrodes is plotted in Figure 4.8. Startup and shutdown procedures can induce large electrode potential variations. The cathode potential rises quickly (within seconds) to approximately +200 mV versus RHE, and then remains stable. The anode potential decreases rapidly, then stabilizes for a long period of time, and then falls down to the voltage value of the cathode after 80 min.

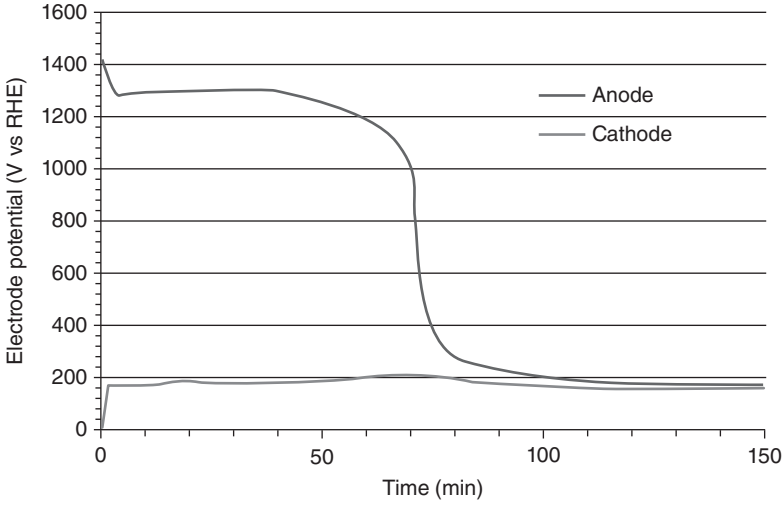

Figure 4.8 Potential time behaviour of the hydrogen and oxygen electrodes after shutdown of the electrolyser. (Redrawn from Ref. [24], Raney Ni electrodes, 10 M KOH, 100 °C.)

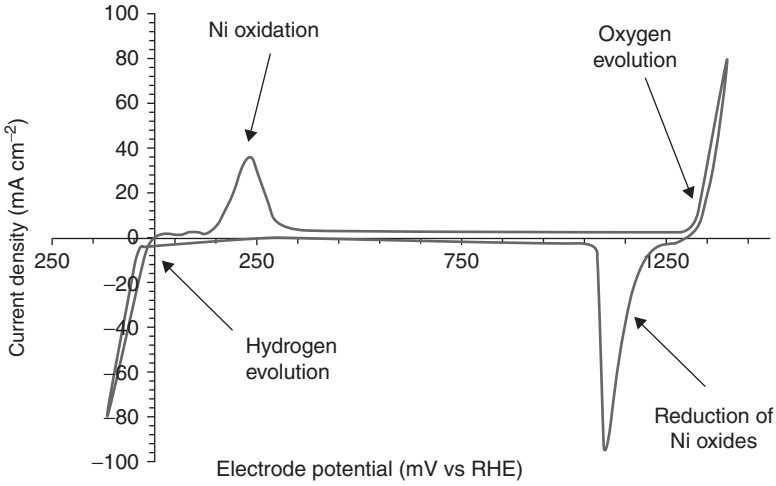

Figure 4.9 Cyclic voltammetry of a Raney nickel electrode (Redrawn from data of Ref.[24], 1 mV s^{-1}, 10 M KOH, 100 °C).

This behaviour is attributed to the discharge of pseudo-capacitances due to the oxidation of nickel at the cathode and to the reduction of nickel oxides formed during operation at the anode (Figure 4.9).

Accumulation of startup/shutdown cycles is equivalent to oxidation/reduction cycles for the catalysts. Mechanical stress due to swelling of catalyst surface and dissolution of oxides can cause catalyst losses. Jović *et al.* [25] proposed an accelerated stress test on cathodic catalysts to compare their stability to polarity inversion of the electrodes that could appear during the replacement of old electrodes of an electrolyser with new ones. This accelerated stress test, called 'service life' test, consists of a succession of cycles including potentiostatic and galvanostatic phases and cyclic voltammetry. A clear loss of the catalyst layer is observed after the 'service life' test (Figure 4.10). The Ni–MoO_2 catalyst coating was found to be much more stable than the Ni–MoOx composite coating.

4.2.4
Diaphragm/Separator

Cell separators, also called diaphragms, are usually made of a porous and electrically insulating material and placed between anodes and cathodes. They should be stable in the standard conditions of operation of electrolysers (30 wt% KOH at 80 °C, highly oxidizing conditions at the anode, reducing conditions at the cathode, gas bubbling, etc.). Their major functions in the electrochemical cell are the separation of the electrodes of different polarity to prevent any short circuit between these electronic conducting parts (electrodes). Then, they must also prevent the recombination of H_2 (formed at the cathode) and O_2 (formed at the anode) by avoiding gas crossover. While serving in all these functions, the

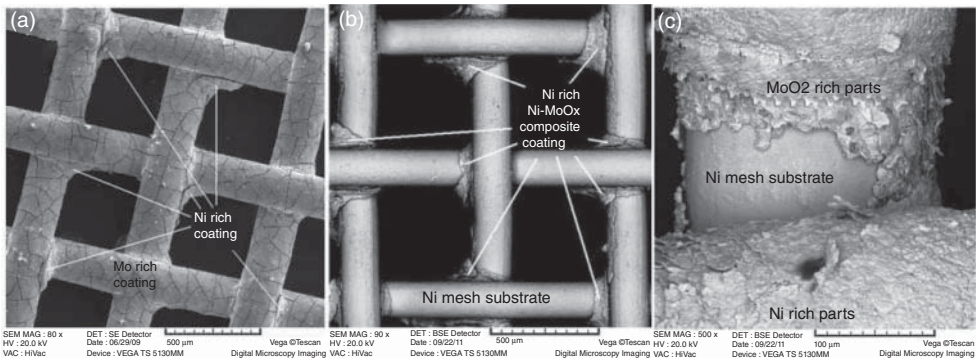

Figure 4.10 Catalyst (Ni–MoOx and Ni–MoO_2)-coated Ni mesh before (a) and after 'service life' test. (b) NiMoOx coating and (c) Ni–MoO_2 coating.

separator should also be a highly ionic conductor for transportation of OH^- ions from the cathode to the anode. Functions are summarized in Figure 4.11. The ionic current passes through the liquid electrolyte present in the pores of the diaphragm. This is why its ionic conductivity depends on the porosity and the tortuosity of the material and on the conductivity of the liquid electrolyte filling the pores. To enhance ionic conductivity of the separator and lower gas crossover, hydrophilic materials are required. Calculation of the ionic conductivity of such porous media is usually a complex process. Simple models are, however, available in the literature [26]. The first commercial separators were made of microfibrous chrysotile asbestos ($Mg_3(Si_2O_5)(OH)_4$). However, asbestos is not very resistant to corrosion caused by the strong alkaline environment at high temperatures. Moreover, asbestos is classified as a carcinogenic material and in 1999 asbestos was forbidden for commercial use in the European Union [27]. However, the European Chemicals Agency (ECHA) has proposed to extend its authorization for the use of chrysotile in the production of diaphragms for existing electrolysis installations until they reach the end of their service life

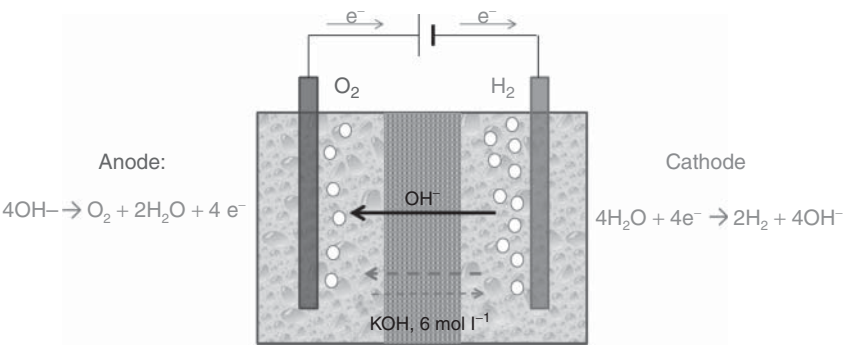

Figure 4.11 Schematic view of usual electrolysis cell with a porous separator.

or until suitable asbestos-free substitutes become available. This authorisation would be prolonged to December 31 2025 [28].

From the 1970s onwards, many organic and inorganic material substitutes to asbestos have been introduced as gas separation material. Inorganic materials such as oxide-ceramic materials YSZ, $NiTiO_3/NiO$, $BaTiO_3/ZrO_2/K_2Ti_6O_{13}$ supported on metallic nets (cermets) were used but large surface area samples were very expensive. On the other hand, organic materials such as polysulphone, polyphenylene sulphide, polyphenyletheretherketone, polytetrafluoroethylene (PTFE) and other hydrophobic polymers do not show a sufficiently hydrophilic properties. Therefore, a composite made of a very stable hydrophobic polymer binder mixed with hydrophilic ceramics or polymers was proposed to combine high chemical stability, mechanical strength and electrolyte pore filling capabilities. PTFE-bonded potassium titanate and polysulphone-bonded zirconia show excellent stability in a hot (until 150 °C) and caustic environment with a rather low specific resistance (approximately $0.2\,\Omega\,cm^{-2}$). Typical thicknesses are a few hundreds of microns, significantly thinner than asbestos diaphragms (thickness of several millimetres).

One of the most popular materials used as a separator is composed of a polysulphone network (Figure 4.12) and zirconium oxide as the inorganic filler. This material, also known as Zirfon® Perl , was developed by VITO Research [29] and is commercialized by Agfa-Gevaert Group (Agfa Specialty Products) [30]. It contains 85 wt% of hydrophilic ZrO_2 powder with a high specific surface area of $22\,m^2\,g^{-1}$ as hydrophobic agent and 15 wt% polysulphone, which gives the material its mechanical strength [31]; 0.5 mm thick Zirfon® separators present excellent chemical stability and a low ionic resistance, leading to a significant improvement in the water electrolysers performance [31, 32].

Zirfon® Perl (Figure 4.13) is commercially available with two types of polymer mesh having between 50% and 70% of open area:

- the Zirfon PERL® LT (low temperature) uses a polypropylene (PP)-based mesh and its maximum recommended operating temperature is limited to 80 °C;
- for higher operating temperature, the Zirfon PERL® HT (high temperature) is made of an ethylene tetrafluoroethylene (ETFE)-based mesh and maximum temperature of operation is approximately 120 °C.

More recently [33], it was found that a sulphonated poly-ether-ether-ketone (Figure 4.14) porous membrane could also be used as an alternative separator. Results obtained in water alkaline electrolysis using a 50 kW electrolyser stack were found very promising.

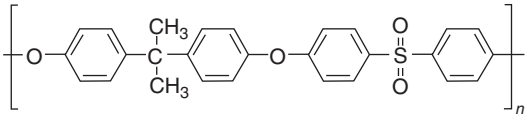

Figure 4.12 Chemical structure of polysulphone.

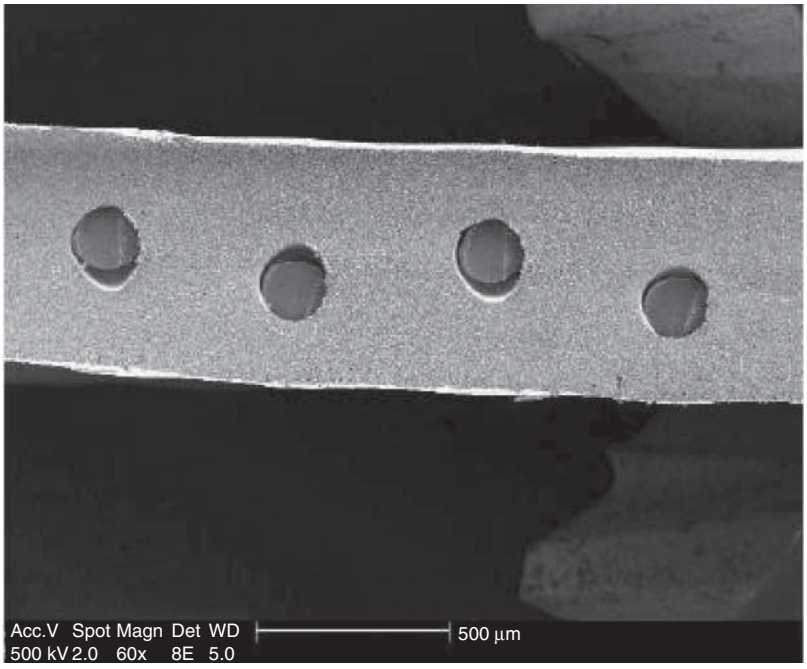

Figure 4.13 Cross section of a 500 µm thick ZIRFON Perl 500 UTP separator [11]; the separator contains an open mesh polymer fabric, which is symmetrically coated with a mixture of a polymer and zirconium oxide.

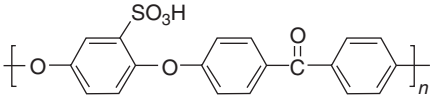

Figure 4.14 Chemical structure of sulphonated poly-ether-ether-ketone (s-PEEK).

Performance was compared with the commercially available Zirfon HTP 500 separator under normal operating conditions (400 mA cm^{-2}, 10 bars, 80 °C, electrolyte KOH 30 wt%) and under transient operation including numerous shutdown cycles. Results of performance and stability conducted on s-PEEK separators showed a similar cell voltage (about 2.5 V $cell^{-1}$) and higher gas purity than the ones obtained with the commercial Zirfon HTP 500 diaphragm.

4.2.4.1 **Zero-Gap Assembly**

As discussed before, the electrolyte volume stored in the electrochemical cells is determined by the distance (gap) between the electrodes. This distance ranges between a millimetre and several centimetres. The ohmic losses in the electrolyte increase with the distance between the electrodes. On the other hand, when the electrolyte volume is too small, the reactant concentrations change rapidly during operation. A major advance in the design of alkaline electrolysers came in 1967

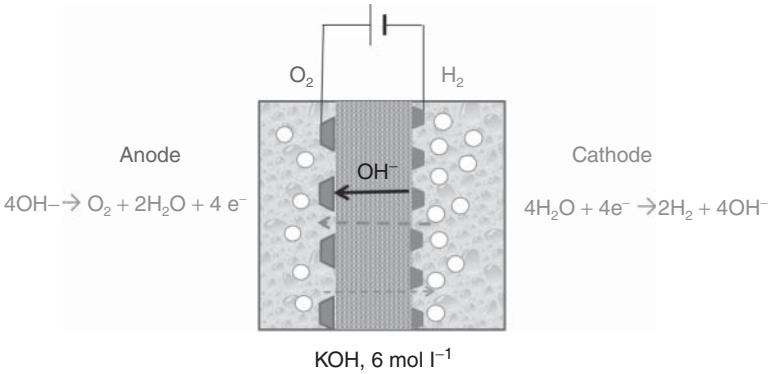

Figure 4.15 Schematic view of a zero-gap electrolysis cell, a large mesh at the anode (Raney nickel coating) and a fine mesh at the cathode (catalyst coating). The thickness of the separator used in zero-gap electrolysis cell is typically about 400 μm.

when Costa and Grimes proposed the concept of 'zero-gap' assembly (Figure 4.15) of the electrodes [34]. The electrodes are placed directly in contact with the porous separator, aiming to reduce the cell resistance by reducing the distance between the two electrodes. Mesh-type or porous electrodes have to be used in order to let the electrolyte fill the pores of the separator. Even though the assembly of such electrochemical cells is more complex than for gap cells, significant increase of the current density was obtained [35].

4.2.4.2 Anionic Membranes

In order to further reduce the internal resistance of the electrolysers and operate the cells at high pressure, the possibility of using a non-porous membrane with high anionic conductivity has also been investigated. Another advantage of using OH^- conductive polymer electrolyte instead of KOH electrolyte is that only deionized water needs to be supplied to the electrolyser. Porous catalyst layers are deposited on each sides of the membrane to form a membrane–electrodes assembly (MEA) very similar to what currently used in proton exchange membrane (PEM) water electrolysis (Figure 4.16).

The main requirements of OH^--conducting membranes are:

- good mechanical and thermal stability in contact with water and during operation;
- insulator regarding electronic conductivity;
- efficient transfer of OH^- ions from one electrode to the other (high ionic conductivity);
- very low permeability to gases to avoid gas crossover between the anodic and cathodic compartments; and
- low cost.

Anion exchange membranes already exist and some are commercially available. However, mobility of hydroxide ions is significantly lower than that of protons

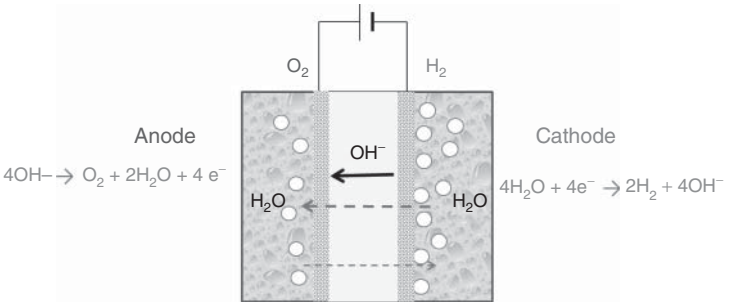

Figure 4.16 Schematic view of an alkaline water electrolysis cell using an anionic exchange membrane and porous electrodes at the cathode and the anode. The thickness of the anionic exchange membranes typically ranges between 100 and 250 μm.

(approximately 15 times) and it is difficult to reach conductivity similar to that of proton-conducting membranes. Moreover, many of these membranes still suffer from a lack of chemical stability at high pH, necessary for good ionic conductivity. They are usually classified into three different categories [36]. The first category contains 'heterogeneous membranes' (Figure 4.17), made of an anion exchange material embedded in an inert compound. Because of the presence of a chemically inert structure, these membranes usually present good mechanical strength. However, these membranes are usually relatively thick (250–600 μm) and it is difficult to obtain a homogeneous dispersion of the exchangeable ionic groups within the whole membrane. The electrical contact between the ionic exchange groups in the membrane and the electrodes is generally of poor quality. Moreover, under long-term operation, a slow extraction of the anionic exchange groups takes place, leading to a loss of ionic conductivity.

A second category of membrane consists of a 'interpenetrating polymer networks' (or IPNs) shown in Figure 4.18. This is basically a combination of

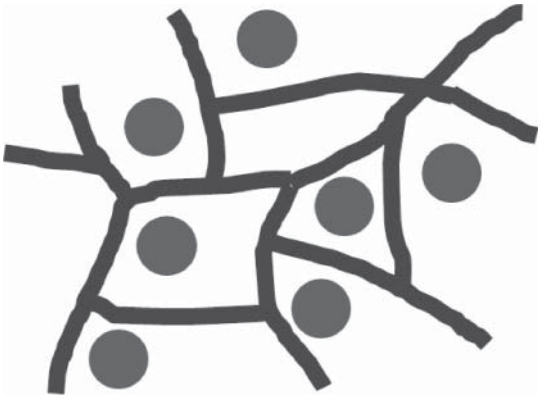

Figure 4.17 Schematic drawing showing the structure of a heterogeneous membrane with an anion exchange material (balls) embedded in a chemically inert structure (linear network).

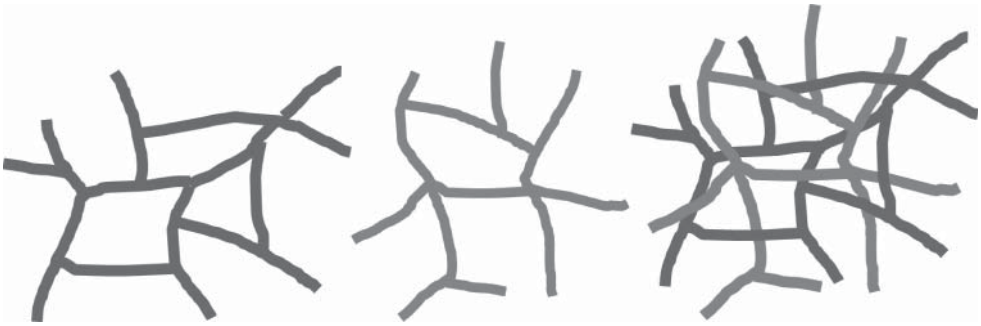

Figure 4.18 Drawing explaining the structure of an interpenetrating polymer networks with a chemically inert polymer matrix (light grey network) and an anion exchange polymer (dark gray network) mixed together.

two polymer networks without any covalent bonds between them. IPNs also have some heterogeneous structures composed of a polymer matrix with good thermal, chemical and mechanical properties, mixed with a conductive polymer to transport anions. These structures are relatively easy to produce and a wide variety of polymers can be used. However, because the conductive polymer is not bounded to the polymer matrix, it can slowly diffuse out of the membrane during operation, thus reducing ionic conductivity.

The third category is that of 'homogeneous membranes' (Figure 4.19). Ionic conductive groups are now covalently bound to the polymer backbone and distributed homogeneously over the entire polymer matrix. Radiation-induced grafting [37] is one of the most widely used methods for the preparation of anionic exchange membranes [38]. However, considering the large-scale production of anionic exchange membranes by radiation-induced grafting, the electrical power required is very large and the membranes will remain expensive.

Figure 4.19 Drawing explaining the structure of a homogeneous membrane with an anion exchange material (balls) covalently bound in a chemically inert structure (network).

A list of commercial suppliers of anionic membrane materials is compiled in Table 4.2 [39].

It should be noted that the development of a membrane satisfying both chemical stability and performance requirements (as listed above) is one half of the problem. In addition, it is of major importance to also develop an ionomer compatible with the membrane material and meeting the same requirements, in order to produce the catalyst layers. Tokuyama Co. Ltd. (Japan) developed an ionomer for its membrane (Figure 4.20). This ionomer (referenced as ' Neosepta As-4') is given for a IEC (ion exchange capacity) of 1.4 $m_{eq} \cdot g^{-1}$ and a conductivity of 14 mS cm^{-1}.

Despite the lack of stability of the anionic membranes, some water electrolysers have been developed and performances have been evaluated. Wu *et al.* [41] used a heterogeneous membrane made with a porous PTFE film filled with a quaternary ammonium polymethacrylate ionomer. They observed a quite low degradation of performance over a 120 h ageing test (37 μV h^{-1} at 22 °C at a current density of 100 mA cm^{-2}).

Another interesting recent work was conducted by Faraj *et al.* [42] with the company Acta S.p.A (Italy). This company has commercially launched an alkaline membrane water electrolyser [43] that uses an alkaline exchange membrane placed in a dilute aqueous K_2CO_3 electrolyte that guarantees ionic conductivity and pH buffering (approximately 10). The MEA used electrodes made of non-precious group metal catalysts produced by Acta S.p.A [44] at both the anode and the cathode and a commercially available anion exchange ionomer (AS4 from Tokuyama corporation). The system is quite compact with current densities that can reach 500–600 mA cm^{-2} and a differential pressurization of gases is possible up to 30 bars. In this work, the authors studied the performance of a membrane made of a low-density polyethylene (LDPE) film modified by UV-induced grafting of vinylbenzyl chloride. Electrochemical performance of a MEA made with this membrane was compared to a MEA using a commercial Tokuyama Co. membrane (reference not specified). Experiments were conducted on a 10 cm^2 single cell at a cell temperature of 45 °C and constant current density of 460 mA cm^{-2}, feeding only the anode side with an aqueous solution of 1 wt% K_2CO_3. The cathode side was not fed with electrolyte, and the water required for hydrogen production passed through the membrane by electro-osmosis. The hydrogen gas compartment was pressurized to 20 bars while oxygen was kept at atmospheric pressure. Ageing tests conducted for 500 h showed an average increase of cell voltage of 300 μV h^{-1} on the experimental membrane, whereas it was limited to 80 μV h^{-1} for the commercial membrane-based MEA. Degradation of performance cannot solely be explained by the increase of the AC cell resistance, periodically measured at 1 kHz. On the MEA made of the commercial membrane, this resistance remained stable (0.22–0.23 Ω cm^2), while it increased from 0.30 to 0.43 Ω cm^2 on the MEA made of the experimental membrane. Such increase of high-frequency resistance, which is generally attributed to the membrane internal resistance and the membrane electrode interface, only weights for a third of the observed voltage degradation. The rest of the performance lost could be due to a decrease of the

Table 4.2 List of suppliers of commercial anionic exchange membranes data from Ref.[39] (Xu et al. J. membr. Sci. (2005)).

Company	Membrane type	Commercial name	IEC ($m_{eq}\ g^{-1}$)	Thickness (μm)	Resistivity ($\Omega\ cm^{-2}$)
Asahi Chemical Industry Co. Japan	—	Aciplex A-XXX	—	140–240	1.4–4.2
Asahi Glass Co. Ltd., Japan	PS-*b*-EB-*b*-PS	Selemion XXV	—	110–170	1.5–3.5
Tokuyama Co. Ltd., Japan	IPN (poly(styrene-*co*-divinylbenzene))	Neosepta AXX	1.3–3.5	100–240	0.2–6.0
Tianwei Membrane Co. Ltd., China	—	TWXXX	1.2–2.1	160–230	2–10
Shanghai Chemical Plant of China, China	Heterogeneous PE	PE3362	1.8–2.0	450	13.1
Solvay S.A., Belgium	—	Morgane ADP	1.3–1.7	130–170	1.8–2.9
MEGA a.s., Czech Republic	—	Ralex	1.8	>700	8–13
FuMA-Tech GmbH, Germany	PEEK	FAA-3-PK-130	1.43	130	1.9
PCA Polymerchemie Altmeier GmbH, Germany	—	PC-SA D	—	80–100	—
Ionics Inc., USA	Heterogeneous membrane	103PZL 183	—	—	—
RAI Research Corp., USA	IPN	R-1030	—	—	—
CSMCRI, Bhavnagar India	LDPE/HDPE (IPN)	IPA	0.8–0.9	160–180	2.0–4.0

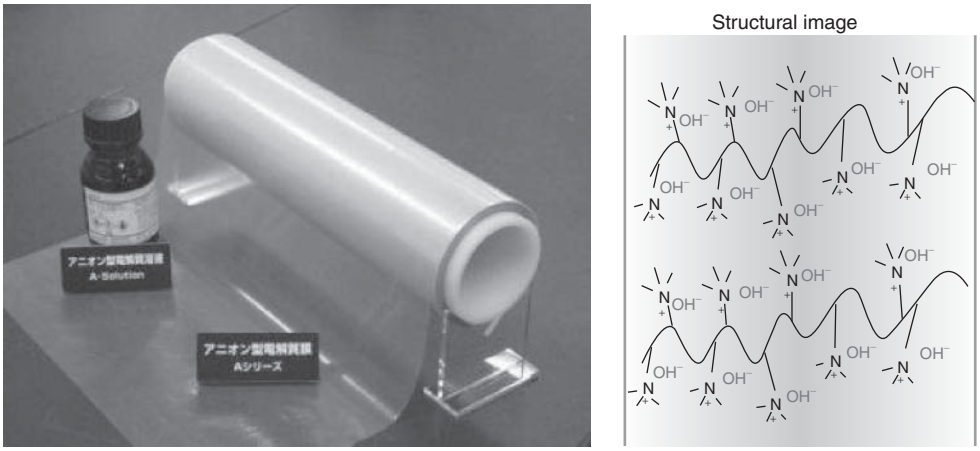

Figure 4.20 (a) Picture of a Neosepta membrane (linear hydrocarbon backbone with quaternary ammonium group) and bottle of the corresponding ionomer (Tokuyama Co. Ltd., Japan) [40] (b) chemical structure odf the polymer.

electrochemically active surface area of the electrodes (degradation of the catalyst layers, which is a mixture of a catalyst powder and an ionomer).

4.3
Electrochemical Performances of Alkaline Water Electrolysers

4.3.1
Polarization Curves

Polarization curves (plots of cell voltage vs. current density) are the key performance indicators used to evaluate and compare the performances of water electrolysis cells. As discussed in the different chapters of this book, polarization curves can differ significantly from one technology to another, depending on different parameters (mainly the conception of the electrolyser, operating temperature and pressure). Some examples for several alkaline water electrolysis cells are plotted in Figure 4.21. The first steep portions of these curves are due to activation polarization at the electrodes. At higher current densities, the linear relationship is due to the cell resistance. Mass transport limitation can also be observed at higher current densities.

In Figure 4.21, electrolyte composition and operating temperatures are roughly the same. However, cell voltage of the zero-gap-type electrolyser (DLR prototype) is far lower than that of the usual concept one. There is no voltage difference between the Bamag electrolyser, which is composed of catalyst-coated electrode plates, and the Lurgi electrolyser, which uses nickel-plated wire gauze as electrodes. The cell voltage of the Teledyne electrolyser using porous nickel electrodes is lower than that of the two electrolysers with conventional structure. This is due

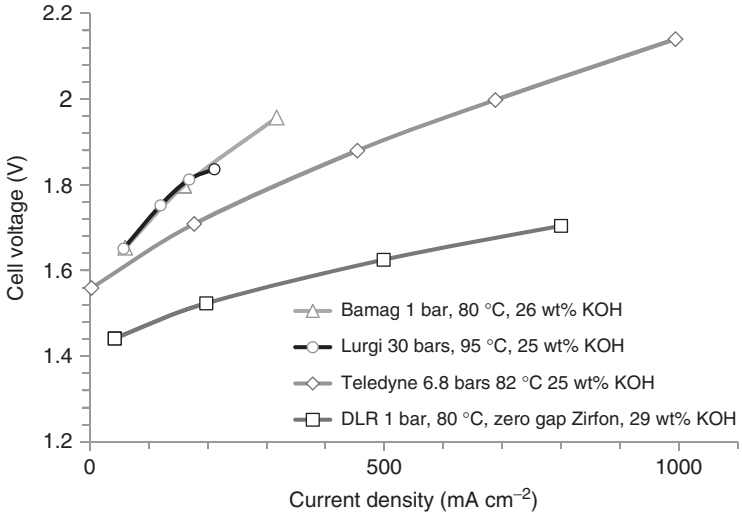

Figure 4.21 Polarization curves of different alkaline electrolysers [45].

to the higher electrocatalytic activity of the porous nickel structure, compared to Ni-coated plates (Bamag) or meshes (Lurgi).

4.3.2
Comparison of Electrolyser Performances

To compare the performance of different type of electrolysers, it is convenient to determine their efficiency ε. Efficiency of the water splitting reaction is calculated by considering on the one hand the energy supplied to the electrolyser and on the other hand the amount of hydrogen that will actually be recovered at the electrolyser outlet. The energy E_{el} supplied to the electrolyser powered by a DC power source is:

$$E_{el}(J) = U \cdot I \cdot t = n_{cell} \cdot U_{cell} \cdot I \tag{4.3}$$

where U is the cell voltage in volt (V), I is the current in amperes (A) and t the duration of operation (in s); 'n_{cell}' is the number of cells in the electrolyser and 'U_{cell}' is the average cell voltage.

Assuming that there is no parasitic reaction, the hydrogen and oxygen flows are directly related to the current that crosses the electrochemical cell:

$$\varphi_{H_2}(\text{mol s}^{-1}) = \frac{I \cdot n_{cell}}{2F} \tag{4.4}$$

where 'n_{cell}' is the number of cells in the electrolyser and 'F' the Faraday constant (96 485 A·mol^{-1}). When a current I is supplied for t seconds, then the amount of hydrogen produced is:

$$n_{H_2}(\text{mol}) = \frac{I \cdot n_{cell}}{2F} \cdot t \tag{4.5}$$

In standard conditions of temperature (273.15 K) and absolute pressure (100 kPa), the energy produced when hydrogen is burned in pure oxygen to form water vapour (i.e. the enthalpy of combustion) is $\Delta H_C^\circ = 242\,\text{kJ mol}^{-1}$. When liquid water is formed, the latent heat of water condensation has to be added and the total energy produced is $286\,\text{kJ mol}^{-1}$. The first value is usually called the 'lower heating value' (LHV) and the second the 'higher heating value' (HHV). Energy produced by the electrolyser is then given by the following equations:

$$E_{H_2\text{-}H_2O\ (vap)}(\text{J}) = \frac{I \cdot n_{cell}}{2F} \cdot t \cdot 242\,000 \tag{4.6}$$

$$E_{H_2\text{-}H_2O(l)}(\text{J}) = \frac{I \cdot n_{cell}}{2F} \cdot t \cdot 286\,000 \tag{4.7}$$

Then the electrolyser efficiency 'ε' can be calculated by dividing the energy contained in the hydrogen collected at the outlet of the electrolyser by the electrical energy supplied:

$$\varepsilon_{H_2-H_2O\ (vap)} = \frac{\frac{I \cdot n_{cell}}{2F} \cdot t \cdot 242\,000}{n_{cell} \cdot U_{cell} \cdot I \cdot t} = \frac{\frac{1}{2F} \cdot 242\,000}{U_{cell}} = \frac{242\,000}{2F \cdot U_{cell}} \tag{4.8}$$

$$\varepsilon_{H_2-H_2O(l)} = \frac{286\,000}{2F \cdot U_{cell}} \tag{4.9}$$

The efficiency ε is totally independent of the amount of hydrogen produced. It depends mainly on operating current density, temperature and pressure. This is why the cell efficiency is not always considered as the most appropriate way to compare the performance of different electrolysers. In practice, the performances of electrolysers are often compared by taking into consideration two parameters: (i) the hydrogen production rate, which is a measure of the capacity of the hydrogen production unit (units are usually $\text{Nm}^3\text{H}_2\ \text{h}^{-1}$ or $\text{kgH}_2\ \text{h}^{-1}$) and (ii) the energy consumption at nominal operating conditions of operation (temperature, pressure and current density) expressed per unit of volume or mass (in $\text{kWh Nm}^{-3}\text{H}_2$ or $\text{kWh kg}^{-1}\text{H}_2$). By plotting the volumetric energy consumption measured (i) at the stack level and (ii) at the system level, as a function of the hydrogen production rate (Figure 4.22), it is possible to show that the energy consumption measured at the stack level is significantly lower than the energy consumption measured at the system level, especially at low current density (low hydrogen flow rate). The difference is due to the fact that the measurements made at the stack level do not take into account parasitic reactions, H_2 and O_2 crossover between compartments, the energy consumption of ancillary equipments and the energy required to purify/dry gases. Of course, this difference tends to decrease at higher operating current density.

4.3.3
Operation at Elevated Temperatures

Most commercial water electrolysers operating at 70–90 °C use 25–35 wt% KOH solutions. Practical efficiencies range from 65% to 75% (1.85 to 1.7 V·cell^{-1}) at

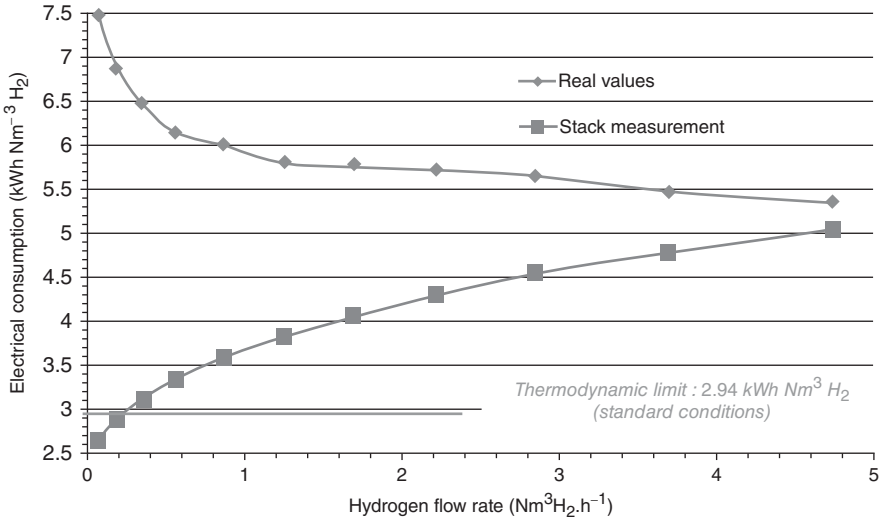

Figure 4.22 Electrical energy consumption versus hydrogen capacity. Comparison of measurements performed at the stack level (■) and at the system level (⧫).

current densities of approximately 200 mA cm^{-2}. By increasing operating temperature, higher efficiencies can be obtained.

4.3.3.1 Thermodynamics

Concerning thermodynamics aspects, the electrical energy required to split water molecules decreases with increasing temperature until water evaporation. However, the heat demand increases and the total energy demand (sum of electrical energy and heat) is almost constant at any temperature for both liquid water and vapour (steam) water. The evolution of $E_{rev}(T, P)$ follows the general equation:

$$E_{rev}(T, P) = \frac{-\Delta G_f^0}{2F} + \frac{RT}{2F} \ln\left(\frac{a_{H_2}\, a_{H_2}^{1/2}}{a_{H_2O}}\right) \tag{4.10}$$

where ΔG°_f is the Gibbs free energy of formation at standard conditions (−237 178 kJ mol^{-1}), R is the constant of perfect gases (8.3145 J mol^{-1} K^{-1}), a_{H_2} is the hydrogen activity, a_{O_2} is the oxygen activity, a_{H_2O} is the activity of water and T is the temperature in Kelvin.

Ganley [47] has conducted experiments on high-temperature alkaline electrolysis cell (up to 400 °C). Some of the experiments (Figure 4.23) used a sealed electrolysis cell under self-generated steam partial pressure. The maximum pressure reached was 8.7 MPa. The cell voltage was found to decrease linearly with the temperature (Figure 4.24). But the slope was found far more important than the expected one, considering the evolution of $E_{rev}(T, P)$. The possibility to split water with less than 500 mV at a current density of 200 mA cm^{-2} and

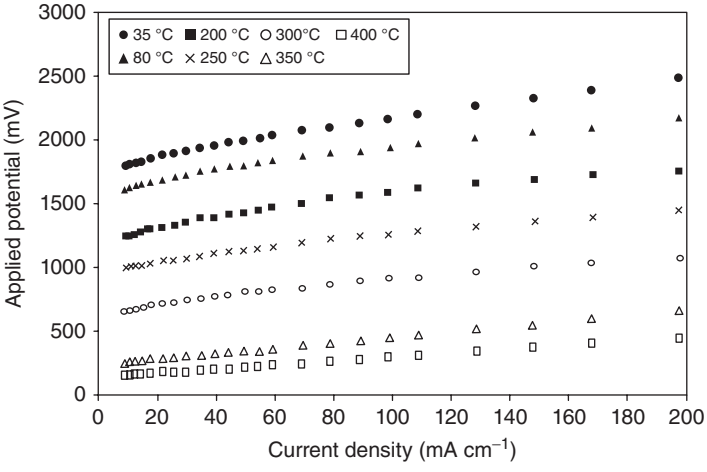

Figure 4.23 Polarization curves of (sealed) alkaline electrolysers, recorded at different. (•) 35 °C; (triangle) 80 °C; (square) 200 °C; (x) 250 °C; (o) 300 °C; (open triangle) 350 °C; (open square) 400 °C. Ref. [47] (Ganley et al. IJHE (2009))

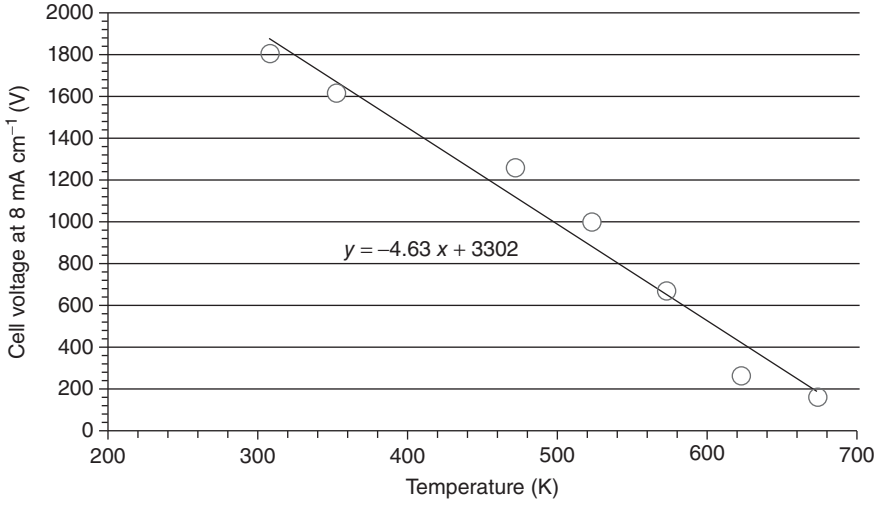

Figure 4.24 Evolution of the cell voltage recorded at 8 mA cm^{-2} versus temperature. Red-Drawn from data of Ref. [47] (Ganley et al. IJHE (2009)

temperature of 400 °C was observed. The reasons for this unexpected very low potential measured at high temperatures were not clarified. It was suggested that parasitic reactions involving the reaction species (recombination of hydrogen and oxygen) could occur in the closed cell, leading to mixed potential values on each electrode.

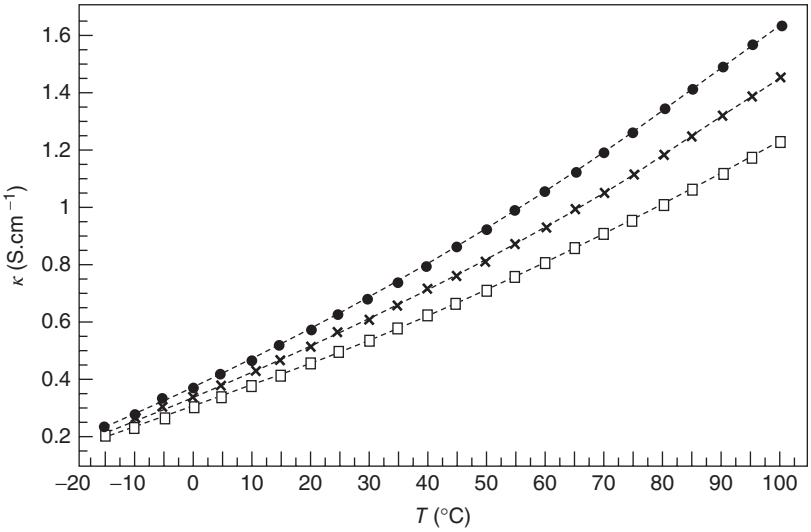

Figure 4.25 Variation of specific conductivity *k*, with temperature *T* (•) 15 mass%; (x) 20 mass%; (full square) 25 mass% KOH [11].

4.3.3.2 Kinetics

Main effects of higher operating temperature on electrode kinetics have been observed for the oxygen evolution reaction on nickel electrodes. The exchange current density for this reaction was found to increase more than three orders of magnitude from 80 to 264 °C [48]. The effect of temperature on the HER is less significant.

4.3.3.3 Electrolyte Conductivity

Usually, the ionic conductivity of electrolytes increases with temperature [10, 11]. This is the case for aqueous KOH, as shown in Figure 4.25 [11].

By increasing the operating temperature from 70 to 150 °C, it is possible to significantly increase the efficiency of the electrolyser and to facilitate the thermal management (cooling) of the cells. However, the chemical stability of the electrolyser components is a key parameter and working at temperature higher than 100 °C also necessitates the use of pressurized electrolysers that negatively impacts capital expenses.

4.3.4 Operation at Elevated Pressures

Many practical applications require pressurized hydrogen:

- for hydrogen storage in metal hydrides ($P > 1.2$ MPa with <5 ppm O_2 and H_2O);
- for hydrogen transport in pipelines (H_2 into CH_4 and biogases – power to gas): 1.3–8.2 MPa [49];

for hydrogen filling in tube trailers (22 MPa);
for hydrogen storage in car tanks (35–70 MPa);
for hydrogen storage in hydrogen refuelling stations (90 MPa).

4.3.4.1 Hydrogen Compression

Pressurized water electrolysis is limited to approximately 0.5 MPa. Although higher operating pressures can be reached, the impact of pressurization vessels on capital expenses tends to become unacceptable. Higher pressures (e.g. 90 MPa are required for hydrogen refuelling stations) can be reached using mechanical compression, but gas compression requires significant amounts of energy. The compression work is the difference between the final and the initial energy states of the gas. The compression work required for an isothermal compression process is given by the simple following equation:

$$W = P_0 V_0 \cdot \ln\left(\frac{P_1}{P_0}\right) \tag{4.11}$$

where W is the specific compression work ($\mathrm{J\,kg^{-1}}$), P_0 is the initial pressure (Pa), P_1 is the final pressure (Pa), V_0 is the initial specific volume ($\mathrm{m^3\,kg^{-1}}$); $V_0 = 11.11\,\mathrm{m^3\ kg^{-1}}$ for H_2.

However, when the gas is compressed in an insulated cylinder, the flow of heat transferred to the surroundings is null. Increase of the internal energy of the gas during compression leads to a temperature rise. In the ideal isothermal case, the temperature remains constant, while it rises considerably under adiabatic conditions. For an ideal gas undergoing an adiabatic process, the energy required to increase the pressure is higher than in isothermal process. It is given by:

$$W = \left[\frac{n}{n-1}\right] P_0 V_0 \cdot \left[\left(\frac{P_1}{P_0}\right)^{\frac{n}{n-1}} - 1\right] \tag{4.12}$$

where W is the specific compression work ($\mathrm{J\,kg^{-1}}$), P_0 is the initial pressure (Pa), P_1 is the final pressure (Pa), V_0 is the initial specific volume ($\mathrm{m^3\,kg^{-1}}$) ($V_0 = 11.11\,\mathrm{m^3\ kg^{-1}}$ for H_2), and n the adiabatic coefficient (ratio of specific heats) ($n = 1.41$ for H_2).

Multistage compressors equipped with intercoolers (used to evacuate excess heat) operate somewhere between the isothermal and adiabatic condition limits. Adiabatic, isothermal and multistage compressions of hydrogen are compared in Figure 4.26.

Electrolysers operating at elevated pressure require only pressurization pumps to inject feed water into the process loop. For example, the energy required to supply pressurized water to an electrolyser producing $8\,\mathrm{Nm^3\,h^{-1}}$ hydrogen at a constant rate of $2.2 \times 10^{-6}\ \mathrm{m^3\ s^{-1}}$ (with a pump efficiency of 75%) is very low. Compared to the data of Figure 4.26, the energy required to pressurize a liquid is low compared to the energy required for pressurizing gases.

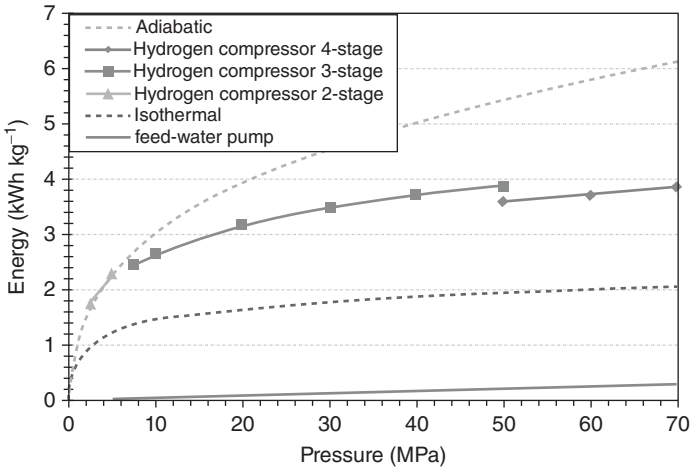

Figure 4.26 Energy consumption of hydrogen compression. Comparison of the energy consumption of isothermal, adiabatic and multistage processes to a feed water pump [50, 51].

4.3.4.2 Pressurized Electrolysers

The first pressurized industrial alkaline water electrolyser was developed by Ewald Arno Zdansky for the Swiss group Lonza. A 3 MPa electrolyser was commercialized in 1951 by the company Lurgi (Germany). This company acquired all the Lonza's patents (32 patents deposited by Zdansky between 1950 and 1956 [52–54]). Compact, high-pressure water electrolysers were also used to produce oxygen on board the nuclear-powered submarines, as part of the life-supporting system. In 1959, Treadwell Corp. (USA) installed its electrolytic oxygen generator (EOG) Model 7L16 aboard USS *Nautilus* [55], producing 2.5 $Nm^3O_2\,h^{-1}$. In 1965, a new model of EOG (Model 6L16), operating at 20.6 MPa and producing 4.2 $Nm^3O_2\,h^{-1}$ was aboard all 637, 688 and 726 class submarines. In 1970, more than 100 electrolytic oxygen generators were in operation in submarines [56].

4.3.4.3 Advantages and Disadvantages

Increasing the operating pressure of the electrolyser has a major effect on the energy consumption of the hydrogen purification unit but it only slightly modifies the energy consumption for splitting the water molecule [57]:

- *LHV*: 2.94 kWh Nm^{-3} (33 kWh kg^{-1}) at atmospheric pressure, 3.16 kWh Nm^{-3} (35.8 kWh kg^{-1}) at 10 MPa.
- *HHV*: 3.54 kWh Nm^{-3} (39.7 kWh kg^{-1}) at both atmospheric pressure and 10 MPa.

Increasing the operating pressure has some positive effects on alkaline water electrolysers. As the pressure increases, the size of gas bubbles tends to decrease and a larger amount of gases are dissolved into the electrolyte (Figure 4.27). Consequences are a reduction of the 'shadow effect' due to the presence of

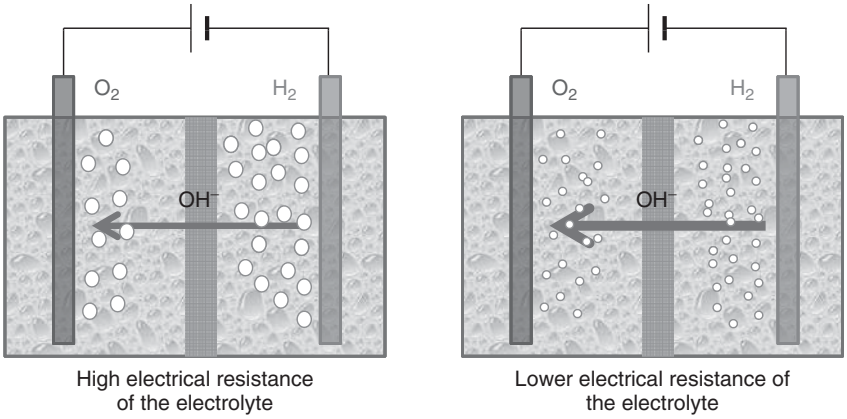

Figure 4.27 Schematic diagrams explaining the shadow effect of gas bubbles in the electrolyte during water electrolysis.

non-conductive gas bubbles in the electrolyte, which tends to increase the ohmic resistance of the electrochemical cell.

Higher operating pressures tend to reduce the voltage of the electrolysis stack, and, consequently, to reduce the energy required to produce hydrogen. Another advantage of high pressure lies in the fact that it is easier to dry the hydrogen when produced at high pressure. The saturation pressure of water in gases is 0.1 MPa at 100 °C. When the pressure is increased, the ratio of the amount of water to remove to the hydrogen that is produced tends to decrease.

On the less positive side, high pressure also increases some parasitic reactions due to the large amount of gases dissolved in the electrolyte at high pressure: As the pressure of the system increases, the partial pressure of each gas in the compartments increases. Then, diffusion of gases across the diaphragm is increased. The flow of hydrogen towards the oxygen compartment and vice versa is linearly dependent on the partial pressure of the gases. Moreover, pressure increases the amount of gas dissolved in the electrolyte (that fills the porous structure of the diaphragm) and forms microbubbles that can reach the size of the pores within the diaphragm. Then, after gas/liquid separation, electrolytes coming from each compartment (O_2 and H_2) are usually mixed together and reinjected in the electrolyser. A recent work [58] showed that hydrogen bubbles in aqueous solutions, even at atmospheric pressure, are very stable: continuing to have a diameter of around 0.4 μm for an unexpectedly long time (after 9 h, only 50% of the number of bubbles had disappeared).[1)] Consequences are that the purity of produced gases decreases rapidly when increasing the pressure. Another consequence is the reduction of the faradaic efficiency of the electrolyser: if 3% of the hydrogen produced goes to the oxygen compartment and 1% of the oxygen produced goes to the hydrogen compartment, the amount of hydrogen really usable (at the exit of a

1) Open porosity of Zirfon separators is usually in the micrometre range.

deoxidation unit) is reduced by approximately 5%. The mixture of gases could also rapidly reach the safety limit (50% of the LEL: 2.5% H_2 in O_2), and this can have a major influence on the operating range of the electrolyser (at low current density, gas diffusion remains constant, but less gas is produced, then the H_2 that crosses over the diaphragm to the O_2 compartment is less diluted). Finally, a compromise has to be found between pressure, costs of construction, efficiency and range of operation.

4.3.4.4 Best Solution?

Combining the best performance of pressurized electrolysers and mechanical compressors, it appears (Figure 4.28) that the energy consumption required to reach 70 MPa can be minimized using a pressurized electrolyser that operates between 2 and 6 MPa (a range that can be further refined by taking into account the characteristics of the entire electrolysis unit, that is, electrolyser + H_2 dryer + compressor).

Data from Ref. [51] indicate that the lowest energy consumption to reach 70 MPa of hydrogen is reached for an alkaline electrolyser operating at a pressure between 5 and 10 MPa. Similar results were obtained on PEM water electrolysers [60, 61] with an optimal operating pressure ranging between 4 and 7 MPa. It should be noted that the optimal pressure changes with the flow of hydrogen produced: optimal pressure decreases when the current density of the electrolyser increases.

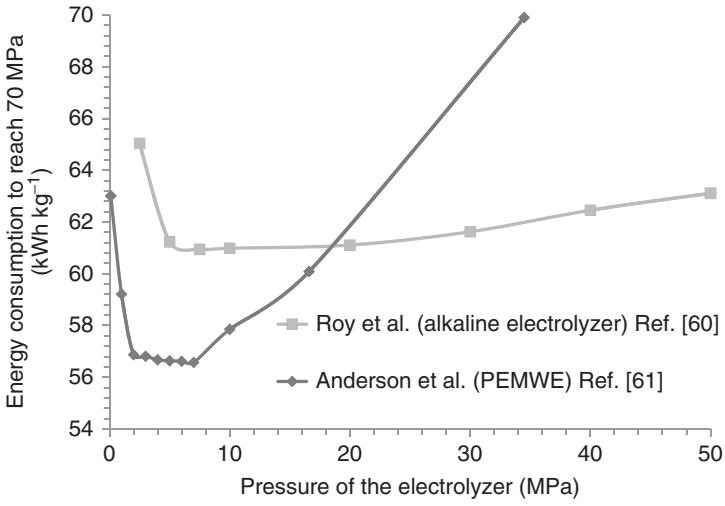

Figure 4.28 Energy required for the production of dry pressurized hydrogen (70 MPa) using a pressurized electrolyser and a mechanical multistage compressor [59, 60].

4.4
Main Suppliers, Commercial Developments and Applications

Alkaline electrolysis is a very mature technology and is the current standard for small-scale to medium-scale onsite hydrogen production (steam methane reforming is preferred for larger volumes).

4.4.1
Markets for Electrolysers

The commercial market for small electrolysers (producing less than 1 $Nm^3H_2\ h^{-1}$), to very large electrolysers (producing more than 1000 $Nm^3H_2\ h^{-1}$) is obviously very different. The market can be categorized into three different segments: small size (producing less than 1 $Nm^3H_2\ h^{-1}$), medium size (1–10 $Nm^3H_2\ h^{-1}$) and large size (more than 100 $Nm^3H_2\ h^{-1}$).

4.4.1.1 Small-Scale Electrolyser Market (Less than 1 $Nm^3H_2\ h^{-1}$)

The small-scale electrolysers are mainly used to replace the storage compressed hydrogen cylinders (up to 10 Nm^3H_2) and bundles (typically 110 Nm^3H_2). The possibility to produce onsite and on request high-purity hydrogen from water and electricity is very convenient for numerous applications. Hydrogen is mostly used as a fuel gas for flame application (oxygen + hydrogen): its clean and pure combustion flame produces high and concentrated thermal power for soldering and brazing of metals, glass, quartz, crystal and similar materials, jewels, and so on. Another specific application is the inflation of meteorological balloons. Few cubic metres of hydrogen (less than 2 $Nm^3\ H_2$) are required to inflate the large sounding balloons of a total lift of 2000 g [62, 63]. Several manufacturers propose small-scale industrial electrolysers. Some data are compiled in Table 4.3. Electric energy consumption of small-scale electrolysers is higher than that of larger electrolysers. This is due to the electrical consumption of the auxiliaries (pumps, AC/DC converters, control panel, valves, etc.) that is almost the same whatever the size of the electrochemical cell. Also, energy consumption is usually less significant in small systems and reduction of capital expenses is preferred over efficiency.

4.4.1.2 Medium-Scale Electrolysers Market (1–10 $Nm^3H_2\ h^{-1}$)

Larger electrolysers are used in the industry sector to produce onsite hydrogen and replace the use of hydrogen bundles or tube trailers (2000–3000 Nm^3H_2). Industrial applications for electrolysers of such a size are still wide:

- *Metallurgy application*: high-purity hydrogen is used to produce heat for soldering, brazing and thermal treatment of metal pipes, tubes, plates and sheet. Coating processes use the high-temperature hydrogen flame for wire spraying applications. Hydrogen is also used as a protective or reducing atmosphere to prevent metal oxidation during metal annealing, sintering and surface treatment.

Table 4.3 Small-scale (less than 1 $Nm^3 H_2 h^{-1}$) electrolyser's characteristics; data from some of the most important manufacturers.

Manufacturer	Country	Electrolyte	Maximum pressure (MPa)	Capacity ($Nm^3 h^{-1}$)	Energy ($kWh Nm^{-3}$)	Maximum power (kW)	Remarks
Accadue	Spain	25–30 wt% KOH	3	0.25–1	7.1 to 4.8	1.8–4.8	—
Acta	Italy	AEM	0.3	0.25–1	5.2 to 4.8	1.3–4.8	—
Avalence	USA	28 wt% KOH	13.8	1.3	5.5	7.2	—
Erre due	Italy	—	0.25	0.66	5.45	3.6	—
H_2Nitidor	Italy	25–30 wt% KOH	3	0.25–1	7.1 to 5.3	1.8–5.3	—
Idroenergy	Italy	—	0.18	0.4–1.07	7.5 to 5.5	3–5.9	—
McPhy	Italy/France	—	0.19–0.3	0.4–1	7–7.4	2.8–7.4	—
Sagim	France	—	1	0.1–1	6–8	0.6–8	Monopolar, storage 6–24 Nm^3H_2

- *Powerplant cooling system*: hydrogen is used to cool the windings of the large power plant generators, because of the hydrogen's high heat capacity and low density [64]. Hydrogen gas, pressurized up to 6 bars, is circulated in a closed loop from the active parts to the heat exchangers. A continuous hydrogen flow is necessary to compensate the seal losses and maintain the best operating performance.
- *Food processing industry*: hydrogenation of food oil to produce margarine or edible protein; hydrogenation of non-edible oil to produce animal food or raw material for soap.
- *Float glass production*: protection against oxidation of the molten metal (typically tin) used as bed for floating molten glass during the manufacturing of sheet of glass.

The performances of several commercial systems are compiled in Table 4.4.

4.4.1.3 Large Scale Electrolysers (10 to More than 100 $Nm^3H_2 \cdot h^{-1}$)

Very large electrolysers (producing hundreds of $Nm^3H_2 h^{-1}$) have been used to produce ammonia. Even though some industrial processes still require large amounts of hydrogen and have difficulties to be directly connected to a natural gas pipeline (for H_2 production by methane steam reforming), the real market of such very large electrolysers is related to the development of hydrogen as an energy vector. This is the case for fuel cell vehicles. Car and autobus filling stations should be equipped with a large electrolyser able to produce enough hydrogen to fill the tanks of fuel cell vehicles. A fuel cell car tank contains 4–5 kg of hydrogen at 70 MPa. On a bus, the tank capacity is usually 30–40 kg hydrogen at 35 MPa. The number of hydrogen refuelling stations is gradually increasing (Table 4.5).

Table 4.4 Medium-scale (1–10 $Nm^3H_2 \cdot h^{-1}$) electrolyser's characteristics; data from some of the most important manufacturers.

Manufacturer	Country	Electrolyte	Maximum pressure (MPa)	Capacity ($Nm^3\ h^{-1}$)	Energy ($kWh\ Nm^{-3}$)	Maximum power (kW)	Remarks
Accadue	Spain	25–30 wt% KOH	3	2–10	5.1 to 4.8	10.2–47.8	—
Avalence	United States	28 wt% KOH	13.8	1.3	5.5	7.2	—
ELT	Germany	26 wt% KOH	Atm	2–480	4.6 to 4.3	9.2–2064	Dry gas; Bamag
ERRE due	Italy	—	0.5–3	2.7–10.7	5.4	14–57	—
H_2Nitidor srl	Italy	25–30 wt% KOH	3	2–50	5.1 to 4.7	10.2–236	—
Hydrogenics	United States	30 wt% KOH	1–2.5	10	4.9 to 5.4	49–54	—
Idroenergy	Italy	—	0.18–0.6	2.4–80	5.8 to 4.7	13.9–377	—
Kapsom Mechanical	China	KOH	1.6–3.2	2–1000	—	—	—
McPhy	Italy	—	1.2	1.6–60	6.6 to 5.3	10.5–315	—
Pure Energy Centre	Unnited Kingdom	—	1.2	2.6–42.6	5.8 to 5.4	15–230	Dry gas
SAGIM	France	—	1	1–5	8 to 6.7	8–33	Monopolar, storage 6–24 Nm^3H_2
Shandong Saikesaisi Hydrogen Energy	China	KOH	0.4–5	0.3–2.04	6.9	0.5	—
Suzhou Jingli Hydrogen Production Equipment	China	—	3.2	2–10	5 to 4.9	10–49	—
Teledyne ES	United States	—	1	2.8–11.2	—	—	—
Yangzhou Chungdean Hydrogen Equipment	China	—	3.2	2.5–10	6	15–60	—

Table 4.5 Example of existing hydrogen filling stations capacity for fuel cell vehicles.

H_2 station location	H_2 production capacity $kgH_2 \cdot day^{-1}$; $Nm^3H_2 \cdot h^{-1}$	Supply pressure (MPa)
Brussels, Belgium	65; 30	35
Santa Monica, CA, USA	35; 16	70
Los Angeles, CA, USA	65; 30	70
Oslo, Norway	260; 121	35
Brugg, Switzerland	120; 56	35
Berlin airport of Schönefeld, Germany	214; 100	35–70
Lilleström, Norway	50; 23	70

Electrolysers with hydrogen production capacity ranging from 10 to $100\,Nm^3H_2\,h^{-1}$ perfectly fit with hydrogen needs in small refuelling stations (as long as the number of fuel cell vehicles remains low). The performances of several commercial systems are compiled in Table 4.6.

Electrolysers can also be used for the stabilization electric grid connected to renewable energy (photovoltaic solar farms and wind farms). To adapt the electricity delivery of the renewable energies to the demand of the grid, conversion of electrical energy into hydrogen is a promising solution for energy storage. The extra energy is converted into hydrogen and stored on metal hydrides or transported through a gas network for later use; electricity production and storage are then fully decoupled. Hydrogen can also be mixed in a proportion of 10–15% to biomethane (CH_4 ~ 60% and CO_2 ~ 35%) to increase its heating value and supply the residential, commercial and industrial markets as natural gas does. Large electrolysers are required for such applications (Table 4.7).

4.4.2 Commercially Available Electrolyser Designs

Most of the industrial electrolysers are built according to the filter-press principle proposed by Dr. O. Schmidt in 1900. Three main technologies are available on the market:

- Oerlikon electrolyser: use large square electrodes, operate at atmospheric pressure and do not require circulation pumps.
- Norsk Hydro electrolyser: composed of circular electrodes, operate at atmospheric pressure.
- Zdansky/Lonza electrolyser: pressurized and composed of large circular electrochemical cells.

4.4.2.1 Oerlikon-Type Electrolyser

Contemporary declinations of the Oerlikon–Brown–Boveri electrolyser of 1902 have retained the simplicity and robustness of the system to produce large amounts of hydrogen with a minimum of maintenance. Without any electrolyte

Table 4.6 Large-scale (10–100 $Nm^3 H_2 \cdot h^{-1}$) electrolyser's characteristics; data from some of the most important manufacturers.

Manufacturer	Country	Electrolyte	Maximum pressure (MPa)	Capacity ($Nm^3\ h^{-1}$)	Energy ($kWh\ Nm^{-3}$)	Maximum power (kW)	Remarks
Accadue	Spain	25–30 wt% KOH	3	20–50	4.7	95–236	—
Accagen	Switzerland	KOH	4	60–120	5	300–600	—
ELT	Germany	26 wt% KOH	atm	2–480	4.6 to 4.3	→ 2000	Bamag type, dried gas
ERRE due	Italy	—	0.5–4	16–170	5.4	86–912	—
H_2 Logic	Denmark	—	0.4	5.3–6.6	5.75	30.5–38	Hydrogen refuelling station built in 48 h
H_2 Nitidor	Italy	25–30 wt% KOH	3	2–50	5.1 to 4.7	10.2–236	—
Ht-Hydrotecknic	Germany	—	atm	75–225	5.3	396–1188	—
Hydrogenics	United States	30 wt% KOH	1–2.5	10–60	4.9–5.4	49–324	—
Idroenergy	Italy	—	0.18–0.6	2.4–80	5.8 to 4.7	13.9–377	—
Kapsom Mechanical	China	KOH	1.6–3.2	2–1000	—	—	—
McPhy	Italy/France	—	1.2	1.6–60	6.6–5.3	10.5–315	—
Pure Energy Centre	United Kingdom	—	1.2	2.6–42.6	5.8–5.4	15–230	Integrated H_2 purification system
Spirare Energy	China	—	4	60	4.6	276	—
Suzhou Jingli Hydrogen Production	China	—	1.6–3.2	20–100	4.8–4.6	96–460	—
Teledyne ES	United States	—	1	28–78	—	—	—
Yangzhou Chungdean Hydrogen Equipment	China	—	3.2	20–80	6–5	120–400	—

Table 4.7 Very large-scale (more than 100 $Nm^3 H_2 h^{-1}$) electrolyser's characteristics; data from some of the most important world manufacturers.

Manufacturer	Country	Electrolyte	Maximum pressure (MPa)	Capacity ($Nm^3 h^{-1}$)	Energy ($kWh Nm^{-3}$)	Maximum power (kW)	Remarks
ELT	Germany	26 wt% KOH	Atm	2–480	4.6 to 4.3	→ 2200	Bamag type; dried gas
ELT	Germany	25 wt% KOH	3	200–1400	4.6 to 4.3	→ 6000	Lurgi type; dried gas
ERRE due	Italy	—	0.5-4	16–170	5.4	→ 920	—
H_2 Nitidor	Italy	25–30 wt% KOH	3	100–200	4.7	→ 940	—
Ht-Hydrotecknic	Germany	—	Atm	75–225	5.3	→ 1200	—
IHT	Switzerland	—	3.2	760	4.65	3500	—
Kapsom Mechanical	China	KOH	1.6–3.2	2–1000	—	—	—
McPhy	Germany	—	3	100–400	5	2000	—
NEL	Norway	25 wt% KOH	Atm	150–485	4.75	→ 2300	—
Suzhou Jingli Hydrogen Production Equipment Co., Ltd	China	—	1.6	150–1000	4.6 to 4.4	→ 4400	—
Yangzhou Chungdean Hydrogen Equipment	China	—	3.2–1.5	120–1000	5	→ 5000	—

recirculation pump, this electrolyser is simple to operate and it is possible to check visually the operation of each cell, by looking at the diphasic mixture of electrolyte and gas flowing in the transparent tubes connected from the top of the electrolysis cell to the gas–liquid separation tanks. This type of electrolyser was installed by Brown–Boveri (Switzerland) in Aswan (Egypt) in 1977. The 144 electrolysers installed with a nominal power rating of 162 MW were able to produce up to 32 400 $Nm^3\ H_2 \cdot h^{-1}$. Examples of actual commercialized apparatus are the Bamag-type electrolyser from ELT (using electrodes up to 3 m^2) and the McPhy with very large electrolysers of 2 MW (Figures 4.29 and 4.30).

It has to be noted that this type of electrolyser can be pressurized by using a pressurization vessel. This is the case for the electrolyser developed by GHW in the framework of a hydrogen project at Munchen Airport, Germany, realized by ARGEMUC (ArbeitsGEmeinschaft Flughafen MUenChen) between 1997 and 2006 [66]. A 30 bars pressure electrolyser of approximately 450 kW, producing 94 $Nm^3\ H_2\ h^{-1}$ at nominal power load, was connected to the existing power network to produce pressurized hydrogen (Figure 4.31). It was composed of two adjacent cell blocks of approximately 225 kW each, each of which is located in a 3 MPa pressure vessel.

In 2004 it was planned to develop 'small' cell areas (0.8 m^2) for units of up 1 MW per single cell and 2.3–2.5 m^2 for units bigger than 1 MW. The production power range per electrolyser unit was planned up to 700 Nm^3 of hydrogen (3 MW). These

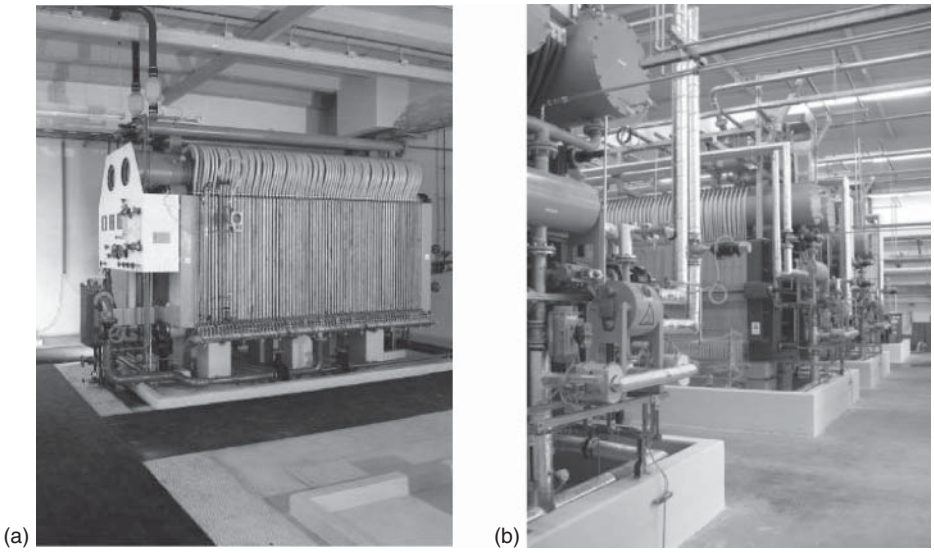

Figure 4.29 (a) Bamag electrolyser commercialized by ELB Elektrolysetechnik GmbHuntil 2.2 MW (480 $Nm^3\ H_2\ h^{-1}$) (*http://www.elektrolyse.de/vkp/modules.php?name=Content&pa=showpage&pid=5*) and (b) McPhy electrolysers type McLyzer 425-AT installed at Audi A.G. plant (three electrolysers, 2 MW each, producing 425 $Nm^3\ H_2\ h^{-1}$ each) *http://forschung-energiespeicher.info/en/projektschau/gesamtliste/projekt-einzelansicht//Weltweit_erste_industrielle_Power_to_Gas_Anlage.*

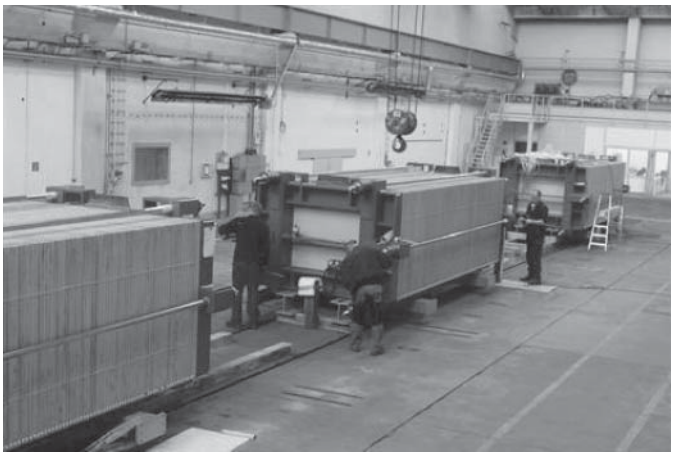

Figure 4.30 2 MW electrolysers stack under fabrication [65].

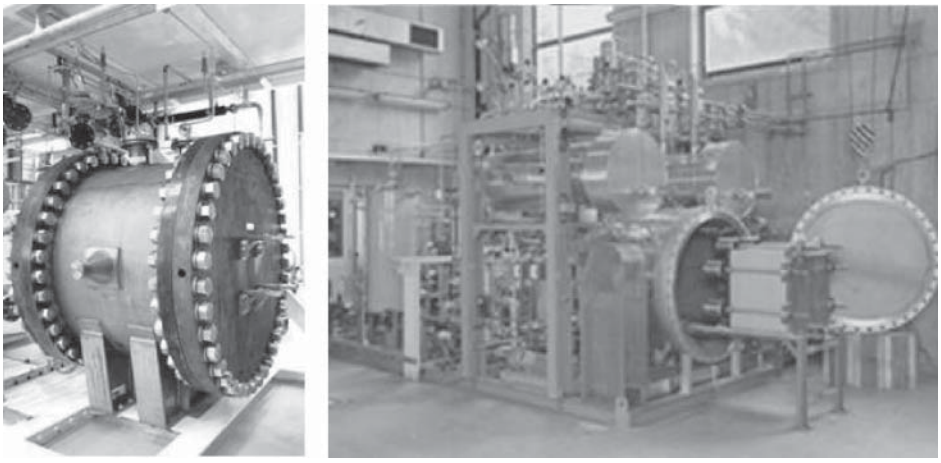

(a) (b)

Figure 4.31 (a) GHW's advanced 500 kW, 30 bar PME electrolyser shown at HYFORUM (May 2004), Beijing [67]. (b) GHW 100 kW test plant.

new devices had no circulation pump. Lye circulation was achieved by the gas lifting effect of the product gases generated in the cell. The energy consumption for the system was said to be about 4 kWh Nm^{-3} H_2. On the basis of this concept, the McPhy company now proposes the 'McLyzer 030-60' system, with a production capability of 30 Nm^3 $H_2 \cdot h^{-1}$ at 5.8 MPa.

4.4.2.2 Norsk Hydro-Type Electrolyser

Norsk Hydro-type electrolysers were developed in the 1930s. They are considered to be one of the most efficient and reliable type of water electrolyser. More than 500 electrolysers are installed in the world. These electrolysers were developed for

continuous production over several years (a stack replacement is recommended after 8–10 years of continuous operation). Main developments of these atmospheric electrolysers are now focused on the dynamic behaviour to allow immediate startup from stand-by, quick response time to dynamic load changes and a broader operational range of hydrogen production (5–100% instead of 25–100%). Increasing the pressure of operation of the stacks is another challenge for such type of electrolyser. Nel recently developed a new electrolyser (NEL P.60) producing 60 $Nm^3\ H_2 \cdot h^{-1}$ from one single cell stack at 1.5 MPa outlet pressure directly from the electrolyser (Figure 4.32). The operational range has been enlarged to 10–100% and the response time to dynamic load change is said to be less than 1 s (*http://www.nel-hydrogen.com/docs/P60_memo.pdf*).

The same concept is also used by numerous manufacturers with electrolysers operating at pressure lower than 10 bars (Figures 4.33 and 4.34).

4.4.2.3 **Zdansky/Lonza-Type Electrolyser**

This electrolyser was the first high-pressure system that became commercially available. It was possible to produce a large amount of hydrogen at a pressure of 3 MPa. The Zdansky–Lonza technology is commercialized by ELB Elektrolysetechnik GmbH. The largest electrolyser can deliver up to 1400 $Nm^3\ H_2 \cdot h^{-1}$ in a single stack (Figure 4.35) [71].

Several companies developed pressurized electrolysers producing hydrogen directly at pressures higher than 3 MPa (Figures 4.36).

Figure 4.32 Picture of a NEL electrolyser (50–485 $Nm^3\ H_2\ h^{-1}$, 4.4 $kWh \cdot Nm^3\ H_2$, 80 °C, atmospheric pressure) [68].

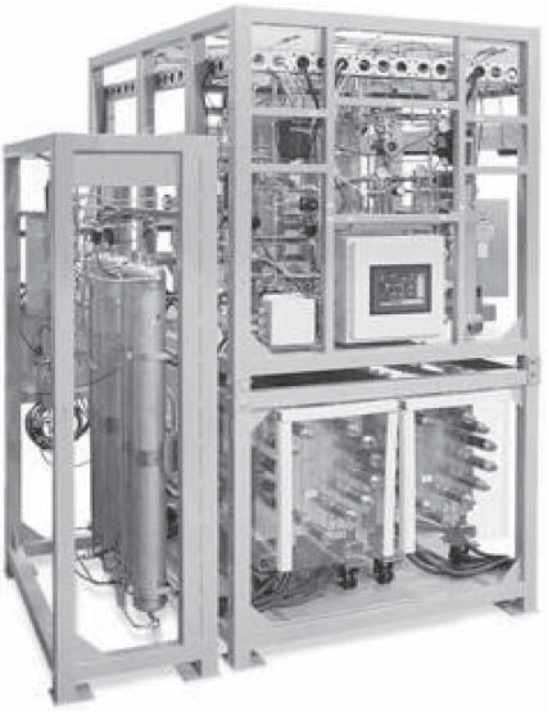

Figure 4.33 Titan EL from Teledyne *http://www.teledynees.com/index.php/products/detail/titan-el*.

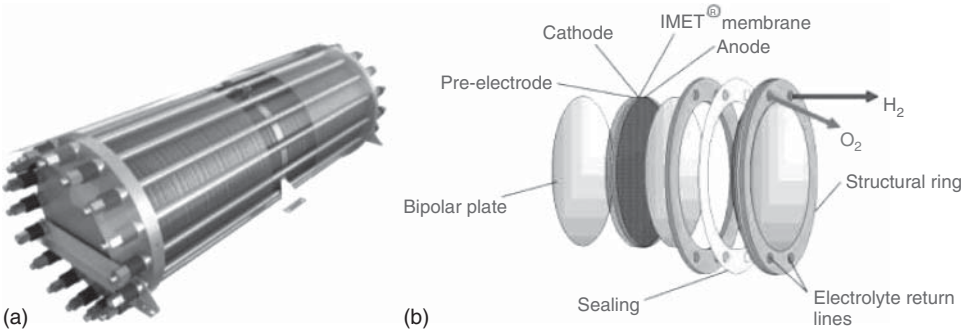

Figure 4.34 (a) Hydrogenics HySTAT™ cell stack (10 bars 15 Nm^3 H_2 h^{-1}, 4.2 kWh $Nm^{-3}H_2$) (b) single cell structure [69, 70].

4.4.3 Advanced Designs

4.4.3.1 Metal Foam as Electrodes

Allebrod *et al.* have conducted experiments in which metallic meshes used in zero-gap electrolysers were replaced by metallic foams and proposed to call this design

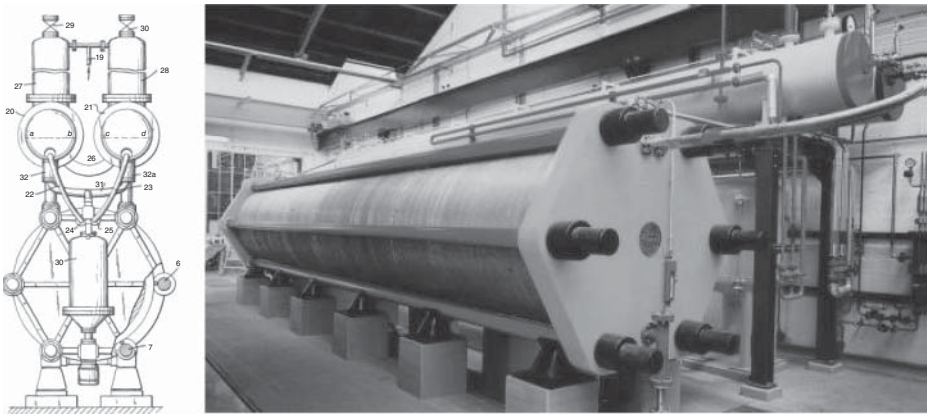

(a) (b)

Figure 4.35 (a) Schematic drawing of the Zdansky–Lonza electrolyser (patent 1959) and (b) ELT high-pressure electrolyser.

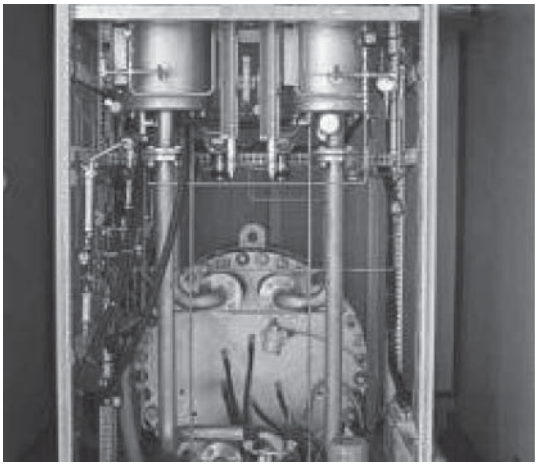

Figure 4.36 AccaGen electrolyser composed of a single electrolysis module of 60 $Nm^3\,h^{-1}$ or single 40′ container for 120 $Nm^3\,h^{-1}$; operated up to 4 MPa (energy consumption of 5 kWh $Nm^{-3}H_2$) *http://www.accagen.com/products-and-services/products/electrolysers*.

'foam based alkaline electrolysis cells'. They used inconel foam on the cathode and silver nanoparticles coated the nickel foam on the anode as gas diffusion electrodes (Figure 4.37).

A controlled amount of $SrTiO_3$ powder was placed between the two electrodes and the whole structure was pressed at a pressure of 13 kN cm^{-2}. After sintering in controlled atmosphere (9% H_2/Ar) at 1000 °C for 6 h, a mesoporous $SrTiO_3$ structure (mean pore size of 63 nm) sandwiched between the foam electrodes was obtained (Figure 4.38).

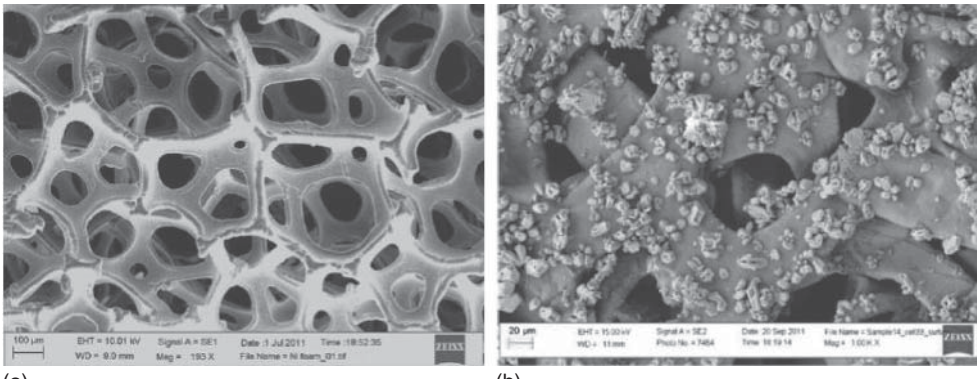

(a) (b)

Figure 4.37 SEM picture of nickel foam (a) and silver nanoparticles-coated nickel foam (b) electrodes used as anode for the 'foam-based alkaline electrolysis cells'. Ref [46] (Allebrod et al. JPS (2013))

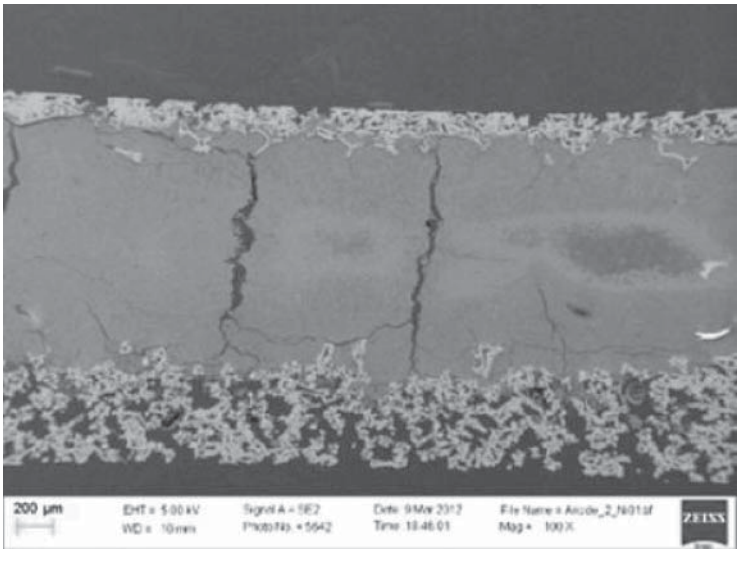

Figure 4.38 SEM picture of the cross section of the structure composed of the silver particles-coated nickel foam (top), mesoporous $SrTiO_3$ sintered powder and inconel foam (bottom). Ref [46] (Allebrod et al. JPS (2013))

The sample was placed in an autoclave filled with a 22.5 wt% KOH aqueous solution and used as an electrochemical cell for water electrolysis. Experiments were conducted at temperatures and pressures up to 250 °C and 42 bar, respectively. A current density of 1 A cm^{-2} was measured at a cell voltage of 1.5 V (2 A·cm^{-2} at 1.75 V). Even though this structure is far more expensive than the conventional one, the use of metallic foams with high surface area as electrodes and mesoporous

sintered oxides powder should be a promising way for high-temperature and/or high-pressure electrolysers.

4.4.3.2 Gas Diffusion Electrodes

An advanced concept of alkaline water electrolyser with gas diffusion electrodes and recirculation of the electrolyte between the electrodes has been proposed by Marini *et al.* [72] (Figure 4.39).

A schematic drawing showing the principles of this electrolysis setup is provided in Figure 4.39. Each electrode assembly consists of a cell separator, active layer, gas diffusion layer (GDL) and a nickel net used as current collector. The active layer consists of 5–10% PTFE mixed with 70% of Raney nickel and with another catalyst and/or a conducting material. The gas diffusion layers are made of carbon black (cathode) or nickel powder (anode) bonded with 20% PTFE. The separator layer is made with ZrO_2 powder (~50 nm particle size) and a PTFE suspension, bonded with the active layer (25 μm thick stretched polypropylene sheet was also used in replacement of the previous separator). The two-electrode assembly is separated by a 1.5 mm thick gasket, which defines the electrolyte compartment. As the electrolyte circulates between the electrodes, the differential pressure between the two gas compartments and between the gas compartments and the electrolyte are crucial. Indeed, if the electrolyte pressure is less than the gas pressure, gas will flow in the electrolyte and the catalyst layer will partly lose the ionic contact with the electrolyte, thus increasing the cell resistance. On the other hand, if the electrolyte pressure is too high, the electrolyte will cross the hydrophobic gas diffusion layer and accumulate in the gas compartments. The first results presented on this electrolyser show performance close to conventional filter-press electrolysers (2.4 V at 500 mA and 80 °C). Ageing tests conducted over 100 days did not show any significant performance degradation.

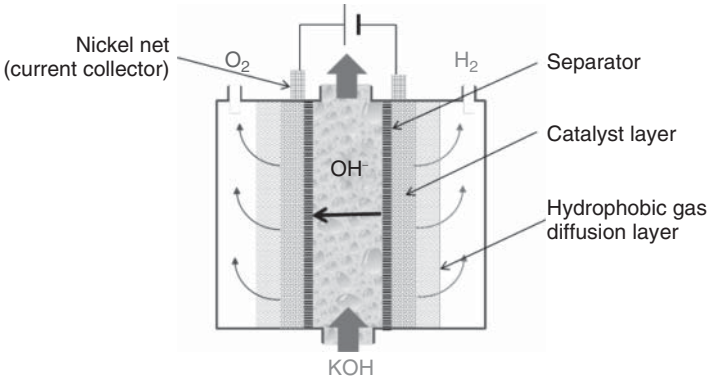

Figure 4.39 Scheme of principle of the alkaline electrolyser with gas diffusion layers and electrolyte circulation between the electrodes.

4.4.3.3 Very High-Pressure Electrolysers

The American company Avalence has been developing a monopolar alkaline water electrolyser (Avalence Hydrofiller) for several years, with the aim of producing hydrogen at a pressure of 45 MPa without the use of a compressor (Figure 4.40). Numerous publications and presentations are available in the literature, describing the system [73–75]. The electrolysis cell is cylindrical and is filled with 28 wt% KOH aqueous solution used as electrolyte. The Avalence Hydrofiller 50-6500 is configured with 48 individual electrolysis cells, with each set of 24 cells wired in series. The approximate operating voltage is 50 V for a current of 130 A (hydrogen output of 0.2 kg h^{-1}). The name of the electrolyser 'Hydrofiller 50-6500' refers to the production capability of 50 standard cubic feet of H_2 per hour (1.4 $Nm^3\ h^{-1}$) and the possibility to reach an operating pressure of 6500 psi (44.8 MPa).

A nickel rod placed in the middle of the cell is used as anode. Initially, the outer electrode, used as cathode, was coated with nickel. However, the nickel coating

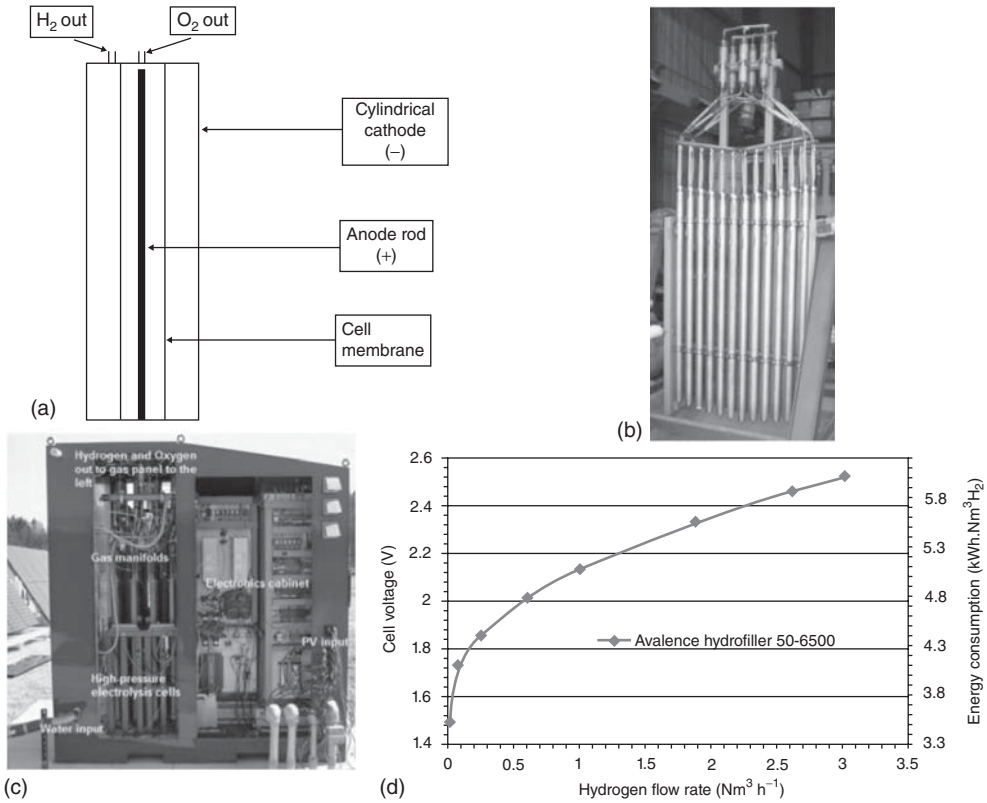

Figure 4.40 (a) Scheme of principle of the Avalence Hydrofiller electrolyser [74]. (b) Picture of a 24-cell electrolyser, according to [72]. (c) Picture of the cabinet containing 48 electrolysis cells and the electronics, connected to a PV plant and (d) Polarization curve of the Avalence Hydrofiller electrochemical cells at 24 °C and 13.8 MPa [74].

was found to dissolve and to foul the electrolyte. Therefore, a steel cathode surface is now used. The two electrodes are separated by a polymer membrane. One of the most important parameters of this system is that the differential pressure of hydrogen and oxygen outputs has to be kept as low as possible, using a very sensitive pressure balancing system. Despite this, the first experiments concluded that the gas purity was not good enough to run the system at a pressure of 45 MPa. Several membranes with various chemical properties and various membrane thicknesses have been tested to increase the gas purity by reducing hydrogen cross-permeation. The original hydrophobic polyethylene membrane was replaced by a hydrophilic polysulphone - based one and the membrane thickness was adjusted to reduce hydrogen permeation (73).

Using a more efficient membrane and improving the sealing design as well as the anolyte and catholyte circulation, it was possible to reach an oxygen purity of 99.7% at 17 MPa. An electrolyser was successfully tested over a 109-day period, from the fall of 2008 until the fall of 2009, at the GM Proving Ground in Milford (USA), limiting the hydrogen output pressure to 13.8 MPa. Several improvements are proposed to increase the performance and the purity of gases at high pressure.

4.5 Conclusions

The purpose of this chapter was to review state-of-the-art alkaline water electrolysis, to present basic principles, to describe technology developments, to identify some limitations in existing technology and to draw some perspectives in view of future market applications. Alkaline water electrolysis is a somewhat old technology that appeared at the industrial scale at the beginning of the twentieth century. Alkaline water electrolysers are simple and robust devices that are used to produce hydrogen and oxygen of electrolytic grade from water dissociation. The technology has mostly been used for applications in the industry sector, in particular for hydrogen production for ammonia synthesis. Systems that can deliver up to several hundred of $Nm^3\ H_2\ h^{-1}$ have been successfully developed and implemented in different places throughout the world. The main advantages of this technology are: (i) low cost; (ii) high reliability and durability and (iii) the possibility to operate at elevated pressure (prototypes operating above 10 MPa have been successfully tested). On a less positive side, alkaline water electrolysers are not compact, operate at moderate current density and are not totally appropriate for operation using transient power sources. In spite of its well-established maturity, the technology is still the subject of research and development. The last generation of alkaline water electrolysers are more efficient, more reliable and more capable to comply with the requirements set for applications in combination with fluctuating renewable energy sources.

Nomenclature

A	membrane area (m^2)
a_i	activity of species i
C_i	concentration of species i in mol m^{-3}.
D_i	diffusion coefficient of species i ($m^2\ s^{-1}$)
E	free energy electrolysis voltage (V)
F	Faraday constant (96 485 C mol^{-1})
f_i	fugacity of species i
G	Gibbs free energy (J mol^{-1})
H	enthalpy (J mol^{-1})
I	current (A)
i	current density (A cm^{-2})
i_0	exchange current density (A cm^{-2})
L	membrane thickness (m)
m	mole number
n	number of electrons exchanged during the electrochemical reaction
P	pressure (Pa)
p_i	partial pressure of component i in a gas mixture (Pa)
R	resistance (Ω)
r	specific resistance (Ω m^2)
R_{PG}	constant of perfect gas (0.082 J K^{-1} mol^{-1})
S	entropy (J mol^{-1} K^{-1})
t	time (s)
T	absolute temperature (K)
U_{cell}	cell voltage (V)
V	thermoneutral electrolysis voltage (V)
V_0	specific volume (m^3 kg^{-1})
W	work (J) or work density (J·kg^{-1})
x, y, z	space coordinates

Greek Symbols

Δ	difference
ε	cell efficiency (%)
η	overvoltage (V)
φ	electrode absolute potential (V)
ρ	electrical resistivity (Ω m)
σ	electrical conductivity (S m^{-1})

Subscripts or Superscripts

°	standard conditions (298 K, 1 bar)
Cell	electrolysis cell

d	dissociation
e	electrolyte
f	formation
i	species *i*
r	real
rev	reversible
th	theoretical

Acronyms

CCS	carbon capture and storage
DLR	Deutsches Zentrum für Luft- und Raumfahrt (German Aerospace Center)
GDL	Gas Diffusion Layer
HER	hydrogen evolution reaction
IEC	ion exchange capacity
LEL	lower explosivity limit
OER	oxygen evolution reaction
PEM	proton exchange membrane
PTFE	polytetrafluoroethylene
Raumfahrt	(German Aerospace Center)
SEM	scanning electron spectroscopy

References

1. Paets Van Troostwyk, A. and Deiman, J.R. (1789) Lettre de MM. Paets van Troostwyk et Deiman; A M. de la Métherie, Sur une manière de décomposer l'eau en Air inflammable & en Air vital. *Observations sur la Physique, sur L'Histoire Naturelle et sur les Arts*, **XXXV** (II), 369–378.
2. Guillaume, C.-E. (1891) La production industrielle de l'hydrogène et de l'oxygène par l'électrolyse de l'eau. *La Nature*, **940** (Juin), 106–110.
3. Engelhardt, V. (1904) in *The Electrolysis of Water Processes and Applications*, Monographs on Applied Electrochemistry, vol. 1 (ed. V. Engelhardt), The Chemical Publishing Company, Vienna, p. 140.
4. Schmidt, O. (1899) Apparat zur Elektrolyse von Wasser. Patent DE 111,131, Jun. 13, 1899.
5. Kreuter, W. and Hofmann, H. (1998) Electrolysis: the important energy transformer in a world of sustainable energy. *Int. J. Hydrogen Energy*, **23** (8), 661–666.
6. Vieira Da Rosa, A. (2013) *Fundamentals of Renewable Energy Processes*, third Edition, Academic Press, ISBN: 978-0-12-397219-4; p. 389.
7. IEA Energy Technology Essentials (2007) Hydrogen Production and Distribution, April 2007, *http://www.iea.org/techno/essentials5.pdf* (accessed 4 September 2014).
8. Schroeder, V. and Holtappels, K. (2005) Explosion characteristics of hydrogen-air and hydrogen-oxygen mixtures at elevated pressures. Fist ICHS, Paper 120001, Pisa, Italy.
9. Holtappels, K. (2002) Report on the Experimentally Determined Explosion Limits, Explosion Pressures and Rates of Explosion Pressure Rise – Part 1:

Methane, Hydrogen and Propylene, Vol. 1, pp. 1–149.
10. Gilliam, R., Graydon, J., Kirk, D., and Thorpe, S. (2007) A review of specific conductivities of potassium hydroxide solutions for various concentrations and temperatures. *Int. J. Hydrogen Energy*, **32** (3), 359–364.
11. See, D.M. and White, R.E. (1997) Temperature and concentration dependence of the specific conductivity of concentrated solutions of potassium hydroxide. *J. Chem. Eng. Data*, **42** (6), 1266–1268.
12. Index Mundi *http://www.indexmundi.com/commodities/?commodity=nickel* (accessed 4 September 2014).
13. Platinum Today *http://www.platinum.matthey.com/prices/price-charts* (accessed 4 September 2014).
14. Hall, D.E. (1981) Electrodes for alkaline water electrolysis. *J. Electrochem. Soc.*, **128** (4), 740–746.
15. Raney, M. (1925) Method of preparing catalytic material. US Patent 1,563,587, Dec. 1, 1925.
16. Manabe, A., Kashiwase, M., Hashimoto, T., Hayashida, T., Kato, A., Hirao, K., and Nagashima, I. (2013) Basic study of alkaline water electrolysis. *Electrochim. Acta*, **100**, 249–256.
17. Raney, M. (1927) Method of producing finely divided nickel. US Patent 1,628,190, May 10, 1927.
18. Kumar, M., Awasthi, R., Sinha, A.S.K., and Singh, R.N. (2011) New ternary Fe, Co, and Mo mixed oxide electrocatalysts for oxygen evolution. *Int. J. Hydrogen Energy*, **36** (15), 8831–8838.
19. Gerken, J.B., Shaner, S.E., Massé, R.C., Porubsky, N.J., and Stahl, S.S. (2014) A survey of diverse earth abundant oxygen evolution electrocatalysts showing enhanced activity from Ni–Fe oxides containing a third metal. *Energy Environ. Sci.*, **7**, 2376–2382.
20. Vandenborre, H., Vermeiren, P., and Leysen, R. (1984) Hydrogen evolution at nickel sulphide cathodes in alkaline medium. *Electrochim. Acta*, **29** (3), 297–301.
21. Danilovic, N., Subbaraman, R., Strmcnik, D., Stamenkovic, V., and Markovic, N. (2013) Electrocatalysis of the HER in acid and alkaline media. *J. Serb. Chem. Soc.*, **78** (12), 2007–2015.
22. Hu, W. (2000) Electrocatalytic properties of new electrocatalysts for hydrogen evolution in alkaline water electrolysis. *Int. J. Hydrogen Energy*, **25** (2), 111–118.
23. Han, Q., Chen, J., Liu, K., and Wei, X. (2009) A study on the composite $LaNi_5$/Ni–S alloy film used as HER cathode in alkaline medium. *J. Alloys Compd.*, **468** (1-2), 333–337.
24. Divisek, J., Schmitz, H., and Steffen, B. (1994) Electrocatalysts materials for hydrogen evolution. *Electrochim. Acta*, **39** (11/12), 1723–1731.
25. Jović, V.D., Lačnjevac, U., Jović, B.M., and Krstajić, N.V. (2012) Service life test of non-noble metal composite cathodes for hydrogen evolution in sodium hydroxide solution. *Electrochim. Acta*, **63**, 124–130.
26. Bagotsky, V.S. (2006) *Fundamentals of Electrochemistry*, 2nd edn, John Wiley & Sons, Inc, Hoboken, NJ.
27. European Commision, Enterprise and Industry Directorate-General (0000) Commission Directive 1999/77/EC of 26 July 1999 *http://ec.europa.eu/enterprise/sectors/chemicals/files/markrestr/derogation_chrysotile_asbestos_diaphragms_en.pdf*
28. European Chemical Agency (2014) Annex XV Restriction Report Amendment to a Restriction Substance Name: Chrysotile IUPAC Name: Chrysotile EC Number: - CAS Nnumber(S): CAS No 12001-29-5 and 132207-32-0, 17 January 2014.
29. VITO *https://www.vito.be/* (accessed 1 September 2014).
30. Agfa *http://www.agfa.com/sp/global/en/binaries/Zirfon%20Perl%20UTP%20500_v7_tcm611-56748.pdf* (accessed 1 September 2014).
31. Vermeiren, P., Leysen, R., Beckers, H., Moreels, J.P., and Claes, A. (2006) The influence of manufacturing parameters on the properties of macroporous Zirfon® separators. *J. Porous Mater.*, **15** (3), 259–264. doi: 10.1007/s10934-006-9084-0
32. Vermeiren, P., Adriansens, W., Moreels, J.P., and Leysen, R. (1998) Evaluation of the Zirfon separator for use in alkaline

water electrolysis and Ni-H_2 batteries. *Int. J. Hydrogen Energy*, **23** (5), 321–324.

33. Otero, J., Sese, J., Michaus, I., Maria, M.S., Guelbenzu, E., Irusta, S., and Arruebo, M. (2013) Sulphonated PEEK diaphragms used in commercial scale alkaline water electrolysis. *J. Power Sources*, **247**, 967–974.
34. Costa, R.L. and Grimes, P.G. (1967) Electrolysis as a source of hydrogen and oxygen chem. *Eng. Prog.*, **63** (4), 56–58.
35. Wendt, H. and Hofmann, H. (1985) Cermet diaphragms and integrated electrode-diaphragm units for advanced alkaline water electrolysis. *Int. J. Hydrogen Energy*, **10**, 375–381.
36. Merle, G., Wessling, M., and Nijmeijer, K. (2011) Anion exchange membranes for alkaline fuel cells: a review. *J. Membr. Sci.*, **377** (1-2), 1–35.
37. Varcoe, J. and Slade, R. (2007) (ethylene-co-tetrafluoroethylene)-derived radiation-grafted anion-exchange membrane with properties specifically tailored for application in metal-cation-free alkaline. *Chem. Mater.*, **19** (10), 2686–2693.
38. Couture, G., Alaaeddine, A., Boschet, F., and Ameduri, B. (2011) Polymeric materials as anion-exchange membranes for alkaline fuel cells. *Prog. Polym. Sci.*, **36** (11), 1521–1557.
39. Xu, T. (2005) Ion exchange membranes: state of their development and perspective. *J. Membr. Sci.*, **263** (1-2), 1–29.
40. Fukuta, K. (2011) Electrolyte materials for AMFCs and AMFC performance. Alkaline Membrane Fuel Cell Workshop, Arlington, VA, May 8–9
41. Wu, X., Scott, K., Xie, F., and Alford, N. (2014) A reversible water electrolyser with porous PTFE based OH – conductive membrane as energy storage cells. *J. Power Sources*, **246**, 225–231.
42. Faraj, M., Boccia, M., Miller, H., Martini, F., Borsacchi, S., Geppi, M., and Pucci, A. (2012) New LDPE based anion-exchange membranes for alkaline solid polymeric electrolyte water electrolysis. *Int. J. Hydrogen Energy*, **37**, 14992–15002.
43. Acta *http://www.actaspa.com/products/* (accessed 4 September 2014).
44. Acta *http://www.actaspa.com/products/fuel-cell-and-electrolysis-catalysts/* (accessed 4 September 2014).
45. Evangelista, J., Phillips, B., and Gordon, L. (1975) *Electrolytic Hydrogen Production An Analysis and Review* (pp. 1–49). NASA Technical Memorandum, NNASA TM X-71856 Cleveland, OH.
46. Allebrod, F., Chatzichristodoulou, C., and Mogensen, M.B. (2013) Alkaline electrolysis cell at high temperature and pressure of 250 °C and 42 bar. *J. Power Sources*, **229**, 22–31.
47. Ganley, J.C. (2009) High temperature and pressure alkaline electrolysis. *Int. J. Hydrogen Energy*, **34** (9), 3604–3611.
48. Miles, M.H., Kissel, G., Lu, P.W.T., and Srinivasan, S. (1976) Effect of temperature on electrode kinetic parameters for hydrogen and oxygen evolution reactions on nickel electrodes in alkaline solutions. *J. Electrochem. Soc.*, **123** (3), 332–336.
49. Di Bella, F., and Osborne, C. (2010) Development of a centrifugal hydrogen pipeline gas compressor. 2011 DoE Hydrogen Program Merit Review.
50. Bossel, U. (2006) Does a hydrogen economy make sense? *Proc. IEEE*, **94** (10), 1826–1837.
51. Roy, A., Watson, S., and Infield, D. (2006) Comparison of electrical energy efficiency of atmospheric and high-pressure electrolysers. *Int. J. Hydrogen Energy*, **31** (14), 1964–1979.
52. Zdansky, E.A. (1956) Improvements relating to electrolyzers for the decomposition of water. Patent GB 837,864, Switzerland.
53. Zdansky, E.A. (1959) Decomposer. US Patent 2,881,123, Switzerland.
54. Zdansky, E.A. (1959) Electrolytic water decomposer. US Patent 2,871,179, Switzerland.
55. Treadwell Corporation. Company Information/Timeline, *http://www.treadwellcorp.com/about-timeline.php* (accessed 4 September 2014).
56. Treadwell Corporation. Treadwell Corporation – Profile, *http://www.hellotrade.com/treadwell-corporation/profile.html* (accessed 4 September 2014).

57. Onda, K., Kyakuno, T., Hattori, K., and Ito, K. (2004) Prediction of production power for high-pressure hydrogen by high-pressure water electrolysis. *J. Power Sources*, **132** (1-2), 64–70.
58. Aoki, K., Toda, H., Yamamoto, J., Chen, J., and Nishiumi, T. (2012) Is hydrogen gas in water present as bubbles or hydrated form? *J. Electroanal. Chem.*, **668**, 83–89.
59. Roy, A., Watson, S., Infield, D., 2006 "Comparison of electrical energy efficiency of atmospheric and high-pressure electrolysers" *International Journal of Hydrogen Energy* **31** 1964–1979.
60. Anderson, E., Dalton, L., Carter, B., and Ayers, K. (2012) Elimination of mechanical compressors using PEM-based electrochemical technology. WHEC 2012, Toronto, Canada.
61. Marangio, F., Pagani, M., Santarelli, M., and Calì, M. (2011) Concept of a high pressure PEM electrolyser prototype. *Int. J. Hydrogen Energy*, **36** (13), 7807–7815.
62. Sagim *http://www.sagim-gip.net/html-anglais/produits-annexes.html* (accessed 4 September 2014).
63. Department of the Army (USA)(2007) Chapter 7 Balloon inflation and launching procedures, in *Tactics, Techniques, and Procedures for Field Artillery Meteorology*, Field Manual No. 3-09.15, Department of the Army, Washington, DC, 25 October 2007.
64. Gibney, J.J. (0000) GE Generators – An Overview, GE Industrial & Power Systems, GER3688B, *http://site.ge-energy.com/prod_serv/products/tech_docs/en/downloads/ger3688b.pdf* (accessed 4 September 2014).
65. Fuel Cell Today (2012) Enertrag Delivers Three 2 MW Alkaline Electrolyser, News, 23 November 2012.
66. Burmeister, W. (1999) Hydrogen Project at Munich Airport, *http://ieahia.org/pdfs/munich_airport.pdf* (accessed 4 September 2014).
67. Brand, Rolf (2004) GHW presents advanced pressurized alkaline electrolyzer at HYFORUM. *Hydrogen Fuel Cell Lett.*, **XIX** (7), July 2004.
68. Taalesen, Atle (2011) Nel Hydrogen, Hydrogen and Fuel Cells in the Nordic Countries, Malmö, Sweden, October 2011, 25–26.
69. Schmid, R. (2012) Electrolysis for grid balancing, Where are we? Symposium – Water Eelectrolysis and Hydrogen as a Part of the Future Renewable Energy System, *http://www.hydrogennet.dk/fileadmin/user_upload/PDF-filer/Aktiviteter/Kommende_aktiviteter/Elektrolysesymposium/Raymond_Schmid_Hygrogenics_120510_Copenhagen_Symposium_Final.pdf* (accessed 5 September 2014).
70. De Maeyer, R. (2010) HySTAT TM on site hydrogen. Visit Waterstofregio to Oevel.
71. ELB Elektrolysetechnik GmbH Industrial Hydrogen Production (0000) Pressure Electrolyser Based on the LURGI System Datasheet, *http://elektrolyse.de/wordpress/?page_id=38* (accessed 5 September 2014).
72. Marini, S., Salvi, P., Nelli, P., Pesenti, R., Villa, M., Berrettoni, M., and Kiros, Y. (2012) Advanced alkaline water electrolysis. *Electrochim. Acta*, **82**, 384–391.
73. Dunn, P. and Mauterer, D. (2011) High-Capacity, High Pressure Electrolysis System with Renewable Power Sources, DOE Merit Review, 11 May.
74. Kelly, N., Gibson, T., and Ouwerkerk, D. (2008) A solar-powered, high-efficiency hydrogen fueling system using high-pressure electrolysis of water: design and initial results. *Int. J. Hydrogen Energy*, **33** (11), 2747–2764.
75. Kelly, N.A., Gibson, T.L., and Ouwerkerk, D.B. (2011) Generation of high-pressure hydrogen for fuel cell electric vehicles using photovoltaic-powered water electrolysis. *Int. J. Hydrogen Energy*, **36** (24), 15803–15825.

5
Unitized Regenerative Systems

Pierre Millet

5.1
Introduction

The water–hydrogen–oxygen redox system can be used in redox batteries. From a technology viewpoint, the first option is to couple a water electrolysis cell and a H_2/O_2 fuel cell. This kind of tandem device can store electricity into chemicals by splitting water molecules into gaseous hydrogen and oxygen, and can restitute electricity by the 'cold' combustion of hydrogen and oxygen in a fuel cell. A second and more challenging option is to combine the water electrolyser and the fuel cell into a single unit that can operate reversibly. Such an integrated or hybridized device is called a unitized regenerative fuel cell (URFC). This is basically a redox battery that operates reversibly, either as a power sink (water electrolysis mode equivalent to battery loading) or as a power source (fuel cell mode equivalent to battery discharge). The capacity of such a device is potentially unlimited, being determined by the size of the hydrogen/oxygen gas reservoirs. As for any conventional fuel cell, the atmosphere can be used as the oxygen sink and in that case the capacity of the URFC is determined only by the size of the hydrogen reservoir. URFCs can potentially be used in different energy management systems for transport, domestic and space applications. A brief review of historical background and practical applications can be found in Ref. [1]. In this chapter, basic principles of URFCs are reviewed. Low-temperature URFCs based on polymer electrolyte membranes (PEMs) cells and high-temperature URFCs based on solid oxide cells are described and compared.

Hydrogen Production: by Electrolysis, First Edition. Edited by Agata Godula-Jopek.
© 2015 Wiley-VCH Verlag GmbH & Co. KGaA. Published 2015 by Wiley-VCH Verlag GmbH & Co. KGaA.

5.2 Underlying Concepts

5.2.1 Thermodynamics

The thermodynamics of the water splitting reaction has been described in detail in Chapter 2, section 2.1. Here, I'm making reference to chapter 2 of the book (fundamentals of watger splitting). I leave it up to you to decide what is the way to make reference to this chapter. Let us consider it again but now from the viewpoint of reversibility. The splitting or dissociation reaction of liquid water is:

$$H_2O(l) \rightarrow H_2(g) + \frac{1}{2} O_2(g) \tag{5.1}$$

In spite of a favourable entropy contribution, this is a non-spontaneous transformation due to the non-favourable enthalpy term. In standard conditions of temperature and pressure ($T° = 298$ K, $P° = 1$ bar), enthalpy, entropy and free (Gibbs) energy standard changes of reaction (5.1) are, respectively:

$$\Delta H_d{}^\circ(H_2O(l)) = +285.840 \text{ kJ mol}^{-1}(\text{endothermic})$$

$$\Delta S_d{}^\circ(H_2O(l)) = +163.15 \text{ J mol}^{-1} \text{ K}^{-1}$$

$$\Delta G_d{}^\circ(H_2O(l)) = \Delta H_d{}^\circ(H_2O(l)) - T \cdot \Delta S_d{}^\circ(H_2O(l)) = +237.22 \text{ kJ mol}^{-1}$$

The thermodynamics of reaction (5.1) is a function of operating temperature T and pressure P:

$$\Delta G_d(T,P) = \Delta H_d(T,P) - T\,\Delta S_d(T,P) > 0 \tag{5.2}$$

$\Delta H_d(T, P)$, ΔS_d (T, P) and $\Delta G_d(T, P)$ are, respectively, the enthalpy change (in J mol^{-1}), the entropy change (in J mol^{-1} K^{-1}) and the Gibbs free energy change (in J mol^{-1}) of reaction (5.1) occurring at T and P. Data for reaction (5.1) at atmospheric pressure are plotted in Figure 5.1 over an extended temperature range. ΔG_d (J mol^{-1}) of electricity and $T\Delta S_d$ (J mol^{-1}) of heat are required to split 1 mole of water.

In spite of an unfavourable entropy change contribution, the reverse reaction (hydrogen combustion in oxygen) is a strongly exothermic and spontaneous process:

$$H_2(g) + \frac{1}{2} O_2(g) \rightarrow H_2O(l) \tag{5.3}$$

Changes of thermodynamic state functions are opposite in sign to those of reaction (5.1):

$$\Delta H_c{}^\circ(H_2O(l)) = -285.840 \text{ kJ mol}^{-1}(\text{exothermic})$$

$$\Delta S_c{}^\circ(H_2O(l)) = -163.15 \text{ J mol}^{-1} \text{ K}^{-1}$$

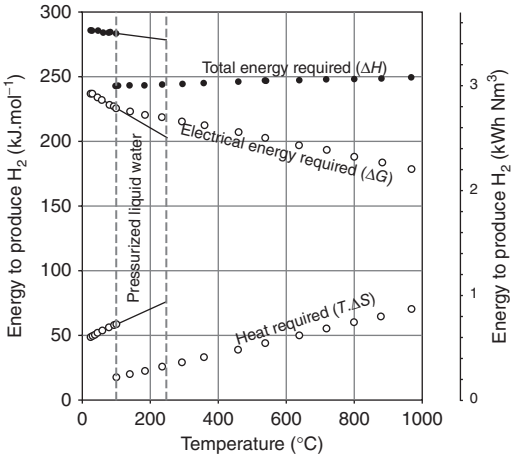

Figure 5.1 $\Delta G(T)$, $\Delta H(T)$ and $T{\cdot}\Delta S(T)$ of the water splitting reaction at $P = 1$ bar. (—) data for pressurized liquid water up to 250 °C.

$$\Delta G_c{}^\circ(H_2O(l)) = \Delta H_r{}^\circ(H_2O(l)) \; - \; T \cdot \Delta S_r{}^\circ(H_2O(l)) \; = -237.22 \;\; \text{kJ} \;\; \text{mol}^{-1}$$

For a combustion reaction occurring at given temperature T and pressure P, one can write:

$$\Delta G_c(T,P) = \Delta H_c(T,P) - T\,\Delta S_c(T,P) > 0 \tag{5.4}$$

In Equation 5.4, $\Delta H_c(T, P)$, $\Delta S_c\ (T, P)$ and $\Delta G_c(T, P)$ are, respectively, the enthalpy change (in J mol^{-1}), the entropy change (in J mol^{-1} K^{-1}) and the Gibbs free energy change (in J mol^{-1}) of reaction (5.3) occurring at T and P. They are opposite in sign to those of reaction (5.1) and data of Figure 5.1 are their absolute values.

In electrochemical experiments, it is more convenient to measure potential and voltage than energy levels. Both quantities are inter-related. As discussed in chapter 2, the electricity (nFE) required at equilibrium to split 1 mole of water according to reaction (5.1) is equal to the Gibbs free energy change (ΔG_d) of the water dissociation reaction:

$$\Delta G_d \; - \; n\,F\,E_d = 0 \text{ where } \; \Delta G_d \; > \; 0 \tag{5.5}$$

where

- $n = 2$ is the number of electrons exchanged during the electrochemical splitting of one water molecule;
- $F \approx 96\,485$ C mol^{-1} is the Faraday constant, that is, the electric charge of 1 mole of electrons;
- E (in volts) is the free energy electrolysis voltage associated with reaction (5.7);
- ΔG_d (in J mol^{-1}) is the free energy change associated with reaction (5.7).

Conversely, the open-circuit electromotive force E (or open circuit voltage) of a hydrogen/oxygen fuel cell operating according to reaction (5.2) is related to

the Gibbs free energy change (ΔG_c) of the reaction of hydrogen combustion in oxygen:

$$\Delta G_c + n F E_c = 0 \text{ where } \Delta G_c < 0 \tag{5.6}$$

Because $|\Delta G_d| = |\Delta G_c|$, $E_d = E_c$.

Two different thermodynamic voltages are usually used to characterize the electrochemical transformations. First, the free energy electrolysis voltage E in volts is defined as:

$$E\ (T, P) = \frac{\Delta G_d\,(T, P)}{n\ F} \tag{5.7}$$

The enthalpy or thermoneutral voltage V in volts is defined as:

$$V\,(T, P) = \frac{\Delta H\,(T, P)}{n\ F} \tag{5.8}$$

Both voltages at 1 bar of gases are plotted in Figure 5.2 as a function of operating temperature.

Whereas hydrogen can be burned directly in air or in oxygen to produce heat, it can also be burned in an electrochemical fuel cell to convert part of this heat into electrical work of more added value. Assuming that water splitting and hydrogen combustion are two reversible processes, one can write:

$$H_2O(l) \Leftrightarrow H_2(g) + \frac{1}{2}\,O_2(g) \tag{5.9}$$

The general reaction isotherm (also known as the van't Hoff isotherm) [2] relates the Gibbs free energy change of the reaction to the equilibrium constant K according to:

$$\Delta G^\circ = -RT\ \mathrm{Ln}\ K^\circ \tag{5.10}$$

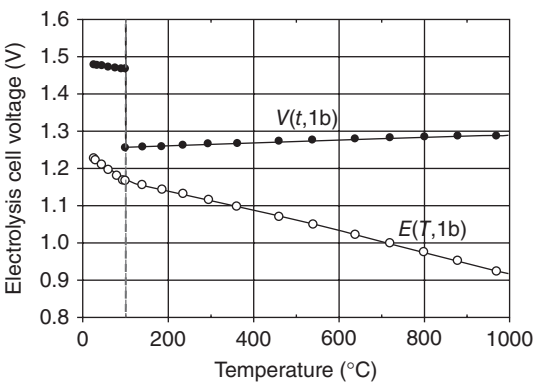

Figure 5.2 Role of operating temperature on the free energy electrolysis voltage $E(T)$ and the enthalpy electrolysis voltage $V(T)$ of water ($P = 1$ bar).

The equilibrium constant K is defined as:

$$K = \frac{f_{H_2} f_{O_2}^{1/2}}{a_{H_2O}} \tag{5.11}$$

where f denotes gas fugacity and a activity. Application of Equation 5.10 to reaction (5.3) yields a very small value of $K_d^\circ = 2.7 \times 10^{-42}$. This is an indication that Equation 5.9 is totally deplaced to the liquid water side. The application of Equation 5.10 to reaction (5.3) yields $K_c^\circ = 3.8 \times 10^{41}$. This is a confirmation that the combustion of hydrogen in oxygen is a complete reaction.

5.2.2
Half-Cell Reactions

A URFC is based on two redox couples: the high-potential water/oxygen couple and the low-potential water/hydrogen couple. In acidic electrolytes, hydrated protons convey charges from the anode to the cathode. Half-cell reactions in water electrolysis and fuel cell modes are:

$$\text{Anode, electrolysis}: \ H_2O \rightarrow \frac{1}{2} O_2 + 2\,H^+ + 2\,e^- \tag{5.12}$$

$$\text{Cathode, electrolysis}: \ 2\,H^+ + 2\,e^- \rightarrow H_2 \tag{5.13}$$

$$\text{Positive, fuel cell}: \ \frac{1}{2} O_2 + 2\,H^+ + 2\,e^- \rightarrow H_2O \tag{5.14}$$

$$\text{Negative, fuel cell}: \ H_2 \rightarrow 2\,H^+ + 2\,e^- \tag{5.15}$$

In solid oxide electrolytes, oxide ions O^{2-} convey the charges from the cathode to the anode. Half-cell reactions in water electrolysis and fuel cell modes are:

$$\text{Anode, electrolysis}: \ O^{2-} \rightarrow \frac{1}{2} O_2 + 2\,e^- \tag{5.16}$$

$$\text{Cathode, electrolysis}: \ H_2O + 2\,e^- \rightarrow H_2 + O^{2-} \tag{5.17}$$

$$\text{Positive, fuel cell}: \ \frac{1}{2} O_2 + 2\,e^- \rightarrow O^{2-} \tag{5.18}$$

$$\text{Negative, fuel cells}: \ H_2 + O^{2-} \rightarrow H_2O + 2\,e^- \tag{5.19}$$

Half-cell reactions (5.12) and (5.16) are called the oxygen evolution reactions or OERs.

Half-cell reactions (5.13) and (5.17) are called the hydrogen evolution reactions or HERs.

Half-cell reactions (5.14) and (5.18) are called the oxygen reduction reactions or ORRs.

Half-cell reactions (5.15) and (5.19) are called the hydrogen oxidation reactions or HORs.

5.2.3
Process Reversibility

In electrochemistry, the Butler–Volmer relationship relates the overvoltage η (in volts) set across a metal–electrolyte interface to the current density i (in A cm^{-2}) that flows across this interface:

$$i = i_0 \left\{ \exp\left[\frac{\beta\ n\ F}{R\ T}\ \eta\right] - \exp\left[-\frac{(1-\beta)\ n\ F}{R\ T}\ \eta\right] \right\} \tag{5.20}$$

where η is the overvoltage, that is, the difference between the actual voltage set across the interface and the equilibrium voltage; i_0 is the exchange current density in A cm^{-2}; R is the constant of perfect gas (0.082 J K^{-1} mol^{-1}) and T is the absolute temperature in K.

Equation 5.20 provides some insight into the concept of electrochemical reversibility. The sign of the current flowing across the interface changes when the sign of the overvoltage η is changed. Reversibility is also a kinetic concept. The difference between a reversible and an irreversible charge transfer process is dictated by the value of the exchange current density. The higher the magnitude of the exchange current density, the more reversible the reaction (Figure 5.3).

The effect of operating temperature on the reversibility and the kinetics of a URFC can be analysed by plotting polarization curves in fuel cell and water electrolysis modes at two significantly different operating temperatures (Figure 5.4). At an elevated temperature (1000 °C) using a solid oxide cell, the transition from fuel cell to electrolysis modes (the potential at which there is a change in the sign of the current flowing across the cell) requires a change of only a few millivolts, at a well-defined cell potential (≈ 0.9 V in this case), which is equal to the thermodynamic voltage of reactions (5.1) and (5.2). This is an indication that the two electrochemical reactions taking place at the positive

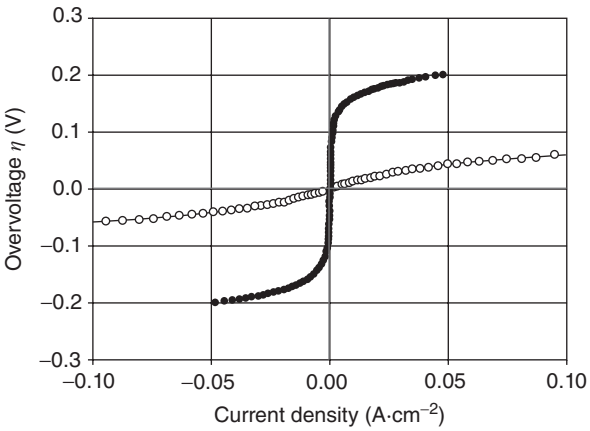

Figure 5.3 Comparison of reversible (○) and irreversible (•) charge transfer processes. Polarization curves were calculated at 25 °C from Equation 5.20 with: (○): $i_0 = 10^{-2}$ A cm^{-2} and (•): $i_0 = 2 \times 10^{-5}$ A cm^{-2}.

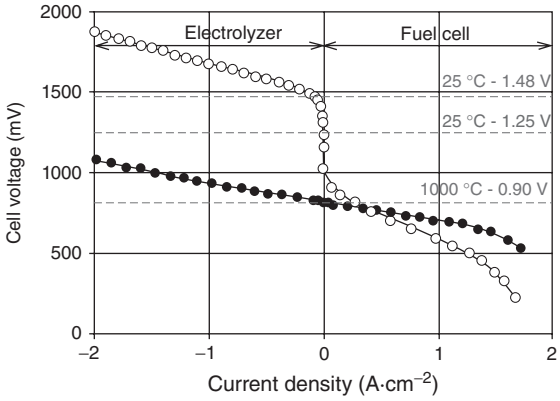

Figure 5.4 Reversibility of the water splitting reaction at low (25 °C) and elevated (1000 °C) operating temperature.

and negative electrodes are both reversible. At room temperature, the situation is significantly different. Large overvoltages are required to shift from water electrolysis to fuel cell modes of operation. This irreversibility is not due to the hydrogen electrode for which the two reactions (HER during charge and HOR during discharge) are highly reversible but to the oxygen electrodes: both the OER (during charge) and the ORR (during discharge) are highly irreversible (Figure 5.5). In addition to that, mass transport limitations due to the diffusion-controlled transport of gaseous reactants to the reaction sites tend to further slow down the kinetics.

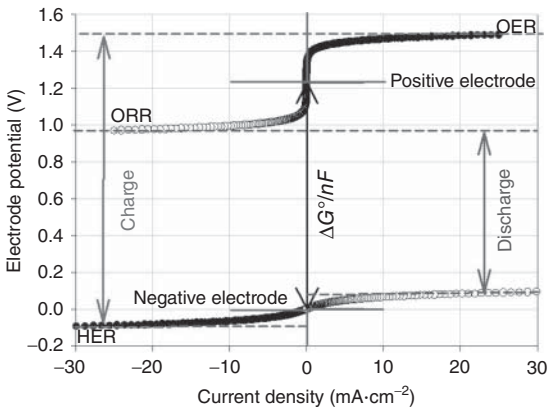

Figure 5.5 Overvoltage–current density relationships on smooth surfaces for OER = oxygen evolution reaction on Ir°; HER = hydrogen evolution reaction on Pt°; ORR = oxygen reduction reaction on Pt° and HOR = hydrogen oxidation reaction on Pt°.

5.3
Low-Temperature PEM URFCs

5.3.1
Principles

In this section, basic principles of low-temperature (PEM) URFCs are introduced. In a first configuration (A in Figure 5.6), the URFC requires two fully reversible electrodes. In the water electrolysis mode (battery charging, top left), water is oxidized at the anode (on iridium dioxide) into gaseous oxygen and protons according to reaction (5.12), and protons migrate through the membrane (also referred to as solid polymer electrolyte or SPE) down to the cathode where they are reduced (on platinum) to gaseous hydrogen according to reaction (5.13). In the fuel cell mode (battery discharge, bottom left), oxygen is reduced at the positive electrode (cathode, platinum) into water according to reaction (5.14) and hydrogen is oxidized at the negative electrode (anode, platinum) into protons according to reaction (5.15). In this configuration, each compartment cell always deals with the same gas. In the left compartment, hydrogen is produced during electrolysis and hydrogen is consumed during the fuel cell operation. In the right compartment, oxygen is produced during electrolysis and oxygen is consumed during the fuel cell operation. In other words, this configuration requires fully reversible catalysts. From a catalyst viewpoint, three of the four reactions involved in the process require platinum: HER, ORR and HOR. The last one (OER) requires iridium dioxide. This is why the oxygen electrode requires a mixture of iridium dioxide and platinum. That mixture can be optimized in term of composition and structure. The first option is to

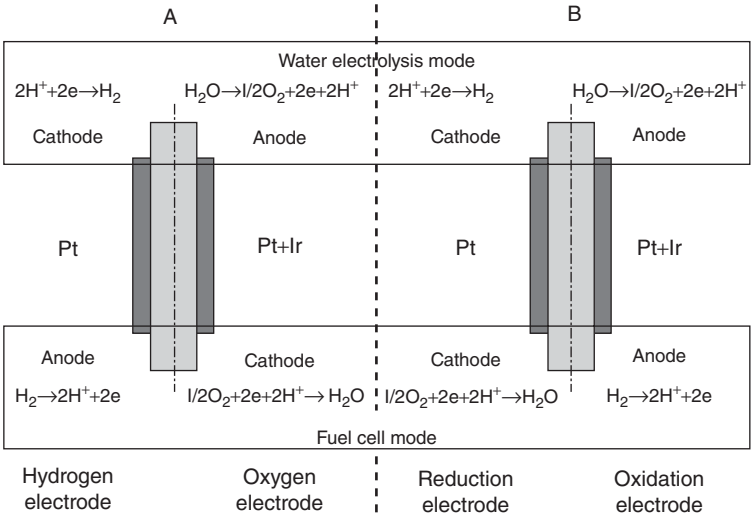

Figure 5.6 schematic diagram of two main URFC designs showing individual cellbreak reactions [1].

deposit two layers onto the SPE, one of Pt nanoparticles and one of iridium dioxide atop each other. A second option is to coat homogeneous mixtures. The problem comes from the ORR that requires a carbonaceous gas diffusion layer (GDL) while for the OER, sintered titanium plates are preferred. Because carbon is not stable at elevated operating potentials (from a thermodynamic viewpoint, carbon is oxidized according to $C + 2H_2O \rightarrow CO_2 + 4H^+ + 4e^-$ at a potential of only +0.206 V versus the Reversible Hydrogen Electrode or RHE [3]), configuration A cannot be easily implemented.

In a second configuration (B in Figure 5.6), URFC compartments are not specialized in terms of gases but in terms of the redox process. The left compartment is the reduction compartment where protons are reduced into evolving hydrogen through the HER reaction in the electrolysis mode and where oxygen is reduced into water through the ORR reaction during operation in the fuel cell mode. The right compartment is the oxidation compartment where water is oxidized into evolving oxygen through the OER reaction in the water electrolysis mode and where hydrogen is oxidized into protons through the HOR reaction in the fuel cell mode. The B-configuration has one major advantage and one major drawback. The major advantage is that there is no need of carbonaceous supporting material in the oxidation compartment (hydrogen is readily oxidized on a layer of unsupported platinum). Compared to the A-configuration, the most sluggish reaction (the ORR) that requires carbon-supported platinum nanoparticles and a GDL can take place on the same catalyst than the HER. The major drawback is that it is necessary to invert gas circulation when the URFC switches from the fuel cell to water electrolysis modes and vice versa. From an engineering viewpoint, this is a complication that requires a purge of cell compartments and circuitry and that may raise some safety issues. In particular, at the end of operation in the water electrolysis mode, hydrogen evolved in the left compartment and oxygen evolved in the right compartment must be purged before hydrogen and oxygen from the tanks are introduced in the cell.

Water management in the fuel cell mode is also an issue. During water electrolysis operation, liquid water is pumped through both cell compartments. When the cell is switched into the fuel cell mode, there is a need to sufficiently dry the compartments in order to let gases reach catalytic sites. This can be done by circulation of a dry inert gas (e.g. nitrogen) but this drying process needs to be properly managed in order to prevent membrane drying. Switching from the fuel cell to the water electrolysis mode is usually not a problem whereas the reverse is more challenging and more time-consuming.

5.3.2
Cell Structure and URFC Stack

The detailed structure of a URFC cell is pictured in Figure 5.7. URFC cells can be stacked together to increase power density and capacity, just like in PEM fuel cells or in PEM water electrolysis technology. The photograph of a prototype URFC stack (nominal power consumption during operation in the

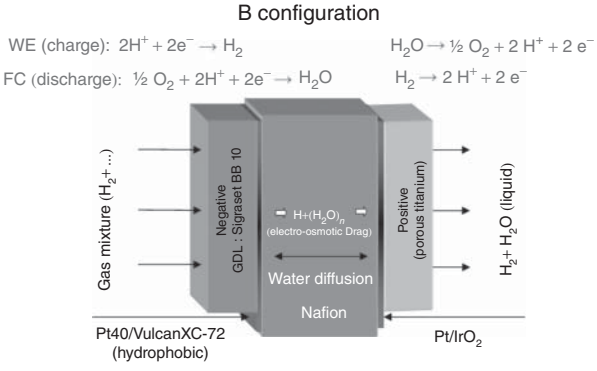

Figure 5.7 Schematic diagram of a PEM URFC cell.

water electrolysis mode = 1.5 kW; nominal power output during operation in the fuel cell mode = 0.5 kW) is provided in Figure 5.8 [4].

5.3.3 Performances

5.3.3.1 Water Electrolysis Mode

The current–voltage relationship of a PEM water electrolysis cell can be approached using the following equation [5]:

$$E_{\text{cell}}(T,P) = E_{\text{T,P}} + \frac{R\ T}{\alpha^{\text{a}}\ F}\ Ln\ \left(\frac{i}{i_0^{\text{a}}}\right) + \frac{R\ T}{\alpha^{\text{c}}\ F}\ Ln\ \left(\frac{i}{i_0^{\text{c}}}\right) + i\ R_j \tag{5.21}$$

where E_{cell} (T, P) is the water electrolysis voltage (V) at temperature T and pressure P of operation; $E_{\text{T,P}} = \Delta G(T,P)/nF$ is the thermodynamic voltage (V), at T, P; $\alpha^{\text{a}} = \alpha^{\text{c}} \approx 0.5$ are the charge transfer coefficients of the anodic OER and cathodic HER respectively; i is the current density in A cm^{-2}; $i_0{}^{\text{a}}$ and $i_0{}^{\text{c}}$ are the

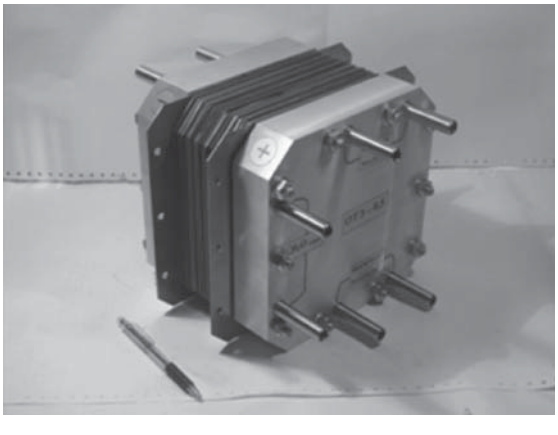

Figure 5.8 Photograph of a PEM URFC stack.

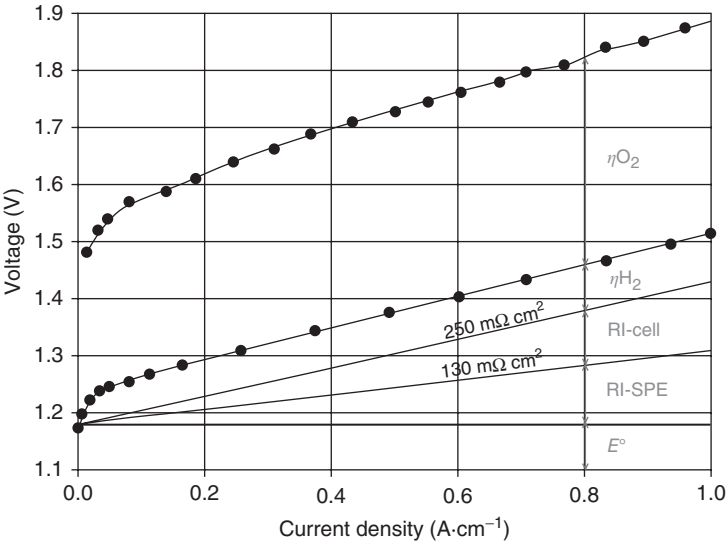

Figure 5.9 Polarization curve measured on a PEM water electrolysis cell at 80 °C showing the main contributions.

exchange current densities of the OER and HER, respectively, in A cm^{-2}; F is the Faraday constant 96 486 mol^{-1} R is the cell resistance (including membrane resistance and other electronic resistances) in Ω cm^{-2}. By adding the contribution of the different terms, the current–voltage polarization curve is obtained. Figure 5.9 shows the different voltage terms that contribute to the polarization curve of a PEM water electrolysis cell operating at 80 °C. The thermodynamic voltage ($E°$ = 1.18 V at 80 °C) is the major contributing term. Next, the linear term is due to the internal cell resistance, which is the sum of the ionic resistance of the proton-conducting membrane and the various electronic resistances of non-electrolyte internal cell components (current collectors, cell spacers, bipolar plates; they include both bulk resistances and contact resistances). The resistance of the SPE is a function of the membrane thickness and equivalent weight (EW). The next term is the HER overvoltage η_{H_2}, which is usually small, the reaction being a fast process on platinum surfaces in acidic media. The last term, which is the most significant in terms of magnitude, is the OER overvoltage η_{O_2}.

5.3.3.2 Fuel Cell Mode

Assuming that the HOR is a fast process, the current–voltage relationship of a PEM fuel cell can be approached using the following equation [6]:

$$E_{\text{cell}} = E_{T,P}° - \frac{R\ T}{\alpha\ F}\ \text{Ln}\left(\frac{i}{i_0}\right) - \frac{R\ T}{\alpha\ F}\ \text{Ln}\left(\frac{i_L}{i_L - i}\right) - i\ R_i \tag{5.22}$$

where E_{cell} is the fuel cell voltage (V); $E_{T,P}°$ is the thermodynamic voltage (V), at temperature (T) and under pressure (P); $\alpha \approx 0.5$ is the charge transfer coefficient; i is the current density in A cm^{-2}; i_0 is the exchange current density (of the ORR at

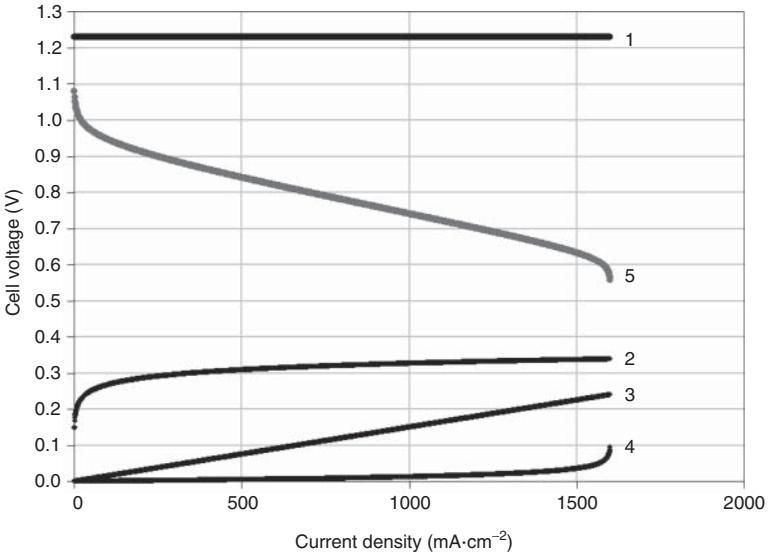

Figure 5.10 Calculated polarization curves of a PEM fuel cell at 25 °C using Equation 5.22: 1 – thermodynamic voltage,2 – charge transfer losses (mainly ORR), 3 – ohmic drop due to internal resistances, 4 – mass transport (O_2) losses and 5 – global polarization curve. $T = 333$ K, $R = 8.314$ J mol^{-1} K^{-1}, $\alpha = 1$, $n = 2$, $i_L = 1.6$ A cm^{-2}, $i_0 = 3 \times 10^{-6}$ A cm^{-2} and $R = 0.15\,\Omega \cdot$ cm^{-2}.

the cathode) in A cm^{-2}; i_L is the limiting current density at the positive electrode due to oxygen diffusion in A cm^{-2}; F is the Faraday constant 96 485 C mol^{-1} (C = coulomb, not °C) R is the cell resistance (including membrane resistance and other electronic resistances) in Ω cm^{-2}. Addition of these different voltage contributions yields the global current–voltage polarization curve. The different polarization losses calculated from Equation 5.22 are plotted in Figure 5.10. The thermodynamic voltage $E°$ is a function of operating temperature, gas pressure and oxygen purity. Losses due to charge transfer processes are mainly because of the ORR. The ohmic drop due to the cell resistance is a function of membrane thickness and equivalent weight. A value of 150 mΩ cm^2, as pictured in Figure 5.10, is responsible for an ohmic drop of 150 mV at 1 A cm^{-2}. This is common good practice. Mass transport losses are due to diffusion–controlled gas transport to the reaction sites. Oxygen transport is the main contributor. A limiting current is reached at high current densities. The value of the limiting current will depend on oxygen purity (pure oxygen or air), on gas pressures but also on cell design and mass transport properties of GDLs. The global polarization curve (plot 5 in Figure 5.10) is the sum of these different terms.

5.3.3.3 URFC Mode

As discussed above, a URFC is a compromise between a water electrolysis cell and a fuel cell, in terms of design, selection of cell components and catalysts compositions. Some typical polarization curves obtained in the URFC mode with

different catalyst compositions are plotted in Figure 5.11. Reference polarization curves measured on a conventional PEM water electrolysis and on a conventional PEM fuel cell are also plotted for comparison. Results show that the composition of the catalyst layer is critical for the performances. In some favourable cases, performances of the URFC can compete with best practices of individual PEM water electrolysers and fuel cells. The idea that a low-temperature URFC is a poor electrolyser and a poor fuel cell is therefore not exact. However, it should be emphasized that the key performance indicator for a URFC is not only its electrochemical performances but also its ability to maintain these performances over a significant number of alternative fuel cell/water electrolysis cycles. The data of Figure 5.11 shows that the maximum power density measured on the URFC operating in fuel cell mode is approximately 500 mW cm^{-2}. Gibbs free energy efficiencies $\varepsilon_{\Delta G}$ (see definition in Section 2.1) measured at 80 °C as a function of operating current density are plotted in Figure 5.12. As discussed

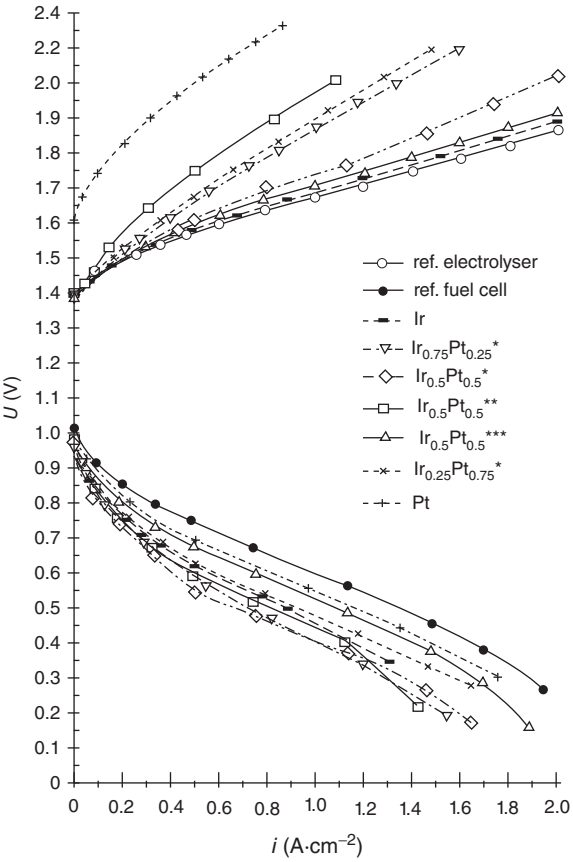

Figure 5.11 Polarization curves of a low-temperature URFC for different catalyst compositions at 80 °C [1].

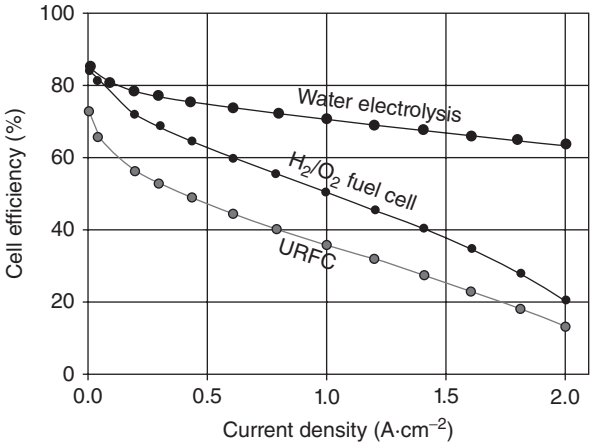

Figure 5.12 Typical plots of the efficiency of PEM water electrolysis cell, fuel cell and URFC as a function of operating current density, at 80 °C.

in Chapter 2, section 2.1, efficiencies of electrochemical cells are close to 100% at zero current (electrochemical interfaces at equilibrium) but tend to decrease when the operating current density is raised. This is because dissipation terms (cell resistance and charge transfer processes at anodes and cathodes) are directly proportional to the operating current density, a general characteristic of non-equilibrium processes [7]. The efficiency of the PEM water electrolysis cell is larger than the efficiency of the fuel cell at any current density. An efficiency value of $\varepsilon_{\Delta G} \approx 70\%$ at $1\,\mathrm{A\,cm^{-2}}$ is common good practice, at least at the lab scale. Although PEM fuel cell are using thinner membrane electrolyte than PEM water electrolysis cells (hence their internal resistance is lower), their efficiency is less because of the sluggish kinetics of the ORR combined with mass transport limitations of gaseous reactants to the reaction sites. As a consequence, the full cycle efficiency (electricity to electricity via hydrogen production and storage combining water electrolysis and fuel cell) is usually less than 50% (Figure 5.12) except at current densities less than a few hundred $\mathrm{mA\,cm^{-2}}$. The cycle efficiency at the nominal current density of $1\,\mathrm{A\,cm^{-2}}$ is usually in the 35–40% range.

5.3.4
Limitations and Perspectives

A PEM URFC is a low-temperature redox battery that uses the water/hydrogen and water/oxygen redox couples to store electricity in a reversible way. Such devices are of interest because chemical reactants can be stored outside the electrochemical cell. Therefore, the capacity of the battery is determined by the size of the reservoirs, not by the size of the battery. If the Earth atmosphere is used as the oxygen reservoir, then the capacity of the battery is only determined by the volume/pressure of the hydrogen reservoir. The main characteristics of

PEM URFCs do not significantly differ from those of individual PEM water electrolysis cells and fuel cells. The main challenge comes from the highly irreversible oxygen electrode. As in PEM fuel cell technology, the ORR requires a GDL made of carbon materials that cannot sustain the conditions found at the anode of PEM water electrolysis (operating potential of +2.0 V under evolving oxygen). The problem can be circumvented by using the B-configuration shown in Figure 5.6.

Main characteristics of PEM URFCs are:

- *Performances and efficiency*: when appropriate catalyst compositions are used, performances and efficiency of a PEM URFC are close to those of conventional water electrolysis cells and fuel cells, at least at the lab scale. The global efficiency of a PEM URFC (electricity → electricity) operating at 1 A cm^{-2} is within the 35–40% range.
- *Cyclability/durability*: PEM URFCs can sustain several hundred cycles of operation without significant degradation losses. Cyclability depends largely on the nominal current density of operation. In the A-configuration of Figure 5.6, the carbon substrate used to support platinum nanoparticles that catalyse the ORR is not stable. In the B-configuration of Figure 5.6, platinum used at the positive electrode for hydrogen oxidation in fuel cell mode is prone to oxidation and dissolution in the polymer electrolyte. This is a factor that tends to reduce the lifetime of the device.
- *Operation under pressure*: because the chemicals produced during the water electrolysis step (battery charge) are gaseous, the capacity of the URFC is directly related to the pressure of operation. Principles and characteristics of pressurized PEM water electrolysis have been reported in a previous chapter. Commercial PEM water electrolysers deliver compressed hydrogen in the 15–50 bar range at no significant extra cost of electricity. The pressure can then be further raised using appropriate compressors (up to 800 bars for mobility applications). Therefore, PEM URFCs using high-pressure hydrogen storage tanks such as those developed for the automotive industry could have a significant capacity but gas compressors are required. There is no specific problem for the URFC to operate under pressure except that SPEs used in PEM technology are based on (perfluorosulphonated acid (PFSA) polymeric materials), which are prone to gas cross-permeation effects through the poly tetra fluoro ethylene (PTFE) backbone. Cross-permeation effects can be reduced by using thicker SPEs but this tends to further reduce the cycle efficiency.
- *Cost issues*: PEM technology uses expensive materials: platinum group metals (PGMs) as electrocatalysts and PFSA materials as SPE. But significant progress has been made over the last few decades to reduce PGM loadings (and in some cases get rid of PGMs) and develop alternative cheaper polymer materials and it can be expected that such advances will also benefit URFC technology in the future.

5.4 High-Temperature URFCs

5.4.1 Principles

A URFC can also operate at elevated temperatures (>800 °C) using the solid oxide technology. The main advantage of this kind of cell is that the water/oxygen redox couple becomes fully reversible (see Figure 5.4) and the A-configuration of figure 5.6 can be more easily implemented. The principles of a URFC cell based on solid oxide technology are pictured in Figure 5.13.

5.4.2 Cell Structure

Earlier developments of high-temperature solid oxide cells were using tubular geometries but more integrated planar geometries have been developed over the last few decades. The structure of a solid oxide URFC operating in water electrolysis mode is pictured in Figure 5.14. The electrochemical cell itself contains three ceramic layers. A dense oxide-ion-conducting ceramic membrane placed in the middle is used as an electrolyte and cell separator. This membrane is clamped between two porous ceramic electrodes (the positive and negative electrodes). Two grooved end plates also called interconnects placed on each side of the electrochemical cell delimit the unit cell. They are used for the distribution of gaseous reactants (fuel cell mode) or for the collection of reaction gases (electrolysis mode)

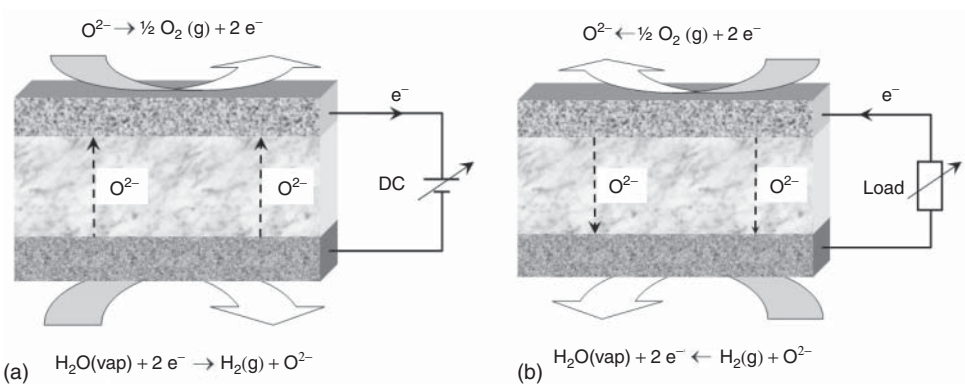

Figure 5.13 Schematic diagram of a solid oxide steam electrolysis cell (a) and a solid oxide fuel cell (b).

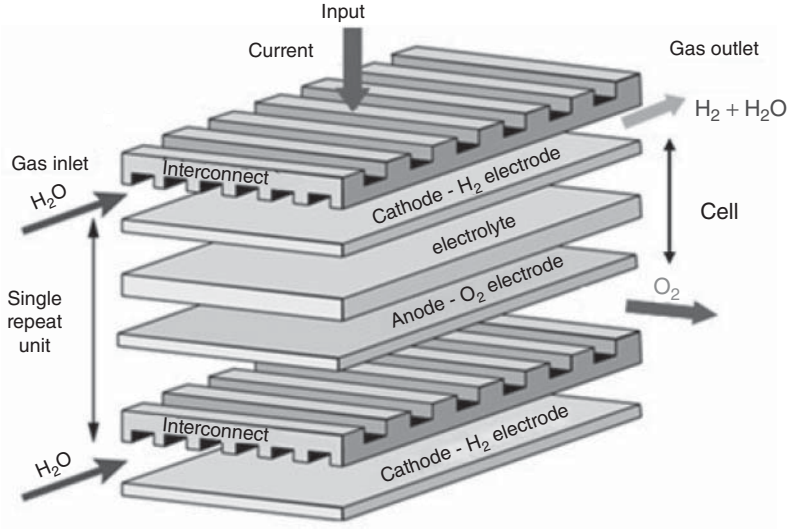

Figure 5.14 Structure of a solid oxide electrolysis cell (see chapter 3) that can be used as URFC.

and to convey electricity to/from the cell. Peripheral glassy sealants are used to ensure gas tightness.

In the planar design of Figure 5.14, the electrolyte (0.1–0.2 mm thick zirconia film) is used as the mechanical support of the cell. This design is called electrolyte-supported cells (ESCs) and electrodes have a thickness of approximately 50 μm. The problem is that the ion conductivity of the zirconia membrane becomes appropriate only at elevated operating temperatures (between 850 and 1000 °C), a temperature range that requires expensive and sometimes difficult to manufacture materials such as $LaCrO_3$, Cr-based alloys (Ducralloy) or special ferritic stainless steels or Ni-based alloys for the interconnects. The situation can be improved using the so-called anode-supported-cell (ASC) or cathode-supported-cell (CSC) design. In such cells, the thickness of the electrolyte membrane is reduced down to ≈5–20 μm to enhance ionic conductivity and thus allow operation at lower temperatures (650–850 °C). Because such thin electrolyte layers are not able to provide an appropriate mechanical support for the cell, the thickness of the hydrogen electrode is increased up to 0.2–1.5 mm without any significant prejudice. Using this design, elevated current densities can be reached and cheaper stainless steels can be used as interconnects. Improved lifetimes and reduced costs have been reported, opening the way to commercial applications. Materials used in high-temperature steam electrolysis (HTSE) are similar to those used in solid oxide fuel cells (SOFCs). Hence, URFCs do not require too specific developments.

5.4.3 Performances

5.4.3.1 Water Electrolysis Mode

HTSE cell or stack performances depend on the cell design considered. When operating at the same temperature, the electrochemical performances of a HTSE cell based on ESC design are much lower than those of a cell based on the CSC design. From a practical viewpoint, standard ESC cells operating at 800 °C are running at a maximum current density of ≈0.5 A cm^{-2} and 1.3 V. Higher current densities can be obtained but at higher temperatures (e.g. 0.6 A cm^{-2}, 1.3 V at 850 °C [8]). CSC cells are more efficient and can reach higher current densities. Details about cells based on LSM oxygen electrode operating at 850 °C at 1 A cm^{-2} and 1.3 V have been reported in 2008 in the literature [9]. Using LSCF oxygen electrodes, the same current density can be achieved but at only 800 °C [10, 11]. Current densities as high as −2.0 A cm^{-2} or even above can be achieved at the thermoneutral voltage at 800 °C using advanced CSC cells (Figure 5.15).

5.4.3.2 Fuel Cell Mode

Some typical polarization curves measured on a solid oxide fuel cell using oxygen as oxidant with different concentrations are reported in Figure 5.16. Performances strongly depend on the oxygen concentration in the oxidant gas and on the operating temperature [12]. A SOFC can operate at elevated current densities, in the multi A cm^{-2} range. Main polarization losses are plotted in Figure 5.17. When thin ceramic membranes are used, main losses come from concentration polarization (mass transport limitations at high current densities) and charge transfer (activation) kinetics (see chapter 3).

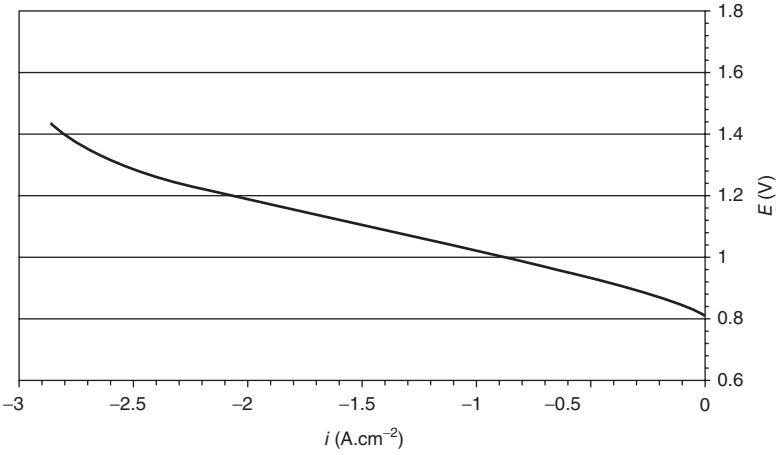

Figure 5.15 *i–V* curve of an advanced CSC cell made of Ni–YSZ/YSZ/GDC/LSC tested at 800 °C in 90%H_2O/10%H_2; steam conversion rate = 68% at −2.5 A cm^{-2} (see chapter 3).

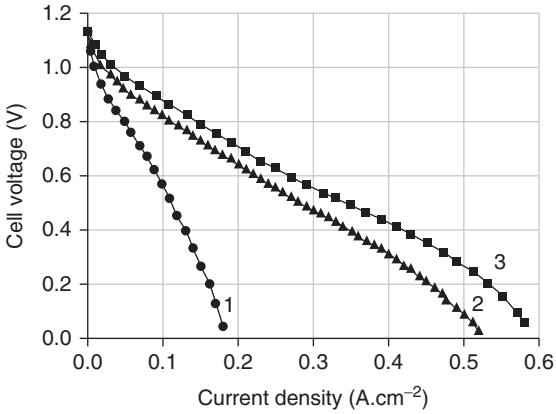

Figure 5.16 Polarization curves of a solid oxide fuel cell at 800 °C. Fuel: H_2. Oxidant: (1) 8% O_2 + 92% N_2; (2) 21% O_2 + 79% N_2 and (3) 100% O_2 [12].

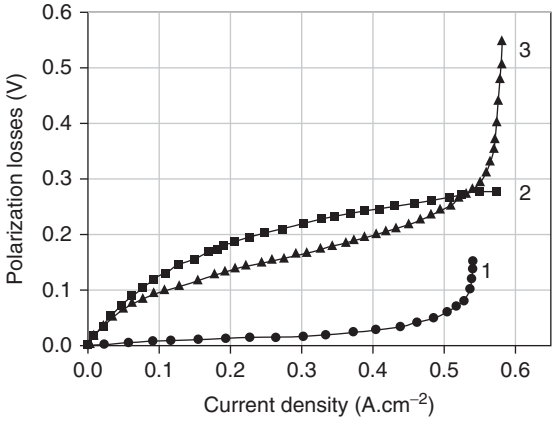

Figure 5.17 Different polarization losses at 800 °C. Fuel: H_2 (3% H_2O). Oxidant: air. (1) Cathodic concentration polarization; (2) activation polarization and (3) anodic concentration polarization.

5.4.3.3 **URFC Mode**

The typical performances of a solid oxide URFC operating at 1000 °C are plotted in Figure 5.18. As discussed above, the electrochemical reactions implying the water/oxygen and proton/hydrogen redox couples are fully reversible and there is no need to implement configuration B of Figure 5.6 at such temperatures. Although the energy required to split 1 mole of water is almost the same at room temperature and at high temperature (the main difference being due to the heat of vapourization, as shown in Figure 5.1), the electrical efficiencies of both water electrolysis and fuel cell reaction are much higher than those obtained at low temperature using PEM technology because part (≈one-third) of the energy requirements can be supplied as heat. As a consequence, the electrical efficiency

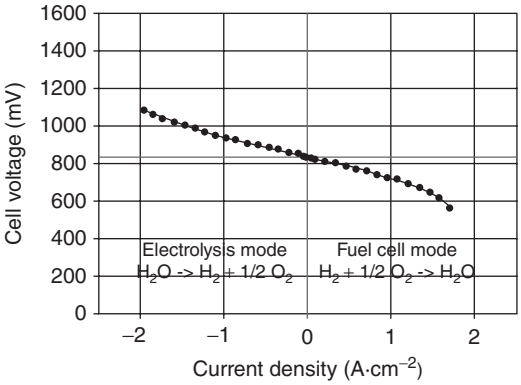

Figure 5.18 Polarization curves of a high-temperature URFC operating at 1000 °C.

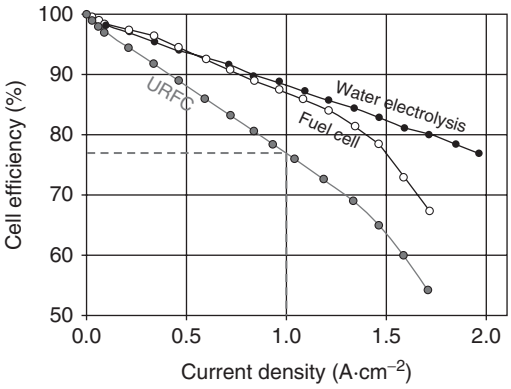

Figure 5.19 Plot of the efficiency of a solid oxide water electrolysis cell, a fuel cell and URFC as a function of operating current density, at 1000 °C.

of the solid oxide URFC is significantly higher than the efficiency of the PEM URFC (≈78–80% at 1 A cm^{-2} as shown in Figure 5.19).

5.4.4
Limitations and Perspectives

As for PEM URFCs, limitations of solid oxide URFCs are those of the solid oxide technology.

- *Performances and efficiency*: performances of solid oxide URFC are limited by those of solid oxide steam electrolysis cell, whose performance is lower than that of an SOFC. However, their efficiency (electricity → electricity) is approximately twice that of PEM URFCs, within the 75–80% range.
- *Cyclability/durability*: when solid oxide technology operates in stationary conditions of temperature and power, then durability is better due to constant

R&D efforts. Degradation rates in HTSE technology (>2%/1000 h) are higher than in SOFC technology (<1%/1000 h) and therefore durability of solid oxide URFCs are expected to be like those of HTSE cells [13, 14]. However, load cycling and temperature cycling have very significant deleterious effects on both performance and durability.

- *Operation under pressure*: there are few reports concerning the developments of HTSE cells or stack operating under pressure.

5.5 General Conclusion and Perspectives

In the hydrogen economy, the water splitting reaction is considered as a key reaction to transform zero-carbon electricity into zero-carbon hydrogen and the electrochemical combustion of hydrogen in oxygen (or air) in a fuel cell is used for power generation. Electricity storage and electricity restitution can be obtained by coupling a water electrolyser to a fuel cell. A step further towards higher integration and lower capital expenses can be achieved by designing large capacity redox batteries with external gas storage that use water and its reduced (hydrogen) and oxidized (oxygen) redox forms. In the literature, such devices are usually referred to as unitized regenerative fuel cells (URFCs). Basically, a URFC is a hybrid technology device that merges a water electrolysis cell and a fuel cell for reversible electricity storage. Because water electrolysis and fuel cell technologies are usually ranked as a function of operating temperature, so are URFCs. In the low-temperature range (<250 °C), PEM technology is the most appropriate technology for the design of URFCs. Proof of concepts have been demonstrated and some technology developments have been made (up to the kilowatts range). The main challenge comes from the irreversibility of the water–oxygen redox couple (for both water oxidation into oxygen and oxygen reduction into water), which is a source of low efficiency (a maximum of 35–40% can be obtained for electricity-to-electricity cycles at 1 A cm^{-2}). Also, the need to combine the oxygen evolution reaction (that requires iridium dioxide as electrocatalyst) and the hydrogen oxidation reaction (that requires platinum as electrocatalyst) is the cause of some corrosion issues and fast ageing. In the high-temperature range (>650 °C), solid oxide technology prevails. In this temperature range, the water–oxygen redox couple is fully reversible. As a result, cell design is simplified and higher efficiencies can be achieved (75–80% can be obtained for electricity to electricity at 1 A cm^{-2}). Although there are few (if any) market applications for URFCs at the moment, the development of the hydrogen economy will certainly boost R&D activities in the field and systems of larger capacity will be developed in the future.

Nomenclature

A	membrane area (m^2)
a_i	activity of species i
E	free energy electrolysis voltage (V)

F	Faraday constant (96 485 °C mol^{-1})
f_i	fugacity of species i
G	Gibbs free energy (J mol^{-1})
H	enthalpy (J mol^{-1})
I	current (A)
i	current density (A cm^{-2})
i_0	exchange current density (A cm^{-2})
L	membrane thickness (m)
n	number of electrons exchanged during the electrochemical reaction
P	pressure (Pa)
R	resistance (Ω)
r	specific resistance (Ω m^2)
R	constant of perfect gas (0.082 J K^{-1} mol^{-1})
S	entropy (J mol^{-1} K^{-1})
t	time (s)
T	absolute temperature (K)
U_{cell}	cell voltage (V)
V	thermoneutral electrolysis voltage (V)
W	electrical work (J)
x, y, z	space coordinates

Greek symbols

Δ	difference
ε	cell efficiency (%)
η	overvoltage (V)
φ	electrode absolute potential (V)
ρ	electrical resistivity (Ω m)
σ	electrical conductivity (S m^{-1})

Subscripts or superscripts

°	standard conditions (298 K, 1 bar)
cell	electrolysis cell
d	dissociation
e	electrolyte
i	species i
r	real
t	theoretical

Acronyms

ASC	anode-supported cell
CSC	cathode-supported cell
ESC	electrolyte-supported cell

EW	equivalent weight of membrane (equiv. g^{-1})
GDC	Gadolinium Doped Ceria
GDL	gas diffusion layers
HER	hydrogen evolution reaction
HOR	hydrogen oxidation reaction
HTSE	high temperature steam electrolysis
LSCF	Lanthanum Strontium Cobalt Ferrite
OER	oxygen evolution reaction
ORR	oxygen reduction reactions
PEM	polymer electrolyte membrane
PFSA	perfluorosulphonated acid
PGM	platinum group metals
PTFE	poly tetra fluoro ethylene
RHE	Reversible Hydrogen Electrode
SOFC	solid oxide fuel cell
SPE	solid polymer electrolyte
URFC	Unitized Regenerative Fuel Cell
YSZ	Yttria Stabilized Zirconia

References

1. Grigoriev, S.A., Millet, P., Dzhus, K.A., Middleton, H., Saetre, T.O., and Fateev, V.N. (2010) Design and characterization of bi-functional electrocatalytic layers for application in PEM unitized regenerative fuel cells. *Int. J. Hydrogen Energy*, **35**, 5070–5076.
2. Peters, A.P.H. (2010) *Concise Chemical Thermodynamics*, CRC Press.
3. Bard Allen, J., Roger, P., and Joseph, J. (1985) *Standard Potentials in Aqueous Solution, Monographs in Electroanalytical Chemistry and Electrochemistry*, CRC Press, New York.
4. Grigoriev, S.A., Millet, P., Porembsky, V.I., and Fateev, V.N. (2011) Development and preliminary testing of a unitized regenerative fuel cell based on PEM technology. *Int. J. Hydrogen Energy*, **36**, 4164–4168.
5. Hamann, C.H., Hamnett, A., and Vielstich, W. (1998) *Electrochemistry*, Wiley-VCH Verlag GmbH, Weinheim.
6. Barbir, F. (2012) *PEM Fuel Cells*, Elsevier.
7. Kjelstrup, S. and Bedeaux, D. (2008) *Non-Equilibrium Thermodynamics of Heterogeneous Systems*, World Scientific Publishing.
8. O'Brien, J.E., Stoots, C.M., Herring, J.S., Condie, K.G., and Housley, G.K. (2009) The high-temperature electrolysis program at the idaho national laboratory: observations on performance degradation. International Workshop on High Temperature Water Electrolysis Limiting Factors, INL/CON-09-15564.
9. Hauch, A., Ebbesen, S., Jensen, S., and Mogensen, M. (2008) Highly efficient high temperature electrolysis. *J. Mater. Chem.*, **18**, 2331–2340.
10. Brisse, A., Schefold, J., and Zahid, M. (2008) High temperature water electrolysis in solid oxide cells. *Int. J. Hydrogen Energy*, **33**, 5375–5382.
11. Mougin, J., Mansuy, A., Chatroux, A., Gousseau, G., Petitjean, M., Reytier, M., and Mauvy, F. (2013) Enhanced performance and durability of a high temperature steam electrolysis stack. *Fuel Cells*, **13** (4), 623–630.
12. Yoon, K.Y., Huang, W., Ye, G., Gopalan, S., Pal, U.B., and Seccombe, D.A. Jr.,

(2007) Electrochemical Performance of Solid Oxide Fuel Cells (SOFCs) manufactured by single step co-firing process. *J. Electrochem. Soc.*, **154** (4), B389.

13. Brisse, A. and Schefold, J. (2012) High temperature electrolysis at EIFER, main achievements at cell and stack level. *Energy Procedia*, **29**, 53–63.
14. Mocoteguy, P. and Brisse, A. (2013) A review and comprehensive analysis of degradation mechanisms of solid oxide electrolysis cells. *Int. J. Hydrogen Energy*, **38**, 15887–15902.

6
High-Temperature Steam Electrolysis

Jérôme Laurencin and Julie Mougin

6.1
Introduction

Electrolysis of water can be performed either at low temperature using liquid water or at high temperature using steam. In this chapter, the latter process will be presented, the so-called high-temperature steam electrolysis (HTSE).

The global electrolysis remains the same: $H_2O \rightarrow H_2 + \frac{1}{2} O_2$.

However, the main advantage of this technology is that the dissociation of steam requires less energy compared to liquid water, as presented in Figure 6.1. In addition, when the temperature increases, a part of the electrical energy needed to dissociate the water molecule can be replaced by heat. When heat sources are available at low prices, which is often the case compared to electricity, the replacement of electricity demand by heat gives rise to high efficiencies and contributes to the decrease of the cost of hydrogen production.

However, there is an optimum temperature that can be used for HTSE, mainly due to the limitations of the materials, as very high temperature can be detrimental in terms of durability. For this reason, the HTSE operating temperature range is around 700–900 °C.

6.2
Overview of the Technology

An HTSE involves a stack of several single-repeat units (SRUs) (Figure 6.2). The electrochemical cell, the so-called solid oxide electrolysis cell (SOEC), that is one of the electrolyser's components, comprises three ceramic layers: a dense electrolyte and two porous electrodes (cathode and anode, where hydrogen and oxygen are respectively produced) placed on both sides of the electrolyte. Taking into account the operating temperature range, the electrochemical cell is made of ceramics.

Hydrogen Production: by Electrolysis, First Edition. Edited by Agata Godula-Jopek.
© 2015 Wiley-VCH Verlag GmbH & Co. KGaA. Published 2015 by Wiley-VCH Verlag GmbH & Co. KGaA.

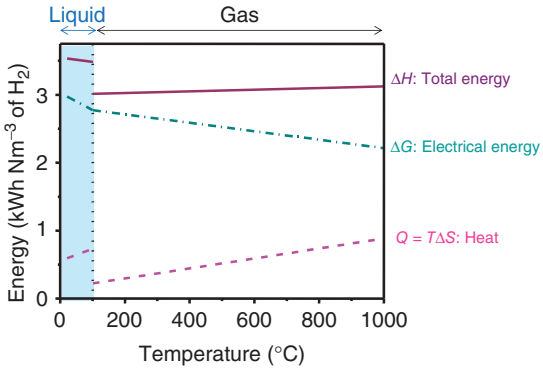

Figure 6.1 Energy need for the electrolysis reaction as a function of temperature; enthalpy (ΔH), Gibbs enthalpy (ΔG), entropy ($T\Delta S$) [1].

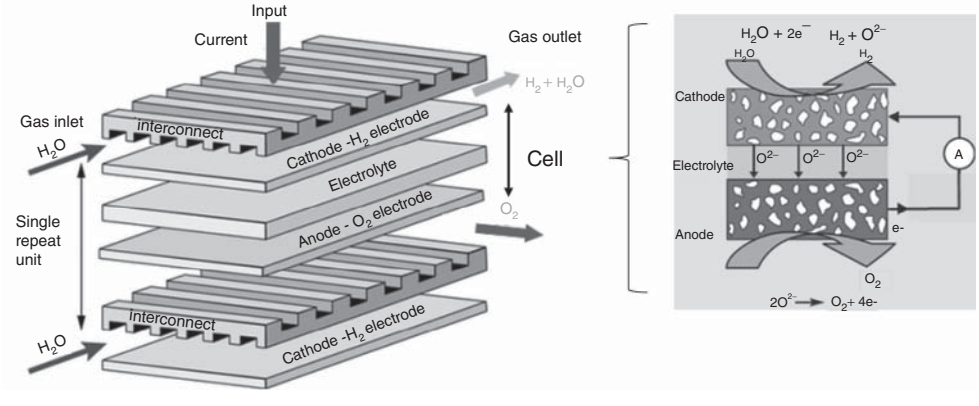

Figure 6.2 Schematic representation of a single repeat unit (SRU) including the three-layer cell (cathode/electrolyte/anode) and two half-interconnects; highlight of the anodic and cathodic half-reactions occurring in the cell.

The stack further features interconnects, which serve the purpose of carrying the electric current along, ensuring fluid distribution for every cell and acting as separators between the anode of a cell and the cathode of the adjacent one.

In addition, a stack comprises sealings to ensure, on the one hand, the gastightness of the stack towards the outside ambiance and, on the other hand, the anodic and the cathodic compartments of each cell.

The gaseous atmospheres consist of a water–hydrogen (H_2O/H_2) mixture on the cathode side and oxygen (O_2) on the anode side. Consequently, the stresses acting on the constituent materials of such a high-temperature electrolyser (HTE) are not very different from those involved in solid oxide fuel cells (SOFCs). For these reasons, and also taking into account that SOFCs have been developed for some decades and are currently reaching a maturity compatible for market commercialization as can be seen in some countries such as Japan or the United States, for

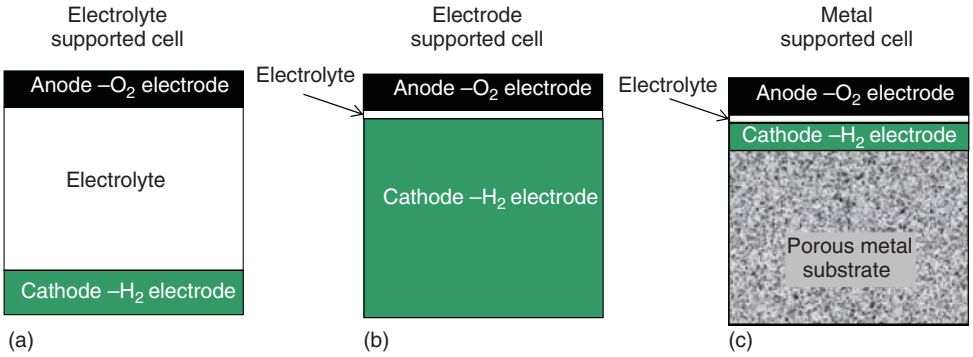

Figure 6.3 Schematic representation of the three types of cells: (a) electrolyte-supported cell, (b) electrode-supported cell and (c) metal-supported cell.

example, HTSE components and materials are for the time being similar to those considered for SOFCs.

Thus, SOECs are similar to SOFCs and several cell designs are considered.

First SOFCs, manufactured by Westinghouse in the early 1970s, had a tubular shape and were operated at 1000 °C. The concept demonstrated high robustness regarding thermal cycling, but was considered as lacking the potential for low-cost mass manufacturing. In addition, the support of the cell was a thick porous support tube made of calcia-stabilized zirconia that presented high impedance to air flow towards the cathode, which reduced the cell performance.

Then considerable efforts were put on planar designs using the electrolyte (zirconia) as the mechanical support of the cell (thickness 0.1–0.2 mm), to manufacture so-called electrolyte-supported cells (ESCs). In this design, the electrodes with a thickness of around 50 μm were deposited on both sides of the mechanical supporting electrolyte (Figure 6.3). The high electrolyte thickness requires an operating temperature between 850 and 1000 °C in order to increase the ion conductivity of the zirconia. The high operating temperature requires special materials such as $LaCrO_3$, Cr-based alloys (Ducralloy) or special ferritic stainless steels or Ni-based alloys for the stack interconnects. These materials are expensive and difficult to manufacture in the case of $LaCrO_3$.

A second generation of planar cells was developed in which the electrolyte thickness was decreased to 5–20 μm to decrease electrolyte resistivity and to allow reduced operating temperatures. However, the thin electrolyte is not able to mechanically support the cell and therefore the thickness of the SOFC anode (hydrogen electrode) is increased in the range of 0.2–1.5 mm (Figure 6.3). This geometry is named the anode-supported cell (ASC) for SOFC operation and has to be renamed as the cathode-supported cell (CSC) for SOEC operation or more generally the ESC. Thanks to the thin electrolyte, the operating temperature can be decreased to 700–800 °C. High current densities can be obtained and cheaper stainless steels can be used to produce interconnects and stacks. These elements lead to an improvement in lifetime and cost, further reduction of operating

temperature aiming at further lifetime improvement and a decrease in cost with the operating temperature below 650 °C.

For HTSE operation, both ESC and CSC cells are considered by the different teams involved in this topic around the world.

In these 'self-supported' cells, one of the ceramic layers plays the role of the mechanical support, which is not the primary electrochemical function of the component. A third and more recent generation of SOFC uses an 'external' electrochemically inactive metallic support on which the ceramic components of the cell are deposited as thin layers (Figure 6.3). This type of cell is named the metal-supported cell (MSC). This cell geometry is still under development for SOFC, and only a few tests in the SOEC mode have been performed.

As to the characteristics desired with respect to cell materials, these differ according to the component considered: ceramic materials for the electrolyte would be preferable for the anode (i.e. the site where oxygen is released) and a ceramic–metal composite – generally referred to as a cermet – for the cathode (i.e. the hydrogen production site).

The electrolyte consists of a material exhibiting adequate gastightness (density >95%, zero open porosity), good ion conductivity (10^{-2} S cm^{-1} at operating temperature), a thermal expansion coefficient close to that of the electrodes (in order to limit mechanical stresses), further proof of being chemically inert with respect to the electrode materials, stability in both oxidizing and reducing environments and, finally, mechanical stability in HTSE operating conditions. In most cases, the electrolyte material is yttria-stabilized zirconia (YSZ), that is to say zirconia (zirconium oxide) stabilized with yttria (yttrium oxide), generally with 8 mol% of yttria due to its higher conductivity compared to other rates. Other zirconia-based electrolytes such as scandia-stabilized zirconia are also considered for the lowest operating temperatures, but researchers are still verifying their capabilities, in terms of stability and ageing resistance, which makes them all the more a relatively costly compound.

As regards the electrodes, the materials selected must exhibit high electronic conductivity (>100 S cm^{-1}), together with – if possible – a degree of ionic conductivity, in order to limit ohmic losses and delocalize the electrochemical reaction across the bulk of the electrode.

These electrodes are characterized by their high porosity – this property being indispensable – to permit steam diffusion in the SOEC mode, but equally to allow the removal of hydrogen at the cathode and oxygen at the anode. This porosity must be optimized to preclude any local overpressure, such as would tend to delaminate the electrodes' constituent layers. More specifically, the hydrogen electrode requires good catalytic properties for water reduction and an ability to remain stable in a reducing environment. As for the oxygen electrode, this must exhibit suitable catalytic properties for the oxidation of O^{2-} ions, while remaining stable in an oxidizing environment.

In mechanical terms, the cell must also exhibit adequate strength, in particular with regard to the ceramic layer called upon to serve as a mechanical support (this applying either to the electrolyte or one of the electrodes, depending on the

type of cell selected). Finally, again with regard to developing a process that is economically viable, it is imperative that the constituent materials for the electrochemical cells be available in quantity at a low cost.

For the hydrogen electrode, the material is a cermet, generally a nickel/yttria-stabilized zirconia (Ni/YSZ) cermet. Nickel figures indeed as the most effective electrocatalyst discovered to date. Materials of the nickel/gadolinia-doped ceria (Ni/GDC) or nickel/samaria-doped ceria (Ni/SDC) type are also under investigation as substitutes to the conventional Ni/YSZ cermets to achieve higher conductivity at low temperature. Some teams are also looking into all-oxide materials for the hydrogen electrode, acting as mixed conductors; however, performances are still far from those of conventional cermets.

For the oxygen electrode, a material belonging to the perovskite family is generally considered as it has an ABO_3 structure. The strontium-doped lanthanum manganite (LSM, $La_{1-x}Sr_xMnO_{3-\delta}$) is considered as the reference compound and is often found in ESCs as it is particularly suitable to operations above 800 °C. However, since it is a purely electronic conductor, it is generally mixed with YSZ, the electrolyte material, to form an LSM – YSZ compound, thus exhibiting a mixed electronic and ionic conductivity thanks to LSM and YSZ, respectively, which allows extending the electrochemically active reaction site area. For ESCs operating at lower temperatures (below 800 °C), mixed ionic and electronic conductors (MIECs) are preferred, and among them is another perovskite referred to as lanthanum strontium cobalt ferrite (LSCF, $La_{1-x}Sr_xCo_{1-y}Fe_yO_{3-\delta}$). For the lowest temperatures (below 700 °C), LSC ($La_{1-x}Sr_xCoO_{3-\delta}$)is considered because of its higher conductivity. It must be noted that intermediate layers between the oxygen electrode and the electrolyte might be intercalated in the case of LSCF or LSC, with the aim of minimizing the reactivity between the electrolyte and the electrode materials and also to promote the adhesion of the electrode, which presents a thermal expansion coefficient mismatch with the electrolyte. This layer generally consists of GDC or yttria-doped ceria (YDC), as it then proves chemically compatible both with the zirconia-based electrolyte and the electrode material. Thus, many ESCs, developed to operate at temperatures around 700 – 750 °C, feature an LSCF anode, together with a ceria-based barrier layer (GDC or YDC) acting as a barrier. Finally – looking more to the future – materials from the nickelate family ($A_2NiO_{4+\delta}$, A being Nd, La or Pr) are currently undergoing development and qualification for the purposes of HTSE operation [2, 3].

As regards the interconnects, the material must, first of all, exhibit good electrical conductivity, high oxidation resistance, fulfil the specific conditions prevailing in HTSE (in terms of temperature and environment) and, second, not impair the electrochemical cells' proper operation. A twofold constraint thus applies to the interconnect: in mechanical terms, the challenge is to preclude any rupture of the ceramic cells the interconnect is attached to and, consequently, to select a material exhibiting comparable thermal expansion characteristics; in chemical terms, the aim of the design studies is to suppress any risk of emitting compounds that would be detrimental to the electrodes. These technical imperatives are compounded by a further requirement of an economic nature: the HTSE system must

remain inexpensive. For this purpose, the material used for the interconnect must be easily 'workable', that is it must lend itself to cutting, machining and/or stamping. For operating temperatures below 900 °C as currently considered, metallic interconnects are considered that are made of alloys affording oxidation resistance at high temperature because of the formation of chromium-rich oxide layers (stainless steels, nickel-based alloys). However, such layers are fairly poor electrical conductors and in addition emit volatile chromium compounds that are likely to contaminate the cell through the phenomenon of chromium poisoning, as such vapours are condensed at the electrochemical active sites of the cell. Among the alloys currently under consideration are ferritic stainless steels. Inexpensive as they are, these steels further exhibit advantageous properties: they prove particularly suitable for shaping and welding purposes, exhibit expansion behaviours compatible with that found for the cell and are resistant to prolonged exposure to high temperatures. On the other hand, their surface properties are not altogether satisfactory: their oxidation resistance in steam, in particular, is poor and the protective chromium oxide formed proves to be electrode-poisoning. Research organizations and manufacturers are currently striving to optimize the composition of such steels, in particular by seeking to control the nature of the naturally forming oxide layers. For instance, the Crofer® 22 APU grade (an iron–chromium alloy containing 22 wt% chromium), developed by ThyssenKrupp VDM, with the addition of manganese to the alloy, promotes the formation, at the very surface, of a mixed manganese–chromium oxide. This oxide affords the twofold benefit of emitting lower quantities of chromium-compound vapours and of proving to be a far better conductor than chromium oxide by itself – even though the latter oxide does still form beneath this mixed oxide. Hence, additions of rare earths (of lanthanum, for instance) are made, to bring down oxide growth rate: the ensuing thinner layer exhibits better adhesion, and hence better conduction properties. Finally, titanium is added, to bring down the chromium oxide's resistivity. This grade specifically developed for SOFC is suitable for SOEC. Sandvik also developed a specific grade named Sanergy HT, another 22 wt% Cr ferritic stainless-steel grade containing Mn, but with Mo and Nb rather than Ti.

Unfortunately, the effectiveness of such solutions proves altogether limited, with regard to ensuring SOFC and HTSE operation over extended timescales. Thus, efforts are consequently conducted to obtain improved surface properties by means of coatings. Investigations are focusing more particularly on chromium-free oxides, exhibiting low electrical resistivity, while affording the ability to prevent, or markedly slow down, oxidation of the underlying alloy. The chief compound investigated in this respect is a mixed manganese–cobalt oxide, exhibiting a spinel structure, with the composition $(Co, Mn)_3O_4$. The benefit it affords is its high conductivity: about a thousand times higher than that exhibited by chromium oxide, at 800 °C. A commercial solution is available, commercialized by Sandvik, as pre-coated strips that are covered by a very thin Co coating (a few hundred nanometres) deposited by a vacuum process. As high-temperature oxidation takes place and the protective $(Co, Mn)_3O_4$ is formed from the Co coating, with the Mn coming from the steel.

Other compounds, for example lanthanum perovskites, however, derived from electrode compositions are equally proving to be of interest to researchers. Numerous deposition techniques are also being considered. Most of these involve combining the coating operation with a post-treatment procedure for the purposes of achieving the proper stoichiometry and/or deposit densification.

Concerning the sealings, SOFC solutions can be considered. However, specifications in terms of gastightness are more severe. Indeed, while an SOFC can be operated even if not fully gastight, SOEC cannot, as each molecule of hydrogen produced but not recovered at the outlet leads to a decrease of the process efficiency. Glass and glass–ceramic sealants are the most used solutions. They exhibit strong bonding to the interface; their adherence to the cell provides hermetic sealing and thus most of the requirements for SOEC are fulfilled. Although glass presents the faculty of self-healing, which can be very beneficial in case of cracking, its excessive devitrification at operating temperatures leads to drastic changes in its physicochemical properties. Glass–ceramic sealants are thus often preferred as their crystallization can be controlled. However, for such materials the self-healing faculty is partially or even completely lost; therefore, glass–ceramic properties have to be completely determined, starting from their vitreous state, in order to be perfectly adapted to adjacent cell components. Their performance depends on their components, compositions and arrangement in the network structure, which is very complex and not yet fully understood. The formulation process of glass–ceramics is highly complex, especially due to the large number of elements that can be included [4]. Glass–ceramics from several systems have been investigated and their suitability for sealing applications within SOECs has been checked. It was concluded that glass–ceramics based on the $CaO-Al_2O_3-SiO_2$ (CAS) system meet most of the requirements for efficient sealing, especially in terms of chemical durability.

6.3 Fundamentals of Solid-State Electrochemistry in SOEC

SOEC electrochemical performance is characterized by the polarization curve. This curve plots the evolution of cell voltage, U, which is recorded at the cell terminal, as a function of current density, i. Basically, the '$U-i$' curve is composed of two contributions: the reversible voltage, U_{rev}, which assumes that the thermodynamic conditions are fulfilled and the cell polarization that arises under current. In electrolysis mode, cell polarization or 'overpotential' increases the voltage in operation according to:

$$U(i) = U_{rev} + |\eta| \tag{6.1}$$

The global overpotential η depends on the current density and originates from the irreversible character of the electrolysis process (see Chapter 1). It results in an increase in the electrical demand for steam electrolysis, when the current density, or the associated hydrogen production rate, is increased. This loss in the global

SOEC efficiency corresponds to an entropy production in the system, leading to heat release in the cell. The generation of heat modifies the SOEC thermal regimes by balancing the heat absorbed by the endothermic electrolysis reaction.

This section 6.3 aims to detail the mechanisms that are likely to contribute to the global cell overpotential. In this objective, the term η will be decomposed in a sequence of independent contributions; each term will be ascribed to a process that limits the cell efficiency and, hence, the hydrogen production rate. In this framework, this section has been split into three subsections:

1) The first one has been devoted to the global decomposition of the cell polarization curve.
2) In the second subsection, the reader can find a fine description of the fundamental equations governing the electrochemical behaviour of SOEC electrodes.
3) The impact of thermal SOEC operating modes on the polarization curve is addressed in the third section.

6.3.1 Cell Polarization Curve

6.3.1.1 Expression of the Cell Voltage *U*(*i*)

Considering the typical SOEC planar configuration, the cell voltage is equal to the difference between the electric potentials recorded on each side of the cell. This measurement corresponds to the difference between electrical potentials, φ_{e^-}, taken at the cell terminals (i.e. on the metallic interconnects that ensure the current collection) (Figure 6.4):

$$U(i) = \varphi^1_{e^-} - \varphi^2_{e^-} \tag{6.2}$$

It may be noted that the subscript e^- indicates that φ_{e^-} is related to an 'electronic' potential picked up in an electronic conducting phase. In this section, the current density is considered negative by convention ($i < 0$).

As illustrated in Figure 6.4, the expression of the cell voltage (Equation 6.2) can be decomposed into a sum of seven contributions. They are related to the difference in the electrical potentials all along the cell thickness:

$$\begin{aligned} U(i) = {} & (\varphi^1_{e^-} - \varphi^{ACC}_{e^-}) + (\varphi^{ACC}_{e^-} - \varphi^{AFL}_{e^-}) + (\varphi^{AFL}_{e^-} - \varphi^{Anode}_{io}) + (\varphi^{Anode}_{io} - \varphi^{Cathode}_{io}) + \cdots \\ & \cdots + (\varphi^{Cathode}_{io} - \varphi^{CFL}_{e^-}) + (\varphi^{CFL}_{e^-} - \varphi^{CCC}_{e^-}) + (\varphi^{CCC}_{e^-} - \varphi^2_{e^-}) \end{aligned} \tag{6.3}$$

Locations of these potentials are depicted in Figure 6.4. The terms $\varphi^{ACC}_{e^-}$ and $\varphi^{CCC}_{e^-}$ refer to the potentials taken on each side of the cell in the electrode current collectors (CCs). The terms $\varphi^{AFL}_{e^-}$ or $\varphi^{CFL}_{e^-}$ denote the potentials in the electronic conducting phases at the interfaces between the electrode current collector (ECC) and the anode or cathode functional layer (FL); whereas φ^{Anode}_{io} or $\varphi^{Cathode}_{io}$ corresponds to the electrical potentials taken in the ionic conducting phase at the anode/electrolyte or cathode/electrolyte interfaces. It may be noted that the subscript 'io' indicates that the potential φ_{io} is related to the ionic conductor.

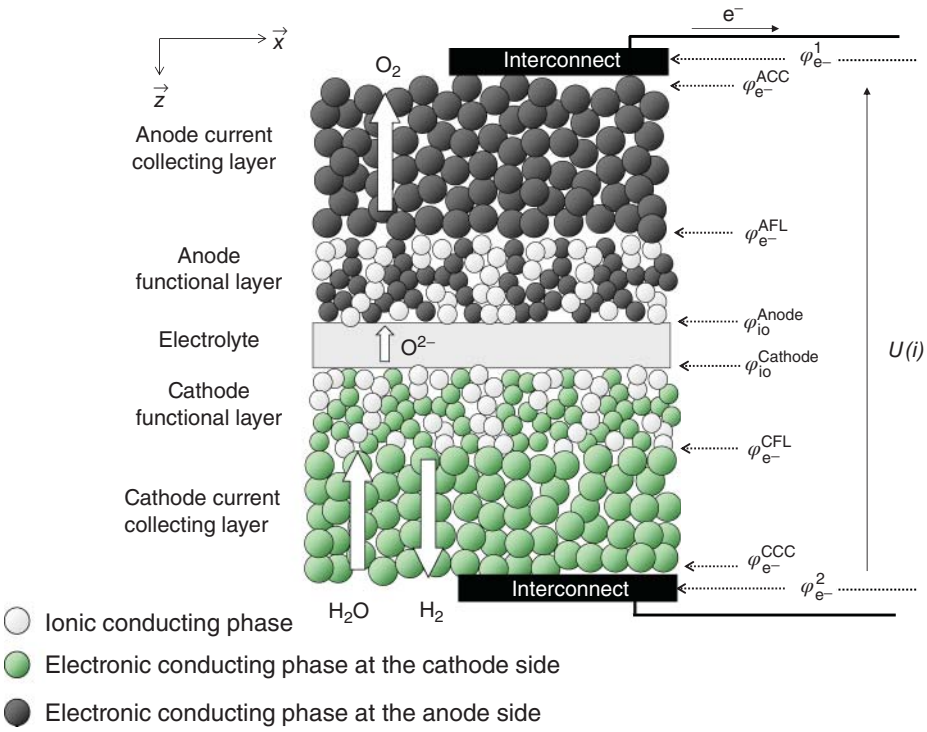

Figure 6.4 Schematic representation of the SOEC. Locations of the electrical potentials given in Equation 6.3 are also indicated.

The seven components that contribute to the cell voltage are detailed subsequently.

6.3.1.2 Ohmic Losses and Contact Resistances

Ohmic Losses into the Current Collecting Layers and Electrolyte Membrane The potential difference across the anode and cathode current collector (CCC) layers are simply caused by their electrical resistivities to the current flow. Since the electron transport obeys the classical Ohm's law, the associated voltage losses are expressed as functions of the conductivities of both CC layers (i.e. $\sigma_{e^-}^{\text{eff_ACC}}$ or $\sigma_{e^-}^{\text{eff_CCC}}$):

$$\left(\varphi_{e^-}^{\text{ACC}} - \varphi_{e^-}^{\text{AFL}}\right) = R_{\text{ACC}}^{\text{eff}} \times |i(x)| \quad \text{with} \quad R_{\text{ACC}}^{\text{eff}} = \frac{\ell_{\text{ACC}}}{\sigma_{e^-}^{\text{eff_ACC}}}$$

$$\left(\varphi_{e^-}^{\text{CFL}} - \varphi_{e^-}^{\text{CCC}}\right) = R_{\text{CCC}}^{\text{eff}} \times |i(x)| \quad \text{with} \quad R_{\text{CCC}}^{\text{eff}} = \frac{\ell_{\text{CCC}}}{\sigma_{e^-}^{\text{eff_CCC}}} \tag{6.4}$$

where $\ell_{\text{ACC or CCC}}$ represents the thickness of the considered layer. The term $\sigma_{e^-}^{\text{eff_ACC}}$ or $\sigma_{e^-}^{\text{eff_CCC}}$ refers to an 'effective' conductivity that is a combination of the 'intrinsinc' conductivity of the dense material and the microstructure properties

of the porous layer (see details Section 6.3.2.5). The term $i(x)$ refers to the local current density that evolves all along the cell length (i.e. in the $\vec{x}$ direction: see system of coordinates in Figure 6.4). Similarly to the collecting layer, the diffusion of the O^{2-} oxygen ions through the electrolyte is hindered by its bulk resistivity. The voltage drop due the electrolyte resistance is also dependent on the ionic conductivity σ_{io} of the dense material as follows:

$$\left(\varphi_{io}^{Anode} - \varphi_{io}^{Cathode}\right) = R_{electrolyte} \times |i(x)| \quad \text{with} \quad R_{electrolyte} = \frac{\ell_{electrolyte}}{\sigma_{io}} \tag{6.5}$$

where $\ell_{electrolyte}$ denotes the thickness of the electrolyte membrane.

Contact Resistances at the Electrode/Interconnect Interfaces Metallic interconnects are applied on the cell under a compressive load. The non-perfect electrical contact at the electrode/interconnect interface creates a resistance that induces a loss in cell voltage [5]:

$$(\varphi_{e^-}^{1} - \varphi_{e^-}^{ACC}) = R_c^{Anode} \times |i(x)| \text{ and } (\varphi_{e^-}^{CCC} - \varphi_{e^-}^{2}) = R_c^{Cathode} \times |i(x)| \tag{6.6}$$

where R_c^{Anode} and $R_c^{Cathode}$ denote, respectively, the contact resistances at the anode and cathode sides. As cathodic Ni–YSZ cermet presents much higher conductivity than anodic materials, the contribution $R_c^{Cathode}$ is usually neglected compared to the anode contact resistance R_c^{Anode} [6].

6.3.1.3 Anode and Cathode Polarization: Role of the Electrochemical Process on the Cell Polarization Curve

'Local' and 'Resulting' Electrode Potential As depicted in Figure 6.4, the FL is a porous composite made up of an electronic and ionic conductor. As a consequence, the electrochemical reaction can occur in the whole interlayer at the sites where the ions, electrons and gas species meet. These sites correspond to intricate lines in the structure that are usually called 'triple phase boundary lengths' (TPBls) (Figure 6.5).

Inside the FL, there is a step of electrical potential between the electronic and the ionic conductor that is due to an excess of charge on each side of the metal/electrolyte interface. This difference in Galvani potential corresponds to the well-known Helmotz double layer [7, 8], which yields the local electrode potential E (Figure 6.5):

$$E(x, z) = \varphi_{e^-}(x, z) - \varphi_{io}(x, z) \tag{6.7}$$

The electrochemical active zone can spread on the whole FL at TPBls [9]. The electrochemical reactions locally absorb or generate charges and gas species that modify the electronic, ionic and gas fluxes. This phenomenon leads to a steep evolution of the local electrode potential all along the thickness of the active layer (see Section 6.3.2 for further details). Thus, the 'resulting' potential for the SOEC electrode can be defined as the difference of electronic and ionic potentials taken on

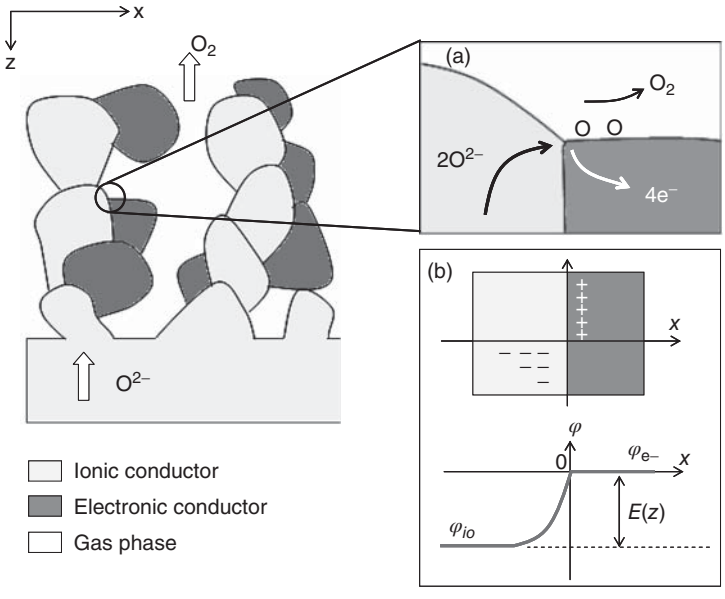

Figure 6.5 Representation of a porous SOEC anode functional layer. (a) Zoom on a triple phase boundary line where the charge transfer takes place. (b) Schematic of the potential distribution along the interface. (Adapted from Ref. [7].)

each side of the FL [9]:

$$E^{\text{Anode}}(x) = \left(\varphi_{\text{e}^-}^{\text{AFL}} - \varphi_{\text{io}}^{\text{Anode}}\right) \text{ and } E^{\text{cathode}}(x) = \left(\varphi_{\text{e}^-}^{\text{CFL}} - \varphi_{\text{io}}^{\text{Cathode}}\right) \tag{6.8}$$

These expressions of electrode potential encompass all the phenomena that participate in the electrochemical process within the FL. It may be noted that the anodic potential is positive ($E^{\text{Anode}} > 0$) while the cathodic one is negative ($E^{\text{Cathode}} < 0$). In operation, the anode potential increases while the cathode potential decreases. Both electrode polarizations result in a higher cell voltage according to Equation 6.3.

Reversible Potential and Limitation by Gas Conversion We consider in this paragraph an 'ideal' electrode that can operate by infinitesimal changes. This assumption means that the system evolves without energy dissipation or entropy production. In this condition, the electrode potential E reduces to a 'reversible' or thermodynamic contribution, denoted as E_{rev}, for which any change in net free energy, $|\Delta G|$, is balanced by the minimum electrical work $nF|E_{\text{rev}}|$ that is requested for electrolysis (see Chapter 1):

$$|\Delta G| = nF|E_{\text{rev}}| \tag{6.9}$$

where n is the number of exchange electrons involved in the reaction and F the Faraday constant. The reversible electrode potential can be expressed according

to the Nernst equation as a function of the temperature T, the gas constant R and the activities of gas species [10].

Ideal gas behaviour and atmospheric pressure condition are generally assumed for SOEC electrodes. Activities are then equal to partial pressure, and, thus, the 'Nernst' or 'reversible' electrode potential is written as follows (see system of coordinates in Figure 6.4):

$$O^{2-} \rightarrow \frac{1}{2}O_2 + 2e^- : \Delta G^0_{\text{Anode}} + RT\ln\left(P^{\text{canal}}_{O_2}(x)\right)^{1/2} = 2F\left(\varphi^{\text{Anode}}_{e^-,\text{rev}}(x) - \varphi^{\text{Anode}}_{\text{io, rev}}(x)\right)$$
$$\rightarrow E^{\text{Anode}}_{\text{rev}}(x) = E^{\text{Anode}}_0(T) + \frac{RT}{4F}\ln P^{\text{canal}}_{O_2}(x) \text{ with } E^{\text{Anode}}_0(T) = \frac{\Delta G^0_{\text{Anode}}}{2F} \tag{6.10a}$$

$$H_2O + 2e^- \rightarrow H_2 + O^{2-} : \Delta G^0_{\text{Cathode}} + RT\ln\frac{P^{\text{canal}}_{H_2}(x)}{P^{\text{canal}}_{H_2O}(x)}$$
$$= 2F\left(\varphi^{\text{Cathode}}_{\text{io, rev}}(x) - \varphi^{\text{Cathode}}_{e^-,\text{ rev}}(x)\right)$$
$$\rightarrow E^{\text{Cathode}}_{\text{rev}}(x) = E^{\text{Cathode}}_0(T) + \frac{RT}{2F}\ln\frac{P^{\text{canal}}_{H_2O}(x)}{P^{\text{canal}}_{H_2}(x)} \text{ with } E^{\text{Cathode}}_0(T)$$
$$= \frac{-\Delta G^0_{\text{Cathode}}}{2F} \tag{6.10b}$$

where ΔG^0 corresponds to the free energy in the standard conditions. The terms P^{canal}_i denote the partial pressure of the species i taken in the channel of gas distribution designed in the interconnect. At this stage, as the thermodynamic conditions are assumed to be fulfilled, the mass transfer across the electrode is not a limiting step. As a consequence, the partial pressures in the channel of gas distribution are equal to the ones in the vicinity of the active TPB sites (i.e. close to the interface with the electrolyte).

The reversible electrode potentials can be shared by one contribution at the open circuit potential (OCP) (i.e. $i = 0$) and a second one that modifies the electrode polarization under current (i.e. $i \neq 0$). This modification is denoted as ΔV_{rev}. Mathematical expressions for ΔV_{rev} can be directly deduced from Equation 6.10 leading to the relations (6.11) for the anode:

$$E^{\text{Anode}}_{\text{rev}} = E^{\text{Anode}}_{\text{OCP}} + \Delta V^{\text{Anode}}_{\text{rev}} \rightarrow E^{\text{Anode}}_{\text{0CP}} = E^{\text{Anode}}_0 + \frac{RT}{4F}\ln P^{\text{canal}}_{O_2_i=0} \tag{6.11a}$$

$$\text{and } \Delta V^{\text{Anode}}_{\text{rev}}(x) = \frac{RT}{4F}\ln\frac{P^{\text{canal}}_{O_2_i\neq 0}(x)}{P^{\text{canal}}_{O_2_i=0}} \tag{6.11b}$$

and the relations (6.12) for the cathode:

$$E^{\text{Cathode}}_{\text{rev}} = E^{\text{Cathode}}_{\text{OCP}} + \Delta V^{\text{Cathode}}_{\text{rev}} \rightarrow E^{\text{Cathode}}_{\text{0CP}} = E^{\text{Cathode}}_0 + \frac{RT}{2F}\ln\frac{P^{\text{canal}}_{H_2O_i=0}}{P^{\text{canal}}_{H_2_i=0}} \tag{6.12a}$$

$$\text{and} \quad \Delta V_{\text{rev}}^{\text{Cathode}}(x) = \frac{RT}{2F} \ln \frac{P_{\text{H}_2_i=0}^{\text{canal}} \times P_{\text{H}_2\text{O}_i\neq 0}^{\text{canal}}(x)}{P_{\text{H}_2_i\neq 0}^{\text{canal}}(x) \times P_{\text{H}_2\text{O}_i=0}^{\text{canal}}} \tag{6.12b}$$

where $P_{j_i=0}^{\text{canal}}$ and $P_{j_i\neq 0}^{\text{canal}}$ correspond, respectively, to the partial pressure of each species j at OCP ($i = 0$) and under current ($i \neq 0$).

$\Delta V_{\text{rev}}^{\text{Anode}}$ and $\Delta V_{\text{rev}}^{\text{Cathode}}$ correspond to the 'reversible' electrode polarizations. As shown by Equations 6.11 and 6.12, they are ascribed to a modification of gas composition that takes place all along the cell because of the electrolysis reaction. This means that, even for an ideal 'thermodynamic' process, polarizations are inevitably caused by the gas conversion that modifies the fluid composition from the inlet to the cell outlet. For instance, when oxygen is produced at the anode, O_2 partial pressure in operation is higher than the one at OCP ($P_{O_2_i\neq 0}^{\text{canal}} > P_{O_2_i=0}^{\text{canal}}$). According to Equation 6.11b, such an evolution results in $\Delta V_{\text{rev}}^{\text{Anode}}$ terms higher than zero ($\Delta V_{\text{rev}}^{\text{Anode}} > 0$), which increase the electrode potential and the cell voltage simultaneously. At the cathode side, gas conversion is due to the consumption of steam and the production of hydrogen. It results in a polarization $\Delta V_{\text{rev}}^{\text{Cathode}}$ lower than 0 ($\Delta V_{\text{rev}}^{\text{Cathode}} < 0$), which decreases the electrode potential and increases the cell voltage.

At very high steam conversion rate, all the water is consumed in such way that the steam partial pressure decreases sharply at the cell outlet. Consecutively, hydrogen partial pressure reaches values close to unity. In these conditions, the cathodic polarization due to the gas conversion tends to an unbounded limit according to Equation 6.12b. This behaviour yields very high cell voltages, leading to a limiting current density when the steam conversion rate reaches 100%.

If the cathode inlet is fed with air, the stream will be enriched in oxygen up to the cell outlet. The rise of oxygen partial pressure from 0.21 to 1 also induces electrode polarization. However, unlike the cathode side, $\Delta V_{\text{conc}}^{\text{Anode}}$ increases to a bounded value according to Equation 6.11b.

Electrode Irreversible Overpotentials Aside from the Nernst contribution, the electrode potential is also impacted by some irreversible processes occurring in the electrode. They are associated with the real electrode operation that leads to the production of entropic terms. These irreversibilities induce the so-called activation and concentration overpotentials, respectively denoted as η_{act} and η_{conc}. They can be seen as a supplementary potential necessary to overcome a barrier induced by the energy dissipated by the whole electrochemical process:

$$E^{\text{Anode}} - E_{\text{rev}}^{\text{Anode}} = \eta^{\text{Anode}}(x) \ \text{ with } \ \eta^{\text{Anode}}(x) = \eta_{\text{conc}}^{\text{Anode}}(x) + \eta_{\text{act}}^{\text{Anode}}(x) \quad (\eta^{\text{Anode}} > 0) \tag{6.13a}$$

$$E^{\text{Cathode}} - E_{\text{rev}}^{\text{Cathode}} = \eta^{\text{Cathode}}(x) \ \text{ with } \ \eta^{\text{Cathode}}(x) = \eta_{\text{conc}}^{\text{Cathode}}(x) + \eta_{\text{act}}^{\text{Cathode}}(x) \quad (\eta^{\text{Cathode}} < 0) \tag{6.13b}$$

The potential losses due to η_{act} and η_{conc} are thus linked to the mechanisms that limit the kinetic rate of the global electrochemical reaction. The concentration overpotential is attributed to a mass transfer limitation across the porous electrode, while the activation overpotential is associated to the electrochemical reaction mechanisms itself.

It is assumed in this paragraph that the global overpotential η can be expressed from the well-known generalized Butler–Volmer equation [10]:

$$i(x) = i_0^{\text{Anode}} \left\{ \left(\frac{P^{\text{TPBs}}_{O_2_i\neq O}(x)}{P^{\text{canal}}_{O_2_i\neq O}(x)} \right)^{1/2} e^{\frac{-(1-\alpha^{\text{Anode}})2F(\eta^{\text{Anode}}(x))}{RT}} - e^{\frac{\alpha^{\text{Anode}}2F(\eta^{\text{Anode}}(x))}{RT}} \right\}$$
$$\text{with } (\eta^{\text{Anode}} > 0;\ \ i < 0) \tag{6.14a}$$

$$i(x) = i_0^{\text{Cathode}} \left\{ \left(\frac{P^{\text{TPBs}}_{H_2_i\neq O}(x)}{P^{\text{canal}}_{H_2_i\neq O}(x)} \right) e^{\frac{(1-\alpha^{\text{Cathode}})2F(\eta^{\text{Cathode}}(x))}{RT}} - \left(\frac{P^{\text{TPBs}}_{H_2O_i\neq O}(x)}{P^{\text{canal}}_{H_2O_i\neq O}(x)} \right) e^{\frac{-\alpha^{\text{Cathode}}2F\left(\eta^{\text{Cathode}}(x)\right)}{RT}} \right\} \text{ with } (\eta^{\text{Cathode}} < 0;\ \ i < 0) \tag{6.14b}$$

where α is the symmetrical factors and i_0 the electrode exchange current density. In these expressions, it may be noted that the activity of oxygen ions is taken to be unity ($a_{O^{2-}} = 1$).

Concentration Overpotentials The porous electrode opposes a resistance to the gas transfer from the gas channel distribution to the electrochemical active sites (TPBs). This limitation to the gas transport across the electrode induces some partial pressure gradients, which are strongly dependent on the microstructural properties of porous electrodes. This phenomenon results in a modification of fluid composition at TPBs so that polarization losses arise in operation. These cell polarizations are ascribed to the so-called concentration overpotentials η_{conc}.

Concentration overpotentials are exacerbated at high current densities as these operating conditions impose high gas fluxes through the electrodes. Therefore, the expression for η_{conc} can be deduced from the generalized Butler–Volmer equation when $|i| \gg 0$ so that cell polarization is dominated by the concentration overpotential ($\eta \to \eta_{conc}$). If we consider in addition that the system is rapid at high temperature ($i_0 \gg i$ so that $|i|/i_0 \to 0$), the concentration overpotential can be derived from Equation 6.14 as follows:

$$\eta_{conc}^{\text{Anode}}(x) = \frac{RT}{4F} \ln \frac{P^{\text{TPB}}_{O_2_i\neq 0}(x)}{P^{\text{canal}}_{O_2_i\neq 0}(x)} \tag{6.15a}$$

$$\eta_{conc}^{\text{Cathode}}(x) = \frac{RT}{2F} \ln \frac{P^{\text{canal}}_{H_2_i\neq 0}(x) \times P^{\text{TPB}}_{H_2O_i\neq 0}(x)}{P^{\text{TPB}}_{H_2_i\neq 0}(x) \times P^{\text{canal}}_{H_2O_i\neq 0}(x)} \tag{6.15b}$$

Gas transfer across the porous electrodes is likely to be driven as much as by a permeation flow than a diffusional process. However, the effective gas diffusivities of typical SOEC electrodes are high compared to their permeability coefficient. It means that the viscous flow associated to an elevation of pressure in the electrode can be considered negligible compared to the diffusive fluxes [11–13]. As a consequence, concentration overpotentials arising in an SOEC electrode are mainly controlled by an insufficient gas diffusion through the electrode.

This claim is especially well verified at the cathode side. Indeed, the release of one hydrogen compound is accompanied by the consumption of one water molecule. Therefore, the H_2O and H_2 species flow at the same rate but in an opposite direction. In these conditions, any increase of total pressure near the electrode/electrolyte interface due to the generation of hydrogen will be roughly balanced by the opposite steam flow. Unlike the cathode, the oxygen production at the anode side could result in an increase in pressure in a region close to the interface with the electrolyte [14].

Governing equations for gaseous species transport within the typical porous SOEC electrodes are given in detail in the next section 6.3.2.

Activation Overpotentials Aside from the mass transfer limitation, the activation overpotentials encompass the irreversible phenomena that occur in the active FL. It can be, for example, the migration rate of the oxygen ions across the ionic structure of the FL (Figure 6.5). The activation overpotentials also include the limitation due to the kinetic rates of each multi-elementary reaction involved in the electrochemical process. Indeed, at high temperature, the global electrochemical reaction is not generally limited by a single step, such as the charge transfer, but is rather described by a sequence of elementary reactions. The more likely reaction pathways for SOEC electrodes are discussed in the next section.

At the 'macroscopic' cell level, several studies [15–18] have shown that the global activation overpotential could be modelled by the well-known Butler–Volmer equation. However, it has to be mentioned that this approach remains purely phenomenological as the Bulter–Volmer formalism is rigorously adapted only for a single charge transfer happening at the electrode/electrolyte interface.

The equation for expressing 'global' activation overpotentials can then be deduced from the generalized Butler–Volmer relation (Equation 6.14) at low current density for which $\eta \rightarrow \eta_{\text{act}}$ and $P_i^{\text{canal}} \approx P_i^{\text{TPB}}$:

$$i(x) = i_0^{\text{Anode}} \left\{ \mathrm{e}^{\frac{-\left(1-\alpha^{\text{Anode}}\right)2F\left(\eta_{\text{act}}^{\text{Anode}}(x)\right)}{RT}} - \mathrm{e}^{\frac{\alpha^{\text{Anode}}2F\left(\eta_{\text{act}}^{\text{Anode}}(x)\right)}{RT}} \right\} \tag{6.16a}$$

$$i(x) = i_0^{\text{Cathode}} \left\{ \mathrm{e}^{\frac{\left(1-\alpha^{\text{Cathode}}\right)2F\left(\eta_{\text{act}}^{\text{Cathode}}(x)\right)}{RT}} - \mathrm{e}^{\frac{-\alpha^{\text{Cathode}}2F\left(\eta_{\text{act}}^{\text{Cathode}}(x)\right)}{RT}} \right\} \tag{6.16b}$$

where the symmetrical factors α are usually taken as 0.5 for both electrodes [16]. The parameters $i_{0,\text{anode}}$ and $i_{0,\text{cathode}}$ represent the 'apparent' anode and cathode

exchange current densities, respectively. They are expressed in amperes normalized by the active electrode surface area. They must not be mixed with the 'real' kinetic constant for charge transfer that is used at the 'microscopic' scale (see following section 6.3.2). Indeed, the term i_0 characterizes the electrode ability regarding its global electrochemical activity. In other words, the higher the 'apparent' exchange current density, the lower is the 'global' activation overpotential. Note that this parameter is usually obtained by fitting the experimental data at low current density.

According to the global approach presented in this section, the 'apparent' exchange current density is a parameter that encompasses the phenomena that hinder the electrochemical kinetic rates (apart from the one due to the mass transfer limitation that is already taken into account in the concentration overpotential). From this point of view, the 'apparent' exchange current density is likely to depend on several parameters such as the atmosphere, the temperature, the O^{2-} mobility in the FL and the electrode microstructural properties.

First of all, it is obvious that the electrode exchange current density is directly related to the electrochemical activity of materials. Moreover, as the electrolysis reactions are based on thermally activated processes, the value of i_0 strongly depends on the local temperature. Further details on this thermal behaviour are discussed in Section 6.3.3.2.

The 'apparent' exchange current density is also affected by the electrode microstructure. For instance, the exchange current density increases with the density of TPBls. Indeed, higher densities of TPBls directly enhance the electrode efficiency by offering more sites for the electrochemical reaction. Therefore, it is worth keeping in mind that any value of i_0 is strongly correlated to the microstructural characteristics of the FL.

Nevertheless, despite this dependence with the electrode microstructural properties, it is possible to give some typical values for i_0 that are the most representative of SOEC electrodes. Thus, values within the range of 500–600 mA cm^{-2} are reported for Ni–8YSZ cathodes operated at 800 °C [16, 18]. At the same temperature, the exchange current density for LSM–8YSZ anodic composites is roughly equal to 200 mA cm^{-2} [16, 18], whereas the typical value for MIECs such as LSC approaches 500 mA cm^{-2} [19].

6.3.1.4 Global Decomposition of the Cell Polarization Curve

As the interconnect plates are good electronic conductors, the potentials $\varphi^1_{e^-}$ and $\varphi^2_{e^-}$ and hence the cell voltage $U = \varphi^1_{e^-} - \varphi^2_{e^-}$ (Figure 6.4) can be considered constant all along the cell length. This assumption means that, for a given cell voltage, the local current densities $i(x)$ are distributed in such a way that Equation 6.17 is verified at each position x along the cell length. This last relation has been obtained by introducing into the Equation 6.3 each contribution to the cell polarization curve detailed in the previous section:

$$U = U_{rev}(x) + \eta_{ohmic}(x) + \eta^{Anode}_{act}(x) + \eta^{Anode}_{conc}(x) - \eta^{Cathode}_{act}(x) - \eta^{Cathode}_{conc}(x) \quad (6.17)$$

- The term U_{rev} refers to the 'thermodynamic' or 'reversible' voltage. It can be decomposed into one component at the open circuit voltage (OCV) and a second contribution that arises in operation. This second contribution simply refers to the cell polarizations due to the gas conversion (cf. Equations 6.11 and 6.12):

$$U_{rev} = U_{OCV} + \Delta V_{rev}^{Anode} - \Delta V_{rev}^{Cathode} \text{ with } U_{OCV} = E_{OCP}^{Anode} - E_{OCP}^{Cathode} \quad (6.18)$$

  It is worth mentioning that the gas conversion losses depend only on the operating conditions defined by the current density and the gas feeding conditions. These 'thermodynamic' contributions are thus 'unavoidable' and will be the same whatever the SOEC materials. In these conditions, cell polarization curves can be compared only if the contributions ΔV_{rev}^{Anode} and $\Delta V_{rev}^{Cathode}$ are identical. In other words, assessment in performances of different cells is relevant only if the $U-i$ curves are compared at the same gas conversion rates (i.e. for identical conditions of inlet gas fluxes that lead to the same steam conversion and oxygen production rates).
- The ohmic overpotential η_{ohmic} includes the ionic resistances of the electrolyte and the electronic resistances of both CC layers (cf. Equations 6.4–6.6):

$$\eta_{ohmic} = (R_{electrolyte} + R_{ACC}^{eff} + R_{CCC}^{eff} + R_c^{Anode} + R_c^{Cathode}) \times |i(x)| \quad (6.19)$$

  The effective resistances induced by the electrode collecting layers are usually low as the effective conductivities of typical porous electrodes are high at the SOEC operating temperature (i.e. $\approx 650-1200\,\Omega^{-1}\,cm^{-1}$ for an Ni–YSZ cathode [20–22] and $\approx 70-140\,\Omega^{-1}\,cm^{-1}$ for an LSM anode [22, 23]). Conversely to the electrodes, the ionic conductivity of the dense electrolyte remains relatively poor in spite of the high temperatures of operation (i.e. $\approx 0.026-0.044\,\Omega^{-1}\,cm^{-1}$ at 800 °C for 8YSZ: cf. Section 6.3.3.2). The ionic losses represent a significant contribution to the total cell overpotential. As shown in Equation 6.5, they are strongly dependent on the electrolyte thickness, and hence on the cell configuration. Therefore, the CSC geometry has been designed to lower the ohmic losses by reducing the thickness of the electrolyte.
  In the SOEC stack, the contact resistance of the electrode/interconnect junction depends on many parameters. Besides the natures of the involved materials, the contact resistance is a function of the local design of the contacts [5, 24] and the compressive load applied on the stack [5, 25]. Note that an interlayer or a metallic grid is usually added between the interconnect and the electrode to reduce the contact resistivity. Despite all of these precautions, typical contact resistance of $0.05\,\Omega\,cm^2$ is reported for a typical SOEC planar stack [26]. As a consequence, improvements of electrode/interconnect electrical contact remain an important issue regarding the global SOEC stack performance.
- The activation overpotentials, η_{act} in Equation 6.17, depend on the electrode characteristics through the electrode exchange current densities. As already mentioned for i_0, it is obvious that the electrochemical activity of materials directly impacts the activation overpotentials. Moreover, these overpotentials

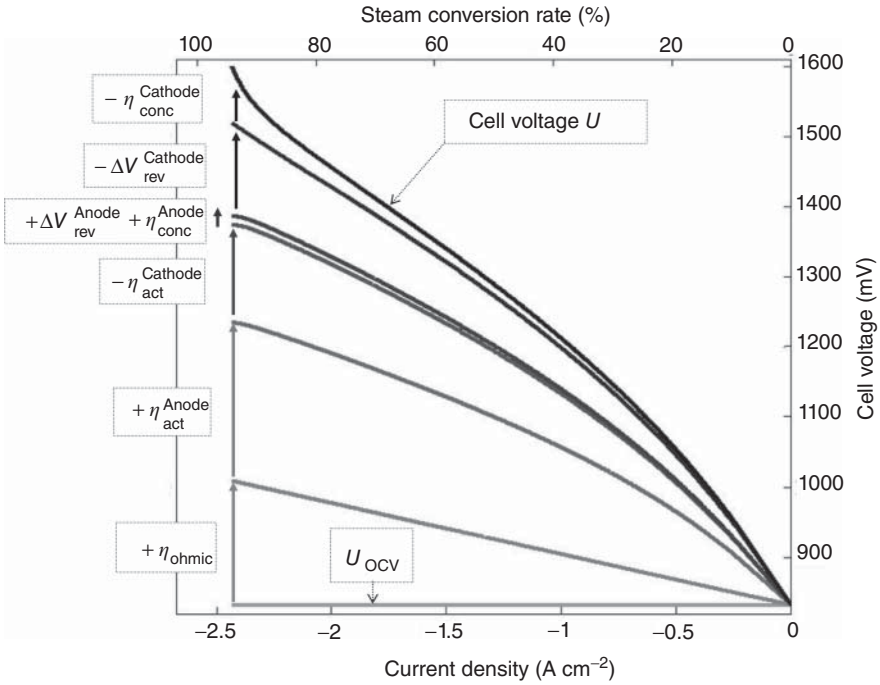

Figure 6.6 Decomposition of a typical polarization curve for cathode-supported cell (Ni–8YSZ//8YSZ//LSM–8YSZ, $T = 800\,°C$, $R_c = 5 \times 10^{-2}\ \Omega\ cm^2$, air feeding at the anode side, composition of the inlet cathodic gas: 90% H_2O + 10% H_2, electrode microstructural properties are given in Ref [9], $\ell^{\text{support}}_{\text{cathode}} = 1$ mm, $\ell_{\text{electrolyte}} = 10$ μm, $\ell_{\text{anode}} = 40$ μm). Numerical decomposition calculated by using the model presented in Ref [17].

are also mitigated by the microstructure features of the FLs that also play a key role in the electrode efficiency.

- The concentration overpotentials η_{conc} are a function of the resistance that the porous medium opposes in the gas flow. Concentration overpotentials are then strongly affected by the layer thickness and by the morphological characteristics of the porous network.

To conclude this section, Figure 6.6 shows a polarization curve for a typical CSC manufactured with the classical materials (i.e. Ni–8YSZ for the cathode, 8YSZ for the electrolyte and LSM–8YSZ for the anode). The cell voltage has been decomposed into the different polarization losses thanks to a numerical analysis published in the articles [17, 18]. Note that in this representation, the resulting current density and the overpotentials are integrated on the cell active surface area. Such kinds of numerical decomposition [15, 17] have shown that the LSM–YSZ anode activation overpotentials are significant. Conversely, the polarization due to the Ni–YSZ cathode overpotentials is much more restricted. Concentration overpotentials are moderated for thin electrodes. However, in the case of thick CSCs, concentration overpotentials can increase drastically with current density.

6.3.2
Fundamental for Electrochemistry, Mass and Charge Transfer in SOEC Electrodes

This section aims to give the basic phenomena and the fundamental equations governing the SOEC electrode behaviour. The reader who might not be interested in such level of details may skip this section and go directly to the next one.

A local approach is adopted hereafter by taking into consideration a slice of the electrode. As illustrated in Figure 6.7, the elementary slice is located along the cell length at a position between x and $x + \mathrm{d}x$ (cf. system of coordinate in Figure 6.4). At this position, the gas conversion rate and the partial pressures in the canal $P^{\mathrm{Canal}}_{j=\mathrm{H_2},\,\mathrm{H_2O},\cdots}(x)$ are fixed and used as boundary conditions. The 'reversible' or thermodynamic electrode potential $E^{\mathrm{Electrode}}_{\mathrm{rev}}(x)$ is then given according to Equation 6.10. It should be noted that in this section the current density is positive if considering the anode and negative for the cathode (i.e. anode: $i > 0$ and $E > 0$; cathode: $i < 0$ and $E < 0$).

Governing equations and basic phenomena are first presented for the case depicted in Figure 6.7. It corresponds to a classical active FL composed of a pure electronic conducting electrode mixed with the electrolyte material (such as the LSM–YSZ composite in Figure 6.7a or the Ni–YSZ cermet in Figure 6.7b). Specific operating mechanisms of single-phase electrodes made of an MIEC are detailed elsewhere (see Section 6.3.2.4). The role of the electrode microstructure on electrochemistry is discussed at the end of this section.

6.3.2.1 Electronic and Ionic Charge Transport into the Electrode

Electronic Flow into the Electrode Current Collector and Functional Layer As mentioned in Section 6.3.1.2, the current density $i_{\mathrm{e}^-}(x)$ is described through the classical Ohm's law. Under the assumption of an unidirectional electronic flow perpendicular to the electrolyte interface (i.e. in the $\vec{z}$ direction), Ohm's law can be written for any elementary strip of electrode positioned between z and $z + \mathrm{d}z$:

$$\vec{i}_{\mathrm{e}^-} = -\sigma^{\mathrm{eff}}_{\mathrm{e}^-} \times \mathrm{grad}(\varphi_{\mathrm{e}^-}) \quad \Rightarrow \quad i_{\mathrm{e}^-} = -\sigma^{\mathrm{eff}}_{\mathrm{e}^-} \frac{\mathrm{d}\varphi_{\mathrm{e}^-}}{\mathrm{d}z} \quad 0 \le |z| \le \ell_{\mathrm{FL}} + \ell_{\mathrm{CC}} \quad (6.20)$$

where $\sigma^{\mathrm{eff}}_{\mathrm{e}^-}$ denotes the effective conductivities of the electronic conducting phase related to the CC or the FL. If we consider the systems illustrated in Figure 6.7, the local coordinate z ranges from the electrode/electrolyte interface up to the top of the CC (i.e. $0 \le |z| \le \ell_{\mathrm{FL}} + \ell_{\mathrm{CC}}$).

- It is worth mentioning that the ECC is a purely resistive medium without any electronic source. This means that the current density is constant through the collecting layer so that Equation 6.20 can be directly integrated along the layer

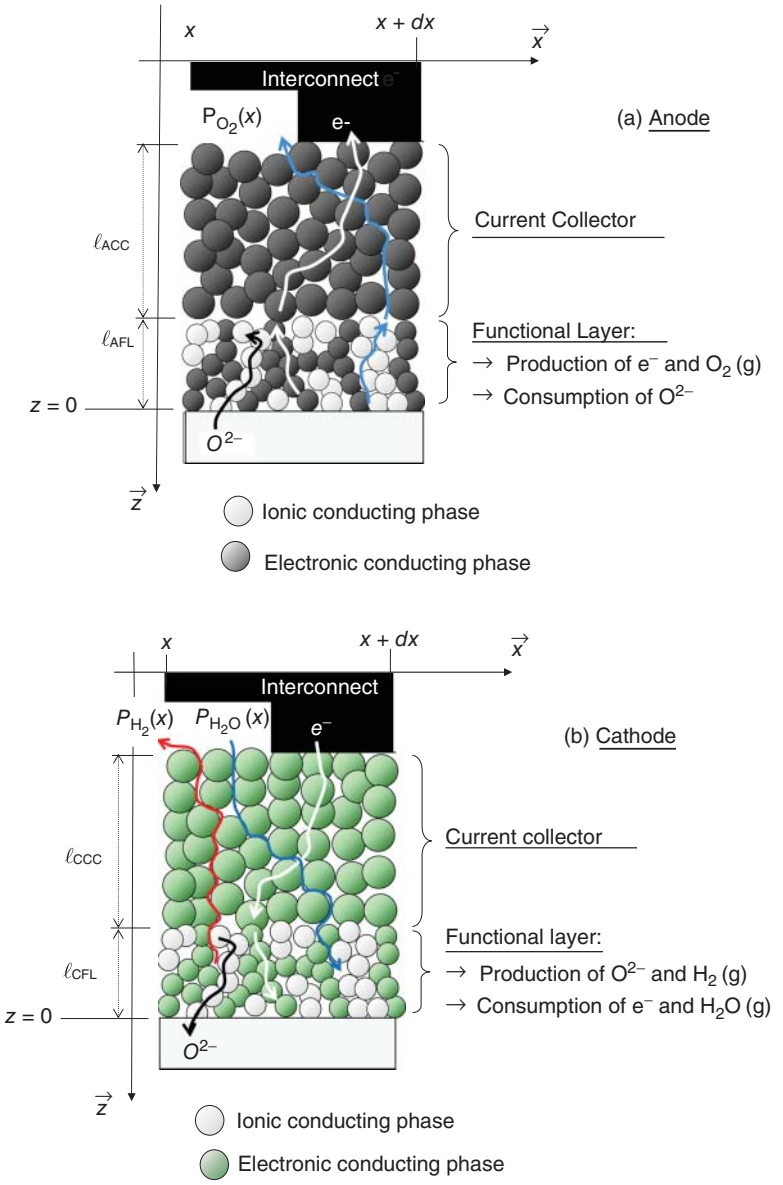

Figure 6.7 Scheme of an electrode slice considered for the local approach (case of (a) the anode and (b) the cathode). The system of local coordinates and the flow directions of gaseous, ionic and electronic species are also represented.

thickness. The result of this integration leads to the electrode ohmic losses presented in Section 6.3.1.2 (cf. Equation 6.4):

$$\int_{\varphi_{e^-}^{z=-\ell_{FL}-\ell_{CC}}}^{\varphi_{e^-}^{z=-\ell_{FL}}} -\mathrm{d}\varphi_{e^-} = \int_{z=-\ell_{FL}-\ell_{CC}}^{z=-\ell_{FL}} \frac{i_{e^-}}{\sigma_{CC}^{eff}}\mathrm{d}z \quad \Rightarrow \quad \left(\varphi_{e^-}^{z=-\ell_{FL}-\ell_{CC}} - \varphi_{e^-}^{z=-\ell_{FL}}\right) = \frac{\ell_{CC}}{\sigma_{CC}^{eff}} \times i_{e^-}$$

$$\text{(for current collector : } \ell_{FL} \leq |z| \leq \ell_{FL} + \ell_{CC} \text{ see Figure 6.7)} \qquad (6.21)$$

- Due to the electrochemical reaction in the FL, electrons are either consumed at the anode or produced at the cathode. The electron consumption or production yields sources that are generated or absorbed into the electronic conducting phase. These electrical sources are related to a specific current density $j(z)$, which is expressed in amps per unit volume of electrode. The term $j(z)$ is assumed to be positive at the anode as the electrons are released and negative at the cathode as they are absorbed. In both cases, they increase the absolute value of the current density from the electrode/electrolyte interface up to the interface with the ECC (where electrons are collected if considering the anode or supplied if considering the cathode: see Figure 6.7). This typical evolution is illustrated in Figure 6.8 for an LSM–YSZ anode.

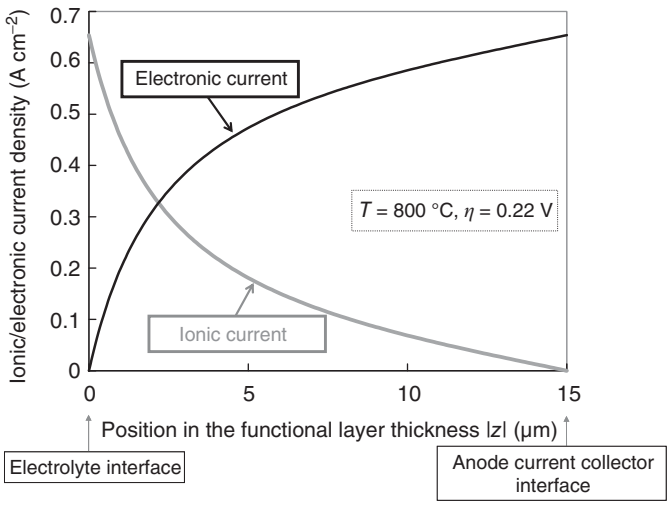

Figure 6.8 Evolution of the ionic and electronic current densities in the thickness of a typical anode functional layer at $T = 800\,°C$, $\eta = 0.22\,V$ for $i = 0.65\ A\ cm^{-2}$. The curves have been computed with the electrode model describe in Ref [27]. (LSM/LSM–8YSZ, $\ell_{AFL}^{LSM\text{-}8YSZ} = 15\ \mu m$, $\ell_{CCC}^{LSM} = 15\ \mu m$, $P_{O_2}^{canal} = 0.21$, material conductivities: $\sigma_{io} = 2.6 \times 10^{-2}\ \Omega^{-1}\ cm^{-1}$, $\sigma_{e^-} = 128\ \Omega^{-1}cm^{-1}$, AFL microstructure properties: $\varepsilon_{gas}/\varepsilon_{8YSZ}/\varepsilon_{LSM} = 0.5/0.26/0.24$, $\tau_{gas}/\tau_{8YSZ}/\tau_{LSM} = 1.3/3.5/1.6$, $\bar{r}_p^{gas} = 1\ \mu m$, $\xi_{TPB} = 5\ \mu m^{-2}$, $S_p = 10\ \mu m^{-1}$, CCC microstructure properties: $\varepsilon_{gas}/\varepsilon_{LSM} = 0.5/0.5$, $\tau_{gas}/\tau_{LSM} = 1.3/1.3$, elementary kinetic modelled into a charge transfer at TPBls and an oxygen associative desorption step: see Section 6.3.2.3).

The modifications of the current density inside the FL can be described through simple charge balances. For an electrode slice of thickness dz, the variations in current density are then written as follows:

$$\mathrm{div}(\vec{i}_{e^-}) = -j(z) \Rightarrow \mathrm{d}i_{e^-}(z) = -j(z)\mathrm{d}z \ \ (\text{for functional layer} : 0 \geq |z| \geq \ell_{FL}) \tag{6.22}$$

Note that the combination of Equation 6.22 for electrical conservation and Equation 6.20 for charge fluxes yields the well-known Laplace equation (i.e. $\mathrm{div}(-\sigma_{e^-}^{eff} \times \mathrm{grad}(\varphi_{e^-})) = -j$).

Ionic Flow into the Functional Layer Within the FL, an ionic current density i_{io} has to be considered in the ionic conducting phase. Indeed, as depicted in Figure 6.7a for anodic polarization, oxygen ions have to be transferred from the electrolyte up to the electrochemical active sites. For cathodic polarization, oxygen ions are released in the ionic conducting phase and flow from the active sites towards the electrolyte (Figure 6.7b). As the O^{2-} transport into the ionic material is based on a solid-state diffusion process, the ionic current density i_{io} is expressed by the classical Ohm's law:

$$\vec{i}_{io} = -\sigma_{io}^{eff} \times \mathrm{grad}(\varphi_{io}) \ \Rightarrow \ i_{io} = -\sigma_{io}^{eff}\frac{\mathrm{d}\varphi_{io}}{\mathrm{d}z} \ \ (\text{for functional layer} : 0 \geq |z| \geq \ell_{FL}) \tag{6.23}$$

where σ_{io}^{eff} denotes the effective conductivity of the electrode ionic conducting phase.

The source terms $j(z)$, which are linked to the electrochemical reactions, also modify the ionic current all along the FL. As a consequence, the variation in ionic current density can also be described through simple charge balances (such as the ones written for the electronic contribution in Equation 6.22):

$$\mathrm{div}(\vec{i}_{io}) = +j(z) \Rightarrow \mathrm{d}i_{io}(z) = +j(z)\mathrm{d}z \ \ (\text{for functional layer} : 0 \geq |z| \geq \ell_{FL}) \tag{6.24}$$

At the electrode/electrolyte interface, the absolute value of the ionic current density $|i_{io}|$ is equal to its value inside the electrolyte. Because of the electrochemical reaction, it decreases continuously all along the thickness of the FL. In other words, as shown in Figure 6.8, the ionic current is 'transformed' into an electronic contribution all along the FL.

Along with this process, it can be remarked that electro neutrality has to be respected at each position in the FL. This condition means that the ionic and electronic current must vary in opposite ways. Therefore, any modification of the ionic current in the FL thickness must be balanced by the reverse variation in electronic current:

$$\mathrm{d}i_{io}(z) = -\mathrm{d}i_{e^-}(z) \ \ (\text{for functional layer} : 0 \geq |z| \geq \ell_{FL}) \tag{6.25}$$

Note that this last equation is redundant with Equation 6.22 (or Equation 6.21) as both reflect the same phenomenon.

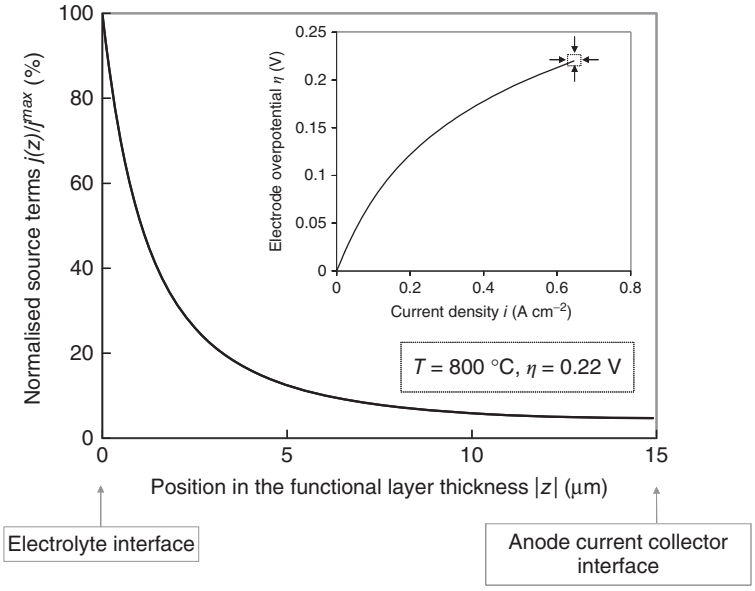

Figure 6.9 Distribution of the source term $j(z)$ in a typical anode functional layer at $T = 800\,°C$, $\eta = 0.22$ V for $i = 0.65\,A\,cm^{-2}$. Inset shows the polarization curve of the studied electrode (see conditions reported in the legend of Figure 6.8). The curves have been computed with the electrode model describe in Ref. [27].

Distribution of the Source Terms *j(z)* in the Functional Layer: Extent of the Electrochemical Active Zone Repartition of source terms $j(z)$ in the thickness of the FL is a direct representation of the distribution of the electrochemical reactions. Figure 6.9 shows the profile of $j(z)$ calculated for a commercial SOEC anode. A steep decrease can be observed in the electronic sources from the electrolyte interface up to the ACC. This evolution characterizes the possibility for the electrochemical reactions to extend within the FL.

The distribution of $j(z)$ is totally governed by the ability of the ionic, electronic and gas species to reach the electrochemical active sites. It has been shown that diffusion of gas across a thin FL is not limiting and does not influence the distribution of $j(z)$ [27]. Moreover, the electronic conductivities of SOEC electrode materials are much higher than their ionic conductivities (for instance, $\sigma_{io}^{8YSZ} \ll \sigma_{e^-}^{Ni}$). As a consequence, the distribution of the electrochemical reaction is mainly controlled by the 'low' mobility of oxygen ions flowing from (or towards) the electrolyte interface. This phenomenon explains why the electrochemical reactions mainly occur in a region nearby the electrolyte interface and decrease steadily within the FL (Figure 6.9).

For typical SOEC electrodes, it has been shown that the electrochemical reactions can spread into the electrode over a limited distance from the electrolyte interface. Several studies have been devoted to assess the thickness of this electrochemically active zone. It has been found that its dimension ranges

between 5 and 40 μm [27–31], depending on material conductivities, electrode microstructure properties [27, 28] and temperatures [30]. The extent of the electrochemical reaction is also modified in operation by the electrode polarization [28]. In general, thicknesses of typical SOEC FLs are roughly designed to match with the dimension of the active zone. In practice, the thicknesses of SOEC FLs do not exceed a few tens of micrometres (10 μm $\leq \ell_{FL} \leq$ 30 μm) and can be considered wholly active regarding the electrochemical reactions [9, 27].

Correlation Between Electrical Conductivities and Profile of Electrochemical Reactions
It is worth mentioning that electronic and ionic conductivities of SOEC electrode materials can strongly deteriorate after a long-term operation at high temperature (see Section 6.4.2). This degradation has potentially a strong impact on the distribution of the electrochemical reactions and, hence, on the electrode performances:

- As an illustration, the repartition of $j(z)$ has been calculated for the extreme case where the effective conductivity of the electronic conducting phase is equal to the effective conductivity of the ionic phase (i.e. $\sigma_{io}^{eff} = \sigma_{e^-}^{eff}$). The resulting profile of the source terms is plotted in Figure 6.10 for the anode. It can be observed that the electrochemical reactions are more homogeneously distributed than the previous repartition given in Figure 6.9 (at the same electrode overpotential). Indeed, in Figure 6.10, the reactions become favoured on each side of the

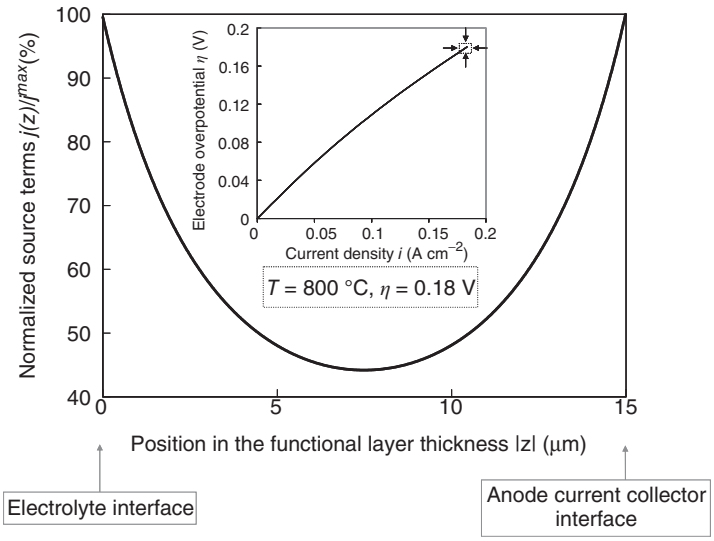

Figure 6.10 Distribution profile of the source term $j(z)$ across the anode functional layer with an effective conductivity ratio $\sigma_{io}^{eff}/\sigma_{e^-}^{eff} = 1$ (at $T = 800\,°C$, $i = 0.18$ A cm^{-2}, $\eta = 0.18$ V, $\sigma_{io}^{eff} = \sigma_{e^-}^{eff} = 2.6 \times 10^{-2}\ \Omega^{-1}\,cm^{-1}$). Inset shows the polarization curve of the studied electrode (see conditions reported in the legend of Figure 6.8). The curves have been computed with the electrode model describe in Ref. [27].

active FL and remain non-negligible in the bulk of the layer. This profile of the electrochemical reactions is explained by the specific assumption adopted here (of identical ionic and electronic effective conductivities). In that case, the distribution of the source terms along the thickness of the FL is governed as much by the diffusion of oxygen ions from the electrolyte as the electronic flux towards the ECC. As a consequence, the electrochemical reactions spread simultaneously from both sides of the FL, resulting in the symmetrical profile presented in Figure 6.10.

- Nevertheless, the very poor electronic conductivities of the FL result in low electrode performances. For instance, the electrode overpotential increases from $\eta = 0.115$ V for the 'fresh' electrode to $\eta = 0.179$ V for the 'aged' one (for the same current $i = 0.18$ A cm^{-2}: see inserts in Figures 6.9 and 6.10). This analysis shows that electrode performance depends on the material effective conductivities of the FL. This is especially true for the ionic conducting phase as its very low value limits the extent of the reactive zone [27]. From this point of view, any degradation of the ionic conductivities will be dramatic regarding the electrode efficiency.

6.3.2.2 Gas Transport in the Electrode

Gas Transfer Phenomena In a porous medium such as an SOEC electrode, gas transfer may originate from three distinct phenomena [32]:

- First of all, the gas flow can be driven by a gradient of concentration across the electrode. This mass transfer is related to the 'ordinary' or 'molecular' diffusion for which the gas flux N_i is due to a gradient of concentration (or partial pressures) across the electrode. As illustrated in Figure 6.11a for a gas mixture composed of two species, A and B, the flux of A is counterbalanced by the flux of B as there is no accumulation of molecules in the electrode (in mathematical terms, $N_A \propto \text{grad}(P_A)$ and $N_A = -N_B \propto \text{grad}(P_B)$ as $P_A = P_T - P_B$). The proportionality between the flux and gradient of concentrations is then described by a unique parameter, named the effective 'binary' diffusion coefficient, $D^{\text{eff}}_{\text{A,B}}$, which is related to the system of two molecules. This coefficient takes into account the effect of molecule interactions and the microstructure of electrode porosity. The diffusive molar fluxes are expressed by the well-known Fick's law as follows:

$$N_A = -\frac{D^{eff}_{A,B}}{RT} \times grad(P_A) = -N_B = \frac{D^{eff}_{A,B}}{RT} \times grad(P_B)$$
$$(P_T = \text{constant: see Figure 6.11a}) \tag{6.26}$$

One can note that the underlying mechanism for molecular diffusion comes from the thermal motion of gas and is controlled by the collision frequency between the molecules. Therefore, the diffusive molecular flux is predominant for microstructures presenting large pores so that the interaction of gas species with the pore walls is negligible.

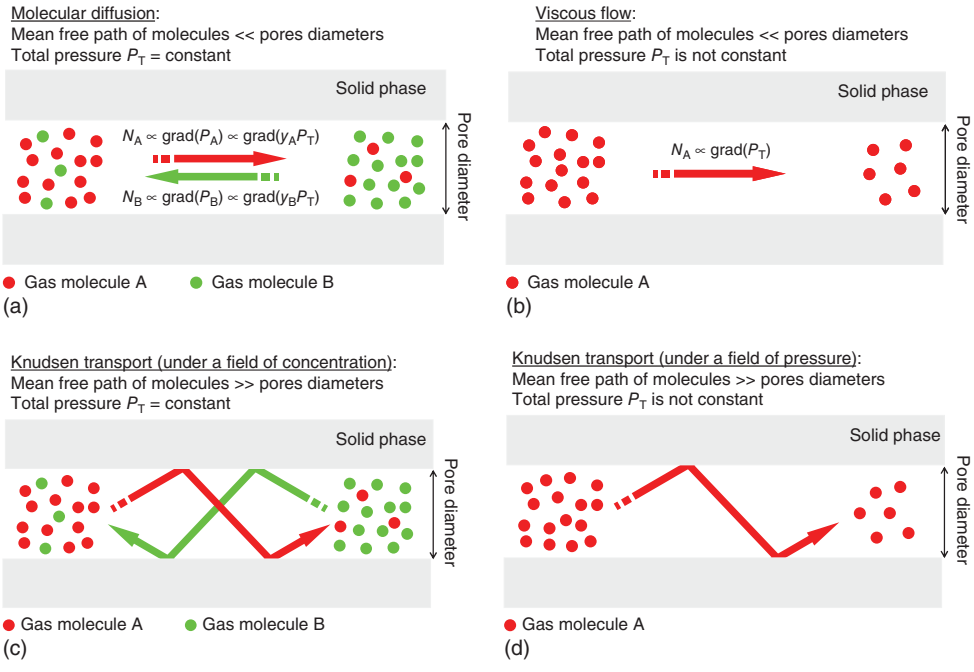

Figure 6.11 Schematic representation of (a) molecular diffusion, (b) viscous flow, and Knudsen transport driven by a field of (c) concentration or (d) total pressure.

- In addition to the molecular diffusion, the gaseous species can flow trough the electrode by a convective process. In this case, the 'convective' or 'viscous' flux is driven by a gradient of total pressure P_T that can arise across the electrode. Expression of flow rate through the porous electrode is provided by the well-known Darcy's law that derives from the Navier and Stokes equations. In this approach, the gas flux is proportional to the gradient of total pressure, the gas dynamic viscosity μ (in Pa s) and a permeability coefficient B_0, which depends on electrode microstructural characteristics:

$$N_A = -\frac{B_0 P_T}{\mu RT} \times \text{grad}(P_T) \quad \text{(see Figure 6.11b)} \tag{6.27}$$

- Unlike the transport processes by molecular diffusion or viscous flow, the 'Knudsen' regime predominates when the mean pore diameter D_p is smaller than the mean free path of molecules λ (i.e. the Knudsen number defined as the ratio of λ/D_p is higher than 1). In this condition, the molecules do not interact among themselves as the gas flux is exclusively governed by the collision of gas species with the wall of the porous medium.

In the Knudsen region, there is no fundamental distinction between viscous flow and diffusion, and the molar flux can be driven either by a gradient of concentration or pressure (Figure 6.11c and d). Therefore, in both cases, fluxes are described

through a single effective 'Knudsen' coefficient denoted as $D^{\text{eff}}_{\text{A,k}}$:

$$N_{\text{A}} = -\frac{D^{eff}_{A,k}}{RT} \times grad(P_{\text{A}}) \quad \text{(see Figure 6.11c) or}$$

$$N_{\text{A}} = -\frac{D^{eff}_{A,k}}{RT} \times grad(P_{\text{T}}) \quad \text{(see Figure 6.11d)} \tag{6.28}$$

As already discussed in Section 6.3.1.3, the convective flow can be reasonably neglected at the cathode side, as there is no net change in the number of molecules in the gas stream (for the reduction of one molecule of steam, one molecule of hydrogen is produced by the electrochemical reaction). Furthermore, even at the anode side where oxygen is released, the elevation of pressure in the open porosity remains fairly low so that the convective flux can be assumed negligible compared to the diffusive one [33, 34].

Regarding the diffusive processes, the relative weight of Knudsen and molecular diffusion is directly linked to the microstructure characteristics of the percolated gas phase. It is worth keeping in mind that the mean pore diameter of SOEC electrodes ranges from 0.5 to 1.5 μm depending on the fine microstructure of the FL [9] or the coarse microstructure of the CC [9]. In this range of porosity size, effective Knudsen and molecular diffusivities are on the same order of magnitude. For example, considering a mean pore diameter of 1 μm, the effective Knudsen coefficient for H_2O is equal to $D^{\text{eff}}_{\text{H}_2\text{O,k}} = 7.5 \times 10^{-5}$ m^2s^{-1} at $T = 800\,°\text{C}$. This value is close to the one related to the effective molecular diffusivity for the H_2-H_2O binary system: $D^{\text{eff}}_{\text{H}_2\text{O,H}_2} = 8.5 \times 10^{-5}$ m^2s^{-1} (coefficients given for a ratio of porosity to 'apparent' tortuosity factor of $\varepsilon/\tau = 0.1$: see Section 6.3.2.5 for more details on the effect of microstructure). As a consequence, neither the Knudsen nor the molecular diffusion fluxes are negligible in classical SOEC electrodes.

Governing Equations for Multi-component Gas Transport in SOEC Electrode Under steady-state conditions, several continuum models may accurately describe the gas transport across the porous SOEC electrodes. In general, Fick's law or the Stefan–Maxwell or the 'dusty gas' models can be employed to predict the gas transport in porous solids [33, 35–37]. As already mentioned, the classical Fick's model stands to describe the molecular diffusion for a binary system (i.e. H_2-H_2O, for instance). It can be extended by taking into account convective transport and Knudsen diffusion. For a mixture of two gases, A and B, the molar flux N_{A} (resp. N_{B}) is given by [33, 35]

$$N_{\text{A}} = \frac{-1}{RT} \times \frac{D^{\text{eff}}_{\text{A,k}} D^{\text{eff}}_{\text{A,B}}}{D^{\text{eff}}_{\text{A,k}} + D^{\text{eff}}_{\text{A,B}}} \times \frac{\text{d}(y_{\text{A}} P_{\text{T}})}{\text{d}z} - \frac{B_0 y_{\text{A}} P_{\text{T}}}{\mu RT} \times \frac{\text{d}P_{\text{T}}}{\text{d}z} \quad (0 \le |z| \le \ell_{\text{FL}} + \ell_{\text{CC}}) \tag{6.29}$$

where P_{T} is the total pressure. The term y_{A} denotes the molar fraction for the gas species A, while $D^{\text{eff}}_{\text{A,k}}$ and $D^{\text{eff}}_{\text{A,B}}$ refer to the effective Knudsen and binary diffusion coefficients, respectively. B_0 is the permeability coefficient and μ is the gas viscosity.

The extended Fick's model is the most simple to handle and implement in SOEC numerical analysis. It provides satisfactory estimations [33], especially in $CO-CO_2$ gas mixtures [35]. Unfortunately, its prediction is not fully suitable for SOEC electrodes, especially in an H_2-H_2O gas mixture [35]. Stepfan–Maxwell equations allow describing the molecular diffusion of a multi-component gas mixture. This model does not seem to be fully relevant for SOEC application as it does not take into account the Knudsen diffusion. In spite of this shortcoming, the Stefan–Maxwell model can produce good approximations at high porosity and low current density [34, 35]. The most appropriate model for mass transfer in an SOEC electrode is the dusty gas model [35, 37], which is widely employed in SOEC models [15–18, 27, 38, 39]. Indeed, it encompasses the Knudsen transport as well as the molecular diffusion for a mixture of several gas species [35–37].

$$\frac{N_i}{D_{i,\mathrm{k}}^{\mathrm{eff}}} + \sum_{j=1, j\neq i}^{n} \frac{y_j N_i - y_i N_j}{D_{i,j}^{\mathrm{eff}}} = \frac{-P_{\mathrm{T}}}{RT}\left(\frac{\mathrm{d}y_i}{\mathrm{d}z}\right) + \frac{-y_i}{RT}\left(\frac{\mathrm{d}P_{\mathrm{T}}}{\mathrm{d}z}\right)\left(1 + \frac{B_0 P_{\mathrm{T}}}{D_{i,\mathrm{k}}^{\mathrm{eff}}\mu}\right)$$
$$(0 \leq |z| \leq \ell_{\mathrm{FL}} + \ell_{\mathrm{CC}}) \tag{6.30}$$

It may be noted that the last term of Equation 6.30 is related to the viscous flow driven by the pressure gradient $\mathrm{d}P_{\mathrm{T}}/\mathrm{d}z$. If the pressure is assumed to be roughly constant in the electrode, the dusty gas model reduces to the set of Equation 6.31:

$$\frac{N_i}{D_{i,\mathrm{k}}^{\mathrm{eff}}} + \sum_{j=1, j\neq i}^{n} \frac{y_j N_i - y_i N_j}{D_{i,j}^{\mathrm{eff}}} = \frac{-P_{\mathrm{T}}}{RT}\left(\frac{\mathrm{d}y_i}{\mathrm{d}z}\right) \quad (0 \leq |z| \leq \ell_{\mathrm{FL}} + \ell_{\mathrm{CC}}) \tag{6.31}$$

In order to calculate the molar fractions in the electrode, the system of Equation 6.31 must be solved analytically or numerically in both the CC and FL of the electrode.

- Within the ECC, there are no chemical or electrochemical reactions. The gas fluxes are constant across the layer as they are not modified by any source term. The boundary conditions required to solve the system (Equation 6.31) are then provided, on the one hand, by the molar fractions in the canal and, on the other hand, by the molar fluxes through the electrode layer. These molar fluxes are linked to the cell current densities according to Faraday's law:

$$\text{At the cathode side}: N_{\mathrm{H_2}} = -N_{\mathrm{H_2O}} = \frac{i_{\mathrm{e^-}}}{2F}; \text{ At the anode side}: N_{\mathrm{O_2}} = -\frac{i_{\mathrm{e^-}}}{4F}$$
$$(\text{for current collector}: \ell_{\mathrm{FL}} \leq |z| \leq \ell_{\mathrm{FL}} + \ell_{\mathrm{CC}}) \tag{6.32}$$

A methodology is detailed in [17] to integrate the system of Equation 6.31 with the previously mentioned boundary conditions. It has been developed for a gas mixture composed of hydrogen, steam and, if necessary, nitrogen used as a dilution gas. The proposed analytical solutions allow expressing the molar fraction in the thickness of the CCC.

Numerical applications of these expressions have shown that, considering the ESC configuration, the difference in partial pressures through the thin ECC is negligible, whereas it becomes significant at high current density across the

substrate of the CSC design [17]. This result is consistent with the large concentration overpotentials that can arise under current for this cell geometry.

At the anode side, the set of Equation 6.31 can be easily integrated for an O_2-N_2 gas mixture. Considering that the nitrogen flux is nil in the electrode, the oxygen molar fraction across the layer is given by

$$y_{O_2}(z) = \frac{D^{\text{eff}}_{O_2,k} + D^{\text{eff}}_{O_2,N_2}}{D^{\text{eff}}_{O_2,k}} + \left(y^{\text{canal}}_{O_2} - \frac{D^{\text{eff}}_{O_2,k} + D^{\text{eff}}_{O_2,N_2}}{D^{\text{eff}}_{O_2,k}} \right) \text{Xexp}\left(-\frac{RT}{P_T}\frac{i}{4F}\frac{D^{\text{eff}}_{O_2,k}}{D^{\text{eff}}_{O_2,k} \times D^{\text{eff}}_{O_2,N_2}} \left(z - z^{\text{canal}}\right) \right)$$

$$(\text{for anode current collector}: \ell_{\text{AFL}} \le |z| \le \ell_{\text{AFL}} + \ell_{\text{ACC}}) \tag{6.33}$$

- Unlike the ECC, the gas species are consumed or produced by the electrochemical reactions inside the FLs. The molar fluxes are then continuously modified in the thickness of the electrode active layer. As a consequence, the set of Equation 6.31 describing the molar fluxes must be associated with equations of mass conservation. For each slice of active layer dz (Figure 6.7), mass balances on N_i molar fluxes are expressed as follows:

$$\text{At the cathode side}: \ \mathrm{d}N_{H_2O} = -\mathrm{d}N_{H_2} = \frac{+j(z)}{2F}\mathrm{d}z \quad (\text{for functional layer}: 0 \ge |z| \ge \ell_{\text{FL}})$$

$$\text{At the anode side}: \ \mathrm{d}N_{O_2} = \frac{+j(z)}{4F}\mathrm{d}z \ (\text{for functional layer}: 0 \ge |z| \ge \ell_{\text{FL}}) \tag{6.34}$$

6.3.2.3 Expression of the Source Terms: Kinetic of the Electrochemical Process

Volume-specific currents $j(z)$ in Equations 6.22, 6.24 and 6.34 correspond to the source terms generated in the cell by the electrochemical reactions. The terms $j(z)$ are linked to the kinetic rates $\nu(z)$ of the global reaction mechanism that potentially occur in the whole FL:

$$j(z) = nF\nu(z) = nF\{\nu_{\text{ox}} - \nu_{\text{red}}\} \ \ (\text{for functional layer}: 0 \ge |z| \ge \ell_{\text{FL}}) \tag{6.35}$$

where n denotes the number of the exchange electrons: $n = 4$ for oxygen production at the anode side ($2O^{2-} \underset{k_{\text{red}}}{\overset{k_{\text{ox}}}{\leftrightarrow}} O_2 + 4e^-$) whereas $n = 2$ for steam reduction at the cathode side ($H_2O + 2e^- \underset{k_{\text{ox}}}{\overset{k_{\text{red}}}{\leftrightarrow}} H_2 + O^{2-}$).

Assuming that the reaction mechanism is limited by a single charge transfer, the kinetic equation for expressing $j(z)$ is given by the general Butler–Volmer relation. However, at high temperature, the reaction pathway is not controlled by a single rate-determining step such as the fundamental charge transfer. In general, the whole reaction can be constituted by several intricate mechanism pathways, each pathway being decomposed in a sequence of elementary reactions. In this framework, the difficulty lies in the identification of the most relevant mechanism

that must be decomposed in a series of elementary reactions. Some of them can be considered as rate-determining steps (i.e. their velocities are non-zero: $v_i \neq 0$), while the others are supposed at the thermodynamic equilibrium (i.e. their velocities are nil $v_i = 0$ so that activities of the reactants a_r and products a_p are simply linked through the thermodynamic equilibrium constant, $K_e = \frac{k_+}{k_-} = \frac{\Pi a_p^{\gamma_p}}{\Pi a_r^{\gamma_r}}$).

It is clear that the reaction mechanism is related to each material but it is also admitted that the mechanism depends on the electrode microstructure. Moreover, the domain of validity of such a reaction mechanism is restricted over a range of temperature, gas composition and pressure. It is also observed that the direction of electrode polarization (in anodic or cathodic polarization) is likely to modify the reaction pathways and the associated rate-determining steps [40, 41].

Several studies have been dedicated to ensure a better understanding of the fundamental mechanistic processes in the SOFC mode of operation (i.e. anodic polarization for H_2 electrodes and cathodic polarization for O_2 electrodes) [42–47]. Nevertheless, despite several efforts, there is still no clear consensus on elementary reaction pathways on classical materials such as an Ni–YSZ cermet [42] or an LSM–YSZ composite [46]. In comparison to the SOFC mode, very few studies have been dedicated to SOEC conditions [27, 39–41, 48]. Therefore, at the time of writing, the interpretation of steam electrolysis in terms of elementary kinetics remains unclear and is still under investigation. It is beyond the scope of this presentation to discuss extensively all the potential multistep reactions mechanisms in steam electrolysis. In other words, the aim of this section is not to provide an exhaustive and detailed description of all the potential elementary mechanisms in SOEC, but rather to introduce and illustrate the theory by some possible and simple reactive pathways on the LSM–YSZ anode and Ni–YSZ cathode.

Elementary Kinetics for LSM-YSZ Anode Among diverse plausible pathways, it has been proposed that the mechanism for O_2 production on the LSM–YSZ electrode could be opposite to the one established in SOFC mode for cathodic polarization [27]. This claim might be restricted for electrodes supplied by air, so that, in both anodic and cathodic polarizations, the electrode is operated in the same range of oxygen partial pressures. In such a condition, it has been proposed to split the mechanism into two rate-determining steps (Figure 6.12):

1) The first step is related to the charge transfer that takes place at the LSM/YSZ/gas TPBls. It leads to the formation of oxygen atoms $O - s_{LSM}$ adsorbed on the surface of LSM particles (Figure 6.12):

$$2O^{2-}_{YSZ} + 2s_{LSM} \underset{k_{red}}{\overset{k_{ox}}{\leftrightarrow}} 2O - s_{LSM} + 4e^-_{LSM} \quad (\text{for functional layer} : 0 \geq |z| \geq \ell_{FL}) \tag{6.36}$$

where s_{LSM} denotes the adsorption sites on the surface of the LSM material. The kinetic rate of this elementary electrochemical reaction can be expressed in the framework of the generalized Butler–Volmer relation as follows:

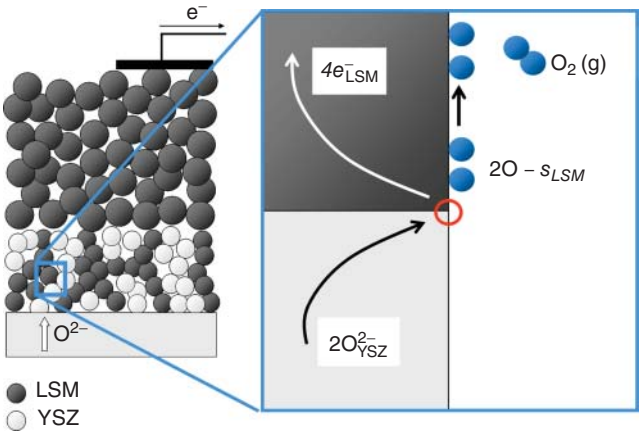

Figure 6.12 A plausible mechanism for O_2 production in LSM–YSZ anode.

$$\nu_{(36)}(z) = k_{ox} e^{\frac{\alpha_{ox} 4FE(z)}{RT}} \Gamma^2 \theta_s^2(z) - k_{red} e^{\frac{-\alpha_{red} 4FE(z)}{RT}} \Gamma^2 \theta_{O-s}^2(z) \quad (0 \geq |z| \geq \ell_{FL}) \quad (6.37)$$

The term Γ corresponds to the surface density of available adsorption sites, while θ_{O-s} and θ_s represent the coverage rates of oxygen-adsorbed atoms and sites, respectively ($\theta_{O-s} + \theta_s = 1$). It may be noted that the products $\Gamma\theta_{O-s}$ and $\Gamma\theta_s$ simply refer to the concentrations, that is to say the activities of adsorbed oxygen atoms and sites.

2) In the presented mechanism, it is assumed that diffusion of adsorbed oxygen atoms from the vicinity of TPBls onto the surface of LSM particles does not limit the reaction. The validity of this assumption can be controversial as it depends on the electrode microstructural characteristics [48]. Indeed, this hypothesis will be verified only if the effective length of oxygen surface diffusion is much higher than LSM mean particle size. Anyway, assuming that this condition is fulfilled, the second rate-limiting step simply corresponds to the associative desorption of adsorbates to form gaseous molecules in the electrode porosity (Figure 6.12):

$$2O - s_{LSM} \underset{k_{ads}}{\overset{k_{des}}{\leftrightarrow}} O_2(g) + 2s_{LSM} \quad (\text{for functional layer} : 0 \geq |z| \geq \ell_{FL}) \quad (6.38)$$

The rate of this reaction is given by

$$\nu_{(38)}(z) = k_{des} \Gamma^2 \theta_{O-s}^2(z) - k_{ads} P_{O_2}(z) \Gamma^2 \theta_s^2(z) \quad (0 \geq |z| \geq \ell_{FL}) \quad (6.39)$$

where k_{ads} and k_{des} represent the adsorption and desorption kinetic constants, respectively. In the steady-state regime, there is no accumulation of oxygen atoms on the electrode surface so that the kinetic rates $\nu_{(36)}$ and $\nu_{(38)}$ must be equal. Moreover, the kinetic rates are linked to the volume-specific current through Faraday's law, leading to $\nu_{(36)} = \nu_{(38)} = j(z)/4F$.

According to this description, it appears that electrode efficiency is not only controlled by the density of TPBs or the O^{2-} mobility in the YSZ structure of the

FL. In addition, electrode performance must depend on oxygen desorption and, hence, on the LSM/gas interfacial surface area [27].

Elementary Kinetics for Ni-YSZ Cathode Several studies have been dedicated to elucidate the overall H_2 oxidation mechanism on the Ni–YSZ cermet in SOFC mode [41–44]. According to these studies, the pathway would consist of the following multiple elementary steps:

1) It seems that hydrogen adsorption is favoured on Ni particles (i.e. $H_2(g) + 2s_{Ni} \underset{k_{des}}{\overset{k_{ads}}{\leftrightarrow}} 2H - s_{Ni}$).
2) Adsorbed hydrogen atoms diffuse up to the TPBs.
3) The subsequent charge transfer involves the transition of surface species across the Ni/YSZ interface and is referred to as the hydrogen 'spillover' mechanism [42, 43]:

$$H - s_{Ni} + O^{2-} - s_{YSZ} \underset{k_{red}}{\overset{k_{ox}}{\leftrightarrow}} OH^{-} - s_{YSZ} + s_{Ni} + 1e^{-}_{Ni} \tag{6.40a}$$

$$H - s_{Ni} + OH^{-} - s_{YSZ} \underset{k_{red}}{\overset{k_{ox}}{\leftrightarrow}} H_2O - s_{YSZ} + s_{Ni} + 1e^{-}_{Ni} \tag{6.40b}$$

where $O^{2-} - s_{YSZ}$, $OH^{-} - s_{YSZ}$ and $H_2O - s_{YSZ}$ denote the species attached on the YSZ surface.
4) The adsorbed oxygen ion $O^{2-} - s_{YSZ}$, which is a reactant of the electrochemical reaction (6.40a), is transferred from the bulk of YSZ according to $O^{2-}_{YSZ} + s_{YSZ} \leftrightarrow O^{2-} - s_{YSZ}$.
5) Water produced in Equation 6.40b is desorbed in the void of the cermet: $H_2O - s_{YSZ} \leftrightarrow H_2O(g) + s_{YSZ}$.

Among these elementary reactions, the charge transfer (Equation 6.40b) could be the rate-limiting step, whereas the other would be at the thermodynamic equilibrium [44]. However, according to [43], it seems that water desorption from YSZ could also participate in the limitation of the overall reaction rate.

Conversely to anode polarization, very few studies have been dedicated to the mechanism of hydrogen production in SOEC mode. Unfortunately, it appears that the reaction pathway for steam electrolysis is not the reverse of the one proposed for hydrogen oxidation [39–41]. Experimental studies have shown that the overall mechanism depends on the gas composition [39] and could involve a solid–gas interaction [41]. In this framework, it has been proposed that the reactive pathway could be controlled by two rate-limiting steps at high steam partial pressure [39]:

1) Steam would adsorb preferentially on the Ni surface [41]

$$H_2O(g) + 1s_{Ni} \underset{k_{des}}{\overset{k_{ads}}{\leftrightarrow}} H_2O - s_{Ni} \quad (\text{for functional layer} : 0 \geq |z| \geq \ell_{FL}) \tag{6.41}$$

2) And is electrochemically reduced at TPBs:

Table 6.1 A possible sequence of elementary reactions for steam electrolysis on an Ni–YSZ cermet.

Steam adsorption: $H_2O(g) + 1s_{Ni} \leftrightarrow H_2O - s_{Ni}$	(1)
Steam dissociation: $H_2O - s_{Ni} + 1s_{Ni} \leftrightarrow H - s_{Ni} + OH - s_{Ni}$	(2)
Hydroxyl dissociation: $OH - s_{Ni} + 1s_{Ni} \leftrightarrow H - s_{Ni} + O - s_{Ni}$	(3)
Associative desorption: $H - s_{Ni} + H - s_{Ni} \leftrightarrow H_2(g) + 2s_{Ni}$	(4)
Charge transfer: $O - s_{Ni} + 2e^-_{Ni} + 1s_{YSZ} \leftrightarrow O^{2-} - s_{YSZ} + 1s_{Ni}$	(5)
Oxygen incorporation: $O^{2-} - s_{YSZ} \leftrightarrow O^{2-}_{YSZ} + 1s_{YSZ}$	(6)

$$H_2O - s_{Ni} + 2e^-_{Ni} \underset{k_{ox}}{\overset{k_{red}}{\leftrightarrow}} O^{2-}_{YSZ} + H_2(g) + 1s_{Ni} \quad (\text{for functional layer} : 0 \geq |z| \geq \ell_{FL}) \tag{6.42}$$

The velocity of adsorption (Equation 6.41) depends on steam partial pressure in the electrode and the coverage rate on Ni particles θ_{H_2O-s} as follows:

$$\nu_{(41)}(z) = k_{ads} P_{H_2O}(z) \Gamma(1 - \theta_{H_2O-s}(z)) - k_{des} \Gamma \theta_{H_2O-s}(z) \tag{6.43}$$

The kinetic rate of the electrochemical reaction (6.42) is written for two exchange electrons:

$$\nu_{(42)}(z) = k_{red} e^{\frac{-\alpha_{red} 2FE(z)}{RT}} \Gamma \theta_{H_2O-s}(z) - k_{ox} e^{\frac{\alpha_{ox} 2FE(z)}{RT}} P_{H_2}(z) \ \Gamma(1 - \theta_{H_2O-s}(z)) \tag{6.44}$$

In stationary condition without surface diffusion, $\nu_{(41)}$ and $\nu_{(42)}$ are equal. According to the relation (6.35), the source terms associated with the volume-specific current $j(z)$ are given by $-\nu_{(42)} = j(z)/2F$.

As proposed in [40], the previous pathway can be refined by introducing the surface decomposition of steam into adsorbed hydrogen and oxygen atoms: see reactions (2) and (3) of the decomposition given in Table 6.1. In this case, hydrogen adsorbates directly recombine to release gaseous hydrogen (4). Meanwhile, oxygen-adsorbed atoms are electrochemically reduced on the surface at TPBs (5). In this mechanism, steam adsorption (1) and charge transfer (5) can still be considered as the rate-determining steps, while the other reactions remain at the thermodynamic equilibrium. Moreover, it is worth mentioning that surface diffusion of hydrogen adsorbates could also participate in the process by slowing down the global reaction rate [43].

From this short discussion on some likely steam reduction mechanisms on the Ni–YSZ cermet, it must be kept in mind that the overall reaction is not only controlled by charge transfer. Other limiting steps involving adsorption species seem to participate in the overall reactive pathway. From that perspective, further studies are needed to elucidate the mechanistic details on the Ni–YSZ cermet.

6.3.2.4 Specific Operating Mechanisms of Single-Phase SOEC Anode

Anode LSM–YSZ composites can be favourably replaced by single-phase materials that must exhibit a mixed ionic and electronic conduction (i.e. MIEC behaviour). Nowadays, MIEC electrodes such as LSCF ($La_{1-x}Sr_xCo_yFe_{1-y}O_{3-\delta}$)

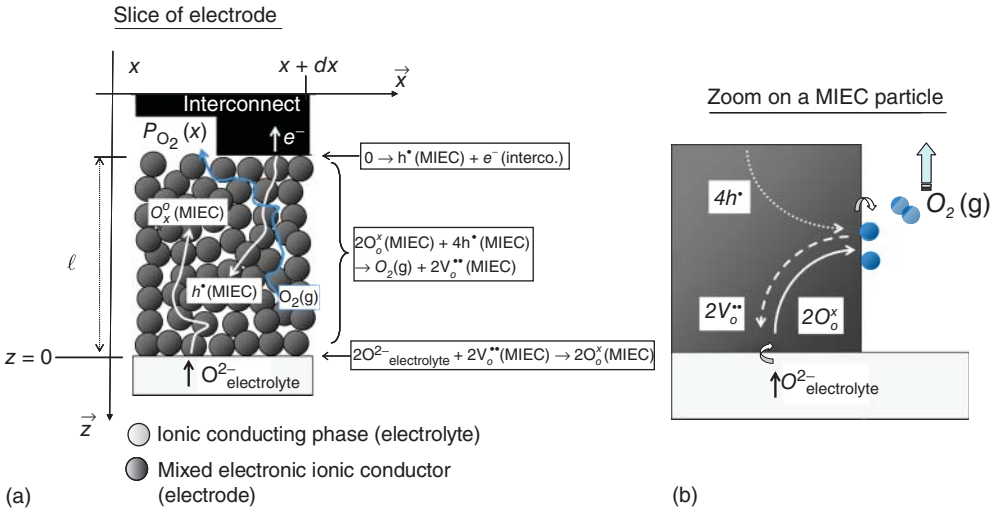

Figure 6.13 Scheme of an electrode slice considered for a single-phase MIEC anode (a). The system of local coordinates and the flow directions of O_2 gas, oxygen atoms and holes in the MIEC are represented (for the sake of clarity, the flow of oxygen vacancies in the MIEC is not depicted). Zoom on an MIEC particle in contact with the electrolyte is also represented (b).

or LSC ($La_{1-x}Sr_xCoO_{3-\delta}$) are usually employed as SOEC anode materials. They correspond to a p-type semiconductor with a high electronic conductivity by holes and a non-negligible ionic conduction by oxygen vacancies. They are generally preferred to the classical LSM–YSZ composite even if these materials present a chemical instability that could limit their utilization [49, 50].

The main advantage of MIECs lies in the fact that the oxygen release is not restricted in the neighbourhood of TPBls, but can extend over the whole gas/electrode interface. This results in a substantial decrease in electrode activation overpotential. The aim of this subsection is to provide a general overview on the specific MIEC operating processes.

Elementary Reactive Pathway By their intrinsic nature, the operating mechanisms of MIECs are radically different from the ones previously detailed for LSM–YSZ double-phase. As depicted in Figure 6.13, the global electrochemical process is generally divided into the following sequential steps [51–55]:

1) A first charge transfer takes place across the anode/electrolyte interface. It corresponds to the direct oxygen ions exchange from the electrolyte into the MIEC:

$$2O^{2-}_{electrolyte} \underset{k_-}{\overset{k_+}{\leftrightarrow}} 2O^{2-}_{MIEC} \quad (\text{at } z = 0) \tag{6.45}$$

where $O^{2-}_{electrolyte}$ and O^{2-}_{MIEC} denote the oxygen ions within the electrolyte and within the MIEC, respectively. When considering the 'Kröger–Vink' notation,

Equation 6.45 can also be expressed in a similar way:

$$2\mathrm{O}_{\mathrm{O}}^{x}(\text{electrolyte}) + 2\mathrm{V}_{\mathrm{O}}^{\cdot\cdot}(\text{MIEC}) \underset{k_-}{\overset{k_+}{\leftrightarrow}} 2\mathrm{O}_{\mathrm{O}}^{x}(\text{MIEC}) + 2\mathrm{V}_{\mathrm{O}}^{\cdot\cdot}(\text{electrolyte}) \quad (\text{at } z = 0) \tag{6.46}$$

The terms $V_{\mathrm{O}}^{\cdot\cdot}$ and $\mathrm{O}_{\mathrm{O}}^{x}$ represent the oxygen vacancies and the oxygen atoms incorporated either in the electrolyte or in the MIEC.

It is worth underlining that the oxygen transfer through the anode/electrolyte interface must be considered as an 'electrochemical' reaction [51, 53–55]. Indeed, the energy barrier of this reaction is affected by the electrical field arising between the two materials. This field stems from the charge transfer that happens across the interface and basically corresponds to the electrode potential $E(z = 0) = \rho_{\mathrm{MIEC}}(z = 0) - \rho_{\mathrm{electrolyte}}(z = 0)$. In other words, the reaction (6.46 or 6.45) involves a passage of charge between the electrolyte and the MIEC indicating its 'electrochemical' nature. As a consequence, the rate of Equation 6.46 must be expressed according to the generalized Butler–Volmer expression as follows [53, 55]:

$$\begin{aligned} v_{(46)} = {} & k_+ \exp\left(\frac{4\alpha^{\mathrm{Anode}} FE}{RT}\right)(1 - a_{\mathrm{O}_{\mathrm{O}}^{x}})^2 \\ & -k_- \exp\left(-\frac{4\left(1-\alpha^{\mathrm{Anode}}\right)FE}{RT}\right)(a_{\mathrm{O}_{\mathrm{O}}^{x}})^2 \\ & (\text{at the anode/electrolyte interface}: \ z = 0) \end{aligned} \tag{6.47}$$

where the oxygen-incorporation rate $a_{\mathrm{O}_{\mathrm{O}}^{x}}$ denotes the oxygen activity in the MIEC. It corresponds to the ratio of oxygen atom concentration to the maximum concentration that can be incorporated in the MIEC (i.e. $a_{\mathrm{O}_{\mathrm{O}}^{x}} = C_{\mathrm{O}_{\mathrm{O}}^{x}}/C_{\mathrm{O}_{\mathrm{O}}^{x}}^{\max}$). Note that $C_{\mathrm{O}_{\mathrm{O}}^{x}}$ is related to the mobile oxygen atoms that are likely to participate in the diffusional transport in the material (i.e. when considering, for example, $\mathrm{La}_{1-x}\mathrm{Sr}_x\mathrm{Co}_y\mathrm{Fe}_{1-y}\mathrm{O}_{3-\delta}$, $C_{\mathrm{O}_{\mathrm{O}}^{x}} = (3-\delta)/V$ where V is the volume of the lattice unit cell). The difference $(C_{\mathrm{O}_{\mathrm{O}}^{x}}^{\max} - C_{\mathrm{O}_{\mathrm{O}}^{x}})$ represents the concentration of oxygen vacancies in the MIEC (i.e. $C_{\mathrm{O}_{\mathrm{O}}^{x}}^{\max} - C_{\mathrm{O}_{\mathrm{O}}^{x}} = \delta/V$). The electrochemical step (Equation 6.46) is considered rapid for usual SOEC materials, in such a way that the reaction can be supposed at the thermodynamic equilibrium. Under this condition, Equation 6.47 can be simplified and replaced by Equation 6.45:

$$\begin{aligned} & v_{(46)} = 0 \Rightarrow \frac{k_+}{k_-} = K_{\mathrm{e}} = \frac{(1 - a_{\mathrm{O}_{\mathrm{O}}^{x}}^{\mathrm{eq}})^2}{(a_{\mathrm{O}_{\mathrm{O}}^{x}}^{\mathrm{eq}})^2} \times \exp\left(\frac{4FE}{RT}\right) \\ & (\text{at the anode/electrolyte interface}: \ z = 0) \end{aligned} \tag{6.48}$$

where K_{e} refers to the thermodynamic equilibrium constant for the reaction (6.46).

2) As depicted in Figure 6.13, the second step of the global process corresponds to the solid-state diffusion of oxygen atoms and holes in the anode material.

3) It is followed by the surface reactions leading to the O_2 release in the electrode porosity. These reactions take place on the gas/MIEC interface and can potentially occur all along the electrode thickness. By taking advantage of studies performed in SOFC mode, it appears that surface reactions should be controlled by two elementary steps. The first one corresponds to the ex-corporation of oxygen atoms O_o^x from the bulk leading to adsorbates $O-s$ onto the MIEC surface:

$$2O_O^x(\text{MIEC}) + 4h^{\cdot} + 2s_{\text{MIEC}} \underset{k_{\text{red}}}{\overset{k_{\text{ox}}}{\leftrightarrow}} 2V_O^{\cdot\cdot}(\text{MIEC}) + 2O - s_{\text{MIEC}} \quad (0 > |z| \geq \ell_{\text{FL}}) \tag{6.49}$$

It is worth underlining that Equation 6.49 involves a charge transfer but corresponds to a simple chemical oxidation [51, 54, 55]. Indeed, charge transfer in Equation 6.49 occurs only in the MIEC, so that the reaction does not involve any interfacial charge exchange. As a consequence, reaction (6.49) is purely chemical and its kinetic rate is simply expressed as follows:

$$\nu_{(49)}(z) = k_{\text{ox}}\Gamma^2\theta_s^2(z)(C_{O_O^x}(z))^2 - k_{\text{red}}\Gamma^2\theta_{O-s}^2(z)(C_{O_O^x}^{\max} - C_{O_O^x}(z))^2 \quad (0 > |z| \geq \ell_{\text{FL}}) \tag{6.50}$$

where the term Γ refers to the surface density of available sites on the electrode surface and θ the coverage rate of sites or adsorbed oxygen atoms ($\theta_s + \theta_{o-s} = 1$). The elementary reaction (6.49) is subsequently followed by the associative desorption of adsorbates to form O_2 gaseous molecules in the voids of the electrode:

$$2O - s_{\text{MIEC}} \underset{k_{\text{ads}}}{\overset{k_{\text{des}}}{\leftrightarrow}} O_2(g) + 2s_{\text{MIEC}} \quad (0 > |z| \geq \ell_{\text{FL}}) \tag{6.51}$$

Note that the velocity of this reaction has already been detailed in the previous section: see Equation 6.40b. Moreover, in the steady-state condition, the rate of oxygen ex-corporation must be equal to the rate of O_2 molecule production (i.e. $\nu_{(49)} = \nu_{(51)}$).

4) As illustrated in Figure 6.13, the last step of the process corresponds to the transport of oxygen molecules by diffusion in the electrode porosity.

In the proposed pathways, one may note that electrochemical oxidation at MIEC/gas/electrolyte TPBs is not considered [55]. Indeed, TPBs are restricted to the MIEC/electrolyte interface ($z = 0$) in such a way that their density is very low. Nevertheless, the direct oxidation at TPBs could occur in parallel to the previous mechanism according to the reaction: $2O_o^x(\text{electrolyte}) + 2s_{MIEC} + 4h^{\bullet} \underset{k_{red}}{\overset{k_{ox}}{\leftrightarrow}} 2V_o^{\bullet\bullet}(\text{electrolyte}) + 2O - s_{MIEC}$. As the rate of this reaction follows a Bulter-Volmer formalism (i.e. $\nu_{TPBs}(z=0) = k_{ox}e^{\frac{4\alpha^{Anode}FE}{RT}}\Gamma^2\theta_s^2 - k_{red}e^{\frac{-4(1-\alpha^{Anode})FE}{RT}}\Gamma^2\theta_{O-s}^2$ its participation to the whole reactive pathway could be activated under polarization, and could even become prevalent at sufficient 'high' anodic over potential [56].

Gas Transfer in Anode Porosity Surface diffusion of adsorbed oxygen atoms is generally assumed to be negligible with respect to the bulk transport of gas molecules. As a consequence, oxygen mass transfer through the electrode can be described in the framework of the 'dusty gas model', which combines molecular and Knudsen diffusion (see Section 4.2.3.2 for details). It is worth noting that the O_2 diffusive flux is modified all along the electrode thickness because of the oxygen production. Evolution of gas flux is taken into account by a mass balance written for each elementary slice of electrode dz:

$$\mathrm{div}(\overrightarrow{N}_{O_2}) = +\nu_{(51)}(z) \Rightarrow \mathrm{d}N_{O_2}(z) = +\nu_{(51)}(z)\mathrm{d}z \;\; (0 > |z| \geq \ell_{FL}) \tag{6.52}$$

where N_{O_2} denotes the oxygen gas flux.

Oxygen Atoms and Holes Transfer in the MIEC Oxygen atoms are released in the MIEC at the anode/electrolyte interface, and then flow towards the gas/electrode surface, where they are oxidized under O_2 molecules. As a consequence, the concentration of oxygen atoms is the highest at the anode/electrolyte interface and decreases all along the electrode thickness. Oxygen atoms flux is determined by a solid-state diffusion that is expressed in the form of the classical Fick's law:

$$\overrightarrow{N}_{O_O^x} = -D_O^{\mathrm{eff}} \times \mathrm{grad}(C_{O_O^x}) \Rightarrow N_{O_O^x}(z) = -D_O^{\mathrm{eff}} \frac{\mathrm{d}C_{O_O^x}}{\mathrm{d}z} \;\; (0 \geq |z| \geq \ell_{FL}) \tag{6.53}$$

where D_O^{eff} is the effective chemical diffusivity of oxygen atoms in the MIEC:

One may note that the oxygen chemical diffusivity corresponds to a phenomenological coefficient that depends on the oxygen self-diffusion coefficient $D_O^{Self-diffusion}$ the oxygen non-stoichiometry δ and oxygen partial pressure P_{O2} [57]. The surface reactions constitute source terms inducing a modification of oxygen diffusive flux all along the electrode thickness. This modification of oxygen flux in the MIEC must be taken into account through the following mass balance:

$$\mathrm{div}(\overrightarrow{N}_{O_O^x}) = -2\nu_{(49)}(z) \Rightarrow \mathrm{d}N_{O_O^x}(z) = -2\nu_{(49)}(z)\mathrm{d}z \;\; (0 > |z| \geq \ell_{FL}) \tag{6.54}$$

Note that the oxygen diffusive flow is counterbalanced by the one of oxygen vacancies so that their respective fluxes are opposite (i.e. $\overrightarrow{N}_{O_O^x}(z) = -\overrightarrow{N}_{V_O^{\cdot\cdot}}(z)$). Moreover, at the anode/electrolyte interface, the oxygen atom flux is directly related to the rate of the oxygen transfer across the interface (Equation 6.46) (i.e. $N_{O_O^x}(z = 0) = -2\nu_{(46)}$).

Finally, the local 'electronic' current densities associated with the hole flow obeys the classical Ohm's law (Equation 6.55a) and must respect a charge balance due to the surface reactions that consumes holes (which can be seen as an 'electron' production) (Equation 6.55b):

$$\overrightarrow{i}_{e^-} = -\sigma_{h^\cdot}^{\mathrm{eff}} \times \mathrm{grad}(\varphi_{\mathrm{MIEC}}) \quad \Rightarrow \quad i_{e^-} = -\sigma_{h^\cdot}^{\mathrm{eff}} \frac{\mathrm{d}\varphi_{\mathrm{MIEC}}}{\mathrm{d}z} \;\; (0 \geq |z| \geq \ell_{FL}) \tag{6.55a}$$

$$\mathrm{div}(\overrightarrow{i}_{e^-}) = -4F\nu_{(49)}(z) \quad \Rightarrow \quad \frac{\mathrm{d}i_{e^-}}{\mathrm{d}z} = -4F\nu_{(49)}(z) \;\; (0 > |z| \geq \ell_{FL}) \tag{6.55b}$$

It can be noticed that the 'electronic' current density is nil at the interface with the electrolyte excepted if the direct oxidation is assumed to occur at TPBs (in that case $i_{e-}(z = 0) = 4Fv_{TPBs}$)

Repartition of Surface Reactions From this set of equations, it can be inferred that the distribution of surface reactions or the profile of current densities in the electrode thickness likely depends on many parameters. For cathodic polarization (in SOFC mode), it has been shown that the repartition is mainly controlled by the effective oxygen chemical diffusivity in the MIEC $D_{O,}^{eff}$ the surface exchange coefficient k_{red} and the electrode microstructural properties [51, 52, 58, 59]. In this condition, it has been found that the oxygen atom flux is the highest at the MIEC/electrolyte interface and decreases exponentially with increasing distance from the electrolyte. The penetration depth of reactions is then expected to spread from the MIEC/electrolyte interface over a distance of a few micrometres in the electrode.

6.3.2.5 Role of Microstructure in the Electrode Behaviour

Aside from the electro-catalytic activities of materials, electrode microstructures also play a major role in cell response. They are key parameters that govern the cell polarization and, hence, the global electrolyser performances [27, 60–63]. Even when considering the same materials, electrochemical cell performances can be widely improved by electrode microstructural optimization.

Several efforts have been made in the last decade to improve SOFC performances by controlling the design of electrode microstructures [64–69]. However, no specific study has as yet been devoted to the optimization of cells operated in electrolysis conditions. Nevertheless, it has to be pointed out that some common recommendations in electrode morphological design are relevant for both modes of operation.

As a general rule, the electrode substrate, which is used as a cell structural support, must present a coarse microstructure to facilitate the gas transportation, and thus reduce the concentration overpotential [60, 62, 70]. Conversely, the FL must exhibit a fine microstructure to optimize the electrochemical process and minimize the activation overpotentials [27, 63, 65]. In this objective, the density in active sites must be increased as far as possible [27]. In addition, the microstructure of the ionic conducting phase must be tailored in order to promote effective O^{2-} conduction within the FL [27]. Indeed, as previously discussed in Section 6.3.2.1, this parameter controls the capacity of the electrochemical reaction to extend from the electrolyte interface within the FL.

The aim of this section is to detail the relationships that link the electrode microstructural parameters to their physical properties such as effective gas diffusivities or electrical conductivities.

Impact of Microstructure on Transport Phenomena: Effective Gas Diffusivities and Electrical Conductivities Gas diffusion through the open porosity or charge transport

through the connected ionic and electronic conducting phases is strongly hindered by the complex microstructure of SOEC electrodes [71–73]. Thus, 'intrinsic' gas diffusivities or charge conductivities are much higher than their effective values in the electrode microstructure. Therefore, the so-called M factor is introduced as the ratio of effective over bulk transport property [73]:

$$\text{Gas diffusivities}: M_{\text{gas}} = \frac{D_{\text{gas}}^{\text{eff}}}{D_{\text{gas}}^{\text{bulk}}}; \text{ Electrical conductivities}: M_i = \frac{\sigma_i^{\text{eff}}}{\sigma_i^{\text{bulk}}}$$
$$(i = \text{ionic or electronic conductor}) \tag{6.56}$$

By definition, the M factor is lower than 1 and is correlated with the morphology of electrode microstructure. In this framework, it depends on three distinct microstructural contributions:

1) First of all, the M factor is related to the percolated phase as the gas (or charge) species can only flow within the connected network. It is then directly proportional to the product of phase volume fraction ε multiplied by the phase connectivity κ (yielding the volumetric percentage of the connected phase).
2) In the electrode microstructure, a supplementary resistance to the gas or charge transfer is caused by some flux constriction effects as the cross-sectional area for diffusion is not constant [72, 73]. This 'bottleneck' phenomenon is described by a 'constrictivity' parameter δ varying between 0 and 1 [73]. For an ideal conductor described by a single cylindrical tube (Figure 6.14a), this parameter can be simply defined by the ratio of minimum over maximum cross-sectional areas.
3) The third contribution of the M factor is related to a parameter that is usually named the 'geometrical' tortuosity factor τ^{geo}. It takes into account the fact that the flow is hampered, since the pathway for diffusion is not straight but sinuous and entangled [73, 74]. For a medium constituted by a bundle of sinuous but parallel capillaries (Figure 6.14b), the geometrical tortuosity factor is rigorously equal to the square of the ratio between the effective path length ℓ_{eff} and the length of the sample ℓ (i.e. $\tau^{\text{geo}} = (\ell_{\text{eff}}/\ell)^2$) [74]. According to this definition, the tortuosity factor is always higher than 1.

Finally, the M factor can be expressed from the previous electrode microstructural parameters according to an empirical relation adapted from Archie's law [73]:

$$\text{Gas diffusivities}: \quad M_{\text{gas}} = (\kappa_{\text{gas}}\varepsilon_{\text{gas}}) \times \frac{\delta_{\text{gas}}}{\tau_{\text{gas}}^{\text{geo}}} \tag{6.57a}$$

$$\text{Electrical conductivities}: M_i = (\kappa_i\varepsilon_i) \times \frac{\delta_i}{\tau_i^{\text{geo}}} \quad (i = \text{ionic or electronic conductor}) \tag{6.57b}$$

However, in complex microstructure such as SOEC electrodes, it is complicated to define and determine accurately the 'constrictivity' parameter [73] or even the geometrical tortuosity factor. Moreover, the relevance of the empirical relation

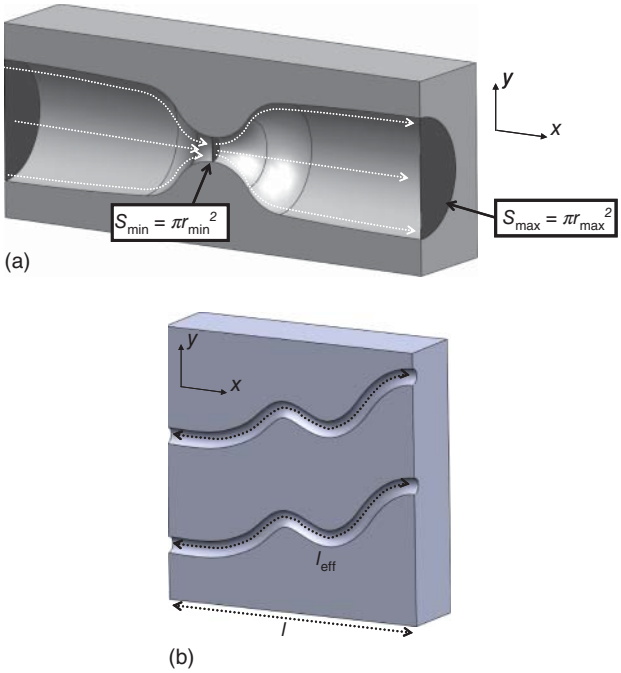

Figure 6.14 Schematic representation of (a) variations in cross-sectional area of a cylindrical pore to define the fluid constriction effect and (b) sinuous but parallel pores to define the geometrical tortuosity factor.

(6.57) for SOEC electrode is not yet fully established. From this point of view, it should be necessary to adapt the law in order to improve its range of predictability. For this purpose, some corrective coefficients could be introduced in the phenomenological law (Equation 6.57) (such as $M_i = A(\kappa_i \varepsilon_i)^{\mathrm{B}} \times \delta_i^{\mathrm{C}} / (\tau_i^{\mathrm{geo}})^{\mathrm{D}}$ where the constants A, B, C and D should be fitted on real electrode microstructures).

To overcome these difficulties, several authors have proposed to directly determine the effective coefficients by employing some homogenization techniques [9, 75–83]. These methods aim to replace a three-dimensional (3D) representation of the real heterogeneous electrode by an equivalent homogeneous medium characterized by its effective properties. The homogenization methods are based on the numerical processing of a 3D representation of the SOEC electrode. They have taken advantage of the recent advances in 3D microstructure imaging (by focused ion beam sectioning tomography or synchrotron X-ray tomography: see Section 6.5.1).

In these methods, the local flows are computed within the conductive digitized structure. For this purpose, Laplace's equation for gas diffusion or charge transfer is solved on the whole 3D reconstructed phase volume:

$$\text{Gas phase}: \quad \frac{-D_{\mathrm{gas}}^{\mathrm{bulk}}}{RT} \mathrm{div}(\mathrm{grad}(y_i^{\mathrm{Local}} P_{\mathrm{T}}^{\mathrm{Local}})) = 0 \tag{6.58a}$$

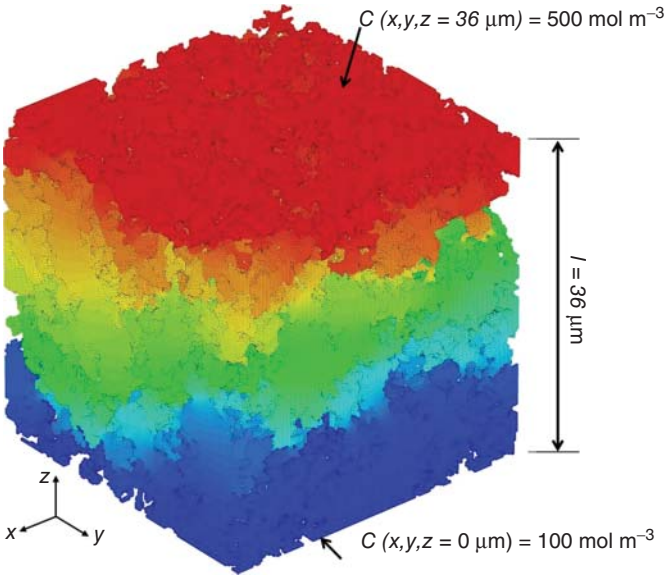

Figure 6.15 Gas concentration field simulated by FEM in the connected porosity of an Ni–YSZ cermet support. Two concentrations have been applied at the lower ($z = 0$) and upper ($z = 36\,\mu$m) surfaces as boundary conditions [75].

$$\text{Ionic or electronic phase}: \quad -\sigma_i^{\text{bulk}}\,\text{div}(\text{grad}(\varphi_i^{\text{Local}})) = 0$$
$$(i = \text{ionic or electronic phase}) \tag{6.58b}$$

where $y_i^{\text{Local}} P_T^{\text{Local}}/RT$ and φ_i^{Local} denote, respectively, the local gas concentration and the local electrical potentials calculated in the heterogeneous structure.

The Lattice–Boltzmann method (LBM) [79–81], the finite element method (FEM) [9, 75–78] or the finite volume method [82] are generally employed to compute Equation 6.58. In practice, each phase of the reconstruction is converted into an independent mesh. Simulations are carried out with zero flux condition at the interfaces within the domain whereas a potential (or flux) boundary condition is applied onto two opposite edges of the analysed domain. For example, Figure 6.15 shows the gas concentration field determined by FEM simulation in the porosity of a commercial Ni–YSZ support [75].

At the 'macroscopic' scale, it is worth remembering that the electrode is considered as a continuum and homogeneous medium represented by its effective property. From this point of view, the macro concentrations $y_i^{\text{Macro}} P_{\text{T}}^{\text{Macro}}/RT$ or potentials $\varphi_{\text{e}^-}^{\text{Macro}}$ can be used as boundary conditions to solve Equation 6.58 at the 'microscopic' scale (i.e. on the heterogeneous domain). The effective diffusion coefficient (or the effective conductivity) is then deduced from the numerical analysis by equating the macro homogeneous flux to the average value computed from

the simulation:

$$\frac{-D_{\text{gas}}^{\text{eff}}}{RT}\text{grad}(y_i^{\text{Macro}}P_{\text{T}}^{\text{Macro}}) = \frac{-D_{\text{gas}}^{\text{bulk}}}{RT} \times \frac{1}{V}\iiint_V \text{grad}(y_i^{\text{Local}}P_{\text{T}}^{\text{Local}})\text{d}V \quad \text{(gas phase)} \tag{6.59a}$$

$$-\sigma_i^{\text{eff}}\text{grad}(\varphi_i^{\text{Macro}}) = -\sigma_i^{\text{bulk}} \times \frac{1}{V}\iiint_V \text{grad}(\varphi_i^{\text{Local}})\text{d}V$$
$$(i = \text{ionic or electronic phase}) \tag{6.59b}$$

In homogenization problems, the reconstructed volume must be sufficiently large to be statistically representative of the studied heterogeneous materials. Furthermore, it can be shown that the calculated effective property depends on the choice of the boundary conditions. However, it is beyond the scope of this section to discuss these details. The reader interested in such homogenization methods could refer to specialized book reviews [84] or articles [85].

Once the effective transport property is known, the result is usually presented in chemical science engineering through an 'apparent' tortuosity factor [9, 75–83]:

$$\tau_{\text{gas}}^{\text{app}} = (\kappa_{\text{gas}}\varepsilon_{\text{gas}}) \times \frac{D_{\text{gas}}^{\text{bulk}}}{D_{\text{gas}}^{\text{eff}}} \quad \text{(gas phase)} \tag{6.60a}$$

$$\tau_i^{\text{app}} = (\kappa_i\varepsilon_i) \times \frac{D_i^{\text{bulk}}}{D_i^{\text{eff}}} \quad (i = \text{ionic or electronic phase}) \tag{6.60b}$$

In this approach, the phase volume fraction and connectivity are also deduced from the 3D reconstruction by direct geometrical analysis. Although the 'apparent' tortuosity factor is a parameter that is widely used for SOEC/SOFC electrodes, it corresponds to a purely phenomenological representation of the microstructure morphology. Indeed, it encompasses both the geometric tortuosity and the 'constrictivity' parameter.

Impact of Microstructure on Intrinsic Knudsen Diffusivity Up to now, it has been implicitly assumed that the 'intrinsic' properties of gas and solids are independent of the electrode microstructure. This claim is obviously correct for the bulk of electrical conductivities that depend only on the physical nature of materials. This is also verified for the molecular diffusivity, since this coefficient is exclusively controlled by interactions of molecules among themselves.

Unlike electrical conductivities or molecular diffusion coefficients, Knudsen diffusivities depend on the local geometry of porosity as this mechanism of gas transport is governed by the collisions of gaseous species with the pore wall. Therefore, in the framework of the kinetic theory of gases, it has been demonstrated that the 'intrinsic' Knudsen coefficient is basically proportional to a structural parameters

K_0 [33], which is usually taken as the mean pore radius $\bar{r}$ [17, 70]:

$$D_{i,\mathrm{k}}^{\mathrm{bulk}} = \bar{r}\frac{2}{3}\sqrt{\frac{8RT}{\pi M_i}} \quad (i = \mathrm{H_2},\ \mathrm{H_2O},\ \text{etc} \ldots) \tag{6.61}$$

As for the constrictivity or tortuosity factor, the mean pore radius of a complex connected network is also difficult to define properly. However, different geometrical concepts can be used to deduce this parameter from 3D electrode reconstructions.

If the mean pore diameter is seen as a characteristic length of the gas phase, it can be calculated with mathematic morphological tools such as the two-point correlation or covariance function [84, 86]. Moreover, analysis of the reconstruction in terms of pore size distribution should allow estimating this parameter [87].

Impact of Microstructure on Electrochemical Reaction Rates Morphological characteristics of the FL have also a direct impact on the electrochemical reaction rates. Indeed, by offering more or less active sites for the electrochemical reactions, electrode microstructure is one of the key parameters to promote the electro-catalytic activities of materials. In this framework, two main microstructure parameters have to be considered depending on the electrode multi-step mechanism:

- In a composite electrode made of an electronic and an ionic conductor (i.e. Ni–YSZ cermet or LSM–YSZ cerer), the fundamental step of charge transfer can only occur at the 'active' TPBls. These sites are simply defined by the linear contacts with the three percolated phases where ions, electrons and gas can effectively meet. They must be distinguished from the total TPBl, which includes the 'inactive' lines related to the non-connected phases. For a composite electrode, the kinetic constant of charge transfer is thus directly scaled up by the density of 'active' TPBls $\xi_{\mathrm{TPBl}}^{\mathrm{Actif}}$ [27] (see relations (6.37) or (6.42)):

$$k_{\mathrm{ox}} \text{ and } k_{\mathrm{red}} \propto \xi_{\mathrm{TPBl}}^{\mathrm{Actif}} \text{ for the electrochemical reactions (6.37) and (6.44)} \tag{6.62}$$

- For a MIEC electrode, it can be noticed that the kinetic constants related to the direct oxidation at MIEC/electrolyte/gas TPBs will be also proportional to the density of TPBs (see section 6.3.2.4).
- Among the several electrode reaction pathways, the gas adsorption/desorption step constitutes a common rate-limiting reaction, especially at high polarization (cf. Section 6.3.2.3). In this case, the adsorption/desorption kinetic constants must depend on the electrode surface area that is accessible by the gaseous species. This parameter corresponds to the electrode-specific surface area S_{p}, classically defined as the surface area of the open porosity normalized by the volume of the gas phase.

For an anodic MIEC, the charge transfer is likely to takes place all along the surface of the single phase material. In such a condition, the kinetic constants of

surface reactions (which correspond to the oxygen release from the bulk (Equation 6.49) and the subsequent oxygen desorption (Equation 6.51) are then unambiguously proportional to the specific surface area of electrode material:

$$k_{ox} \text{ and } k_{red} \propto S_p \text{ for the reaction (6.49) of oxygen ex-corporation} \quad (6.63a)$$

$$k_{des} \text{ and } k_{ads} \propto S_p \text{ for the oxygen associative desorption (Equation 6.51)} \quad (6.63b)$$

However, for composite electrodes, the adsorption or desorption step is potentially not the same on the surface of the electronic and ionic conductors. In this case, the kinetic constants should be distinguished between the two conductors and scaled up by their respective surface areas in contact with the gas. For example, as discussed in Section 4.2.3.3 for the LSM–YSZ anode, it seems that oxygen adsorbates are preferentially attached on the surface of LSM

Table 6.2 Comparison of some microstructural parameters of typical Ni–YSZ cathodes.

	Ni–YSZ			
	Electrode active layer or functional layer		**Cell support**	
Phase volume fraction (%)	Ni	28.2 | 21.8 | 24.5 | 24.5| 36.9| 28.5	Ni	21.7 | 24.6
	YSZ	49.0 | 28.4 | 26.0 | 26.0| 40.1| 49.3	YSZ	31.7 | 41.4
	Pores	22.8 | 49.8 | 49.5 |49.5 | 23.0| 22.2	Pores	46.6 | 34.0
Connectivity (%)	Ni	97.1 | 92.82| n/a | 86.7| 99.3| 98.5	Ni	96.7 | 94.8
	YSZ	99.7 |97.16 | n/a |96.6 | 100 | 99.9	YSZ	99.2 | 99.3
	Pores	88.0 | 99.82| n/a |100 | 98.8| 77.6	Pores	99.2 | 96.9
'Apparent' tortuosity factors	Ni	5.50 | 12 | 6.94 | 11 | n/a | n/a	Ni	8.65 | n/a
	YSZ	2.28 | 7.5 | 9.84 |6.58 | n/a | n/a	YSZ	3.63 | n/a
	Pores	10.1 | 2.0 | 1.83 | 1.95| n/a | n/a	Pores	2.22 | n/a
Specific surface area ($\mu m^2\ \mu m^{-3}$)	Ni	6.54 | n/a | n/a | 3.83 | 4.11 | 2.17	Ni	5.87 | 1.34
	YSZ	5.50 | n/a | n/a | 7.79 | 6.01 | 3.11	YSZ	6.01 | 2.17
	Pores	9.09 | n/a | n/a | 4.25 | 7.56 | 2.28	Pores	4.24 | 1.82
Density of TPBls ($\mu m\ \mu m^{-3}$)	Total	4.63 | 2.05 | 2.55 | 2.44 | 3.06 | 4.36	Total	3.46 | 2.14
	Active	3.30 | n/a | 1.65 | n/a | 2.89 | n/a	Active	2.61 | n/a
Mean pore diameter (μm)		0.94 | n/a | n/a | n/a | n/a | 0.378		2.6 | 0.541
Reference[a)]		[9] | [80] | [79] | [89] | [90] | [91]		[9] | [91]

a) All values of tortuosity factors are given for one direction.

particles (Figure 6.12). According to this reactive pathway, the kinetic constants for the desorption step (Equation 6.40a) must be proportional to the LSM/gas interfacial surface area.

Until shortly before the capacity to obtain 3D electrode reconstruction, the TPBs could only be estimated through indirect methods. Nowadays, the density of total TPBls can be determined from the 3D reconstruction by counting all the segments in contact with the three phases. (Different methods are given in the literature and a short review can be found in [79, 88].) One may note that their active part can be easily obtained if the analysis is restricted to the connected phases. Finally, electrode-specific surface areas can also be deduced from the 3D reconstruction by using specific algorithms or mathematical morphological tools.

Typical Electrode Microstructure Parameters Tables 6.2 and 6.3 summarize some microstructure parameters recently determined on typical SOEC/SOFC electrodes. A large scattering on the data can be observed even when considering

Table 6.3 Comparison of microstructural parameters of typical LSM–YSZ and LSCF cathodes.

	LSM–YSZ		LSCF	
Phase volume fraction (%)	LSM YSZ Pores	24 | 23.1 | 34 26 | 26.3 | 32 50 | 50.6 | 34	LSCF Pores	51.7 | 63.2 48.3 | 36.8
Connectivity (%)	LSM YSZ Pores	90 | 76.2 | 98.2 100 | 98.2 | 99.8 100 | 100 | 98.2	LSCF Pores	n/a | >99% n/a | >99%
'Apparent' tortuosity factors	LSM YSZ Pores	n/a | n/a | n/a 3.5 | n/a | n/a 1.6 | n/a | n/a	LSCF Pores	2.06 | 1.56 1.92 | 2.32
Specific surface area ($\mu m^2\ \mu m^{-3}$)	LSM YSZ Pores	a) | 9.51 | n/a a) | 12.6 | n/a a) | 7.86 | n/a	Pores	4.4 | 7.83
Density of TPBls ($\mu m\ \mu m^{-3}$)	Total Active	7.5 | 10.2 | 6.6 5 | 6.73 | 6.0	n/a	
Mean pore diameter (μm)		n/a | n/a | 0.34	—	
References		[88] | [90] | [92]		[93] | [94]

a) Surface area normalized by the sample volume (μm^{-1}) 1.9/3/4 for LSM/YSZ/pores.

the same electrode composition. This apparent discrepancy in microstructure characteristics must be ascribed to the different manufacturing routes that are generally used for SOEC/SOFC cell fabrication. Moreover, even for the same processing method, conditions in terms of sintering temperature, dimensional characteristics of the initial powder, percentage of pore formers, etc. represent as many crucial parameters that deeply impact the final electrode microstructure.

6.3.3 Role of Temperature in SOEC Operation

6.3.3.1 Cell Thermal Regimes

As detailed in Chapter 1, water splitting into hydrogen and oxygen is an endothermic reaction that requires an energy input. This request in energy corresponds to a positive enthalpic term (i.e. $^{i}/_{2F}\Delta H_{H_2O}(T) > 0$) that must be brought to the system. At high temperature, water is in the form of vapour, and then, $\Delta H_{H_2O}(T)$ denotes the enthalpy of steam formation expressed in joules per mole.

During the electrolysis process, energy absorbed by the reaction is basically provided by the electrical work that corresponds to a change in free energy, $\Delta G = U \times i < 0$. This electrical energy demand for steam electrolysis is increased in operation due to the irreversibilities that increase the cell voltage. At low polarization, electrical work is not sufficient for the steam electrolysis, and thus, a part of the total energy demand is supplied in the form of heat. Conversely, at high polarization, the electrical supply exceeds the energy required for water splitting. In this condition, only a part of the electrical work is used for steam electrolysis, the other part being dissipated as heat.

Endothermic and Exothermic Modes of Operation The electrolysis process leads to a modification in the system entropy ΔS. The overall energetic balance for the electrolyser is thus written as follows:

$$\Delta Q = T\Delta S = \frac{i}{2F}\Delta H_{H_2O} + U \times i$$
$$\text{(Heat sources} = \text{Enthalpy for steam decomposition}(>0) + \text{Electrical work}(<0)) \tag{6.64}$$

The global modification in system entropy is accompanied by heat sources that can be either endothermic or exothermic. If exothermic, heat is released into the cell ($\Delta Q < 0$) and must be exhausted from the electrolyser. If endothermic, heat is absorbed by the cell ($\Delta Q > 0$) and must be brought to the electrolyser.

When the current density is applied during cell polarization ($i < 0$), the thermal regime will pass from an endothermic region at low cell voltage to an exothermic one at high cell voltage:

- Indeed, at high cell polarization ($|i| \gg 0$ and $|\eta| \gg 0$), the absolute value of electrical work is higher than the enthalpy necessary for steam electrolysis (i.e. $\frac{i}{2F}\Delta H_{H_2O} < |U \times i|$). In other words, the entropic terms associated with the irreversibilities are higher than the endothermic nature of steam reduction.

The resulting thermal sources are exothermic ($\Delta Q < 0$) and will induce cell warming.

- Conversely, at low cell polarization ($|i| \rightarrow 0$ and $|\eta| \rightarrow 0$), the absolute value of electrical work is lower than the enthalpy necessary for steam electrolysis (i.e. $\frac{i}{2F}\Delta H_{H_2O} > |U \times i|$). In this case, energy released by the irreversibilities becomes lower than the thermal sinks due to steam reduction. The resulting thermal sources ($\Delta Q > 0$) are endothermic and will induce cell cooling.
- Between the two regimes, the 'thermo-neutral' condition ($\Delta Q = 0$) is defined as the enthalpy for water splitting that is equal to the supplied electrical work (i.e. $\frac{i}{2F}\Delta H_{H_2O} = |U^{\Delta Q=0} \times i|$). In this condition, heat release due to the irreversibilities is strictly counterbalanced by the enthalpy demand for the steam electrolysis reaction. One may note that the 'thermo-neutral' condition is independent of current density and is fulfilled for a given cell voltage defined by $U^{\Delta Q=0} = \frac{\Delta H_{H_2O}(T)}{2F}$. For example, the thermo-neutral voltage is $U^{\Delta Q=0} \approx 1.28\,\mathrm{V}$ at $T = 800\,^{\circ}\mathrm{C}$.

Electrolyser Temperature It is expected that SOEC temperature will be deeply affected by the thermal regimes of steam electrolysis. However, it is worth noting that the level of cell temperature is also strongly dependent on the system design and the associated thermal boundary conditions. For instance, when considering a single cell operated in a test bench, the SOEC heating (or cooling) will be mitigated by the controlled furnace temperature. In this case, it can be roughly assumed that the cell is operated in an isothermal condition (with a temperature imposed by the furnace control set point).

Let us consider now an elementary unit constituted of the cell sandwiched between the two interconnect plates. If the unit is located in the central part of the stack, the heat flux can be considered negligible in the staking direction. Therefore, adiabatic conditions can be assumed on the surfaces connecting two adjacent elementary units (Figure 6.16a). Thermal boundary conditions are then given by the temperature of gases introduced in the electrolyser and by the temperature considered for the stack-insulating enclosure (Figure 6.16a). In this condition, two modes of thermal transfer ensure the heat exchanges with the cell:

1) Firstly, heat can be exhausted (or brought) by the anodic and cathodic gas flow. This corresponds to the convective heat transfers that take place all along the gas channel distribution.
2) Moreover, because of the high temperatures of SOEC operation, radiation is the predominant mode of heat transfer between two solid surfaces. As a consequence, heat can also be transferred by the radiative heat exchanges between the edge of the electrolyser (i.e. free surface defined by the outline of the stack) and the wall of the stack-insulating enclosure (Figure 6.16a).

As an illustration in Figure 6.16b, the temperature computed in the central part of a typical planar SOEC stack has been plotted versus current density and cell voltage. For the calculation, gas temperature introduced in the electrolyser and the

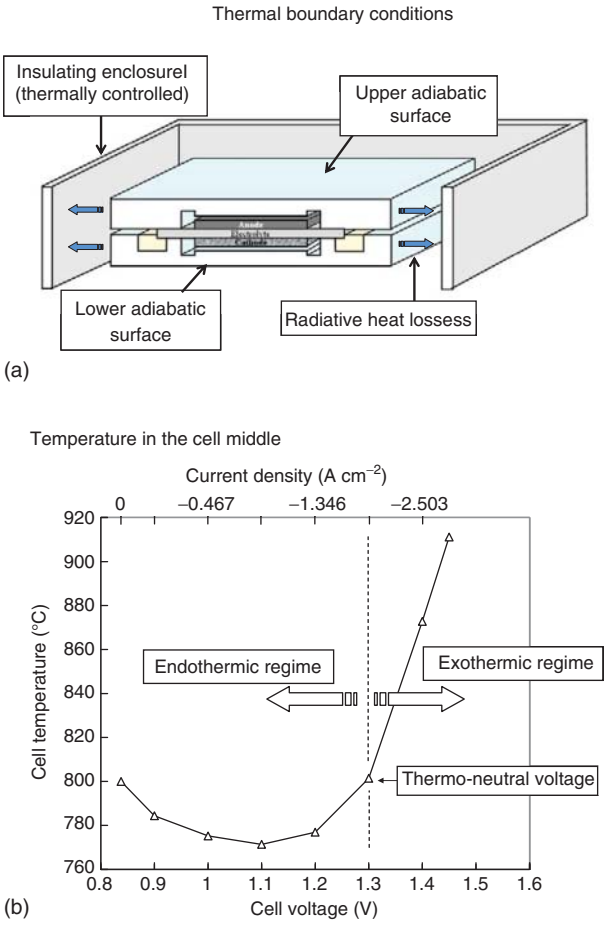

Figure 6.16 (a) Thermal boundary conditions for an elementary unit of a typical electrolyser stack and (b) temperature taken in the middle of a cathode-supported cell plotted as a function of current density and cell voltage. Temperatures of stack enclosure and gas inlets are fixed at 800 °C. Temperature field and electrochemistry are computed with the model presented in Ref. [17] (Ni–8YSZ//8YSZ//LSM–8YSZ, $R_c = 5.10^{-2}\,\Omega\ \text{cm}^2$. Air feeding at the anode side, composition of the inlet cathodic gas: 90% $H_2O + 10\%\ H_2$, electrode microstructural properties are given in Ref. [9], $\ell_{\text{cathode}}^{\text{support}} = 1$ mm, $\ell_{\text{electrolyte}} = 10$ μm, $\ell_{\text{anode}} = 40$ μm, interconnect thickness = 10 mm).

temperature of the stack enclosure have been supposed to be controlled and maintained at 800 °C. As expected, it is found that cell temperature is equal to ≈800 °C when the cell operates at the thermo neutral voltage (1.28 V). Below this voltage, the endothermic sinks induce cell cooling. However, it may be noted that the temperature decrease remains fairly low in this thermal regime. Conversely, a steep temperature elevation is found as soon as the voltage exceeds the thermo-neutral

voltage. In other words, the stack heating in the exothermic mode of operation is much higher than the one for a single-cell environment.

6.3.3.2 Impact of Cell Temperature on Polarization Curve

Temperature modification is likely to have a strong impact on cell performances. Indeed, most of the processes that are involved in steam electrolysis are temperature-dependent. As a general rule, it must be kept in mind that any increase in temperature is accompanied by an improvement in cell performances.

Role of Temperature on Electrolyte Conductivity Ionic conductivity of solid electrolytes is a physical property that exhibits a thermally activated behaviour. As a general rule, SOEC electrolyte resistance is significantly lowered when temperature is increased.

Electrical characteristics of usual 8YSZ electrolytes have been widely studied and present strong temperature dependence. Nonetheless, the reported values for this material present a large scattering in the open literature [67, 95–97]. Indeed, ionic conductivity of solid-state electrolyte is a physical property that is largely dependent on material microstructure [97–99] (and, subsequently, of the electrolyte manufacturing conditions). Nevertheless, it is worth underlining that the thermal evolution of ionic conductivity can be expressed in the form of an Arrhenius law with a pre-exponential factor that is inversely proportional to the temperature [8]:

$$\sigma_{\text{io}}^{\text{electrolyte}} = \frac{\sigma_0}{T} \times \exp\left(\frac{-E_{\sigma_{\text{io}}}}{RT}\right) \tag{6.65}$$

where $E_{\sigma io}$ refers to the activation energy of oxygen ions mobility. For the 8YSZ electrolyte, an activation energy on the order of 83 kJ mol^{-1} must be considered in the range of SOEC operating temperature [67, 96]. According to the data given in [67], a temperature increase from 800 to 850 °C results in an improvement in conductivity of 51%. The increase in ionic conductivity directly reduces the ohmic losses in the cell polarization curve (see Equation 6.5 in Section 6.3.1.2). This constitutes a major effect that explains a large part of the SOEC temperature dependence, especially for the thick ESC design.

Role of Temperature in Elementary Reactions Most of the elementary steps that are involved the reaction mechanism are also thermally activated. The kinetic constant for charge transfer is thus expressed through a modified expression of the Arrhenius law, which explicitly takes into account the temperature dependence of the pre-exponential factor [27, 38]:

$$k_{\text{red}} \text{ and } k_{\text{ox}} \propto \left(\frac{T}{T_0}\right)^{\beta} \times \mathrm{e}^{\frac{-\Delta H_{\text{ox}}}{RT}} \tag{6.66}$$

where T_0 is reference temperature and β the temperature exponent (that is taken in practise either as 1 [27] or 0 [38]). It may be noted that the kinetic for charge transfer generally presents a high activation energy that could be in the range of

≈200 kJ mol^{-1} for steam reduction in an Ni–YSZ cermet [100] or ≈294 kJ mol^{-1} for O_2 production in an LSM–YSZ composite [27].

Moreover, adsorption or desorption of gas molecules on the surface of materials is also potentially a thermally activated process with kinetic constants that follow the same expression as the previous one [101]. As an illustration, activation energy reported for steam desorption on an Ni catalyst (i.e. $H_2O - s_{Ni} \rightarrow H_2O(g) + s_{Ni}$) is equal to 60–63 kJ mol^{-1} [38, 102]. Activation energies for the associative desorption of hydrogen (i.e. $2H - s_{Ni} \rightarrow H_2(g) + 2s_{Ni}$) would be in the range of 80–100 kJ mol^{-1}. These reported values are measured for H_2 molecule adsorption on single Ni crystal surfaces (i.e. $E_a = 95 - 96$ kJ mol^{-1} [103, 104] on the Ni (1 1 1) and Ni (1 0 0) planes, and 89 kJ mol^{-1} [104] on the Ni (1 1 0) plane). Unlike adsorption, it is worth mentioning that there is no barrier energy for the dissociative adsorption of hydrogen on a nickel surface [105].

Finally, one may note that surface diffusion of adsorbed atoms over the active sites is also a thermally activated process. Indeed, the motion of adsorbed species must overcome an energy barrier to jump from one site to the other. However, it is worth remembering that this mode of mass transfer is still poorly understood (even if it could constitute a key process at TPBs). Accordingly, literature data on surface diffusion coefficients are scarce for SOEC materials and often rely on density functional theory (DFT) simulations to determine the activation energies. A compilation of diffusion coefficients is summarized in [43] for species adsorbed on Ni or YSZ surfaces. For instance, it is reported that the activation energy for the diffusion of hydrogen atoms on Ni ranges from 11 to 19 kJ mol^{-1}, while the one for water adsorbates on YSZ is on the order of 55 kJ mol^{-1}.

Role of Temperature in the Global Electrochemical Process The global electrochemical reaction that occurs in the FL is controlled by the sequence of elementary reactions but also by the oxygen ion transport in the bulk of the ionic conductor (see Section 4.2.3.1). As all these phenomena are thermally activated, the resulting electrode exchange current density is expressed through an Arrhenius law:

$$i_0 = i_{00} \times e^{\frac{-E_a}{RT}} \tag{6.67}$$

The global electrode activation energy E_a includes the energy barrier for the electrochemical reaction pathway and the contribution for the ionic oxygen conductivity. Activation energy of 120 kJ mol^{-1} is thus reported [9] for a typical Ni–8YSZ cermet. It combines the contribution for O^{2-} conduction (≈83 kJ mol^{-1}) and the contribution of the highest energy barrier of the sequential elementary reactions (i.e. ≈200 kJ mol^{-1} for charge transfer). Therefore, a cell temperature elevation from 800 to 850 °C yields a noticeable increase in Ni–8YSZ exchange current density from the typical value of 530 to 965 mA cm^{-2}.

The increase with temperature of both electrode exchange current densities results in a decrease of the associated activation overpotentials (see Equation 6.16 in Section 6.3.1.3). This reduction of electrode polarization in temperature obviously leads to significant improvement in cell performances. This statement is

especially true for the CSC design, for which the electrode activation overpotentials constitute the prevalent contribution to the global cell polarization (as the ohmic losses are low: see decomposition in Figure 6.6).

Role of Temperature in Gas Transport It is worth mentioning that gas transport through the porous electrodes is not a thermally activated process. On the contrary, the dependence of gas diffusivities with temperature is rather weak. As a consequence, any reasonable SOEC temperature elevation will not significantly facilitate the gas transfer across the electrode.

Indeed, as already shown in Equation 6.61, the Knudsen coefficient is proportional to the square root of the temperature (i.e. $D_{i,\mathrm{k}}^{\mathrm{bulk}} \propto \sqrt{T}$). The binary diffusion coefficients exhibit temperature dependence in $T^{3/2}$ or $T^{1.75}$ (according to the solution of the Boltzmann equation by the Chapman–Enskogg procedure [106] or the Fuller theory [107], respectively) :

$$\text{Chapman} - \text{Enskoggmodel}: D_{i,j} = \frac{0.0018583\sqrt{1/M_i + 1/M_j}}{P_{\mathrm{T}}\ \Omega\ \sigma_{i,j}^2} \times T^{3/2} \quad (6.68a)$$

$$\text{Fuller model}: \quad D_{i,j} = \frac{0.00143}{P_{\mathrm{T}}(V_i^{1/3} + V_j^{1/3})^2\sqrt{\frac{2}{1/M_i + 1/M_j}}} \times T^{1.75} \quad (6.68b)$$

where Ω denotes the collision integral (dimensionless) and σ_{ij} the average collision diameter (in angstroms) [12, 106, 108]. The terms V_i represent the molar diffusion volumes whose values are tabulated in [109]. It may be noted that values of diffusivities deduced from the Chapman–Enskogg and Fuller expressions are quite similar in the temperature range of SOEC operation, and from a practical point of view, both models can be employed indifferently.

The thermal behaviour of Knudsen and molecular gas diffusivities means that the related concentration overpotentials (see Section 6.3.1.3) are not significantly affected by temperature. In other words, any reasonable temperature modification of the electrolyser will not change the cell polarization losses due to the mass transfer limitation through the electrodes.

Impact of Temperature on Cell Performances This section aims to give an insight into the effect of temperature modification on the global electrolyser performances. For this purpose, the polarization curve of a typical cell has been computed in an isothermal condition at $T = 800\,°\mathrm{C}$. The resulting U–i curve is plotted in Figure 6.17 and is compared to the one obtained considering the stack thermal boundary conditions depicted in Figure 6.16a. In this situation, only temperatures of gas inlets and stack enclosure are fixed (in the present case at 800 °C). Cell temperature is then free to evolve during polarization and the resulting temperature profile is given in Figure 6.16b.

- Under the thermo-neutral voltage, that is to say in the endothermic mode of operation, cell temperature in the stack is cooled below 800 °C (Figure 6.16b). As

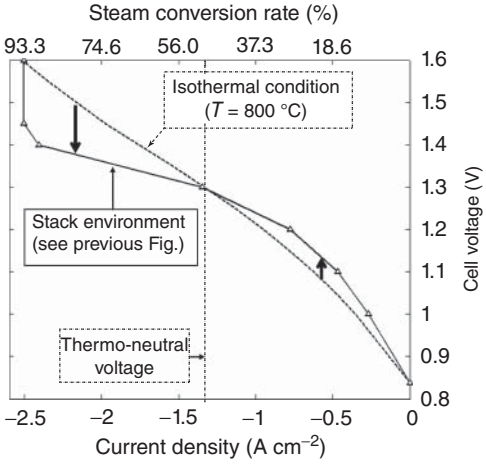

Figure 6.17 Polarization curves for a cathode-supported cell calculated considering (i) an isothermal condition at $T = 800\,°C$ or (ii) for the thermal boundary conditions and cell temperatures given in Figure 6.16 (a stack environment). Temperature field and electrochemistry are computed with the model presented in Ref. [17] (Ni–8YSZ//8YSZ//LSM–8YSZ, $R_c = 5 \times 10^{-2}\,\Omega\ cm^2$. Air feeding at the anode side, composition of the inlet cathodic gas: 90% $H_2O + 10\%\ H_2$, electrode microstructural properties are given in Ref. [9], $\ell^{support}_{cathode} = 1$ mm, $\ell_{electrolyte} = 10$ μm, $\ell_{anode} = 40$ μm, interconnect thickness = 10 mm).

illustrated in Figure 6.17, the cell cooling leads to an extra voltage loss compared to the isothermal case, resulting in a global deterioration of the electrolyser performances. At $i = -0.5\ A\ cm^{-2}$, the temperature decrease is roughly equal to ≈29 °C (Figure 6.16b), yielding a supplementary cell voltage drop of ≈50 mV. As previously discussed, this thermal effect must be attributed to the temperature dependence of both (i) electrolyte ohmic resistance and (ii) electrode activation overpotentials.

- At the thermo-neutral voltage, the two polarization curves intersect (Figure 6.17), as cell temperatures become equal to 800 °C in both cases.
- Above the thermo-neutral voltage, the steep temperature elevation results in a significant reduction of cell polarization losses. However, at high steam conversion rate, the polarization curve computed with the stack environment assumption reaches a limiting current density so that cell performances become increasingly similar in both cases. Such a condition of operation means that the current density is bounded by the polarization losses induced by the steam starvation at the electrochemical active sites. This is the result of two contributions: (i) the cathode concentration overpotential due to the mass transfer limitation and (ii) the 'reversible' polarization associated with the high steam conversion rate (see Section 6.3.1.3). One must remember that the former phenomenon is not thermally activated while the 'reversible' polarization is by nature independent of temperature. Therefore, the appearance of the limiting current density is not significantly affected by temperature.

6.3.4
Summary and Concluding Remarks

As shown in this section, electrical demand in operation for HTSE increases with increasing current density and the associated hydrogen production rate. The loss in the global electrolyser efficiency comes from different phenomena. First of all, gas conversion takes place all along the cell and induces an increase in cell voltage. This increase can lead to a limiting current density if steam is fully converted into hydrogen. Aside from this 'reversible polarization', some irreversible losses arise in operation and are also accompanied by an increase in electrical demand. They have been split into three contributions: the ohmic polarization and the activation and concentration overpotentials.

Ohmic polarization stems from the ionic resistance of the electrolyte and, to a lesser extent, from the electronic resistivity of electrodes. Ohmic losses are thus predominant for thick ESC design. In this framework, the CSC geometry has been designed to reduce the ohmic polarization by making thinner electrolytes.

Concentration overpotentials are caused by the difficulty of gas to diffuse through the porous electrodes. These contributions are generally low for cells fed under hydrogen and steam. Nevertheless, they can lead to large overpotentials in the case of CSCs operated at high current density.

Activation overpotentials correspond to the supplementary energy barrier that is requested to trigger the electrochemical reactions. Except for the limitation by gas diffusion already taken into account in concentration overpotential, activation overpotential includes all the phenomena that hinder the rate of the electrochemical reaction. These phenomena are related to the underlying local mechanisms controlling the overall reaction. In this regard, activation overpotentials strongly depend on the nature of the materials and the rate-determining steps of the electrochemical process. Currently, the understanding of the elementary reactive pathways in steam electrolysis is an important issue to improve both cell efficiency and durability.

Moreover, electrode microstructure also plays a major role in cell performances. Indeed, electrode microstructural properties are key parameters that have a direct impact on gas diffusion and material electrochemical activities. From this point of view, optimization of cell microstructures in electrolysis mode represents a strategic axis for further SOEC developments.

Finally, ohmic polarization and activation overpotentials are thermally activated processes such that the cell electrochemical performances are highly temperature-dependent. Moreover, SOEC operation presents three thermal regimes depending on the polarization (endothermic, thermo-neutral or exothermic). This intrinsic thermal behaviour of cells can lead to some technical difficulties to manage the stack electrolyser temperature (see Section 6.4.3).

6.4 Performances and Durability

As mentioned previously, the maturity of HTSE is lower than that of SOFC. However, several teams around the world are performing experiments to evaluate the potentialities of this technology in terms of performance and durability. Several scales are considered. First, experiments are performed at the single-cell level, the cell being either a button cell (a few square centimetres of active area) or a larger one (around 100 cm^2 of active area). This type of test generally carried out in a test bench with ceramic housing and performing grid CCs allows the determination of the intrinsic characteristics of the cell. Second, tests are carried out at the single repeat unit level, with the cell size around 100 cm^2 but in a stack-representative environment, that is to say with the interconnects and sealings. Finally, tests at the stack level are carried out, generally with a few cells (3–5 cells), but more recently with a larger number of cells (above 10, with some tests with 60 cells stacks). This last type of test allows validating the scaling up of the technology. It must be noted that for larger powers, the size of the stack is not increased indefinitely but an arrangement of modules with multiple stacks is rather considered. Finally, only a few tests at the system level have been carried out.

In this section, results in terms of performance and durability at the different testing scales will be presented.

6.4.1 Performances

Figure 6.18 presents the typical range of $i-V$ curves achieved with HTSE technology compared to other water electrolysis technologies (alkaline and polymer electrolyte membrane (PEM) water electrolysis). It may be noted from Figure 6.18 that HTSE typical voltages are lower compared to the other technologies, which is directly linked to the fact that the energy required to split the steam molecule is lower compared to the energy required to split the water molecule, with lower overpotentials. Thus, the power consumption, which is the product of the voltage V by the current I, will be lower for HTSE, leading to better efficiency. In addition, the current, represented in Figure 6.18 in terms of current density (current divided by the active area), is directly linked to the hydrogen production through Faraday's law, $Q_{H_2} = I/2\,F$, with Q_{H_2} the flow rate of hydrogen produced, I the current and F the Faraday constant. Thus, the higher the current (or current density), the greater will be the hydrogen production. Figure 6.18 shows that HTSE is an efficient process to increase the hydrogen production rate. For both reasons, high hydrogen production rate and lower voltage, both the capital expenditure (CAPEX) and operational expenditure (OPEX) are promising.

Cell or stack performances depend on the cell design considered. As mentioned in Section 3.2, ESC and CSC are the two main designs considered, which mainly differ in electrolyte thickness, which is responsible for the main ohmic losses.

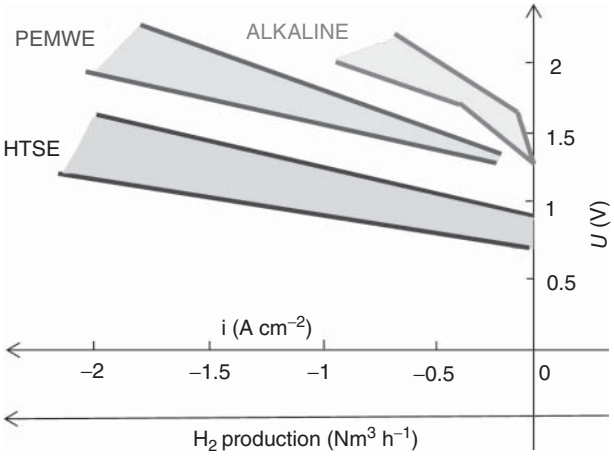

Figure 6.18 Typical range of performance represented by *i*–*V* curves achieved with HTSE technology compared to other water electrolysis technologies (alkaline and PEM water electrolysis). (Figure after [110].)

Thus, performances of ESCs are expected to be much lower than for CSCs at the same temperature; that is why in general ESCs are operated at higher temperature. Generally speaking, standard ESCs reach a maximum current density of $-0.5\,A\,cm^{-2}$ at 1.3 V at 800 °C, and can reach $-0.6\,A\,cm^{-2}$ at 1.3 V at 850 °C [111]. Only advanced ESCs targeting low-temperature operation can reach higher performances, as the one presented in Figure 6.19a. Indeed, thanks to materials tailored for low-temperature operation such as LSC oxygen electrode, a current density of $-0.6\,A\,cm^{-2}$ at 1.3 V at 800 °C is achieved [112].

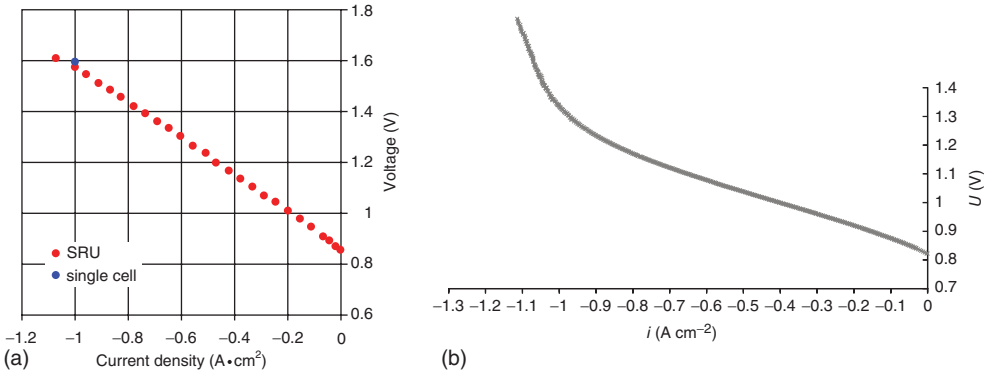

Figure 6.19 (a) *i*–*V* curve of an ESC operated at 800 °C in 90% H_2O/10% H_2 on the hydrogen side, air on the oxygen side, at the single-cell level and in SRU environment; advanced electrode-supported cell, designed for low-temperature operation: Ni–GDC/YSZ/YDC/LSCF. (b) *i*–*V* curve of a CSC operated at 800 °C in 90% H_2O/10% H_2 on the hydrogen side, air on the oxygen side and at the single-cell level; classical cell made up of Ni–YSZ/YSZ/YDC/LSCF.

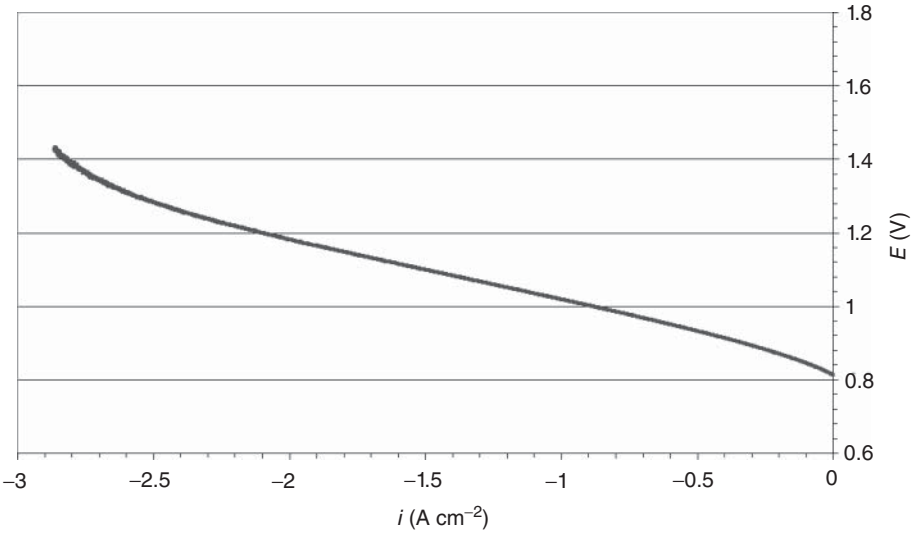

Figure 6.20 *i–V* curve of an advanced CSC made up of Ni–YSZ/YSZ/GDC/LSC tested at 800 °C in 90% H_2O/10% H_2; steam conversion rate SC = 68% at – 2.5 A cm^{-2}.

On the contrary, CSCs give rise to improved performances. Values of −1 A cm^{-2} at 1.3 V at 850 °C were reported by Hauch *et al.* [113] with an LSM oxygen electrode. The same current density can be achieved but at 800 °C with an LSCF oxygen electrode [114, 115]. Current densities as high as −2.0 A cm^{-2} or even above can be achieved at the thermo-neutral voltage at 800 °C with advanced CSCs, the major difference being the use of an LSC oxygen electrode (Figure 6.20).

In addition, it must be noted that direct comparison between the different results is very difficult, as experimental conditions vary quite a lot, as the test benches are different and also the operating parameters, mainly temperature, gas composition and gas flow rate, which are expected to play a major role in the performance.

Performances at the stack level are less numerous.

Most of the results published concern stacks in the range of 3–6 cells. O'Brien reports performances at the 10-cell stack level in the range of −0.4 A cm^{-2} below the thermo-neutral voltage at 800 °C [116]. Ebbesen reports results of a six-cell stack, with a performance at 850 °C of −0.25 A cm^{-2} at the thermo-neutral voltage for the worse cell, and above −0.5 A cm^{-2} for the other cells. Diethelm reports current densities between −0.32 and −0.52 A cm^{-2} at the thermo-neutral voltage at 700 °C on a six-cell stack. [117]. Petitjean highlights performances above −1 A cm^{-2} at the thermo-neutral voltage at 800 °C for a five-cell stack [26]. Ebbesen reports performance results at the six-cell stack scale. At 850 °C, a stack containing six Ni–YSZ/YSZ/LSM–YSZ CSCs presents a current density between −0.25 A cm^{-2} for the worse cell and a value above −0.6 A cm^{-2} for the best cells at 1.3 V [118].

In most of these results, it may be noted that a certain scattering among the different cells of the stacks is observed. Only few papers reports stack results with a small scattering between the different cells. Reytier reports a performance of $-1.9\ \mathrm{A\ cm^{-2}}$ at the thermo-neutral voltage at 800 °C, with no scattering between the three cells of the short stack as shown in Figure 6.21 [119]. In addition, it must be noted that very high performance is achieved, thanks to the use of advanced ESCs.

As mentioned earlier, the aim of single-cell tests is primarily to know the intrinsic behaviour of the cell. Thus, it is interesting to compare single-cell and stack results even if it is not always easy as experimental conditions can vary. However, when it can be done, results tend to show that stack performances are generally below single-cell performances or even SRU ones. Only a few papers compare stack performances to single-cell ones under the same conditions, as reported by Petitjean *et al.* [26] and Reytier *et al.* [119]. Figure 6.22 presents the comparison in the same testing condition of a single cell, an SRU and a five-cell stack. One can see that the $i-V$ curves obtained in these three conditions are almost superimposed, showing that the stack design is rather optimized. Figure 6.21 illustrates the same statement on another stack, with the comparison of a three-cell stack with an SRU, the stack being slightly less performing.

Tests of larger stacks are far less numerous. We can quote works performed at INL in the United States that tested several stacks, including large stacks of 60 cells and modules of several stacks leading to a total of 720 cells for a power of 15 kW [120]. As far as published results are concerned, the test quoted earlier is the

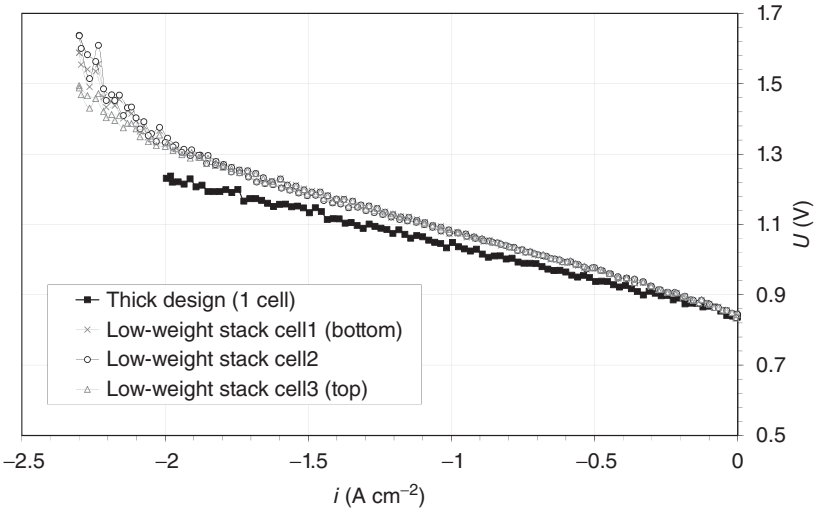

Figure 6.21 Comparison of the performances of the two designs at 800 °C, 90 vol% $H_2O + 10$ vol% H_2 on the hydrogen side, air on the oxygen side, SC = 85% at $i = -2\ \mathrm{A\ cm^{-2}}$ for the low-weight stack, SC = 54% at $i = -2\mathrm{A\ cm^{-2}}$ for the thick and robust one.

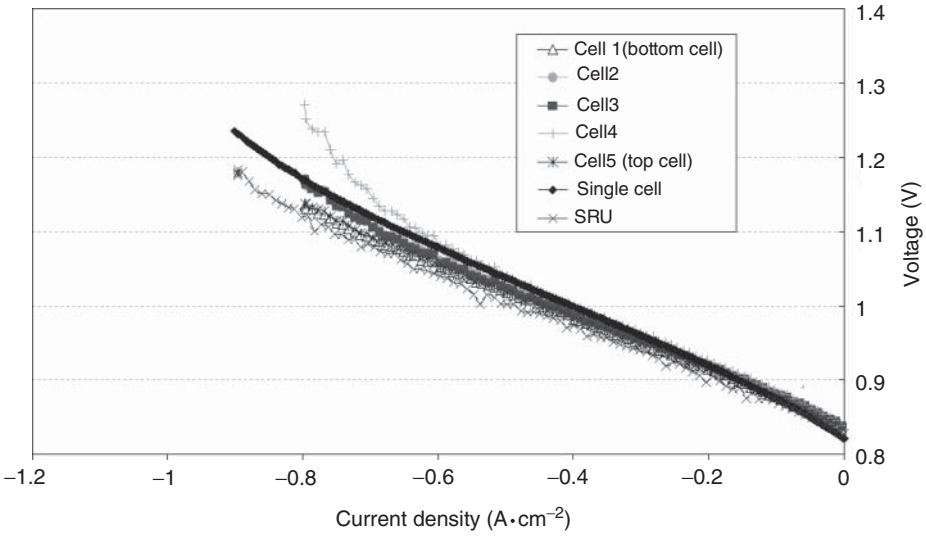

Figure 6.22 *i–V* curves of single-cell, SRU and five-cell stack, at 800 °C in 90 vol% H_2O + 10 vol% H_2, SC = 50% at − 0.8 A cm^{-2}.

largest known. Performance results were not reported, but the hydrogen production, which was equal to 5.7 Nm^3 h^{-1} for the whole system, gives the impression that the performances were rather low. In 2012, the same team reported results at the scale of a 4 kW stack, composed of two stacks of 40 cells, with a current density of −0.4 A cm^{-2} at the thermo-neutral voltage [116].

Li *et al.* [121] report recent results at the scale of a 30-cell stack. An average current density slightly above −0.2 A cm^{-2} is achieved at the thermo-neutral voltage at 800 °C with CSCs made of Ni–YSZ/YSZ/LSM.

Reytier *et al.* [119] reported the performance of a 10-cell stack, with performances above −1.2 A cm^{-2} at the thermo-neutral voltage at 800 °C, and more recently other results at the scale of 10- and 25-cell stacks (Figure 6.23) [122]. One can see in this figure that performances above −1.6 A cm^{-2} at the thermo-neutral voltage at 800 °C have been achieved on both sizes of stacks, with a low scattering between cells.

Finally, we can underline that in the literature, performances are often qualified in terms of current densities through *i–V* curves. However, another important parameter is the hydrogen outlet flow rate. Indeed, if the gastightness of the stack is not good, the hydrogen (and oxygen) produced from the current passing through the stack is not recovered in the exhaust tubes, and thus the efficiency of the electrolyser is not good. Thus, the measurement of the hydrogen (and oxygen) outlet flow rates is of primary importance. Only a few papers consider this parameter. As an example, results reported by Mougin *et al.* [112, 123] show that when the stack is fully gastight, the hydrogen flow rate measured at the outlet is perfectly equal to the one calculated from Faraday's law, assuming 100% efficiency.

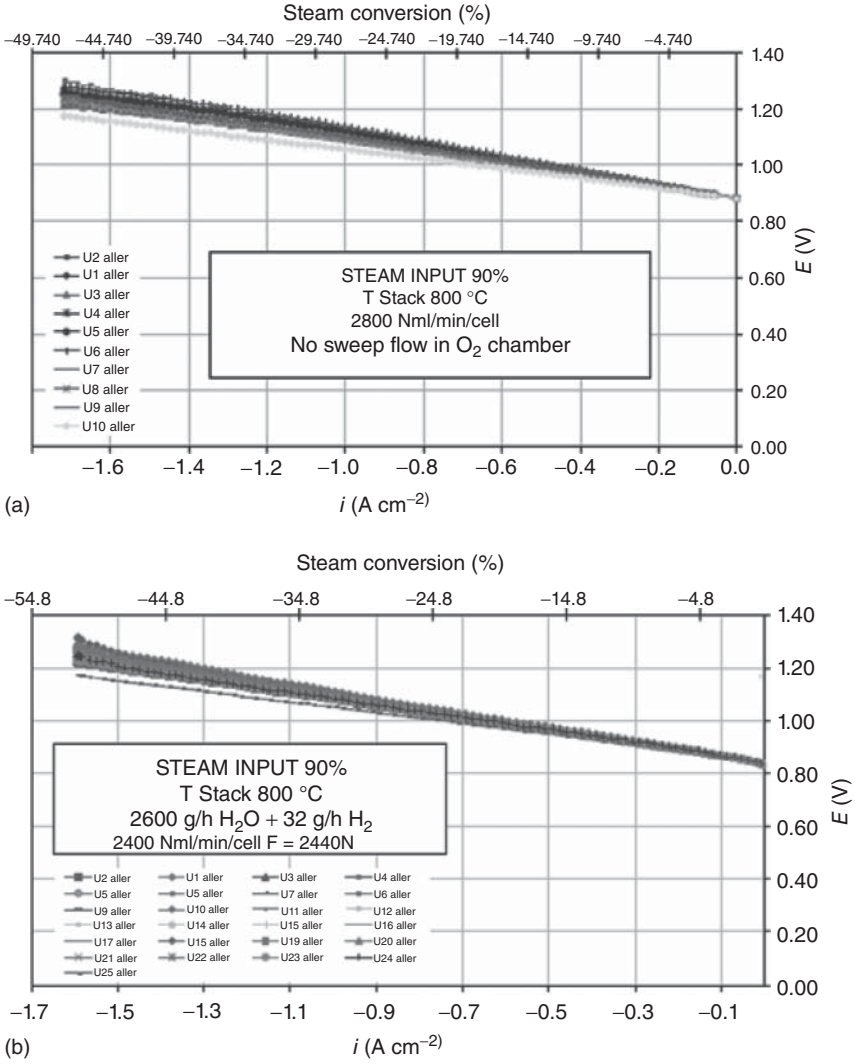

Figure 6.23 i–V curves at 800 °C in 90 vol% H_2O + 10 vol% H_2 of (a) 10-cell stack, flow rate = 28 N ml min^{-1} cm^{-2} and (b) 25-cell stack, flow rate = 24 N ml min^{-1} cm^{-2}.

6.4.2
Durability

The same teams who conducted performance measurements quoted earlier often conduct durability tests. Measurements from a few hundred hours up to 9000 h are reported at different scales (single-cell, SRU or stack). As for performance results, a direct comparison between all the data available is difficult, as operating parameters might differ from one test to another. In addition, degradation rates taken

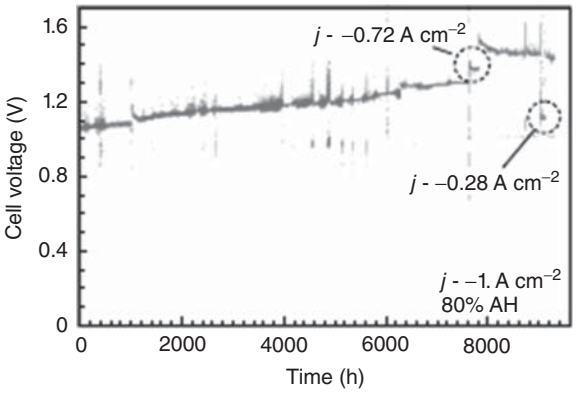

Figure 6.24 Evolution of voltage versus time for a CSC tested at 780 °C at $-1\ A\ cm^{-2}$ over the first 5600 h, the corresponding steam conversion rate being 36%, before a decrease of the current density [126].

from durability tests can be expressed in different ways, either from the durability curve representing the evolution of one parameter (voltage or current) versus time or from $i-V$ curves taken before and after the durability tests. Then the unit can be $mV\ h^{-1}$ or mV/1000 h if the test is performed at a fixed current, or $mA\ h^{-1}$ or mA/1000 h if the test is performed at a fixed voltage or $m\Omega\ cm^2\ h^{-1}$ or 1000 h if the results are taken from the $i-V$ curves. All these degradation rates can be converted into %/h or 1000 h of degradation when divided by the initial value. If all values are expressed in %/1000 h they can be compared, but this comparison might be dangerous as the evolutions of the different parameters over time are intrinsically not similar. In addition, in most cases, the degradation over time is not linear, and an expression in %/1000 h represents an approximation.

Nevertheless, some trends can be stated.

In the first part of this section, we will consider stationary durability tests, that is to say the operating parameters are fixed for the whole duration of the test, even if in some cases some uncontrolled incidents in the test rig or in the lab lead to unintentional transient operation (load cycling, shutdown, etc.).

First, it seems that degradation rates in HTSE are higher than in SOFC. Indeed, when degradation rates below 1%/1000 h are often reported in SOFCs even at stack level, HTSE studies rather report degradation rates above 2%/1000 h [124, 125].

As an illustration, Figure 6.24 presents the durability curve obtained by Schefold on a CSC over 9000 h [126]. The corresponding degradation rate over the first stationary durability period of 5600 h lies between 2.4%/1000 h and 1.7%/1000 h, with a tendency to decrease over time.

More recently, some degradation rates below 1%/1000 h are reported, but they often correspond to the best cell within a stack and/or are obtained in mild testing conditions (mainly low current densities). For example, Fu *et al.* report a degradation rate of 0.4%/1000 h for the best cell within a six-cell stack,

whereas the other cells present rates around 2%/1000 h, for a test performed at −0.6 A cm^{-2} at 700 °C. In addition, some strong instabilities of the cell voltage are observed several times in the stack, making any degradation rate measurements difficult [127]. Nguyen *et al.* report durability tests on a two-cell short stack operated between −0.3 and −0.875 A cm^{-2} over 9000 h. The average degradation rate around 1.5%/1000 h is reported for the whole 9000 h of the test [128].

Table 6.4 summarizes some durability results taken from the literature, in a non-exhaustive way, and moreover some durability results are not expressed by the authors in terms of % of degradation per 1000 h. It highlights that testing conditions might be very different from one test to another, and maybe because of this, no clear trend regarding the impact of the type of test (cell or stack) and of the different operating parameters (temperature, current density or steam conversion rate) can be easily stated. Only a few parametric studies varying one parameter (T, i or SC) while the other is constant are available and tend to show that an increase of temperature, current density and steam conversion is detrimental (see Figure 6.25 for the effect of current density and SC). However, more systematic

Table 6.4 Summary of some of the results of durability tests reported in the literature.

Type of test	Temperature (°C)	Test duration (h)	Operating point (i in A cm^{-2} or U in V)	Steam conversion rate SC (%)	Degradation rate (%/1000 h)	References
CSC	850	1316	−0.5 A cm^{-2}	28	2	[129]
CSC	850	800	−0.5 A cm^{-2}	70	5	[130]
CSC	750	1000	−0.5 A cm^{-2}	—	1.7	[131]
CSC	780	9000	−1 A cm^{-2}	36	3.8	[126]
CSC	800	1000	−0.5 A cm^{-2}	17, 34, 69, 83	6.0–14.4, increase with SCC	[115]
ESC SRU	8000	4000	−0.4 A cm^{-2} −0.6 A cm^{-2} −0.8 A cm^{-2}	25, 37.5 50	1.6 2.4 2.7	[112]
MSC	800	2000	−0.3 A cm^{-2}	—	3.3	[132]
CSC and SRU	800	1000	−0.5 A cm^{-2}	25	6	[112]
CSC SRU	700	700	−0.5 A cm^{-2}	32	1.8	[133]
6-CSC stack	650	1160	−0.26 A cm^{-2}	50	0.4–5.1	[117]
5-CSC stack	800	2700	−0.5 A cm^{-2}	25	7–13	[26]
3-CSC stack	700	700	−1 A cm^{-2}	40	1.9–3.6	[119]
10-ESC stack	800	2500	1.29 V/cell	—	8.15	[111]
5-CSC stack	850	2651	−0.4 to −0.6 A cm^{-2}	39–58	~3	[124]
5-ESC stack	850	4050	−0.4	39	~5	[124]
5-CSC stack	850	3250	−0.8 to −1 A cm^{-2}	52	~4–5	[124]

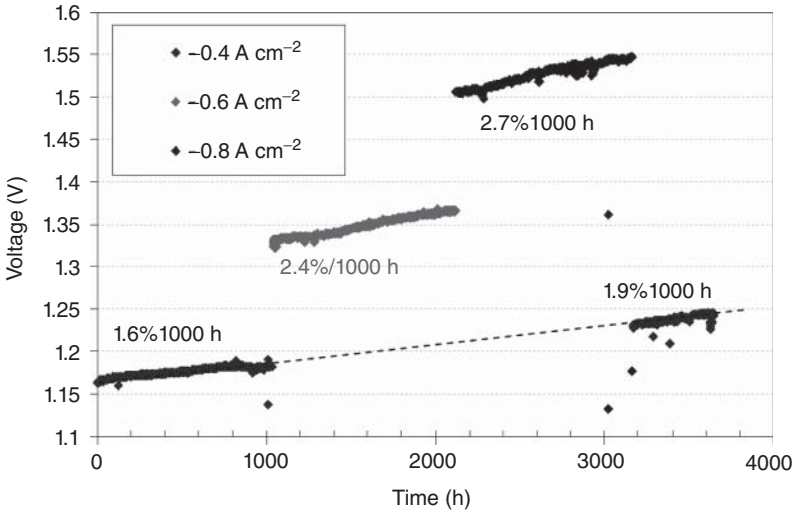

Figure 6.25 Evolution of the cell voltage versus time for a CSC tested in an SRU at 800 °C and constant flow rate for three values of current densities and thus three values of steam conversion rate: $-0.4\,A\,cm^{-2}$ and SC = 25%, $-0.6\ A\ cm^{-2}$ and SC = 37.5% and $-0.8\ A\ cm^{-2}$ and SC = 50% [112].

studies such as those done in SOFC over the past years would be necessary to clarify the impact of the operating parameters on the durability, and to understand the associated degradation mechanisms.

6.4.3
Stack Electrochemical and Thermal Management

It has been shown in Section 3.2 that the stack can be submitted to several thermal modes depending on the voltage: endothermal, thermo-neutral or exothermal.

Depending on the thermal regime, the theoretical efficiency of the stack is different. Indeed, at the thermo-neutral voltage, the heat needed for the electrolysis reaction is exactly compensated by the ohmic losses (Joule heating), leading to an electrical efficiency of 100% [134]. In the exothermal mode, the voltage is higher than the thermo-neutral voltage; hence thermal needs are entirely covered by the Joule heating, which is in excess. The excess heat is dissipated as thermal energy to the environment, in particular to the reaction gases, which in turn leads to a temperature increase. Thus, the electrical efficiency decreases below 100%. Finally, in the endothermal mode, the cell voltage is lower than the thermoneutral voltage, and the heat needed for the reaction is only partly covered by the Joule heating. Thus, some heat has to be supplied externally. It is worth noting that if a high-temperature source above the operating temperature of the HTSE is available, an electrical efficiency above 100% is possible.

In general, stacks are not operated in the exothermal mode for several reasons: first, to maximize the electrical efficiency; second, to avoid strong heating (see Figure 6.13 of Section 3.2); and, third, to minimize degradation, which is expected to be higher in this operating mode. Operation close to the thermo-neutral voltage also has the privileged of making the thermal management easier.

Thanks to a model of HTSE developed by Laurencin *et al*. it is possible to map hydrogen production rates versus cell/stack voltage for given operating conditions (T, anodic and cathodic gas flowrates) [17].

Figure 6.26 presents the maps of temperature in the middle of a cell within a stack (Figure 6.26a), of hydrogen production rate (Figure 6.26b) and of electrical efficiency, taken as the ratio between the energy content of the hydrogen and the electric power used to produce it (Figure 6.26c) [135]. In Figure 6.26a, the region where temperature increase might be dangerous for the cell/stack integrity is highlighted in red and can be considered as forbidden. We see in Figure 6.26b,c that it would correspond to the highest hydrogen production rate but with lower efficiency. One can see from these plots that operating the HTSE close to the thermo-neutral voltage indeed represents a good compromise between thermal management, hydrogen production rate and electrical efficiency (see green circle in Figure 6.26b).

At this point, and in agreement with experimental results at stack level presented earlier, with current density around $-1.5\ \mathrm{A\ cm^{-2}}$ at 1.3 V, an electrical efficiency of 96% lower heating value (LHV) can be calculated (considering a 'free' source of heat). For comparison, efficiencies for alkaline and PEM water electrolysis are rather 62% and 68% respectively.

At the system level, some losses are expected both in electrical converters and in thermal auxiliaries. Taking into account a loss of 8% in all cases, efficiencies become equal to 89% for HTSE, 58% for alkaline electrolysis and 63% for PEM water electrolysis . These values are consistent with those claimed by alkaline and PEM electrolyser manufacturers, and with calculations performed by Ni *et al*. [136]. For HTSE, no real system has been produced and tested for the time being, but signficant increase in efficiency is expected and should be evidenced.

6.5 Limitations and Challenges

The previous sections have shown that HTSE improved performances and efficiency, as well as durability results. However, it clearly appears that degradation rates are still an issue to reach long operation durations, above 25 000 h, such as those targeted for this technology. In addition, as also illustrated earlier, numerous studies have been performed at cell and short stack level, only a couple at stack level with 5–25 cells and very few for larger stacks, while system developments have just started. Thus, the maturity of the technology is much less than the one for alkaline and PEM water electrolyses, and further extensive work is requested for system integration.

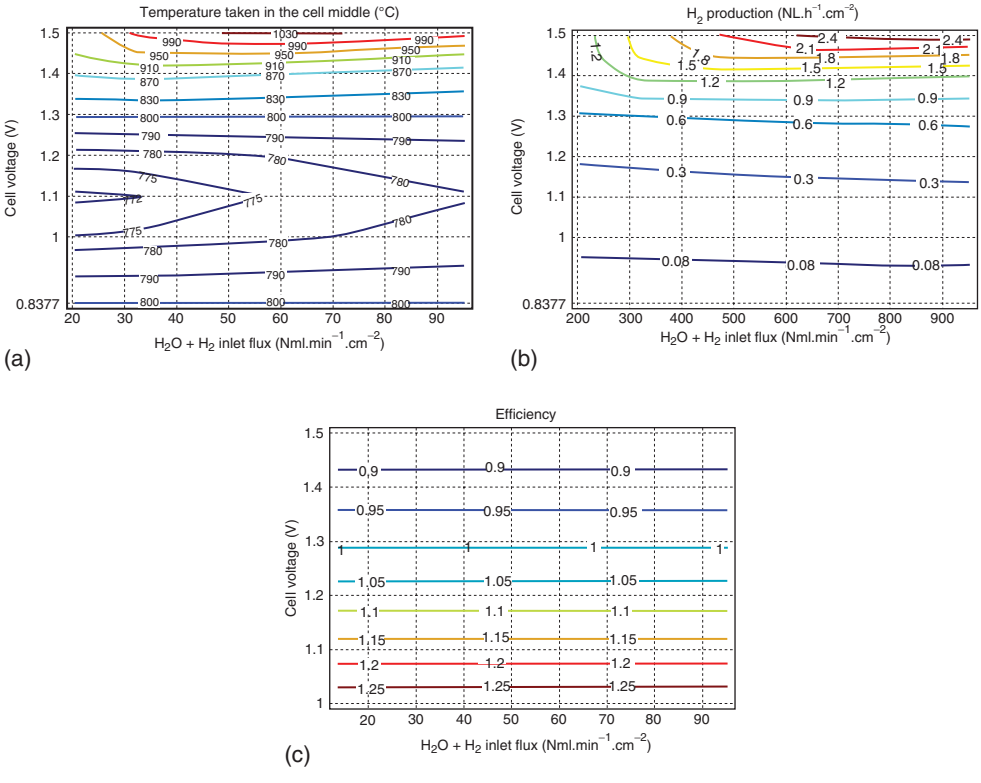

Figure 6.26 Simulated maps of (a) temperature in the middle of a cell within a stack, (b) hydrogen production rate and (c) electrical efficiency; simulation conditions: 90% $H_2O + 10\%\ H_2$ on H_2 electrode, air on oxygen electrode, same gas flow rate on both electrodes, gas inlet and hotbox temperature fixed at 800 °C.

In this section, both topics will be covered, starting with degradation issues that need to be solved and then covering system integration as well as the associated economical considerations.

6.5.1
Degradation Issues

Degradation issues encountered during HTSE operation can be divided into two categories: first, the phenomena occurring during steady-state operation, and, second, the phenomena occurring during cycling. Both will be briefly described in this section.

Cell and other stack components are subject to degradation phenomena during steady-state operation in HTSE mode. Compared to SOFC, studies on SOEC degradation are less numerous. Generally speaking, it can be considered that degradation phenomena in SOEC mode are very close to those in SOFC mode,

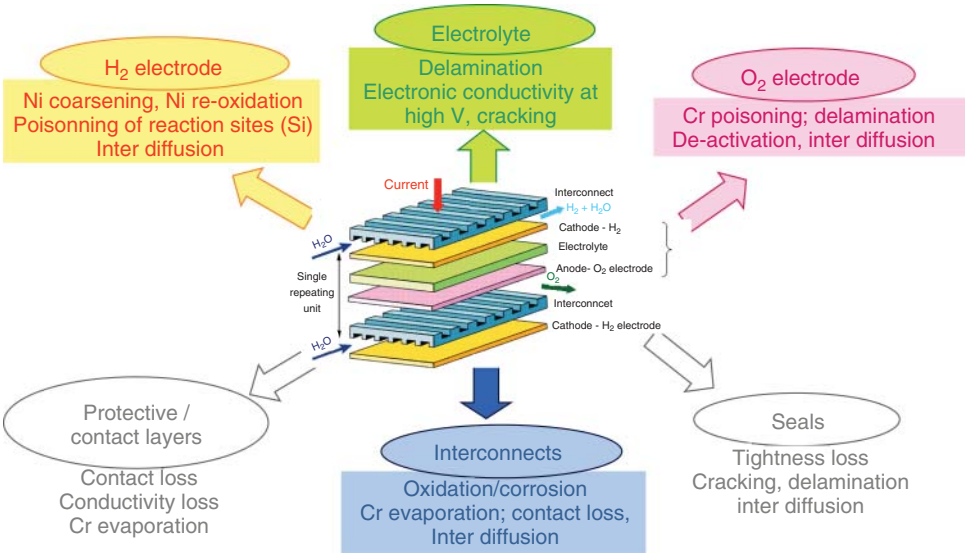

Figure 6.27 Schematic representation of the different degradation phenomena that can occur at the cell and stack component level.

even though some specificities exist and degradation rates are higher in SOEC compared to SOFC as mentioned in Section 3.3.

Figure 6.27 gives an overview of the different degradation phenomena that can be encountered at the cell and stack component levels, as reported in review articles [2, 125, 137, 138].

It may be noted from Figure 6.27 that most of the degradation issues are related to chemical, physico-chemical or electrochemical phenomena that are thermally activated. But some others are related to mechanical phenomena, potentially partly linked to previous chemical/physico-chemical phenomena.

The purpose here is not to describe all degradation mechanisms that are detailed elsewhere [2, 125, 137, 138]. Only major mechanisms specific to HTSE operation will be briefly quoted.

Regarding the hydrogen electrode (Ni–YSZ cermet), we can in particular quote changes in its microstructure, such as Ni coarsening. Compared to SOFC operation, the high steam content in SOEC operation is considered to be an accelerating factor, which might explain at least partly the higher degradation rates in SOEC mode [125]. On the oxygen electrode side, the decomposition of the LSCF perovskite is often reported, as well as its delamination. In SOEC mode, this latter phenomenon is linked to the formation of oxygen at this electrode, which does not exist in SOFC. Electrolyte instability is also a key issue.

Regarding interconnects, the more oxidant atmosphere in SOEC mode compared to the SOFC one, due to the oxygen formation, makes the oxidation phenomenon more severe and the request for efficient protection more crucial.

Finally, it may be noted that degradation phenomena occurring on one component can affect others, such as chromium evaporation from the interconnects that provoke chromium poisoning of the oxygen electrode, or components of the sealing that can enhance corrosion of the interconnect or poison the cell or change in the Ni – YSZ microstructure and even creep that can lead to the electrolyte cracking.

It must be noted that some of the degradation mechanisms can also find their origin in extrinsic causes, such as pollution of the inlet gas or pollution from the BoP components. For example, Ebbesen reports that impurities in cathodic gas leads to cermet poisoning and that efficient gas cleaning can significantly decrease the degradation rate [139].

Therefore, solving degradation issues needs to be considered globally at the stack and even system level to take into account interactions between the various components. Anyway, further studies of degradation mechanisms are requested to understand what happens and to decrease the degradation rates reported in Section 3.3, which are still too high for application.

Cycling operation is also a potential cause of degradation. As for SOFC, thermal cycling of SOEC stacks is a weak point. Even if the operating mode forecasted does not often consider start-up and shutdowns, some thermal cycles will be required over the lifetime of the system, some of them being programmed for periodic maintenance, to which unexpected ones can be added, for example due to building or grid shutdown. The degradation phenomena associated with these cycles have been much less studied than the steady-state operation. One can easily understand that the complex assembly between considerably rigid metallic interconnect plates and brittle ceramic cells, linked together with glass ceramic sealants, makes the transition from 700 – 800 °C to room temperature rather complicated, more so as thermal expansion coefficients (TECs), even when selected as carefully as possible, are not exactly similar. Thus, thermo-mechanical issues at the stack level, as well as within the cell, can be expected, as the cathode/electrolyte/anode also present different values of TEC. For SOFC stacks, some optimizations of the design have been carried out to allow thermal cycling. Similar improvements are expected to be beneficial for SOEC. Very few thermal cycling results are reported in SOEC mode, but we can quote works of Mougin *et al*. [112], who report three thermal cycles on a one-cell stack and one thermal cycle on a three-cell stack, with no impact either on the performances or on the gastightness. These thermal cycling phenomena can affect the cell microstructure, in particular the electrode microstructures, as well as the TEC, which can evolve over cycles. Further studies are required to understand its impact on the degradation rate.

The degradation phenomena quoted earlier occur at different scales, some of them being local and not easy to detect. Thus, in most cases, a combination of classical techniques and of advanced characterization methods is required. For microstructural analyses, we can quote, for example, a combination of different microscopic techniques such as the conventional scanning electron microscopy (SEM), electron probe microanalysis (EPMA) and the focused ion beam (FIB) preparation technique for transmission electron microscopy (TEM), which allows

a post-mortem analysis at a multi-scale level. These complementary techniques can be used to characterize structural and chemical changes over a large and representative sample area (microscale) as well as at the nano-scale level for selected sample details [140]. For porous structures such as the electrodes, 3D image analysis is an essential tool to characterize the microstructures. However, the studied volumes have to be sufficiently large to be representative of the heterogeneous medium. Laurencin *et al.* developed a methodology, based on synchrotron X-ray nano-tomography measurements, which allows obtaining 3D reconstructions of porous supports for SOFC/SOFC cells. The methodology has been applied to investigate the microstructure of a typical Ni–8YSZ cermet substrate. Experimental conditions have been optimized so that a 3D reconstruction of 42 μm × 42 μm × 105 μm has been computed with a voxel size of 60 nm [75]. In addition, thanks to X-ray nano-holotomography, quantitative phase contrast has been performed on large volumes of an Ni–YSZ cermet. Both the electrode FL and the ECC have been characterized in 3D. The X-ray nano-holotomography was performed with an isotropic voxel size of $25 \times 25 \times 25\ nm^3$ and a field of view of about 50 mm. This technique is non-destructive and was used in local tomography mode. After filtering and thresholding, the segmentation of the 3D reconstructions allows precisely separating the network of each phase of the electrode (metallic, ceramic and porosity), giving representative features of the microstructure [141].

During operation, *in situ* diagnostics is often useful in addition to classical $i-V$ curve measurements or the monitoring of the voltage or current evolution over time, especially to understand slow and gradual degradation phenomena. Electrochemical impedance spectroscopy (EIS) is one of the most used methods, extensively in SOFC and in an associated way in SOEC, although studies in the latter mode are less numerous. In addition, modelling and description in equivalent circuits in SOEC mode can differ from SOFC mode and require specific studies. We can quote works of Jensen *et al.* [142], who described degradation phenomena in cells operated in SOEC mode thanks to impedance spectra. Analysis methods of impedance spectra have been developed to facilitate the identification of mechanisms. We can quote the distribution function of relaxation times (DRT) method developed by Ivers-Tiffee *et al.* [143–146] for SOFC, which can advantageously be used for SOEC.

6.5.2
System Integration and Economical Considerations

As mentioned in Section 3.3, the maturity of HTSE is lower compared to that of SOFCs. In addition, it must be noted that contrary to SOFC presenting a market for small units (around 1 kW for domestic micro-cogeneration), HTSE market requires larger units. Therefore, the challenges to build a complete system at such a scale are greater. As far as public information is concerned, no integrated system has been designed, built and operated until now. We can only quote works at Idaho National Laboratory in the United States, where a 15 kW system made of three

electrolysis modules, each consisting of four stacks of 60 cells, yielding 240 cells per module and 720 cells in total has been tested, including the heat exchangers. Peak hydrogen production with this facility was 5700 NL h^{-1}. The 15 kW system was operated for 1080 h, but significant performance degradation was observed [147].

Some demonstration projects are also ongoing in Germany and Denmark, at the scale of a few tens of kilowatts, targeting a coupling with synthetic gas or fuel production units for the power to gas market.

Finally, economical considerations are also a key point. Indeed, HTSE technology has to compete with low-temperature alkaline or PEM electrolysis in terms of cost of the hydrogen produced. No commercial systems are available, and the cost of laboratory demonstration units is not representative of the potential cost of this technology when it will be produced massively. That is why some techno-economical assessments have been carried out, based on real performance and durability data, but extrapolating the stack and system design to larger units, including an estimate of the cost of mass production of these units, to be more representative.

An American study considered the coupling of an HTSE hydrogen production plant with a very high-temperature nuclear reactor (VHTR), which provides both electrical and heat energy (heat for the steam production and overheating, and for the electrolysis reaction) to the HTSE [148]. This economic analysis demonstrated that HTSE can deliver hydrogen at a cost of 3.23 \$ kg^{-1} of hydrogen, assuming an internal rate of return of 10%. This hydrogen cost is lower compared to the one obtained with low-temperature electrolyses. It is even not so far from the cost of hydrogen produced by the widely used steam methane reforming (SMR) technology, which produced hydrogen at around 2.50 \$ kg^{-1} [149].

However, finding such high-temperature heat sources is not easy as VHTRs do not exist yet, and the possibility of operating HTSE systems with heat sources at lower temperature would be necessary for earlier market penetration. Thus, Rivera-Tinoco *et al.* [150] investigated options with heat sources at lower temperatures. They demonstrated that medium-temperature thermal energy sources could be coupled to the high-temperature electrolysis process without resulting in large overcosts.

Finally, because HTSE plants reaching a multi-megawatt power will not be available at short term, and because there might be an interest for smaller units for decentralized hydrogen production on sites presenting a heat source, cost analyses have been performed by Reytier *et al.* [119] for smaller units including a low-weight, performing stack design experimentally validated. Based on these data, an SOEC system coupled with a low-temperature heat source (for steam generation only) is modelled for a production capacity of 100 kg H_2/day. The electrolysis is considered to be done at the pressure of 13 bars at 700 °C with a steam conversion of 60%.

In order to compare the SOEC system with the conventional water electrolysis technologies based on an equivalent market maturity, a cost analysis was conducted considering a manufacturing scale of 100 system/year, 30% margin on

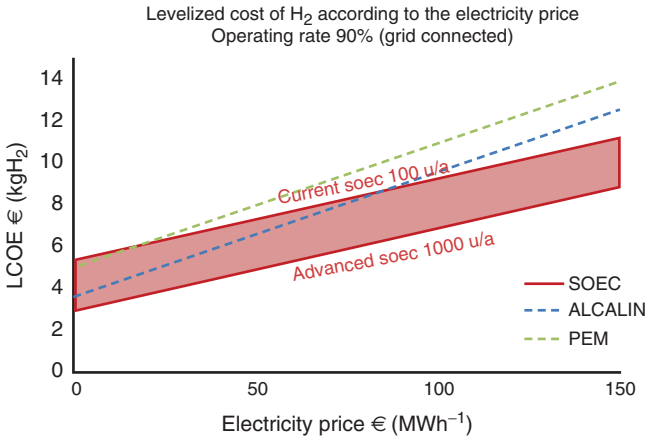

Figure 6.28 Levelized cost of hydrogen versus electricity price; comparison of SOEC with alkaline and PEM electrolyses.

the manufacturing cost and 20% contingencies. The calculations give a selling price of the system of 11.2 € $Nm^{-3}\,h^{-1}$ for the SOEC system compared with 6.5 € $Nm^{-3}\,h^{-1}$ for the alkaline and 11 € $Nm^{-3}\,h^{-1}$ for the PEM system according to supplier sources. It is worth noting that PEM is currently only produced in small volumes and the announced price should correspond to a lower production scale. Despite a higher price, the SOEC system keeps a reasonable competitive position as compared to the conventional technologies. Considering the achievement of the developments in progress on the durability, performance and design of the stack, as well as a mass production effect, this selling price could drop to 5 € $Nm^3\,h^{-1}$ [122].

Figure 6.28 presents the levelized cost of hydrogen versus the electricity cost for SOEC compared to alkaline and PEM electrolyses. Figure 6.28 shows that the energetic efficiency of the SOEC prevails over its higher investment and becomes competitive with alkaline, for a high operating rate, allowing better amortization, and for an electricity price above 100 € MWh^{-1}, which concerns many European countries. Moreover, the advanced SOEC shows the very promising potential of the developments in progress. Whatever the electricity price, SOEC produces cheaper hydrogen compared to PEM water electrolysis.

6.6 Specific Operation Modes

6.6.1 Pressurized Operation

Whatever the electrolysis technology considered, the hydrogen produced always requires to be stored before being used. Due to its low volumetric density, it

requires to be stored pressurized between 10 to a few tens of bars for injection into the natural gas grid and up to 350 or 700 bars for transportation. Hydrogen compression is not easy and consumes a part of the energy contained in the hydrogen, decreasing the overall process efficiency. On the contrary, compression of liquid water is much easier, and that is why alkaline and PEM water electrolyses consider a pressurized operation at a few bars to a few tens of bars, with some attempts above 100 bars. To compete with these technologies and to gain some points on the global efficiency, operating HTSE under pressure is interesting and some studies have been carried out, although they are not numerous. Works at INL are reported, with a testing station that is able to operate up to 50 bars at stack level [151]. Experimental results on a 10-cell stack have been published up to 15 bars, highlighting the possibility to operate HTSE stacks under pressure [152]. Despite a higher OCV, the slope of the $i-V$ curves decreases with increasing pressure, indicating lower area-specific resistance (ASR) values associated with higher-pressure operation because of improved gas diffusion in the porous electrodes at high pressure. Thus, there is a double beneficial effect of pressure, with improved cell/stack performances and better global process efficiency. Works are also performed in this field at the Technical University of Denmark (DTU) in Denmark and at the Atomic Energy Commission (CEA) in France.

6.6.2 Reversible Operation

As mentioned in Section 3.1, SOECs are similar to SOFCs, and can thus by nature be operated in both modes, which is not the case for the two other most developed electrolysis technologies, alkaline electrolysis and PEM water electrolysis, which require different catalysts or active materials in the fuel cell and electrolysis modes. This specificity is particularly interesting for application to the market of renewable energy storage. Indeed, as detailed in Chapter 5, intermittent renewable energies need to be stored, and hydrogen is one of the storage options, being produced by electrolysis when excess of electricity is available and being used in a fuel cell to produce electricity when needed. Thus, an electrolyser and a fuel cell are required, both being operated only part time. A reversible system would be advantageous as only one system has to be purchased, minimizing the investment cost, which is in addition operated full time, thus maximizing the return on investment.

Some works have started quite recently to investigate transient operation and reversible operation. It has been first demonstrated that transient operation (cycles from zero current to defined values leading to voltages below, at or above the thermo-neutral voltage) is possible [112, 153, 154].

While reversible performance curves ($i-V$ curves) plotted in both SOEC and SOFC modes are common, either using the same gas mixture (generally 50% H_2O/50% H_2) or different mixtures (richers in steam in SOEC and in hydrogen in SOFC), long-term tests with several number of SOEC–SOFC cycles are less

numerous. Nguyen [155] reports a few long cycles, whereas Borglum [156] presented in 2013 much shorter cycles, more representative of such a reversible operation, during oral presentation but not in proceedings. These results, obtained at the scale of a 28-cell stack for a test duration of 900 h, prove the feasibility at the scale of a large stack and show that degradation is not accelerated with this type of cycles.

6.6.3
Co-Electrolysis

Thanks to the high operating temperature, this HTSE technology is also likely to electrolyse different compounds, and not only steam. For instance, CO_2 can also be electrolysed, as well as a mixture of H_2O and CO_2, which produces syngas, that is to say $H_2 + CO$ [110]. Depending on the H_2O/CO_2 ratio at the inlet, several ratios of H_2/CO at the outlet can be obtained that are likely to be further transformed into synthetic gaseous (such as methane) or liquid synfuels (methanol, DME, etc.) through catalytic reactors. Synfuels complement hydrogen for the storage of intermittent renewable energies through the power to gas concept, and are currently raising growing interest.

As an example, Figure 6.29 presents performance curves obtained at the scale of a 25-cell stack in co-electrolysis for two different H_2O/CO_2 ratios. It may be noted that performances in co-electrolysis mode are very close to that in pure steam electrolysis, validating this operation mode. Gas composition at the outlet

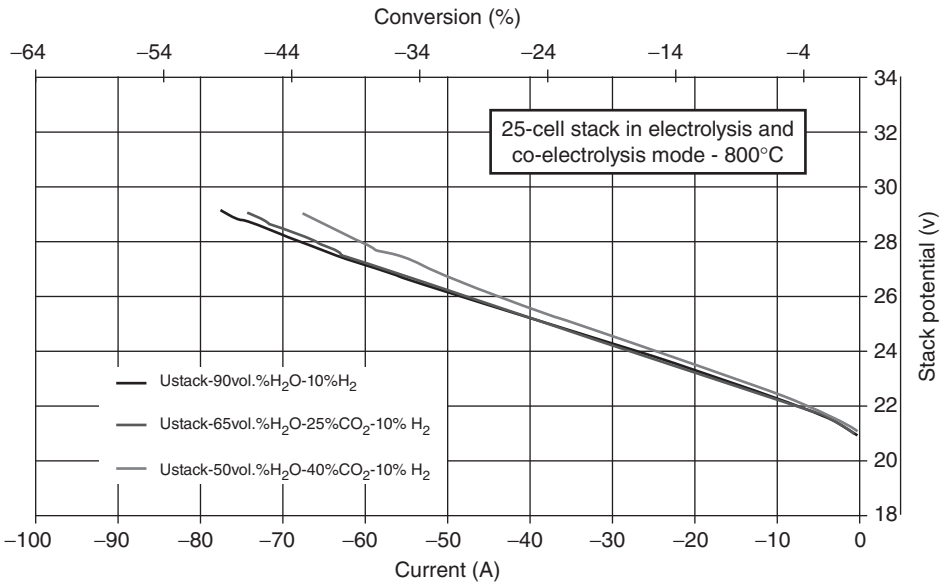

Figure 6.29 *i–V* curves of a 25-cell stack operated at 800 °C in pure steam electrolysis and in co-electrolysis for two H_2O/CO_2 ratios.

has been measured by gas micro-chromatography and was found as expected [18]. Thus, the gas composition of the gas produced can be tailored exactly as required for the following catalytic reactor that produced synfuel [122, 123].

List of Terms

Roman symbols

a_r, a_p	thermodynamic activities of reactants and products of an electrochemical or chemical reaction
B_0	permeability coefficient
$D_{i,k}$	Knudsen diffusion coefficient for the gaseous species i ($D_{i,k}^{eff}$: effective Knudsen diffusion coefficient)
$D_{i,j}$	molecular diffusion coefficient for gaseous species i and j ($D_{i,j}^{eff}$: effective molecular diffusion coefficient)
e^-	electrons
E	local electrode potential (E_{rev} = reversible electrode potential, E_{OCP} electrode potential at OCP, E^{Anode}, $E^{Cathode}$: anode and cathode electrode potentials)
E_a	activation energy
F	Faraday constant
$h^{\cdot}$	holes in a p-type semiconductor
i	electric current density (i_{e^-}, i_{io}: electronic and ionic current densities)
i_o^{Anode}, $i_o^{Cathode}$	anode and cathode exchange current densities
j	specific current density (source terms)
k_+, k_-	kinetic constants in forward and backward direction, respectively
k_{ox}, k_{red}	kinetic constants for charge transfer (through oxidation and reduction, respectively)
k_{ads}, k_{des}	kinetic constants for adsorption and desorption, respectively
K_e	thermodynamic equilibrium constant for a chemical or electrochemical reaction
ℓ_j	thickness of the cell layer j
M_i	molar mass for the gas species i or M factor for gas, ionic or electronic conductor
n	number of exchange electrons
N_i	molar flux for the gas species i
O^{2-}	oxygen ions
O_O^x	oxygen atoms incorporated in the MIEC
P_T	total pressure
P_j^{canal}, P_j^{TPB}	partial pressure of the species j taken in the channel of gas distribution or at TPBls
$\bar{r}$	mean pore radius
R	ideal gas constant

R_j	ohmic resistance for the cell layer j ($R_{\text{electrolyte}}$, R_{c}: electrolyte and contact resistances, $R^{\text{eff}}_{\text{ACC}}$, $R^{\text{eff}}_{\text{CCC}}$: effective resistances of the anode and cathode current collecting layers)
s	adsorption site on material surface
S_{p}	specific surface area
T	temperature
U	cell voltage (U_{rev}: reversible cell voltage, U_{OCV}: cell voltage at OCV)
$v_{(i)}$	kinetic rate of chemical or electrochemical reaction (i)
V_i	molar diffusion volume for the gaseous molecule i
$V_{\text{O}}^{\cdot\cdot}$	oxygen vacancies
y_i	molar fraction of the gaseous species i
$X-\text{s}$	adsorbed species X on material surface

Greek Symbols

α	symmetrical factor
ε	phase volume fraction (ε_{gas}: porosity, ε_i: volume fraction of the ionic or electronic conductor)
δ	constrictivity
κ	phase connectivity (κ_{gas}: connectivity for gas, κ_i: connectivity for the ionic or electronic conductor)
$\xi^{\text{Actif}}_{\text{TPBls}}$	Density of active TPBls
ΔH_{ox}	activation enthalpy for charge transfer
$\Delta H_{\text{H}_2\text{O}}$	enthalpy of steam formation
ΔG	change in free energy
ΔQ	heat sources
ΔS	change in entropy
$\Delta V^{\text{Anode}}_{\text{rev}}$, $\Delta V^{\text{Cathode}}_{\text{rev}}$	potential loss due to the gas conversion at the anode or cathode side
φ	electrical potential (φ_{e^-}, φ_{io}: electronic and ionic potentials, respectively)
$\sigma_{\text{e}^-}, \sigma_{\text{io}}$	electronic and ionic conductivities, respectively
$\sigma_{\text{h}^\cdot}$	conductivity by holes in p-type semiconductor
$\sigma_{i,j}$	average collision diameter for the binary gas mixture of molecules i and j
τ	tortuosity factor (τ_{geo}, τ_{app}: geometrical and apparent tortuosity factor, respectively)
η	overpotential (η_{ohmic}, η_{act}, η_{conc}: ohmic, activation and concentration overpotentials, respectively)
μ	dynamic viscosity
Ω	collision integral
Γ	surface density of available adsorption sites
θ_{s}, $\theta_{X-\text{s}}$	coverage rates of site s and adsorbed species X, respectively

γ_r, γ_p	stoichiometric coefficients of reactants and products of an electrochemical or chemical reaction, respectively

Abbreviations

ACC	anode current collecting layer
CC	current collector
CCC	cathode current collecting layer
CSC	cathode supported cell
DFT	density functional theory
ECC	electrolyte supported cell
FEM	finite element method
FL	functional layer
MIEC	Mixed Ionic Electronic Conductor
OCP	open circuit potential
OCV	open circuit voltage
TPB	triple phase boundary (TPBls: length of TPBs)

References

1. Atkins, P.W. (2002) *Physical Chemistry*, 5th edn, Oxford University Press, Oxford, p. 331.
2. Laguna-Bercero, M.A. (2012) Recent advances in high temperature electrolysis using solid oxide fuel cells: a review. *J. Power Sources*, **203**, 4–16.
3. Chauveau, F., Mougin, J., Bassat, J.M., Mauvy, F., and Grenier, J.C. (2010) A new anode material for solid oxide electrolyser: the neodymium nickelate Nd 2NiO 4+ δ. *J. Power Sources*, **195**, 744–749.
4. Khedim, H., Nonnet, H., and Méar, F.O. (2012) Development and characterization of glass-ceramic sealants in the (CaO-Al_2O_3-SiO_2-B_2O_3) system for solid oxide electrolyzer cells. *J. Power Sources*, **216**, 227–236.
5. Dey, T., Singdeo, D., Bose, M., Basu, R.N., and Ghosh, P.C. (2013) Study of contact resistance at the electrode-interconnect interfaces in planar type solid oxide fuel cells. *J. Power Sources*, **233**, 290–298.
6. Morel, B., Reytier, M., and Oresic, B. (2010) Experimental study of mechanical load effects on contact resistance between interconnectors and electrodes in SOFC or HTE stacks. Proceeding of the 9th European Solid Oxide Fuel Cell Forum, Lucerne, Switzerland, Chapter 12, pp. 12–14.
7. Gellings, P.J. and Bouwmeester, H.J.M. (eds) (1997) *The CRC Handbook of Solid State Electrochemistry*, CRC Press.
8. Déportes, C., Duclot, M., Fabry, P., Fouletier, J., Hammou, A., Kleitz, M., Siebert, E., and Souquet, J.L. (1994) *Electrochimie des Solides*, Presses Universitaires de Grenoble.
9. Usseglio-Viretta, F., Laurencin, J., Delette, G., Villanova, J., and Cloetens, P. (2014) Quantitative microstructure characterization of a Ni-YSZ bi-layer coupled with simulated cathode polarisation. *J. Power Sources*, **256**, 394–403.
10. Bard, A.J. and Faulkner, L.R. (2001) *Electrochemical Methods, Fundamentals and Applications*, 2nd edn, John Wiley & Sons, Inc..
11. Ackmann, T., deL.G.J., Haart, Lehnert, W., and Thom, F. (2000) Proceeding of the 4th European Solid Oxide Fuel Cell Forum, Lucerne, Switzerland, Modelling of mass and heat transport in thick substrate thin electrolyte layer SOFCs, p. 431–438.

12. Jiang, Y. and Virkar, A.V. (2003) Fuel composition and diluent effect on gas transport and performance of anode-supported SOFCs. *J. Electrochem. Soc.*, **150** (7), A942–A951.
13. Kim, J.W., Virkar, A.V., Fung, K.Z., Metha, K., and Singhal, S.C. (1999) Polarisation effects in intermediate temperature, anode-supported solid oxide fuel cells. *J. Electrochem. Soc.*, **146** (1), 69–78.
14. Mawdsley, J.R., Carter, J.D., Kropf, A.J., Yildiz, B., and Maroni, V.A. (2009) Post-test evaluation of oxygen electrodes from solid oxide electrolysis stacks. *Int. J. Hydrogen Energy*, **34**, 4198–4207.
15. Udagawa, J., Aguiar, P., and Brandon, N.P. (2007) Hydrogen production through steam electrolysis: model-based steady state performance of a cathode-supported intermediate temperature solid oxide electrolysis cell. *J. Power Sources*, **166**, 127–136.
16. Ni, M., Leung, M.K.H., and Leung, D.Y.C. (2007) Parametric study of solid oxide steam electrolyzer for hydrogen production. *Int. J. Hydrogen Energy*, **32**, 2305–2313.
17. Laurencin, J., Kane, D., Delette, G., Deseure, J., and Lefebvre-Joud, F. (2011) Modelling of solid oxide steam electrolyser: impact of the operating conditions on hydrogen production. *J. Power Sources*, **196**, 2080–2093.
18. Aicart, J., Laurencin, J., Petitjean, M., and Dessemond, L. (2014) Experimental validation of two-dimensional H_2O and CO_2 Co-electrolysis modeling. *Fuel Cells*, **14** (3), 430–447.
19. Horita, T., Yamaji, K., Sakai, N., Yokokawa, H., Weber, A., and Ivers-Tiffée, E. (2001) Electrode reaction of La_{1-x} Sr_xCoO_{3-d} cathodes on $La_{0.8}Sr_{0.2}Ga_{0.8}Mg_{0.2}O_{3-y}$ electrolyte in solid oxide fuel cells. *J. Electrochem. Soc.*, **148** (5), A456–A462.
20. Simwonis, D., Tietz, F., and Stöver, D. (2000) Nickel coarsening in annealed Ni/8YSZ anode substrates for solid oxide fuel cells. *Solid State Ionics*, **132**, 241–251.
21. Aruna, S.T., Muthuraman, M., and Patil, K.C. (1998) Synthesis and properties of Ni-YSZ cermet: anode material for solid oxide fuel cells. *Solids State Ionics*, **111**, 45–51.
22. Stiller, C., Thorud, B., Seljebø, S., Mathisen, Ø., Karoliessen, H., and Bolland, O. (2005) Finite-Volume modeling and hybrid-cycle performance of planar and tubular solid oxide fuel cells. *J. Power Sources*, **141**, 227–240.
23. Mizusaki, J., Mori, N., Takai, H., Yonemura, Y., Minamiue, H., Tagawa, H., Dokiya, M., Inaba, H., Naraya, K., Sasamoto, T., and Hashimoto, T. (2000) Electronic conductivity, Seebeck coefficient, defect and electronic structure of nonstoichiometric $La_{1-x}Sr_xMnO_3$. *Solids State Ionics*, **132**, 167–180.
24. Koch, S. and Hendriksen, P.V. (2004) Contact resistance at ceramic interfaces and its dependence on mechanical load. *Solid State Ionics*, **168**, 1–11.
25. Sasaki, K., Wurth, J.P., Gschwend, R., Gödickemeier, M., and Gauckler, L.J. (1996) Microstructure-property relations of solid oxide fuel cell cathodes and current collectors. *J. Electrochem. Soc.*, **143**, 530–543.
26. Petitjean, M., Reytier, M., Chatroux, A., Bruguiere, L., Mansuy, A., Sassoulas, H., Di Iorio, S., Morel, B., and Mougin, J. (2011) Performance and durability of high temperature steam electrolysis: from single cell to short-stack scale. *ECS Trans.*, **35** (1), 2905–2913.
27. Lay-Grindler, E., Laurencin, J., Delette, G., Aicart, J., Petitjean, M., and Dessemond, L. (2013) Micro-modelling of solid oxide electrolysis cell: from performance to durability. *Int. J. Hydrogen Energy*, **38**, 6917–6929.
28. Cai, Q., Adjiman, C.S., and Brandon, N.P. (2011) Investigation of the active thickness of solid oxide fuel cell electrodes using a 3D microstructure model. *Electrochim. Acta*, **56**, 10809–10819.
29. Primdhal, S. and Mogensen, M. (1997) Oxidation of hydrogen on Ni/Yttria-Stabilized Zirconia cermet anodes. *J. Electrochem. Soc.*, **144** (10), 3439–3418.
30. Juhl, M., Primdahl, S., Manon, C., and Mogensen, M. (1996) Performance/structure correlation for

composite SOFC cathodes. *J. Power Sources*, **61**, 173–181.

31. Kong, J., Sun, K., Zhou, D., Zhang, N., Mu, J., and Qiao, J. (2007) Ni–YSZ gradient anodes for anode-supported SOFCs. *J. Power Sources*, **166**, 337.
32. Kast, W. and Hohenthanner, C.R. (2000) Mass transfer within the gas-phase of porous media. *Inter. J. Heat Mass Transfer*, **43**, 807–823.
33. Veldsink, J.W., van Damme, R.M.J., Versteeg, G.F., and van Swaaij, W.P.M. (1995) The use of the dusty gas model for the description of mass transport with chemical reaction in porous media. *Chem. Eng. J.*, **57**, 115–125.
34. Vural, Y., Ma, L., Ingham, D.B., and Pourkashanian, M. (2010) Comparison of the multicomponent mass transfer models for the prediction of the concentration overpotential for solid oxide fuel cell anode. *J. Power Sources*, **195**, 4893–4904.
35. Suwanwarangkul, R., Croiset, E., Fowler, M.W., Douglas, P.L., Entchev, E., and Douglas, M.A. (2003) Performance comparison of Fick's, dusty-gas and Stefan-Maxwell models to predict the concentration overpotential of a SOFC anode. *J. Power Sources*, **122**, 9–18.
36. Kong, W., Zhu, H., Fei, Z., and Lin, Z. (2012) A modified dusty gas model in the form of a Fick's model for the prediction of multicomponent mass transport in a solid oxide fuel cell anode. *J. Power Sources*, **206**, 171–178.
37. Mason, E.A. and Malinaukas, A.P. (1983) *Gas Transport in Porous Media: The Dusty-Gas Model*, Elsevier, Amsterdam.
38. Menon, V., Janardhanan, V.M., and Deutschmann, O. (2014) A mathematical model to analyse solid oxide electrolyzer cells (SOECs) for hydrogen production. *Chem. Eng. Sci.*, **110**, 83–93, (2013).
39. Grondin, D., Deseure, J., Ozil, P., Chabriat, J.-P., Grondin-Perez, B., and Brisse, A. (2011) Computing approach of cathodic process within solid oxide electrolysis cell: experiments and continuum model validation. *J. Power Sources*, **196**, 9561–9567.
40. Mizusaki, J., Tagawa, H., Saito, T., Yamamura, T., Kamitani, K., Hirano, K., Ehara, S., Takagi, T., Hikita, T., Ippommatsu, M., Nakagawa, S., and Hashimoto, K. (1994) Kinetic studies of the reaction at the nickel pattern electrode on YSZ in H_2-H_2O atmospheres. *Solid State Ionics*, **70-71**, 52–58.
41. Dasari, H.P., Park, S.-Y., Kim, J., Lee, J.-H., Kim, B.-K., Je, H.-J., Lee, H.-W., and Yoon, K.J. (2013) Electrochemical characterization of Ni-yttria stabilised zirconia electrode for hydrogen production in solid oxide electrolysis cells. *J. Power Sources*, **240**, 721–728.
42. Bessler, W.G., Vogler, M., Störmer, H., Gerthsen, D., Utz, A., Weber, A., and Ivers-Tiffée, E. (2010) Model anodes and anode models for understanding the mechanism of hydrogen oxidation in solid oxide fuel cells. *Phys. Chem. Chem. Phys.*, **12**, 13888–13903.
43. Vogler, M., Biberle-Hütter, A., Gauckler, L., Warnatz, J., and Bessler, W.G. (2009) Modelling study of surface reactions, diffusion, and spillover at the Ni/YSZ patterned anode. *J. Electrochem. Soc.*, **156** (5), B663–B672.
44. Zhu, H., Kee, R.J., Janardhanan, V.M., Deutschmann, O., and Goodwin, D.G. (2005) Modelling elementary heterogeneous chemistry and electrochemistry in solid-oxide fuel cells. *J. Electrochem. Soc.*, **152** (12), A2427–A2440.
45. Adler, S.B. (2004) Factors governing oxygen reduction in solid oxide fuel cell cathodes. *Chem. Rev.*, **104**, 4791–4843.
46. Mitterdorfer, A. and Gauckler, L.J. (1998) $La_2Zr_2O_7$ formation and oxygen reduction kinetics of the $La_{0.85}Sr_{0.15}Mn_yO_3$,$O_2$(g)/YSZ system. *Solid State Ionics*, **111**, 185–218.
47. Deseure, J., Bulter, Y., Dessemond, L., and Siebert, E. (2005) Theoretical optimisation of a SOFC composite cathode. *Electrochim. Acta*, **50**, 2037–2046.
48. Shin, E.-C., Ahn, P.-A., Seo, H.-H., Jo, J.-M., Kim, S.-D., Woo, S.-K., Yu, J.H., Mizusaki, J., and Lee, J.-S. (2013) Polarization mechanism of high temperature electrolysis in a Ni-YSZ/YSZ/LSM solid oxide cell by parametric impedance analysis. *Solid State Ionics*, **232**, 80–96.

49. Yokokawa, H., Tu, H., Iwanschitz, B., and Mai, A. (2008) Fundamental mechanisms limiting solid oxide fuel cell durability. *J. Power Sources*, **182**, 400–412.
50. Endler-Schuck, C., Leonide, A., Weber, A., Uhlenbruck, S., Tietz, F., and Ivers-Tiffée, E. (2011) Performance analysis of mixed ionic-electronic conducting cathodes in anode supported cells. *J. Power Sources*, **196**, 7257–7262.
51. Adler, S.B., Lane, J.A., and Steele, B.C.H. (1996) Electrode Kinetics of porous mixed-conducting oxygen electrodes. *J. Electrochem. Soc.*, **143** (11), 3554–3564.
52. Adler, S.B. (1998) Mechanism and kinetics of oxygen reduction on porous $La_{1-x}Sr_xCoO_{3-\delta}$ electrodes. *Solids State Ionics*, **111**, 125–134.
53. Svensson, A.M., Sunde, S., and Nişancioğlu, K. (1998) Mathematical modeling of oxygen exchange and transport in air-perovskite-yttria stabilised zirconia interface regions, II. Direct exchange of oxygen vacancies. *J. Electrochem. Soc.*, **145** (4), 1390–1400.
54. Deseure, J., Bultel, Y., Dessemond, L., and Siebert, E. (2005) Modelling of dc and ac responses of a planar mixed conducting oxygen electrode. *Solid State Ionics*, **176**, 235–244.
55. Svensson, A.M., Sunde, S., and Nişancioğlu, K. (1997) Mathematical modeling of oxygen exchange and transport in air-perovskite-yttria stabilised zirconia interface regions, I. Reduction of intermediately adsorbed oxygen. *J. Electrochem. Soc.*, **144** (8), 2719–2732.
56. Coffey, G.W. Pederson, L.R. Rieke, P.C. (2003) Competition between bulk and surface pathways in mixed ionic electronic conducting oxygen electrodes, *J. Electrochem. Soc.*, **150** (8), A1139–A1151.
57. Katsuki, M. Wang, S. Dokiya, M. Hashimoto, T. (2003) High temperature properties of $La_{0.6}Sr_{0.4}Co_{0.8}Fe_{0.2}O_{3-\sigma}$ oxygen nonstoichiometry and chemical diffusion constant, *Solid State Ionics*, **156**, 453–461.
58. Rüger, B., Weber, A., and Ivers-Tiffée, E. (2007) 3D-modelling and performance evaluation of mixed conducting (MIEC) cathodes. *ECS Trans.*, **7** (1), 2065–2074.
59. Carraro, T., Joos, J., Rüger, B., Weber, A., and Ivers-Tiffée, E. (2012) 3D finite element model for reconstructed mixed-conducting cathodes: I. Performance quantification. *Electrochem. Acta*, **77**, 315–323.
60. Virkar, A.V., Chen, J., Tanner, C.W., and Kim, J.-W. (2000) The role of electrode microstructure on activation and concentration polarizations in solid oxide fuel cells. *Solid State Ionics*, **131**, 189–198.
61. Cai, Q., Adjiman, C.S., and Brandon, N.P. (2011) Modelling the 3D microstructure and performance of solid oxide fuel cell electrodes: computational parameters. *Electrochim. Acta*, **56**, 5804–5814.
62. Berbei, A., Nucci, B., and Nicolella, C. (2013) Microstructural modelling for prediction of transport properties and electrochemical performance in SOFC composite electrodes. *Chem. Eng. Sci.*, **101**, 175–190.
63. Tanner, C.W., Fung, K.-Z., and Virkar, A.V. (1997) The effect of porous composite electrode structure on solid oxide fuel cell performance. *J. Electrochem. Soc.*, **144** (1), 21–30.
64. Kenny, B. and Karan, K. (2007) Engineering of microstructure and design of a planar porous composite SOFC cathode: a numerical analysis. *Solid State Ionics*, **178**, 297–306.
65. Duong, A.T. and Mumm, D.R. (2012) Microstructural optimisation by tailoring particle sizes for LSM-YSZ solid oxide fuel cell composite cathodes. *J. Electrochem. Soc.*, **159** (1), B39–B52.
66. Zhu, W.Z. and Deevi, S.C. (2003) A review on the status of anode materials for solid oxide fuel cells. *Mater. Sci. Eng.*, **A362**, 228–239.
67. Weber, A. and Ivers-Tiffée, E. (2004) Materials and concepts for solid oxide fuel cells (SOFCs) in stationary and mobile applications. *J. Power Sources*, **127**, 273–283.

68. Tietz, F., Buchkremer, H.P., and Stöver, D. (2002) Component manufacturing for solid oxide fuel cells. *Solid State Ionics*, **152-153**, 373–381.
69. Menzler, N.H., Tietz, F., Uhlenbruck, S., Buchkremer, H.P., and Stöver, D. (2010) Materials and manufacturing technologies for solid oxide fuel cells. *J. Mater. Sci.*, **45**, 3109–3135.
70. Ackmann, T., de Haart, L.G.J., Lehnert, W., and Stolen, D. (2003) Modelling of mass and heat transport in planar substrate type SOFCs. *J. Electrochem. Soc.*, **150**, A783–A789.
71. Berg, C.F. (2012) Re-examining Archie's law: conductance description by tortuosity and constriction. *Phys. Rev. E*, **86**, 046314 (1–9).
72. Lanzi, O. and Landau, U. (1990) Effect of pore structure and potential distributions in a porous electrode. *J. Electrochem. Soc.*, **137** (2), 585–593.
73. Holzer, L., Wiedenmann, D., Münch, B., Keller, L., Prestat, M., Gasser, P., Robertson, I., and Grobéty, B. (2013) The influence of constrictivity on the effective transport properties of porous layers in electrolysis and fuel cells. *J. Mater. Sci.*, **48**, 2934–2952.
74. Epstein, N. (1989) On tortuosity and the tortuosity factor in flow and diffusion through porous media. *Chem. Eng. Sci.*, **44**, 777–789.
75. Laurencin, J., Quey, R., Delette, G., Suhonen, H., Cloetens, P., and Bleuet, P. (2012) Characterisation of SOFC Ni-8YSZ substrate by synchrotron X-ray nano-tomography, from 3D reconstruction to microstructure quantification. *J. Power Sources*, **198**, 182–189.
76. Delette, G., Laurencin, J., Usseglio-Viretta, F., Villanova, J., Bleuet, P., Lay, E., and Le Bihan, T. (2013) Thermo-elastic properties of SOFC/SOEC electrode materials determined from three-dimensional microstructural reconstructions. *Int. J. Hydrogen Energy*, **38**, 12379–12391.
77. Wilson, J.R., Kobsiriphat, W., Mendoza, R., Chen, H.-Y., Hiller, J.M., Miller, D.J., Thornton, K., Voorhees, P.W., Adler, S.B., and Barnett, S.A. (2006) Three-dimensional reconstruction of a solide-oxide fuel-cell anode. *Nat. Mater.*, **5**, 541–544.
78. Joos, J., Carraro, T., Weber, A., and Ivers-Tiffée, E. (2011) Reconstruction of porous electrodes by FIB/SEM for detailed microstructure modelling. *J. Power Sources*, **196** (17), 7302–7307.
79. Iwai, H., Shikazono, N., Matsui, T., Teshima, H., Kishimoto, M., Kishida, R., Hayashi, D., Matsuzaki, K., Kanno, D., Saito, M., Muroyama, H., Eguchi, K., Kasagi, N., and Yoshida, H. (2010) Quantification of SOFC anode microstructure based on dual beam FIB-SEM technique. *J. Power Sources*, **195**, 955–961.
80. Kanno, D., Shikazono, N., Takagi, N., Matsuzaki, K., and Kasagi, N. (2011) Evaluation of SOFC anode polarization simulation using three-dimensional microstructures reconstructed by FIB tomography. *Electrochem. Acta*, **56**, 4015–4021.
81. Grew, K.N., Chu, Y.S., Yi, J., Peracchio, A.A., Izzo, J.R., Hwu, Y., De Carlo, F., and Chiu, W.K.S. (2010) Nondestructive nanoscale 3D elemental mapping and analysis of a solid oxide fuel cell anode. *J. Electrochem. Soc.*, **157** (6), B783–B792.
82. Gunda, N.S.K., Choi, H.-W., Berson, A., Kenney, B., Karan, K., Pharoah, J.G., and Mitra, S.K. (2011) Focused ion beam-scanning electron microscopy on solid-oxide fuel-cell electrode: image analysis and computing effective transport properties. *J. Power Sources*, **196**, 3592–3603.
83. Vivet, N., Chupin, S., Estrade, E., Piquero, T., Pommier, P.L., Rochais, D., and Bruneton, E. (2011) 3D microstructural characterization of a solid oxide fuel anode reconstructed by focused ion beam tomography. *J. Power Sources*, **196**, 7541–7549.
84. Torquato, S. (2001) *Random Heterogeneous Materials, Microstructure and Properties, Interdisciplinary Applied Mathematics*, vol. 16, Springer.
85. Kanit, T., Forest, S., Galliet, I., Mounoury, V., and Jeulin, D. (2003) Determination of the size of the representative volume element for random

composites: statistical and numerical approach. *Int. J. Solids Struct.*, **40**, 3647–3679.

86. Haas, A., Matheron, G., and Serra, J. (1967) Morphologie mathématique et granulométrie en place. *Ann. Mines*, **11**, 736–753, (1967), **12**, 768–782.
87. Holzer, L., Münch, B., Iwanschitz, B., Cantoni, M., Hocker, T., and Graule, T. (2011) Quantitative relationships between composition, particle size, triple phase boundary length and surface area in nickel-cermet anodes for solid oxide fuel cells. *J. Power Sources*, **196**, 7076–7089.
88. Wilson, J.R., Cronin, J.S., Duong, A.T., Rukes, S., Chen, H.-Y., Thornton, K., Mumm, D.R., and Barnett, S. (2010) Effect of composition of (La0.8Sr0.2MnO3-Y2O3-stabilized ZrO2) cathodes: correlating three dimensional microstructure and polarization resistance. *J. Power Sources*, **195**, 1829–1840.
89. Kishimoto, M., Iwai, H., Saito, M., and Yoshida, H. (2011) Quantitative evaluation of solide fuel cell porous anode microstructure based on focused ion beam and scanning electron microscope technique and prediction of anode overpotentials. *J. Power Sources*, **196** (10), 4555–4563.
90. Cronin, J.S., Chen-Wiegart, Y.C.K., Wang, J., and Barnett, S.A. (2013) Three dimensional reconstruction and analysis of an entire solid oxide fuel cell by full-field transmission X-ray microscopy. *J. Power Sources*, **233**, 174–179.
91. Joos, J., Ender, M., Rotscholl, I., Menzler, N.H., and Ivers-Tiffee, E. (2014) Quantification of double-layer Ni/YSZ fuel cell anodes from focused ion beam tomography data. *J. Power Sources*, **246**, 819–830.
92. Nelson, G.J., Harris, W.M., Lombardo, J.J., Izzo, J.R., Chiu, W.K.S., Tanasini, P., Cantoni, M., Van Herle, J., Comminellis, C., Andrews, J.C., Liu, Y., Pianetta, P., and Chu, Y.S. (2011) Comparison of SOFC cathode microstructure quantified using X-ray nanotomography and focused ion beam-scanning electron microscopy. *Electrochem. Commun.*, **13**, 586–589.
93. Joos, J., Ender, M., Carraro, T., Weber, A., and Ivers-Tiffée, E. (2012) Representative volume element size for accurate solid oxide fuel cell cathode reconstructions from focused ion beam tomography data. *Electrochim. Acta*, **82**, 268–276.
94. Lay-Grindler, E., Laurencin, J., Villanova, J., Kieffer, I., Usseglio-Viretta, F., Le Bihan, T., Bleuet, P., Mansuy, A., and Delette, G. (2013) Degradation study of the La0.6Sr0.4Co0.2Fe0.8O3 Solid Oxide Electrolysis Cell (SOEC) anode after high temperature electrolysis operation. *ECS Trans.*, **57** (1), 3177–3187.
95. Yamamoto, O. (2000) Solid oxide fuel cells: fundamentals aspects and prospects. *Electrochem. Acta*, **45**, 2423–2435.
96. Zhang, C., Li, C.-J., Zhang, G., Ning, X.-J., Li, C.-X., Liao, H., and Coddet, C. (2007) Ionic conductivity and its temperature dependence of atmospheric plasma-sprayed yttria stabilised zirconia electrolyte. *Mater. Sci. Eng., B*, **137**, 24–30.
97. Chen, X.J., Khor, K.A., Chan, S.H., and Yu, L.G. (2002) Influence of microstructure on the ionic conductivity of yttria-stabilized zirconia electrolyte. *Mater. Sci. Eng., A*, **335**, 246–252.
98. Badwal, S.P.S. (1995) Grain boundary resistivity in zirconia-based materials: effect of sintering temperatures and impurities. *Solid State Ionics*, **76**, 67–80.
99. Steil, M.C. and Thevenot, F. (1997) Densification of yttria-stabilised zirconia. Impedance spectroscopy analysis. *J. Electrochem. Soc.*, **144** (1), 390–398.
100. Gewies, S., Bessler, W.G., Sonn, V., and Ivers-Tiffee, E. (2007) Experimental and modeling study of the impedance of Ni/YSZ cermet anodes. *ECS Trans.*, **7** (1), 1573–1582.
101. Asnin, L.D., Chekryshkin, Y.S., and Fedorov, A.A. (2003) Calculation of the sticking coefficient in the case of the linear adsorption isotherm. *Russ. Chem. Bull., Int. Ed.*, **52** (12), 2747–2749.

102. Hecht, E.S., Gupta, G.K., Zhu, H., Dean, A.M., Kee, R.J., Maier, L., and Deutschmann, O. (2005) Methane reforming kinetics within a Ni-YSZ SOFC anode support. *Appl. Catal. Gen.*, **295**, 40–51.
103. Lapujoulade, J. and Neil, K. (1972) Chemisorption of hydrogen on the (111) plane of Nickel. *J. Chem. Phys.*, **57** (8), 3535–3545.
104. Christmann, K., Schober, O., Ertl, G., and Neumann, M. (1974) Adsorpion of hydrogen on nickel single crystal surfaces. *J. Chem. Phys.*, **60** (11), 4528–4540.
105. Jiang, S.P. and Badwal, S.P.S. (1997) Hydrogen oxidation at the nickel and platinum electrodes on yttria-tetragonal zirconia electrolyte. *J. Electrochem. Soc.*, **144** (11), 3777–3784.
106. Marrero, T.R. and Mason, E.A. (1972) Gaseous diffusion coefficients. *J. Phys. Chem. Ref. Data*, **1** (1), 3–118.
107. Fuller, E.N., Schettler, P.D., and Giddings, J.C. (1966) A new method for prediction of binary gas-phase diffusion coefficients. *Ind. Eng. Chem.*, **58** (5), 18–27.
108. Chan, S.H., Khor, K.A., and Xia, Z.T. (2001) A complete polarization model of a solid oxide fuel cell and its sensitivity to the change of cell component thickness. *J. Power Sources*, **93**, 130–140.
109. Todd, B. and Young, J.B. (2002) Thermodynamic and transport properties of gases for use in solid oxide fuel cell modelling. *J. Power Sources*, **110**, 186–200.
110. Graves, C., Ebbesen, S., Mogensen, M., and Lackner, K. (2011) Sustainable hydrocarbon fuels by recycling CO_2 and H_2O with renewable or nuclear energy. *Renew. Sustain. Energy Rev.*, **15**, 1–23.
111. O'Brien, J.E., Stoots, C.M., Herring, J.S., Condie, K.G., and Housley, G.K. (2009) The high-temperature electrolysis program at the idaho national laboratory: observations on performance degradation. International Workshop on High Temperature Water Electrolysis Limiting Factors, INL/CON-09-15564.
112. Mougin, J., Chatroux, A., Couturier, K., Petitjean, M., Reytier, M., Gousseau, G., and Lefebvre-Joud, F. (2012) High temperature steam electrolysis stack with enhanced performance and durability. *Energy Procedia*, **29**, 445–454.
113. Hauch, A., Ebbesen, S., Jensen, S., and Mogensen, M. (2008) Highly efficient high temperature electrolysis. *J. Mater. Chem.*, **18**, 2331–2340.
114. Brisse, A., Schefold, J., and Zahid, M. (2008) High temperature water electrolysis in solid oxide cells. *Int. J. Hydrogen Energy*, **33**, 5375–5382.
115. Mougin, J., Mansuy, A., Chatroux, A., Gousseau, G., Petitjean, M., Reytier, M., and Mauvy, F. (2013) Enhanced performance and durability of a high temperature steam electrolysis stack. *Fuel Cells*, **13** (4), 623–630.
116. O'Brien, J.E., Zhang, X., Housley, G.K., Moore-McAteer, L., and Tao, G. (2012) High Temperature Electrolysis 4 kW Experiment Design, Operation, and Results. INL/EXT-12-27082. Idaho National Laboratory.
117. Diethelm, S., Van Herle, J., Montinaro, D., and Bucheli, O. (2012) 10th European Fuel Cell Forum, Lucerne, Switzerland, June 26–29, 2012, p. A1104.
118. Ebbesen, S., Høgh, J., Nielsen, K.A., Nielsen, J.U., and Mogensen, M. (2011) Durable SOC stacks for production of hydrogen and synthesis gas by high temperature electrolysis. *Int. J. Hydrogen Energy*, **36**, 7363–7373.
119. Reytier, M., Cren, J., Petitjean, M., Chatroux, A., Gousseau, G., Di Iorio, S., Brevet, A., Noirot-Le Borgne, I., and Mougin, J. (2013) *ECS Trans.*, **57** (1), 3151–3160.
120. Stoots, C.M., Condie, K.G., Moore-McAteer, L., O'Brien, J.E., Housley, G.K., and Herring, J.S. (2009) Integrated Laboratory Scale Test Report, INL/EXT-09-15283. Idaho National Laboratory.
121. Li, Q., Zheng, Y., Guan, W., Jin, L., Xu, C., and Wang, W.G. (2014) *Int. J. Hydrogen Energy*, **39**, 10833–10842.
122. Reytier, M., Di Iorio, S., Petit, J., Chatroux, A., Gousseau, G., Aicart, J., Petitjean, M., and Laurencin, J.

(2014) 11th European Fuel Cell Forum, Lucerne, Switzerland, July1–4, 2014, p. B1307.

123. Reytier, M., Di Iorio, S., Chatroux, A., Petitjean, M., Cren, J., and Mougin, J. (2014) Stack performances in high temperature steam electrolysis and co-electrolysis. WHEC2014, Gwangju, Korea, June 15–20, 2014.

124. Brisse, A. and Schefold, J. (2012) High temperature electrolysis at EIFER, main achievements at cell and stack level. *Energy Procedia*, **29**, 53–63.

125. Moçoteguy, P. and Brisse, A. (2013) A review and comprehensive analysis of degrada-tion mechanisms of solid oxide electrolysis cells. *Int. J. Hydrogen Energy*, **38**, 15887–15902.

126. Schefold, J., Brisse, A., and Tietz, F. (2012) Nine thousand hours of operation of a solid oxide cell in steam electrolysis mode. *J. Electrochem. Soc.*, **159** (2), A137–A144.

127. Fu, Q., Schefold, J., Brisse, A., and Nielsen, J.U. (2014) Durability testing of a high-temperature steam electrolyzer stack at 700 °C. *Fuel Cells*, **14** (3), 395–402.

128. Nguyen, V.N., Fang, Q., Packbier, U., and Blum, L. (2013) Long-term tests of a Jülich planar short stack with reversible solid oxide cells in both fuel cell and electrolysis modes. *Int. J. Hydrogen Energy*, **38**, 4281–4290.

129. Hauch, A. (2007) *Solid Oxide Electrolysis Cells, Performance and Durability*, Thèse Risoe National Laboratory, Denmark.

130. Ouweltjes, J.P., van Tuel, M., van Berkel, F.S (2009) Bert rietveld. European Fuel Cell Forum, Lucern, Switzerland, p. B0904.

131. Brian, Borglum (2011) *presentation at 220th ECS Meeting*, Electrochemical Processes for Fuels, Boston, MA.

132. Schiller, G., Ansar, A., Lang, M., and Patz, O. (2009) High temperature water electrolysis using metal supported solid oxide electrolyser cells (SOEC). *J. Appl. Electrochem.*, **39**, 293–301.

133. Chatroux, A., Couturier, K., Petitjean, M., Reytier, M., Gousseau, G., Mougin, J., and Lefebvre-Joud, F. (2012) Enhanced performance and durability of a high temperature steam electrolysis stack. 10th European Fuel Cell Forum, Lucerne Switzerland, June 26–29, 2012, p. A1103.

134. Petipas, F., Brisse, A., and Bouallou, C. (2014) Benefits of external heat sources for high temperature electrolyser systems. *Int. J. Hydrogen Energy*, **39**, 5505–5513.

135. Usseglio-Viretta, F., Laurencin, J., Loisy, F., Delette, G., and Leguillon, D. (0000, to be published in) *Int. J. Hydrogen Energy*.

136. Ni, M., Leung, M.K.H., and Leung, D.Y.C. (2008) Technological development of hydrogen production by solid oxide elecrolyzer cell (SOEC). *Int. J. Hydrogen Energy*, **33**, 2337–2354.

137. Sohal, M.S., O'Brien, J.E., Stoots, C.M., Herring, J.S., Hartvigsen, J.J., Larsen, D., Elangovan, S., Carter, J.D., Sharma, V.I., and Yildiz, B. (2009) Critical Causes of Degradation in Integrated Laboratory Scale Cells During High-Temperature Electrolysis, INL/EXT-09-16004. Idaho National Laboratory.

138. Sohal, M.S. (2009), Degradation in Solid Oxide Cells During High Temperature Electrolysis. INL/EXT-09-15617. Idaho National Laboratory.

139. Ebbesen, S.D. and Mogensen, M. (2010) Exceptional durability of solid oxide cells. *Electrochem. Solid-State Lett.*, **13** (9), B106–B108.

140. Wiedenmann, D., Hauch, A., Grobety, B., Mogensen, M., and Vogt, U.F. (2010) Complementary techniques for solid oxide electrolysis cell characterisation at the micro- and nano-scale. *Int. J. Hydrogen Energy*, **35**, 5053–5060.

141. Villanova, J., Laurencin, J., Cloetens, P., Bleuet, P., Delette, G., Suhonen, H., and Usseglio-Viretta, F. (2013) 3D phase mapping of solid oxide fuel cell YSZ/Ni cermet at the nanoscale by holographic X-ray nanotomography. *J. Power Sources*, **243**, 841–849.

142. Jensen, S.H., Hauch, A., Knibbe, R., Jacobsen, T., and Mogensen, M. (2013) Modeling degradation in SOEC impedance spectra. *J. Electrochem. Soc.*, **160** (3), F244–F250.

143. Schichlein, H., Müller, A.C., Voigts, M., Krügel, A., and Ivers-Tiffée, E.

(2002) Deconvolution of electrochemical impedance spectra for the identification of electrode reaction mechanisms in solid oxide fuel cells. *J. Appl. Electrochem.*, **32**, 875–882.

144. Darowicki, K. (1998) Differential analysis of impedance data. *Electrochim. Acta*, **43**, 2281–2285.

145. Sonn, V., Leonide, A., and Ivers-Tiffée, E. (2008) Combined deconvolution and CNLS fitting approach applied on the impedance response of technical Ni/8YSZ cermet electrodes. *J. Electrochem. Soc.*, **155** (7), B675–B679.

146. Leonide, A., Sonn, V., Weber, A., and Ivers-Tiffée, E. (2008) Evaluation and modeling of the cell resistance in anode-supported solid oxide fuel cells. *J. Electrochem. Soc.*, **155** (1), B36–B41.

147. Stoots, C.M., O'Brien, J.E., Condie, K.G., and Hartvigsen, J.J. (2010) High-temperature electrolysis for large-scale hydrogen production from nuclear energy – Experimental investigations. *Int. J. Hydrogen Energy*, **35**, 4861–4870.

148. Sohal, M.S., O'Brien, J.E., Stoots, C.M., McKellar, M.G., Harvego, E.A., and Herring, J.S. (2008) Challenges in Generating Hydrogen by High Temperature Electrolysis Using Solid Oxide Cells. INL/CON-08-14038. Idaho National Laboratory.

149. Manage, M.N., Hodgson, D., Milligan, N., Simons, S.J.R. and Brett, D.J.L. (2011) *Int. journal of hydrogen energy*, **36**, 5782–5796.

150. Rivera-Tinoco, R., Mansilla, C., and Bouallou, C. (2010) Competitiveness of hydrogen production by High Temperature Electrolysis: impact of the heat source and identification of key parameters to achieve low production costs. *Energy Convers. Manage.*, **51**, 2623–2634.

151. O'Brien, J.E., Zhang, X., Housley, G.K., DeWall, K.,Moore-McAteer, L., and Tao, G. (2012) 10th European SOFC Forum, Lucerne, Switzerland, June 26–29, 2012, p. A1108.

152. O'Brien, J.E., Zhang, X., Housley, G.K., DeWall, K., Moore-McAteer, L., and Tao, G. (2012) High Temperature Electrolysis Pressurized Experiment Design, Operation, and Results. INL/EXT-12-26891. Idaho National Laboratory.

153. Petipas, F., Brisse, A., and Bouallou, C. (2013) Model-based behaviour of a high temperature electrolyser system operated at various loads. *J. Power Sources*, **239**, 584–595.

154. Petipas, F., Fu, Q., Brisse, A., and Bouallou, C. (2013) Transient operation of a solid electrolysis cell. *Int. J. Hydrogen Energy*, **38**, 2957–2964.

155. Nguyen, Van Nhu Fang, Qingping, Packbier, Ute and Blum, Ludger (2013) *Int. journal of hydrogen energy*, **38**, 42814290.

156. Borglum, B. and Ghezel-Ayagh, H. (2013) Development of solid oxide fuel cells at versa power systems and fuel cell energy. *ECS Trans.*, **57** (1), 61–66.

157. Nielsen, J. and Hjelm, J. (2014) Impedance of SOFC electrodes: a review and a comprehensive case study on the impedance of LSM:YSZ cathodes. *Electrochim. Acta*, **115**, 31–45.

158. Graves, C., Ebbesen, S.D., and Mogensen, M. (2011) Co-electrolysis of CO_2 and H_2O in solid oxide cells: performance and durability. *Solid State Ionics*, **192**, 398–403.

7
Hydrogen Storage Options Including Constraints and Challenges

Agata Godula-Jopek

7.1
Introduction

Commercially viable hydrogen storage is regarded as one of the most technically challenging key barriers for its widespread application as an effective energy carrier [1–3]. Hydrogen can be stored using six different methods and phenomena: (i) high-pressure gas cylinders (up to 800 bar), (ii) liquid hydrogen in cryogenic tanks (at 21 K), (iii) adsorbed hydrogen on materials with a large specific surface area (SSA) (at $T < 100$ K), (iv) absorbed on interstitial sites in a host metal (at ambient pressure and temperature), (v) chemically bonded in covalent and ionic compounds (at ambient pressure) and (vi) through oxidation of reactive metals, for example, Li, Na, Mg, Al, Zn, with water [2]. Table 7.1 illustrates parameters for the above-given methods [4].

Nowadays the most proven, tested and commercially available hydrogen storage is in gaseous form (compressed) or in liquid form. In order to achieve a satisfying energy density with compressed gas storage systems, the operating pressure has been raised up to 70 MPa (700 bar) [5]. Liquid hydrogen can exist only at temperatures that are below the critical temperature of 33.25 K (−239.9 °C). Other critical parameters are pressure and volume, p_c 1.28 MPa and V_c 64.99 cm^3 mol^{-1}, respectively [6, 4]. In reality, liquid hydrogen is stored usually at lower temperatures of 20 K (−253 °C), because at 20 K it could be stored at atmospheric pressure, whereas at 33 K pressurized storage at 13 bar is needed. The economical way to store hydrogen for automotive applications with respect to mass production still poses a lot of challenges. Set of numerous scientific and technological challenges has been listed for the development of feasible hydrogen storage for mobile applications. The constraints and challenges are, among others, the following: high volumetric and gravimetric hydrogen densities due to weight and space limitations, low operating pressures for safety concerns, fast kinetics for loading and deloading, reversibility, operating temperatures in the range of −50 to 150 °C and costs of hydrogen storage system [1]. For stationary applications gravimetric and volumetric densities are not so critical due to available space/weight and there

Hydrogen Production: by Electrolysis, First Edition. Edited by Agata Godula-Jopek.
© 2015 Wiley-VCH Verlag GmbH & Co. KGaA. Published 2015 by Wiley-VCH Verlag GmbH & Co. KGaA.

Table 7.1 Hydrogen storage methods and relevant parameters.

Storage method	Gravimetric density (mass %)	Volumetric density (kg H_2 m^{-3})	*T* (°C)	*P* (bar)
High-pressure cylinders	13	<40	25	800
Liquid hydrogen in cryogenic tanks	Size dependent	70.8	−252	1
Adsorbed hydrogen	≈2	20	−80	100
Adsorbed hydrogen on interstitial sites	≈2	150	25	1
Complex compounds	<18	150	>100	1
Metal and complexes together with water	<40	>150	25	1

Source: By permission of Wiley VCH.

are possibilities to operate at higher pressures and temperatures. Possible cost-effective gaseous hydrogen storage is by the use of underground cavities similar to those used presently for storage of natural gas (two types: hollow such as mines and caverns and porous). It is assumed that hydrogen storage systems of the same type and the same energy content will be more expensive by approximately a factor of 3 than natural gas storage systems due to lower volumetric heating value of hydrogen. It is expected that apart from estimated losses of the working gas in the amount of 1–3% per year there should not be more technical issues associated with underground hydrogen storage [7]. In case of hydrogen, considerable amounts are currently stored at geological sites such as Teesside in the United Kingdom (operated by Sabic UK Petrochemicals) with three salt caverns being operated at a constant pressure of 45 bar with a brine storage pond used for equilibration of short-term demands, each cavern with 1.5×10^5 scm working gas capacity. Another location is Spindletop in Texas, USA, operated by Air Liquide Phillips and Praxair – dry salt cavern with a working volume 8.5×10^7 scm and a cushion gas amount of 5.8×10^7 scm [8]. At present there is one salt cavern in Germany in the city of Kiel, operating with town gas containing about 60–65% of hydrogen. The cavern of 1330 m depth has a geometric volume of about 3.2×10^4 m^3 and is under operation at 80–160 bar since 1971. Gaz de France has stored hydrogen-rich refinery by-product gases in an aquifer structure near Beynes [7]. Safe and compact hydrogen storage in a solid medium could be considered to be superior to liquid or compressed storage provided that a suitable material is found to fulfil the requirements from US DOE in terms of both gravimetric and volumetric capacities as well as favourable hydrogen loading/deloading characteristics. The latter is particularly important if the hydrogen is to be utilized within the operational envelope of Polimer Electrolyte Membrane Fuel Cell (PEM). In order to develop and demonstrate hydrogen storage technologies for transportation, stationary and portable power, the following objectives have been defined by the US DOE [9].

- By 2015, develop and verify a single-use hydrogen storage system for portable power applications achieving 0.7 kWh kg^{-1} system (2.0 wt% hydrogen) and 1.0 kWh l^{-1} system (0.030 kg hydrogen l^{-1}) at a cost of \$0.09/Wh_{net} (\$3/g $H_{2\ stored}$).
- By 2017, develop and verify onboard automotive hydrogen storage systems achieving 1.8 kWh kg^{-1} system (5.5 wt% hydrogen) and 1.3 kWh l^{-1} system (0.040 kg hydrogen l^{-1}) at a cost of \$12/kWh (\$400/kg $H_{2\ stored}$).
- By 2017, develop novel precursors and conversion processes capable of reducing the high-volume cost of high-strength carbon fibre by 25% from \$13 per pound to ~\$9 per pound.
- By 2020, develop and verify a rechargeable hydrogen storage system for portable power applications achieving 1.0 kWh kg^{-1} system (3.0 wt% hydrogen) and 1.3 kWh l^{-1} system (0.040 kg hydrogen l^{-1}) at a cost of \$0.4/Wh_{net} (\$13/g $H_{2\ stored}$).
- By 2020, develop and verify a hydrogen storage system for MHE applications achieving 1.7 kWh l^{-1} system (0.050 kg hydrogen l^{-1}) at a cost of \$15/kWh_{net} (\$500/kg $H_{2\ stored}$).
- Enable an ultimate full-fleet target of 2.5 kWh kg^{-1} system (7.5 wt% hydrogen) and 2.3 kWh l^{-1} system (0.070 kg hydrogen l^{-1}) at a cost of \$8/kWh (\$266/kg $H_{2\ stored}$) for onboard automotive hydrogen storage.

Figure 7.1 presents the DOE hydrogen storage system targets that were established by applying vehicle performance requirements into storage system needs.

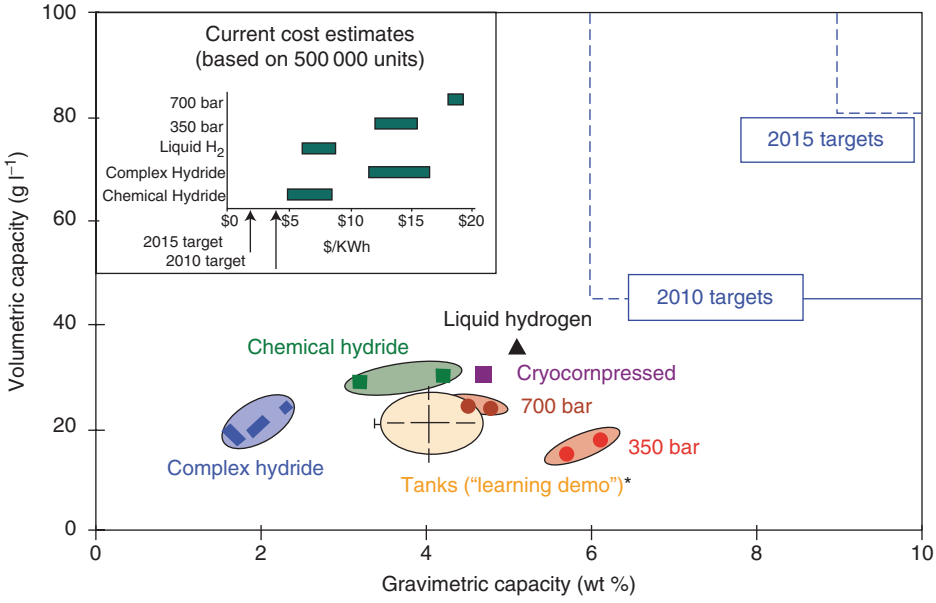

Figure 7.1 Current status of vehicular hydrogen storage systems in comparison to the gravimetric and volumetric system targets including costs estimates (costs exclude regeneration/processing) [10].

The 2010 targets allowed some vehicles to achieve a driving range of 300 miles (482.8 km) for early market penetration. High-pressure or cryogenic hydrogen storage systems are already available in prototype vehicles. Even more challenging targets have been identified for 2015 to enable the required driving range for the full range of light-duty vehicles in the North American market. According to the requirements that have to be met by 2015 for reversible storage of hydrogen gravimetric density should be 9 wt% and the volumetric capacity 81 g of H_2 l^{-1} [10]. As can be seen from Figure 7.1, none of the current vehicular hydrogen storage systems meet the combined gravimetric, volumetric and cost targets for 2010 or 2015.

Considered hydrogen storage options have several critical features that have to be solved. In general, the weight, volume and cost of hydrogen storage systems is too high (especially for automotive application), and the durability of hydrogen storage systems is inadequate. High-pressure cylinders for compressed gas and other high-pressure elements limit the choice of construction materials and fabrication techniques, within weight, volume, performance and cost constraints. In addition, hydrogen refuelling times are too long [11]. Research is also needed on improving hydrogen discharge kinetics and simplifying the reactor required for discharging hydrogen on board the vehicle (such as the volume, weight and operation). For metal hydrides, weight, system volume and refuelling time are the primary issues. In case of high surface area adsorbents, which have low density and low hydrogen binding energies and as such require cryogenic temperatures, volumetric capacity and operating temperature are important. The ultimate goal is for storage systems to be integrated with PEM fuel cell power plants, utilizing available waste heat as effectively as possible. In addition to gravimetric capacity, the research should focus on understanding the volumetric capacity, thermodynamics, kinetics and potential durability/cyclability of materials [10]. Table 7.2 summarizes projected performance of hydrogen storage methods [9].

7.2 Liquid Hydrogen

As said before, liquid hydrogen (LH_2) can exist only at temperatures that are below the critical temperature of 33.25 K (−239.9 °C). Other critical parameters are pressure and volume, p_c 1.28 MPa and V_c 64.99 cm^3 mol^{-1}. In reality, liquid hydrogen is stored usually at lower temperatures of 20 K (−253 °C), because at 20 K it could be stored at ambient pressure, whereas at 33 K pressurized storage at 13 bar is needed. Liquid hydrogen at 20 K exhibits volumetric density of 70.79 kg m^{-3}. Because of the low critical temperature of hydrogen (33 K), liquid hydrogen can only be stored in open systems, because there is no liquid phase existing above the critical temperature.

The hydrogen molecule is composed of two protons and two electrons. Hydrogen molecules exist in two different forms, as *para-* and *ortho*-hydrogen, depending on the nuclear spin orientation of the two atoms. As depicted in Figure 7.2, in the *ortho*-form the electrons of both hydrogen atoms are turning in the same direction whereas in the para-form the direction is opposite.

Table 7.2 Projected DOE performance of hydrogen storage methods.

Projected performance of hydrogen storage methods[a)]				
Hydrogen storage system	**Gravimetric ($kWh\ kg^{-1}$ system)**	**Volumetric ($kWh\ l^{-1}$ system)**	**Cost ($\$\ kWh^{-1}$; projected to 500.000 units/year)**	**Year published**
700 bar compressed (type IV)[b)]	1.7	0.9	19	2010
350 bar compressed (type IV)[b)]	1.8	1.6	16	2010
Cryo-compressed (276 bar)[b)]	1.9	1.4	12	2009
Metal hydride ($NaAlH_4$)[c)]	0.4	0.4	TBD	2012
Sorbent AX-21 carbon, 200 bar)[c)]	1.3	0.8	TBD	2012
Chemical hydrogen storage (AB liquid)[c)]	1.3	1.1	TBD	2012

a) Assumes a storage capacity of 5.6 kg of usable hydrogen.
b) On the basis of Argonne National Laboratory performance and TIAX cost projections.
c) On the basis of Hydrogen Storage Centre of Excellence performance projections.

Source: DOE Technical Plan, Hydrogen Storage, 2012 [9].

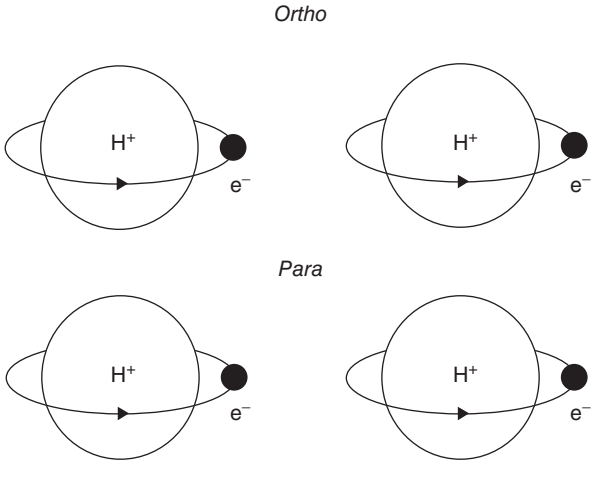

Figure 7.2 *Ortho*- and *para*-form of hydrogen [4]. (By permission of Wiley VCH.)

At room temperature hydrogen contains 25% of the *para*-form and 75% of the *ortho*-form and the latter cannot be prepared in a pure state. The physical properties of both forms are different due to the differences in energy. At a boiling point (20 K) almost all hydrogen exists in a much more stable para-form. The conversion of *ortho*- to *para*-form is exothermic and temperature dependent.

At 300 K the heat of conversion is 270 kJ kg^{-1} and increases as the temperature decreases, where it reaches 519 kJ kg^{-1} at 77 K. At temperatures lower than 77 K the enthalpy of conversion is 523 kJ kg^{-1} and nearly constant [2]. As a consequence, until the conversion into the *para*-form is completed in a storage vessel, liquid hydrogen has a source of heat (the enthalpy of conversion will be released in the vessel), which results in the evaporation of the liquid hydrogen (boil off effect). The reaction can be catalysed by charcoal or metal catalysts such as tungsten, nickel or any paramagnetic oxides such as chromium or gadolinium oxides, which accelerate the conversion of the *ortho*- into the *para*-form even before complete liquefaction of hydrogen is achieved and boil-off loss is avoided. The boil-off rate of hydrogen from a liquid hydrogen storage vessel due to heat leaks is a function of the size, shape and thermal insulation of the used vessel. Therefore the main concern of LH_2 storage is an issue of minimizing hydrogen losses from liquid boil-off. Liquefaction process is energy consuming; the typical demand of the installed units for the process is between 36 and 54 MJ kg^{-1} and the goal for future efficiency-optimized installations should be in the range of 25 MJ kg^{-1} [4]. The liquefaction process was first successfully realized by Dewar in 1898, followed in 1900 by the Linde concept of the first liquefier by compression later improved by Claude. The liquefaction process is based on two expansion processes: Joule–Thomson expansion performed by using valves or expansion with energy extraction using an expansion turbine or expander. The simplest liquefaction cycle is the Joule–Thomson cycle (Linde cycle). After compression at ambient temperature the gas is cooled in a heat exchanger, followed by its passing through a throttle valve where it undergoes an isenthalpic Joule–Thomson expansion, producing some liquid. The cooled gas is separated from the liquid and returned to the compressor via the heat exchanger (Flynn 1992). The Joule–Thomson cycle is applicable for gases such as nitrogen. The Claude process is realized by combination of the expansion turbine and Joule–Thomson expansion stage. The cooled gas is separated from the liquid and returned via the heat exchanger to a several-stages compressor (typically two, three or four stages). The Collins process or the modified Claude cycle was originally developed for the liquefaction of helium. Usually the liquefier consists of six heat exchangers and two reciprocating expanders. The refrigeration effect produced in the expanders, proportional to the mass flow and the inlet temperature of the gas, determines the function of the unit: as refrigerator or liquefier. The liquefaction produced in the cycle is directly proportional to the mass flow rate directed to expand through the Joule–Thomson valve [12]. The liquefaction process could also be performed by magnetic refrigeration based on the magnetocaloric effect (MCE) and consists of four steps: (i) adiabatic magnetization, (ii) isomagnetics enthalpic transfer, (iii) adiabatic demagnetization and (iv) isomagnetics entropic transfer. The technique can be applied to extremely low temperatures below 1 K. Ultimately the liquefaction process is energy intensive (12–15 kWh kg^{-1} vs 3.2 kWh kg^{-1} for compression to 700 bar) and expensive (1.61 \$/kg H_2); the costs of a large-scale liquid hydrogen plant depend primarily on the energy costs [13, 14].

7.2.1
Liquid Hydrogen Storage Systems

Low-pressure liquid hydrogen storage systems have high density and reasonably low cost, but they suffer from evaporative losses after a short period of inactivity (1–3 days) [13]. Liquid hydrogen storage tanks can have spherical or cylindrical form and cylindrical can have horizontal or vertical configuration. It is thought that spherical shape cylinders are more advantageous for ships and cylindrical vessels are better for transportation by trucks or railways. Technical data for horizontal and vertical tanks for liquid hydrogen storage as well as for data for tanks depending on their size (local, large/today and large/long term) is presented in [15]. A typical modern liquid hydrogen storage cylindrical tank (capacity of 540 l of liquid hydrogen, outside diameter of 500 mm and an overall length of 5.5 m) has been developed by Linde in Germany for hydrogen-powered buses [16]. It is reported that currently liquid hydrogen tanks can reach gravimetric and volumetric energy densities with 0.06 kg H_2 kg^{-1} or 2 kWh kg^{-1} and 0.04 kg H_2 l^{-1} or 1.2 kWh l^{-1}, respectively [17]. At present NASA at Cape Canaveral in Florida has the largest spherical tank able to store 3400 m^3 of liquid hydrogen at −253 °C [15]. In 2011 Shell Deutschland Oil GmbH opened their first demonstration hydrogen station, within the scope of the 'Clean Energy Partnership' (CEP), located in Berlin. It has the capacity to fill about 250 hydrogen-fuelled vehicles per day, but the station is mainly to be used for demonstration and research purposes [18]. Cryogenic pressure vessels successfully passed cycle testing and a variety of additional tests (pressure cycle and burst, environmental, drop from 3 m, drop from 10 m, gunfire, bonfire and cryogenic cycle and burst following procedures specified by the US Department of Transportation (DOT), the Society of Automotive Engineers (SAE) and the International Organization for Standardization (ISO) [13]. The first cryogenic vessel installed on a Ford Pickup (generation 1 prototype) operated at a maximum pressure of 245 bar with a 135 l internal volume and 9.3 kg LH_2 capacity. Safe operation of a hydrogen-fuelled experimental vehicle with a cryogenic tank (prototype 2) has also been demonstrated. The hydrogen hybrid vehicle was test driven at Lawrence Livermore National Laboratory (LLNL) typical traffic conditions, covering a distance of 1050 km on a single tank fill of LH_2, which was the longest for a hydrogen vehicle [13]. There are few manufacturers of cryogenic vessels, including, among others, Linde in Germany, Air Liquide in France, Air Products and Praxair in the United States, British Oxygen Company in the United Kingdom, Kobe Steel in Japan and JSC Cryogenmash in Russia [15].

For a city bus Linde AG has built a mobile liquid hydrogen storage system as presented in Figure 7.3. A mobile refuelling unit by Linde is shown in Figure 7.4.

The distribution of hydrogen for usage at filling stations is already widely demonstrated worldwide, for example, within EU project Clean Urban Transport for Europe (CUTE). In Figure 7.5 one can see Linde hydrogen refuelling station located at Linde site at Lohhof nearby Munich, under operation since 2007.

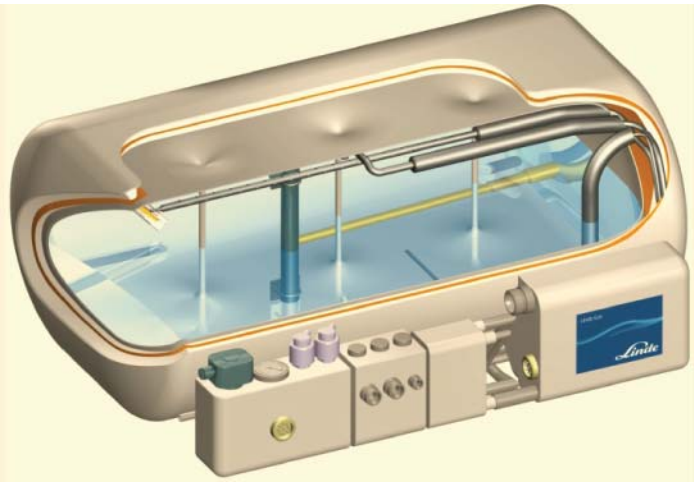

Figure 7.3 Linde mobile refuelling storage. (By kind permission of Linde AG Germany.)

Figure 7.4 Linde mobile refuelling unit. (By kind permission of Linde AG, Germany.)

From an above-ground liquid hydrogen storage tank different types of hydrogen vehicles can be fuelled with both liquid hydrogen and compressed gaseous hydrogen, going through corresponding dispenser systems. Hydrogen is stored in a superinsulated 17.600 l liquid hydrogen tank (with boil-off system to CGH_2 supply).

Figure 7.5 Linde hydrogen refuelling station in Munich. (Reprinted by kind permission of Linde AG, Germany.)

7.3 Compressed Hydrogen

Compressed hydrogen is still the preferred option for storing and distributing hydrogen, especially for the automotive sector due to rapid refuelling capability and well-developed and established infrastructure for compression. Figure 7.6 depicts the evolution of the volumetric density of compressed hydrogen as a function of the pressure for different temperature ranges. Hydrogen density does not increase in a linear way with increasing temperature. At 30 MPa hydrogen density is 20 kg m^{-3} and at 70 MPa the density increases up to 40 kg m^{-3}. Compression of hydrogen from the atmospheric pressure to 30 MPa [19] or higher needs a large amount of energy and can be realized by adiabatic or by isothermal compression. In case of adiabatic compression the process occurs without heat exchange between gas and the surrounding environment. During isothermal compression the temperature remains constant during the process and as such cooling of the gas has to be taken into consideration. The work needed for adiabatic and isothermal compression can be described by the following reactions:

$$\text{Adiabatic compression} \quad W = \frac{\gamma}{\gamma - 1} RT_1 \left\{ \left(\frac{P_2}{P_1} \right)^{\gamma/\gamma-1} - 1 \right\}$$

$$\text{Isothermal compression} \quad W = nRT \ \ln \frac{p_1}{p_2}$$

where

W – amount of work
R – ideal gas constant, $R = 8.3145\,\mathrm{J\,K^{-1}\,mol^{-1}}$
γ – specific heat ratio of the gas, $\gamma = \frac{C_p}{C_v}$

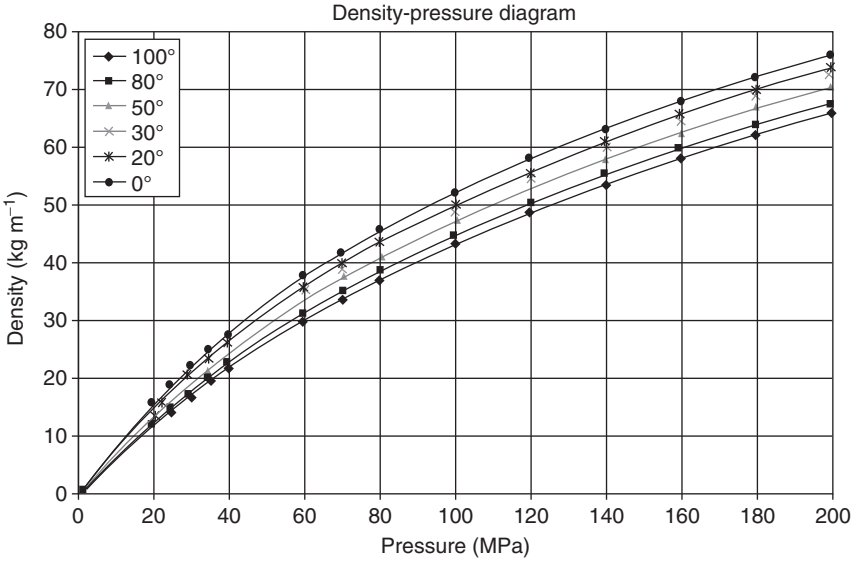

Figure 7.6 Density of compressed hydrogen as a function of pressure at different temperature regimes [4]. (By permission of Wiley VCH.)

T – temperature, K.

In case of adiabatic compression of 1 kg of hydrogen (inlet pressure 2 MPa and outlet pressure 35 MPa) the work is calculated as 5.45 MJ kg^{-1}. Isothermal compression needs 3.03 MJ kg^{-1} [4]. Compression can be realized by using mechanical compressors (piston and piston metal diaphragm) or by non-mechanical compressors (metal hydride compressors, electrochemical compressors) [4, 14]. Compressed gas has to be cooled down to make the process less adiabatic and more isothermal.

7.3.1
Compressed Hydrogen Storage Systems

Mostly compressed hydrogen is available in pressurized containers up to 30 MPa (300 bar). In order to achieve a satisfying energy density with compressed gas storage systems, the operating pressure has been raised up to 70 MPa, which is one of the greatest challenges in developing high-compressed tanks nowadays. Special care must be taken when selecting the material for the tank, and with regard to safety and balance of plant components such as pipelines, valves and regulators. Specific features of hydrogen while in contact with the tank material have to be considered. Such phenomena include among others hydrogen embrittlement, hydrogen attack, permeation through metals and non-metals, resistance to external corrosion, resistance to dynamic and impact loads, prevention of leaks and compatibility mode with static and cyclic pressurization. Apart from the static and dynamic pressure loads, pressure cylinders have to be resistant towards the

temperature of about 140 °C during the fast filling process due to compression energy [20]. It seems that these extreme structural requirements can be achieved in an economical way only with hybrid structures. Carbon fibre composite pressure tanks up to 70 MPa can achieve a gravimetric storage density of 6 wt% and volumetric storage density of 30 kg m^{-3} [1].

Composite storage cylinders offer light weight, corrosion resistance and dimensional stability and can store gas at higher pressures, but they cannot guarantee safe operation for the time being [21]. Also, it is possible to choose the orientation of the composite fibres to ensure optimal usage of the material for the given usage. Composite are basically sensitive to combined thermomechanical loads (the strength and stiffness are temperature dependent); therefore numerous studies have been performed on analysing the properties, structural integrity and behaviour of composite cylinders. They include, among others, investigations on multilayered glass and epoxy composite high-pressure cylinders under plane strain and closed-end conditions [22], analysis of composite hydrogen storage cylinders under transient thermal loads and subjected to high pressure and localized flame impingements using final element model [21, 23], analysis of thermal stresses in multilayered hollow cylinders using final difference model and Laplace transforms [24], calculations on transient thermoelastic stresses in thick-walled composite anisotropic pipes [25]. In the case of composite cylinders there are two design types.

Type III are completely made from carbon fibres (with a metal liner for gas tightness and taking small parts of the load) and type IV has a plastic/synthetic liner for gas tightness (the liner does not take any structural loads). A number of high-pressure cylinders of type III and IV (both for 350 and for 700 bar) are available for automotive applications. According to detailed characteristics analysed by Klell [17], the obtainable net volume of cylinders can vary from 34 to 100 l (type III) and from 36 to 120 l (type IV). Energy densities are higher than for steel cylinders and can reach gravimetric hydrogen content of 0.049 kg H_2 kg^{-1} with gravimetric and volumetric energy densities of 1.633 kWh kg^{-1} and 0.533 kWh l^{-1} (type III, 350 bar); the respective values for 700 bar type III cylinders are 0.036 kg H_2 kg^{-1}, 1.2 kWh kg^{-1} and 0.833 kWh l^{-1}. For a 700 bar pressure cylinder of type IV the maximal gravimetric hydrogen content is 0.055 kg H_2 kg^{-1}, equivalent to 1.833 kWh kg^{-1} and volumetric energy density of 0.767 kWh l^{-1} [17]. Commercially available containers (called type I) are typically made from stainless steel and available in nominal pressures from 200 to 300 bars (20–30 MPa) with similar gravimetric and volumetric energy densities of about 0.333 kWh kg^{-1} or 0.3 kWh l^{-1} (tank volume 2.5 l) up to 0.4/0.367 kWh kg^{-1} or 0.4/0.533 kWh l^{-1} (tank volume 50 l), respectively. Unfortunately, they are rather heavy; the weight of the tank of 2.5 l is 3.5 kg (3.6 l) and the tank of 50 l weighs from 58 to 94 kg (60.1–64.7 l) [17]. Cylinders of type II have a thin metal liner partially with a mesh for stability. According to Klell [17], the price for tank systems can vary from about 40 EUR per 1 kWh of stored hydrogen energy for 350 bar type III cylinder up to about 150 EUR per 1 kWh for 700 bar type IV cylinders.

7.4 Cryo-Compressed Hydrogen

Compressed hydrogen stored at cryogenic temperatures (CcH_2) is a compromise between liquid hydrogen and compressed gas storage at ambient temperatures. CcH_2 refers to the storage of hydrogen at cryogenic temperatures in a container that can be pressurized to 250–350 bar, opposite to current cryogenic containers storing liquid hydrogen at near-ambient pressures. Cryo-compressed hydrogen storage can include liquid hydrogen, cold compressed hydrogen or hydrogen in a two-phase region (saturated liquid and vapour) [26]. CcH_2 storage takes advantage of LH_2-based infrastructure and can be compatible to the 350 bar CGH_2 infrastructure. Cryo-compressed hydrogen has a density of 71 kg m^{-3} max or 272 bar max pressure. With volumetric storage capacities of 41.8–44.7 kg H_2 m^{-3} the CcH_2 system meets the US DOE 2015 volumetric target, which is 40 kg H_2 m^{-3}, but not the ultimate target of 70 kg H_2 m^{-3}. With gravimetric system capacities of 5.5–9.2 wt% CcH_2 system with Al shell approaches the ultimate gravimetric target, which is 7.5 wt%. Options involving cryogenic hydrogen have <41% WTW (well-to-wheel) efficiencies [27].

7.4.1 Cryo-Compressed Hydrogen Storage Systems

Cryo-compressed hydrogen storage shows good performance and interesting perspectives for the fuelling station business case. It has been noted that despite the fact that the technology risks of cryo-compressed are still high, no show stopper has been discovered until now. BMW continues developing CGH_2 700 and 350 bar CcH_2 vehicle storage in parallel [28]. A criterion for the application of the CcH_2 tank for an automotive use is a combination of the advantageous properties of CGH_2 pressure tanks and liquid hydrogen tanks, and simultaneously minimizing the demands made on the critical subsystems of both storage types [29].

The BMW Linde CcH_2 pump prototype is in operation since April 2004 with performance of 80 g l^{-1} at 300 bar, 100 kg H_2 h^{-1} (up to 120 kg h^{-1}), <1% Lower Heating Value (LHV) compression energy. Hydrogen delivered (status September 2012) ~45 000 kg (>7000 refuellings with subscale and full size tank systems). The BMW CcH_2 filling station is in operation since November 2011. Active research and development on cryo-compressed hydrogen systems is ongoing (projects: Cryosys, Hymod, Cryocode, Cryofuel) [30].

In Figure 7.7 a concept of the BMW cryo-compressed storage tank (prototype 2011) is shown. It is based on the idea of compressing liquid hydrogen to a supercritical pressure level and storing it as cryo-compressed hydrogen gas in an insulated pressurized vessel suitable for cryogenic temperatures. The design of the cryo-compressed storage tank is similar to that of a liquid hydrogen tank.

It consists of an inner vessel – a carbon-fibre-reinforced composite pressure vessel with a metal liner – an all-enveloping layer of vacuum superinsulation with

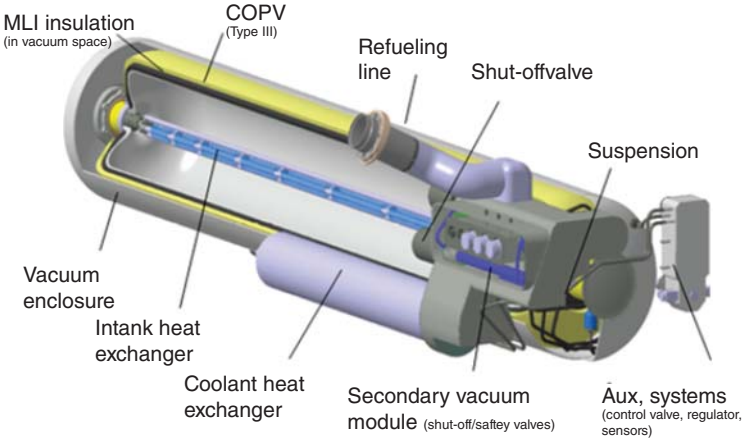

Figure 7.7 BMW prototype 2011 system layout of superinsulated cryogenic cylinder [31]. (Reprinted by kind permission of BMW.)

multilayer radiation shields to minimize heat input into the inner vessel and a lightweight outer vessel that acts as a vacuum enclosure [29].

It has been highlighted that core components of the BMW CcH_2 storage have experimentally proven their compliance with requirements of high-density storage, quick loss-free refuelling and durability [31]. Compared with the hydrogen storage tanks available today, the cryo-compressed storage tank has the highest system-based volumetric and gravimetric storage density potential (2.0 kWh kg^{-1} and 1.2 kWh l^{-1} for CcH_2 at 350 bar, 1.6 kWh kg^{-1} and 0.8 kWh l^{-1} for CGH_2 at 700 bar, 2.0 kWh kg^{-1} and 0.6 kWh l^{-1} for CGH_2 at 350 bar). In addition, hydrogen storage tanks can have considerably higher volumetric and gravimetric system storage densities than Li-ion batteries (0.15 kWh kg^{-1} and 0.25 kWh l^{-1}). The operational envelope of BMW cryo-compressed storage covers pressures of up to 35 MPa and temperatures from +65 °C down to −240 °C, applying high loads on composite and metallic materials of the cryogenic pressure vessel compared to ambient carbon–fibre-reinforced pressure vessels [29]. BMW is convinced that the storage of hydrogen in cryo-compressed tanks offers many more advantages, opportunities and potential as compared with pressurized hydrogen and liquid hydrogen storage technology. Both cryo-compressed hydrogen and compressed hydrogen infrastructure allows high refuelling flexibility at filling stations with different hydrogen supply paths. It has been shown that the typical automotive life cycle requirements and safety can be fulfilled by the CcH_2 storage system. Validation of safe operation and structural durability (pressure and temperature cycling, static pressure and vehicular vibrations) on the storage vessel and key components has been successfully performed. For example, test series with 1 and 20 cycles on the CcH_2 prototype tank followed by burst tests in each case have proven that there is no degradation of the static strength of the inner tank; however, further tests are necessary. When comparing adiabatic expansion energies of different hydrogen storage systems it can be concluded that in case of failure,

the low adiabatic expansion energy of hydrogen at cryogenic temperatures (5–16 times lower) provides a high level of safety [29]. As of today, single-flow cryo-compressed refuelling without the need for precooling the vehicle tank seems to be potentially the fastest and the most efficient method. In such case the filling station requires only a cryo-pump and liquid hydrogen storage tank; there is no need for high-pressure tank arrays and additional equipment such as heat exchangers and gas compressors [29].

Technical assessment of cryo-compressed hydrogen storage tank systems for automotive applications has been performed including onboard and offboard performance and costs [26]. The assessment was based on the Gen-3 tank design as shown below and the prototype vessel, which was constructed by the LLNL and Structural Composites Industries (SCI). The Gen-3 system concept has been analysed for its potential to meet 2010, 2015 and ultimate US DOE targets for hydrogen storage for fuel cell and hydrogen-fuelled vehicles and included both hydrogen storage system required on the vehicle (onboard) and thermal management, fuel cycle, energy costs and infrastructure needed to refuel the onboard system (offboard). The prototype cryo-compressed storage vessel has hydrogen storage volume of 151 l (total system volume is 253 l, system weight is 145 kg) and can store 10.7 kg of liquid hydrogen at 20.3 K and 1 bar pressure. The pressure vessel consists of 9.5 mm thick aluminium liner wrapped with carbon fibre composite. Fibre wound vessel is surrounded by a vacuum gap filled with multilayer superinsulation. In addition, 3 mm stainless steel outer shell and balance of plant equipment constitute the system. Filled with gaseous hydrogen the system is able to store 2.8 kg of compressed hydrogen at 272 bar and 300 K. Filled with liquid hydrogen the system shows nominal usable volumetric capacity of 44.5 kg m^{-3} and gravimetric capacity of 7.1 wt% (1.5 kWh l^{-1} and 2.3 kWh kg^{-1}, respectively) [26] (Figure 7.8).

Technical assessment of cryo-compressed hydrogen storage tank for automotive application versus 2010, 2015 and ultimate DOE targets for onboard hydrogen storage for light-duty vehicles is depicted in Table 7.3.

Regarding gravimetric system capacities, the cryo-compressed option exceeded the DOE 2010 target of 4.5 wt% (scaled Gen-3 system 5.5–9.2 wt% and prototype Gen-3 system 7.1–12 wt%) and meets 2015 and ultimate targets. In case of volumetric capacities and given DOE targets scaled Gen-3 with 41.8–44.7 kg H_2 m^{-3} well exceeded the 2010 target of 28 kg H_2 $m^{-3}$and meets the 2015 target of 40 kg H_2 m^{-3}, but is below the ultimate target of 70 kg H_2 m^{-3} (Gen-3 meets about 60–64% of the set ultimate target value).

7.5
Solid-State Hydrogen Storage Including Materials and System-Related Problems

An efficient and compact way of storing hydrogen in a solid state seems to be the most challenging and demanding part of the hydrogen economy for mobile applications (Figure 7.9); therefore this way of storing hydrogen is the area where

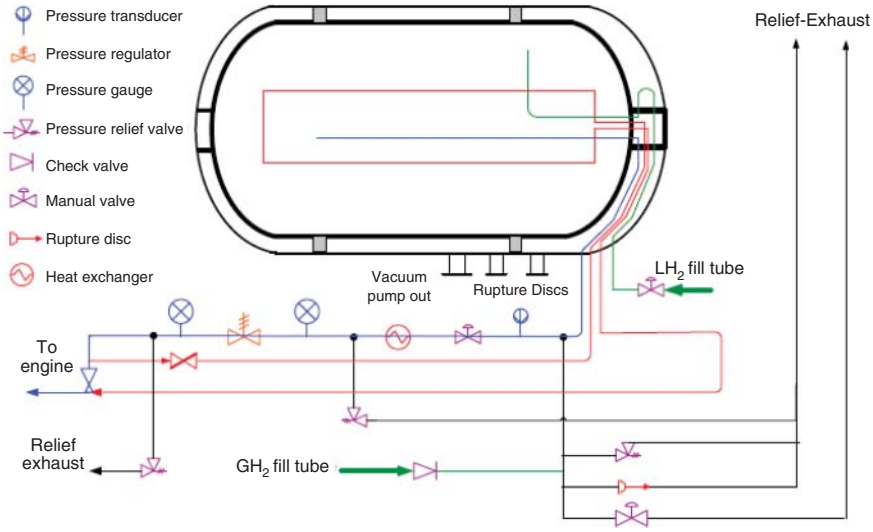

Figure 7.8 Design schematic of the Gen-3 cryo-compressed H_2 storage tank system [26].

Table 7.3 Summary results of the assessment of the prototype and LLNL Gen-3 cryo-compressed H_2 storage systems [26].

Performance and cost metric	Units	Scaled Gen-3	Prototype Gen-3	2010 targets	2015 targets	Ultimate targets
Usable storage capacity (nominal)	kg H_2	5.6	10.4	—	—	—
Usable storage capacity (maximum)	kg H_2	6.6	12.3	—	—	—
System gravimetric capacity	wt%	5.5–9.2	7.1–12	4.5	5.5	7.5
System volumetric capacity	kg H_2 m^{-3}	41.8–44.7	44.5–47.1	28	40	70
Storage system cost	\$ kWh^{-1}	12	8	4	2	TBD
Fuel cost	\$ gge^{-1}	4.80	—	2–3	2–3	2–3
Cycle life (1/4 tank to full)	Cycles	18 000	18 000[a)]	1000	1500	1500
Minimum delivery pressure	atm	3–4	3–4	4/35	3/35	3/35
System fill rate	kg H_2 min^{-1}	1.5–2	1.5–2	1.2	1.5	2.0
Minimum dormancy (full tank)	W-d	4–30	7–47	—	—	—
H_2 loss rate (maximum)	g h^{-1} kg^{-1} H_2	0.2–1.6[b)]	—	0.1	0.05	0.05
WTW efficiency	%	41.1	—	60	60	60
GHG emissions (CO_2 equivalent)	kg kg^{-1} H_2	19.7	—	—	—	—
Ownership cost	\$/mile	0.12	—	—	—	—

a) Warm cycles.
b) During vent time, tank 50–100% initially full.
FC/ICE – Fuel Cell/Internal Combustion Engine; GHG – Greenhouse Gas.

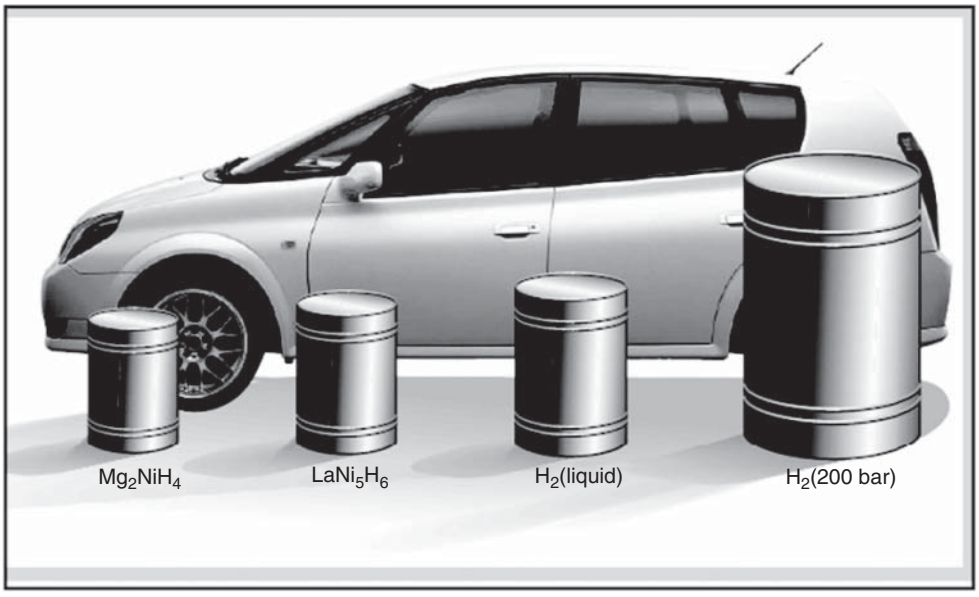

Figure 7.9 Alternatives for storage of 4 kg hydrogen with volume relative to the size of a car [32].

considerable international effort is spent. The lack of a suitable hydrogen storage material currently limits the utilization of hydrogen more widely in the automotive sector, especially in fuel cell vehicles [32]. Although gaseous or liquid hydrogen storage is a potential candidate for onboard storage, the losses due to the boil-off effect as described in the section above and requirement of high liquefaction energy are the principal demerits. Therefore solid-state hydrogen storage is potentially superior when considering energy efficiency, safety and gravimetric and volumetric storage capacities.

With regard to the technical targets and requirements set by the US DOE for onboard hydrogen storage systems for light-duty vehicles [10], some materials meet the criteria in terms of gravimetric and volumetric hydrogen storage capacities but it looks that for the time being they could not satisfy the targets on a system level (0.055 kg H_2/kg and 0.040 kg H_2 l^{-1} system in 2017). This is presented in Figure 7.10.

In addition there are several other factors that severely limit or prevent their practical application, such as non-reversibility/cyclability, thermodynamic barriers and slow kinetics of hydrogen uptake/release. Such material should be safe, light-weight and an inexpensive storage medium when compared with gaseous and liquid storage.

Two categories of hydrogen storage in a solid state, chemical and physical, can be considered depending on the nature of the bonding created between the solid material or compound and hydrogen. In chemical storage the hydrogen is chemically held to compound atoms within a solid (formation of chemical bonds).

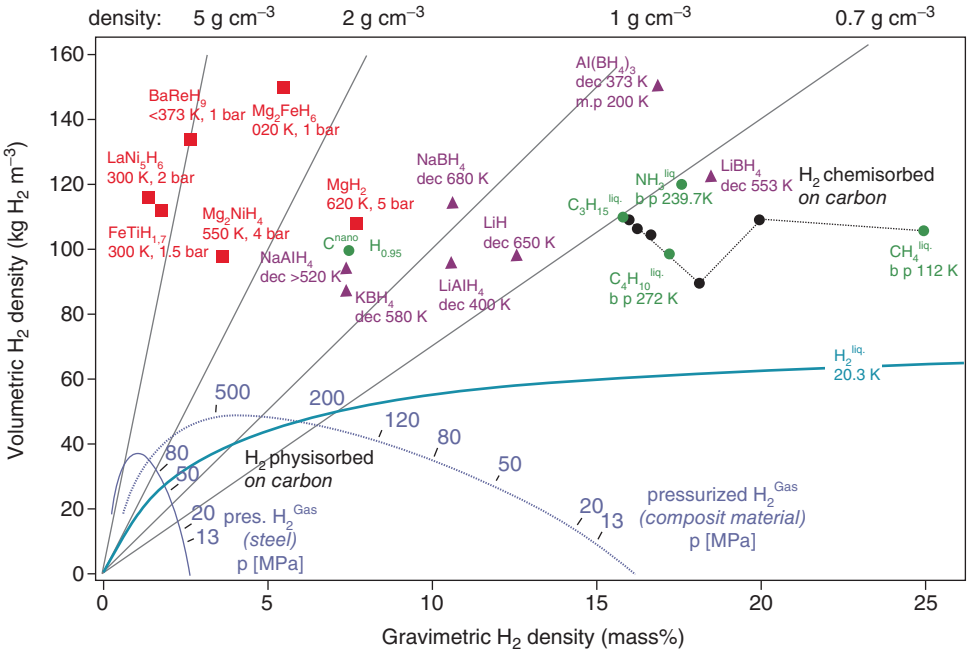

Figure 7.10 Volumetric and gravimetric hydrogen density of some selected hydrides [2].

As a consequence, hydrogen uptake and release (loading and unloading) involves a chemisorption step before the absorption of hydrogen in the bulk surface and the creation of chemical bonds. Chemical storage often requires high temperatures for releasing hydrogen. During physical storage the hydrogen molecule interacts with the atoms at the surface of the solid surface or a porous solid by much weaker van der Waals interactions. The interaction involves two terms: an attractive term that diminishes with the distance between the molecule and the surface to the power of −6 and a repulsive term that diminishes with the distance to the power of −12 [33]. As a result, the potential energy of the molecule shows a minimum at a distance of approximately one hydrogen molecule radius (approximately 0.2 nm) of the adsorbate. The energy minimum is of the order of 0.01–0.1 eV (1–10 kJ·mol^{-1}) [2]. Because of the weak interaction, significant physisorption is only observed at low temperatures below 273 K and/or very high pressures. State of the art on solid-state hydrogen storage focusing on both physical and chemical aspects of hydrogen storage has been presented by Reardon *et al.* [34]. Newly emerging routes towards meeting the practical demands required from solid-state hydrogen storage system have been highlighted, including the role of nanostructuring techniques to modify kinetics and thermodynamics, as well as the role of inorganic nanostructures as evolving intermediate materials between physical and chemical hydrogen storage systems has been described. Both physical and chemical storage ways can benefit from nanomodifications. The role of altering reaction enthalpies

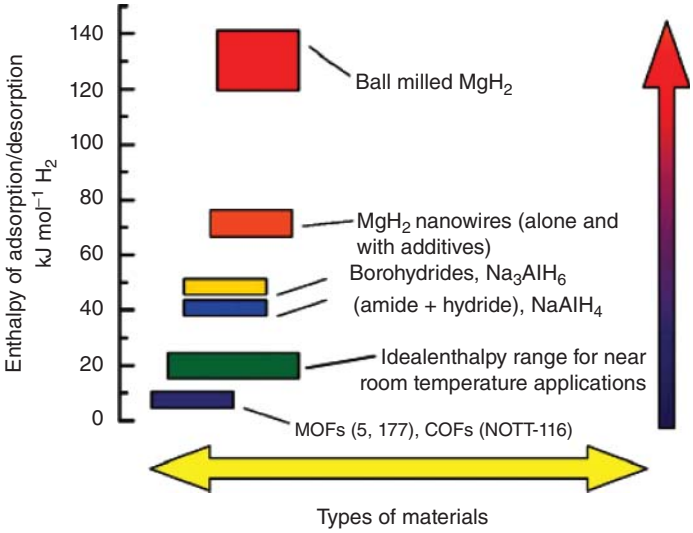

Figure 7.11 The enthalpy of adsorption ranges for various types of storage materials [34].

of novel lightweight hydrides has been widely analysed by Dornheim [35]. The classical way of destabilizing hydrides is by substitution of the metal lattice and as such new intermetallic hydrides are formed. This concept has been successfully demonstrated on conventional metal hydrides, leading to the creation of a large number of hydrides with different thermodynamic properties and extended towards complex and lightweight hydrides. An attractive concept to modify the reaction enthalpies of single-component hydrides is by mixing them with suitable reactive additives. The first results of the substitution of H-sites by F^- anions-substituted systems show promising results for complex hydrides. It has been demonstrated that the hydrogen uptake/release ability of lightweight metal hydrides can be improved by the use of nanoadditives such as transition metals as catalysts. It has been proven that nanodesign approach can have a significant effect on improving sorption kinetics and enhancing interaction strength and thus reducing the temperature of hydrogen release when compared to the bulk [34]. Figure 7.11 depicts enthalpies of adsorption/desorption of several types of storage materials. It can be seen that the enthalpies of adsorption/desorption of chemisorbed materials are different to physisorbed ones. Chemisorbed materials enthalpies are above and physisorbed enthalpies are below the ideal enthalpy for near-ambient temperature of hydrogen sorption (15–25 kJ mol^{-1} H_2).

7.5.1
Physical Storage – Overview

Activated carbons (ACs), zeolites, graphene, coordination polymers such as metal organic frameworks (MOFs), covalent organic frameworks (COFs) and polymers are among porous materials that are widely investigated for hydrogen storage by

physisorption. As said above, during the mechanism of physisorption (or physical adsorption) the hydrogen is stored in a molecular way only on the surface of a solid material. Thus only porous materials with a high SSA are suitable candidates for molecular hydrogen storage. Molecular adsorption of hydrogen occurs by weak dispersive forces (van der Waals forces in the range of 1–10 kJ mol^{-1}) and is completely reversible and a non-activated process, meaning that hydrogen can be adsorbed on and released from the surface without any losses in several cycles. Adsorption being an exothermic process releases heat and due to low polarizability of the hydrogen molecule, the heat of adsorption is low. The adsorption process on porous materials is best described by the adsorption isotherms (e.g. Langmuir, Brunauer–Emmet–Teller – BET, Henry). Benard and Chahine [19] discussed the use and the limitations of physisorption as a storage media for hydrogen. The best adsorbent can be determined by the following optimizing parameters: the characteristic binding energy of the hydrogen molecule with the material, the available surface for adsorption processes and the bulk density of the adsorbate. The binding energy is the factor that determines the operating temperature of a hydrogen storage system based on the solid. Ideally, the binding energies of carbon-based materials should be between 0.2 and 0.8 eV (19.29–77.1 kJ mol^{-1}) [36], making possible that hydrogen remains at operational conditions without the need of applying high pressures and can be released after moderate heating. The ideal hydrogen storage material would have very high surface area, over 2000 $m^2\,g^{-1}$. The amount of hydrogen stored on the porous surface can be expressed by the absolute storage capacity and excess storage capacity. The absolute storage capacity is determined from the theoretical calculations and refers to the amount of hydrogen adsorbed on a porous medium, not taking into account the gas phase. The excess adsorption is based on experimental measurements and is described as a difference between the quantity of a gas stored at a given temperature and pressure in a given volume containing the adsorbent and the quantity that would be stored under the same conditions in the absence of gas–solid interactions. The difference between the excess and absolute adsorption can be expressed as follows [37]:

$$N_{ex} = N_{ads} - \rho_g(V_0 - V_g) = N_{ads} - \rho_g(V_a),$$

where

N_{ex} – excess adsorption
N_{ads} – the amount of gas adsorbed on a sample
ρ_g – gas density
$V_0 - V_g$ – difference between the real free volume and the free volume measured with helium in the absence of the adsorbed phase
V_a – volume occupied by the adsorbed phase.

At low temperatures and high pressures the absolute adsorption is different from the excess adsorption. The former absolute adsorption for porous materials at 77 K is the Langmuir type (the formation of a monolayer on a surface; at the plateau the maximum uptake of hydrogen is reached), whereas the latter does not reach a plateau at high pressures. At room temperatures only a very small

amount of hydrogen is stored on porous surfaces; it can increase at low temperatures, typically of liquid nitrogen at 77 K.

Carbon-based nanoporous materials such as AC, single-walled carbon nanotubes (SWNTs), multi-walled carbon nanotubes (MWNTs) and graphite have attracted a lot of attention and interest in the last decade and have thus been investigated as promising adsorbents for hydrogen storage applications by many authors, among others [19, 37–44]. Pure carbon materials have binding energy in the range 4–15 kJ mol^{-1}; lower values are typical for graphite and AC whereas higher values are usual for SWNTs and MWNTs. It has been observed that depending on the chosen method and experimental conditions the hydrogen storage capacities on SWNTs can vary from 0.02 to nearly 10 wt% [43] as depicted in Figure 7.12.

At cryogenic conditions Pradhan *et al.* [45] obtained 6 wt% on SWNTs; however, Gundiah *et al.* [46] report significantly lower values, from 0.2 to 0.4 wt%. Poirier *et al.* [47] under 77 K and 4 MPa reached maximum excess adsorption from 1.5 to 2.5 wt%, but at room temperature (pressure 4 MPa) it was less than 0.4 wt%. The maximum storage capacity observed by Gundiah *et al.* [46] was 3.7 wt% on MWNTs prepared by the pyrolysis of ferrocene and acetylene, additionally treated with acid. Other carbon samples differently prepared showed lower values; for example, MWNTs synthesized by the pyrolysis of acetylene reached only 0.2 wt%, whereas MWNTs obtained by the pyrolysis of ferrocene showed 1.0 wt%, the value on MWNTs prepared by the arc-discharge method being well graphitized was 2.6 wt%. AC having high surface area of

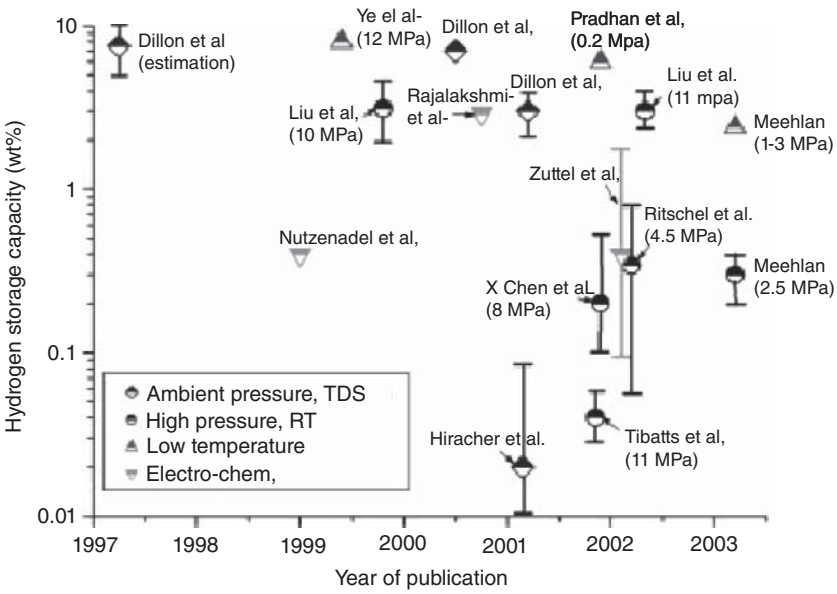

Figure 7.12 Hydrogen storage capacities in SWNTs by different authors, methods and operational condition. (By permission of Wiley VCH [4].)

500–2500 $m^2 g^{-1}$ can adsorb hydrogen in the microscopic pores. Most of them are strongly adsorbing micropores having diameter less than 2 nm and mesopores with diameter from 2 to 50 nm, performing mainly the role of transport channels. In macropores with diameter 100–200 nm the adsorption process on its surface is negligible and, like mesopores, they act as transporting channels. It has been reported that [48] under ambient temperature and 6 MPa the storage capacity of hydrogen on AC was only 0.5 wt%, but at 77 K and pressures 4.5–6 MPa the value significantly increased up to 5.2 wt%. Experiments performed on AC obtained by carbonization of walnut shells and sawdust mixed with phosphoric acid showed hydrogen capacity of 2.2–2.8 wt% at 77 K and pressures 1.2–1.5 MPa. A lot of attention has been given to prospects of hydrogen storage in graphene, two-dimensional one-atom thick crystal build from carbon atoms arranged in a honeycomb geometry and graphene-based structures. A progress in the active field of graphene-based nanomaterials for energy storage applications has been reviewed [49]. Most of the activities started in 2008; thus this field is young, active and promising. Theoretically, graphene is an ideal material, which could fulfil DOE targets for hydrogen storage. Theoretical investigations showed that for graphene layers separated by a distance of 6 Å, one monolayer of hydrogen can be accommodated within the intergraphene structure (yielding a 2–3 wt% storage capacity at 5 MPa). An attractive possibility is to store two layers of hydrogen molecules in a single graphene–graphene interlayer by having two graphene layers separated by 8 Å, which could lead to gravimetric storage capacities of 5.0–6.5% of H_2 [49]. Graphene is stable and robust; on the other hand, it is mechanically stable thus enabling new loading/deloading ways under room temperatures. The maximum gravimetric density in graphene with chemisorptions can reach 8.3 wt% at high pressure and low temperature, corresponding to a fully saturated graphene sheet with 1 : 1 C : H stoichiometrically. At room temperature gravimetric density is in the range of 3–4 wt% [50]. Because of weak interactions between molecular hydrogen and graphite/graphene several ways of improving binding, gravimetric and volumetric storage capacities have been investigated. One route included chemical incorporation of alkali atoms (Li, Na, K). It has been found that each Li atom adsorbed on graphene and nanostructured graphene is capable of adsorbing up to four hydrogen molecules and as such the gravimetric density increases to about 10 wt%. On the basis of the density functional theory (DFT) it has been calculated that Ca atoms adsorbed on graphene and fullerenes can obtain about 8.4 wt% and be recycled at room temperatures [51]. Using DFT calculations a hydrogen storage capacity of 5.13 wt% on Al-doped graphene (one Al atom replaces one C atom) is predicted at 300 K and 0.1 Gpa with an adsorption energy E_b −0.260 eV/H_2. This is close to the target specified by US DOE with a storage capacity of 6 wt% and a binding energy of −0.2 to −0.4 eV/H_2 at ambient temperature and modest pressure for commercial applications. It was found that Al can alter the electronic structure of the graphene layer and hydrogen molecules. It is believed that the uptake capacity of hydrogen would increase if more metal atoms are adsorbed on the surface of graphene and the binding energies between metal atoms and the graphene nanostructure would

be strengthened if more charge is transferred between them [51, 52]. DFT simulations showed that by binding Ti atoms to four hydrogen molecules if attached to both graphene sides, gravimetric capacities of above 7 wt% can be obtained. By incorporating Pd atoms into graphene an increase of gravimetric densities at 30 bar and room temperature has increased from 0.6 to 2.5 wt%. An interesting simulation concept to control hydrogen storage with changes of graphene curvature has been explored. "When needed, hydrogen can be forced to desorb by changing the convexities into concavities". Because this configuration is unstable, hydrogen will spontaneously desorb. Because of variation of hydrogen binding energy, chemisorption is the favourable process on a convex whereas hydrogen release is favourable on concave sites of graphene sites. On the basis of the simulations, a multilayered graphene storage system has been suggested, which may lead to a hydrogen system controlling changes of curvature for the uptake and release of hydrogen [50] (Figure 7.13).

Investigated hydrogen physisorption storage behaviour demonstrated on hierarchical graphene-based material, fabricated using a vacuum-based, low-temperature heating process followed by inert gas-protected thermal treatment and composed of micropores of about 0.8 nm, mesopores of about 4 nm and macropores above 50 nm, with BET surface area of up to 1305 $m^2\,g^{-1}$, has shown a significantly enhanced capacity of more than 4.0 wt% [53]. It is expected that for practical applications, the hydrogen storage capacity for hierarchical graphene material could further be improved by metal doping, surface functionalization and edge-site tailoring. Experimental investigations on thermally exfoliated graphene (TEG) indicated that hydrogen uptake capacity increases linearly with the surface area of about 0.5 wt% H_2 per 500 mg g^{-1} SSA at 77 K and 1 bar. Further improvement in the hydrogen uptake was obtained by organic functionalization and crosslinking of TEG. Functionalized and crosslinked TEG (f-TEG) showed enhanced hydrogen uptake capacities compared with the original TEG (hydrogen

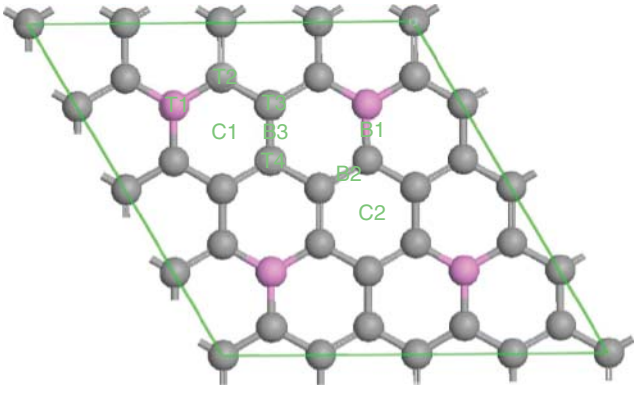

Figure 7.13 Nine different adsorption sites on Al-doped graphene. The grey and pink balls are, respectively, C and Al atoms [52].

uptake per unit surface area of f-TEG was about 1.9 wt% per 500 $m^2 g^{-1}$ at 77 K and 2 bar) [54].

MOFs (also known as coordination frameworks, coordination network materials or coordination polymers) are a class of physical storage materials that have been researched extensively for hydrogen storage purposes in recent years, with very high specific surface of 1000–6000 $m^2 g^{-1}$ [19] and densities down to 0.21 g cm^{-3}. They could be considered as synthetic analogues of zeolitic materials, usually with a three-dimensional framework. MOFs consist of inorganic clusters that are connected through strong bonds via organic linkers. The frameworks of MOFs are interconnected allowing an ordered network of channels or pores. The porosity of MOFs allows gas storage of small molecules, for example, CO_2, CH_4 and H_2. Gas can be captured and released from the pores of these structures and this process is reversible. MOFs became candidates for hydrogen storage materials since 2003, when MOF-5 consisting of an inorganic composition $Zn_4O(BDC)_3$ (BDC is 1,4-benzenedicarboxylate) with a cubic three-dimensional extended porous structure was synthesized. Such MOF-5 was able to absorb hydrogen up to 4.5 wt% at 78 K and 1 wt% at room temperature and 20 bar [55]. Hydrogen uptake has been measured on seven MOF compounds at cryogenic temperature and the maximum excess hydrogen densities found was in the range from 2.0 to 7.5 wt%. The maximum values have been obtained for MOF-177 with 7.5 wt% and IRMOF-20 with 6.7 wt%, with high volumetric densities, 32 and 34 g l^{-1}, respectively. A linear correlation between surface area of MOFs under investigation and hydrogen saturation uptake has been observed [56]. The following hydrogen gravimetric capacities and respective SSA at 77 K have been experimentally determined on selected MOFs. MOF-5 indicates 4.5 wt% (2000 $m^2 g^{-1}$), MOF-177 7.5 wt%, IRMOF-6 4.8 wt% at 50 bar (3300 $m^2 g^{-1}$), IRMOF-11 3.5 wt% at 35 bar (2340 $m^2 g^{-1}$), IRMOF-20 6.7 wt%, CU_2(QPTC) 6.06 wt% at 20 bar (2932 $m^2 g^{-1}$), HKUST-1 3.6 wt% at 10 bar (1958 $m^2 g^{-1}$), MIL-101 6.1 (5550 $m^2 g^{-1}$) [34]. Figures 7.14 and 7.15 depict gravimetric and volumetric densities , respectively, for selected MOFs [56].

High gravimetric hydrogen uptake takes place at cryogenic temperatures (77 K) and at room temperature it decreases to about 1 wt% [55]. It has been suggested that hydrogen binding energy of 15 kJ mol^{-1} at room temperature for porous materials be considered as potential hydrogen storage medium. It has been suggested that in order to deliver hydrogen in an effective way, the hydrogen enthalpy should be in a range of 22–25 kJ mol^{-1} at room temperature and pressures in a range of 30–1.5 bar [34]. Several strategies have been investigated to increase the enthalpy by modification of the internal nanostructure. They include metal sites exposing for hydrogen binding, doping MOFs with metal ions, impregnation involving the insertion of another framework or non-volatile guest, hydrogen spillover involving the dissociation step of hydrogen onto the metal surface, catenation occurring when two separate MOF frameworks self-assemble within each other, and are summarized by Reardon *et al.* [34]. Structure analysis and gas sorption studies on a subfamily of MOFs, a nanotubular MOFs, have been investigated [57]. Explorations on PCN-19 (porous coordination network (PCN)

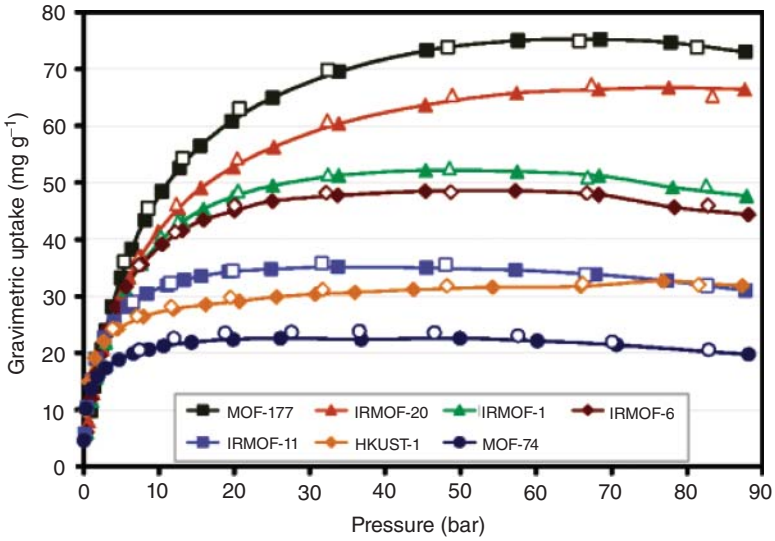

Figure 7.14 High-pressure isotherms for activated materials at 77 K in gravimetric units representing surface excess adsorption. Filled markers represent adsorption; open markers represent desorption [56].

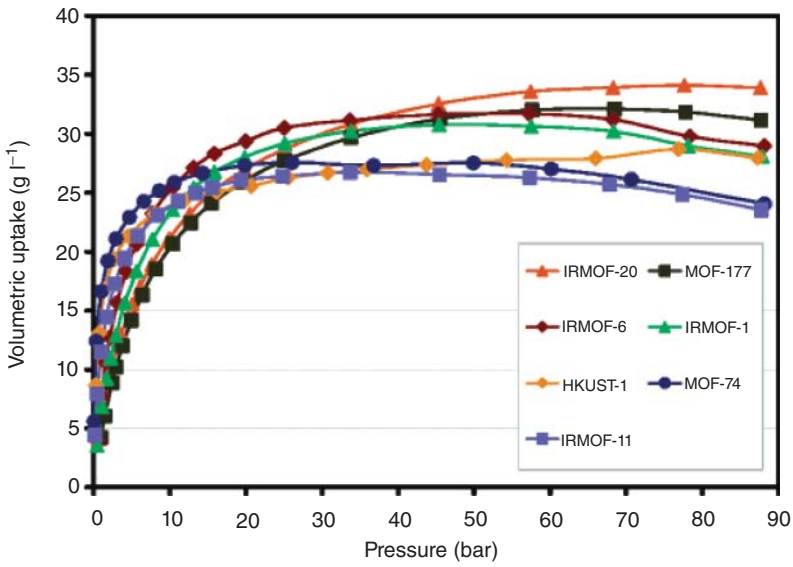

Figure 7.15 High-pressure isotherms for activated materials measured at 77 K in volumetric units, [56].

at 50 °C has shown that it can absorb 0.95 wt% (excess) at 77 K and 760 Torr. With increasing pressure to 48 bar, the excess gravimetric hydrogen uptake of PCN-19 reached 1.67 wt% at 77 K, while the absolute gravimetric hydrogen adsorption capacity achieved is 2.20 wt%. These values are lower than those of MOFs, which can be attributed to the much lower surface area of PCN-19 compared to MOFs. Recently, COFs (where the organic structural building units are held together by strong covalent bonds, for example, C–C, C–O, B–O and Si–C) have been found to be promising candidates for hydrogen storage because of their low density and ultrahigh porosity. Theoretical studies on prototypical COFs using Grand Canonical Monte Carlo (GCMC) simulation predicted that three-dimensional COFs are the most promising candidates for practical hydrogen storage. It has been demonstrated that the synthesis of ordered COFs is possible and that predesigned structures and properties can be achieved by selection of the building elements and conditions during preparation [58]. The highest predicted excess hydrogen uptakes at 77 K are 10.0 wt% for COF-105 at 8 MPa and 10.0 wt% for COF-108 at 10 MPa [59]. With this value COFs are much better than representative MOFs with highest measured hydrogen uptake of 7.5 wt% for MOF-177 [56]. On the basis of the total adsorption isotherms it is assumed that COF-108 may be able to store up to 18.9 wt% of hydrogen at 77 K and 10 MPa, followed by COF-105 with 18.3 wt%, COF-103 with 11.3 wt%, COF-102 with 10.6 wt%, COF-5 with 5.5 wt% and COF-1 with 3.8 wt% [59]. The maximum volumetric hydrogen uptake is 49.9 g l^{-1} for COF-102, 49.8 g l^{-1} for COF-103, 39.9 g l^{-1} for COF-108, 39.5 g l^{-1} for COF-105, 36.1 g l^{-1} for COF-1 and 33.8 g l^{-1} for COF-5. To sum up, it seems that the best COFs for hydrogen storage are COF-105 and COF-108, giving the highest values reported for associative hydrogen storage of any material [59]. Interesting studies on integrating bonding features of MOFs and COFs were carried out by Wu *et al.* [60] who assumed that such a combination could offer perfect opportunities for the development of new porous materials dubbed 'MOCOFs', in which the coordinating bonds of MOFs and covalent bonds of COFs could confer unique advantages in hybrid materials. Hydrogen adsorption measurements showed that BIF-9-Li can adsorb 1.23 wt% (volumetric uptake of 9.23 kg m^{-3}) at 77 K and 1 bar, whereas BIF-9-Cu reached 1.06 wt% (volumetric uptake 8.58 kg m^{-3}) under similar conditions. Also, polymers have been investigated and optimized for gas storage possibilities. The suited included among others polyacetylene, $(C_2H_2)_n$, polyaniline (PANI), polypyrrole (PPY), polyurea (P-Urea) and polyamide amine (PAMAM), polystyrene (PS) and polymers of intrinsic microporosity (PIMs) [34].

7.5.2
Chemical Storage – Overview

In chemical storage, the hydrogen is chemically bound in a compound. Thus, the loading and unloading of hydrogen (uptake-release process) involves chemisorption steps before the absorption of hydrogen in the bulk and the formation of chemical bonds. As a result, in chemical storage hydrogen is relatively strongly

bound and many of the challenges in using such materials are related to the thermodynamics and kinetics of dehydrogenation. Solid-metal hydrogen compounds can be formed due to the reaction between hydrogen and metals, intermetallic compounds and alloys. Metal hydrides are formed by metals and alloys that can reversibly store (absorb) large amounts of hydrogen, simultaneously releasing heat during the absorption process. Conversely, hydrogen is released (desorbed) when heat is delivered to the compound. This process can be described by the following equation:

$$\mathrm{Me} + \frac{x}{2}\mathrm{H}_2 \leftrightarrow \mathrm{MeH}_x$$

Metal hydrides are important energy storage materials. They are still extensively investigated for onboard applications. Metal hydrides can be used not only as a potential storage hydrogen materials, such as, for example MgH_2, but it can also serve as the precursors for the production of future complex hydrides. For example, $LiAlH_4$ can be produced on a large scale by the reaction of LiH with $AlCl_3$ dispersed in the solvent or by milling AlH_3 with NaH [61, 62]. There is a wide spectrum of metal hydride applications in industry. They are used for hydrogen storage in stationary and mobile applications, in electrochemistry (battery, catalysts), in hydrogen processing for the purpose of separation from mixed gas streams [63], purification, separation of isotopes, compression and gettering (e.g. inert gas purification or vacuum maintenance). Metal hydrides are also used for thermal applications, such as heat storage, heat pumping, refrigeration or in materials processing, such as, magnet processing.

Light metals such as Li, Na, Mg, Al, B, Be form a wide variety of metal hydrogen compounds (light metal hydrides). They are especially interesting due to their light weight and the ability to accommodate one or more hydrogen per metal atom. Despite high hydrogen storage densities they have high desorption temperatures, poor kinetics and non-reversible thermodynamics. Simple binary metal hydrides can be divided into three types based on the nature of the metal–hydrogen bonds: ionic or saline hydrides, covalent metal hydrides and metallic hydrides [64]. Ionic or saline hydrides include binary hydrides of all alkali and alkaline earth metals from calcium to barium and there hydrogen exists as negatively charged ion H^-. Covalent metal hydrides are composed of hydrogen and non-metals, having in general low melting or boiling points. Most covalent hydrides are in liquid or gas form at room temperature, and in solid form they are usually unstable. Examples include silanes (SiH_4), aluminium borohydride $Al(BH_4)_3$, hydrocarbons. Hydrocarbons containing hydrogen include aromatic hydrocarbons such as cyclohexane, methylcyclohexane, decaline and heteroaromatics, such as carbazole or benzoquinone. Hydrogen storage capacities of such hydrocarbons are in the range of 6–8 wt% [4]. Metallic hydrides where hydrogen acts as a metal and built metallic bonds are formed by transition metals include rare earth and actinides, for example, TiH_2 or ThH_2. Intermetallic compounds are formed by alloying a metal, usually a rare earth or alkaline earth metal with a high affinity to hydrogen (A), typically forming a stable binary hydride with another element (B), which is often a transition metal with a low affinity to hydrogen and

Table 7.4 Metallic hydrides of intermetallic compounds including the prototype and the structure.

Intermetallic compound	Prototype	Hydrides	Structure
AB_5	$LaNi_5$	$LaNiH_6$	Haucke phases, hexagonal
AB_2	ZrV_2, $ZrMn_2$, $TiMn_2$	$ZrV_2H_{5.5}$	Laves phases, hexagonal or cubic
AB	TiFe, ZrNi	$Ho_6Fe_{23}H_{12}$	Cubic, CsCl or CrB type
A_2B	Mg_2Ni, Ti_2Ni	Mg_2NiH_4	Cubic, $MoSi_2$ or Ti_2Ni type
AB_3	$CeNi_3$, Yfe_3	$CeNi_3H_4$	Hexagonal, $PuNi_3$ type
A_2B_7	Y_2Ni_7, Th_2Fe_7	$Y_2Ni_7H_4$	Hexagonal, Ce_2Ni_7 type
A_6B_{23}	Y_6Fe_{23}	$Y_2Ni_7H_3$	Cubic, Th_6Mn_{23} type

Source: Reprinted by permission of Wiley VCH [4].

forming only unstable hydrides. According to their stoichiometry, intermetallic compounds can thus be classified as depicted in Table 7.4 [65].

A careful choice of A and B element can provide a source of hydrogen across a wide range of pressures. The classical example of an ammonia borane (AB_5) hydride is $LaNi_5$. The absorption–desorption of hydrogen on $LaNi_5$ can be described by the following equation:

$$LaNi_5 + 3H_2 \leftrightarrow LaNi_5H_6; \quad \Delta H = -31\,\text{kJ}\,\text{mol}^{-1}$$

In general, in addition to nickel and boron, AB_5 can be composed of elements such as Co, Al, Mn, Fe, Sn, Si, Ti and many others. Modern alloys of this family are mainly based on a lanthanide mixture with different metals such as Ce + La + La + Nd + Pr (element A) and Mn + Co + Al + Fe + … (element B). In general, AB_5 compounds do not show high gravimetric hydrogen capacities, but they are easy to activate and are tolerant to small amounts of oxygen and water in hydrogen. The stability of metal hydrides is usually presented in the form of van't Hoff plot. It can be seen that isothermal pressure–composition hysteresis is located in the lower part of the van't Hoff plot [66]. Mechanically grinding a small amount of palladium or platinum with AB_5 type intermetallic hydrogen storage alloys significantly improved the hydrogen absorption and desorption performances of the alloys [67] (Figure 7.16).

The AB_5 family represents a group of 330 compounds, A_2B 103 compounds and AB 156 compounds [68]. The AB_2 group of intermetallics represents the widest range of possible materials with nearly 509 compounds. These AB_2 alloys are more difficult to activate than other intermetallic hydrides, but once activated they show good hydrogenation–dehydrogenation kinetics. A-elements can be from the IVA group (such as Ti, Hf, Zr) and/or can include rare earth metals with atomic number 57–71. B-elements are represented by a large variety of transition and non-transition metals. Gravimetric hydrogen capacities are typically slightly higher than those of AB_5. Some examples include compounds in the range from 1.5 wt% ($ZrFe_{1.5}Cr_{0.5}$) to 2.43 wt% ($TiCr_{1.8}$). Details on intermetallic compounds and their hydrogen storage properties including specific elements, alloys and engineering

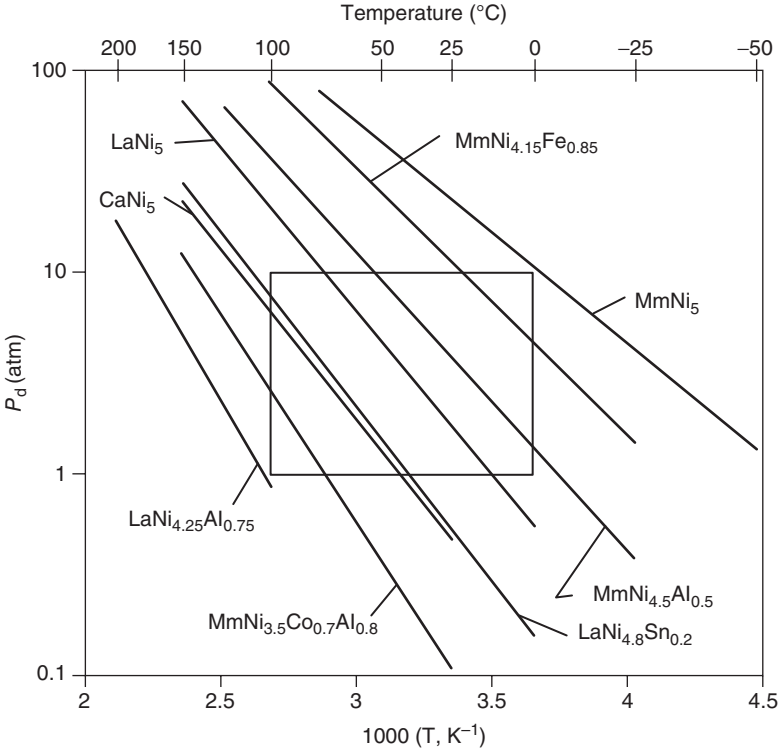

Figure 7.16 van't Hoff plots of AB_5 metal hydrides. (Reprinted by permission of Wiley VCH [4].)

properties are available in the databases by the International Energy Agency (IEA), supported by the US DOE and the Sandia National Laboratories (SNLs) [68, 69].

An illustration of the metal hydride family tree is shown in Figure 7.17 [66].

Complex chemical hydrides show several opportunities over the binaries in many respects. Borohydrides, aluminohydrides (alanates) and amides are close to meeting US DOE targets in terms of storage capacity, reversibility, cost and toxicity [32]. A good overview of the properties of the major hydrogen storage classes, including conventional metal hydrides (e.g. $LaNiH_6$), complex hydrides (e.g. $NaAlH_4$), chemical hydrides (e.g. NH_3BH_3), sorbent systems (e.g. MOF-5), with trends for technical challenges, is given by Yang *et al.* [70]. A review of lightweight complex hydrides [71] presents a lot of detailed information of these materials from synthesis, crystal structure, thermodynamics and kinetics of hydrogenation–dehydrogenation processes to hydrogen storage capacities. Materials that are described are, among others, alanates, borohydrides, amide–imide systems, amineboranes and alanes. It has been highlighted that hydrogen storage in such kind of materials is an emerging and promising field of investigations for renewable energy systems. It seems that alanates, especially $NaAlH_4$, belong to complex hydrides followed by borohydrides and amide

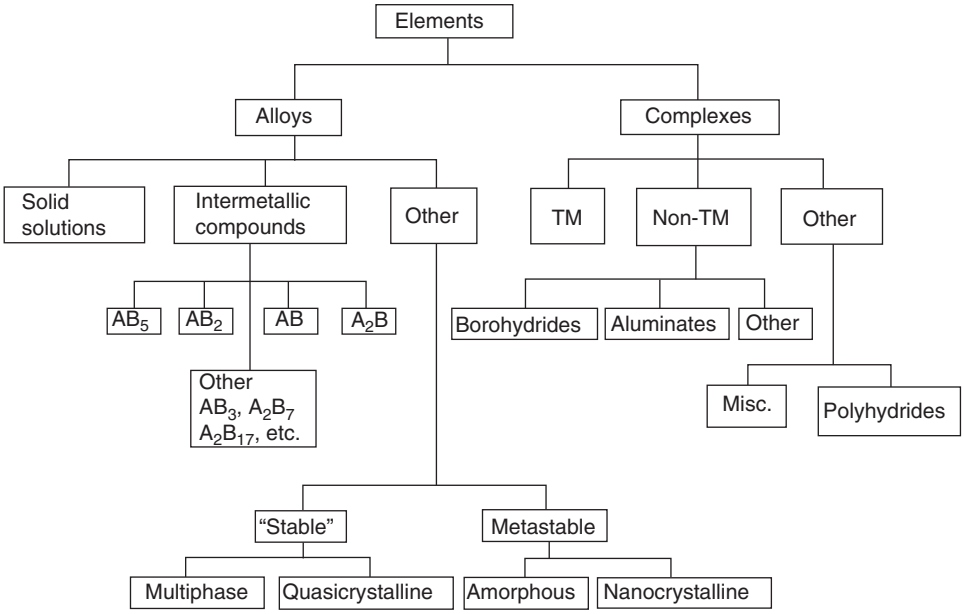

Figure 7.17 Hydriding alloys and complexes family tree; TMs stands for transition metals, non-TMs stands for non-transition metals [4].

systems. Sodium borohydride, $NaBH_4$, has been very intensively investigated as a potential material for hydrogen storage with a theoretical gravimetric capacity of 7.5 wt% (material level). After numerous efforts in both research and development, US DOE recommended a No–Go for sodium borohydride for onboard automotive hydrogen storage, suggesting work on AB, another promising hydrogen storage material [72, 73]. The reasons for the recommendation focused mainly on storage capacity versus DOE targets, formation of sodium metaborane, $NaBO_2$ by-product and, as a consequence, its recycling and, last but not the least, high costs. In response to this recommendation, researchers have continued their interest in $NaBH_4$, mainly focusing on utilizing its solid form rather than aqueous solution. Such systems show improved hydrogen storage capacities compared to the traditional way based on catalytic hydrolysis. An extensive summary of the research including noble and non-noble metal catalysts and evaluation of several alternative designs for storage system was published in 2011 [74].

7.5.2.1 Solid-State Hydrogen Storage System Coupled with Electrolyser

Magnesium hydride MgH_2 (6.7 wt%) as a potential candidate for hydrogen storage has gained a lot of attention. The world's first unit, coupling industrial-scale electrolyser with 100 kg solid state hydrogen storage unit (energy content of 3.3 MWh), based of magnesium hydride MgH_2 as a hydrogen source, has been successfully demonstrated by the French company McPhy in September 2013.

(a) (b)

Figure 7.18 (a) McPhy magnesium hydride disk containing 600 l of hydrogen and (b) compacted MgH_2 disks. (Reprinted by kind permission of McPhy Energy, Grenoble, France.)

The demonstration was the result of the first phase of the French PUSHY project and is the first in the commercial range. The main reason for using magnesium hydride is based on several benefits, such as totally reversible hydrogen storage, high cycling stability, energy, costs and maintenance savings when compared to existing hydrogen storage solutions (about 10–25% of the energy content of the gas is used for compression), significant reduction in safety risk when compared to compressed or cryogenic storage and, last but not the least, low unloading pressure of 2 bar at PEM fuel cell or hydrogen gas turbine inlet. McPhy magnesium hydride is manufactured in the form of disc; one contains 600 l of hydrogen (Figure 7.18). When put in containers, solid storage can contain up to hundreds of kilograms or even several tons by multiplying the number of containers.

Four kilograms of hydrogen storage prototypes were validated in 2011. At present McPhy is capable of providing (high energy system – HES, based on McPhy phase change material – PCM, as a heat storage to increase the efficiency of the system, mainly for energy applications) adiabatic storage of 25 kg of hydrogen (275 Nm^3, equivalent of 830 kWh) and HDS (high density system, technology without PCM, mainly for industrial use enabling storage of more hydrogen in the same volume when compared to HES) non-adiabatic storage of 100 kg of hydrogen (1100 Nm^3, equivalent of 3.3 MWh). McPhy's solid-state storage based on MgH_2 has been coupled with McPhy's alkaline electrolysers with scalable hydrogen generation capacities from 10 to X000 $Nm^3\,h^{-1}$ and the characteristics are shown in Table 7.5.

Examples of a small electrolyser (12 $Nm^3\,h^{-1}$) and McLyzer 60 (McPhy aggregates hydrogen production units to create larger-output hydrogen production units of 60 $Nm^3\,h^{-1}$ at 12 bar) allowing optimization of costs and energy efficiency are presented (Figures 7.19 and 7.20).

McPhy's flexible hydrogen generator comprising alkaline electrolyser and hydrogen storage, which has been demonstrated in 2013 is shown in Figure 7.21. 'While such systems enable the supply of onsite hydrogen for industry, they also mark a world premiere in the transition to renewable energies, enabling approaches such as "power-to-gas" and hydrogen mobility to become both

Table 7.5 Characteristics of large- and small-/medium-scale electrolysers.

Characteristics	Large-scale electrolysers	Small- and medium-scale electrolysers
Working pressure (bar)	Up to 60	Up to 12
Hydrogen production	Scalable units up to X000 $Nm^3 h^{-1}$ • Atmospheric pressure, 500 $Nm^3 h^{-1}$ to 2 MW module • Up to 60 bar, 100 $Nm^3 h^{-1}$ to 500 kW module • Multi MW engineered solutions	Scalable units up to X00 $Nm^3 h^{-1}$ • Baby PIEL (0.4 $Nm^3 h^{-1}$) • Standard pressure @ 3 bar to 1–12 $Nm^3 h^{-1}$ • Medium pressure @ 8 bar to 3–24 $Nm^3 h^{-1}$ • 60 $Nm^3 h^{-1}$, 20 ft container @ 10 bar
Gas purity (before purification)	99.9% water saturated	99.5% water saturated
Electric energy consumption (kWh Nm^{-3} H_2)	4.5	5.2
Max water consumption (l Nm^{-3} H_2)	0.8	0.8

Source: McPhy Energy, Grenoble, France.

Figure 7.19 An example of a small electrolyser. (Reprinted by kind permission of McPhy Energy, Grenoble, France.)

technical and commercial realities' – McPhy News, La Motte-Fanjas, France, 27 September 2013.

Other projects to demonstrate combination of solid-state hydrogen storage systems and electrolysis are as follows: (i) INGRID 2012–2016 – hydrogen generation by electrolysis from renewable electricity, storage in solid form and then reusage to create electricity via a fuel cell or to supply the hydrogen market and (ii)

Figure 7.20 McLyzer 60, McPhy aggregates hydrogen production skid units to create larger-output hydrogen production units of 60 $Nm^3 h^{-1}$ at 12 bar) allowing optimization of costs and energy efficiency. (Reprinted by kind permission of McPhy Energy, Grenoble, France.)

Figure 7.21 McPhy's own flexible hydrogen generator. (Reprinted by kind permission of McPhy Energy, Grenoble, France.)

HyCube – using a platform of a 400 kW photovoltaic farm and a hydrogen energy storage chain, comprising an electrolyser, hydrogen storage and a fuel cell.

7.6 Summary

Three main approaches for hydrogen storage can be distinguished: compressed gas hydrogen at pressures up to 700 bar at ambient temperature, cryogenic storage in the form of liquid hydrogen and hydrogen stored in a solid-state form. Each way as presented above has its own merits and demerits. Storage under high pressure results in high installation space requirements; hydrogen-absorbent materials are too heavy and result in complex energy and heat management. Liquid hydrogen storage reaches the highest gravimetric and volumetric storage densities. Hydrogen in order to be further utilized or integrated with,

for example, renewable energy sources, shall be stored in a way that is the most appropriate for a given application. For different integration scenarios several key components shall be taken into account, which are described in detail in Chapter 8. *Integration of water electrolysis with renewable energy sources*.

Table 7.6 [27] compares performance and cost metrics for compressed, cryo-compressed hydrogen liquid, compressed (300 and 700 bar) and cryo-compressed hydrogen and porous material (MOF-177) as a reference.

Table 7.6 Performance and cost comparison for liquid, compressed, cryo-compressed hydrogen, MOF-177 versus DOE 2010, 2015 and ultimate targets [27].

Performance and cost metric	Units	CH_2 350-T4	CH_2 700-T4	LH_2	CcH_2	MOF-177	2010 Targets	2015 Targets	Ultimate targets
Tank	—	1-Tank	1-Tank	—	—	—	—	—	—
Usable storage capacity (nominal)	kg H_2	5.6	5.6	5.6	5.6	5.6	—	—	—
Usable storage capacity (maximum)	kg H_2	5.6	5.6	5.6	6.6	5.6	—	—	—
System gravimetric capacity	wt%	5.5	5.2	5.6	5.5–9.2	4.0	4.5	5.5	7.5
System volumetric capacity	kg H_2 m^{-3}	17.6	26.3	23.5	41.8–44.7	34.6	28	40	70
Storage system cost	\$ kWh^{-1}	15.5	18.9	TBD	12	18	4	2	TBD
Fuel cost	\$ gge^{-1}	4.2	4.3	TBD	4.8	4.6	2–3	2–3	2–3
Cycle life (1/4 tank to full)	Cycles	NA	NA	NA	5500	5500	1000	1500	1500
Minimum delivery pressure FC/ICE	atm	4	4	4	3–4	4	4/35	4/35	3/35
System fill rate	kg H_2 min^{-1}	1.5–2	1.5–2	1.5–2	1.5–2	1.5–2	1.2	1.5	2.0
Minimum dormancy (full tank)	W-d	NA	NA	2	4–30	2.8	—	—	—
H_2 loss rate (maximum)	g h^{-1} kg^{-1} H_2	NA	NA	8	0.2–1.6	0.9	0.1	0.05	0.05
WTW efficiency	%	56.5	54.2	22.3	41.1	41.1	60	60	60
GHG emissions (CO_2 equivalent)	kg kg^{-1} H_2	14.0	14.8	TBD	19.7	19.7	—	—	—
Ownership cost	\$/mile	0.13	0.14	TBD	0.12	0.15	—	—	—

References

1. Marnellos, G.E., Athanasiou, C., Makridis, S.S., and Kikkinides, E.S. (2008) Integration of hydrogen energy technologies in autonomous power systems, in *Hydrogen-based Autonomous Power Systems. Techno-Economic Analysis of the Integration of Hydrogen in Autonomous Power Systems* (eds E.I. Zoulias and N. Lymberopoulos [Buchverf.]), Springer-Verlag, London, ISBN: 978-1-84800-246-3.
2. Zuttel, A. (2004) Hydrogen storage methods. *Naturwissenschaften*, **91**, 157–172.
3. Winter, C.-J. (2009) Hydrogen energy – Abundant, efficient, clean: a debate over the energy-system-of-change. *Int. J. Hydrogen Energy*, **34**, S1–S52.
4. Godula-Jopek, A., Jehle, W., and Wellnitz, J. (2012) *Hydrogen Storage Technologies. New Materials, Transport and Infrastructure*, Wiley-VCH Verlag GmbH & Co. KGaA, Weinheim, ISBN: 978-3-527-32683-9.
5. Anders, S. (2007) Thermal loading cases of hydrogen high pressure storage cylinders. International Conference on Hydrogen Safety, San Sebastian, Spain, September 11–13, 2007.
6. Atkins, P.W. (1998) *Physical Chemistry*, 6th edn, Oxford University Press.
7. Sherif, S.A., Barbir, F., and Veziroglu, T.N. (2005) Wind energy and the hydrogen economy – review of the technology. *Solar Energy*, **78**, 647–660.
8. Wackerl, J., Streibel, M., Liebscher, A., and Stolten, D. (2013) Geological storage for the transition from natural to hydrogen gas, in *Transition to Renewable Energy Systems* (eds D. Stolten and V. Scherer [Buchverf.]), Wiley-VCH Verlag GmbH & Co. KGaA, Weinheim, ISBN: 978-3-527-33239-7.
9. US Department of Energy (2012) *http://www1.eere.energy.gov/hydrogenandfuelcells/mypp/pdfs/storage.pdf* (accessed 5 September 2014).
10. Read, C., Thomas, G., Ordaz, G., and Satyapal, S. (2007) U.S. department of energy's system targets for on-board vehicular hydrogen storage. *Mater. Matter*, **2** (2), 3.
11. Krishna, R., Titus, E., Maryam, S., Olena, O., Sivakumar, R., Jose, G., Rajkumar, A., Sousa, J.M.G., Ferreira, A.L.C., and Campos Gil, J. (2012) Hydrogen storage for energy application, in *Hydrogen Storage* (ed. J. Liu [Buchverf.]), IntachISBN: 978-953-51-0731-6.
12. Atrey, M.D. (1998) Thermodynamic analysis of Collins helium liquefaction cycle. *Cryogenics*, **38**, 1199–1206.
13. Aceves, S.M., Petitpas, G., Espinosa-Loza, F., Matthews, M.J., and Ledesma-Orozco, E. (2013) Safe, long range, inexpensive and rapidly refuelable hydrogen vehicles with cryogenic pressure vessels. *Int. J. Hydrogen Energy*, **38**, 2480–2489.
14. Leon, A. (2008) Hydrogen storage, in *Hydrogen Technology. Mobile and Portable Applications*, Springer-Verlag, Berlin, Heilderberg, ISBN: 978-3-540-79027-3.
15. Tietze, V. and Luhr, S. (2013) Near-surface bulk storage of hydrogen, in *Transition to Renewable Energy Systems* (eds D. Stolten and V. Sherer [Buchverf.]), Wiley-VCH GmbH & Co. KGaA, Weinheim.
16. Larsen, H., Feidenhans, R., and Sonderberg Petersen, L. (2004) Hydrogen and its Competitors. Report 3, Risø National Laboratory, November 2004.
17. Klell, M. (2010) Storage of hydrogen in the pure form, in *Handbook of Hydrogen Storage. New Materials for Future Energy Storage* (ed. M. Hirscher [Buchverf.]), Wiley-VCH Verlag GmbH & Co.KGaA, Weinheim, ISBN: 987-3-527-32273-2.
18. The Linde Group (2011) Shell Opens Hydrogen Service Station with Linde Technology in Germany, *http://www.the-linde-group.com/en/news_and_media/press_releases/news_2011_06_20.html* (accessed 5 September 2014).
19. Benard, P. and Chahine, R. (2007) Storage of hydrogen by physisorption on carbon and nanostructured materials. *Scr. Mater.*, **56**, 803–808.
20. Anders, S. (2007) Thermal loading cases of hydrogen high pressure storage

cylinders. International Conference on Hydrogen Safety, San Sebastian, Spain, September 2007.

21. Hu, J., Sundararaman, S., Chandrashekhara, K., and Chernicoff, W. (2007) Analysis of composite hydrogen storage cylinders under transient thermal loads. International Conference on Hydrogen Safety, San Sebastian, Spain, September 2007.
22. Kaynak, I.H. and Akcay, I. (2005) Analysis of multilayered composite cylinders under thermal loading. *J. Reinf. Plast. Compos.*, **24**, 1169–1179.
23. Hu, J., Chen, J., Sundararaman, S., Chandrashekhara, K., and Chernicoff, W. (2008) Analysis of composite hydrogen storage cylinders subjected to localized flame impingements. *Int. J. Hydrogen Energy.*, **33**, 2738–2746.
24. Lee, Z.Y., Chen, C.K., and Hung, C.I. (2001) Transient thermal stress analysis of multilayered hollow cylinder. *Acta Mech.*, **151**, 75–88.
25. Jacquemin, F. and Vautri, A. (2004) Analytical calculation of the transient thermoelastic stresses in thick walled composite pipes. *J. Compos. Mater.*, **38**, 1733–1751.
26. Ahluwalia, R.K., Hua, T.Q., Peng, J.-K., Lasher, S., McKenney, K., and Sinha, J. (2010) Technical assessment of cryo-compressed hydrogen storage tank systems for automotive applications. *Int. J. Hydrogen Energy*, **35**, 4171–4184.
27. R.K. Ahluwalia, J.-K. Peng, T.Q. Hua (2011) Cryo-compressed hydrogen storage: performance and cost review. Compressed and Cryo-Compressed Hydrogen Storage Workshop, Crystal City Marriott, Arlington, VA, February 2011.
28. Kunze, K. (2012) Performance of a cryo-compressed hydrogen storage. WHEC, Toronto, Canada, 2012.
29. Kircher, O., Greim, G., Burtscher, J., and Brunner, T. (2011) Validation of cryo-compressed hydrogen storage(CCH2) – a probabilistic approach. International Conference on Hydrogen Safety, San Francisco, CA, 2011.
30. Kampitsch, M. (2013) BMW – Status Foerderprojekte, NIP VOLLVERSAMMLUNG, 17.06.2013.
31. Kunze, K. (2011) *Cryo-Compressed H2-Storage – Recent Advances and Experimental Results*, FCHE, Washington, DC, February 2011.
32. Mandal, T.K. and Gregory, D.H. (2009) Hydrogen storage materials: present scenarios and future directions. *Annu. Rep. Prog. Chem. Sect. A*, **105**, 21–54.
33. Zuttel, A., Wenger, P., Sudan, P., Mauron, P., and Orimo, S.-I. (2004) Hydrogen density in nanostructured carbon, metals and complex materials. *Mater. Sci. Eng.*, **B108**, 9–18.
34. Reardon, H., Hanlon, J.M., Hughes, R.W., Godula-Jopek, A., Mandal, T.K., and Gregory, D.H. (2012) Emerging concepts in solid-state hydrogen storage: the role of nanomaterials design. *Energy Environ. Sci.*, **5**, 5951–5979.
35. Dornheim, M. (2010) Tailoring reaction enthalpies of hydrides, in *Handbook of Hydrogen Storage. New Materials for Future Energy Storage* (ed. M. Hirscher [Buchverf.]), Wiley-VCH Verlag GmbH & Co. KGkA, Weinheim, ISBN: 978-3-527-32273-2.
36. Iniguez, J. (2008) Modelling of carbon-based materials for hydrogen storage, in *Solid-State Hydrogen Storage, Materials and Chemistry* (ed. G. Walker [Buchverf.]), Woodhead Publishing Limited, Cambridge.
37. Panella, B. and Hirscher, M. (2010) Physisorption in porous materials, in *Handbook of Hydrogen Storage. New Materials for Future Energy Storage* (ed. M. Hirscher [Buchverf.]), Wiley-VCH Verlag & Co, KGaA, Weinheim, ISBN: 978-3-527-32273-2.
38. Schimmel, H.G., Kearley, G.J., Nijkamp, M.G., Visser, C.T., de Jong, K.P., and Mulder, F.M. (2003) Hydrogen adsorption in carbon nanostructures: comparison of nanotubes, fibers and coals. *Chem. Eur. J.*, **9**, 4764–4770.
39. Jurewicz, K., Frackowiak, E., and Beguin, F. (2004) Towards the mechanism of electrochemical storage in nanostructured materials. *Appl. Phys. A*, **78**, 981–987.
40. Li, Y., Zhao, D., Wang, Y., Xue, R., Shen, Z., and Li, X. (2006) The mechanism of hydrogen storage in carbon materials. *Int. J. Hydrogen Energy.*, **32**, 2513–2517.

41. Anson, A., Callejas, M.A., Benito, A.M., Maser, W.K., Izquierdo, M.T., Rubio, B., Jagiello, J., Thommes, M., Parra, J.B., and Martinez, M.T. (2004) Hydrogen adsorption studies on single wall carbon nanotubes. *Carbon*, **42** (7), 1243–1248.
42. Becher, M., Haluska, M., Hirscher, M., Quintel, A., Skakalova, V., Dettlaff-Weglikovska, U., Chen, X., Hulman, M., Choi, Y., Roth, S., Meregalli, V., Parrinello, M., Ströbel, R., Jörissen, L., Kappes, M.M., Fink, J., Züttel, A., Stepanek, I., and Bernier, P. (2003) Hydrogen storage in carbon nanotubes. *C.R. Phys.*, **4** (9), 1055–1062.
43. Fichtner, M. (2005) Nanotechnological aspects in materials for hydrogen storage. *Adv. Eng. Mater.*, **7** (6), 443–453.
44. Yamanakaa, S., Fujikane, M., Uno, M., Murakami, H., and Miura, O. (2004) Hydrogen content and desorption of carbon nano-structures. *J. Alloys Compd.*, **366** (1-2), 264–268.
45. Pradhan, B.K., Harutyunyan, A., Stojkovic, D., Zhang, P., Cole, M.W., Crespi, V., Goto, H., Fujiwara, J., and Eklund, P.C. (2002) Large cryogenic storage of hydrogen in carbon nanotubes at low pressures. *Mater. Res. Soc. Symp. Proc.*, **706**, Z10.3.1–Z10.3.6.
46. Gundiah, G., Govindaraj, A., Rajalakshmi, N., and Dhathathreyan, K.S. (2003) Hydrogen storage in carbon nanotubes and related materials. *J. Mater. Chem.*, **13**, 209–213.
47. Poirier, E., Chahine, R., Benard, P., Lafi, L., and Dorval-Douville, G. (2006) Hydrogen adsorption measurements and modeling on metal-organic frameworks and single-walled carbon nanotubes. *Langmuir*, **22** (21), 8784–8789.
48. David, E. (ed.) (2005) An overview of advanced materials for hydrogen storage. *J. Mater. Process. Technol.*, **162-163**, 169–177.
49. Pumera, M. (2011) Graphene-based nanomaterials for energy storage. *Energy Environ. Sci.*, **4**, 668–674.
50. Tozzini, V. and Pellegrini, V. (2013) Prospects for hydrogen storage in graphene. *Phys. Chem. Chem. Phys.*, **15**, 80–89. doi: 10.1039/c2cp42538f
51. Ao, Z.M. and Peeters, F.M. (2010) High-capacity hydrogen storage in Al-adsorbed graphene. *Phys. Rev. B*, **81**, 205406-1–205406-7.
52. Ao, Z.M., Jiang, Q., Zhang, R.Q., Tan, T.T., and Li, S. (2009) Al doped graphene: a promising material for hydrogen storage at room temperature. *J. Appl. Phys.*, **105**, 074307-1–074307-6.
53. Guo, C.X., Wang, Y., and Li, C.M. (2013) Hierarchical graphene-based material for over 4.0 wt. % physisorption hydrogen storage capacity. *ACS Sustainable Chem. Eng.*, **1**, 14–18.
54. Jin, Z., Lu, W., O'Neill, K.J., Parilla, P.A., Simpson, L.J., Kittrell, C., and Tour, J.M. (2011) Nano-engineered spacing in graphene sheets for hydrogen storage. *Chem. Mater.*, **23**, 923–925.
55. Rosi, N.L., Eckert, J., Eddaoudi, M., Vodak, D.T., Kim, J., O'Keeffe, M., and Yaghi, O.M. (2003) Hydrogen storage in microporous metal-organic frameworks. *Science*, **300**, 1127–1129.
56. Wong-Foy, A.G., Matzger, A.J., and Yaghi, O.M. (2006) Exceptional H2 saturation uptake in microporous metal-organic frameworks. *J. Am. Chem. Soc. Commun.*, **128**, 3494–3495.
57. Ma, S., Simmons, J.M., Yuan, D., Li, J.-R., Weng, W., Liu, D.-J., and Zhou, H.-C. (2009) A nanotubular metal-organic frameworks with permanent porosity: structure analysis and gas sorption studies. *Chem. Commun.*, 4049–4051.
58. Uribe-Romo, F.J., Hunt, J.R., Furukawa, H., Klock, C., O'Keeffe, M.l., and Yaghi, O.M. (2009) A crystalline imine-linked 3-d porous covalent organic framework. *J. Am. Chem. Soc. Commun.*, **131** (13), 4570–4571.
59. Han, S.S., Furukawa, H., Yaghi, O.M., and Goddard, W.A. III, (2008) Covalent organic frameworks as exeptional hydrogen storage materials. *J. Am. Chem., Soc. Commun.*, **130**, 11580–11581.
60. Wu, T., Zhang, J., Zhou, C., Wang, L., Bu, X.i., and Feng, P. (2009) Zeolite RHO-type net with the lightest elements. *J. Am. Chem. Soc.*, **131**, 6111–6113.
61. Eigen, N., Keller, C., Dornheim, M., Klassen, T., and Borman, R. (2007) Industrial production of light hydrides for hydrogen storage. *Scr. Mater.*, **56**, 847–851.

62. Eigen, N., Kunowsky, M., Klassen, T., and Bormann, R. (2007) Synthesis of NaAlH4-based hydrogen storage material using milling under low pressure hydrogen atmosphere. *J. Alloys Compd.*, **430** (1-2), 350–355.
63. Sheridan, J.J., Eisenberg, F.G., Greskovich, E.J., Sandrock, G.D., and Huston, E.L. (1983) Hydrogen separation from mixed gas streams using reversible metal hydrides. *J. Less-Common Met.*, **89** (2), 447–455.
64. Huot, J. (2010) Metal hydrides, in *Handbook of Hydrogen Storage. New Materials for Future Energy Storage* (ed. M. Hirscher [Buchverf.]), Wiley-VCH Verlag GmbH & Co. KGaA, Weinheim, ISBN: 978-3-527-32273-2.
65. Zuettel, A. (2004) Hydrogen storage methods. *Naturwissenschaften*, **91**, 157–172.
66. Sandrock, G. (1999) A panoramic overview of hydrogen storage alloys from a gas reaction point of view. *J. Alloys Compd.*, **293-295**, 877–888.
67. Shan, X., Payer, J.H., and Jennings, W.D. (2009) Mechanism of increased performance and durability of Pd-treated metal hydriding alloys. *Int. J. Hydrogen Energy*, **34**, 363–369.
68. Sandrock, G. and Thomas, G. (2001) The IEA/DOE/SNL on-line hydride databases. *Appl. Phys. Mater. Sci. Process.*, **2** (72), 153–155.
69. Sandia National Laboratories (2007) Hydride Information Center for Metal-Hydrogen Systems, Properties, Applications and Activities, September 2007, *http://hydrogenmaterialssearch.govtools.us/pdf/Hydride%20Databases%20Introduction%20GS%202-10-11.pdf.*
70. Yang, J., Sulik, A., Wolverton, C., and Siegel, D.J. (2010) High capacity hydrogen storage materials: attributes for automotive applications and techniques for materials discovery. *Chem. Soc. Rev.*, **39**, 656–675.
71. Jain, L.P., Jain, P., and Jain, A. (2010) Novel hydrogen storage materials: a review of lightweight complex hydrides. *J. Alloys Compd.*, **503**, 303–339.
72. Demirci, U.B., Akdim, O., and Miele, P. (2009) Ten-years effort and a no-go recommendation for sodium borohydride for on-board automotive hydrogen storage. *Int. J. Hydrogen Energy.*, **34**, 2638–2645.
73. Demirci, U.B. and Miele, P. (2009) Sodium borohydride versus ammonia borane, in hydrogen storage and direct fuel cell applications. *Energy Environ. Sci.*, **2**, 627–637.
74. Muir, S.S. and Yao, X. (2011) Progress in sodium borohydride as a hydrogen storage material: development of hydrolysis catalysts and reaction systems. *Int. J. Hydrogen Energy*, **36**, 5983–5997.

8
Hydrogen: A Storage Means for Renewable Energies

Cyril Bourasseau and Benjamin Guinot

8.1
Introduction

Issues related to climate change, environment pollution and security of energy supply have pushed several countries to reconsider their energy production means and to examine their dependence on other countries. Within this context, renewable energies (solar, wind, biomass, geothermal, etc.) can be considered as an answer to these problems. However, most renewable energy sources are intermittent by nature and the production from such sources can be difficult to forecast with great accuracy. In the first section of this chapter, we discuss how these particularities have important impacts on the operation of existing electrical networks when considering an intensive integration of renewable energies. We will also examine the different solutions to allow a higher penetration of renewable intermittent energies than it is today observed in most countries. Among them, energy storage and related storage functions will be detailed further before focusing on advantages and drawbacks of hydrogen production from electrolysis as a renewable electricity storage means.

However, intermittency and power characteristics of renewable sources impose technical and operational requirements for water electrolysis at multiple levels. It seems important to bring to the reader's attention the challenges related to the coupling of renewable sources with electrolyser systems. To do so, the second section of this chapter reviews the associated requirements and their impact on system design, power electronics and process control. Furthermore, the impact of intermittency on electrolysis system performances and reliability will be analysed in terms of produced hydrogen characteristics, efficiency and system lifetime. From this, perspectives on implementable improvements of system design and operation will be given. On the basis of selected key criteria, a qualitative comparison will be provided on the suitability of proton exchange membrane (PEM), alkaline and high-temperature steam electrolysis (HTSE) for integration with renewable sources.

In the third section of this chapter, examples of integration schemes for various applications, both off-grid and grid-connected, are proposed. To illustrate

Hydrogen Production: by Electrolysis, First Edition. Edited by Agata Godula-Jopek.
© 2015 Wiley-VCH Verlag GmbH & Co. KGaA. Published 2015 by Wiley-VCH Verlag GmbH & Co. KGaA.

these schemes, a few demonstration projects of hydrogen production by electrolysis powered by renewable energy are presented.

In the last section, the integration of electrolysis with renewable energies are analysed from a techno-economic point of view. A review of potential new markets is also discussed to highlight the role that electrolysis can play in an energy mix dominated by renewable energies. Second, we discuss why systems integrating electrolysis for energy or non-energy purposes are becoming increasingly complex and how modelling and simulation can play an important role in assessing their economic value.

8.2 Hydrogen: A Storage Means for Renewable Energies (RE)

8.2.1 Renewable Energy Sources: Characteristics and Impacts on Electrical Networks

By nature, the production of electricity from renewable energy sources is very different from the one obtained from conventional productions such as coal, nuclear or gas power plants. Most renewable energy sources (solar energy, wind energy, wave energy, etc.) are intermittent and our capacity to forecast their behaviour is limited. Furthermore, unlike conventional power plants, the scale of renewable power plants is smaller than the one of conventional power plants leading to a production essentially connected to distribution networks instead of transmission networks (decentralized production). The apparition of electrical power injection on distribution networks has important consequences on their management as they have been initially designed essentially to distribute electrical energy coming from transmission networks.

8.2.1.1 Intermittency and Limited Forecast of Renewable Production and Electrical Load

A power production is said to be intermittent when the energy source is not continuously available. Examples of intermittent electrical production are wind (onshore and offshore), tidal, photovoltaic (PV) and run-off river power plants. Figure 8.1 illustrates an example of a daily PV production from an 80 Wp module. We can see in this figure how important power variations may occur within the day.

In the common understanding, the notion of intermittency is extended to include the fact that the production is exposing unmanaged and undesired power level changes due to uncontrolled factors, essentially of meteorological nature. The ability to forecast the power production from renewable sources is very specific to the nature of the energy source. For example, tidal energy production offers probably the best chances to be perfectly predictable as the evolution of the sea level at the coast is well known. Forecast of power generation from renewable sources is an intensively investigated subject. Particularly, PV and wind

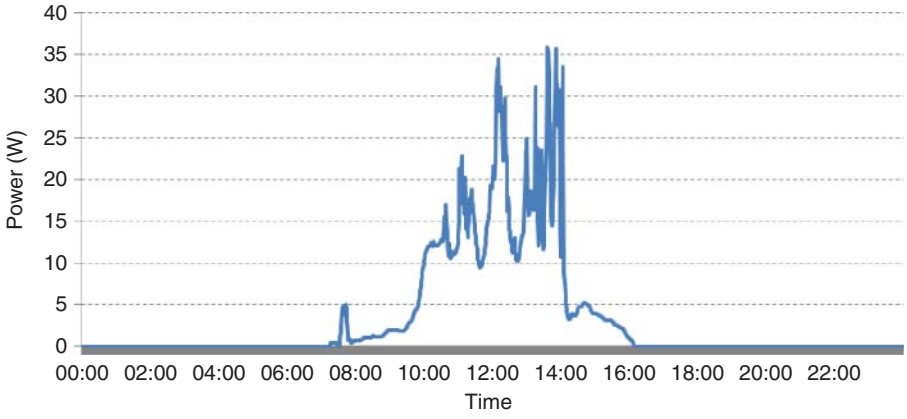

Figure 8.1 Example of a production profile of an 80 Wp PV module (7 January 2008, south of France).

power forecasting have seen an increasing interest with the intensification of these productions on electrical networks. Forecasting PV and wind productions requires an estimation of the renewable energy source that can be used by PV and wind farms (respectively, incoming solar radiation and wind speed). Different levels of forecast can be distinguished depending on the timescale at which they are necessary. For example, PV and wind production can usually be predicted from a couple of minutes up to several months ahead. These different timescales usually address different needs and are based on different forecasting methods [1, 2]. Long-term forecasting assesses the availability of the energy source on a monthly basis in order to determine a potential electrical energy production from a given power plant. This information can be particularly useful when negotiating long-term energy contracts. Forecasts of 24–48 h are suitable for power plants participating in day-ahead electricity markets. Building market offers in terms of hourly energy volume and price requires indeed a good estimation of the potential production for each hour of the coming day. Finally, short-term forecasts (several hours down to a few minutes ahead) are necessary for specific situations such as insular grids and micro-grids in which fast changes in renewable energy productions must be anticipated in order to facilitate and optimize the real-time control of the different production means (see Section 8.2.1.2).

It is important to mention that the need for a perfectly accurate forecast of energy sources (wind speed, solar radiation, etc.) is not equivalent for all energy sources. PV modules have no inertia associated in their production. In other words, as soon as the sun gets covered by clouds, the electricity production falls instantaneously. It can represent an important change in production in the case of a large PV power plant (several megawatts). On the other hand, rotors of wind turbines manufactured today are larger and heavier. They have more inertia and are less disrupted by fast changes in wind speed [3]. Consequently, minutes-ahead forecast of energy sources can be important for PV power plants, although less

for wind power plants. The advantage of inertia is not negligible when it comes to facing the difficulties in perfectly forecasting changes in wind speed, which is more complex than forecasting changes in incoming solar radiation.

Both intermittency and capacity to forecast determine the extent to which power generation from a renewable source can be dispatched. A production is said to be non-dispatchable when it cannot be controlled. It is worth mentioning that all production technologies, including production units from renewable energies, can be dispatchable downwards. In other words, the electricity production can be intentionally reduced. For example, wind turbines can rely on pitch control to adjust their power output (adjustment of the angle of attack between the airflow and the blade). Similarly, power electronics can reduce the production of PV modules by modifying their operating point.

8.2.1.2 Impacts of Non-Dispatchable Power Sources on Electrical Networks

Integration of power production from intermittent sources into electrical networks is not achieved without consequences. This is particularly true when the share of such power production means in the global mix becomes important. The maximum share of intermittent sources in a given mix largely depends on the characteristics of the network, the other production means (number, flexibility, etc.) and the meteorological conditions [4]. An upper value of 30% is often given but without case-specific assessment.

At each moment, the total electricity production injected into the grid and the total electricity consumption (power withdrawn from the grid) must be equal. When a difference between these two quantities appears, it results in a variation of the network frequency that deviates from the nominal frequency (50 or 60 Hz depending on the utility frequency). The frequency keeps deviating until the equilibrium is reached again (e.g. the production equals the consumption) (Figure 8.2).

It is essential to mention that electrical devices are designed to work at a given frequency (nominal frequency). Operating electrical devices at a different frequency can lead to premature fatigue and failure of the devices. Consequently, maintaining the frequency very close to its nominal value is essential and is part of the required quality points of the supplied electrical energy. One of the difficulties that electrical networks have been facing ever since they were built is that electricity consumption cannot be perfectly anticipated (no one is asked to inform the network operator that one is about to switch on the light!). This means that to maintain the frequency around its nominal value, in other words, to maintain the production equal to the consumption, the production level needs to follow the consumption at each instant. Consequently, there is a need for fully dispatchable power production units. These units must be able to rapidly increase or decrease their power production according to the load level. On the basis of the information provided previously (see Section 8.2.1.1) it is clear that an intermittent power production cannot follow changes in consumption and the integration of this power production into an electrical network highly depends on the ability of other production units to handle this lack of flexibility.

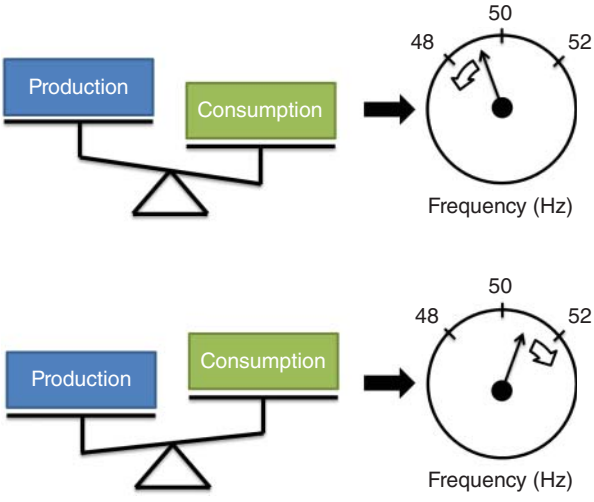

Figure 8.2 Impact of production and consumption imbalances on the frequency of the electrical network.

As previously stated, most renewable power production units are connected to distribution networks due to their power levels. The decision regarding whether a production unit should be connected to the distribution or the transmission network depends, among other aspects, on its maximum power level. It is worth mentioning though that most offshore wind farms and some large onshore wind farms are connected to the transmission network. Historically, production was centralized in large power plants requiring high-capacity lines to 'evacuate' the amount of energy produced (transmission networks). For example, power plants with a capacity higher than 2 GW are largely widespread across the world (essentially nuclear, coal and hydraulic power plants) [5]. Transmission networks are operated at high voltage (110 kV and above) to reduce transmitted intensity and thus ohmic losses. They are connected to distribution networks that operate at lower voltages (voltage levels closer to those required by electrical appliances). Figure 8.3 illustrates schematically the structure of the electrical network. It can be seen in this figure that the transmission network has been designed with a mesh structure in order to manage sudden loss of transmission lines when distribution networks are usually designed with a radial structure.

The increasing power injection into distribution networks raises technical issues. Some examples are listed here [6]:

- Impact on the usual top–down power transit. If the locally injected power is more important than the local demand, the extra power will have to go up to the transmission network. This highlights the need for bidirectional equipments.
- Impact on planning, control and operation of networks.
- Impact on the voltage profile due to power injection/consumption.
- Impact on the protection scheme of distribution networks.

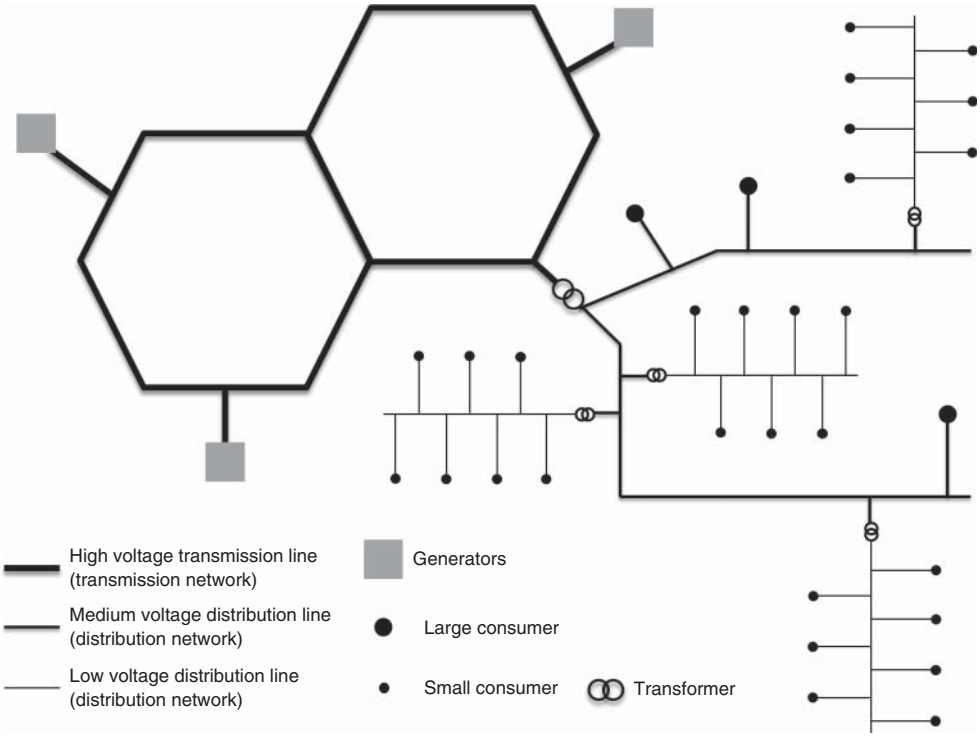

Figure 8.3 Illustration of the structure of the electrical network.

It is worth mentioning that renewable power injection into the transmission network is not without consequences either. Transmission system operators (TSOs) are facing new issues such as follows:

- Congestion in areas with strong renewable power injection.
- Diminution of operation margins of the entire production park.
- Risks of important and sudden loss of power due to meteorological forecast errors.

8.2.1.3 Solutions for Higher Penetration of Renewable Energies

As stated earlier, the increasing injection of renewable power into electrical networks globally reduces operation flexibility. To ensure the reliability of the electrical system, the existing flexibility must be maintained. Several solutions have been identified and can be categorized into the following actions:

- Actions on the structure of the electrical networks.
- Management of power sources and electrical loads.
- Introduction of energy storage systems.

The first solution consists in reinforcing and further developing electrical grid infrastructures. The main objective is to mutualize renewable energy production over a wide region, such as Europe, covered by different meteorological conditions. Within such a region, when the wind is not blowing in one location, it might be blowing somewhere else, or solar energy might be available in another place, and so on. Mutualizing all these sources can only be achieved by reinforcing existing grid infrastructures (increasing the capacity of transmission lines) and increasing interconnection capacities between countries (by the use of high-voltage direct current (HVDC) lines). This vision of largely interconnected networks is often referred to as a 'super grid'.

Another way of increasing operation flexibility in power networks is by acting on the power sources and electrical loads. As stated previously (see Section 8.2.1.2), acting on power sources is the solution adopted today allowing electrical systems to work. A power production from renewable energy sources (solar, wind) is generally operated in such a way that it delivers the maximum amount of power it can provide based on the site meteorological conditions. In this case, the only possible control is to intentionally reduce the level of produced power. For example, it is possible to change the operating point of PV modules by controlling the inverter to which these modules are connected. This allows the PV modules to produce less than what is physically possible. Similarly, it is possible to change the pitch angle of wind turbine blades to decrease their efficiency and lower their production. In order to make renewable energy–based production units dispatchable like conventional power plants, a possibility would be to operate them at partial power. This would allow at each moment to increase or decrease the production according to the fluctuations of the load. However, this would result in losing part of the potential energy of a given site. The development of communication technologies opens new perspectives regarding the adjustment of production and consumption. As mentioned earlier, power systems have been relying almost exclusively on 'supply-side management'. Nevertheless, some studies and demonstration projects aim to explore further the 'demand-side management'. Some loads are said to be 'deferrable' when the power consumption at a given moment can take place at another instant. It is obviously not the case for many electricity uses. For example, if we consider lighting, no one would accept to have to wait for the light to come after turning it on! However, 'demand-side management' can be suitable for several other types of residential, commercial and industrial loads. The most popular example, extensively used in electro-intensive countries, is the domestic hot water heated by an electrical resistance. In this case, the electricity consumption is postponed during the night to take advantage of better prices. Managing electrical loads can then be another valuable option to increase the flexibility on power networks.

The third option consists in introducing energy storage in our electrical networks. To face an increase in production or a decrease in consumption, the energy storage system could be used to absorb the available power, allowing the production level to be maintained. Inversely, when the consumption increases or when the production decreases, the energy storage system would operate in discharge

mode to supply the required amount of energy for a full satisfaction of the connected loads. The introduction of plug-in electric vehicles is incontestably adding new electricity consumptions in power networks. However, they can also be seen as a new storage capacity if their batteries can also be used in discharge mode to supply electricity to the network.

8.2.2 Energy Storage on Electrical Networks

As stated before, energy storage is identified as a means to increase the penetration level of renewable and intermittent energies into the grid. However, a first difficulty arises when facing the diversity of storage technologies that are available on the market or in development today. Furthermore, even within the narrowed context of renewable energy integration, the possible uses of energy storage are numerous. From these two points emerges the practical question of choosing the right technology for a given storage application.

8.2.2.1 Technologies Characteristics

The development of electrical energy storage technologies has been ongoing almost ever since the use of electricity has spread around the world. It is today drawing more attention with the rapid development of renewable and intermittent energies. Consequently, there exist today a large number of storage technologies. A first way to classify these technologies is to distinguish physical technologies from electrochemical technologies [7]. Among the physical technologies, one can mention gravity-based technologies, superconducting magnetic energy storage, compressed gas, inertia and thermodynamic heat storage. Among electrochemical technologies, one can mention all battery technologies (lead–acid, lithium, vanadium, sodium–sulphur, etc.), supercapacitors and, finally, hydrogen technologies. However, from a grid integration point of view, the physicochemical processes that govern the different technologies have little importance and all these technologies are usually compared according to evaluation criteria that are really of concern when it comes to deploy an energy storage system in an application [7–9]. Examples of relevant criteria are listed here:

- Energy capacity
- Maximal charge and discharge powers
- Self-discharge
- Efficiency
- Ageing (calendar and cycling)
- Costs (investment, operation, maintenance, replacement)
- Specific energy/power (per unit of mass, volume or surface)
- Response time
- Grey energy (amount of energy required to manufacture and transport a component)
- Maturity.

On the basis of these criteria, several two-dimensional charts can be created to visualize how the different technologies compare to one another based on the selection of two criteria. An example of 2D chart based on the maturity of technologies and their suitability for power or energy applications is provided in Ref. [8].

8.2.2.2 Past, Present and Future Technology Choices

Storage technologies have been integrated in electrical networks essentially to increase operation flexibility. The main reason is that electrical networks were not interconnected as they are today. As mentioned before, interconnections allow transporting a large amount of electrical energy from one region to another. They also have another major advantage. By interconnecting all production units, they allow a mutualization of the contributions provided by each power production unit to frequency regulation. This sharing of regulation capabilities allows an interconnected network to face more critical unplanned events such as a sudden reduction of intermittent power production or the loss of several conventional production units. An interesting historical example is the storage unit installed in 1986 in West Berlin, Germany, and operated by Bewag. This 17 MW/14 MWh storage unit was based on lead–acid batteries and was used for frequency regulation (the West Berlin electrical network was isolated from East Germany) [10]. Two years after the electrical connection of West Berlin to Western Europe, the storage facility was decommissioned as the mutualization of the different connected production units provided enough flexibility to guarantee the reliability of the network operation.

Pumped hydrostorage (PHS) technology and lead–acid batteries have been the preferred technologies for decades. Today, PHS is the most prevalent technology worldwide with an installed capacity much greater than all other technologies combined. It represents indeed 99% of the total storage capacity (Figure 8.4) when hydrogen represents only 4 MW. Recently, efforts of research and development (R&D) on sodium–sulphur batteries have been concretized by the installation of several systems based on this technology. It is worth mentioning also the recent

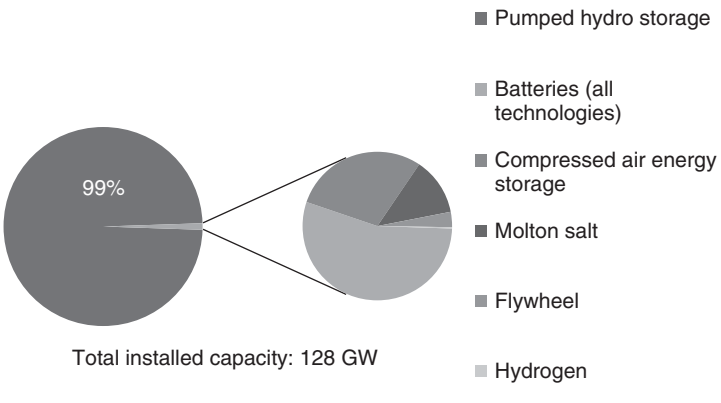

Figure 8.4 Storage capacity installed worldwide per technology in 2012 [11].

development of flywheels and the multiplication of their installations. Finally, lithium-based batteries are considered as one of the most promising technologies for the very near future and a lot of uncertainties persist regarding the impact of the development of this technology on its electrochemical competitors.

8.2.2.3 Possible Roles of Energy Storage on the Grid

Given the operational constraints of electrical networks and the consequences of renewable energy integration, it is worth examining the possible roles that energy storage can play in these networks. Services provided by energy storage can be seen as an association between a technical function and an objective. We can then identify a given service as a function–objective couple. For example, during low power demand periods, a wind farm may be shut down if the local grid to which it is connected cannot 'evacuate' the produced power. In order to increase the annual energy production of this farm (objective), an energy storage unit could be installed nearby to store the produced energy every time the electrical network is unable to absorb it (function). Each technical action (function) can satisfy several objectives and, inversely, a given objective may be fulfilled by several functions.

Several works intend to identify exhaustively all possible functions and objectives that storage can have in electrical networks [12, 13]. It is worth pointing out that not all storage function–objective couples are related to renewable energies. A detailed overview of all function–objective couples is out of the scope of this book so we describe only some functions directly related to renewable energy integration.

Four storage functions are illustrated by the following figures. Peak production shaving (Figure 8.5) consists in storing the production above a given power threshold. To reuse the example given previously of the wind farm connected to a constrained network, the power injection threshold may depend on the local power demand and can represent the maximum level of power that the local grid can handle. The objective of such a function could be in this case to maximize the annual production of the wind farm (production that would be lost otherwise) and, at the same time, to defer investment in new grid transmission capacities, which, if realized, would lead to underused new capacities.

Production smoothing (Figure 8.6) consists in using a storage system alternatively in charge and discharge to avoid fast fluctuating wind or PV power injection into the grid. The objective of such a function could be to relieve other production units of their obligation to furnish power reserve.

Production shifting (Figure 8.7) consists in storing produced energy at a given moment in time to discharge this energy later in the day, later in the week or later in the year (seasonal storage). This function would be particularly useful in the context of an energy mix based on a large amount of renewable energy. For example, the majority of PV energy could be stored during summer when the PV production is maximal and used during winter when less PV energy is available.

Production guarantee (Figure 8.8) consists in using a storage system in association with a renewable power plant to make this combination equivalent to a conventional dispatchable power plant. In this case, a production profile can be

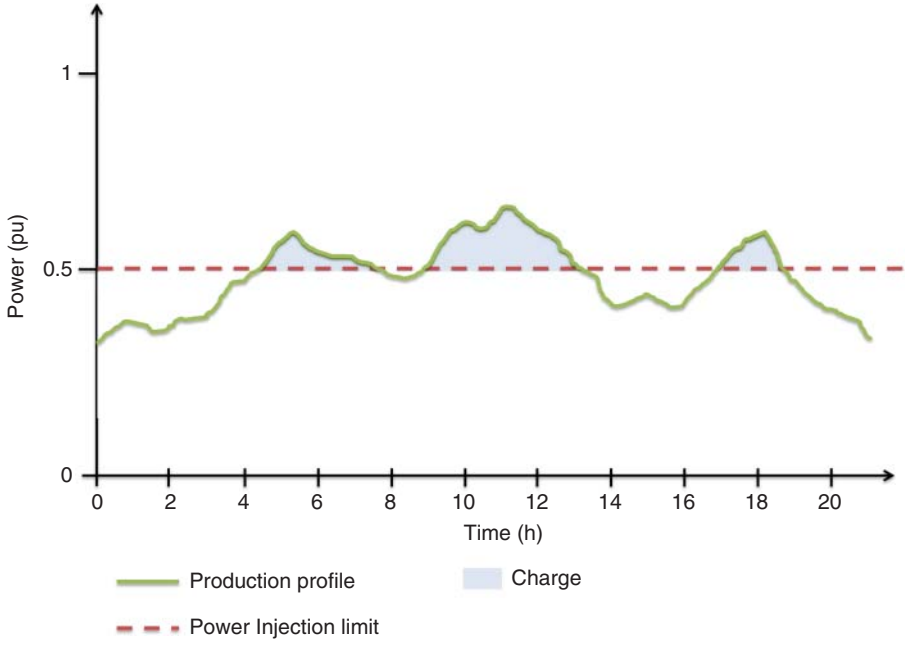

Figure 8.5 Illustration of the peak production shaving storage function.

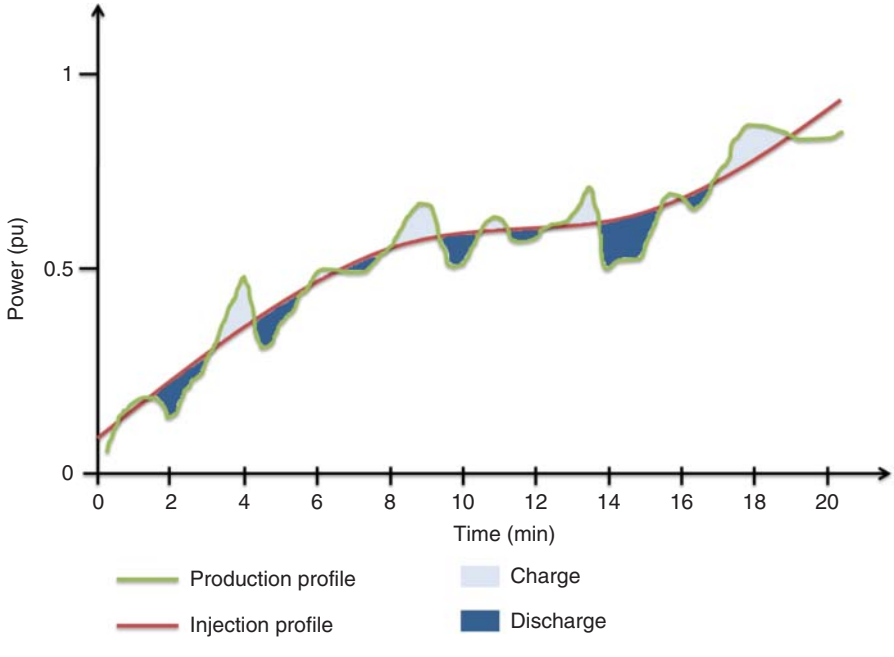

Figure 8.6 Illustration of the production smoothing storage function.

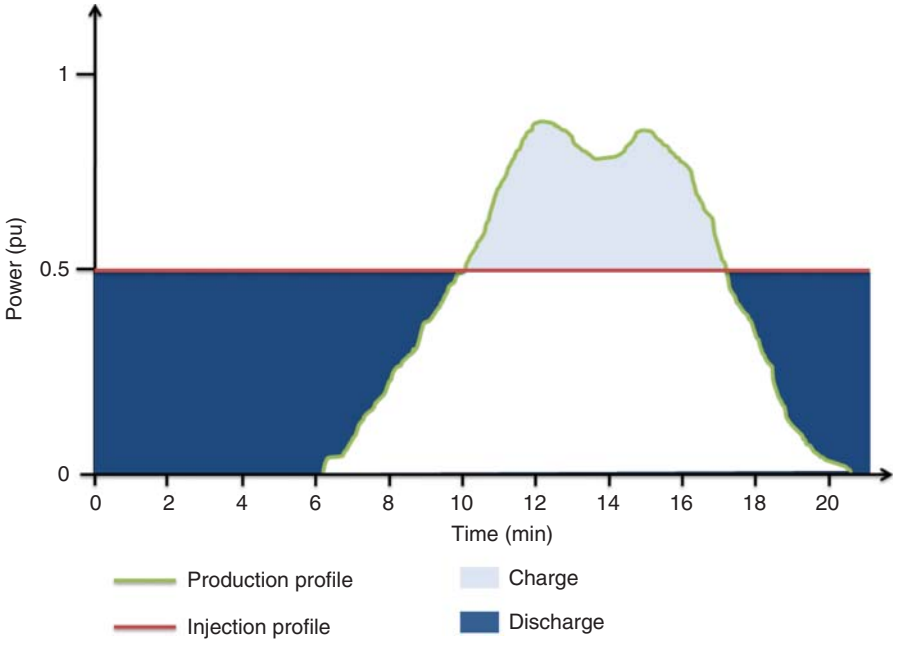

Figure 8.7 Illustration of the production shifting storage function (illustration for a day).

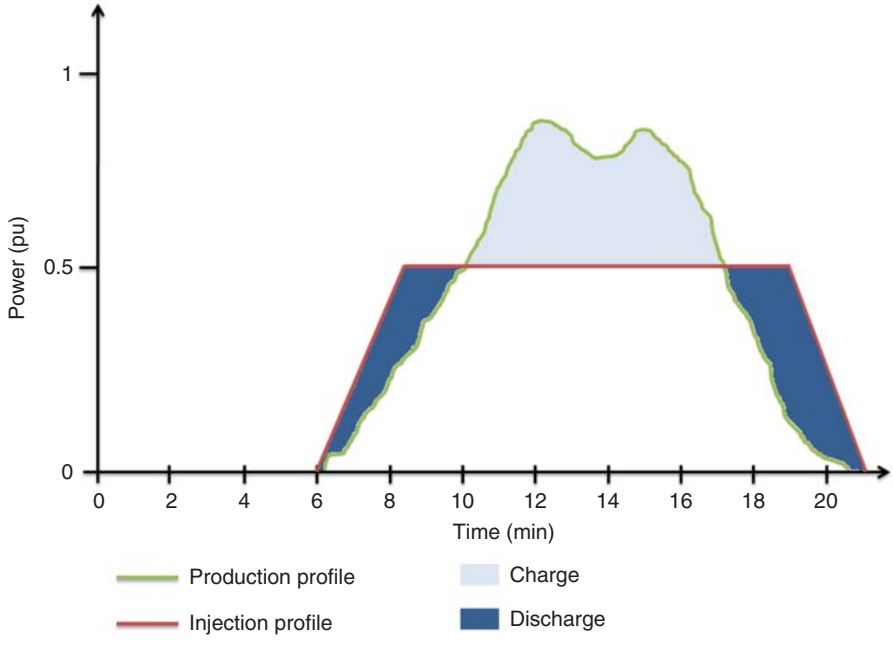

Figure 8.8 Illustration of the production guarantee storage function.

announced in advance to the grid operator or energy market stakeholders and the renewable energy producer can use the storage system to fulfil its contractual engagements. Figure 8.8 illustrates a situation where the PV power plant daily injects a trapezoidal power profile into the grid.

8.2.3 Hydrogen for Energy Storage

The storage functions described previously are usually linken to technologies such as batteries, PHS, compressed air energy storage, and so on. However, hydrogen can also be seen as a means to store energy and, as it can also be used to produce electricity, it can be seen as a reversible electricity to electricity storage means.

8.2.3.1 Power to Hydrogen: Use of Electrolysis to Store Electrical Energy

Storing electricity requires an energy carrier in order to hold part of the energy content of the electrical energy. All storage technologies (batteries, PHS, etc.) use such an energy carrier. For example, compressed air is an energy carrier used in several industrial applications (pneumatic hammer, dental drill, etc.). Usually, only energy carriers that are easily transportable are considered. For example, water stored at a height (potential energy) is not considered as an energy carrier as it would need to be transported several metres above the ground in order not to lose its energy content.

Energy carriers used today are essentially electricity itself, natural gas and products derived from oil (gasoline, diesel, kerosene, etc.). It is worth pointing out that natural gas and oil are often considered energy sources (although this point could be largely debated if one assumes that the only energy sources are sunlight and geothermal). It is important to understand that this debate does not apply to electricity and hydrogen, which are only energy carriers as they must be produced and do not exist as such in nature.

Using natural gas and petroleum products as energy carriers leads to widely known environmental issues (global warming due to CO_2 emissions, fine particles pollution, etc.). Electricity and hydrogen, if produced from clean energy sources (renewable energies), constitute interesting alternatives from an environmental point of view. However, electricity cannot be stored and needs therefore to be transformed into another form of energy (including hydrogen) if a later use in time is desired.

Electrolysis can be used to convert available electrical energy into chemical energy (in the so-called power to hydrogen process). It produces hydrogen and oxygen from water and electricity. Hydrogen is then usually stored in gaseous, liquid or solid state. Most of the time, oxygen is released in the atmosphere but it may also be stored for later use.

Unlike battery technologies, electrolysis and hydrogen offer the advantage of a separation between charging power and stored energy. For example, if lead–acid batteries are used as a storage unit, the power and energy needs of a given application are met by connecting in series/parallel several individual lead–acid batteries.

Each individual battery has a maximum charging power and an energy capacity. Consequently, increasing the storage capacity by increasing the number of batteries necessarily increases the charging power. Depending on the application, the required balance between power and energy needs may not be similar to the balance obtained for a single battery. Therefore, it is either the energy need or the charging power need that will determine the number of required batteries. This will lead to either an oversized charging capacity or an oversized storage capacity. Electrolysis and hydrogen rely on two different objects. This allows decoupling charging power (through the electrolyser size) and stored energy (through the hydrogen storage size). In applications with contrasted needs in terms of charging power and stored energy, this decoupling can have major economic advantages. Furthermore, batteries usually suffer from one important issue, which is the link that exists between the charging regime and the amount of energy that can be stored. It can be observed in almost all battery technologies that when a high charging intensity is applied, the battery voltage quickly reaches the value indicating the end of charge, which requires stopping the charge. This results in an amount of energy stored less important than when a low charging current is applied. An electrolyser does not suffer from this drawback and, apart from the difference in efficiency according to the operating point, the amount of hydrogen produced does not depend on the power point but only on the consumed energy.

Unlike most battery technologies, hydrogen tanks have no self-discharge (or very limited). Furthermore, storing energy as hydrogen in its gaseous state can benefit from the existing gas transportation and distribution networks. Although originally designed for natural gas, investigations are ongoing to determine to which extent hydrogen can be mixed into natural gas [14] and transported with natural gas pipelines. A step further also currently investigated would be to convert the produced hydrogen along with carbon dioxide into synthetic methane (power to methane, or more generally through the so-called power to gas concept). If successfully developed, synthetic methane could take advantage of the enormous volume of pipelines and of their variable pressures, which constitute a very large energy storage capacity. Finally, hydrogen and carbon dioxide can also be combined in order to produce synthetic liquid hydrocarbons such as diesel or kerosene. This full set of electrochemical reactions is commonly referred to as 'power to liquids'.

8.2.3.2 Attractiveness of Hydrogen: Not Only an Energy Carrier

Among all energy carriers to which electricity can be transformed, hydrogen is particularly interesting in the sense that, apart from its capacity to be transformed again into energy, it can be used in several contrasted applications (Table 8.1) in which its energy content is not the only factor of interest.

According to [15], ammonia production represents the main hydrogen use across the world (55%) followed by refining (25%) (Figure 8.9). These two activities represent approximately 80% of the hydrogen use worldwide.

Among the different uses of hydrogen mentioned in Table 8.1, oxyhydrogen flame illustrates particularly well the diversity of hydrogen applications. It is used,

Table 8.1 Overview of the different uses of hydrogen.

Industry	Application	Use of hydrogen
Chemistry	Refinery	*Hydrotreatment:* removal of impurities by reaction with hydrogen *Hydrocracking*: production of jet fuel, diesel, gasoline kerosene and other products from gas oil in the presence of hydrogen
	Synthesis of chemical products	*Ammonia:* reaction of hydrogen with nitrogen to produce ammonia *Methanol:* reaction of carbon monoxide or carbon dioxide with hydrogen to produce methanol
	Laboratory analysis	*Gas chromatography:* hydrogen is used as carrier gas for chromatography
Food	Synthesis of solid fats	*Hydrogenation:* hydrogen is used to convert liquid vegetable oils into solid or semi-solid fats (margarine)
	Synthesis of sorbitol	*Sorbitol*: reaction of cellulose with hydrogen to produce sorbitol
Glassmaking	Fusion and crystallization of glass	*Oxyhydrogen flame:* Reaction of hydrogen and oxygen to produce high-temperature flame used to process glass
	Float glass manufacturing	*Protective atmosphere:* hydrogen is used in combination with nitrogen to create a protective atmosphere to prevent oxidation
Electronic	Growth of epitaxial films	*Epitaxy*: method used to grow high-quality crystals for semiconductor materials. Hydrogen is used in epitaxial silicon growth based on vapour-phase epitaxy (hydrogen reacts with silicon tetrachloride)
	Quartz fusion	*Oxyhydrogen flame:* reaction of hydrogen and oxygen to produce high-temperature flame used to melt quartz
Metallurgy	Soldering/cutting/brazing	*Oxyhydrogen flame:* reaction of hydrogen and oxygen to produce high-temperature flame used in soldering, cutting and brazing of different metals
	Thermal treatment	*Protective atmosphere:* hydrogen is used in combination with nitrogen to create a protective atmosphere for the annealing heat treatment
Energy	Nuclear reactor	*Protective atmosphere:* hydrogen is used in combination with nitrogen to create a protective atmosphere to prevent oxidation
	Cooling of electrical generators	*Coolant*: hydrogen is used as a coolant in turbo generator (combined-cycle gas turbines)

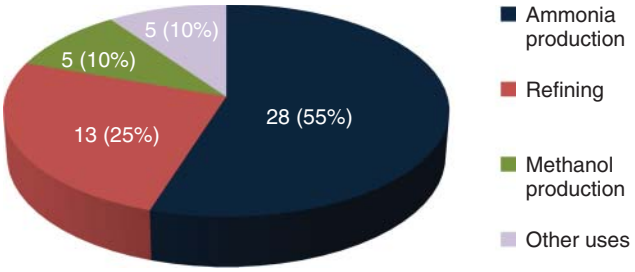

Figure 8.9 Estimated world hydrogen use in million tonnes per year in 2008.

for example, in metallurgy, plumbing, glassmaking, electronics and jewellery. Oxyhydrogen flame presents also the advantage of working underwater, leading to a large panel of submarine applications.

It is worth pointing out that these industrial applications differ in terms of required hydrogen specifications. The three main factors that determine the characteristics of hydrogen are purity, mass flow rate (minimum, maximum fluctuations with time) and pressure level. For example, the use of hydrogen in electronic applications often requires very pure hydrogen. If hydrogen is used for mobility application, it is usually required to have a high specific weight in terms of stored hydrogen mass per unit of occupied volume or per unit of mass of storing material. In this case, storage at the highest possible pressure can be a solution to increase the specific weight.

8.2.3.3 Use of Hydrogen to Produce Electricity

Hydrogen can be used to produce electrical energy, mechanical energy and thermal energy by combining with oxygen. Use of hydrogen in a fuel cell directly produces electricity and heat. The association of an electrolyser, a hydrogen storage device and a fuel cell is often denoted as a hydrogen chain. This chain constitutes a fully reversible energy storage device. The use of hydrogen in a fuel cell can be seen as the discharge phase. Hydrogen can also be used in a motor or turbine to produce mechanical and thermal energy (hydrogen-fuelled aircraft, rocket propellant). For hydrogen turbines, the mechanical energy can in its turn drive an alternator and produce electricity.

Comments made previously on the ability of electrolysis to decouple charging power and stored energy apply here also. Discharging power (power produced in a fuel cell or in a hydrogen turbine) is completely independent of the amount of energy that is stored in a hydrogen tank. This is another advantage of using a hydrogen chain as an energy storage device. The three main components (electrolyser, hydrogen storage, fuel cell) can be sized individually. With this ability, a hydrogen chain can tackle several storage applications in which the need for charging power, discharging power and stored energy can be very different.

The major disadvantage of using a hydrogen chain as an energy storage device is the relatively low overall efficiency (25–35% without hydrogen compression) in

comparison to other technologies (e.g. Li–ion batteries 90% and lead–acid batteries 80%). However, in most applications, the comparison cannot be based only on efficiency as it is not the only impacting criteria. For example, self-discharge, footprint, lifetime, reliability and costs may also be determining factors.

8.3 Electrolysis Powered by Intermittent Energy: Technical Challenges, Impact on Performances and Reliability

As presented in previous chapters, liquid water electrolysis can today be considered as a well-established technology. Indeed, alkaline water electrolysis has been used industrially for decades and PEM electrolysers have been available commercially for many years, although in limited sizes. Hydrogen in general and water electrolysis as a production means has been considered for a long time as applicable for energy use. As it was described in the previous section, hydrogen production by electrolysis shows great advantages for energy storage applications as it can be applied at a vast range of scales and can be suitable for long-term storage. As long as electrolysis is powered by renewable electricity, hydrogen becomes a clean energy carrier; this is why integration of water electrolysis with renewable energy sources is of great interest. However, requirements induced by intermittent power on electrolysis systems are largely different from those found in traditional industrial applications. Indeed, the connection of water electrolysers to intermittent power sources imposes some specific system design and operating modes due to the nature itself of these power sources as reviewed in the previous sections. This section aims to describe the specificities of these operating modes and then to explain the impact they may have on performances of an electrolyser. Among the different electrolysis technologies presented in this book, it appears clearly that HTSE does not show the same readiness level when compared to low-temperature water electrolysis. Thus, most of the material presented in this chapter relates to low-temperature electrolysis, that is alkaline and PEM technologies. Nevertheless, some requirements specific to HTSE are discussed. Finally, existing solutions or modifications that could possibly be implemented to favour and optimize coupling of water electrolysis and renewable energy are reviewed. This section should then help to understand which (if any) electrolysis technology is better suited to renewable energy coupling and intermittent operation.

8.3.1 Effect of Intermittency on System Design and Operation

Different system configurations exist to allow generation of hydrogen from water electrolysis, some of them implying direct connection of the renewable source to the electrolysis system, and others, a connection to the electric grid or even a combination of those. However, whichever of these configurations is considered,

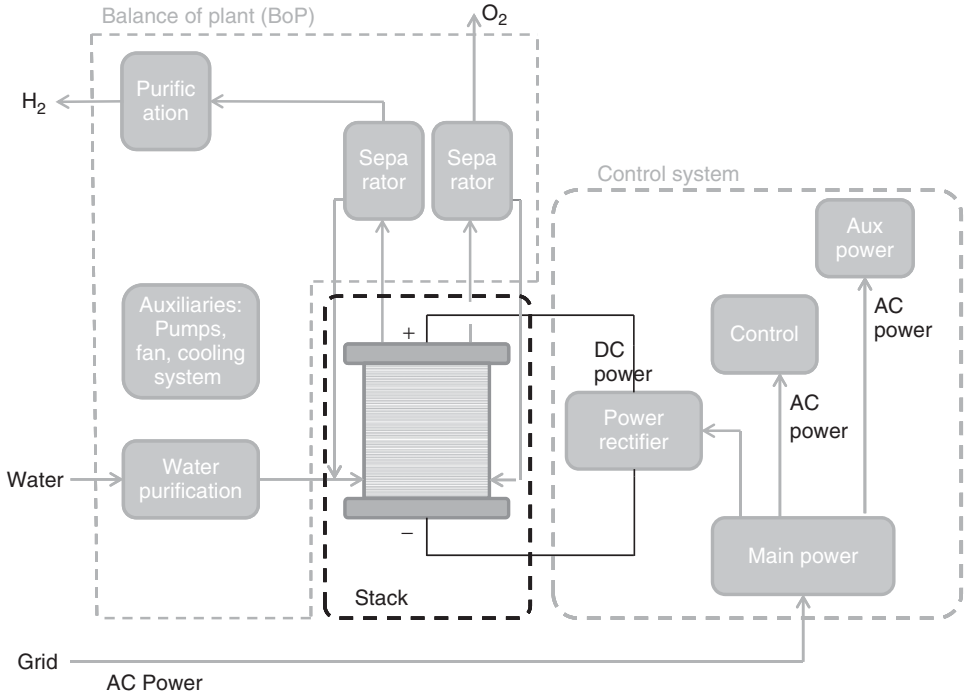

Figure 8.10 Schematic diagram of a water electrolysis system.

the available power to be used by the load might be intermittent and this has an impact on the operation of the electrolysis system and its design.

A commercial electrolysis system is composed of three main blocks as represented in Figure 8.10:

- *The stack*: this is the main component of the system where water is split into hydrogen and oxygen. One electrolysis system can be composed of one or several electrolysis stacks.
- *The control system*: this block is the electric system powering and controlling the process. For the control system, different architectures exist but, for most systems, there is a master control and some specific controls for each electrolysis stack.
- *The balance of plant (BoP)*: this includes the rest of the system composed of elements such as water pumps, gas–liquid separation units, cooling system and all the related piping and instrumentation items.

All components of the system, and not only the production stacks, can be affected by the intermittency and the associated operating modes. An efficient and optimal integration of a renewable power source first requires identifying the technical challenges imposed by intermittency and renewable power source specificities.

8.3.1.1 Impact on Power Electronics and Process Control

As already presented in this book, the electrolysis process requires direct current (DC) to split water into hydrogen and oxygen. As most electrical networks today use alternative current (AC), there is a need for power transformation from AC to DC when an electrolyser is connected to the grid. This configuration has been used for industrial application and is the one proposed as a standard by all electrolysis systems manufacturers.

However, each renewable power source has particular current and voltage characteristics that do not match electrolysis stack and system needs. Furthermore, as mentioned by Fingersh [16], a nearly infinite number of power electronics design can be used on a wind turbine. Consequently, power transformation must be specific to each case, which leads to increased complexity as illustrated in Figure 8.11.

Most of the difficulties in matching the characteristics of electrolysers and renewable power sources can be solved by power converters but each and every power conversion inevitably induces a loss of efficiency for the overall system. Furthermore, an electrolysis system is always a combination of DC-powered parts (the most important ones being the production stacks) and AC-powered components (pumps, fans, common control system parts). The existence of differently powered equipments implies the use of one or several power converters and a choice between AC and DC for the main bus. When the electrolysis system is integrated within a larger system including several power sources and multiple loads, this choice becomes even more complicated and crucial. The decision on the electrical design of the system and the nature of the main bus depends on the complete system. Indeed, not only should the electrolyser be taken into account but also the nature and diversity of power sources constituting the energy system (including fuel cell if electrical power is produced from hydrogen) and

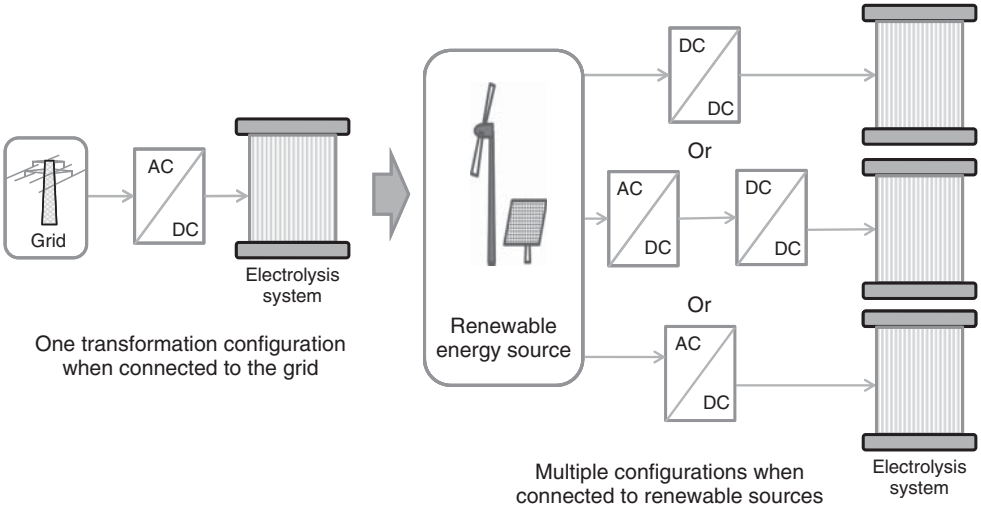

Figure 8.11 Complexification of power conversion.

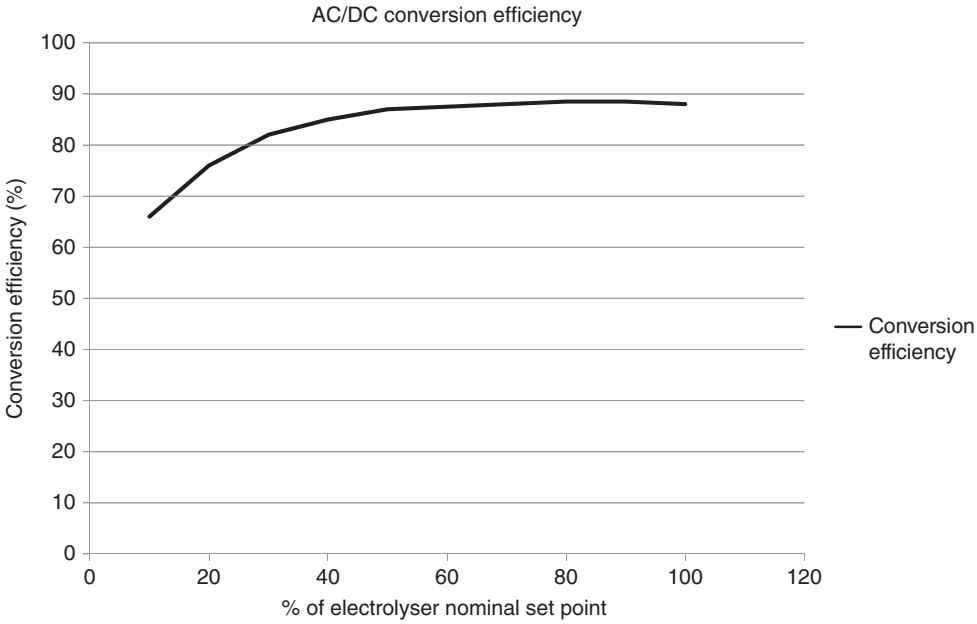

Figure 8.12 Efficiency of an AC/DC converter obtained on a 5 $Nm^3 h^{-1}$ PEM electrolyser.

the nature and diversity of loads. Choices must be made in order to ensure the quality of power provided to the loads (stability of voltage and frequency, purity of waveform). These choices also depend on availability of converters at low cost. Little *et al.* [17] describe the different reasons that led to the decision of a main DC bus for the West Beacon Farm stand-alone power supply that included a 34 kW electrolyser. In this article, drawbacks associated with the use of a DC bus are also reviewed. As many different configurations may exist, this diversity can complicate the standardization of electrolysis systems and impact the cost of the system. That is why, as of today, technical choices are often made based on off-the-shelf available components in order to reduce the total cost of the system.

As any power transformation reduces the energy efficiency of the system, the number of transformations should ideally be limited and great care should be taken in the choice of power converters. This is even more important when dealing with a highly fluctuating power source as converter efficiency depends largely on the inlet power characteristics. Typically, an AC–DC conversion process is expected to be around 90% efficient at nominal power but efficiency can fall significantly at partial load as illustrated in Figure 8.12. DC–DC converters typically show a maximum efficiency above 90% but it is also strongly related to load and voltage inputs and outputs. As a renewable energy–powered electrolyser may spend most of its operational time at part load, the importance of power conversion is then easily understandable.

The topology of power supply has also an influence on the energy consumption of the electrolysis stack. As presented by Ursùa *et al.* [18], power converters can be classified into two main groups: thyristor-based (ThPC) and transistor-based (TrPC) power converters. On the basis of experiments carried out with an electrolyser power supply emulator, it was shown that the stack energy consumption is lower when power is supplied by a TrPC compared to a ThPC. Efficiency gain up to 10% was observed with a ThPC supply. This is related to the quality of DC and voltage that is available for electrolysis parts. Mazloomi [19] also demonstrates that electrolysis efficiency depends on applied voltage waveform. The quality of DC is strongly related to the power converter, the renewable source and its associated intermittency and it has been observed that it has an impact on electrolysis efficiency. However, full quantification of this impact still requires more research to be conducted.

System process control should also be compatible with intermittent operation. This is of course true for each individual control element and its characteristics but also for the control scheme itself. Indeed, several ways of controlling an electrolyser may exist. The major parts of electrolysis systems, especially those of rather small size, were initially designed to be controlled so that they can maintain a specific stack internal pressure or ensure a given outlet flow rate of hydrogen. In these configurations the process control is realized through the downstream of the stacks, that is based on the hydrogen demand. This control scheme was well adapted to industrial applications where the objective was the production of hydrogen itself and the electrolysis process was controlled by the demand. However, when directly connected to an intermittent energy source, the electrolysis system must be controlled by applying appropriate and available current through the stacks or voltage across the stacks. Most of the electrolysis system manufacturers now offer this type of control scheme. The choice between current control and voltage control will depend on the overall architecture of the system and the function that the electrolysis system is supposed to fulfil. If the electrolyser is the only electric load, current-controlled stacks seem more appropriate. The control set point can then be directly a flow rate of hydrogen or current through the stacks. As the electrolyser is directly powered by a fluctuating renewable source, the control loop must include the measurement of available power, and process this information in order to deduce the current to apply and avoid inequality between electrical production and consumption. To ensure rapid power transience, a fast-operating process control is necessary. If the electrolyser is not the only electric load and is not in charge of ensuring the instantaneous balance, then voltage control can be applied. In this case, the bus voltage can, for example, be imposed by a battery bank that has the responsibility of instantaneous electric balance. The electrolyser will in turn draw current based on the applied voltage across the stack. The voltage of the DC bus will be constantly fluctuating based on renewable power, battery state of charge and load demand.

High-frequency power and voltage transience and sudden power failures have to be anticipated when considering renewable energy sources. These characteristics require specific power equipment such as an uninterruptible power system

(UPS) to ensure safe shutdown of the system and battery banks to handle power transience faster than what the electrolysis system can guarantee.

The integration of the electrolysis system with the renewable power source greatly complicates the power adaptation and the control scheme. Although existing power electronic devices are able to adapt to any configuration, great care must be taken in the design of the electrolysis system within its environment to limit the losses associated with power conversion and to ensure sufficient quality of applied current in the stacks.

8.3.1.2 Requirements to Allow Dynamic Operation

Besides specific electrical characteristics (current and voltage) adaptation, coupling to variable renewable energy sources imposes some drastic dynamic constraints. When an electrolyser is directly connected to the grid for a constant-load industrial application, these constraints barely exist as electrolysis will either be producing at its nominal set point or be stopped. As renewable sources are characterized by their intermittency and their irregularity, some specific abilities are required for the electrolyser system to be able to follow the fluctuating power.

First of all, the electrolyser must be able to handle frequent start and stop requests due to sudden loss of power caused, for example, by clouds passing by (in case of PV powered electrolysis) or by wind speed diminution below the rated level. An electrolyser that would run only when excess renewable energy is available, for example, must be able to start up quickly in response to a signal in order to make maximum use of available energy. This requirement is often not compatible with the start and stop procedure of the electrolysis process, which generally lasts several minutes to several tens of minutes depending on the technology and the size of the equipment. This incompressible time can be due to technical requirements (system pressurization time, start-up verification of components, etc.) or safety precautions (slow current increase, hydrogen leak testing, extraction flow rate verification, safety sensors warm-up time, etc.). The most time-consuming event at start-up seems to be the pressurization of the system including stacks, separators, piping and purification system. The pressurization time obviously depends on the working pressure and the volume of the system. Figure 8.13 illustrates the main steps of a 5 $Nm^3\,h^{-1}$ PEM electrolyser start-up sequence. It can be seen from this figure that about 7 min are required to see the first molecules of hydrogen at the outlet of the system.

Second, in order to operate an electrolyser with intermittent renewable power, the system must be able to work on a wide operating range. Indeed, if the electrolyser is supposed to follow the exact profile provided by the renewable energy source, its ideal operating range would be 0–100%. Thus, it would then be able to fully adapt to the available power and this implies of course operation at low duty. However, most of the electrolysers today have restricted operability ranges, mainly due to safety requirements. Whichever technology (alkaline, PEM) is considered, a crossover phenomenon through the membranes take place. This leads, on both sides of the electrolysis stack (anode and cathode), to a mixture of oxygen

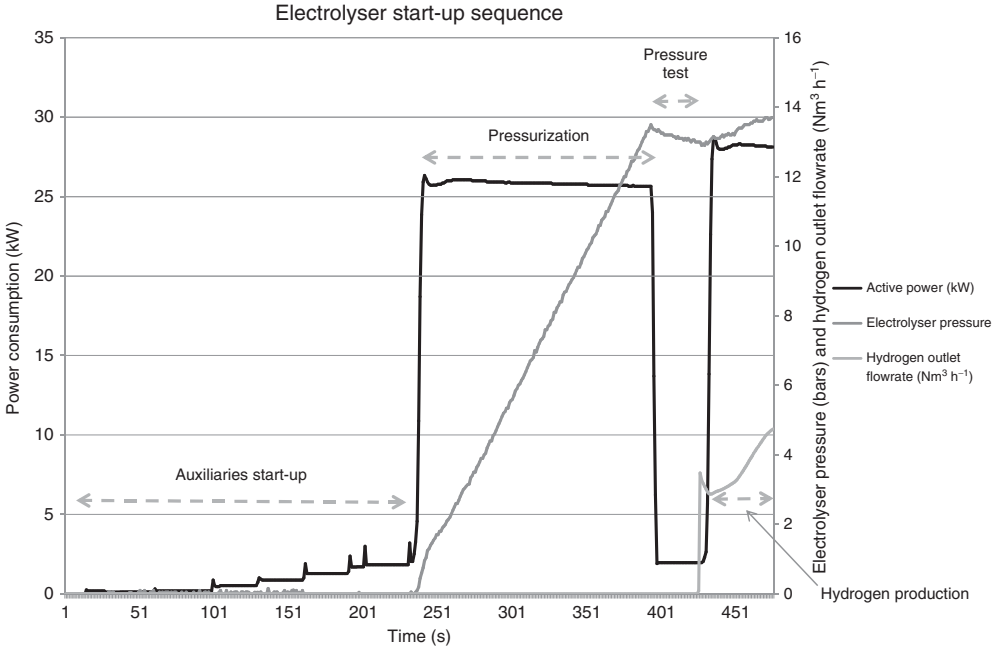

Figure 8.13 Example of a PEM electrolyser start-up sequence.

and hydrogen. For safety reasons, it must be ensured at any given time that the gas mixture remains non-hazardous.

Finally, the system must be able to handle fast power transience and maintain adequate response time over the whole operating range. These requirements are usually taken care of through the control scheme and the implemented control loop that have a strong relation with power electronics. The ability to allow quick response times for a process depends on many parameters such as electric behaviour, power converter technology, signal information transfer, thermal capacity, electrochemical phenomenon and design of the stacks. The observed current increase per unit of time for medium-size PEM electrolysers is higher than 50 A s^{-1} when the system is running. Large-scale alkaline electrolysis systems used to show longer response time when compared to PEM systems. However, commercial alkaline electrolysers can already bear current variation of about 10 A s^{-1} [18] and developments related to advanced alkaline electrolysis will contribute to demonstrate similar performances between PEM and alkaline technologies.

It should then be remembered that the dynamic operation must be possible for the whole system and not only the electrochemical part, namely the production stacks. Indeed, the production stack environment is critical in an electrolysis system to handle fluids (water, steam, gas) and electricity (power conditioning) and ensure proper thermal management. All these components have a specific dynamic response and they must be compatible with an intermittent and dynamic control.

8.3.1.3 Impact on Downstream Elements

As presented earlier, an electrolysis system is composed of one or several stacks, some power and control elements and the BoP. Depending on the application aimed at by the produced hydrogen, the overall system also includes other components such as compression system, hydrogen storage (gas, liquid or solid form), filling station or chemical reactor. The intermittency of power sources impacts not only the electrolyser design and operation but also these additional components. All the elements must be able to withstand a dynamic operation and it may be necessary to adapt the system to intermittency. For instance, if compression of hydrogen is needed by the application, then a buffer tank may be required to smoothen the pressure and flow rate variations at the inlet of the compressors and gas boosters. Indeed, these elements are mechanical parts that usually and preferably work at constant load. In addition, if the hydrogen must be available for an intermittent demand (hydrogen tank-filling station, for example), then sizing of all components must be done taking into account the variability of both the power source and application in order to respect the contractual load. Adequate sizing of process components can then become difficult when a wide operating range is required.

Ensuring flexible operation of the BoP and the downstream elements often means adding or oversizing several pieces of equipment. This leads to increased capital cost as these elements may be used at their nominal point only for a limited period of time. It also leads to increased operational cost as these elements may consume more power when not at their nominal point and age prematurely due to intermittent operation.

8.3.2 System Performances and Reliability under Dynamic Operation

As described previously in this chapter, intermittent power constraint can have a strong influence on design and dynamic requirements for the electrolysis system. These design and operation choices will in turn have a strong impact on performances of the system and reliability as it will not operate, most of the time, at its nominal point. Although it can sometimes be difficult to clearly link loss of technical performance or components failures to intermittent working conditions, this paragraph will review the possible impact of intermittency on hydrogen production characteristics, energy efficiency and reliability of the system.

The connection of electrolysers to renewable power sources has been widely studied using simulation and a few demonstration projects have illustrated the potential of hydrogen for energy storage. However, it is fair to say that the impact of cyclic and intermittent operation has not been adequately addressed in the public literature. The impact on efficiency can quite easily be evaluated but the effect on stacks and system degradation is much more complicated and has received little attention. This may be due to several reasons among which the following can be mentioned:

- Industrial applications so far have not required intermittent operation (this is especially true for alkaline electrolysis).
- PEM electrolysis has been historically used in controlled laboratory environments.
- High-temperature electrolysis is relatively new.

Furthermore, most of the demonstrations projects integrating renewable power and hydrogen were focused on proving that different components can be linked together and on improving reliability of operation but very few were designed or run long enough to study degradation effects. Most of the systems were designed for maximum reliability using off-the-shelf components but very little has been done yet to improve components, architecture and system efficiency.

8.3.2.1 Impact on Hydrogen Production Characteristics

The hydrogen produced by a water electrolyser can be characterized by its flow, pressure, temperature and purity. Although it is quite obvious from what was discussed before that the hydrogen output flow rate is directly linked to the power available for electrolysis, and more precisely the current going through the stacks, as illustrated by Faraday's law already presented in previous chapters, it is important to understand that pressure, temperature and purity are also affected by the intermittent operation.

Temperature Frequent start and stop as well as intermittent and variable power operation have a direct impact on the heat generated by electrolysis stacks and, consequently, on the system operating temperature and hydrogen temperature. Even though it may not have any impact on the quality of the hydrogen produced, as usually downstream purification system can handle a variation of temperature, it has an important consequence on system efficiency, which will be reviewed in the next section. The amount of heat generated by the electrolysis stacks depends mostly on the Joule effect occurring in the electrolyte, which is a function of the current running through the stacks. As described by Ulleberg [20], the thermal behaviour of an electrolysis system depends on the heat generated by the stacks and the heat losses due to the external environment and auxiliary cooling. Indeed, to avoid system operation at too high temperature, electrolysers always include a cooling system. Its design is based on stack system size and usually maintains an optimal temperature at the maximum operating current. At low current set point, the heat generation is, however, much lower than at high set point and, as a consequence, the temperature of the stack decreases. When subjected to intermittent power, the temperature of the stack constantly fluctuates and the system often operates below nominal temperature. Figure 8.14 illustrates the stack temperature evolution of a 25 kW PEM electrolyser powered by PV on a cloudy day. The temperature evolves from 15°C to about 50°C with a general pattern largely influenced by the available PV power.

Owing to fundamental technology differences, PEM and alkaline electrolysis systems do not have the same heat capacity for a same given hydrogen production range. They will therefore not show the same temperature evolution even

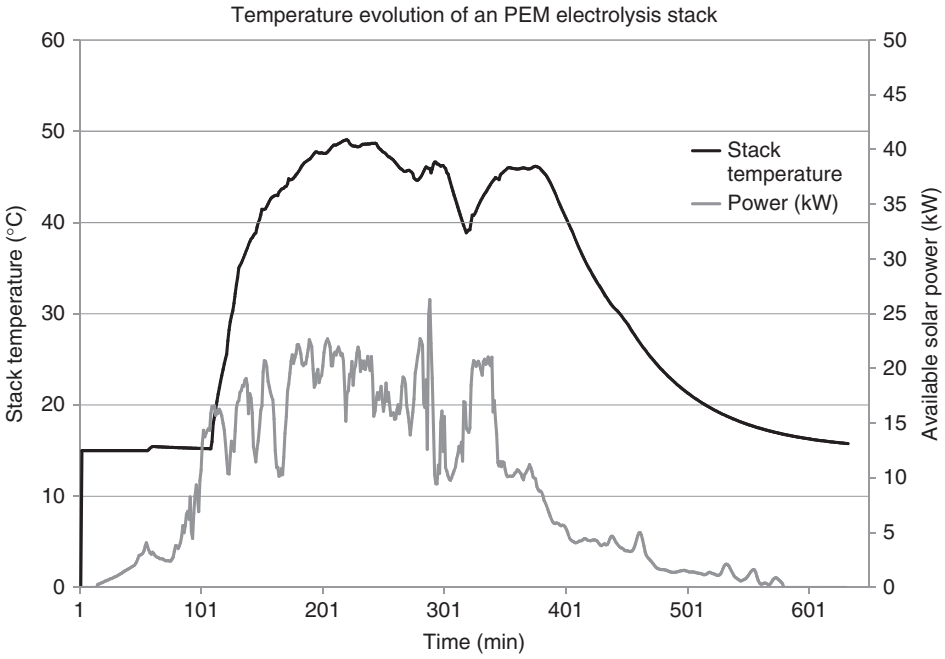

Figure 8.14 Stack temperature evolution on a cloudy day.

though they are powered by the same intermittent profile. In any case, the purification of the hydrogen, and particularly the removal of water pollution, is necessary in most applications. This will require cooling down the produced gas to condense the water and therefore the temperature at the outlet of the system will be constant and close to the ambient temperature. Variation of stack temperature will have a limited influence on the cooling power requirement.

Pressure Pressure in the electrolysis system is also affected by the variation of flow rate. Indeed, to avoid pressure rise (or reduction) in the system when flow rate increases (or decreases), produced gas must be instantly absorbed by the downstream elements. Owing to fluid dynamics of elements constituting the system, this is of course not possible and pressure varies within the system. This effect can be limited using back pressure regulator or downstream regulation elements but a fluctuating flow rate will anyway inevitably mean a fluctuating pressure. Depending on the downstream hydrogen storage technology (pressure, liquid, solid) or application (fuelling station, chemical process, etc.), additional equipment, such as a buffer volume, may be required to handle pressure variations. This leads to additional complexity of the system and increased cost.

Purity Low duty operation also has an impact on the purity of the gases at the outlet of the production stacks. Indeed, the hydrogen generated by an electrolyser contains a certain amount of oxygen, while the oxygen generated contains a certain amount of hydrogen. This is due to the inevitable permeation of gases through the membrane, which happens whichever electrolysis technology is considered. The rate of permeation depends on several parameters (membrane material and thickness, operating pressure and temperature) and can account for up to several points of efficiency loss. At low load, the permeation speed of hydrogen or oxygen through the membrane can be comparable to the actual production rate of the molecules, thus leading to the formation of an unsafe mixture. That is the main reason why the lower operating point is most of the time voluntarily limited by the manufacturer. This phenomenon is more important in alkaline technology than PEM technology and the low quality of hydrogen at low load may force to oversize the purification system or to install additional safety features, which induce additional costs (higher capital and operation costs) compared to a system invariably operating at nominal load. As experimentally demonstrated by Ursùa *et al.* [21], the oxygen in the hydrogen impurity quickly rises with the decrease of current. For the considered alkaline electrolyser at 55°C, the amount of hydrogen in the oxygen would be multiplied by 5 from full power to low operating set point.

It was also experimentally demonstrated [21] that the impurity in hydrogen or oxygen increases with operation temperature and pressure, two parameters that are strongly influenced by intermittency.

Intermittent operation also induces frequent production starts and stops of the system and stacks. During stand-by of stacks, permeation still occurs through the membrane and if gases are not evacuated, then a hazardous mixture can be present inside the system. This is usually dealt with by manufacturers by only authorizing a short period of stand-by time under pressure and forcing depressurization after a certain amount of time, typically less than 20 min. These depressurizations also induce a loss of hydrogen and require long restart time when availability of power is back.

Safety Safety problems related to the intrinsic characteristics of the hydrogen molecule and the corrosive property of alkaline or acid electrolytes are inherent to electrolysis technologies. However, associated risk can be amplified by intermittent operation due to the fact that pressure and temperature are fluctuating. Indeed, pressure and temperature variations will induce high mechanical stresses to the stacks, to the BoP, especially to components ensuring tightness of the system, and might increase the risk of gas or liquid leaks.

8.3.2.2 Impact on System Efficiency

When considering the performance of an integrated renewable energy source with a hydrogen system, the achieved operational efficiency is more crucial than optimal nominal efficiency as the system will spend most of its time operating at partial load. The real performance of the electrolysis system is importantly impacted

by parameters like pressure, temperature and operating power range, which are strongly related to the dynamic operation of the system.

When considering only production stacks, efficiency is generally higher at low current density (i.e. low operating level), due to the limited Joule effect. However, when considering the overall system including BoP, it clearly appears that the specific consumption (usually expressed in kilowatt-hour per normal cubic metre of hydrogen) increases when operating point decreases. It can even be observed that the system specific power consumption greatly and rapidly increases at very low load as illustrated by Figure 8.15. The system-specific consumption will be three to four times more important at low load, which of course has a strong impact on overall efficiency of a system powered by an intermittent source. One of the factors that have a major impact on efficiency at low load is the high auxiliary energy demand for fans, pumps and control systems. Typical auxiliary demand for a PEM or alkaline electrolyser can represent 10% of the total power consumption for a large-scale electrolyser operating at nominal set point to more than 80% for a small-scale system operating at low duty.

Today, in most of the electrolysis systems, the BoP power consumption can be considered as almost constant on the whole operating range and is not dependent on the operating point. This leads to a relative 'weight' of the auxiliaries, which greatly increases with decreasing operating current. Figure 8.16 illustrates the specific consumption of auxiliaries for a 5 $Nm^3\,h^{-1}$ PEM electrolyser, which corresponds to a constant power demand (2 kW) over the full operating range.

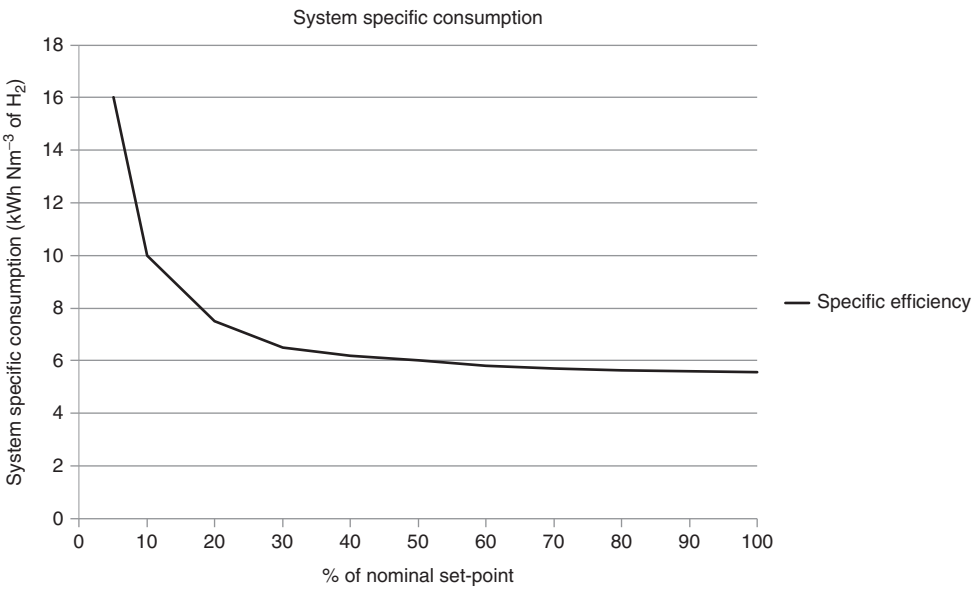

Figure 8.15 Example of a system-specific consumption obtained on a 5 $Nm^3\,h^{-1}$ electrolyser system.

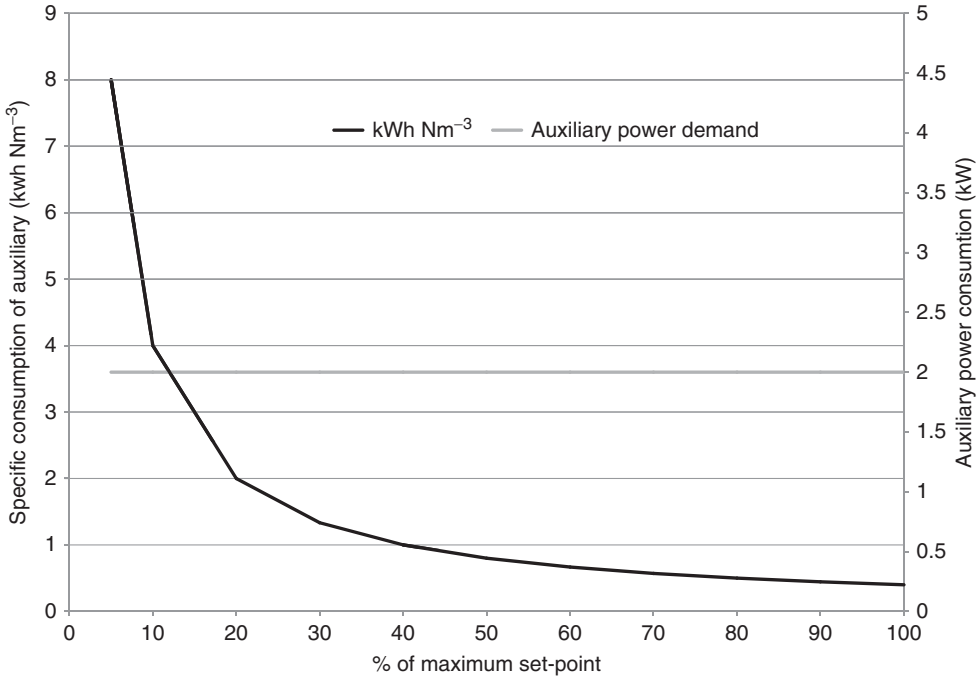

Figure 8.16 Auxiliary power consumption for a 5 $Nm^3 h^{-1}$ PEM electrolyser.

Frequent start and stop also have a strong impact on efficiency. Indeed, every time the system is stopped, it must be depressurized (mostly for safety reasons as presented before) and some of the hydrogen produced is lost, as it gets vented to the atmosphere. The amount of lost hydrogen is directly linked to the volume of the system mainly composed of stack volume, piping, gas–liquid separators and purification system. Appropriate design and sizing of the components is then critical to limit vented hydrogen quantity.

As seen previously in this book, efficiency of the electrolysis is improved when operating temperature is higher. Most of the systems are then designed to operate at an optimal temperature, which is often a compromise between technical feasibility, economics, performance and degradation. Alkaline electrolysers can usually operate up to 120°C and PEM electrolysers up to 80°C. As PEM and alkaline electrolysis is an exothermic process, stacks require cooling and a cooling system is usually designed to remove the heat generated at nominal power. When operated at partial power or when experiencing frequent stops, the system is therefore not operated at optimal temperature, showing then reduced performances.

It was mentioned previously in this book that, thermodynamically, the lower the pressure, the better is the efficiency of the electrochemical reaction. However, it is generally accepted that, due to other phenomena such as the reduction of the bubble size facilitating the electrochemical reaction for alkaline electrolysis, better

efficiency of the system at high pressure can be anticipated. Furthermore, hydrogen storage is often necessary as production and usage of hydrogen do not usually occur simultaneously. For these reasons, the working pressure is of great importance for the efficiency of the overall system and it is usually accepted that pressurized electrolysis (10–30 bars) is preferable, even though it is more expensive to build. This is due to the fact that hydrogen has a very low volumetric mass density and is therefore difficult and energetically costly to pressurize. For example, compressing a kilogram of hydrogen from atmospheric pressure to 30 bars can account for up to 10% of the hydrogen low-heating value (33.33 kWh kg^{-1} of H_2). Although the impact of pressurization is not specific to the integration with an intermittent power source, it must be kept in mind when designing the overall system.

Poor performances of electrolysis systems can also be due to gas permeation through the membrane, parasitic reactions and leakage current at the stack level. At very low current density, these phenomena can become predominant over the reaction of water decomposition itself. This leads to a drop in Faraday efficiency and consequently an increase of energy consumption per normal cubic metre of hydrogen produced. This reduction of efficiency at low load is mostly due to poor conception of the stacks and limited selectivity of the catalysts. Such a conception may be deliberate in order to reduce overall capital cost of the system; it can therefore be overcome with a minimum of design work but it will inevitably raise the cost of the system. Figure 8.17 illustrates the decrease of Faraday efficiency with current density for a low-efficiency electrolyser.

Besides the straightforward and quantified impact of temperature variation and partial load operation on electrolysis efficiency, Bergen *et al.* [22] showed that

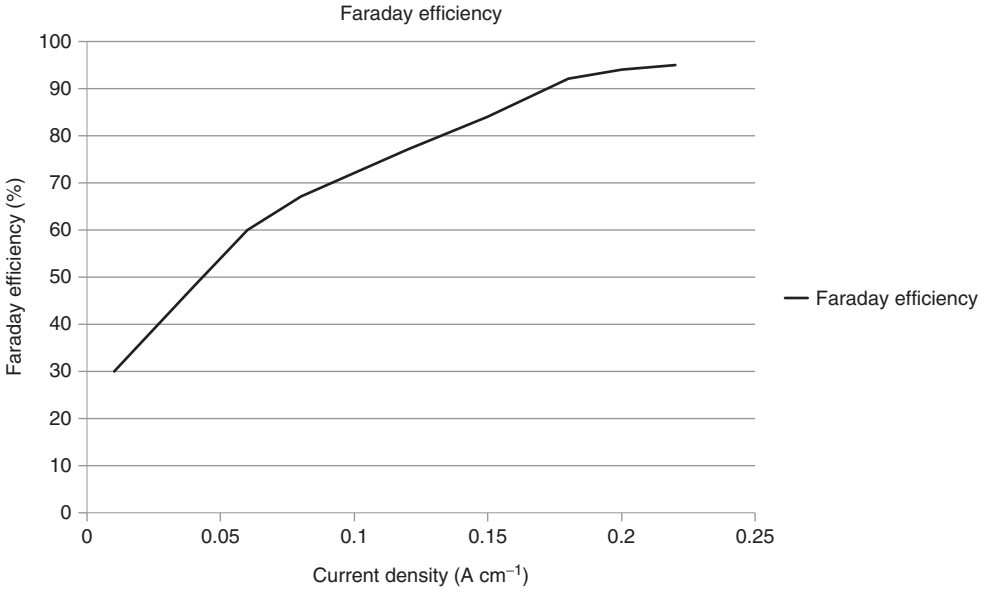

Figure 8.17 Calculated Faraday efficiency for a low-efficiency alkaline electrolyser.

transience-induced performance degradation can be observed on electrolysis systems. Both on–off operation and short time-scale events, that is dynamics events, demonstrated a substantial reduction in electrolyser hydrogen production compared to steady-state performances. A partial recovery of performances was illustrated when a rest period (several hours to days) was applied or when minimum current was maintained through the stacks. The author suggests that accumulation of bubbles of active sites may be responsible for the temporary reduction of efficiency of the alkaline electrolyser. However, the mechanisms responsible for these phenomena have not yet been identified and further work is required to understand the short-term degradation mechanisms of dynamic and intermittent electrolysis operation.

8.3.2.3 Impact of Intermittency on Reliability and Durability

While impressive advancements have been done in the last years on electrolysis system materials, cost reduction and efficiency, there is still a lot to achieve in terms of knowledge on the main causes of failures and degradation modes induced by intermittency. The main reason for this relative lack of knowledge may be that steady-state (or at least controlled) conditions are necessary (or at least preferable) to study durability, which is by nature incompatible with intermittent power sources. Furthermore, degradation testing is long, expensive and difficult to do at an industrial level. Only a few literature studies [23, 24], quantifying performance degradation with time are available but none of them clearly identify causes and aggravating factors related to intermittency.

Water electrolysis systems can suffer from degradation of different types over time and this can be encountered at stack, control system or BoP levels as described hereafter. The objective of this paragraph is not to describe in detail the degradation mechanisms, as it was already done in dedicated parts for each electrolysis technology, but only to recall the main factors and identify if they may be reinforced by intermittency.

Stack Degradation Mechanisms and System Failure The main mechanism of degradation in alkaline electrolysers is corrosion due to the very nature of the liquid electrolyte. The choice of the nature (KOH or NaOH) and the concentration of the electrolyte is always a compromise between performances (related to conductivity of the electrolyte) and risk of material corrosion. The relatively high operating temperature (typically 70–120 °C) of alkaline electrolysers greatly increases the effect of corrosion. Leaks of electrolyte to the outside also contribute to premature stack degradation and the risk gets higher when large electrochemical cells are used. The loss of integrity of diaphragms in the cells is also a main cause of failure of the stack, especially at high pressure. Failure of the diaphragm leads to cross contamination and then to risk of explosion due to mixing of hydrogen and oxygen gases. Finally, wearing of electrodes in an alkaline environment is an observed degradation effect, leading to reduced electrochemical performances.

According to Millet *et al.*, there are two main sources of performance degradation in PEM electrolysers [25, 26]. The first one is the incorporation of traces of

metallic cations released by tubing into the membranes. The migration of these cations to the cathode leads to increased overvoltage and reduced performance. The second source is irreversible processes such as the formation of hot points due to unequal repartition of current across the cells. This can lead to destruction of the membranes first and failure of the system itself as a consequence. Other phenomena such as membrane thinning with age, titanium (bipolar plate material) embrittlement by hydrogen and corrosion are also possible mechanisms leading to degradation of the stacks.

The control system and BoP of electrolyser systems, whatever the technology considered, are also subject to failure. As for the cells and stacks, it is fair to mention that the probability of these failures is increased by higher working temperature or pressure, high current and voltage involved and the nature of liquids and gases involved. However, regarding the BoP of an electrolysis system, there is no inventoried study specifically looking at the impact of intermittency on degradation.

In any case, most of the stacks and systems degradation and deterioration modes lead first to a decrease in efficiency and then to the failure of the system. However, the literature does not clearly provide a direct link between intermittent operation and components or system failures. Nevertheless, two deterioration factors can be intuitively considered as possibly strengthened by intermittent operation. The first one is the high mechanical stress induced by frequent start and stop, fluctuating flow rate and recurrent system depressurizations. Indeed, stacks are rather fragile mechanical assemblies that require perfect leak tightness both inside the stacks and towards the outside environment. Mechanical stress due to continuous pressure and temperature variations can favour degradation of seals and tightening parts, potentially leading to loss of containment and system failure.

The second aggravating factor is the high frequency of voltage and current set point changes across the stacks induced by intermittent power availability and renewable power source characteristics. These variations may also generate stress on both the electrolysis stacks and the power electronics, which can lead to early degradation and failure of these components. Similarly, forcing repeated stand-by conditions on the stacks may have an impact on electrode degradation although there is no clear demonstration of it as yet and research on this topic still needs to be performed.

However, despite all the interrogations still to be answered on the impact of intermittency and the lack of understanding of the mechanisms, it is generally accepted that integration of electrolysis with renewable source does not induce dramatic acceleration of degradation. According to [26], intermittent testing realized with a PEM electrolyser over 3000 h did not show any significant loss of performances. The use of fast-fluctuating input power had no significant effects on the electrochemical performances.

It is often mentioned in the literature that alkaline electrolysers might be more impacted by intermittent operating conditions. Petipas *et al.* [27] refer to a test realized with an alkaline electrolyser showing that the degradation rate increases from 3 $\mu V\,h^{-1}$ under steady-state operation to more than 10 $\mu V\,h^{-1}$ under on–off

operation while PEM electrolysis degrades slower under both steady and transient operations. Despite this commonly accepted fact, there is no systematic study to confirm this allegation from an electrochemistry and system standpoint.

From the available literature, it seems fair to say that the detrimental effects of intermittent operation, frequent start, fluctuating input power and stop and low duty operation have not received enough attention from the water electrolysis community. For any industrial process, reliability and durability are critical in order to ensure sufficient equipment lifetime and thus limit the total cost of ownership (TCO) of a technical solution. Although research work is still required on that subject, past and ongoing hydrogen demonstration projects can give an idea of the main failures or difficulties that were encountered in the field. A number of problems that occurred in relation with alkaline or PEM electrolysers were indeed reported in several articles, although once again, in most studies, no real analysis of the cause is available. Among the different difficulties that are repeatedly mentioned in experienced feedback, the following ones can be highlighted:

- Stack degradation and membrane deterioration (no systematic analysis of the root cause).
- Safety problems with the alkaline electrolytes due to leaks.
- Problems with intermittent and fluctuating power sources such as delayed reaction.
- Difficulties with starting the system after shutdown, especially with cold weather. This can be problematic as electrolysers directly connected to renewable sources may not be installed in a controlled-temperature room and may be frequently stopped when no power is available.
- Extensive maintenance due to insufficiently mature parts of the system in the used conditions.
- Freezing of the membranes in PEM during winter.
- Very rapid stack degradation in some cases and limited warranted lifetime by the supplier.

This list denotes a lack of reliability of components and system, which is probably due to insufficient maturity of (i) electrolysis systems and (ii) their integration with renewable energy sources. Although most of the problems seem easily preventable, it requires technological improvements that will bare a cost either at energetic or economic level.

8.3.2.4 Specificities of High-Temperature Steam Electrolysis

Even though HTSE is still considered in development, it depicts specificities when confronted with intermittent power conditions due to the fact that it operates in the temperature range 700–800 °C. As for liquid water electrolysis, efficiency is impacted by the variable power input and system temperature plays a critical role. Following a system shutdown, for example, the system must be heated up from a low temperature up to the operating temperature before applying any power. This start-up phase may be quite long if the temperature of the system drops relatively low. Once operating temperature is reached, both electric (due to the

renewable source) and thermal (due to the Joule effect) intermittencies occur due to the variability of the power source. It is easy to understand that the impact and dynamics involved are very different from those encountered by low-temperature water electrolysis. Indeed, as presented in Chapter 6, three operating modes exist depending on the operating voltage:

- *Endothermic mode*: operating voltage is below the thermo-neutral voltage so the heat requirement is not satisfied and the temperature decreases.
- *Thermoneutral mode*: operating voltage is at thermo-neutral voltage so the heat required equals the heat produced by the Joule effect and the temperature remains stable.
- *Exothermic mode*: operating voltage is above the thermo-neutral voltage so the Joule heating exceeds the heat requirement and the temperature increases.

The thermal variation of the system will consequently impact the operating mode, making the control of the system rather difficult. The main issue related to the variability of temperature is the induced mechanical stress for the electrolysis cells. The correlation between thermal gradient and failure was shown for solid oxide fuel cell (SOFC) [28] and, due to the similarities between technologies, the conclusion is assumed to be applicable to HTSE.

The existence of three operating modes combined with the power variability of the renewable source is a real challenge for high-temperature electrolysis. To avoid degradation and loss of efficiency, the electrolysis system must be operated close to the thermo-neutral voltage. To allow this, either a restricted operating range or a smart operating and control strategy must be implemented at the system level. This has inevitably an impact on the system, design and efficiency.

The main degradation mechanisms that will impact the electrodes, solid electrolyte, interconnects and contact layers are Chromium (Cr) poisoning, corrosion, delamination, contact losses and loss of tightness. As for conventional water electrolysis, these mechanisms may be reinforced by operation intermittency, especially as it induces temperature and pressure variations. Nevertheless, it is demonstrated in [27] that the solid oxide electrolysis cell voltage degradation rate was not impacted by transient operation during a 600 h test and remained stable at 40 $\mu V\,h^{-1}$. Transient operation was also validated [29] as the different load cycling applied to solid electrolysis cells did not lead to additional degradation for the tested conditions when compared to steady-state operation.

As a conclusion, further work is still needed to evaluate the clear impact of energy intermittency on hydrogen generation systems by water electrolysis. Scientific studies in laboratory environment tend to show that electrolyser systems are compatible with fluctuating conditions over a long period of time. However, it is only by running demonstrations in real conditions and over a sufficiently long period of time that the impact of variable operating conditions will be fully quantified.

8.3.3
Improvements on Design and Operation to Manage Intermittency

From the information presented in the previous paragraphs, it is now quite evident that renewable and intermittent power sources impose some specific requirements on electrolysis systems design, operation and, consequently, have a strong impact on their performances. Design choices at stack and system levels as well as smart operating strategies can be adopted to reduce the detrimental impact of intermittency.

8.3.3.1 Improvements on System Design

A lot of research has been done recently on improving electrochemical performances of alkaline and PEM electrolysis such as better catalyst deposition on electrode surfaces or improving system efficiency by designing high-pressure stacks. This is especially true with the development of advanced alkaline electrolysis seeking to increase current density (from 0.3 to 1 A cm^{-2} [30] demonstrated at laboratory scale), operating temperature (from 80 to 150°C) and pressure (from a few atmospheres to 30 bars). Most of these developments will of course also improve performances when intermittent operation is considered. Nevertheless, specific innovative technical modifications could be implemented as well in order to adapt to renewable energy constraints. Some of them have already been applied by electrolyser manufacturers or systems integrators.

First of all, the integration of electrolysis with renewable source may be improved at the electrical level. As seen before, any power transformation between source and stacks reduces the overall efficiency of the system. Therefore, specific work can be performed on the electrical configuration of the system and the development of components to limit the number of power transformations and improve their efficiencies. As an example, direct powering of stack with DC from PV panels can be considered to enhance performances by avoiding one or several steps of power transformation. This implies adapting the output voltage of solar panels to the voltage range of the electrolysis stack. Nevertheless, as each renewable source and each power plant installation is specific in terms of electrical characteristics (especially voltage level), it quickly becomes impossible to standardize solutions and then very difficult to reduce costs. The Wind2H2 project [31] at National Renewable Energy laboratory, which aimed at integrating wind turbine and PV arrays with an electrolyser, showed that direct coupling with PV demonstrates higher efficiency than a PV system including power electronics when solar irradiance is low (below 500 W m^{-2}). Fingersh [16] also showed that it is possible to efficiently connect electrolysis systems to a variable-speed wind turbine without additional power electronics and thus achieve high efficiency and cost reduction. In reality, one power transformation step is almost always necessary when using standard commercial electrolyser. When considering a system integrating several other components (loads, batteries, fuel cell, etc.) with an electrolysis system, finding the optimal electric scheme becomes even more important and the options more numerous.

Another way to improve overall performances of an electrolysis system is to take advantage of its capacity to handle overload. As stated before, when connected to a renewable source, electrolysers are required to run intermittently at partial load and sizing becomes a very important factor for techno-economic optimization. Instead of sizing the electrolysers for peak input, which may happen scarcely, capital expenditure can be minimized by using smaller electrolysers able to run in overload for short periods of time (several minutes). Both alkaline and PEM electrolysers can run in overload as long as the additional heat generated can be tolerated. However, power equipment and BoP must obviously be sized for overload, which represents additional cost.

It has been mentioned previously that the impact of BoP on the total electrical consumption of a system can become extremely important at partial load. Thus, specific consideration must be given to design and adapt auxiliary component consumption in a hydrogen production set point in order to reduce its impact at low load. Innovative design can also lead to strict simplification of auxiliaries to reduce their power consumption to a minimum.

As seen before, temperature is one of the main parameter influencing electrochemical efficiency. It is also a parameter that is strongly impacted by intermittency of available power. Specific work conducted on thermal management can therefore allow improving general performance of the system. Better thermal regulation can be simply realized by insulating the electrolyser, which would be beneficial in stand-by mode or when no power is available. If waste heat at elevated temperature is available at no cost, stacks can be maintained at their nominal temperature to ensure maximum efficiency. Industrial waste heat recuperation or integration with other hydrogen components (fuel cell or hydride storage) can allow this optimization but this will not be effective at no cost.

The Hbox solar [32] manufactured by ITM Power is an example of electrolysis system integration and optimization of design for a specific application. Hbox solar is a 1.3 kW passive PEM electrolyser, which generates 14 bar hydrogen gas using a direct DC–DC converter between a solar panel and the electrolysis stack. BoP was also optimized by developing, for example, a self-pressurization design limiting the number and the consumption of auxiliary components. It also includes a maximum power point tracking (MPPT) controller for the available PV input through a proprietary control algorithm. A thermal management system limits the temperature decrease of the stacks after darkness or bad weather, leading to improved performances at start-up. This design allows for a very high overall system efficiency, which goes up to 4.5 kWh Nm^{-3}. This value can be compared to 6 or 7 kWh Nm^{-3} [33] for conventional PEM systems of this size when connected to PV modules.

Besides these design modifications, a modular conception of electrolysis systems is also a relatively easy way to provide a certain level of load flexibility without modifying the conception or the environment of the stacks. In that case, each stack can be designed to have little flexibility but the multiplicity of stacks makes the overall system very much adjustable with regard to the set point. This allows for operating each stack close to its nominal point and then improving overall

efficiency. However, this configuration cannot offer full flexibility and will only allow step increase of the system load.

In any case, improved system integration requires the most appropriate components at the optimal size, beginning by the stacks themselves. For large-scale production systems, that is electrical power of tens of megawatts, large-scale stacks are required to reduce the cost of manufacturing and to simplify systems. However, this phase of scale-up may be difficult and, as of today, there are only a few companies offering large-scale equipment. This is especially true for PEM technology for which large-scale systems are usually a combination of smaller-size elements, which limits the cost reduction by the scale effect (although it favours cost reduction by volume effect). Finally, any integration of electrolysis with renewable power will require properly identifying the function and the objective of the hydrogen system to offer the best system for each application.

Of course, all of these system improvements must always be done keeping in mind the TCO of the system. Improvements are always a trade-off between cost and improved performances in order to lower the TCO of the system for a given application.

8.3.3.2 Improvements on Operating Strategies

When considering stable load electrolysis production, there is usually only one way to run a system, which is at the nominal operation set point. However, when considering intermittent operation, the ways of running the system are numerous and the choice becomes crucial. Indeed, as stated by Gahleitner [33], the operating efficiency and the system lifetime are mainly influenced by the power management strategy. This is even more important when the number of electrolysis stacks to manage increases. Indeed, when composed of several stacks assembled in a modular way, each one being able to be controlled individually, many different combinations exist when the global system has to satisfy a given set point. Figure 8.18 illustrates the multiple operating possibilities offered for an electrolysis system depending on its conception.

As an example, Muyeen *et al*. [34] evaluated a novel switching strategy for a hydrogen production system powered by a variable-speed wind turbine and composed of 10 electrolysis units individually controlled. It was shown that this strategy can help units working in full load and thus increases overall system performances and lifetime.

As temperature has a strong impact on the efficiency of the system, thermal management can be of great interest to improve performances. Advanced strategies to run the stacks can, for example, take into account the temperature of the stacks in order to optimize their performances. Particularly for HTSE, it was mentioned previously that the operating strategy must be strongly linked to the stack temperature to limit degradation and ensure high efficiency.

The repeated start and stop sequences anticipated for an intermittent operation of electrolysis also leave some room to improve the management of stand-by periods. Specific strategies can be imagined to allow for quick start and stop with

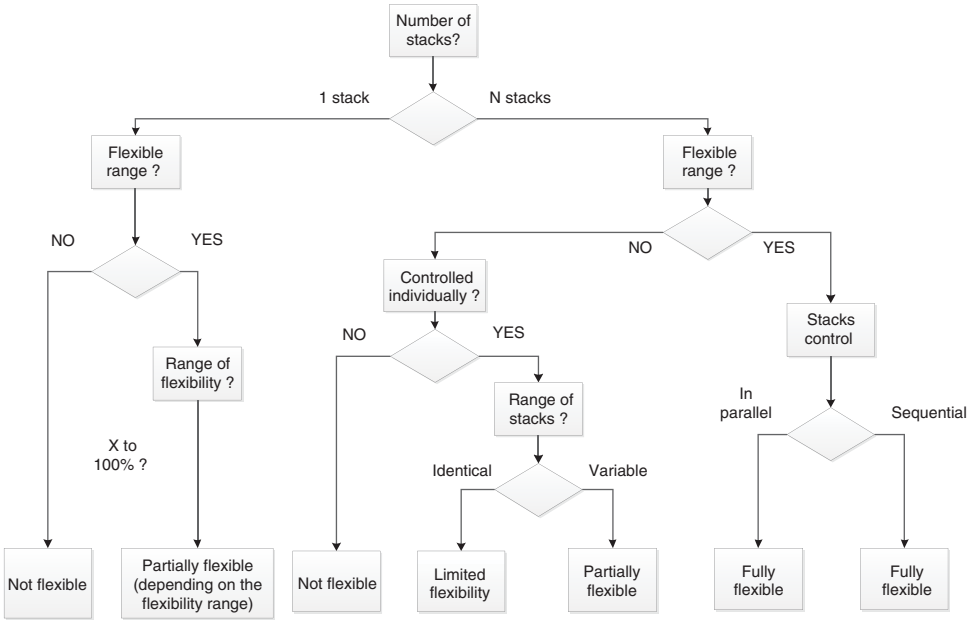

Figure 8.18 Stacks control multiple possibilities.

reduction of the induced loss of power or hydrogen. For instance, a smart management of a multi-stack configuration, including predictive control, may allow avoiding stack shutdown by adapting the strategy to the forecasted available power for the electrolysis systems.

Working on stack stand-by management is all the more important given that experimental work reported in [22] seems to show that limiting on–off sequences, or imposing a minimum shutdown time of several hours, may improve long-term performances compared to repeated start–stop operation. Although no specific mechanism has yet been identified, it was suggested that imposing a minimum current through electrolysis stacks seems to limit the transience-induced degradation. Research work on efficient operating strategies to limit the degradation of electrolysis stacks and systems is critical to improve durability of any electrolysis system. It is also worth mentioning that most electrolysis systems manufacturers carry out specific design work to allow longer time in stand-by mode under pressure. This would allow faster start-up but requires innovative design to avoid safety issues due to oxygen and hydrogen gas mixing due to the crossover in the membrane.

For certain applications, hydrogen production, storage and, finally, usage systems can be integrated in combination with a short-term storage means such as batteries to improve performances. In this case, the overall energetic system strategy becomes all the more important as the system gets more complex. Numerous energy management strategies can be possible and system performance optimization depends on the involved components (renewable sources,

storage technologies, loads to satisfy), their size and the objectives to be fulfilled by the overall system. For instance, the capacity of the short-term storage must be sized in accordance with the operation requirements (minimum current or minimum stop time, for example) of the electrolysis system. The size of the electrolysis system, the intermittency and the load to power will also influence the optimal size of the battery bank. The optimization of operating strategies is a complex multi-factor and multi-component problem. In any case, the operating strategy of the electrolyser itself should always be optimized with regard to the overall system within which it is integrated. A number of different strategies for renewable hybrid hydrogen systems with hydrogen and batteries as storage media can be found in the literature [35–37]. As examples, the following operating modes for the overall system are worth mentioning:

- *Power demand satisfaction*: the overall strategy makes sure that power demand is always satisfied. Other criteria such as economic or efficiency are secondary.
- *Maximum efficiency*: the system tries to operate each component at its maximum efficiency point at any given time.
- *Hydrogen production priority*: any available power compared to a load to satisfy is directed to the electrolyser.
- *Battery protection*: this operating mode tends to protect the batteries from intensive use to prevent early degradation.
- *Fuel cell protection*: this mode tends to protect the fuel cell from intensive use to prevent early degradation.
- *Electrolyser protection*: this mode tends to protect the electrolyser from intensive use to prevent early degradation.

Each system strategy applied determines individual strategies for each component and is based on techno-economic criteria. For a given application, the operating strategy must find the best compromise between load satisfaction and total cost (electricity consumption, protection of components, etc.).

8.3.3.3 Which Technology Best Suited to Intermittent Sources?

As dynamic operation has not been necessary in former industrial applications, it is often believed that electrolysis is not suited for direct coupling to intermittent power sources. It has been shown before that even though technical challenges, technology requirements or adaptation needs exist, there are no insurmountable problems that would prevent electrolysis to be used in integration with renewable power. Integration of electrolysis with renewable power has been demonstrated in several projects as it will be illustrated in the following section. However, allowing intermittent operation without compromising too much on performances may lead to increased complexity for the system and its operation, thereby leading to higher cost of the solution and reduced overall efficiency.

With regard to coupling to intermittent renewable energy sources, PEM electrolysis is often referred to as the preferred technology in various literature studies [24, 25, 33]. However, due to very different technological maturities and insufficient experimental feedback, it still remains difficult to make a clear statement. In

order to initiate a qualitative comparison between electrolysis technologies with regard to intermittent operation, Table 8.2 presents a few selected performance indicators and how each electrolysis technology positions itself.

Today, both alkaline and PEM electrolysis can be considered as suitable for integration with renewable energy. Even though maturity, cost and reliability remain favourable to alkaline technology, PEM electrolysis seems to have a slight advantage from a technical point of view in terms of performances and when integration with renewable energy is considered. However, very little experience is yet available to understand the real impact of intermittency on the performances and durability of each technology. Furthermore, integration schemes are numerous, better configurations still need to be demonstrated and optimized operating strategies may show that alkaline technology remains as suited as PEM electrolysis for renewable source coupling.

HTSE does not yet offer the same maturity. The high operating temperature and the associated thermal inertia do not seem to favour the intermittent operation. However, for some specific cases, especially when waste heat at appropriate temperature is available and with a system based on a modular conception, there is no counter indication showing that HTSE could not be powered by a renewable source [27, 29]. Work presented in [27] suggests that modular operation of high-temperature electrolysers is possible and therefore no specific issue would prevent powering by intermittent renewable source. Finally, the anticipated reversibility of HTSE into fuel cell mode may provide a competitive advantage to HTSE for renewable electricity storage when compared to conventional water electrolysis.

It is often considered that water electrolysis has limited flexible capacity, which is not true. Nevertheless, the dynamic operation has an important impact on performances and needs to be further studied. Some improvements (at system level and on operating strategies) need to be done to ameliorate overall efficiency of the system and limit degradation and required maintenance in order to improve reliability and durability. To acquire sufficient experimental feedback,

Table 8.2 Electrolysis technology comparison.

	Alkaline technology	PEM technology	HTSE technology
Electrolysis efficiency	−	+	++
Ease of thermal management	+	++	−
Quick start-up	+	++	−
Overload capacity	+	++	++
Low duty capacity	+	++	++
Auxiliaries consumption	+	++	+
Hydrogen purity at stacks outlet	+	++	++
Technology maturity	++	+	−
Reliability	++	+	−
Degradation due to intermittency	+	+	+
System capital cost	++	+	−

several demonstration systems have been imagined and studied over the past years. The following part will give an overview of these demonstrations and a short description of the systems studied.

8.4 Integration Schemes and Examples

Several demonstration plants integrating hydrogen production by water electrolysis with renewable power sources have been realized (some of them are still in operation) or are being planned. In the 1980s and 1990s, a number of projects were started in Germany but more recently, demonstration projects have been initiated in different countries worldwide. Observed integration schemes of hydrogen with renewable energy sources can be very different and every case study can be considered as unique.

For each considered application, the integration of electrolysis with renewable energy requires some additional components in order to fulfil the function the system is designed for. These components, illustrated in Figure 8.19, typically are as follows:

- *A hydrogen storage system*: the actual storage of energy under the form of hydrogen can be done in gas phase (from ambient pressure to 700 bars), liquid phase (necessitating energy to cool down the hydrogen) or solid phase (absorption in metal hydrides, for example).
- *A fuel cell system*: to produce electricity back from stored hydrogen.
- A power conditioning system including power transformation and energy management system.
- A connection to the electric grid.
- A short-term energy storage system (such as batteries).
- A downstream hydrogen-handling system (such as a fuelling station, for example).
- An electrical load to satisfy.

The different applications of hydrogen production with renewable energy can be divided into off-grid (autonomous) and grid-connected applications. For each category, the main components and specificities are reviewed and a few representative projects are mentioned and shortly described.

8.4.1 Autonomous Applications

Off-grid applications or autonomous applications are those in which electrolysers and renewable energy sources are not connected to the main electrical grid. In these applications, hydrogen produced by water electrolysis can be considered as completely renewable as the full amount of electrical energy leading to hydrogen production is originated from a renewable source.

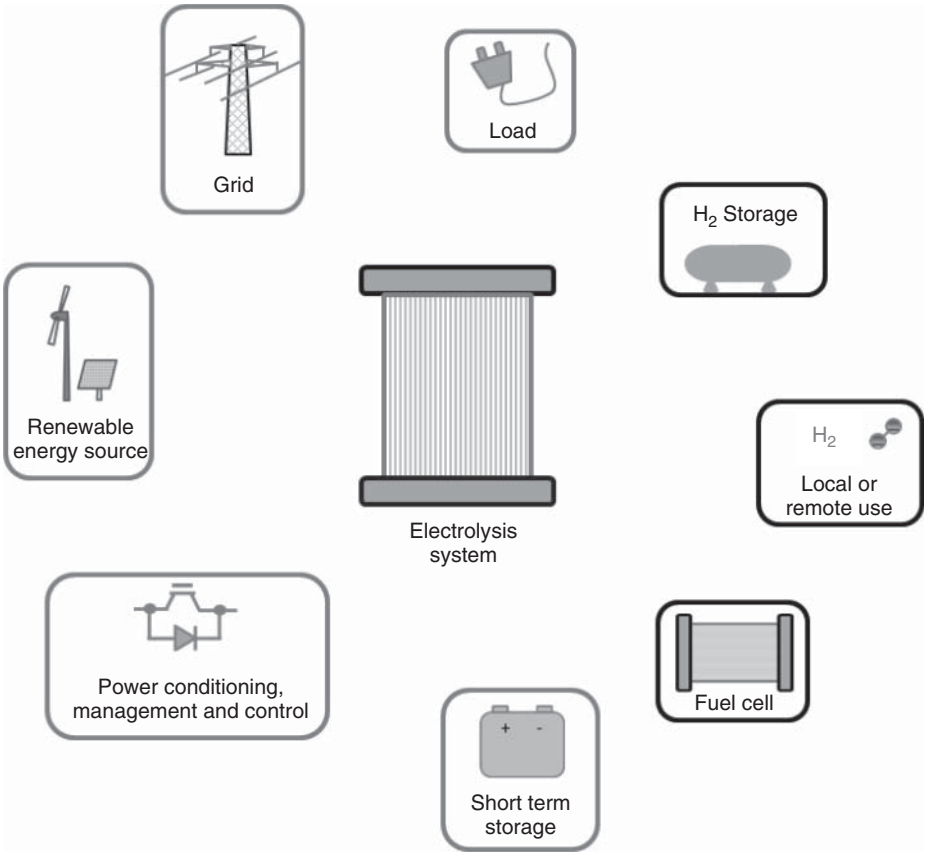

Figure 8.19 Additional elements for integration of electrolysis with renewable energy.

Off-grid applications can be divided into two main configurations as described in the following two sections.

8.4.1.1 Production of Renewable Hydrogen

In this first configuration (Figure 8.20), hydrogen is produced to be used for its chemical properties rather than for electricity production with a fuel cell. Hydrogen can be used locally in a variety of industrial applications (chemistry or metallurgy, for example) or directly as a fuel (locally) for heating or transportation. Renewable hydrogen can also be stored in gas, liquid or solid form and transported to remote utilization locations (industry or hydrogen fuel station) or even conveyed through pipelines to the end users.

R&D work on this configuration has been done mostly by simulation and has focused on PV and wind systems as the renewable source. In such cases, the electrolyser is directly exposed to the variable power supply of the renewable energy source and an AC/DC or DC/DC power converter must be part of the system and

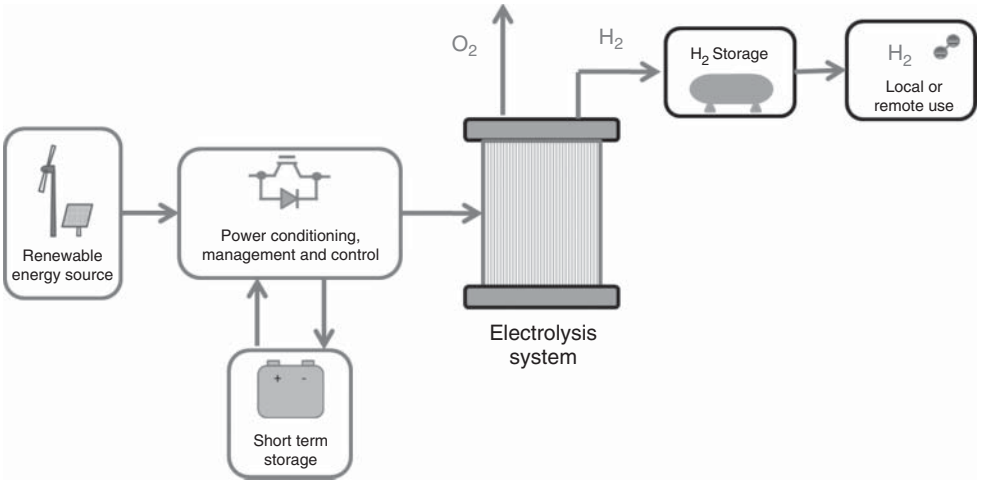

Figure 8.20 Schematic diagram of grid-independent hydrogen production.

able to support fast power transience. A battery bank is often added to the system to facilitate power transience absorption as most of the existing commercial electrolysers are not designed to handle extremely fast power changes.

There are relatively few existing demonstrations of this type even though increasing interest in 'power-to-gas' applications may boost the production of renewable hydrogen. This configuration could indeed draw growing attention towards the production of green hydrogen both for industrial applications looking at limiting their environmental impact and for mobility applications to reduce their dependency on hydrogen produced by fossil fuel reforming. The anticipated deployment of hydrogen fuel cell vehicles in the near future will generate a tremendous increase in hydrogen demand that will need to be fulfilled by green hydrogen from electrolysis (and not from steam methane reforming) to remain sustainable.

In the future, hydrogen will also offer new ways of benefiting from sustainable but isolated worldwide renewable resources (off-shore wind and desert sun especially). Today already, in countries where available land is limited and associated cost is high, developing off-shore wind platforms is increasingly considered. However, in this case, grid connection can become problematic both from a technical and economic point of view. Local off-shore production and storage of wind-hydrogen and its transportation by boat to the land can then be seen as an alternative for bringing energy on shore from the ocean.

8.4.1.2 Stand-Alone Power System with Hydrogen as Storage of Electrical Energy

The second off-grid configuration (Figure 8.21) can be adopted for autonomous systems where the main grid is not accessible, so electricity needs to be generated on site. Stand-alone power supply systems are already being used around the world in remote areas and the use of renewable energy within these systems is growing

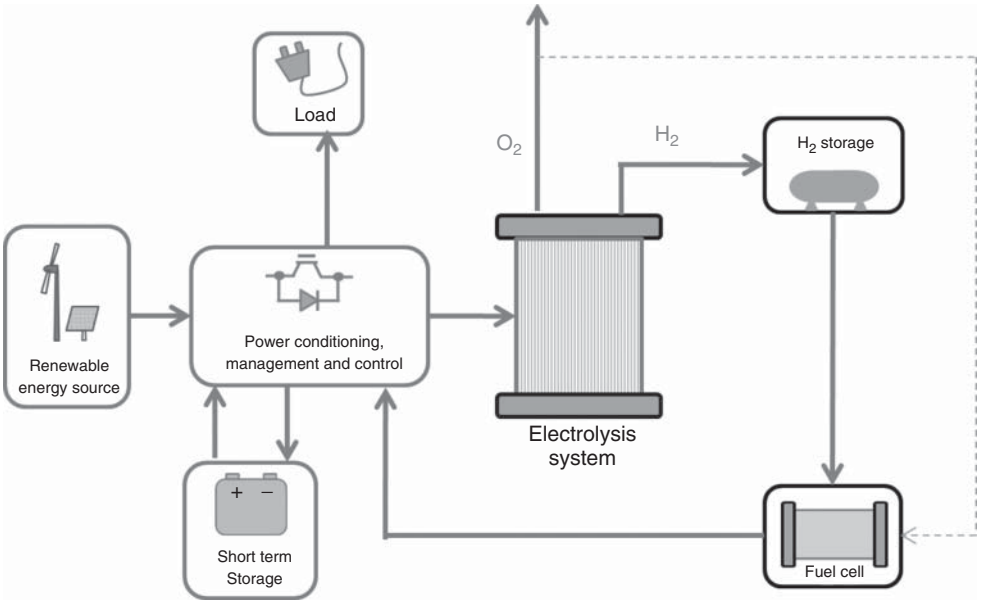

Figure 8.21 Schematic diagram of grid-independent integrated renewable-source hydrogen system.

due to rising fuel prices. Indeed, although they could be conventionally powered with diesel generators, renewable sources coupled with a hydrogen chain can be a viable alternative to allow full autonomy and reduced environmental impact at competitive cost. Wireless telecommunication stations or high-mountain refuges are typical remote area loads that can be considered for such grid-independent installation. Depending on the design of the overall system, hydrogen can be seen either as the main power source or as the back-up power for the renewable source. These integrated hydrogen systems typically include an electrolyser, a storage tank and a fuel cell to supply electricity to the load when the renewable source is not producing enough. To ensure availability of electric energy and thus load satisfaction, energy storage is an imperative and hydrogen storage can be seen as a viable option in certain configurations.

These renewable source–hydrogen configurations have been widely studied in the scientific literature. Most of the time, electrolysers are used in combination or in comparison with other storage media such as battery banks in order to optimize the design of the storage system from a techno-economic perspective. Systems are usually relatively small as considered stand-alone applications are most of the time small remote electrical loads of one to a few kilowatts [38].

In these systems, the excess renewable energy compared to load requirement is used to produce hydrogen. Hydrogen is stored and used later to produce electricity through a fuel cell in order to feed the load when renewable energy is not sufficient (on a cloudy day or at night, during low wind conditions, to compensate seasonal

loss of PV production). A short-term electricity storage means (such as battery) is usually added to deal with fast power (load or production) variations. The power conditioning and management system must be able to control the energy flow between the renewable sources, the electrolyser, the loads, the fuel cell and in certain cases the battery bank.

Alternatively, produced hydrogen can also be used for other applications such as local processes, building heating or for fuel cell vehicles through a fuelling station.

In these configurations, reported applications show that mainly wind and PV power sources are coupled with electrolysis systems. However, small-size hydraulic power and geothermal power stations have also been studied in the literature [39, 40]. The operating conditions of such systems fluctuate greatly as they are imposed by the variability of the wind and solar resources but also by the intermittency of the load. The connection to the power source can be carried out by means of a DC/DC power conditioning stage in the PV case or an AC/DC or DC/DC for the wind systems. For stand-alone systems, a hybrid combination with batteries is often seen as a viable opportunity. Batteries are used for short-term storage and hydrogen storage deals with long-term storage (e.g. seasonal in the case of PV energy) to overcome battery self-discharge. In this case, batteries are also used for transient operations.

Several demonstration projects corresponding to such off-grid applications have been running since the 1990s and it can be anticipated that new projects will continue to arise. Table 8.3 gives a non-exhaustive but representative list of demonstration projects that have been running or are currently in operation in different countries.

An exhaustive review of demonstration and pilot plants is available in [33].

Table 8.3 Off-grid demonstration projects.

Project (start date)	Renewable source	Electrolyser technology	Status	Country	References
Stralsund Project (1990s)	Wind PV	Alkaline (25 kW)	In operation (laboratory)	Germany	[41]
PHOEBUS (1993)	Solar	Alkaline (26 kW)	Out of operation	Germany	[42]
Utsira (2004)	Wind	Alkaline (50 kW)	Out of operation	Norway	[43]
HARI (2004)	Wind PV Micro-hydro	Alkaline (36 kW)	In operation	United Kingdom	[17]
PURE (2005)	Wind	Alkaline (15 kW)	In operation	United Kingdom	[44]

8.4.2 Grid-Connected Applications

For configurations considered as grid-connected applications, depending on the integration scheme, both electrolysers (for power consumption) and renewable sources (for power injection) can be connected to the electric grid. Three specific cases are reviewed in this section.

8.4.2.1 Production of Renewable Hydrogen with Grid Assistance

In this first configuration (Figure 8.22), the final objective of the electrolysis system is the production of hydrogen. When grid power is available, it is then possible to eliminate problems related to intermittent operation by combining renewable power with input power from the grid. Even though the electrolysis system does not operate in an intermittent way, some specific arrangements must be done that may not be required when an electrolyser is only connected to the grid. In particular, power conditioning and control system must enable the electrolyser to receive constant power input by combining input from an intermittent source and input from the grid. The energy management system should be designed to facilitate the control of the overall system.

In this configuration, the electrolyser can be operated at a constant power and is therefore not affected by intermittent operation. If available power from renewable source ($P_{renewable}$) is lower than the desired electrolysis power ($P_{electrolyser}$), then missing electricity is supplied by the electric grid. When $P_{renewable}$ is higher than $P_{electrolyser}$, then the electrolyser is only powered by the renewable source. However, in such a case, the surplus of renewable energy must be downgraded to comply with required equilibrium between electricity production and consumption. This task has to be fulfilled by the power management system, more specifically the power point tracking component for PV or wind energy systems, for example. Downgrading the produced power from a renewable source is limited

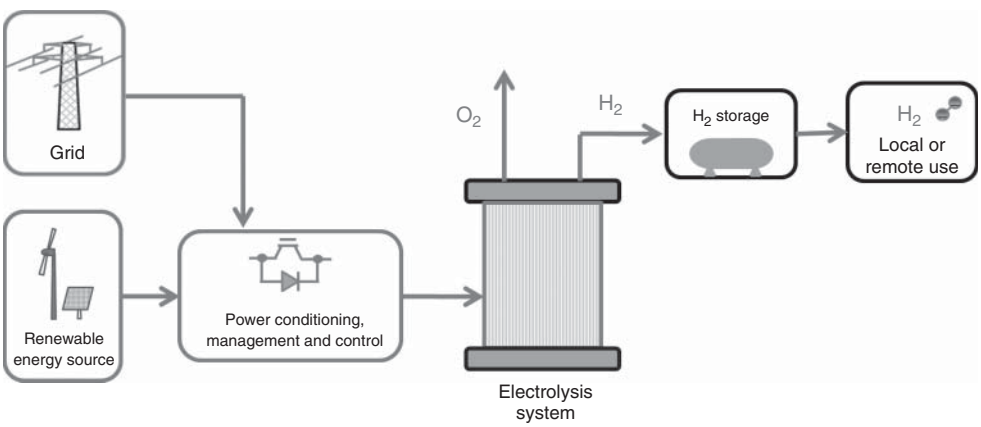

Figure 8.22 Grid-assisted hydrogen generation.

(typically down to 30% minimum for PV, for example). Designing and sizing of the electrolyser system are ideally done based on the peak renewable power to avoid having to shut down the installation due to excess renewable power.

The main advantage of this configuration, besides the fact that intermittent operation is avoided, is that the capacity factor of the electrolyser may reach a value really close to 100%, the only down-time being potentially due to maintenance. This leads to improved economics and reduced production cost of hydrogen. On the other hand, one drawback of grid-assisted hydrogen production is that the hydrogen produced is not 100% renewable and cannot be marketed as such. To this regard, there is no existing regulation or directive giving the methodology to characterize a hydrogen molecule that would have been partly produced from renewable energy. Some specific research and normalization actions are required and are being pursued in order to evaluate and quantify the renewable character of hydrogen and generate guarantees of origin for green hydrogen.

8.4.2.2 Electrolysis for Renewable Energy Storage

In this second configuration (Figure 8.23), the electrolysis system is only powered by renewable energy when the electricity cannot be absorbed by the grid, that is, when there is a surplus of electricity (demand lower than production) or a congestion problem at the grid level. This is also called renewable energy peak shaving. In this configuration, the electrolyser is subjected to the intermittent nature of the renewable source with all the implications that were described previously in this chapter and with the need for a short-term storage means to handle fast

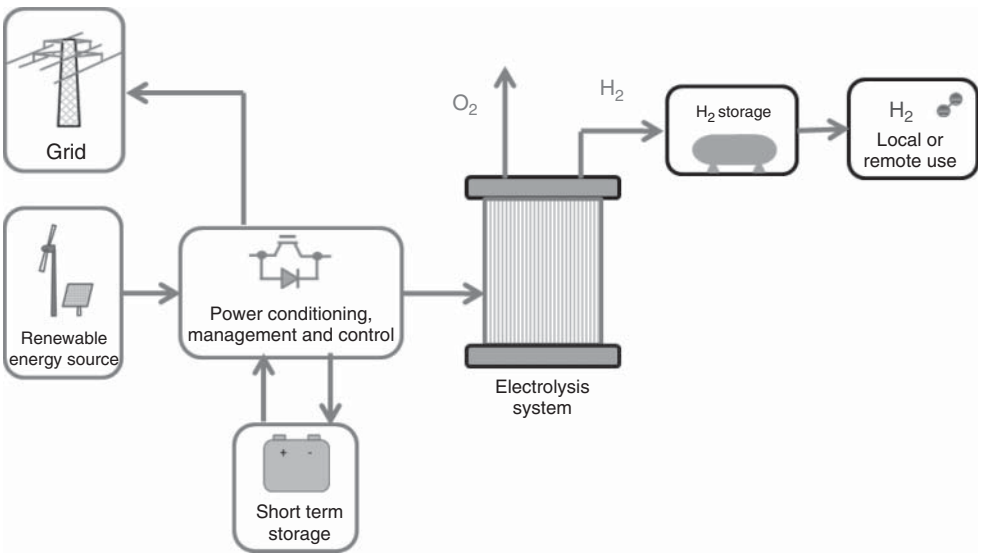

Figure 8.23 Renewable power storage.

power variations. This inevitably has an impact on the capacity factor of the electrolysis system, which is significantly reduced. As a consequence, an electrolysis plant, sized for a given quantity of available electricity will operate under its nominal capacity most of the time. This will affect the TCO of the solution. However, this is not necessarily unacceptable, especially if the global energy efficiency is an objective of the overall energy system or the considered geographical area (region, district, building).

A variation of this configuration is to operate the electrolyser at constant power and inject excess renewable power into the grid (base-load consumption). This is possible assuming that, at any time, the grid is able to absorb the remaining power. When available renewable power is lower than nominal electrolyser power, the hydrogen production system must adapt its operating set point and deal with power variation. Once again, designing and sizing are critical in that configuration and pertinence depend on the application and the objectives of the power and hydrogen system.

The French research project potential use of solid hydrogen (PUSHY) [45], federating actors of the green hydrogen value chain and funded by the French innovation agency Oseo (now known as BPI France), is an example of green hydrogen production for local industrial application. Its objective is to demonstrate the feasibility and viability of renewable hydrogen production with an electrolysis system connected both to a renewable source and to the grid. On the basis of technical and economic parameters, a decision must be made to use the electricity either for hydrogen production or grid injection.

For these first two grid-connected configurations, the use of produced hydrogen can be any heating, industrial or mobility local application. When stored, the hydrogen may also be transported to the required point of use.

8.4.2.3 Renewable Source, Grid and Electrolysis Integrated Energy System

A third integration scheme (Figure 8.24) for renewable energy and hydrogen production electrolysis is the utilization of a hydrogen energy chain (including production, storage and a fuel cell) to enable the injection of a constant or controlled power profile into the grid or into any electric load. When required, available renewable electricity (or from the grid in certain cases) is stored under the form of hydrogen and electricity is produced back later from hydrogen and oxygen in a fuel cell. In this configuration, the electrolysis system can be used to help the grid operation by participating in the instantaneous equilibrium between electricity production by power plants and consumption by the loads that needs to be satisfied at the grid level. In doing so, hydrogen production by electrolysis can contribute to the implementation of grid operation services. It can also facilitate the integration of renewable energy into the grid by reducing the impact of intermittency. Indeed, the stored electricity in hydrogen can be used to fulfil several different functions such as (i) peak shaving, (ii) production and injection smoothing or (iii) supporting renewable plants in meeting their power injection forecast required by the grid operator. In this configuration, the capacity factor of the electrolysis system depends on the service that the hydrogen energy storage system is

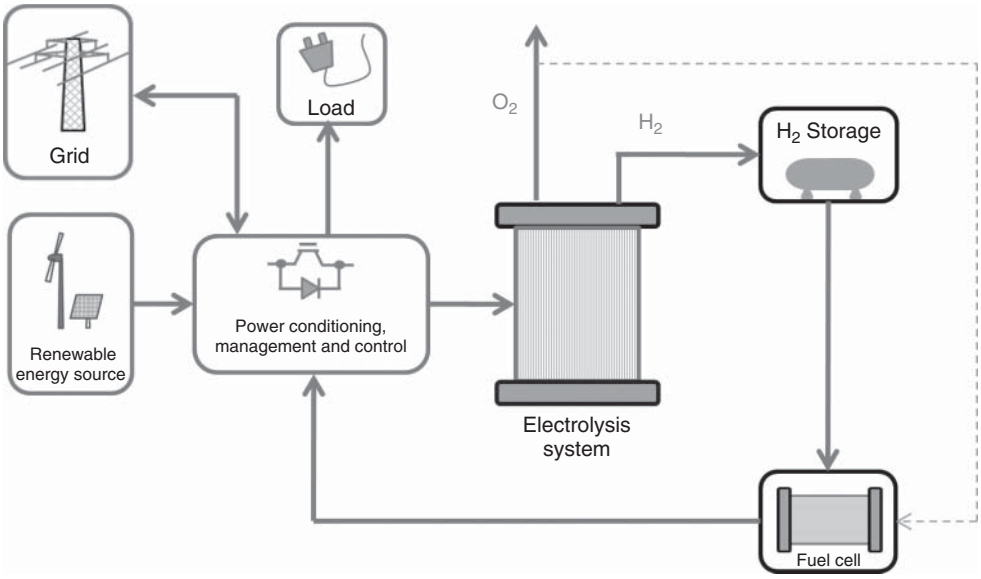

Figure 8.24 Integrated energy system.

supposed to fulfil. It may not be critical to maximize it as provided services can generate high revenues even for short periods of time.

The power conditioning and control system has an extremely complex function in this configuration. It should be able, based on various parameters, to direct electricity from the renewable source either to the grid (or a local load) or to the electrolysis system and be able to switch to the use of the fuel cell system as the main power provider when required by the application and corresponding power injection level. In some cases, the electrolysis system can also be powered totally or partly by the grid if favourable conditions (low electricity price, for example) are satisfied.

A variation of this configuration is the use of electrolysis in a local small-size grid (generally called micro-grid) at a local level (region, island or district) and operating independently from the main grid or being partially connected to it. Depending on the micro-grid characteristics, in combination with other short-term electricity storage systems such as battery hydrogen energy systems can be particularly useful for seasonal storage as it does not suffer self-discharge.

There are relatively few demonstration projects of hydrogen production by electrolysis integrated with renewable energy and connected to the grid. The Myrte Project [46] in Corsica, funded by the French government and the European Union, is an example of electricity storage using hydrogen under pressure for various electric grid applications.

Table 8.4 reviews a few demonstration projects representative of grid-connected integrated renewable hydrogen systems.

Table 8.4 Grid-connected demonstration projects.

Project (start date)	Renewable source	Electrolyser	Status	Country	References
Res2H2 (2007)	Wind	Alkaline (55 kW)	In operation	Spain	[47]
Wind2H2 (2007)	Wind	Alkaline (33 kW)	In operation	United States	[31]
	Solar	PEM (7 kW)			
Myrte (2007)	PV	PEM (60 kW)	In operation since 2012	France (Corsica)	[46]
Sotavento (2008)	PV	Alkaline (300 kW)	In operation	Spain	[48]
	Wind				
Pushy (2011)	Small hydropower	Alkaline (60 kW)	Design studies	France	[45]
Ingrid (2013)	Wind	Alkaline (1 MW)	Design studies	Italy	[49]

An exhaustive review of demonstration and pilot plants is available in [33].

R&D work carried out since the 1980s towards integration of hydrogen production by electrolysis with renewable energy as well as the various past and present demonstration projects validate the feasibility of such integration. Even though systematic analysis of the impact of intermittency was not realized, a number of lessons can be drawn:

- In almost all demonstration projects, PV and wind systems are the considered renewable source. A few demonstrations were realized with thermal solar but their number is limited although their size can be important.
- For most of the demonstrations, alkaline electrolysis was installed, although in recent years PEM electrolysis has been increasingly considered.
- Designing and sizing are the key to an energy-efficient integrated system.
- The design of a system depends on its location, power requirements and load to satisfy.
- Auxiliary units often represent an important share of power consumption and are often subject to a lack of reliability.
- Owing to the complexity of the systems, the control scheme and the operating strategy play a very important role.
- Safety is an important point as flammable gas is involved and its cost is not negligible.
- For all components, improvements are needed with regard to reliability, robustness and cost, especially due to the fact that the system is subject to fluctuating operation.

8.4.3
High-Temperature Steam Electrolysis Integration with Renewable Source

As already mentioned, high-temperature electrolysis shows limited maturity compared to alkaline and PEM electrolysis; therefore there is no existing demonstration project connecting HTSE with renewable power. The main specificity of HTSE being the need for heat source to vaporize water and potentially maintain the high operating temperature (about 800°C), integration with power sources will especially make sense when excess thermal energy is available. Concentrating solar power sources (solar tower, solar dish, solar parabolic and solar Fresnel) as well as geothermal power plants have been identified as the best candidates for integration with high-temperature electrolysis. Depending on the available waste heat temperature, integration schemes may vary and can be of different complexities. Within the electrolysis process, heat integration is of great importance to maximize the energetic efficiency of the overall system (Figure 8.25). PV and wind source can also be considered for integration with HTSE through the schemes presented previously but the efficiency is anticipated to be less as heat must be provided from another source. The connection to

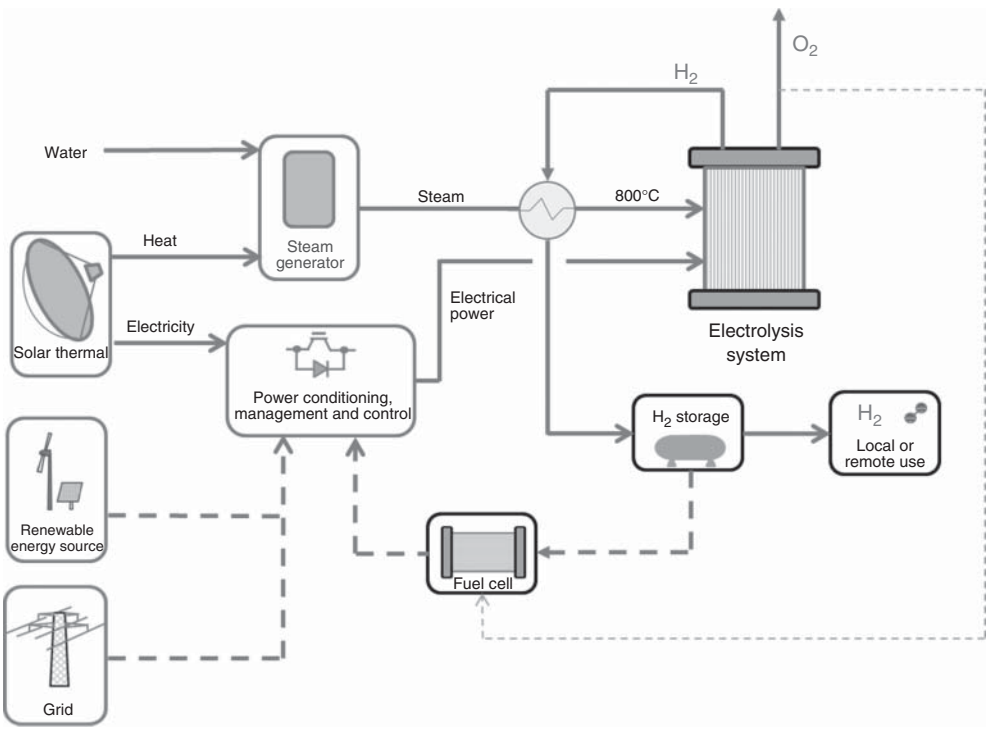

Figure 8.25 Integration of HTSE with renewable energy.

the grid or to an additional renewable source (with no waste heat available) can also be considered and the applications of hydrogen can be similar to those presented before. The system complexity related to high operating temperature should favour applications with minimum intermittency and maximum capacity factor.

To date, there are no demonstration projects of integration of high-temperature electrolysis with renewable energy due to the lack of technical readiness of the technology. However, in recent years, a number of R&D projects dedicated to intermediate-temperature steam electrolysis and HTSE have been carried out with a few of them specifically focused on integration with renewable sources. Among them, it is worth mentioning the following projects funded by the European Commission:

- *ADEL (http://www.adel-energy.eu/)*: this collaborative research project (ADvanced ELectrolyser for Hydrogen Production with Renewable Energy Sources) focuses on the development of cost-competitive, energy-efficient and sustainable hydrogen production based on renewable energy sources. Intermediate-temperature steam electrolysis (i.e. about 600°C) is considered in this project.
- *RELHY (http://www.relhy.eu/)*: this collaborative project focuses on the development of novel or improved, low-cost materials for their integration in efficient and durable components for the next generation of HTSE. Integration of HTSE with wind turbine and nuclear power is specifically considered in this project.

Along with the necessary research to consolidate performances, robustness and reliability of HTSE, its integration with renewable sources will continue to be studied in the near future.

8.5 Techno-Economic Assessment

The objective of this part is to provide an overview of future markets that could be addressed by electrolysis, specifically when integrated with renewable energy sources, and to give some insights on the different market sizes. Furthermore, modelling and simulation of such hydrogen-based systems are introduced in order to highlight the role they can play in techno-economic assessments.

8.5.1 Hydrogen from Electrolysis: Future Markets

As illustrated in Chapter 1, there are several markets that can already be addressed by hydrogen production from electrolysis. All these identified markets rely on the produced product from the electrolysis process (hydrogen). Several new markets are identified today that rely not only on the produced chemical but also on the particularity of electrolysis that uses electricity. For example, today, an electricity

consumer connected to the grid has indeed the potential to value the flexibility it can offer on its consumption. The objective of this part is to briefly introduce some of these new markets and to provide some insights into their economic potential.

8.5.1.1 Hydrogen for Off-Grid Applications

In the past, electricity supply in off-grid sites has been largely dominated by diesel generators. This solution presents, however, technical (reliability), logistical (diesel delivery) and environmental (CO_2, NO_x, fine particle emissions) challenges. Economic issues may also emerge from the rising cost of diesel. With the cost reduction of renewable energies such as PV and wind power, technical solutions for off-grid sites are switching to more green-based solutions. Today, systems hybriding PV and/or wind power with diesel generators are more common and have started leading the market [50]. Furthermore, cost reduction in energy storage technologies opens the way to new solutions entirely based on renewable energies. Depending on diesel cost, these solutions may be economically competitive in comparison to PV-diesel or wind-diesel solutions. Besides, 100% renewable energy–based solutions may be beneficial for sites with difficult access.

A recent study based on a report of Navigant Research (formerly Pike Research) forecasts that remote microgrid market will reach 1.1 GW by 2017 [51]. Moreover, revenues for off-grid base station power are expected to grow from $1.6 billion in 2012 to more than $10 billion in 2020. This shows that an important market growth (+21% in 7–8 years) is anticipated for off-grid applications.

Within this context, hydrogen can play an important role. It can be produced directly on the isolated site from wind or PV power and stored as gas or in metal hydrides. When the local renewable source is insufficient to satisfy the load demand, hydrogen can be used in combination with oxygen (pure oxygen or oxygen from the air) in a fuel cell to produce electricity. Hydrogen can in this case solve most logistical issues (no more need for fuel deliveries) with requirements for site visit only for maintenance of the electrolyser and the fuel cell. Furthermore, it is a non-polluting solution solving as well environmental issues encountered with diesel generators. Unlike batteries, which could also be used as a means to store electrical energy, hydrogen can be stored for long periods without or with very little energy loss (no self-discharge). Today, most researches are focusing on hybrid solutions between hydrogen and batteries with the objective to take advantage of the high efficiency of batteries, the ability of hydrogen to separate power and energy and the long-term storage of hydrogen. Challenges reside in sizing optimization of the different components and on the design of an optimal operation strategy [52–54].

8.5.1.2 Hydrogen for Mobility

Fuel cell vehicles have been drawing attention for several decades without a clear take-off. Apart from the cost of such fuel cell technology, the low penetration of fuel cell vehicles on the automotive market is often explained by the chicken and egg dilemma (no one buys a hydrogen car because there is no infrastructure to

supply hydrogen and no one builds infrastructures because no one drives a hydrogen car). More recently, several hydrogen mobility plans are being investigated in several countries (United States, Japan, Germany, United Kingdom, France, Italy, Norway, Sweden, etc.) with the objective to overcome this dilemma. Among them, the H_2 mobility initiative in Germany is promising to lead the development of hydrogen-refuelling networks in Europe with more than 400 stations planned in Germany for 2023. According to a study from a working group composed of vehicle manufacturers, utilities and electrolyser companies, fuel cell vehicles from about €30 000 could be on the market by 2020 [55]. More ambitious announcements from Honda, Toyota and Hyundai raise the spectre of vehicles on the market in 2015.

Hydrogen production from electrolysis is identified as a key technology. Electrolysis from renewable energy can indeed ensure a sustainable production of hydrogen from both an environmental and energy independence (in the sense country energy independence from importations) point ofview.

8.5.1.3 Power to Hydrogen – A Way to Provide Services to the Network

As seen in Section 8.2.1.2, integration of renewable and intermittent energies into electrical networks is raising technical issues that can impact their effective operation. In situations where the electrical grid can no further absorb a local production (low local demand, low or saturated transmission capacities), electrolysis can be used to consume locally this energy and produce hydrogen. As stated before, instead of storing this hydrogen in tanks (pressure, metal hydrides), it can be injected into the natural gas network offering an enormous amount of storage capacity. Indeed, the length of the gas pipelines and the flexibility on the gas pressure represent an important storage capacity. Several R&D projects are investigating the technical feasibility of such an injection of hydrogen produced from electrolysis into the gas network, including the maximum hydrogen content that could be considered [14, 56]. As stated in Section 8.2.3.1, it is also possible to convert this hydrogen into synthetic methane (methanation). With this extra step, a larger storage volume can be made available.

Another example of service that can be provided to the network by electrolysis is frequency regulation. Thanks to the recent development of fast-response electrolysers, they can be operated at partial load and can rapidly increase (or decrease) their operating point in order to quickly consume more power (or less power). From a network operation point of view, this rapid change in consumption is similar to a rapid change in production and can serve the objective of frequency regulation, which is a service remunerated by the grid operator. For example, an electrolyser Hydrogenics HySTAT™ provides frequency regulation on the Ontario network with fluctuations of its power consumption thanks to signals sent from the grid operator on a second-by-second basis [57].

8.6
The Role of Simulation for Economic Assessment

Economic assessments are determining investment decisions and are thus a very important step in the lifetime of a given project. Results of an economic assessment are highly dependent on assumptions of technical considerations. They determine indeed the accuracy of the evaluation of the service that can be provided and thus, by extension, the revenues that can be expected. Techno-economic assessments are original in the sense that they identify the intimate cause–effect relationships between technical and economic aspects.

As seen previously, today's energy systems are becoming increasingly complex for the reasons that we recall hereafter:

- The change in paradigm of energy production and distribution from a centralized production to a diffuse production.
- The introduction of intermittent energy sources.
- The improvement of some technologies that link up energy vectors separated so far such as electricity, heat and gas.

These considerations modify the existing value chain of energy production, transmission and consumption and open new perspectives for services and products.

As seen in Sections 8.2.2.3 and 8.2.3.2, there are several applications in which electrolysers can play a role (frequency regulation, hydrogen production for industrial purposes, seasonal storage of renewable energy, etc.). Consequently, an electrolyser system operator may be remunerated for providing these different services. Furthermore, an electrolyser system can be integrated into a much more complex system, as illustrated in Figure 8.26, which can also provide other services (management of deferrable loads, electrical mobility, short-term electricity storage, etc.). However, the evaluation of the global benefit is not trivial as some of these services cannot be provided simultaneously but are neither completely exclusive.

In light of these elements, estimating expenses and revenues based on simple calculations is becoming more and more out of reach. The modelling and simulation of energy systems can then play an important role in assessing the economic viability of a given project by virtually putting into operating conditions the desired system.

8.6.1
Objectives of the Simulation

Simulation can be defined for economic assessment as the imitation of the operation of a real-world process or system over time [58]. In our context, it is the imitation of an energy system constituted of one or more electrolysers and operating

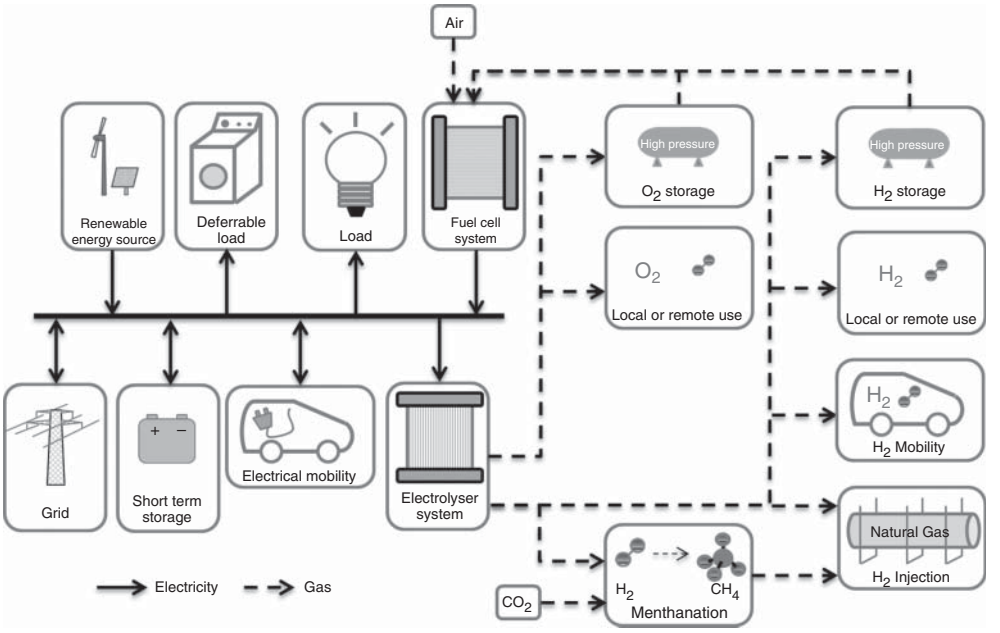

Figure 8.26 Example of energy system integrating electrolysis.

within a given environment. The simulation relies on the modelling of the complete system, which requires the different components (technologies) to be identified. Furthermore, the simulation must also consider the interactions between the system and its environment (meteorological conditions, local constraints, etc.). Finally, to perform this modelling, elements of the business model impacting the operation of our system must be determined and taken into account. Interests of running simulations are many; among them, we will focus on the following:

- Evaluation of the performances of a given component within a system.
- Sizing of components.
- Design and optimization of control strategies.
- Comparison of products and technologies.
- Comparison of business models.

A first need can be to evaluate the performances of a given component when integrated into a system. For example, we may want to investigate how a given PEM electrolyser system is handling the fluctuations of a PV production. Simulation can help determine if the dynamics of the electrolyser system and its main components is compatible with the dynamics of the energy source. Simulation also offers the possibility to observe how the component performances are maintained with time and how the operating conditions influence its lifetime (see Section 8.2.1).

For one or several system functions, choosing a suitable size for each of the constituting components can be a difficult task. It is important to limit the risk

of an inappropriate sizing to avoid undersizing, which may lead to the incapacity of furnishing a required service, or oversizing, which may lead to an inefficient operation. Multiplying simulations can help in testing several options in order to determine the optimal sizing.

The operation of an energy system is of main importance. It impacts indeed both expenses and revenues that can occur within the project lifetime. For example, the operation strategy, if unsuitable for a given application, can lead to premature ageing of a given component and thus to important replacement costs. The operation strategy also determines the revenues that can be generated as it impacts the quality of the supplied service. Consequently, there is a need to elaborate and test several control strategies in order to find the one maximizing the value created by the system at the least possible cost. In practice, the control strategy has the objective of answering questions such as the following:

- Which component do I use at which moment? For example, on an off-grid system comprising PV modules, batteries and a hydrogen chain, how to arbitrate between the recharge of the batteries and the production of hydrogen from electrolysis?
- How do I manage a set of similar components, and how do I optimize their operating point? For example, in an electrolyser system constituted of several stacks, how do I allocate a global available power between the different stacks?

Simulation allows comparing several optimized systems (sizing and operation) constituted of different components. It is then possible to compare several products within the same application (e.g. comparing PEM electrolysers from different suppliers for an application of frequency regulation). It is also possible to compare different technologies to determine the most suitable one for a given application (e.g. comparing a PEM electrolyser with an alkaline electrolyser for an off-grid application).

Finally, simulation can be of great help in testing different business models for which expenses and incomes would be hard to estimate otherwise. For example, a renewable electric energy producer may consider valorizing its production by injecting the energy produced into the grid. He may also consider investing in a decentralized electrolyser to produce hydrogen from the same renewable energy source, hydrogen, that he could valorize with local industrials. He could also benefit from a flexible electrolyser to furnish a frequency regulation service to the grid operator. All these business models can be evaluated through simulation and compared. It is also possible to use simulation to determine how to mix these different options with the hope of increasing the overall value by successively and intelligently alternating these sources of revenues.

8.6.2
Simulation's Main Input Data – Impact on the Robustness of the Results

A simulation consists in dividing a simulation horizon (1 day, 1 month, 1 year, etc.) into elementary portions of time (time step). The durations of the time steps may

be identical (fixed time step) or may vary in order to capture periods of time during which some system components may have a fast dynamic (variable time step). The simulation will then consist in evaluating the state of the system at each time step by evaluating the state of each component as well as the different energy and mass transfers between components. For an energy system integrating an electrolyser, it consists in evaluating at each moment quantities such as the power consumed by the stack, the power consumed by the system, the losses in the power converters, the flow rate of hydrogen produced, the pressure and temperature inside the stack, and so on. There are several elements, described in the following sections, that are required to perform a simulation and that can have a significant influence on the robustness of the results.

8.6.2.1 Components, Architectures and Component Models

As stated in Section 8.6.1, system's components must be identified according to the objective of the system. However, selecting components is not sufficient without specifying the architecture of the system. The architecture illustrates how components are linked together through electrical or fluidic connections. It requires determining the number and locations of power converters, compressors, pressure relief valves and so on.

Another important consideration is the way we represent the different components of the system. For a given component, a model will be required to represent its performances. Furthermore, for techno-economic analyses, an ageing model will also be required in order to assess how performances are maintained with time and to evaluate the impact of a given operation strategy on the component. To do so, simulations over long periods of time (several years) are required as a component's ageing may take several years before impacting the performances of the overall system. Consequently, among the different natures of performance models (2D/3D multi-physics, quasi-physics, empirical, learning), some are incompatible with techno-economic analyses in the sense that they would require too important computing times when performing simulations over several years. Techno-economic simulations favour 0D models, which are faster to compute such as quasi-physics or empirical models. The use of learning models (e.g. artificial neural network) is not very widespread in component modelling for techno-economic assessment. They are indeed suitable to phenomena where the links between inputs and outputs are not trivial. Usually, this is not the case with single components as their behaviour is well understood. Within quasi-physics and empirical models, there are several levels of modelling depending on the required amount of details or available information for a given component. As mentioned in Section 8.3.1, if one considers a PEM electrolyser system, it is constituted of one or several electrolyser stacks and their auxiliaries (water pump etc.). Figure 8.27 illustrates an example of different levels of performance modelling that could be suitable for a techno-economic analysis [59].

As shown in Figure 8.27, the most basic approach is to consider the different elements constituting the electrolyser system as a single element and to model its performances through a constant efficiency. The hydrogen mass flow rate ($Nm^3\ h^{-1}$)

Modeling details level and modeling approaches	Elementary objects modeled	Model inputs	Equations overview
High level			
U–I polarization curve	Electrolyzer cell Auxiliaries	• Cell *I–V* curve parameters • Number of cells • Auxiliaries consumption Parameters	$P_{Syst} = P_{Stack} + P_{Aux}$ $P_{stack} = Nb_{Cells} + P_{Cell}$ $P_{Cell} = V_{Cell} \times I_{Cell}$ $V_{Cell} = f_1(I_{Cell})$ $P_{Aux} = f_2(P_{Stack})$ $m_{H2} = f_4(I_{Stack})$ $I_{Stack} = f_3(I_{Cell})$
Polynomial efficiency	Electrolyzer system	• Polynomial coefficients	$\eta_{Syst} = \sum_{i=0}^{i=n} K_i \times P_{Syst}^{\,i}$ $\dot{m}_{H2} = f_5(\eta_{Syst}, P_{Syst})$
Constant efficiency	Electrolyzer system	• System efficiency	$\dot{m}_{H2} = f_6(\eta_{Syst}, P_{Syst})$
Low level			

Figure 8.27 Examples of different levels of performance models [59].

produced by the electrolyser depends only on the power consumed by the system and on this efficiency. The second approach, denoted 'polynomial efficiency', takes into account the fact that the power level at which the electrolyser system is solicited influences its efficiency. The efficiency of the system is thus evaluated for a given power level and the produced hydrogen mass flow rate is determined based on this computed efficiency. With this approach, the impact of auxiliaries at low duty (see Section 8.3.2.2) can be accounted for. Finally, the last approach consists in considering separately the different parts of the system and thus to model the stack independently of the auxiliaries. In this case, the stack performances model can, for example, be derived from a cell model, which could be represented by its polarization curve ($I-V$ curve). Properties at stack level (voltage, hydrogen flow rate) would be obtained by knowing the number of cells in the series that constitute the stack. This approach allows considering, for example, the starting and stopping phases of the auxiliaries. It is then possible to account for their specific power consumption and duration in order to determine when the stack is ready to produce. It is also possible with this approach to integrate the stand-by power consumption of the auxiliaries (when no hydrogen is produced) or the pressurizing phase of the stack, and so on.

It is important to understand from these explanations that models of components require parameters in order to fit the different models' laws on real data. For example, the $I-V$ curve of an electrolysis cell may be represented by a polynomial function, which would require the polynomial coefficients. A well-chosen set of parameters can then be representative of a given product from a given manufacturer. It is usually possible to test different products and/or manufacturers by using the same model but by adjusting the model parameters according to the

manufacturer's data sheets or experimental characterization results obtained on the equipment.

Ageing is also an important part of the full modelling of a component. As highlighted in [59], there are several ways to consider ageing for a given component as summarized in Table 8.5.

Table 8.5 Examples of modelling approaches for component ageing.

Ageing modelling approach	Description	Example
Absolute lifetime	A constant lifetime is attributed to the component independently of the operating conditions. Replacement of the component occurs when the lifetime has expired. Performances remain constant over time	An electrolyser system with a lifetime of 10 years
Relative lifetime	A relative lifetime is attributed to the component. This lifetime is expressed in operating hours. The component ages only if it is operating and it is replaced once the maximum number of operating hours has been reached. Performances remain constant over time	An electrolyser system with a lifetime of 10 000 h of operation
Absolute performance degradation	Absolute performance degradation rates are attributed to the component. The degradation directly impacts the performances of the system but does not depend on the operating conditions ('absolute'). A replacement criterion must be elaborated based on a 'non-acceptable' level of degradation to determine when the component has to be replaced. Performances and ageing models are not independent	An electrolyser system loses 2% of its initial efficiency every year
Relative performance degradation	Relative performance degradation rates are attributed to the component. They consist in degradation mechanisms that directly impact the performances of the system. The intensity of degradation is directly linked to the operation conditions of the component ('relative'). A replacement criterion must be elaborated based on a 'non-acceptable' level of degradation to determine when the component has to be replaced. Performances and ageing models are not independent	The voltage over the entire operation range of an electrolysis cell increases by 10 μV every hour of operation

Among the different approaches mentioned in Table 8.5, one can identify two families: lifetime and performance degradation. It is important to highlight that 'lifetime' approaches have an impact only on economic indicators of the system as performances remain constant during the simulation. Lifetime approaches determine the frequency at which a given component will have to be replaced in order to evaluate the total replacement costs. A proper evaluation of the total replacement costs improves the accuracy of the economic indicators, which are greatly regarded in an investment decision. On the other hand, 'performance degradation' approaches also impact technical indicators as performances change during the simulation. The simulation can then highlight how this degradation impacts the quality of the service that the component was entitled to provide. Considering ageing with such an approach will not only help in refining the estimation of the total expenses (through replacements costs) but it can also provide precise calculations of the potential revenues from the system as they are highly linked to the quality of the provided service (the service supplied at the beginning of a simulation can be different from the one supplied just before the replacement of the component).

The degree of performance modelling detail and the approach for consideration of ageing can drastically impact the economic evaluation. For example, Ref. [60] examines for a given application two different levels of modelling of a PEM electrolyser system and three approaches for considering its ageing. It is shown how the use of a too simplified model can lead to non-optimal electrolyser system sizing. It is also assessed how this non-optimal sizing impacts the economic evaluation and how it results in providing the decision maker with erroneous information regarding the profitability of a project.

8.6.2.2 **Control Strategies**

As stated before, control strategies play an essential role in the global performances of a given energy system. They derive from the business model(s) for which the system has been designed and they have for objective operating the system in order to satisfy the required services at the least possible cost. Consequently, they must make sure that the system will provide the required services in order to guarantee sufficient revenues for the system. Furthermore, at the same time, they must operate the components in such a way that it limits their ageing (increases lifetime) in order to avoid excessive replacement costs and limit global expenses. Impacts of control strategies on the profitability of a project can be very important, justifying the need for simulation to elaborate, test and compare several strategies. It is important to bear in mind that the final objective of a control strategy is to operate *in fine* a system in real time (e.g. an electrolyser system). Consequently, the control strategy must be designed by taking into account constraints of a real-time process. For example, if we consider an energy system comprising PV modules and a hydrogen chain (electrolyser, storage, fuel cell) designed for the power supply of an off-grid site, a PV production forecast system may not be available as system integrators usually want to keep the system as simple as possible to increase its

robustness. Consequently, in the design of the operating strategy, only the instantaneous PV production should be used as an input variable. Anticipating the PV production for the next hours to determine, for example, start-up and shutdown of the electrolyser would not be appropriate as it would not be representative of the situation once the system is installed on the field.

8.6.2.3 Simulation Temporal Characteristics

The temporal characteristics of the simulation come down to the choice of the time step (for fixed time step simulations) and the simulation horizon (start and stop dates). The possibilities are limited essentially due to computation time. For example, a simulation with a time step of 1 ms over 25 years will be hard to perform on a standard computer. However, depending on the dynamics of the system, the use of a too large time step may result in an important loss of information. This is particularly true for energy systems comprising intermittent energy production such as PV or wind. To illustrate this point, Figure 8.28 shows on two different days the solicitation profiles of an electrical energy storage device integrated in a PV storage grid system when simulated on two different time steps: 1 min and 1 h. We can see that for a highly fluctuating PV production (bottom figure), the balance of charging and discharging energies can largely depend on the time step used (1 min vs 1 h). Consequently, if an electrolyser system were used to produce hydrogen within this application (powered with the available 'charge' energy), performing a simulation on a 1 h time step would have led to an erroneous estimation of the total available energy and thus a wrong estimation of the amount of produced

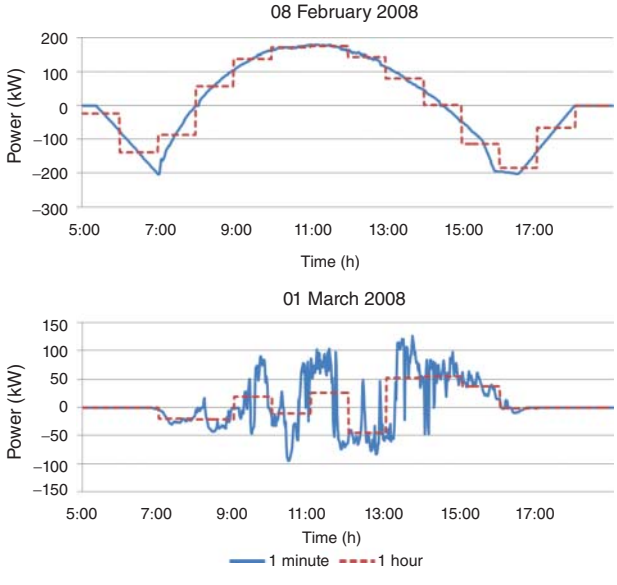

Energy (kWh)		
	Simulation time step	
	Minute	Hour
Charge	774	763 (−1%)
Discharge	627	616 (−2%)

Energy (kWh)		
	Simulation time step	
	Minute	Hour
Charge	252	191 (−24%)
Discharge	161	100 (−38%)

Figure 8.28 Illustration of the influence of simulation time step (top figure: PV profile with very few cloud covers, bottom figure: PV profile highly fluctuating).

hydrogen. Generally, when signals are highly fluctuating, they must be captured by small simulation time steps.

The simulation horizon may also have a great influence on the economic results for several reasons. Firstly, for energy systems comprising renewable sources, the seasonal effect is usually very pronounced, leading to the need to perform simulation at least over an entire year to capture the differences between seasons (change in wind speed, solar radiation, temperature, etc.). Furthermore, meteorological conditions may be very different from one year to the next. Consequently, a simulation over a single isolated year can lead to unrepresentative meteorological conditions in comparison to those seen by the system over a 20- or 25-year period. Secondly, considering ageing may show that simulations over several consecutive years are necessary to refine economic calculations. Economic indicators are indeed computed over a 20–25-year period (see Section 8.6.2.4) but are based on technical results obtained on the simulation horizon. When performance degradation is considered, extrapolation of the obtained degradation over 1 year must be performed to determine the frequency of replacement over the operating period of a given system component. However, degradation mechanisms often lead to non-linear performance losses resulting in erroneous extrapolations and derived replacement costs. These two points highlight the need to perform simulation over several years ideally taking into account contrasted meteorological conditions as highlighted in [60].

8.6.2.4 Simulation Results

There are several types of useful results that can be obtained from a simulation. We will distinguish techno-economic performance indicators that are related to the overall system and component-specific information.

Performance Indicators Performance indicators are usually of technical, economical or environmental nature. They illustrate how the energy system performs with a given set of components, architecture, models, control strategies and within a given environment (meteorological conditions, electricity prices, etc.). Economic indicators are usually computed over the operating time of the energy system (usually between 10 and 25 years), which may be different from the simulation horizon. Examples of technical and economic indicators are illustrated in Table 8.6.

Indicators are the quantities on which comparison between manufacturers, technologies, and control strategies can be performed. They are also used in optimization and sensitivity analyses to assess the impact of changes in component sizing, control strategies model parameters and so on on the system's technical and economic performances (see Section 8.6.3).

Component-Specific Information Other important results that can be obtained from simulations are results specific to a given component. These results have for main objectives to examine the way a given component is solicited within the system. They allow, for example, to identify the consequences of a given

Table 8.6 Examples of techno-economic indicators relevant for a hydrogen-based energy system.

Indicator	Nature	Description
Use rate of renewable energy (%)	Technical	This indicator illustrates the relative use by the system of a given renewable energy source in comparison to its maximum potential. Depending on operating conditions, the renewable production may be down-regulated leading to a non-complete use of its potential
Unmet hydrogen load – mass-based (%)	Technical	For a given hydrogen load profile (e.g. hydrogen consumption of an industrial process), the simulation can highlight that the defined system characteristics (component sizing, architecture, control strategies) do not allow a full satisfaction of the load. It is then possible to compute an indicator illustrating the relative amount of hydrogen not supplied in comparison to the overall demand
Levelized cost of hydrogen production (€ kg^{-1})	Economic	This indicator is computed from all expenses (investment, operations and maintenance, replacement) levelized over the plant operating time and from the levelized amount of hydrogen[a)] that is expected to be produced during the plant operating time. For an energy system with the objective of producing and selling hydrogen (e.g. wind electrolyser system), the levelized cost of hydrogen production is a pertinent indicator to determine the profitability of such a system. It can indeed directly be compared to assumptions on a hydrogen selling price in order to determine the viability of the project
Levelized payback time (years)	Economic	This indicator is very common in economics. It highlights the time required to see the levelized sum of all revenues exceeding the levelized sum of expenses

a) The levelized amount of produced hydrogen has no 'physical' meaning and is just a trick of arithmetic used to compute the levelized production cost.

solicitation regime on the component's ageing. Several types of information, essentially time series and statistical data, are usually derived from simulations.

Time series allow visualizing the evolution of the component's properties with time. For a PEM electrolyser system, it is interesting to observe the total power consumption and the mass flow rate of the produced hydrogen. If the modelling allows it, it can be worth observing also how the pressure is building up inside the stack to see, for example, in how much time the first molecules of hydrogen are available at the system outlet as a function of the input power profile.

Statistical information can be of great interest as well. For example, one can know the number of start/stop cycles of an electrolyser system that occurred during the simulation. It can also be useful to visualize a histogram of the power consumption of the electrolyser system to determine if it is underused or properly used in comparison to its maximum capacity.

8.6.3 Optimization and Sensitivity Analysis

Running a single isolated simulation allows assessing the system performances for a defined set of parameters. However, it is very often required to optimize part of the system or to assess the impact of parameter changes with regard to defined indicators.

8.6.3.1 Principles

Although objectives of optimization and sensitivity analysis are different (see Section 8.6.3.2), they rely on the same principles. The idea is to observe how modifications of model parameters (performances and ageing), component sizing and control strategies parameters impact the values of the different techno-economic indicators of the system. For example, if we consider a wind PEM electrolyser system in which the electrolyser stack is modelled at the cell level, simulating its behaviour will require several types of information:

- Polarization curve (performances).
- Cell active surface, number of cells (sizing).
- Maximum current density (control strategy).
- Cell cost.

Optimization and sensitivity analysis will consist in multiplying simulations in order to link these different parameters to indicators such as the levelized cost of hydrogen production (€ kg^{-1}) or the payback time (years).

8.6.3.2 Objectives

In techno-economic analysis, the main objective when performing optimizations is to determine the optimal sizing of the different components and to optimize the system control strategies. Consequently, parameters related to sizing and control strategies are then considered as optimization variables. Techno-economic indicators of the system are used to quantify the progress of the optimization process when sizing and strategy parameters evolve. Selected indicators are then considered as optimization criteria. Depending on the number of criteria, the optimization is qualified as mono-objective (one criterion) or multi-objective (several criteria). A mono-objective optimization leads to a single solution or multiple equivalent solutions with exactly the same criterion value. When several criteria are used, the solutions obtained belong to the Pareto front and an aggregation method is then required to finally select only one solution.

Sensitivity analyses are used to assess the robustness of the results obtained from a defined set of system parameters. They are usually performed on economic assumptions (investment, operations and maintenance (O&M) costs, replacement costs, discount rate, etc.) or on component performances and ageing (models parameters). Sensitivity analysis can be used to take into account uncertainties in order to have not just a single indicator value as an output but a range of possible values instead. They can also be used to identify and prioritize R&D efforts on components in order to determine, for example, if the focus should be on reducing costs, improving performances or increasing longevity.

8.6.3.3 Main Difficulty and Solutions Related to Simulation

Optimizations are often very time-consuming tasks that constitute a major difficulty. A first solution is to reduce the search space (e.g. reducing the minimum and maximum size to explore) or to increase the step between consecutive sizing. However, the risk with search space reduction is to miss the window of sizing in which the optimal solution actually is or to fall in a local optimum if the step between two consecutive sizes is too large. Furthermore, for multi-component systems, reducing the size of the search space may not be sufficient to reduce the computation time. In these situations, advanced optimization algorithms may be required like those belonging to heuristic and metaheuristic families such as genetic algorithms or particle swarm optimization. These techniques allow performing optimization without testing the entire search space, leading to an important reduction of the computation time and with solutions relatively close to the global optimum.

Sensitivity analyses usually assess the impact of one parameter at a time (the values of all other parameters being fixed). Computation time is in this particular case less problematic than for an optimization. However when multi-parameter sensitivity analyses are required, it may result in computation times similar to those observed in optimizations. This can occur, for example, when using Monte Carlo methods. They consist in designing functions (Gaussian, triangle, etc.) illustrating the probability of occurrence of the studied parameters and multiplying random sampling according to these functions to obtain different sets of parameters to be tested.

8.6.4 Example of Existing Software Products for Techno-Economic Assessments of Hydrogen-Based Systems

There are several commercial and academic software products dedicated to techno-economic assessments of hydrogen-based energy systems [61, 62]. Table 8.7 mentions some examples.

As highlighted in [59], software products can be distinguished based on several points:

Table 8.7 Example of software products for techno-economic assessments of hydrogen-based systems.

Software	Editor	Reference
HOMER 2	HOMER Energy, United States	[63]
iHOGA	Department of Electrical Engineering. University of Zaragoza, Spain	[64]
energyPRO	EMD International A/S, Denmark	[65]
ODYSSEY	New Energy Technologies and Nanomaterials Innovation Laboratory, Atomic and Alternative Energies Commission, France	[59]

- Level of details available for the component models (performances and ageing).
- Flexibility in the definition of the electrical and fluidic architectures.
- Available operation strategies.
- Business models that can be represented.
- Accessible simulation time step and simulation horizon.

As discussed previously, the level of details of the component models can have a great impact on the reliability of the techno-economic assessment. Too simplified models can indeed lead to non-representative behaviours in comparison to what could be observed in reality. Most software products choose to rely on simplified models in order to propose an exhaustive panel of technologies within their tools. Consequently, hydrogen technologies (electrolyser systems, fuel cell systems, hydrogen storages) are often modelled in an approximate way.

As stated in Section 8.4, electrical and fluidic architectures become increasingly complex. Choices of DC or AC buses, type of hydrogen storage and levels of pressure are important factors that still need to be assessed using simulation and flexible tools. Unfortunately, most tools offer limited possibilities in the architecture design (maximum two electric buses, one level of pressure, one type of storage, etc.), leading to unrepresentative modelled systems.

As mentioned in Section 8.6.2.2, control strategies are an essential part of the energy system as they determine the generated revenues and expenses. With the increasing complexity of energy systems, control strategies have to be increasingly elaborate and case-specific. Most tools available today rely on a limited choice of control strategies, and are often unable to handle the complexity of the system. Furthermore, these strategies are rarely parameterized, giving little room for the user to customize them.

The different economic valorizations of electrolysis detailed in Section 8.2.3 (hydrogen for industrial application, hydrogen for mobility, etc.) are often treated independently in available tools. They can thus hardly be used to design multi-service hydrogen-based energy systems and to elaborate and optimize suitable control strategies that represent complex business models.

Finally, simulation time step and simulation horizon are often fixed in these tools. They rely on a 1-year simulation at a time step of 1 h. As mentioned in Section 8.6.2.3, these limitations can have important impacts on computed economic indicators of hydrogen-based energy systems, particularly when a combination with intermittent renewable energies is considered.

All these limitations are regularly highlighted in publications where authors explain how they are constrained to develop their own simulation tool in order to assess the techno-economic performances of a given system. For example, in [59], the development of the ODYSSEY platform is justified by the need for a more open and polyvalent tool. Very often, a simulation environment such as Matlab® – Simulink® is preferred for its flexibility. The major drawback of such a generic environment is the time required to develop the component models, build the system and develop the surrounding code required to perform simulation, compute indicators, perform optimization and so on.

8.7 Conclusion

We have seen in this chapter that the particularities of renewable energy sources induce a need for grid energy storage. Among storage technology candidates, hydrogen production from electrolysis presents interesting features. It is indeed a technology suitable to renewable energy sources as it can adapt its power consumption to available input power. It also offers the advantage of being a fully scalable technology, allowing systems in the range of a few kilowatts to several tens of megawatts. Unlike most storage technologies (batteries, flywheels, etc.), electrolysis allows the separation of the charging power and the stored energy, which can be of great interest when designing a system with contrasted power and energy needs. Hydrogen itself presents several advantages. When produced by electrolysis from renewable energies, it can be considered as a low carbon footprint energy carrier. Furthermore, hydrogen as a product is also used in several industrial applications that grant electrolysis with multiple opportunities of valorization.

Historically, electrolysis systems have been designed to operate continuously at a constant power level to provide hydrogen to industrial applications. The connection to renewable energy sources, due to their intrinsic properties, is imposing drastically different operating modes on electrolysis systems. Intermittency, variability and voltage characteristics introduce increased complexity in electrolysis systems to allow frequent start – stop operation, dynamic behaviour and power adaptation. This complexity is often detrimental to system efficiency, especially at low power load. A few demonstration projects that have been running since the 1980s have highlighted difficulties in managing the intermittency at system design and operation levels. However, experimental feedback dedicated to intermittent operation from these demonstrations is still limited. Nevertheless, it has

appeared that control system remains a key component for such complex systems as it drastically impacts on efficiency. In addition, reliability and robustness of the system and of each individual component require to be improved, especially with regard to fluctuating operation. Further research needs to focus on the improvement of dynamic operation, system efficiency across the entire load curve, reliability of stack, power electronics, BoP and lifetime.

Apart from the limitations mentioned earlier, it seems that no absolute technology barriers impede the integration of electrolysis with renewable energy. Technical solutions already exist to allow dynamic operation of electrolysis systems and their connection to intermittent sources.

Existing and future applications of hydrogen presented in this chapter have highlighted the increasing complexity of electrolyser-based systems. New business models can indeed emerge multiplying the potential valorization of hydrogen. Consequently, the need for modelling and simulation becomes critical to properly assess the economic viability of each business case.

The storage functions in relation to renewable energies that can be fulfilled by electrolysis have very different characteristics (response time, flexibility, efficiency, etc.). Every storage function would require a specific design of the electrolyser system in order to optimize the overall techno-economic performances. However, as highlighted previously, a single electrolyser system can address several storage functions in combination with its first objective of producing hydrogen. Consequently, compromises on the system design must be found to fulfil the technical requirements without deteriorating the economics. In-depth performance modelling and simulation are then necessary to assess techno-economic performances of a given electrolyser system within a given application.

References

1. Kritharas, P.P. and Watson, S.J. (2010) A comparison of long-term wind speed forecasting models. *J. Sol. Energy Eng.*, **132**, 041008–041008.
2. Parks, K., Wan, Y.-H., Wiener, G., and Liu, Y. (2011) *Wind Energy Forecasting: A Collaboration of the National Center for Atmospheric Research (NCAR) and Xcel Energy*, National Renewable Energy Laboratory.
3. Muljadi, E. and Butterfield, C. (2000) *Pitch-Controlled Variable-Speed Wind Turbine Generation*, National Renewable Energy Laboratory.
4. Bayem, H., Capely, L., Dufourd, F., and Petit, M. (2009) Probabilistic study of the maximum penetration rate of renewable energy in an island network. PowerTech, 2009 IEEE Bucharest, pp. 1–5.
5. World Electric Power Plants Database (2011) Platts, a Division of the McGraw-Hill Companies.
6. Hadjsaid, N. (2010) *La distribution d'énergie électrique en présence de production décentralisée*, Edition Lavoisier.
7. Multon, B., Aubry, J., Haessig, P., and Ben Ahmed, H. (2013) *Systèmes de stockage d'énergie électrique*, Techniques de l'ingénieur.
8. ENEA Consulting (2013) Le stockage de l'énergie – Facts & Figures.
9. Delille, G., Francois, B., Malarange, G., and Fraisse, J.-L. (2009) Energy storage systems in distribution grids: new assets to upgrade distribution network abilities. 20th International Conference and Exhibition on Electricity Distribution – Part 1, 2009. CIRED 2009, pp. 1–4

10. Saupe, R. (1988) The power conditioning system for the energy storage plant of BEWAG. Third International Conference on Power Electronics and Variable-Speed Drives, pp. 218–220
11. SBC Energy Institute, Electricity Storage (2013) FactBook Series Leading the Energy Transition.
12. International Electrotechnical Commission (2011) Electrical Energy Storage – White Paper.
13. Eyer, J., Iannucci, J., and Corey, G. (2004) Energy Storage Benefits and Market Analysis Handbook – A Study for the DOE Energy Storage Systems Program.
14. GDF SUEZ (2013) The GRHYD Demonstration Project, *http://www.gdfsuez.com/en/gdf-suez-at-the-center-of-the-national-debate-on-energy-transition/power-to-gas-an-innovative-solution/the-grhyd-demonstration-project* (accessed 03 April 2014)
15. Carbon Counts Company (UK) Ltd (2010) CCS Roadmap for Industry: High-Purity CO2 Sources. Sectoral Assessment – Final Draft Report, 025 CCS Roadmap for Industry.
16. Fingersh, L.J. (2003) Optimized Hydrogen and Electricity Generation from Wind. NREL Technical Report NREL/TP-500-34364, National Renewable Energy Laboratory, pp. 1–12.
17. Little, M., Thomson, M., and Infield, D. (2007) Electrical integration of renewable energy into stand-alone power supplies incorporating hydrogen storage. *Int. J. Hydrogen Energy*, **32**, 1582–1588.
18. Ursúa, A., Marroyo, L., Gubía, E., Gandía, L.M., Diéguez, P.M., and Sanchis, P. (2009) Influence of the power supply on the energy efficiency of an alkaline water electrolyser. *Int. J. Hydrogen Energy*, **34**, 3221–3233.
19. Mazloomi, S.K. and Sulaiman, N. (2012) Influencing factors of water electrolysis electrical efficiency. *Renew. Sustain. Energy Rev.*, **16**, 4257–4263.
20. Ulleberg, Ø. (2003) Modeling of advanced alkaline electrolyzers: a system simulation approach. *Int. J. Hydrogen Energy*, **28**, 21–33.
21. Ursúa, A., San Martín, I., Barrios, E.L., and Sanchis, P. (2013) Stand-alone operation of an alkaline water electrolyser fed by wind and photovoltaic systems. *Int. J. Hydrogen Energy*, **38**, 14952–14967, *http://www.sciencedirect.com/science/article/pii/S0360319913023082* (accessed 18 October 2013).
22. Bergen, A., Pitt, L., Rowe, A., Wild, P., and Djilali, N. (2009) Transient electrolyser response in a renewable-regenerative energy system. *Int. J. Hydrogen Energy*, **34**, 64–70.
23. Stucki, S., Scherer, G.G., Schlagowski, S., and Fischer, E. (1998) PEM water electrolysers: evidence for membrane failure in 100 kW demonstration plants. *J. Appl. Electrochem.*, **28**, 1041–1049.
24. Millet, P., Ranjbari, A., de Guglielmo, F., Grigoriev, S.A., and Auprêtre, F. (2012) Cell failure mechanisms in PEM water electrolyzers. *Int. J. Hydrogen Energy*, **37**, 17478–17487.
25. Millet, P., Mbemba, N., Grigoriev, S.A., Fateev, V.N., Aukauloo, A., and Etiévant, C. (2011) Electrochemical performances of PEM water electrolysis cells and perspectives. *Int. J. Hydrogen Energy*, **36**, 4134–4142.
26. Millet, P., Grigoriev, S.A., and Porembskiy, V.I. (2013) Development and characterisation of a pressurized PEM bi-stack electrolyser. *Int. J. Energy Res.*, **37**, 449–456.
27. Petipas, F., Fu, Q., Brisse, A., and Bouallou, C. (2013) Transient operation of a solid oxide electrolysis cell. *Int. J. Hydrogen Energy*, **38**, 2957–2964.
28. Nakajo, A., Wuillemin, Z., Van herle, J., and Favrat, D. (2009) Simulation of thermal stresses in anode-supported solid oxide fuel cell stacks. Part II: loss of gas-tightness, electrical contact and thermal buckling. *J. Power. Sources*, **193**, 216–226.
29. Couturier, K., Chatroux, A., Donnier-Maréchal, T., Di Iorio, S., Brevet, A., and Lefebvre-Joud, F. (2014) Electrochemical performances of a Single Repeat unit (SRU) in steady-state and transient electrolysis operation at intermediate temperature. Proceedings of the 11th European SOFC and SOE

Forum, Lucerne, Switzerland, July 1–4, 2014.

30. Marini, S., Salv, P., Nelli, P., Pesenti, R., Villa, M., Berrettoni, M., Zangari, G., and Kiros, Y. (2012) Advanced alkaline water electrolysis. *Electrochim. Acta*, **82**, 384–391.
31. NREL (2010) Hydrogen and Fuel Cell Technical Highlights, Wind2H2 Project, *http://www.nrel.gov/hydrogen/pdfs/48435.pdf* (accessed 18 March 2014)
32. ITM Power (2012) (Hbox Solar, a Solar Powered Electrolyser, *http://www.itm-power.com/wp-content/uploads/2012/04/CaseStudy3-HBoxSolar.pdf* (accessed 18 March 2014).
33. Gahleitner, G. (2013) Hydrogen from renewable electricity: an international review of power-to-gas pilot plants for stationary applications. *Int. J. Hydrogen Energy*, **38**, 2039–2061.
34. Muyeen, S.M., Takahashi, R., and Tamura, J. (2011) Electrolyzer switching strategy for hydrogen generation from variable speed wind generator. *Electr. Power Syst. Res.*, **81**, 1171–1179.
35. Ziogou, C., Ipsakis, D., Seferlis, P., Bezergianni, S., Papadopoulou, S., and Voutetakis, S. (2013) Optimal production of renewable hydrogen based on an efficient energy management strategy. *Energy*, **55**, 58–67.
36. Ulleberg, Ø. (2004) The importance of control strategies in PV–hydrogen systems. *Sol. Energy*, **76**, 323–329.
37. Clarke, D.P., Al-Abdeli, Y.M., and Kothapalli, G. (2013) The impact of renewable energy intermittency on the operational characteristics of a stand-alone hydrogen generation system with on-site water production. *Int. J. Hydrogen Energy*, **38**, 12253–12265.
38. Agbossou, K., Kolhe, M., Hamelin, J., and Bose, T.K. (2004) Performance of a stand-alone renewable energy system based on energy storage as hydrogen. *IEEE Trans. Energy Convers.*, **19**, 633–640.
39. Yumurtaci, Z. (2004) Hydrogen production from excess power in small hydroelectric installations. *Int. J. Hydrogen Energy*, **29**, 687–693.
40. Yilmaz, C. and Kanoglu, M. (2014) Thermodynamic evaluation of geothermal energy powered hydrogen production by PEM water electrolysis, **69**, 592–602.
41. Menzl, F. (2004) Windmill, Electrolyser System for Hydrogen Production at Stralsund. IEA-Report, Germany, *http://ieahia.org/pdfs/stralsund.pdf* (accessed 31 March 2014)
42. Meurer, C., Barthels, H., Brocke, W.A., Emonts, B., and Groehn, H.G. (1999) PHOEBUS—an autonomous supply system with renewable energy: six years of operational experience and advanced concepts. *Solar Energy*, **67**, 131–138.
43. Ulleberg, Ø., Nakken, T., and Eté, A. (2010) The wind/hydrogen demonstration system at Utsira in Norway: evaluation of system performance using operational data and updated hydrogen energy system modeling tools. *Int. J. Hydrogen Energy*, **35**, 1841–1852.
44. Gazey, R., Salman, S.K., and Aklil-D'Halluin, D.D. (2006) A field application experience of integrating hydrogen technology with wind power in a remote island location. *J. Power. Sources*, **157**, 841–847.
45. McPhy Energy (2012) PUSHY Demonstration Project, McPhy website, *http://www.mcphy.com/fr/projets/projets-de-demonstration/pushy/* (accessed 31 March 2014).
46. Plateforme Myrte,Universita di Corsica *http://myrte.univ-corse.fr/downloads/* (accessed 31 March 2014).
47. Del Pilar Argumosa, M., Simonsen, B., and Schoenung, S. (2010) Evaluations of Hydrogen Demonstration Projects. Final Report for IEA, HIA Task 18 Subtask B. Madrid, 2010, *http://ieahia.org/pdfs/Task_18_Final_Report.pdf* (accessed 31 March 2014)
48. Sotavento (2008) Sotavento Project: System to Produce Hydrogen, *http://www.sotaventogalicia.com/en/technical-area/renewable-facilities/hydrogen-plant* (accessed 31 March 2014).
49. McPhy energy (2013) INGRID Demonstration Project, McPhy website, *http://www.mcphy.com/en/projects/demonstration-projects/ingrid/* (accessed 3 September 2014).

50. International Energy Agency (2013) Rural Electrification with PV Hybrid Systems – Overview and Recommendations for Further Deployment, IEA (International Energy Agency). Report IEA-PVPS T9-13:2013 *http://www.iea-pvps.org/index.php?id=1&eID=dam_frontend_push&docID=1590* (accessed 3 September 2014)
51. Nayar, C. (2012) Innovative remote micro-grid systems. *Int. J. Environ. Sustainability*, **1** (3), 53–65.
52. Brinkhaus, M., Jarosch, D., and Kapischke, J. (2011) All year power supply with off-grid photovoltaic system and clean seasonal power storage. *Solar Energy*, **85**, 2488–2496.
53. Li, C.-H., Zhu, X.-J., Cao, G.-Y., Sui, S., and Hu, M.-R. (2009) Dynamic modeling and sizing optimization of stand-alone photovoltaic power systems using hybrid energy storage technology. *Renew. Energy*, **34**, 815–826.
54. Castañeda, M., Cano, A., Jurado, F., Sánchez, H., and Fernández, L.M. (2013) Sizing optimization, dynamic modeling and energy management strategies of a stand-alone PV/hydrogen/battery-based hybrid system. *Int. J. Hydrogen Energy*, **38**, 3830–3845.
55. McKinsey & Company (2011) A Portfolio of Power-Trains for Europe: a Fact-Based Analysis.
56. Weisse, M. (2010) Project RH2-WKA – making wind energy a steady power source. Proceedings of the 18th World Hydrogen Energy Conference, Essen, Germany, May 16–21, 2010
57. (2011) Hydrogenics wraps up Ontario utility-scale grid stabilization trial. *Fuel Cells Bull.*, **2011**, 9 *http://www.sciencedirect.com/science/article/pii/S1464285911702218*.
58. Banks, J., Carson, J.S., Nelson, B.L., and Nicol, D.M. (2000) *Discrete-Event System Simulation*, Prentice Hall.
59. Guinot, B., Bultel, Y., Montignac, F., Riu, D., Pinton, E., and Noirot-Le Borgne, I. (2013) Economic impact of performances degradation on the competitiveness of energy storage technologies – Part 1: introduction to the simulation-optimization platform ODYSSEY and elements of validation on a PV-hydrogen hybrid system. *Int. J. Hydrogen Energy*, **38**, 15219–15232.
60. Guinot, B., Bultel, Y., Montignac, F., Riu, D., and Noirot-Le Borgne, I. (2013) Economic impact of performances degradation on the competitiveness of energy storage technologies – Part 2: application on an example of PV production guarantee. *Int. J. Hydrogen Energy*, **38**, 13702–13716.
61. US Department of Energy (2011) Building Energy Software Tools Directory, *http://apps1.eere.energy.gov/buildings/tools_directory* (accessed 04 April 2014)
62. Connolly, D., Lund, H., Mathiesen, B.V., and Leahy, M. (2010) A review of computer tools for analysing the integration of renewable energy into various energy systems. *Appl. Energy*, **87**, 1059–1082.
63. Homer Energy *http://www.homerenergy.com* (accessed 07 April 2014).
64. iHOGA *http://personal.unizar.es/rdufo/index.php?option=com_content&view=article&id=2&Itemid=104&lang=en* (accessed 07 April 2014).
65. energyPRO *http://www.emd.dk/energypro/frontpage* (accessed 07 April 2014).

9
Outlook and Summary

Agata Godula-Jopek and Pierre Millet

Owing to the international energy situation that is calling for novel energy carriers with low carbon footprints, a lot of research and development (R&D) is being conducted for the implementation of a so-called 'hydrogen economy', a societal organization in which hydrogen would replace natural hydrocarbon fuels. In view of this hydrogen economy, water electrolysis has been identified as a key technology for the production of hydrogen of electrolytic grade. Powered by renewable energy sources, it can indeed ensure a sustainable production of hydrogen from both environmental and energy independence viewpoints. Its high potential for transforming zero-carbon electricity sources into the supply of zero-carbon hydrogen and oxygen for miscellaneous end uses has attracted renewed attention over the last decades. Water electrolysis remains a fast-evolving field where massive R&D efforts are being made because much larger and more efficient systems are still needed for implementation at industrial scale.

This book offers a comprehensive review of the state of the art in the field, taking into consideration the main technologies and the different aspects of water electrolysis. It provides a detailed comparison of the existing technologies in terms of materials, manufacturing processes, performances, technology developments and cost. It includes state-of-the-art technologies, worldwide key players for small-, medium- and large-scale units as well as discussions on existing identified limitations and perspectives in view of future market applications.

Liquid water electrolysis can today be considered as a well-established technology. Alkaline water electrolysis has been used industrially for decades and proton exchange membrane (PEM) electrolysers have been available commercially for many years even though in limited sizes.

Alkaline water electrolysis could be classified as an 'old technology' as it was successfully demonstrated on industrial scale at the beginning of the twentieth century. The main advantage of alkaline water electrolysis lies in the fact that alkaline electrolysers can be made from abundant and inexpensive materials like iron or nickel steel. Alkaline water electrolysers are simple and robust. The technology has been used mostly for applications in the industry sector, in particular for hydrogen production for ammonia synthesis. Systems that can deliver up to several hundreds of Nm^3 H_2/h have been successfully developed and implemented

Hydrogen Production: by Electrolysis, First Edition. Edited by Agata Godula-Jopek.
© 2015 Wiley-VCH Verlag GmbH & Co. KGaA. Published 2015 by Wiley-VCH Verlag GmbH & Co. KGaA.

in different places throughout the world. The main advantages of this technology are (i) low cost; (ii) high reliability and durability and (iii) possibility to operate at elevated pressure. On the other hand, alkaline water electrolysers are not compact, they operate at moderate current density and they are not totally appropriate for operation using transient power sources. Despite its well-established maturity, alkaline technology is still the subject of R&D efforts. The last generation of alkaline water electrolysers is more efficient, more reliable and more capable of complying with the requirements set for applications in combination with fluctuating renewable energy sources.

PEM water electrolysis is an efficient, durable and very flexible technology that can sustain successive power on/off cycles, and which is therefore well-suited not only for water splitting using intermittent power sources, but also for the production of hydrogen from off-peak nuclear power electricity.

Compared to the alkaline process, PEM technology remains more expensive in terms of capital expenses. This is partly due to the use of more expensive cell materials such as polymer electrolyte and catalyst but also other internal cell components. The costs are also associated with the use of thin polymer membranes that introduce more severe tolerance constraints on cell component dimensions and require sophisticated manufacturing tools.

For applications in anaerobic environments, PEM offers several decisive advantages: (i) electrolysers are more compact, (ii) they are more efficient at high current density due to a simplified heat management, (iii) they are well adapted to operation with transient power loads, (iv) they are safer in operation as there is no need to use corrosive and leaking liquid electrolytes and last but not least (v) they offer the possibility to operate more safely under pressure for on-board storage or off-board removal of the hydrogen by-product. The latter has been successfully demonstrated on prototypes operating at pressures above 100 bar. This is an interesting feature as emerging markets for mobility and seasonal energy storage applications require compressed gas and therefore pressurized PEM water electrolysis offers some interesting additional perspectives in view of such applications. According to the authors, the potential of PEM water electrolysis is still not fully demonstrated. There are indications that future systems will operate at much higher current densities.

The efficiency of the electrolysis reaction is improved when the operating temperature is raised. Most of the systems are then designed to operate at an optimal temperature, which is often a compromise between technical feasibility, economics, performance and degradation rates. Alkaline electrolysers can usually operate at up to 120 °C and PEM electrolysers up to 80 °C. As PEM and alkaline electrolysis is an exothermic process, stacks require proper cooling infrastructure, which is usually designed to remove the excess heat generated at nominal power. When operated at partial power or when experiencing frequent start/stops, the system is not operated at optimal temperature, showing therefore reduced performances. Frequent start and stop also have a strong impact on efficiency. Every time the system is stopped, it must be depressurized (mostly due to safety reasons) and some of the hydrogen produced is lost, as it is vented

to the atmosphere. The amount of lost hydrogen is directly linked to the volume of the system mainly composed of stacks volume, piping, gas–liquid separators and purification system. Appropriate design and sizing of the components is then critical to limit vented hydrogen quantities. Furthermore, hydrogen storage is often necessary as production and usage of hydrogen do not usually occur simultaneously. For these reasons, the working pressure is of great importance for the efficiency of the overall system and it is usually accepted that pressurized electrolysis is preferable, even though it is more expensive to build. This is due to the fact that hydrogen has a very low volumetric mass density, and therefore its pressurization is difficult and energetically expensive.

A number of problems that occurred in relation with alkaline or PEM electrolysers were carefully investigated and assessed. Among the different difficulties that are repeatedly mentioned, the following can be highlighted:

- Stack degradation and membrane deterioration.
- Safety problems with the alkaline electrolytes due to leaks.
- Problems with intermittent and fluctuating power sources such as delayed reaction.
- Difficulties with starting the system after shutdown, especially during cold weather. This can be problematic as electrolysers directly connected to renewable sources may not be installed in a controlled-temperature room and may be frequently stopped when no power is available.
- Extensive maintenance due to insufficiently mature parts of the system in the conditions of operation.
- Freezing of the membranes in PEM during winter.
- Very rapid stack degradation in some cases and limited warranted lifetime by the supplier.

Although most of the problems seem easily preventable, they require technological improvements that may result in cost increase either at the energetic or economic level or both.

High-temperature steam electrolysis (HTSE) is much less mature than alkaline and PEM technologies; in fact, this technology is considered as relatively new. The developments on a system level have just started and thus further extensive R&D efforts are required for system integration. The HTSE market requires larger units and therefore the challenges associated with building and operating a complete system at such a scale are considered higher. For the time being, no commercial systems are available. It clearly appears that degradation rates are still a problem to be solved in order to reach long operation durations, above 25 000 h, which are targeted for HTSE. Operating temperature ranges of HTSE are also challenging, mainly due to the material limitations, as very high temperature can be detrimental in terms of durability. The main issue related to the variability of temperature is the induced mechanical stress for the electrolysis cells. The existence of three operating modes (endothermic, thermo-neutral and exothermic) combined with the power variability of the renewable source is a real challenge for HTSE. To avoid degradation and loss of efficiency, the electrolysis system must be operated close

to the thermo-neutral voltage value. To allow this, a restricted operating range and control strategy must be implemented at the system level. This has inevitably an impact on the system, design and efficiency. The main advantage of this technology lies in the fact that the dissociation of water steam consumes less electricity in comparison to liquid water. Furthermore, when the temperature increases, a part of the electrical energy needed to dissociate the water molecule can be replaced by the heat. Assuming that heat sources are available at low prices, the replacement of electricity demand by heat increases efficiencies and contributes to the decrease of the overall cost of hydrogen production.

The challenges related to the coupling of renewable sources with electrolyser systems are discussed and assessed in detail. A comprehensive review of the associated requirements and their impact on system design, power electronics and process control is presented, including an analysis of the impact of intermittency on electrolysis system performances and reliability in terms of produced hydrogen characteristics, efficiency and system lifetime.

It is highlighted that among different electricity storage technologies, the electrolytic way of producing hydrogen presents interesting features. It is a suitable technology for renewable energy sources as it can adapt its power consumption to available input power. It also offers the advantage of being a fully scalable technology, allowing systems operation in the range of a few kilowatts to several tenths of megawatts. Unlike most storage technologies, electrolysis allows the separation of the charging power and the stored energy, which can be of a great interest when designing a system with contrasted power and energy needs. Today, in most of the electrolysis systems, the balance of plant power consumption can be considered as almost constant on the whole operating range and is not dependent on the operating point. A qualitative comparison on the suitability of PEM, alkaline and HTSE for integration with renewable energy sources has been performed based on carefully chosen selected key criteria. The comparison led to a conclusion that today both alkaline and PEM electrolysis can be considered as suitable for integration with renewable energy. Even though maturity, cost and reliability remain favourable to alkaline technology, PEM electrolysis seems to have a slight advantage from a technical point of view in terms of performances and when integration with renewable energy is considered. However, very little experience is yet available to understand the real impact of intermittency on the performances and durability of each technology. Better configurations still need to be demonstrated and optimized operating strategies may show that alkaline technology remains as suited as PEM electrolysis for renewable source coupling. HTSE does not yet offer the same maturity; therefore there is no existing demonstration pilot plant connecting HTSE with renewable power. The main specificity of HTSE, which is the need for the heat source to vaporize water and potentially maintain the high operating temperature, for integration with power sources will especially be attractive when excess thermal energy is available. Authors expect that the anticipated larger reversibility of into solid oxide fuel cell (SOFC) mode may provide a competitive advantage to HTSE for renewable electricity storage when compared to conventional water electrolysis.

It is highlighted that there are several markets that can already be addressed by hydrogen production from electrolysis. All these identified markets rely on the hydrogen from the electrolysis process.

On the basis of the insight into production costs from electrolysis and the comparison with other technologies, it is observed that electrolysis becomes competitive with conventional production means like steam methane reforming in some situations. However, improvements on components and system costs, both for capital and operation, must be addressed to reinforce the competitiveness of electrolysis versus incumbent technologies. Furthermore, existing and future applications of hydrogen have highlighted the increasing complexity of electrolyser-based systems.

The following section provides detailed and comprehensive comparison of water electrolysis technologies, technology development status and main manufacturers, and last but not least, material and system roadmap specifications.

9.1 Comparison of Water Electrolysis Technologies

The main characteristics (in terms of cell materials, state-of-the-art performances, capacity and cost) of the three water electrolysis technologies under consideration in this book are compared in Table 9.1.

9.2 Technology Development Status and Main Manufacturers

9.2.1 Alkaline Water Electrolysis

A list of suppliers of commercial alkaline water electrolysers with the main characteristics of some of their products is provided in Table 9.2. Alkaline water electrolysis is a mature technology, used at industrial scale for the large-scale production of electrolytic hydrogen for application in the industry sector. From an economic viewpoint, this is the cheapest way to produce hydrogen of electrolytic grade. Cost (including capital and energy expenses) is in the 1200–1300 € kW^{-1} range with efforts towards 800 €kW^{-1}. Current alkaline electrolysis cells are designed for operation under stationary power conditions and close to nominal operating current density. They can hardly operate at very low current density and this technology exhibits limited flexibility for operation in load-following conditions as required by emerging markets in the energy sector.

Table 9.1 Comparison of main water electrolysis technologies.

	Alkaline [1]	PEM [2]	Solid oxide [3]
Technology status	Commercially mature technologies		R&D
Temperature operating range (°C)	Ambient to 120 [4]	Ambient to 90	700–1000
Electrolyte	25–30 wt% aqueous KOH	PFSA	$Y_2O_3-ZrO_2$, $Sc_2O_3-ZrO_2$, $MgO-ZrO_2$, $CaO-ZrO_2$
Charge carriers	OH^-	H_3O^+	O^{2-}
Cathode catalyst (HER)	Nickel foam/Ni–SS	Platinum	Ni–YSZ or Ni–GDC cermet
Cathode carrier	Nickel foam/Ni–SS $Ni-Mo/ZrO_2-TiO_2$	Carbon	
Anode catalyst (OER)	Ni_2CoO_4, $La-Sr-CoO_3$, Co_3O_4	Ir/Ru oxide [5]	$(La,Sr)MnO_3$, $(La,Sr)(Co,Fe)O_3$,
Anode carrier	No carrier	No carrier	Gd-doped ceria
Cell separator	Asbestos, PAM[a)], ZrO_2-PPS[b)], NiO, Sb_2O_5-PS[c)]	Electrolyte membrane	Electrolyte membrane
Cell sealant	Metallic	Synthetic rubber or fluoroeleastomer	Glass and vitro-ceramics
Current distributor	Ni	Titanium	Ferritic SS (Crofer APU)
Bipolar end plates	Ni	Titanium	Ferritic SS/Ni alloys
Max active surface (cm^2)	15 000–18 000	600–1000	200
Containment material	Nickel-plated steel	Stainless steel	Stainless steel
Pressure operating range (bar)	1–200	1–350 (700)	1–5
Conventional current density ($A\,cm^{-2}$)	0.2–0.5	0.8–2.5	1.0–2.0
Efficiency (%)	60–80	80 [6]	100 [7]
At i ($A\,cm^{-2}$)/U_{cell} (V)/T (°C)	0.2–0.5/2.0/80	1.0/1.8/90	3.6/1.48/950
Capacity ($Nm^3\,h^{-1}$)	1–700	1–100	1–10
Durability (h)	100 000	10 000–50 000	500–2000 [8]
H_2O specification	$\rho > 10$ MΩ cm	$\rho > 10$ MΩ cm	Steam
Load cycling	Medium	Good	No data available
Stop/go cycling	Weak	Good	Weak
Cost (€ kW^{-1})	1300 to 800	2000 to 1200	—

a) Polysulphone-bonded polyantimonic acid.
b) ZrO_2 on polyphenylsulphone (PPS).
c) Polysulphone impregnated with Sb_2O_5 polyoxide.
Source: Adapted from Ref. [9].
HER – Hydrogen Evolution Reaction; YSZ – yttria stabilized zyrkonia; GDC – gadolinia doped ceria; OER – Oxygen Evolution Reaction.

Table 9.2 Some manufacturers of alkaline electrolysers and system characteristics.

Manufacturer	Country	Product name	Capacity range (Nm^3/h)	Pressure (bar g)	Energy consumption ($kWh\ Nm^{-3}$) (ΔH efficiency (%))
IHT	CH		760	30	~4.6 (~65)
NEL Hydrogen	Norway		480	1	~4.5 (~70)
Wasserelektrolyse Hydrotechnik	Germany	EV150	225	1	~5.3 (~55)
Erredue s.r.l	Italy	G256	170	30	~5.3 (~55)
Hydrogenics	Can/EU	HyStat60	60	Oct-25	~5.2 (~60)
Mc Phy	France		60	10	~5.2 (~60)
Teledyne Energy	United States	SLM1000	56	10	N/A (N/A)

Table 9.3 Some manufacturers of PEM water electrolysers and system characteristics.

Manufacturer	Country	Product name	Capacity range ($Nm^3\ h^{-1}$)	Pressure (bar g)	Energy consumption ($kWh\ Nm^{-3}$) (ΔH efficiency (%))
Siemens	Germany	E60	60	30	~4.9 (~60)
Aréva H2Gen	France	E60	60	30	~4.9 (~60)
Proton on-site	United States	Hogen C30	30	30	~5.8 (~50)
ITM	United Kingdom	HPac 40	2.4	15	~4.8 (~60)

9.2.2 PEM Water Electrolysis

PEM can be considered as a commercially emerging technology. Due to its ability to operate at high current densities (in the multi $A\ cm^{-2}$ range), it has been used for decades for oxygen generation in anaerobic environments (underwater and space applications). Emerging markets in the energy sector are calling for more flexible water electrolysis technologies. PEM has strong flexibility aptitudes and most manufacturers of water electrolysis technologies are investing in the development of PEM systems at the MW scale, considering that only PEM will be able to address such markets. A list of some commercial suppliers, showing the level of maturity and main characteristics of their products is provided in Table 9.3. Efficiencies are not so different from those of alkaline water electrolysers but the operating current density is usually twice as high. In terms of cost, low-capacity systems (that deliver less than $100\ Nm^3\ h^{-1}$) are close to $2000\ €\ kW^{-1}$. R&D is now targeting the development of electrolysers at the MW scale, in the $1200-1400\ €\ kW^{-1}$ cost range. Target costs beyond 2020 are $700-800\ €\ kW^{-1}$.

Table 9.4 Some manufacturers of HTSE electrolysers and characteristics of systems under development.

Manufacturer	Country	Power range (kW)	Pressure (bar g)	Energy consumption (kWh Nm^{-3}) (ΔH efficiency (%))
Ceramatec	United States	20–100	10	~3.0 (~60)
SunFire	Germany	200	<30	~3.0 (~60)

9.2.3
Solid Oxide Water Electrolysis

HTSE is an even more recent technology, still under development and sometimes coupled with carbon dioxide reduction (for syngas production). From a technical viewpoint, its origin lies in solid oxide fuel cell technology, which operates at elevated temperature (initially 800–1000 °C, now 650–800 °C) using oxide–ion conducting ceramics as solid electrolyte. The main advantage of this technology is that water evaporation enthalpy can be achieved using waste heat from other industrial processes (e.g. from power-to-gas and power-to-liquid techniques). For the moment, HTSE technology is not considered as a flexible process, especially from the thermal viewpoint. There are few commercial initiatives, the technology still being in R&D phases. The main features of some commercial products under development at the horizon of 2016 are compiled in Table 9.4.

9.3
Material and System Roadmap Specifications

Water electrolysis technologies are the subject of massive R&D efforts aimed at increasing production capacity, improving performances and reducing production costs. These efforts cover material developments, cell design engineering and manufacturing process. Tentative roadmaps related to the improvement of existing materials and operating conditions are provided in Tables 9.5–9.7 for the three water electrolysis technologies under consideration (adapted from[9]). Increasing operating current density at constant levels of performances and durability is considered the best way to reduce capital expenses and reach the 800 € kW^{-1} target for large-scale implementation of low-temperature technologies (PEM and alkaline). Such goals will be difficult to reach if the operating temperature is not raised (150 °C seems a desirable target), a condition that is calling for innovative materials. Concerning HTSE, the approach is to reduce the operating temperature to better manage corrosion and thermal stability issues. Again, innovative materials are required. Higher operating pressure is another objective for hydrogen storage and transportation, in particular for application in the automotive industry.

Table 9.5 Alkaline water electrolysis specifications.

Property	State-of-the-art (2014)	Target 2020–2030	Ultimate goal
Operating current density ($A\,cm^{-2}$)	0.2–0.5	≈0.8	≈1.0–1.2
Operating temperature (°C)	Ambient to 120	Ambient to 150	Ambient to 150
Operating pressure (bars)	1–30	1–100	1–200
Durability (h)	10^5	$>10^5$	$>10^5$
Cyclability	Poor	Improved	High
Production capacity of electrolysis units ($kg\,h^{-1}$)	Up to 50 (≈500 $Nm^3\,h^{-1}$)	>100 (≈1000 $Nm^3\,h^{-1}$)	>1000 (≈10 000 $Nm^3\,h^{-1}$)
Cost (€ kW^{-1})	1300	1000	800

Table 9.6 PEM water electrolysis specifications.

Property	State-of-the-art (2014)	Target 2020–2030	Ultimate goal
Operating current density ($A\,cm^{-2}$)	0–2	0–2.5	0–5
Operating temperature (°C)	50–80	80–100	100–120
Operating pressure (bar)	1–50	1–350	1–700
Enthalpic efficiency with PGM catalysts	80% at 1 $A\,cm^{-2}$	80% at 2 $A\,cm^{-2}$	80% at 4 $A\,cm^{-2}$
Enthalpic efficiency with non-PGM cata (% at 1 $A\,cm^{-2}$)	30–40	60	60
SPE Voltage drop (mV at 1 $A\,cm^{-2}$)	150	100	70
Cathodic PGM (Pt) content ($mg\,cm^{-2}$)	1.0–0.5	0.5–0.05	<0.05
Anodic PGM (Ir, Ru) contents ($mg\,cm^{-2}$)	1.0–2.0	0.5–0.1	<0.1
Durability (h)	10^4	$10^4 - 5 \times 10^4$	$>10^5$
Production capacity of electrolysis units ($kg\,h^{-1}$)	1–10 (≈10–100 $Nm^3\,h^{-1}$)	>10 (>100 $Nm^3\,h^{-1}$)	>100 (≈1000 $Nm^3\,h^{-1}$)
Energy ($kWh\,kg^{-1}$ H_2 at 80 °C, 1 $A\,cm^{-2}$)	56	<50	48
Cost (€ kW^{-1})	2000	1300	800

Table 9.7 Solid oxide water electrolysis specifications.

Property	State-of-the-art	Target 2020–2030	Ultimate goal
Operating temperature (°C)	800–950	700–800	600–700
Operating pressure (bars)	1–5	1–30	1–100
Operating current density (A cm^{-2})	0–0.5	0–1	0–2
Area specific resistance (Ω cm^2)	0.3–0.6	0.2–0.3	—
Enthalpic efficiency	100% at 0.5 A cm^{-2}	100% at 1 A cm^{-2}	100% at 2 A cm^{-2}
Cell voltage degradation (at 1 A cm^{-2})	>10%/1000 h	<1%/1000 h	<0.1%/1000 h
Durability (h)	10^3	10^4	10^5
Electrical modulation	Unknown	0–100	0–100
Load cycles	Unknown	10 000	>10 000
Start-up time (h)	12	1–6	<1–6
Shutdown time	Few hours	Few minutes	Few minutes
Start-up/shutdown cycles	<10	100	1000
Production capacity (kg h^{-1})	<1 (≈10 Nm^3 h^{-1})	10 (≈100 Nm^3 h^{-1})	100 (≈1000 Nm^3 h^{-1})
Energy consumption (800 °C, 1 A cm^{-2})	To be determined	—	—

9.3.1
Alkaline Water Electrolysis

Alkaline water electrolysis is already a mature technology but there is still place for further improvements in order to satisfy the requirements of emerging energy markets. A tentative roadmap for technology improvement is provided in Table 9.5. Major research efforts concern the development of advanced diaphragms with adapted electrodes/catalysts and intermittent operation for the coupling with renewable electricity sources. Challenges concern the lifetime of systems and maintenance costs. An option of interest could be to use hydroxyl–ion conducting fluoro-polymers in place of liquid electrolytes to get closer to PEM technology.

9.3.2
PEM Water Electrolysis

PEM water electrolysis technology is considered to have a significantly large potential for improvement. Whereas commercial units are operating close to 1 A cm^{-2}, the technology is known to be capable of operation in the multi A cm^{-2}

range. To reach this goal at constant cell efficiency performances, it will probably be necessary to raise the operating temperature from 60–70 °C in state-of-the-art systems to the 120–150 °C range. But such an evolution will require the development of appropriate polymer electrolytes and catalyst structures that are not available yet. The development of such materials will require strong R&D commitment at public levels. A tentative roadmap for the improvement of PEM electrolysers is provided in Table 9.6.

9.3.3
Solid Oxide Water Electrolysis

Material science is at the heart of future developments of HTSE for higher durability. Whereas low-temperature water electrolysis technologies are considered as promising for decentralized and flexible applications, HTSE that requires high-temperature heat (available in nuclear or solar power plants) could lend some complementary characteristics to low-temperature sister technologies. A tentative roadmap for the improvement of HTSE electrolysers is provided in Table 9.7.

References

1. Stolten, D. and Krieg, D. (2010) Alkaline electrolysis: introduction and overview, in *Hydrogen and Fuel Cells, Fundamentals, Technologies and Applications*, Wiley-VCH Verlag GmbH, Weinheim.
2. Millet, P., Durand, R., and Pineri, M. (1989) New solid polymer electrolyte composites for water electrolysis. *J. Appl. Electrochem.*, **19**, 162–166.
3. Zahid, M., Schefold, J., and Brisse, A. (2010) *Hydrogen and Fuel Cells, Fundamentals, Technologies and Applications*, Wiley-VCH Verlag GmbH, Weinheim, pp. 227–242.
4. Vandenborre, H., Leysen, R., Nackaerts, H., Van der Eecken, D., Van Asbroeck, P., Smets, W., and Piepers, J. (1985) Advanced alkaline water electrolysis using inorganic membrane electrolyte (I.M.E.) technology. *Int. J. Hydrogen Energy*, **10** (11), 719–726.
5. Marshall, A., Børresen, B., Hagen, G., Tsypkin, M., and Tunold, R. (2009) Hydrogen production by advanced proton exchange membrane (PEM) water electrolyzers-Reduced energy consumption by improved electrocatalysis. *Int. J. Hydrogen Energy*, **34**, 4974–4982.
6. Millet, P., Ngameni, R., Grigoriev, S.A., Mbemba, N., Brisset, F., Ranjbari, A., and Etiévant, C. (2010) *Int. J. Hydrogen Energy*, **35**, 5043–5052.
7. Jensen, S.H., Larsen, P.H., and Mogensen, M. (2007) Hydrogen and synthetic fuel production from renewable energy sources. *Int. J. Hydrogen Energy*, **32**, 3253–3257.
8. Lefebvre-Joud, F., Petitjean, M., Ouweltjes, J.-P., Brisse, A., Schefold, J., Bowen, J.R., Ebbesen, S. D., Ehora, G., Bernuy-Lopez, C., and J.-U. Nielsen (2010) High temperature steam electrolysis performance and durability in the RelHy project. Proceeding of the 9th European Solid Oxide Fuel Cell Forum, Lucerne, Switzerland, June 29–July 2, 2010.
9. Cerri, I., Lefebvre-Joud, F., Holtappels, P., Honegger, K., Stubos, T., and Millet, P. (2012) Scientific Assessment in support of the Materials Roadmap enabling Low Carbon Energy Technologies: Hydrogen and Fuel Cells. JRC Scientific and Technical Reports, EUR 25293 EN–2012, JRC 69375

Index

a

AC/DC converter efficiency, PEM electrolyser 330
activation overpotentials 243
ADEL project 362
Al doped graphene, adsorption sites on 293, 294
alkaline water electrolysers 15
– advantages of 383, 384
– characteristics of 57
– manufacturers and development status of 387, 389
– problems in 385
alkaline water electrolysis 383
– advantage of 121, 144, 145
– Avalence Hydrofiller 160, 161
– bipolar cells, disadvantages of 122
– characteristics of 387, 388
– diaphragm/separator, 128 *see* diaphragm/separator
– disadvantages 144, 145
– economic advantage of 118
– efficiency ϵ 138, 139
– electrical energy consumption vs. hydrogen capacity 140
– electrodes and catalysts, 124 *see* electrodes and catalysts
– electrolyte 123
– Fick's laws 123
– filter press cells 121
– gas diffusion electrodes 159
– Glomfjord electrolysis plants 118
– Gramme machine 117
– hydrogen compressors 143
– hydrogen-oxygen gas 123
– industrial synthesis of 117
– ionic conductivity 142
– kinetics 142
– large scale electrolysers market 148, 151
– limitation of 123
– medium scale electrolysers market 147
– metallic foams electrode 156, 158
– Norsk Hydro electrolyser 150, 154, 156
– Oerlikon electrolyser 150, 153
– OH^- ions 121
– polarization curves 137
– pressurized electrolysers 144, 146
– Schmidt bipolar electrolyser 118, 120
– small scale electrolyser market 147
– specifications of 391, 392
– tank cell 121
– thermodynamics 140, 141
– Zdansky/Lonza electrolyser 150, 155
Alset Technology LLC 5
anaerobic environments 64
anodic catalytic layer 69
apparent tortuosity factor 232
automotive applications
– cryo-compressed hydrogen storage tank systems 286
autonomous applications, 351 *see* off-grid applications
autothermal reforming 14

b

biomass feedstock 17
BMW cryo-compressed storage tank 284, 285
boil-off rate, of hydrogen 278
bottleneck phenomenon 229
Butler-Volmer 52
Butler-Volmer equation 172
Butler-Volmer relation 219

Hydrogen Production: by Electrolysis, First Edition. Edited by Agata Godula-Jopek.
© 2015 Wiley-VCH Verlag GmbH & Co. KGaA. Published 2015 by Wiley-VCH Verlag GmbH & Co. KGaA.

c

carbon capture and storage (CCS) 119
carbon monoxide (CO) 13
catalytic layers 65
cell polarization curve, SOEC
– cell voltage 198, 199
Chapman-Enskogg model 241
Claude process 278
Co-electrolysis 261
Collins process 278
composite storage cylinders 283
compressed hydrogen, 281 *see also* cryo-compressed hydrogen
– adiabatic compression 281, 282
– cost and performance comparison 305
– isothermal compression 281, 282
– storage systems 282, 283
– volumetric density of 281, 282
concentration overpotentials 243
constrictivity parameter 229
contact resistances at interfaces 200
coordination frameworks, 295 *see* metal organic frameworks (MOFs)
coordination network materials, 295 *see* metal organic frameworks (MOFs)
coordination polymers, 295 *see* metal organic frameworks (MOFs)
cost effective gaseous hydrogen storage 274
covalent organic frameworks 297
Crofer(®) 22 APU 196
cryo-compressed hydrogen
– cost and performance comparison 305
cryo-compressed hydrogen storage tank systems 286
cyanobacteria 19
cyclic voltammetry (CV) measurement 80, 82, 83

d

degradation process 93
diaphragm/separator
– anionic membranes 132, 135
– heterogeneous membranes 133, 134
– ionic conductor 129
– ionomer membranes 135
– IPN 133
– OH^-- membranes 132
– oxide-ceramic materials 130
– polysulfone network 130
– s-PEEK separators 131
– zero-gap assembly 132
discharging power 326
distribution networks
– increasing power injection on 315
durability, of HTSE 249–251

e

electrochemical impedance spectroscopy (EIS) characterization 84–87
electrochemical reaction rates, microstructural impact on 233, 235
electrode supported cell
– schematic representation of 193
electrodes and catalysts
– fluorescence-based screening method 125, 126
– hydrogen evolution reaction 127
– Ni–MoOx composite coating 128
– nickel-iron alloy 124
– oxygen evolution reaction 124
– Raney nickel electrodes 127, 128
electrolysers, characteristics of 303
electrolysis
– balanceofplant 328
– efficiency 337–341
– HTSE, 343 *see also* high temperature steam electrolysis (HTSE)
– hydrogen production
– – pressure 336
– – purity 337
– – safety 337
– – temperature 335, 336
– integration with renewable energy
– – components for 351, 352
– – grid connected applications, 356 *see* grid connected applications
– – off-grid applications, 351 *see* off-grid applications
– intermittency effect 327
– – battery protection 349
– – downstream elements 334
– – dynamic constraints 332, 333
– – electrolyser protection 349
– – fuel cell protection 349
– – hydrogen production 349
– – maximum efficiency 349
– – operating strategies 347, 348
– – power demand satisfaction 349
– – power electronics and process control 329–332
– – reliability and durability 341–343
– – system design 345–347
– – technology selection 349–351
– stack and control system 328
– techno-economic assessment 362–364, 376–378

electrolyte supported cells (ESCs) 183
– schematic representation of 193
endothermic operating mode 344
enthalpies of adsorption/desorption, storage materials 290
enthalpy formation 40
entropy formation 40
equilibrium constant 171
ethylene tetrafluoroethylene (ETFE) 130
exothermic operating mode 344

f

Faraday efficiency 51, 52, 340
Faraday law 121
Fuel Cell Electric Vehicles, FCEV 9
fermentative bacteria 19
ferritic stainless steels 196
Fick's law 122
Fick's model 217
fluid constriction effect 230
fluorescence-based screening method 125
fossil fuels 11
Fuller model 241

g

galvanic chain 46
gas concentration field, by FEM simulation 231
gas diffusion layer (GDL) 85, 159, 175, 178
gas transfer phenomena, in SOEC electrode 215, 217
gaseous hydrogen 41, 72
gaseous oxygen 72
gasification technology 16
Gen-3 cryo-compressed H2 storage systems 287
geometrical tortuosity factor 229, 230
German aerospace center 20
Gibbs free energy change (ΔG_b) 33, 36, 51, 168, 169
glass-ceramic sealants 197
Gramme machine 117
Grand Canonical Monte Carlo (GCMC) simulation
graphene
– density functional theory 293, 294
– maximum gravimetric density 293
– thermally exfoliated graphene 294
gravimetric hydrogen density, of hydrides 288, 289
green algae 18, 19
grid assisted hydrogen generation 356
grid connected applications
– electrolysis for renewable energy storage 357, 358
integrated energy system 358–360
– renewable hydrogen production 356, 357
grid independent hydrogen production 353
grid independent integrated renewable source-hydrogen system 354

h

H_2 oxidation mechanism, on Ni-YSZ cathode 222, 223
half cell reaction mechanism
– in acidic media 52, 53, 55
– in alkaline media 56, 57
Hbox solar 346
Henry's law 88
high cell polarization 236
high temperature
– cyclability/durability 186
– HTSE cell 184
– performances and efficiency 186
– pressure 187
– principles of 182
– solid oxide fuel cell 184
– structure of 182, 183
high temperature steam electrolyser
– SRU 191, 192
high temperature steam electrolysis (HTSE)
– advantage of 191
– challenges of 385
– Co-electrolysis 261
– degradation issues 254
– – during cycling operation 256
– – microstructural analyses 256
– – during steady state operation 254–256
– durability of 249–251
– integration with renewable source 361, 362
– manufacturers and development status of 390
– operating temperature range of 191
– performances of 244–249
– pressurized operation mode 259, 260
– reversible operation mode 260, 261
– specifications of 392, 393
– specificity of 386
– stack electrochemical and thermal management of 252–254
– system integration and economic considerations 257–259
– tests for 244
homogenization techniques 230
HTSE, 385 *see* High temperature steam electrolysis (HTSE)

HyCube 304
hydride destabilization 290
hydrogen
– application of 2
– biomass and biomass-derived fuels 16, 18, 19
– cost reduction 8
– electrolysis 14–16
– energy source 1
– future 6
– gasification technology 16
– and methanol 3
– physical properties of 1
– primary energy demand 9–11
– reforming processes 13, 14
– renewable and non-renewable energy sources 11
– storage systems 6
– transport sector 6, 9
– water splitting processes 18, 20, 21
hydrogen compressors 143
hydrogen economy 383
hydrogen evolution reaction (HER) 52–54, 68, 76, 124, 127, 173
hydrogen gas aerostat 2
hydrogen insertion reaction (HIR) mechanism 53
hydrogen oxidation reaction (HOR) 55
hydrogen storage 385
– for automotive applications 273
– compressed hydrogen 281–283
– constraints and challenges of 273
– covalent organic frameworks, 297 *see* covalent organic frameworks (COFs)
– cryo-compressed hydrogen 284–287
– at geological sites 274
– in graphene 293–295
– liquid hydrogen, 276 *see* liquid hydrogen
– metal organic frameworks, 295 *see* metal organic frameworks (MOFs)
– methods and phenomena of 273
– performance of 276
– porous materials
– – absolute and excess storage capacity 291
– – activated carbon 292, 293
– – adsorption process 291
– – binding energy 291
– – Langmuir type 291
– – multi-walled carbon nanotubes 292
– – physisorption mechanism 290
– – at room temperatures 291
– – single-walled carbon nanotubes 292
– renewable energy sources, 312 *see* renewable energies (RE)
– solid state, 286 *see* solid state hydrogen storage
– vehicular systems, status of 275
hydroxyl ions (OH^-) 121

i
INGRID 2012-2016 303
interconnects 195
internal combustion engines (ICE) 11
interpenetrating polymer networks (IPN) 133
intrinsic Knudsen diffusivity, microstructural impact on 232, 233
ionic resistance 177
iridium 76

j
Joule-Thomson expansion process 278
Joule–Thomson cycle 278

k
Kelvin temperature 140
Knudsen number 216
Knudsen transport, in SOEC electrode 216
Krasil'shchikov mechanism 87

l
light duty vehicles, H2 storage systems for 288
Linde cycle 278
Linde hydrogen refueling station 279, 281
Linde mobile refueling storage 280
Linde mobile refueling unit 280
liquefaction process 278
liquid hydrogen (LH_2)
– cost and performance comparison 305
– critical parameters of 276
– hydrogen loss, minimization of 278
– storage systems 279–281
liquid water electrolysis 383
low cell polarization 237
low density polyethylene (LDPE) 135
low temperature PEM URFCs
– cost issues 181
– cyclability/durability 181
– fuel cell mode 177, 178
– performances and efficiency 181
– polarization curves of 179
– pressure 181
– principles of 174, 175
– structure of 175
– water electrolysis mode 176, 177

m

M factor 229
magnesium hydride (MgH_2) 301
magnetocaloric effect (MCE) 278
McPhy French company
– high density system 302
– high energy system 302
– magnesium hydride disk 302
membrane – electrodes assembly (MEA) 67, 93, 97, 98, 135
– catalytic layers, structure of 71
– coating processes 69
– electrocatalyst 68, 69
metal organic frameworks (MOFs) 295, 297
metal supported cell (MSC) schematic representation of, 193
metallic interconnects 196
methanol 13
minimum ignition energy (MIE) 3
mixed ionic and electronic conduction (MIEC)
– advantage of 224
– elementary reactive pathway 224–226
– gas transfer in anode porosity 227
– oxygen atoms and holes transfer 227
– surface reactions, repartition of 228
mixed manganese – cobalt oxide compound, benefit of 196
modern liquid hydrogen storage cylindrical tank 279
modified Claude cycle, 278 *see* Collins process
molecular adsorption, of hydrogen 291
molecular diffusion, in SOEC electrode 215, 216
multi-component gas transport, in SOEC electrode 217–219

n

Nafion membranes 65, 66
Nafion-like solid polymer electrolytes 71
nickel/yttria-stabilized-zirconia (Ni/YSZ) cermets, for hydrogen electrode 195

o

O_2 production mechanism, on LSM-YSZ electrode 220–222
off-grid applications
– renewable hydrogen production 352, 353
– stand-alone power system 353–355
ohmic losses, SOEC 199, 200
ohmic polarizations 243
ohmic resistances 72, 76, 87
operational expenses (opex) 35, 64
ortho- and para- form, of hydrogen 276, 277
oxidative methanol reforming (OMR) 14
oxygen evolution reaction (OER) 53—55, 124, 173
oxyhydrogen flame 324

p

partial oxidation 14
peak production shaving storage function 320, 321
PEM water electrolysers
– manufacturers and development status of 389
PEM water electrolysis
– advantages of 384
– vs. alkaline process 384
– characteristics of 387, 388
– problems in 385
– specifications of 392
performance, of HTSE 244–249
photosynthetic bacteria 19
photovoltaic (PV) production, of 80Wp module 312, 313
PHS technology, 319 *see* pumped hydro storage (PHS) technology
Platforma Solar de Almeria 20
platinum group metals (PGM) 181
polybenzimidazole (PBI) materials 109
polymer electrolyte membrane (PEM) cells
– bipolar plates 74
– chemical/faradaic efficiency 88
– current – gas distributors 72, 73
– EIS characterization 84–87
– electrode/electrolyte characteristics 78
– full-cell characterization 82
– gas cross-permeation model
– – features of 90
– – low current densities 91
– – mole number of hydrogen 91
– – silica/zirconium oxide 92
– gas permeability 89, 90
– half-cell characterization 80, 82
– Henry's law 88
– MEA, 67 *see* membrane electrodes assembly (MEA)
– optimal operation 79
– perfluorosulfonated materials 87
– polarization curves 76, 77
– spacers 74, 75
polymer electrolyte membrane fuel cell (PEMFC) 2
polymer electrolyte membrane (PEM) water electrolysis 63
– advantages 64, 105
– autonomous systems 102
– challenging issue 106

polymer electrolyte membrane (PEM) water electrolysis (*contd.*)
– cost analysis 100, 102
– current densities 110
– de-ionized process 100
– diagnosis tools and maintenance 97, 98
– homogeneous distribution 96
– iridium replacement 108
– limitations 105
– markets and applications 104, 105
– monopolar design 94
– platinum replacement 107
– polymer-based sealants 96
– pressures measurement 110, 111
– process flow-sheet of 100
– SPE cell 63, 65
– specifications 106
– stack performances 96
– and system characteristics 103
– temperature operation, polymeric proton conductors for 109
polynomial efficiency 369
polypropylene (PP) 130
poly(tetrafluoroethylene) (PTFE) 89, 92
porous coordination network (PCN-19) 295
power to liquids 324
powerplant cooling system 148
pressurized operation mode, of HTSE 259, 260
production guarantee storage function 320, 322
production shifting storage function 320, 322
production smoothing storage function 320, 321
pumped hydro storage (PHS) technology 319

r
RELHY project 362
renewable energies (RE)
– hydrogen 323
– – characteristic factors 326
– – electricity production 326, 327
– – electrolysis usage 323, 324
– – uses of 324–326
– impacts on electrical networks 312
– – forecast limitations 312–314
– – increasing penetration 316–318
– – intermittency 312–314
– – non-dispatchable power sources 314–316
– – production and consumption imbalance 314, 315
– – structure, schematic illustration of 315, 316
– storage on electrical networks
– – characteristics 318, 319
– – on grids 320, 322, 323
– – lead-acid batteries 319
– – lithium based batteries 320
– – PHS technology 319
– – in West Berlin 319
reversible operation mode, of HTSE 260, 261

s
Scandia-stabilized zirconia 194
simulation
– component specific information 373, 375
– components, ageing modelling approach for 370, 371
– control strategies 371, 372
– definition of 365
– economic assessment 365
– objectives of 365–367
– optimisation and sensitivity analysis 375, 376
– performance indicators 373
– performance modelling levels 368, 369
– temporal characteristics 372, 373
Single Repeat Unit (SRU)
– schematic representation of 191, 192
software products, for techno-economic assessments 376–378
solid oxide electrolysis cell (SOEC)
– anode and cathode polarization 206, 208
– – activation overpotentials 205–207
– – concentration overpotentials 204, 205, 208
– – electrode irreversible overpotential 203, 204
– – local and resulting electrode potential 200, 201
– – Ohmic overpotentials 207
– – reversible potential 201–203
– cathode supported cell 193
– cell polarization curve 198
– ceramic layers and electrodes in 191
– contact resistances at interfaces 200
– electrochemical impedance spectroscopy 257
– electrode microstructure 228
– – electrical conductivities 228–232
– – electrochemical reaction rates 233, 235
– – gas diffusivities 228–232
– – intrinsic Knudsen diffusivity 232, 233
– – of ionic conducting phase 228
– – parameters of LSM-YSZ and LSCF cathodes 235
– – parameters of Ni-YSZ cathodes 234, 235

– electrode slice for local approach 209, 210
– electronic and ionic conductivity, of electrode 214, 215
– electronic flow into electrode current collector and functional layer 209
– gas transfer phenomena 215, 217
– glass and glass ceramic sealants 197
– ionic flow into functional layer 211, 212
– levelized hydrogen vs. electricity cost 259
– LSM-YSZ anode, O_2 production on 220–222
– MIEC, 224 *see* mixed ionic and electronic conduction (MIEC)
– multi-component gas transport 217–219
– Ni-YSZ cathode, H_2 oxidation on 222, 223
– Ohmic losses 199
– overpotential η 197
– reaction mechanisms 219
– role of temperature
– – electrolyser temperature 237–239
– – endothermic and exothermic modes of operation 236, 237
– – on cell performance 241, 242
– – on elementary reactions 239, 240
– – on gas transport 241
– – on global electrochemical process 240, 241
– – on 8YSZ electrolyte conductivity 239
– source terms *j(z)* distribution of, 213, 214
– steam electrolysis 236
solid oxide fuel cells (SOFCs) 182, 184, 192
– anode supported cell 193
– electrolyte supported cell 193
– metal supported cell 194
solid oxide water electrolysis
– characteristics of 387, 388
– manufacturers and development status of 390
– specifications of 392, 393
solid polymer electrolyte (SPE) 174
solid polymer electrolyte (SPE) cell 63, 65
– durability issues 92, 93
– Henry's law 88
– monopolar design 94
– poly(tetrafluoroethylene) 89, 92
– structure of 89
solid state hydrogen storage
– chemical storage 288, 297–301
– coupled with electrolyser 301–304
– merits of 288
– physical storage 289–297
stack electrochemical and thermal management, of HTSE 252–254
stacks degradation mechanisms 341–343
stand alone power systems (SAPS) 4
steam electrolysis, on Ni-YSZ cermet 223
steam methane reformers (SMR) 102
steam reforming 14
Stefan-Maxwell model 218
Stoichiometric fraction 1
strontium-doped lanthanum manganite, for oxygen electrode 195
sulfonated poly-ether-ether-ketone (s-PEEK) 131
super grid 317
system failure 341–343

t

TEG, 294 *see* thermally exfoliated graphene (TEG)
thermally exfoliated graphene (TEG) 294, 295
thermo-neutral condition 237
thermochemical water splitting cycles 20
thermodynamics 140, 141, 168, 169, 171, 172
– endergonic transformation 36
– Gibbs free energy change 36
– operating temperatures 35
– state function changes 34
– water dissociation voltage
– – pH dependence of 37, 38
– – pressure dependence of 41–44, 46
– – temperature dependence of 39, 41
thermoneutral operating mode 344
transistor-based (TrPC) power converters 331
transmission system operators (TSO) 316
triple phase boundary lengths (TPBls) 200, 201

u

underground hydrogen storage 274
unitized regenerative fuel cell (URFC) 191
– Butler-Volmer equation 172
– definition 167
– high temperature, 182 *see* high temperature
– low temperature PEM, 174 *see* low temperature PEM URFCs
– polarization curves 172
– redox couples 171
– thermodynamics 168, 169, 171, 172
US DOE
– objectives of 274, 275

v

viscous flow, in SOEC electrode 216
volumetric hydrogen density, of hydrides 288, 289

w
water electrolysis system, schematic representation of 328
water splitting reaction
– energy degradation 48
– energy efficiency of 50, 51
– Faradaic efficiency of 51, 52
– gap cell 47
– half cell reaction mechanism 52, 53, 55–57
– operating pressure 56, 58
– operating temperature 56
– polarization curve measurement 48, 50
– SPE cell 47, 48
– thermodynamics, 33 *see* Thermodynamics
– zero-gap cell 47

x
X-ray nano-holotomography 257

y
yttria-stabilized zirconia 194

z
Zirfon® Perl separators 130